A NOVEL MEASUREMENT SETUP FOR IMPEDANCE-BASED ANALYSIS OF 3D TISSUE MODELS: DESIGN, CHARACTERIZATION AND APPLICATION



DISSERTATION

zur Erlangung des
DOKTORGRADES DER NATURWISSENSCHAFTEN (Dr. rer. nat.)
der Fakultät für Chemie und Pharmazie
der Universität Regensburg

vorgelegt von
Simone Bäumler (geb. Ruckdäschel)
aus Weiden i. d. Opf.
im Jahr **2024**

Promotionsgesuch eingereicht am: 12. September 2024

Promotionskolloquium: 17. Dezember 2024

Diese Arbeit wurde angeleitet von: Prof. Dr. Joachim Wegener

Prüfungsausschuss:

Vorsitzender: Prof. Dr. Ursula Storch

Erstgutachter: Prof. Dr. Joachim Wegener

Zweitgutachter: Prof. Dr. Achim Göpferich

Drittprüfer: Apl. Prof. Dr. Rainer Müller

MEINER FAMILIE.



If You Always Do What You´ve Always Done,

You´ll Always Get What You´ve Always Got.

Henry Ford (1863–1947)

CONTENTS

1 INTRODUCTION 1

1.1 2D AND 3D TISSUE MODELS 3

1.2 SPHEROIDS AS 3D TISSUE MODELS 7

1.2.1 3D TISSUE MODELS IN GENERAL 7

1.2.2 FORMATION TECHNIQUES OF SPHEROIDS 10

1.2.3 MICROENVIRONMENT OF SPHEROIDS 15

1.2.4 APPLICATION STRATEGIES OF SPHEROIDS 18

1.3 TECHNIQUES FOR 3D TISSUE MODEL ANALYSIS 21

1.3.1 OVERVIEW OF DIFFERENT TECHNICAL APPROACHES 21

1.3.2 OVERVIEW OF IMPEDANCE-BASED APPROACHES 24

2 OBJECTIVES 33

3 THEORETICAL BACKGROUND 37

3.1 ELECTROCHEMICAL IMPEDANCE SPECTROSCOPY 39

3.1.1 PHYSICAL BACKGROUND 39

3.1.2 DATA ACQUISITION, REPRESENTATION, AND PROCESSING 42

3.1.3 IMPEDANCE ELEMENTS IN EQUIVALENT CIRCUITS 43

3.1.4 EQUIVALENT CIRCUIT MODELS 46

3.2 ELECTRICAL PROPERTIES OF TISSUE MODELS 49

3.2.1 EQUIVALENT CIRCUIT MODEL FOR SPHEROIDS 49

3.2.2 DERIVATION OF THE TRANSFER FUNCTION 51

3.2.3 SIMULATED SPECTRA OF SPHEROID PARAMETERS 52

3.3 ELECTRIC CELL-SUBSTRATE IMPEDANCE SENSING 55

3.3.1 BASIC PRINCIPLES OF ECIS™ MEASUREMENTS 55

3.3.2 EQUIVALENT CIRCUIT MODEL OF CELL MONOLAYERS 57

4 MATERIALS AND METHODS 59

4.1 CELL CULTURE TECHNIQUES 61

4.1.1 CELL LINES 61

4.1.2 GENERAL CULTURE CONDITIONS 61

4.1.3 SUBCULTIVATION 62

4.1.4 CRYOPRESERVATION 63

4.1.5 FORMATION OF SPHEROIDS 64

4.1.6 GROWTH STUDIES OF SPHEROIDS 64

4.1.7 PREPARATION OF BUFFERS AND SOLUTIONS 66

4.1.8 CELL VIABILITY ASSAY FOR 2D AND 3D TISSUE MODELS 68

4.2 MICROSCOPIC TECHNIQUES 70

4.2.1 MICROSCOPES 70

4.2.2 TIME-LAPSE MICROSCOPY 72

4.2.3 CYTOCHEMICAL STAINING 75

4.3 IMPEDANCE ANALYSIS: MEASUREMENT MODES AND DEVICES 77

4.3.1 IMPEDANCE MEASUREMENT MODES 77

4.3.2 FLOW CHANNEL-BASED MEASUREMENT SETUP 79

4.3.3 FUNNEL-BASED MEASUREMENT SETUP 79

4.3.4 ECIS™-BASED MEASUREMENT SETUP 83

4.3.5 IMPEDIMETRIC MODEL STUDIES 85

5 SETUP DEVELOPMENT AND CHARACTERIZATION 87

5.1 THE MEASUREMENT SETUP 89

5.1.1 MEASUREMENT PRINCIPLE 89
5.1.2 FREQUENCY DEPENDENT IMPEDANCE 91
5.1.3 PARASITIC IMPEDANCE CONTRIBUTION 99
5.2 EVOLUTION OF THE FUNNEL DESIGN 102
5.2.1 VARIATION OF THE FUNNEL HOLE DIAMETER 103
5.2.2 VARIATION OF THE FUNNEL APERTURE LENGTH AND INLET ZONE 108
5.2.3 MATERIALS FOR THE FUNNEL FABRICATION 109
5.2.4 DETERMINATION OF THE FUNNEL FLOW BEHAVIOR 112
5.3 DISCUSSION: COMPARISON TO ALTERNATIVE SYSTEMS 114
5.4 SUMMARY AND OUTLOOK 116
6 CHARACTERISTICS OF MCF-7 AND U-373 MG SPHEROIDS 119
6.1 SPHEROID FORMATION 121
6.2 SPHEROID GROWTH KINETICS 123
6.2.1 SPHEROIDS FORMED WITH DIFFERENT CELL NUMBERS 124
6.2.2 SPHEROIDS EXPOSED TO DIFFERENT SERUM CONCENTRATIONS 129
6.2.3 SPHEROIDS EXPOSED TO DIFFERENT PH VALUES 131
6.3 SPHEROID ADHESION 134
6.4 DISCUSSION 137
6.4.1 COMPARISON OF SPHEROID FORMATION 137
6.4.2 COMPARISON OF GROWTH KINETICS 139
6.4.3 COMPARISON OF SIZE DISTRIBUTION 142
6.4.4 COMPARISON OF MICROENVIRONMENTAL CHANGES 144
6.4.5 COMPARISON OF ADHESION KINETICS 146
6.5 SUMMARY AND OUTLOOK 148

7 MODEL STUDIES WITH MCF-7 AND U-373 MG TISSUE MODELS 153

7.1 MODEL STUDY: THE NOVEL MEASUREMENT SETUP 155

7.1.1 INFLUENCE OF SPHEROID SIZE ON THE IMPEDANCE SIGNAL 155

7.1.2 INFLUENCE OF AGE ON THE SPHEROID CELL DYNAMIC 158

7.1.3 INFLUENCE OF PH ON THE SPHEROID CELL DYNAMIC 161

7.1.4 DISCUSSION: INFLUENCE OF TISSUE MODEL CONDITIONS 163

7.1.5 SUMMARY OF IDEAL TISSUE MODEL CONDITIONS 170

7.2 MODEL STUDY: CELLULAR RESPONSE TO PERMEABILIZATION 172

7.2.1 VIABILITY ANALYSIS OF THE SPHEROID AND CELL MONOLAYER 172

7.2.2 IMPEDIMETRIC ANALYSIS OF THE CELL MONOLAYER 174

7.2.3 IMPEDIMETRIC ANALYSIS OF THE SPHEROID DURING FIXATION 176

7.2.4 IMPEDIMETRIC ANALYSIS OF THE SPHEROID DURING PERMEABILIZATION 180

7.2.5 TIME-LAPSE MICROSCOPY ANALYSIS OF THE SPHEROID 185

7.2.6 DISCUSSION: INFLUENCE OF FIXATION 188

7.2.7 DISCUSSION: INFLUENCE OF PERMEABILIZATION 194

7.2.8 SUMMARY OF THE MODEL STUDY OF PERMEABILIZATION 205

7.3 MODEL STUDY: CELLULAR RESPONSE TO ACTIN CYTOSKELETON DEGRADATION 212

7.3.1 VIABILITY ANALYSIS OF THE SPHEROID 212

7.3.2 IMPEDIMETRIC ANALYSIS OF THE CELL MONOLAYER 213

7.3.3 IMPEDIMETRIC ANALYSIS OF THE SPHEROID 216

7.3.4 TIME-LAPSE MICROSCOPY ANALYSIS OF THE SPHEROID 217

7.3.5 DISCUSSION: INFLUENCE OF ACTIN CYTOSKELETON DEGRADATION 220

7.3.6 SUMMARY OF THE MODEL STUDY OF ACTIN CYTOSKELETON DEGRADATION 229

7.4 MODEL STUDY: CELLULAR RESPONSE TO OSMOTIC PRESSURE 233
7.4.1 IMPEDIMETRIC ANALYSIS OF THE CELL MONOLAYER 233
7.4.2 IMPEDIMETRIC ANALYSIS OF THE SPHEROID 236
7.4.3 TIME-LAPSE MICROSCOPY ANALYSIS OF THE SPHEROID 240
7.4.4 DISCUSSION: INFLUENCE OF OSMOTIC PRESSURE 243
7.4.5 SUMMARY OF THE MODEL STUDY OF OSMOTIC PRESSURE 261
7.5 SUMMARY 270
7.6 OUTLOOK 275
8 SUMMARY 277
9 ZUSAMMENFASSUNG 281
10 REFERENCES 285
11 APPENDIX 303
11.1 SUPPLEMENTARY INFORMATION 304
11.2 LIST OF ABBREVIATIONS AND SYMBOLS 321
11.3 MATERIALS AND INSTRUMENTATIONS 324
DANKSAGUNG 329
CURRICULUM VITAE 331
EIDESSTATTLICHE ERKLÄRUNG 333

CHAPTER 1

INTRODUCTION

1.1 2D AND 3D TISSUE MODELS 3

1.2 SPHEROIDS AS 3D TISSUE MODELS 7

1.3 TECHNIQUES FOR 3D TISSUE MODEL ANALYSIS 21

The application of cell culture as an *in vitro* tool is widely used to enhance the understanding of cell biology, tissue morphology and engineering, disease mechanisms, and pharmaceutical drug activity. For the simulation of the *in vivo* physiological microenvironment, various tissue models of cultivating cells in the form of a cellular monolayer or a three-dimensional system have been investigated in recent years. In contrast to the two-dimensional model, three-dimensional cell culture allows cells to grow in all directions, e.g. within an artificial scaffold, and thereby create their own microenvironment. In this way, it was shown that 3D tissue models are more physiologically relevant to represent native systems. Since these models exhibit an intermediate level of complexity, they bridge the gap between traditional cell culture and animal models (Pampaloni et al., 2007). This thesis focuses on the application of multicellular spheroids as 3D tissue models, which comprise spherical cell aggregates formed by a few hundred to several thousand cells. The spheroids can be derived from various cell lines using different standardized protocols and commercially available growth substrates. In general, these tissue models are applied in various fields of research, for example in medicine, fundamental research, and application-orientated approaches such as in drug screening. Various analytical techniques have been developed for monitoring and studying cellular responses within multicellular spheroids. In this thesis, special emphasis is placed on devices that have been investigated in recent years based on electrochemical impedance spectroscopy, which is a label-free, non-invasive technique that enables continuous monitoring.

In the following, an overview of spheroids as 3D tissue models, a comparison to 2D cell cultures, and a review of the analytical techniques and different measurement setups are provided.

1.1 2D AND 3D TISSUE MODELS

To study the mechanisms underlying the formation, function, and pathology of tissues and organs, two model systems mimicking human tissues are applicable: the *in vivo* whole-animal systems and the *in vitro* cell culture systems (Fig. 1.1; Yamada and Cukierman, 2007).

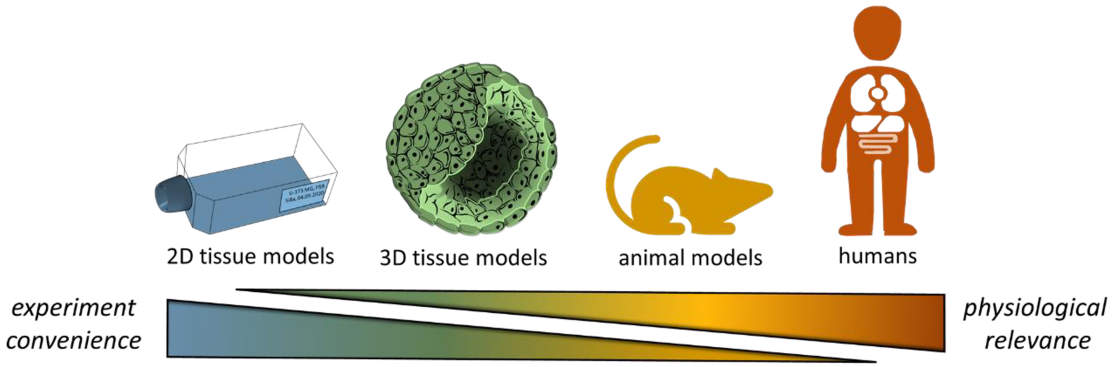

Fig. 1.1 Illustration* of model systems mimicking human tissues, ordered by physiological relevance and experimental convenience.

*illustration is simplified and not to scale
(adapted from Lee et al., 2023)

Animal experiments are mainly used in preclinical drug testing, but their application is strictly regulated. Based on the book "The Principles of Humane Experimental Technique" published in 1959 by British scientists William Russell and Rex Burch, the *3R principle* was established (Russel and Burch, 1959). The 3R principle aims to avoid the use of animals (replacement) or reduce the number of animals (reduction) and their suffering in experiments to the absolute minimum (refinement; https://bf3R.de). This principle was later implemented in the European Directive 2010/63/EU on the protection of animals used for scientific purposes and in German law in 2013 with the amended Animal Welfare Act (*Tierschutzgesetz*) and the Ordinance on the Protection of Laboratory Animals (*Tierschutz-Versuchstierverordnung*). To follow this principle, the reduction and replacement of animals in experimental systems can be achieved using cell culture-based testing. Whereas animal models are highly complex, the most commonly used 2D cell monolayer cultures exhibit low complexity and less similarity to real tissues (Antoni et al., 2015; Souza et al., 2016). Therefore, many advances have been made to mimic the *in vivo* environment in *in vitro* systems. In this way, novel approaches such as the use of stem cell assays, organ-on-a-chip systems, and *in silico* models have been investigated. Additionally, another recent approach is the use of 3D tissue models, which this thesis focuses on, that represent an intermediate level of complexity that bridges the gap between traditional cell culture and animal models (Pampaloni et al., 2007).

Both approaches, namely the 2D and 3D tissue models, represent different properties of cell physiology and morphology, providing distinct advantages and disadvantages, as summarized based on the reviews of Kapałczyńska et al. (2018) and Lee et al. (2023) in Tab. 1.1.

Tab. 1.1 Overview of different properties of cell physiology and morphology in 2D and 3D tissue models following the reviews of Kapałczyńska et al. (2018) and Lee et al. (2023).

technique	**2D tissue models**	**3D tissue models**
time of tissue formation	within a few minutes to a few hours (short time)	within a few hours to a few days (long time)
culture quality	high reproducibility, simplicity of culture, easy results interpretation	poor reproducibility, difficulty of culture, challenging results interpretation
in vivo imitation	limited imitation of the natural structure of the tissue or tumor mass *in vivo*	extensive imitation of the natural structure of the tissue or tumor mass *in vivo*
cellular characteristics	no *in vivo*-like microenvironment	*in vivo*-like microenvironment, diverse phenotype and polarity
access to essential compounds	variable access to oxygen, nutrients, metabolites, and signaling molecules in dependence on the cultivation conditions	variable access to oxygen, nutrients, metabolites, and signaling molecules in dependence on the 3D tissue morphology
molecular mechanism	altered gene expression, cell topology, and biochemistry	preserved gene expression, cell topology, and biochemistry
drug sensitivity	homogeneous exposition and sensitive response	inhomogeneous exposition based on drug diffusion within the tissue model, multicellular resistance, low drug efficacy
costs of culture maintenance	inexpensive, commercially available assays and supplies	expensive, time-consuming, fewer commercially available assays

With the use of the conventional two-dimensional cell cultures, a monolayer of adherent cells is generated on a flat glass or plastic surface forming a homogenous cell environment within a few hours. This culture model provides a simple and cost-effective method of performing high throughput screenings based on commercially available, well-known assays. Due to their simplicity, the 2D tissue models offer high reproducibility and easy interpretation of the cellular responses obtained, providing

a useful tool in basic research and drug discovery to obtain insights into tissue function and mechanistic processes within the cell layer (Hickman et al., 2014). However, this model is not able to reflect *in vivo* tissue characteristics since the cells grown in monolayer culture exhibit altered cell interactions or gene expression in comparison to real tissues (Yamada and Cukierman, 2007). For instance, cell differentiation can be largely suppressed in cell monolayer culture, as demonstrated by fibroblasts grown on a flat surface forming stress fibers and becoming immotile, whereas the cells display an actin cortex and extended filopodia and resemble the *in vivo* situation when cultured in 3D (Walpita and Hay, 2002).

The cultivation of cells as 3D tissue models provides another dimension of cellular interactions and thus more closely mimics the native structure combined with the *in vivo* microenvironment. However, this feature results in increased complexity of 3D tissue models, which is associated with difficult and time-consuming culturing methods (as described in chapter 1.2.2), extended cultivation periods, and reduced reproducibility of the models generated compared to 2D tissue models (Hickman et al., 2014). Thus, the cell behavior differs in many aspects depending on the type of culture chosen.

As reported in the literature, significant differences in cell proliferation rate, gene expression, and chemotherapeutic resistance have been investigated between the two culture models based on the cultivation of the identical cell line as a 2D or 3D tissue model, respectively. In several cell lines, a significantly lower cell proliferation rate was observed in 3D tissue models compared to 2D cell cultures which may be due to the fact that cells in 2D cultures receive the same, homogeneous amount of nutrients and growth factors from the culture medium. In addition, flat adherent monolayers allow necrotic cells to detach while providing space for proliferating cells (Edmondson et al., 2014). In contrast, in 3D tissue models, cellular detachment of internally located cells is not feasible, while the lack of access to essential compounds with limited diffusion into each layer results in a microenvironment that reflects multiple stages of proliferating, quiescent, apoptotic, hypoxic, and necrotic cells (as described in chapter 1.2.3; Khaitan, 2006). The limited diffusion of nutrients or metabolites into or out of the three-dimensional structure also affects the stimulation of cells by exposure to, for example, chemotherapeutic agents. Since the availability of cells to cytotoxic compounds varies in both 2D and 3D tissue models, the cellular response is determined by the cellular architecture. As cells grown in 2D culture receive a homogeneous amount of chemotherapeutic drugs across the monolayer, the cellular response may lead to incorrect test results in drug discovery due to the unnatural microenvironment (Desoize and Jardillier, 2000). In contrast, a 3D tissue model contains cells at different stages of the cell cycle to a greater extent than 2D tissue models and therefore tends to be less affected by the same compound concentration (Edmondson et al., 2014). For instance, Souza

et al. reported that the prostate cancer cell lines they tested were more sensitive to paclitaxel treatment and more resistant in 3D cell culture (Souza et al., 2018), while similar tendencies were observed in breast cancer tissue models (Imamura et al., 2015). The phenomenon of multicellular resistance in 3D tissue models is attributed to several factors, as described in chapter 1.2.3, and may also be caused by general changes in gene expression levels. Recent studies have confirmed that cells may display different gene expression profiles depending on the cell culture system. For example, Bogheart et al. compared the transcriptional profiles of two lung carcinoma cell lines and reported that the results obtained in 3D culture were more similar to real tissue samples compared to 2D culture when taking additional characteristics such as cell confluence, diameter, and volume into account (Bogheart et al., 2018). Consistent with this, Li et al. also observed enhanced resistance to drug-induced apoptosis in human hepatoma HepG2 spheroids, resulting from higher levels of cell-cell adhesion and a greater proportion of cells in G1 phase cell cycle arrest, in addition to elevated levels of E-cadherin, cytochrome c, and other proteins (Li et al., 2008). Thus, the up- and downregulation of specific gene patterns may be directly related to the rate of proliferation and the cellular response to cytotoxic compounds.

As a result, both 2D and 3D tissue models represent different characteristics of cell physiology and morphology, providing distinct advantages and disadvantages in research. While cell monolayer culture is a useful tool in basic applications due to its simplicity, three-dimensional culture systems were shown to mimic real tissue systems more effectively based on their intermediate complexity compared to 2D cell monolayers. Consequently, extensive effort is currently devoted to developing more advanced methods for studying 3D tissue models to improve tumor modeling, cancer treatment therapies, and disease testing methodologies.

1.2 SPHEROIDS AS 3D TISSUE MODELS

In recent years, three-dimensional tissue models have emerged as a useful tool in biomedical studies and drug screening. As a result, a variety of different model types have been investigated based on their origin or structural concept, making the application of 3D tissue models a versatile field of research in which multicellular spheroids serve as cellular aggregates, which can be generated from many different types of cell lines by applying various formation techniques. Based on the spherical architecture, spheroids represent their own microenvironment characterized by distinct cellular properties and are thus effectively applied as models for real tissues and microtumors *in vitro*.

1.2.1 3D TISSUE MODELS IN GENERAL

A 3D tissue model is an artificially created culture system in which cells can grow in all dimensions and interact with the surrounding environment. This allows for the spatial organization of cells similar to native models by providing cell-cell and cell-matrix interactions, tissue-specific stiffness, oxygen, nutrient, and metabolic waste gradients, and a combination of tissue-specific scaffolding cells (Griffith and Swartz, 2006). The 3D tissue models represent a specific microenvironment in which cells proliferate, aggregate, and differentiate, making the culture system suitable for improving the prognostic ability of *in vitro* test systems by presenting realistic tissues outside the body.

In general, 3D tissue models provide a variety of advantages as outlined in the overview (Tab. 1.2; Antoni et al., 2015; Yamada and Cukierman, 2007). Based on their specific microenvironment and cell physiology, the models have been shown to mimic real tissue systems more accurately in comparison to conventional two-dimensional cell cultures. In addition to representing cell-cell and cell-extracellular interactions in combination with native characteristics such as morphology or cell differentiation, 3D tissue models serve to reduce and refine animal testing in various research areas. As a result, the field of 3D culture has grown exponentially in recent years and promises broad applications in drug development and toxicity testing for a wide range of diseases, from cancer to neurological disorders (Langhans, 2018). Despite their numerous advantages, the limitations of these tissue models also have to be considered regarding the lack of vascularization and regulation of molecule transport inside the models and, for instance, their implementation for high-throughput screening or difficulties in image analysis and visualization (Tab. 1.2; Antoni et al., 2015; Yamada and Cukierman, 2007). Therefore, various improvements in new culture platforms and imaging systems, e.g. using light-sheet microscopy, need to be investigated to overcome these key challenges.

Tab. 1.2 Overview of the advantages and limitations of 3D tissue models in general (Antoni et al., 2015; Yamada and Cukierman, 2007).

advantages of 3D tissue models
❖ improved physiology and more accurate representation of the *in vivo* scenario compared to routine 2D cell culture
❖ reflection of tumor viability, morphology, proliferation, and cell differentiation *in vitro*
❖ cell-cell and cell-extracellular matrix interaction and signaling
❖ reduction/refinement of animal testing
❖ enhanced resistance to drug-induced apoptotic stimuli by multicellular resistance
❖ well-established responses to mechanical stimuli of cells
❖ better accessibility for rapid experimental manipulation and cytotoxicity testing in comparison to animal testing
❖ use in drug discovery and pharmacological application for dose evaluation *in vitro*
❖ advanced real-time and/or fixed microscopy imaging compared to animals
❖ potential for tissue engineering, integration into fluid flow systems, and organ-on-a-chip design
❖ imitation of tumor heterogeneity by cellular co-culturing
limitations of 3D tissue models
❖ lack of vascularization and regulation of molecule transport
❖ imitation of static or short-term conditions unlike the progression of *in vivo* systems
❖ variable reproducibility between different batches of generated tissue models
❖ dependence of tissue model imaging on scaffold size, tissue material transparency, and microscope penetration depth
❖ difficult implementation into high-throughput screening
❖ requirements for the optimization and validation of assays for determining the cellular response to drug interactions
❖ challenges pertaining to the control of homogeneous culture conditions throughout the tissue model such as temperature and pH

In terms of 3D tissue models, several culture models can be distinguished based on their origin or structural concept, such as (I) organotypic explant cultures, (II) multicellular spheroids and organoids, (III) bioprinted tissues, and (IV) tissue-engineered models using immortalized cell lines, stem cells, or explants.

(I) In the case of organotypic explant cultures, dissected organ slices of a particular organism and region of interest are cultured on a semi-porous membrane or embedded in a 3D collagen gel (Stoppini et al., 1991; Toda et al., 2002). Since explantation preserves the cytoarchitecture and cellular differentiation of the original tissue, the samples serve as complex and realistic models for studying the maintenance of structural and connective organization (Shamir and Ewald, 2014), brain physiology, and neuronal activity (Holopainen, 2005; Minami et al., 2017), as well as pharmacodynamic profiling of human tumors (Vaira et al., 2010).

(II) Spheroids and organoids are 3D tissue models composed of multiple cells using different cultivation concepts (Gunti et al., 2021). Organoids are complex clusters of organ-specific cells created by directing stem cells to self-organize into viable 3D structures. Within the aggregate, complex interactions between multiple cell types occur, performing organ-like functions. As a result, organoid cultures mimic the structure and function of real organs, such as lungs or hearts, in the form of miniaturized versions of the organs from which they are derived and are thus applicable in a wide range of research (Velasco et al., 2020). In contrast, the concept of multicellular spheroids was first introduced by Sutherland et al. in the 1970s by culturing Chinese hamster lung cells in suspension (Sutherland et al., 1971). Spheroids are based on the creation of round, three-dimensional cell clusters in which a few hundred up to several thousand cells form various layers. This structure is typically composed of a single cell type derived from well-established cell lines and exhibits a specific microenvironment characterized by cells present in different phases of the cell cycle. In this way, spheroids mimic the physical and biochemical characteristics as *in vivo* and serve as fundamental models for drug screening due to their structural simplicity and easier cultivation procedure compared to organoids (Gunti et al., 2021).

(III) To create bioprinted tissue models, the 3D bioprinting technique is used, which is defined as the creation of a 3D structure through the controlled and typically automated deposition of a biological material or “bio-ink” (Vanaei et al., 2021; see chapter 1.2.4 (III)). In this way, complex tissue structures are constructed as duplicates of the *in vivo* tissue or organ of interest using printable solutions that contain the necessary elements of the desired 3D microenvironment (Deo et al., 2020). Bio-inks can be customized and mixed by combining different cells, native proteins, growth factors, and signaling molecules. In addition, the properties of bio-inks can be modified depending on the printing method and application by applying cooling or exposure to light or heat (Ma et al., 2018), while concentrated bio-inks may be required to create dense, stiff structures such as bone biomimetics (Zhou et al., 2016) or dense tumor microenvironment

models (Swaminathan et al., 2019). Bioprinted tissue models are flexible and versatile for diverse research applications but require further optimization with respect to increased cell death during printing as a result of high shear forces and compatibility with different cell types (Law et al., 2021).

(IV) Modular tissue engineering comprises a novel and promising method for building tissue equivalents in a bottom-up approach. It is based on the creation of living building blocks using an appropriate cell source (primary cells, stem cells, organoids), and suitable tissue architecture (scaffolds, hydrogels, bioprinting), which are then optionally assembled with additives (growth factors, proteins, nanoparticles) to create more biomimetically customized tissue models (Ouyang et al., 2020; Moysidou et al., 2021). Moreover, this approach also enables the generation of vascularized tissues via modular assembly of pre-formed vascularized tissue blocks (Homan et al., 2019; see chapter 1.2.4 (IV)). Thus, it is essential to identify the structural and functional role of each component of the native tissue and carefully select the range of features necessary to reproduce these specific characteristics. As outlined by Moysidou et al., tissue engineering offers a versatile tool that promises to revolutionize many aspects of biomedical research and to change paradigms in the understanding of human biology, as well as in the diagnosis and treatment of diseases (Moysidou et al., 2021).

This brief overview summarizes the variety of 3D tissue models that have been established and applied to address various scientific topics in the field of biomedical research. According to the specific requirements of the application, different complexity levels of 3D tissue models are available, ranging from multicellular spheroids to bioprinted tissues or tissue-engineered models. In this thesis, the 3D tissue model of multicellular spheroids is utilized due to their high diversity of compatible cell lines, high reproducibility, and applicability in different assay approaches.

1.2.2 FORMATION TECHNIQUES OF SPHEROIDS

Multicellular spheroids can be generated from a variety of cell lines using different formation techniques depending on the specific cell types and culture conditions. The common principle of all techniques is the prevention of cells from adhering to the culture substrate to promote cell-cell interaction and the formation of three-dimensional aggregates. In general, the mechanism of spheroid formation can be illustrated as a three-step process (Fig. 1.2; Lin et al., 2006).

After seeding a certain number of cells, the suspended individual cells attach to each other and form a loose aggregate. This initial step is naturally promoted by cell-cell interactions through the secretion of

long-chain extracellular matrix (ECM) fibers such as collagen or fibronectin and a high expression of integrins, leading to the subsequent attachment of adjacent dispersed single cells (Robinson et al., 2004).

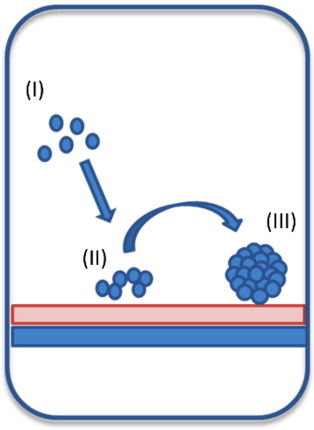

THREE-STEP PROCESS

(I) cell seeding of a certain number of cells and formation of a loose aggregate

(II) organization of cells within the aggregate; formation of a spherical structure; establishment of cell-cell contacts

(III) strengthening of cell-cell contacts; differentiation of cells; formation of a round and compact spheroid shape

Fig. 1.2 Illustration* of the three-step process of spheroid formation on a non-adhesive surface.
*illustration is simplified and not to scale

In the second phase, no morphological changes are observed as the cells begin to organize into a compact, spherical structure (Lin et al., 2006). During this lag period, cells establish cell-cell contacts, and begin to rearrange their positions within the cell aggregate, thereby forming a spheroid. This process can be improved by providing appropriate culture conditions such as growth medium, optimal nutrient supply, and controlled environmental factors. Finally, cell-cell adhesions are strengthened between adjacent cells. The cells on the outer surface of the spheroid undergo specific differentiation into tightly packed, polarized cells that act as a physical barrier very similar to epithelial cells (O´Brien et al., 2002; Ivascu and Kubbies, 2007). In this way, a compact spheroid is formed within hours or days, depending on the cell type and formation technique used.

A variety of spheroid formation techniques have been developed with the basic requirement of achieving stronger adhesion between cells than between the cells and the substrate on which they are grown (Fig. 1.3). The methods are categorized into the classical approaches of using physical stimuli to promote cell agglomeration (e.g., (I) hanging drop, (II) liquid overlay technique, and (III) magnetic levitation), (IV) scaffold-based culture technologies providing physical support, and specialized culture platforms (e.g., (V) microfluidic devices).

(I) The hanging drop method is performed by seeding suspended cells in a drop of 10 µL on the inner side of the lid of a Petri dish, which is then inverted while the drop is held in place due to surface tension (Foty, 2011). In this way, no surface is available for cell adhesion and self-aggregation is promoted by microgravity causing concentration and aggregation of the cells at

the liquid-air interface during incubation (Lin and Chang, 2008). As a result, one spheroid per drop is formed with a defined size dependent on the initial cell concentration used. The hanging drop method provides a controlled environment for simple and reproducible spheroid formation. For routine use, multiwell arrays are commercially available and high-throughput screening approaches have been developed in which up to 384 uniform spheroids are formed in parallel, cultured for long periods, and applied for drug testing using liquid handling robots and plate readers (Tung et al., 2011; Zhao et al., 2019). The hanging drop cultures have also been used to generate cardiac spheroids mimicking key *in vivo* features of the human heart (Polonchuk et al., 2017). In combination with the microfluidic platforms that enable formation, consistent exchange of cell media, and analysis of multicellular spheroids, the hanging drop approach offers a promising technology for body-on-a-chip research (Aijian and Garrell, 2015; Birchler et al., 2016).

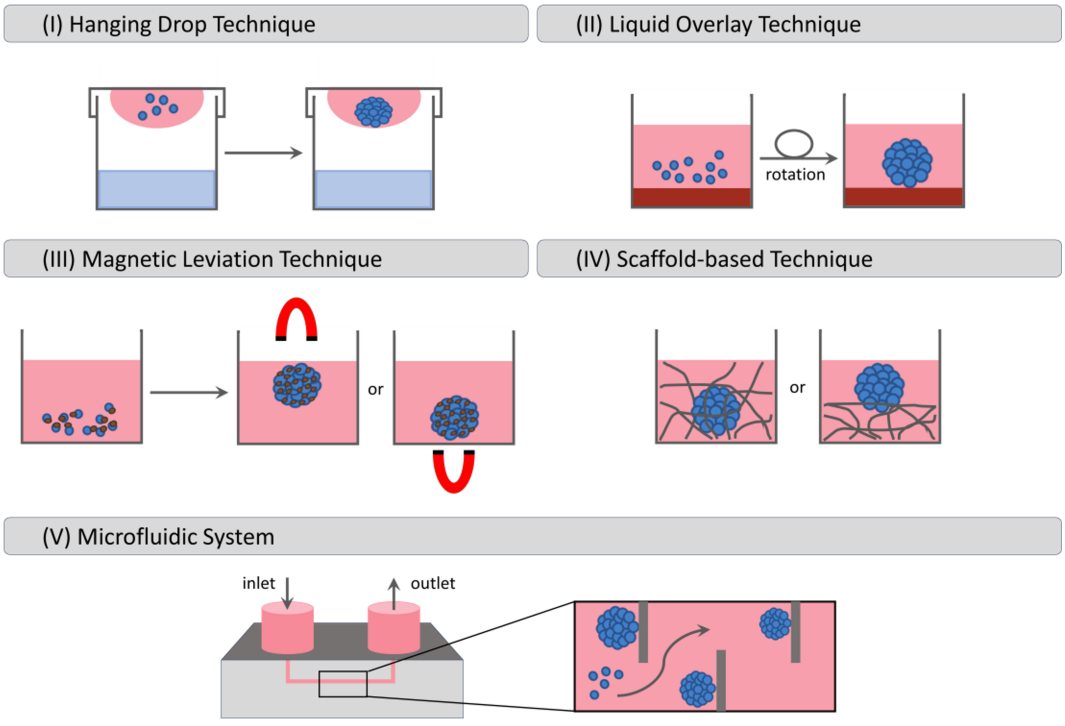

Fig. 1.3 Overview* of different spheroid formation techniques.

*illustration is simplified and not to scale
(adapted from Roy et al., 2023)

(II) In the liquid overlay technique, low attachment plates or non-adhesive substrates are used for spheroid formation, whereby either commercially available ultra-low attachment plates can be utilized or different substrates such as agarose (Hamilton, 1998), polyethylene glycol, and polydimethylsiloxane are used to coat the bottom of 96-well plates or Petri dishes (Hirschhaeuser et al., 2010). Thus, cell-surface adhesion is prevented, and cell-cell adhesion is

strengthened, encouraging cells to aggregate into a three-dimensional structure. After cell seeding, the cells are collected centrally on the bottom of the well by applying centrifugation (Ivascu and Kubbies, 2006; Laurent et al., 2013) or orbital shaking (Frankel et al., 2000; Ong et al., 2010) to enhance cell aggregation. In this way, one single spheroid per well is formed with a defined size in relation to the initial cell concentration used. Based on this principle, Fang et al. developed a specialized chip containing agarose microwells in which more than 200 gradient-sized spheroids are formed simultaneously utilizing a liquid-dome method (Fang et al., 2019). The liquid overlay technique provides a cheap and simple method to form multicellular spheroids of a variety of different cell types in a mainly reproducible size (depending on the cell type) without the need for special equipment and with the possibility of scaling up (Lin and Chang, 2008; Shen et al., 2021).

(III) Magnetic cell levitation is an emerging technique for spheroid formation based on the principle of mimicking the non-gravitational environment with magnetic forces (Yaman et al., 2018). For this purpose, cells are labeled with magnetic nanoparticles and seeded in suspension on a low-adhesion plate. An external magnetic field is applied to promote cell-cell aggregation and spheroid formation (Yaman et al., 2018). This principle has been reported to provide cell aggregates of uniform size and shape that are adjustable in their compactness and size depending on the direction, strength, and duration of the magnetic forces applied (Souza et al., 2010; Anil-Inevi et al., 2018). Magnetic cell levitation has been used for spheroid formation and tissue engineering (Souza et al., 2010; Lewis et al., 2016), and has also been applied in a high-throughput assay for toxicity screening (Timm et al., 2013). Despite the potential of this technique, it is important to note that it requires specialized equipment and that the effects of external forces on cells are generally unknown (Shen et al., 2021).

(IV) In scaffold-based 3D culture, cells are embedded or encapsulated in a framework of biological or synthetic materials that provide a physical support framework (Langhans, 2018). These structures are prepared by the use of either naturally derived polymers such as alginate and collagen, which are mimicking key properties of the ECM such as stiffness, pH, or adhesive sites, or synthetic polymers such as polyethylene glycol and polydimethylsiloxane (Lee and Kim, 2021). Depending on the material or the polymer concentration, the density of the scaffold is modulated, and thus the distance between adjacent cells is varied, resulting in different cell characteristics. While shortening the distance between cells promotes spheroid formation, a porous structure allows aggregates to migrate within the scaffold and promotes cell-to-cell signaling (Shen et al., 2021). Thus, the selection of a 3D cell culture scaffold for a given

application should consider material properties that define physical factors such as porosity, stiffness, and stability in culture, as well as biological properties such as cell compatibility and adhesiveness (Caliari and Burdick, 2016). For example, rigid polymers can provide the physical support found in specialized tissues such as skin or bone, and microplates with micropatterned surfaces can be designed for specific applications such as supporting cell networks (Langhans, 2018). Despite the advantage of generating a variety of different scaffold types and compositions, the technology requires a high degree of expertise to produce reproducible scaffolds and generates cell aggregates of heterogeneous sizes (Roy et al., 2023).

(V) Microfluidic technology refers to the fabrication of miniaturized devices that contain chambers and channels in which fluid flow is geometrically confined (Cui and Wang, 2019). The micropatterned plates are fabricated from polyethylene glycol, polydimethylsiloxane, or agarose using lithography and 3D printing techniques to create a specific number of wells in the substrate with a defined diameter or to form retention pillars within the fluid flow path (Hardelauf et al., 2011). After adding the cell suspension by filling the microfluidic channels, the cells settle into the wells or are retained by retention pillars forming one spheroid per well. By utilizing these microfluidic devices, spheroids can either be formed or maintained under controlled perfusion with a steady supply of oxygen and nutrients while metabolic waste products are removed. Despite the need for specialized equipment, microfluidic devices can reduce the use of spheroid-forming cells and are suitable for screening experiments.

Overall, numerous spheroid formation techniques were developed based on different principles for achieving cellular aggregation. Each method offers certain advantages and disadvantages, as outlined in the respective chapters or in more detail in the reviews of Lin and Chang (2008), Shen et al. (2021), and Roy et al. (2023). A general overview of the basic compatibility of cell types and formation techniques is provided by Lee and Kim (Lee and Kim, 2021). Raghavan et al. showed that the hanging drop method produces smaller spheroids from MCF-7 breast cancer cells compared to the liquid overlay technique within the same culture period (Raghavan et al., 2016). In this context, Han et al. provide a comparison between the liquid overlay technique and the hanging drop method in terms of spheroid size and overall outcome for different cell types (Han et al., 2021). These reports noted the need to establish standardized protocols for generating spheroids of reproducible size and morphology. Therefore, the selection of the appropriate method has to be based on different criteria that determine the applicability for the particular research topic, considering the production efficiency, the degree of spheroid uniformity and reproducibility, the possibility of maintenance and manipulation of the spheroid physiology, as well as the monetary and laboratory/technical aspects (Lin and Chang, 2008).

1.2.3 MICROENVIRONMENT OF SPHEROIDS

The characteristic microenvironment of multicellular spheroids reflects numerous aspects of the microenvironment present in native tissue. Since tumors and spheroids both originate from single-cell aggregates, with the main difference of undergoing vascularization, Mueller-Klieser referred to multicellular spheroids as an *in vitro* model of an early avascular stage of tumor growth (Mueller-Klieser, 1987). Thus, the similarity of providing basic properties such as oxygen and nutrient gradients, hypoxia, and the formation of a central core composed of necrotic cells is evident (Sutherland, 1988). Large spheroids with a diameter of more than approximately 500 µm can mimic various properties of tumors with sizes ranging from 0.5–1 mm^3 (Nath and Devi, 2016). Moreover, similar mechanisms have been found upon exposure to various drugs and other pharmacological molecules, making spheroids an appropriate tissue model.

Based on the three-dimensional cellular architecture, an increasing number of cell-cell interactions are established within multicellular spheroids that are similar to those in real tissues. After spheroid formation, cellular connections are strengthened, and the cellular behavior changes while organizing within the aggregate (Jauković et al., 2020). The cells show morphological changes with reduced nuclear and cytoplasmic volume, thereby becoming more compact over time. Furthermore, cytoskeletal rearrangements appear, as indicated by a loss of cytoskeletal tension accompanied by weak, parallel-aligned actin filaments and increased expression of cell adhesion proteins (Jauković et al., 2020). The outer spheroid layer is formed by densely packed elongated cells that provide the size-volume efficient round spheroid shape and protect the body from external mechanical damage.

Both spheroids and *in vivo* tumors exhibit increased expression of ECM proteins such as collagens, fibronectin, and laminin. The ECM serves as a structural support for cells within a tissue, while increased expression of this component activates intracellular signaling pathways for cell proliferation, differentiation, and survival (Lu et al., 2012). Thus, it is essential for tissue maintenance and tumor function. Additionally, the deposition of ECM proteins, cell-ECM, and cell-cell interactions leads to an increased tissue density and forms a physical barrier between adjacent cells. As a result, the penetration of compounds and their delivery to cells is limited. Since spheroids lack vascularization, gradients of important metabolites arise within the 3D tissue model (Fig. 1.4). Due to the limited mass transport effect (Costa et al., 2016), oxygen, lactate, and nutrient uptake is diminished towards the center, whereas toxic metabolites such as CO_2 or waste accumulate in the central regions of the spheroid. These gradients are amplified with increasing spheroid size growth and/or incubation time.

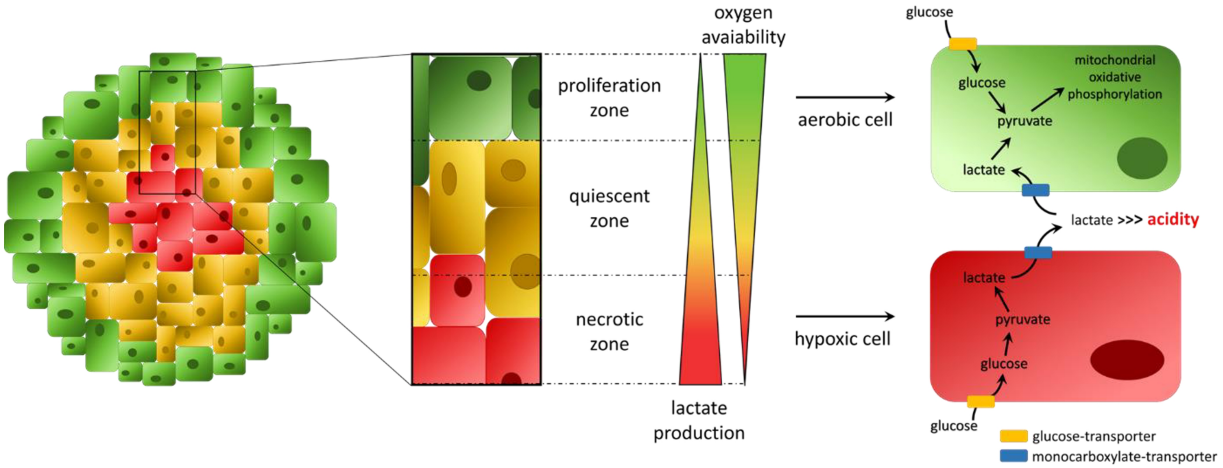

Fig. 1.4 Schematic illustration* of the microenvironment of a spheroid containing three metabolic zones: proliferation zone, quiescent zone, and necrotic zone. Cellular metabolism is affected by the distribution of oxygen within the three-dimensional tissue model, resulting in nutrient and oxygen gradients from the periphery to the core and, in reverse, gradients of metabolic waste and lactate accumulation.

*illustration is simplified and not to scale

(adapted from Nunes et al., 2018)

As a result of the reduced oxygen availability and partial pressure in the center of the spheroid, a hypoxia gradient is established and an altered energy metabolism is induced. The energy supply of the cells is provided by the anaerobic metabolism of glucose, which produces lactate as a by-product (Fig. 1.4; Hirschhaeuser et al., 2011). Hence, an acidic environment is created that further affects cell cycle progression in terms of reduced proliferation and G0/G1 cell cycle arrest. This leads to the formation of concentric zones in a core-shell-like structure exhibiting their own environments (Fig. 1.4). At the periphery of the spheroid, proliferating viable cells are present and an intermediate zone contains viable but quiescent cells while the center of the spheroid is composed of necrotic cells. The spacing or thickness of all three zones can vary with different cell lines, seeding densities, and growth conditions.

In general, the spheroid exhibits an energetically low state which, in combination with the characteristic cellular architecture and metabolic changes, leads to an overall increase in antioxidant capacity combined with a decrease in drug sensitivity similar to tumors *in vivo* (Jauković et al., 2020). This phenomenon of multicellular resistance observed in spheroids and tumors is related to enhanced resistance against radiation damage and therapeutic drugs. Fundamentally, the penetration of drug components is impaired, as the multitude of cell junctions in conjunction with the increased deposition of ECM proteins leads to an increased interstitial fluid pressure (Costa et al., 2016). Simultaneously, the gene expression of producing membrane proteins that actively transport drugs or other molecules to the outside of the cell is upregulated and thus promotes multicellular resistance. To yield an effective therapeutic impact, some therapeutic compounds require oxygen to generate reactive oxygen species capable of damaging cell membranes and DNA. Since spheroids provide a hypoxic and acidic

environment causing protonation of mainly weak alkaline drugs, the efficacy and cellular uptake of these compounds are reduced (Nunes et al., 2018). As reviewed by Breslin and Driscoll, the greatest resistance to anticancer drugs in 3D cell cultures may also be due to alterations in receptor proteins, drug transporters, and enzymatic metabolic activity (Breslin and Driscoll, 2016). Thus, the multicellular resistance of spheroids and tumors is based on the combination of all these microenvironmental properties.

The multidrug resistance is quantitatively reflected by the comparison of the drug potencies in cell monolayer culture versus 3D tissue models. It is expressed as the EC_{50} value describing the concentration effective in producing 50 % of the maximal response. For instance, Desoize and Jardillier reported that the EC_{50} values of spheroids derived from A549 human lung cells were consistently higher compared to monolayer cells and that the drug concentration had to be increased by a factor of 10 to 1,000 for spheroid treatment, depending on the drug applied (Desoize and Jardillier, 2000). Additionally, Horning et al. reported that MCF-7 human breast cancer cells in 3D culture were more resistant to typical anticancer drugs (e.g., doxorubicin and paclitaxel) than in 2D culture, with a 12- to 23-fold difference in EC_{50} values (Horning et al., 2008). In the literature, several examples of therapeutic strategies targeting spheroid resistance mechanisms have been reported. For instance, anti-adhesive agents have been applied to spheroids to block the E-cadherin function and thereby address the effect of E-cadherin expression on multidrug resistance (Green et al., 2004). Other studies examine the use of therapeutics that reduce glucose transport and downregulate the rate of glycolysis (Wartenberg et al., 2003) or investigate hypoxia-activated prodrugs that undergo chemical reduction and become active when exposed to hypoxic environments (Mistry et al., 2017). By identifying the mechanisms enabling spheroids to develop a drug resistance profile in detail, it may be possible to develop new and more effective therapeutic agents.

Based on the characteristic spheroid microenvironment including the cellular architecture, metabolic aspects, and drug sensitivity, a variety of different properties were observed to be common to tumors *in vivo*. To create even more realistic and predictive 3D cultures to improve the prognostic ability of *in vitro* test systems, the heterogeneity of *in vivo* tumors has to be considered. Therefore, heterotypic mixtures or co-cultures of different cell types have been studied, representing different geno- and phenotypes within a single spheroid body. A summary of various tumor spheroid co-cultures and their applications for therapy testing is provided by Hirschhaeuser et al. (Hirschhaeuser et al., 2010). In this way, the spatial organization of cells between different cell types is considered similar to native tumor models by providing cell-cell and cell-matrix interactions in combination with complex transport dynamics for nutrients within the model system. In the context of mimicking the environment as

authentically as possible, the major challenge is to promote vascularization in tumor spheroids. Various reports have described different strategies in this regard, especially tumor-on-a-chip models with vasculature. Although these approaches yield vascularization, the overall degree of tumor vascularity in most studies is still below that observed *in vivo* and needs to be improved in future applications (Wan et al., 2023).

1.2.4 APPLICATION STRATEGIES OF SPHEROIDS

Due to high levels of diversity and the ability to model *in vivo* microenvironmental aspects, the application of multicellular spheroids is becoming prominent in different fields of biomedical research. These spheroids serve as a promising tool to obtain results with higher predictive value for clinical outcomes regarding their application in (I) pathological studies and (II) drug screening, as well as providing (III) alternatives to animal testing while also being used as (IV) tissue building blocks.

(I) Spheroids offer an improved physiological relevance as 3D tissue models representing the development and the environment of *in vivo* tumors. Thus, spheroids are applied in pathological studies mimicking tumor aggregation and cell differentiation due to their characteristic three-dimensional architecture, multiple cell-cell and cell-ECM connections, and the resulting multicellular resistance (see chapter 1.2.3). Therefore, specific cell lines or stem cells originating from the region of interest are applied to most accurately mimic the essential features. To facilitate insights into the complex processes of tissue development and maintenance, the differentiation and formation of organ-like structures can be simulated by culturing stem cell-derived spheroids under various conditions. In this context, the osteogenic differentiation of human mesenchymal stem cell spheroids (Hildebrandt et al., 2010), or the initiation of cardiac differentiation of P19 embryonic carcinoma stem cells into embryonic bodies (Bain et al., 1994; Hupf, 2018) has been demonstrated. Through this approach, the mechanism of aggregation and differentiation can be investigated in detail by varying experimental parameters or using different trigger reagents. The spheroid model can also be extended by the use of co-cultured cell mixtures for spheroid formation. This approach allows the analysis of intercellular heterotypic signaling pathways between different cell types and their spatial organization within a single spheroid body, thus mimicking the heterogeneity of real tumor tissue in a more realistic way (Hirschhaeuser et al., 2020).

(II) One of the key technologies of spheroids is their application in drug discovery and drug development due to their similar metabolic and proliferation gradient distribution to tissues *in vivo* (Hirschhaeuser et al., 2010). In particular, the evaluation of drug penetration, therapeutic

efficacy, and target affinity under physiological conditions can be addressed by using, among others, fluorescence microscopy (Khawar et al., 2021). The most frequently studied parameter of drug effect is cytotoxicity, which can easily be monitored over time by measuring the size and shape of spheroids (Mittler et al., 2017). According to Langhans, it should be taken into account that the response to a broad spectrum of drugs depends not only on a specific cell line or tumor type but also on the surrounding environment (Langhans, 2018). Thus, the response to therapeutic agents can range from drug resistance to increased sensitivity based on the tissue-specific composition of the ECM, interaction with adjacent cells, and the presence of immunoregulatory factors. As a result, the use of spheroids in drug discovery enables the prediction of drug efficacy, toxicity, and side effects prior to animal or human testing, and thereby increases the effectiveness of clinical trials (Langhans, 2018).

(III) In terms of personalized medicine, the human system can be reproduced on a miniaturized scale by generating three-dimensional tissue models from patient-derived primary tumor cells. Therefore, biobanks of appropriate patient material serve as a basis for spheroid formation, which enable the investigation of individual responses to specific drugs or therapies (Gilazieva, 2020). In this context, multicellular spheroids may also serve as disease models for investigating the development and progression of various diseases in a realistic and controlled environment. Moreover, the development of body-on-a-chip or spheroids-on-a-chip approaches offers promising concepts for simulating the complexity of native tissues and studying the synergetic effects of various factors such as nutrients, metabolites and gas flow, shear stress, and mechanical and hydrodynamic forces (Langhans, 2018). These visionary approaches can circumvent the drawbacks of mouse models, which, in addition to high cost and ethical considerations, do not always accurately replicate human diseases or capture drug side effects such as liver toxicity (Langhans, 2018). However, the high complexity of these miniaturized human models requires further research to provide reliable and reproducible experimental applications.

(IV) In the field of 3D bioprinting and biofabrication, tissue spheroids are utilized as modular tissue building blocks for the reconstruction of functional tissues and organs (see chapter 1.2.1 (III) and (IV)). As noted by Jakab et al., this application strategy is based on the ability of the spheroid bodies to behave as a viscoelastic fluid and to fuse within appropriate hydrogel scaffolds through tissue-fusion processes (Jakab et al., 2004). Thus, larger tissue constructs are formed in a similar way as in embryonic development after positioning the building blocks in proximity. In this way, several complex tissues such as the liver, pancreas, cardiac muscle, or bone tissue have

been created (Lin and Chang, 2008). According to Mironov et al., the goal of organ printing technology is to produce 3D vascularized functional living human organs suitable for clinical implantation (Mironov et al., 2008). To this end, different methods for generating vasculature have been developed in recent years, which are categorized as either direct printing of pre-vascularized tissue or indirect printing of perfusable matrices with sacrificial materials (Zhu et al., 2021). As a result, biofabricated tissues may provide a tool for tissue transplantation in the context of regenerative medicine. Due to the immense complexity of mimicking native tumors, 3D bioprinting is still in the infant stage and maintains a large gap between *in vitro* studies and *in vivo* applications, as indicated by Zhu et al. (Zhu et al., 2021). However, these strategies provide perspectives for future directions in the fabrication of advanced vascular constructs.

Overall, significant efforts have been made to implement spheroids in different applications to achieve progress in the fields of pathology, pharmacology, medicine, and biophysics. In this context, however, three key challenges must be considered, and continuously addressed by (I) consistently producing spheroids of uniform size and shape, (II) validating the evaluation techniques of spheroid results and responses, and (III) developing novel high-throughput platforms. Based on these fundamentals, spheroid application strategies represent a versatile, advanced field of research with great potential.

1.3 TECHNIQUES FOR 3D TISSUE MODEL ANALYSIS

Common analytical techniques have been developed for monitoring cellular activities within multicellular spheroids. These methods are mainly based on well-established protocols and technologies for analyzing 2D tissue models that were modified and adjusted to comply with the requirements of three-dimensional models using, among others, increased fluorescence dye respective compound concentrations or longer incubation times. The applicability of the assays was confirmed by studying distinct changes in the spheroid microenvironment concerning alterations of the cellular structure, behavior, and viability.

1.3.1 OVERVIEW OF DIFFERENT TECHNICAL APPROACHES

In general, different technical approaches such as microscopy imaging, flow cytometry, or colorimetric assays and mathematical modeling are applicable for 3D tissue model analysis (Tab. 1.3). In this chapter, several examples of the presented techniques are outlined, following the review by Costa et al. (Costa et al., 2016).

(I) Optical microscopy is a typical tool for characterizing the size, morphology, and internal organization of tissue models. Time-lapse microscopy studies enable the recording of spheroid growth behavior or the impact of specific compounds affecting morphological changes (Friedrich et al., 2009; Ma et al., 2012). However, imaging of 3D cell cultures is challenging due to the thickness of the tissue and the light scattering phenomenon resulting from mismatching refractive indices of the cellular components which limits the amount of light penetration into the specimen and the ability to observe internal structures (Richardson and Lichtman, 2015). As a result, several optical clearing methods for rendering spheroids with enhanced transparency have to be applied (Costa et al., 2019). Moreover, since the difficulty of gaining adequate light penetration also arises in the use of fluorescence microscopy, either thin slices of 3D tissue models are used to facilitate imaging at a submicron resolution (Graf and Boppart, 2010) or optical sectioning microscopies are utilized. These microscopic approaches are capable of capturing images of a thin, single plane of the specimen with minimal interference from the remaining portions, which are then combined into a 3D reconstruction of the entire specimen. Confocal laser scanning microscopy (CLSM), multiphoton microscopy (MPM), and light-sheet fluorescence microscopy (LSFM) are commonly used for this purpose. In general, fluorescence microscopy is gaining importance as it allows the observation of fluorescent markers that stain

a specific area or molecule of interest within cells, and thus enables the analysis of the penetration of fluorescently labeled drugs into the tissue.

Tab. 1.3 Overview of selected techniques for 3D tissue model analysis with a brief description, relevant specifications, and references.

	technique	description	specification	reference
I	**optical microscopy**	Visualization of morphology and internal cellular organization.	– light microscopy	– Friedrich et al., 2009 – Ma et al., 2012
			– fluorescence microscopy	– Graf and Boppart, 2010 – Bruns et al., 2012
II	**electron microscopy**	Visualization of morphology and localization of internal cellular organization with high resolution.	– scanning electron microscopy – transmission electron microscopy	– Li et al., 2008 – Uroukov and Patton, 2008 – Amaral et al., 2010
III	**flow cytometry**	Cell counting, sorting, and detection for biomarkers of interest.		– Khaitan et al., 2006 – Beaumont et al., 2015
IV	**gene expression**	Identification and quantification of various protein levels determining cell proliferation and cell cycle kinetics.	– Western blot – qPCR	– Khaitan et al., 2006 – Brophy et al., 2009
V	**colorimetric assays**	Quantification of cell viability, cell proliferation, and cytotoxicity for evaluating cytotoxic effects of different simulating compounds.	– alamarBlue™/ PrestoBlue™ assay – lactate dehydrogenase assay – acid phosphatase assay	– Walzl et al., 2014 – Ho et al., 2012 – Friedrich et al., 2009
VI	**mathematical modeling**	Extraction of relevant biological information and prediction of biological effects upon variation of distinct influencing factors.		– Ward and King, 1997 – Achilli et al., 2014

(II) Electron microscopy, both in scanning or transmission mode, facilitates an even more detailed image acquisition showing high magnification and resolution at the nanoscale level. For instance, Amaral et al. utilized transmission electron microscopy to analyze the cell morphology and differentiation in MCF-7 spheroids (Amaral et al., 2010). Since sample preparation is time-consuming and includes performing fixation, embedding, and sectioning, the application is intended for addressing specific problems rather than routine use.

(III) Flow cytometry is used for cell counting and additional sorting of cells based on the detection of specific targets of interest. In this way, the cellular uptake of drugs and nanoparticles in spheroids is quantified due to their cytotoxic potential of inducing apoptosis. For instance, by using the Hoechst dye diffusion method, the inner and outer cells of a spheroid are distinguishable, while additional staining of G1 arrested cells localizes the spheroid center (Beaumont et al., 2015). Since the cells have to be analyzed individually, the spheroids must be disaggregated to obtain a suspension of single cells.

(IV) In terms of characterizing gene expression patterns in spheroids, the presence of specific proteins in cell lysates is determined. While Western blot analysis is semiquantitative due to its sensitivity in detecting low levels of proteins, qPCR quantifies gene expression by synthesizing complementary DNA transcripts from RNA. Both methods allow the identification of different proteins that play an essential role in tumor progression and thus enable, for instance, the analysis of therapeutic efficacy by assessing the expression of pro- or anti-apoptotic markers (Khaitan et al., 2006). As shown by Brophy et al., the difference between spheroid formation of liver cells under rocked versus rotated conditions was examined in the context of bioartificiality based on the expression of liver-related genes (Brophy et al., 2009).

(V) Colorimetric assays are used to assess how cell viability is affected by the cytotoxic effect of a compound of interest as a function of its concentration. In general, these techniques are based on cell membrane-permeable and non-fluorescent indicator compounds applied after cytotoxic treatment. On contact with vital cells, these compounds are converted to an absorbance or fluorescence active product by an enzymatic reaction occurring in the cytoplasm or mitochondria. For instance, in the alamarBlue™ assay, the indicator resazurin is reduced by mitochondrial enzymes via NADH or NADPH dehydrogenase to resorufin. The acid phosphatase assay protocol uses *p*-nitrophenyl phosphate as a phosphatase substrate which turns yellow when dephosphorylated by viable cells via intracellular acid phosphatase. By measuring the absorbance at a specific wavelength, the intensity directly correlates with the amount of vital and metabolically active cells within a spheroid or cell monolayer, which enables the calculation

of the cytotoxicity index in relation to various control conditions. As the experimental protocols are usually optimized for monolayer cultures, the limited mass transport within the spheroids must be considered, leading to an insufficient homogeneous distribution of the cytotoxic and colorimetric compounds. To improve the penetration of the reagents into the spheroids, increased compound concentrations, prolonged incubation periods, or as indicated by Valley and coworkers, the horizontal stirring of the spheroids in the compound solution can be applied (Valley et al., 2014).

(VI) In recent years, several mathematical models have been developed that are capable of either extracting relevant biological data or predicting, for example, spheroid growth and the biological effect and penetration depth of various compounds into the tissue models. The equations and algorithms are trained on specific features studied using the actual spheroid model, specifically the round shape, initial exponential growth, and gradient of nutrients, oxygen, and pH value. Concerning the growth of spheroid models, the Gompertzian function was developed to calculate the exponential size increase, and Piccinini et al. reconstructed the changing 3D structure depending on the incubation period using MATLAB® (The MathWorks, Inc., MA, USA; Piccinini et al., 2015).

Overall, a variety of techniques and tools are available to analyze, determine, and calculate various aspects of 3D tissue models. The combination of these different methods provides a comprehensive view of the various properties of the spheroid as described. In this way, manipulation strategies, such as exposure to chemical stimuli, can be evaluated in comparison to a standardized condition. Apart from the high information content, the limitations of these methods arise from their invasiveness, the need for labeling and continuous monitoring, or their design as endpoint assays.

1.3.2 OVERVIEW OF IMPEDANCE-BASED APPROACHES

For studying three-dimensional cell models in a label-free manner, measurement setups are currently being developed to analyze spheroids as a whole entity. In this context, electrical impedance spectroscopy (EIS) has recently emerged as a non-invasive and label-free technique for three-dimensional culture analysis (for the theoretical background of EIS, see chapter 3.1) that provides continuous monitoring, easy automatization, and simple implementation. It has been used for a variety of applications and is increasingly utilized for biological applications since EIS is extremely informative for dynamic systems due to a low amplitude signal and real-time data acquisition with high temporal resolution (Lvovich, 2012). This enables the characterization of biological tissues and monitoring of tissue model alterations induced by therapeutics and toxins. Since experimental approaches requiring

the attachment of cells to planar electrodes for monitoring cell-substrate interactions are inadequate for the assessment of multicellular spheroids, researchers have employed a variety of techniques, including microfluidic channels or microcavity traps. In the following, examples of fundamental spheroid measurement devices, microfluidic-based devices, and multiple spheroid measurement devices.

I FUNDAMENTAL SPHEROID MEASUREMENT DEVICES

Several approaches for trapping spheroids between a set of electrodes can be applied for the development of novel fundamental measurement setups. The challenge of these approaches is to make the spheroid accessible for impedance measurements with the best sensitivity and without affecting its morphology. However, since every possible method of trapping a spheroid partially alters the natural morphology of the spheroid and stresses the cell layers in the outer zone, some EIS-based measurement setups promise the lowest interferences and reproducible trapping strategies.

(I) The group of Andrea Robitzki has published most of the reports on the development and use of devices for EIS measurements of spheroids, which are based on different concepts.

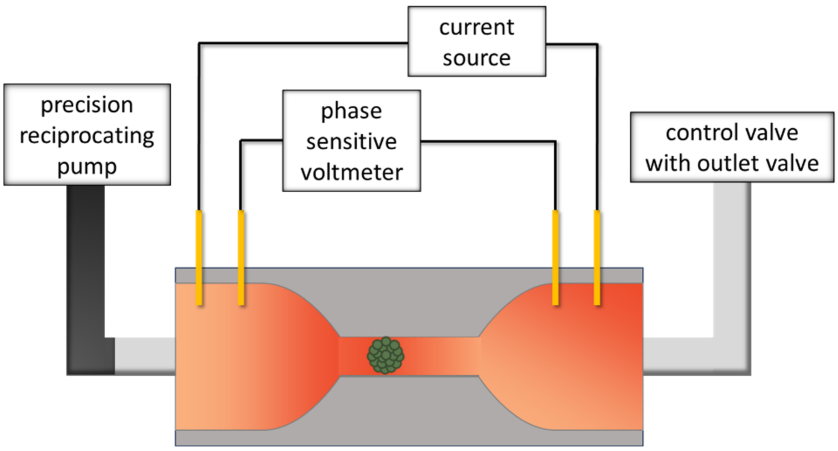

Fig. 1.5 Schematic illustration* of the impedance measurement setup for fundamental spheroid studies developed by Thielecke et al. (Thielecke et al., 2001a). The capillary system is filled with cell culture medium and the spheroid is kept in position within the aperture using a precision reciprocating pump, which is connected via a flexible tube filled with oil. For impedance measurements, a sinusoidal current was applied through the two outer electrodes and the impedance magnitude as well as the phase angle were determined between the two inner electrodes.

*illustration is simplified and not to scale

(adapted from Thielecke et al., 2001a)

One of the devices consists of a glass capillary with an inner diameter of 400 µm and funnel-shaped parts at both ends. On each side of this measuring tube, two holes were drilled for the insertion of a total of four platinum wires serving as electrodes (Thielecke et al., 2001a; Fig. 1.5). After filling the system with a culture medium, the spheroid was positioned in the center of the

capillary using a pump. A sinusoidal current was applied and controlled through the two outer electrodes to measure a voltage drop of 10 mV across the inner electrode. The magnitude and the phase angle were determined between the two inner electrodes. With this measurement setup, it was possible to discriminate impedimetrically between control spheroids and transfected spheroids with decreased growth and increased necrosis. As a result, this setup was used in further studies for EIS-based detection of physiological changes in spheroids after drug stimulation and gene modification (Bartholomä et al., 2005). In addition, the approach has been used for osteogenic differentiation of mesenchymal stem cells (Hildebrandt et al., 2010).

(II) Another experimental system from the group of Andrea Robitzki contains an electrode array unit with planar gold circular electrodes and iridium micro-ring electrodes (Thielecke et al., 2001b). Here, the spheroids were positioned on the planar electrodes by controlled suction into the cavities adapted to the electrodes with central microholes using a micromanipulator and a microscope. A three-electrode arrangement was used to eliminate counter-electrode effects, as demonstrated in proof-of-concept experiments investigating the effects of dimethyl sulfoxide as well as Triton X-100 on tumor spheroids. The results showed that in the frequency range of 50 kHz to 500 kHz, the spheroids induced changes in impedance values caused by morphological changes after substance treatment. In addition, a simplified equivalent circuit model and a suitable transfer function for data fitting were investigated. Based on this fundamental approach, an array for measuring multiple spheroids was established consisting of cavities around the electrodes and microholes for a suction-controlled spheroid positioning procedure, as described in chapter III, example I.

(III) The next EIS microdevice contained a microchannel that was fabricated using a photoresist and then sealed with glass at the top and bottom (Bürgel, 2013). Spheroids were pulled through the 500 x 500 µm cross-section channel by gravity while passing through an electric field applied by a set of opposing platinum electrodes at the top and bottom. This setup has been used to monitor spheroid growth and to demonstrate the effect of growth-inhibiting drugs on spheroids derived from liver or colon carcinoma cells. Overall, this flow-through approach was found to provide more reliable impedance signals compared to immobilized spheroids.

(IV) Another measurement approach consists of a planar organic electrochemical transistor with source, drain, and gate tracks in combination with a micro-trap (Curto et al., 2018). The transistor was fabricated on glass using lift-off lithography, whereby a nozzle-shaped micro-trap was positioned on top of the planar electronics. A transistor channel with a cross-section of 25 x 25 µm was positioned to the left of the nozzle trap, while the gate was aligned directly to

the micro-trap. By applying voltage to the gate, ions from the electrolyte were injected into the channel, changing the electronic charge density and the drain current. The positioning of the spheroids was controlled by a gravity-driven flow by varying the liquid level in the two liquid reservoirs connected at either end of the micro-trap. Using this EIS-based device, differences were demonstrated between spheroids made from fibroblast and epithelial cells alone, as well as when both cell types were combined. Finally, the performance of the platform was evaluated by detecting changes in spheroid resistance in real time after treatment with Triton X-100.

(V) An additional micro-trap based device consisted of a commercially available polyethylene terephthalate foil with a conductive tin oxide layer and a flow channel containing two buffer reservoirs (Hupf, 2018). The flow channel was bonded to the foil above a non-conductive stripe where the tin oxide was chemically etched away, while the two reservoirs were placed on the remaining conductive surface. For spheroid positioning, a hydrodynamically driven flow has to be created by manually varying the liquid level in the two buffer reservoirs, which results in the spheroid body being trapped at the 250 x 250 µm central constriction within the flow channel. A digital microscope was used to control the position of the spheroid throughout the measurement. With this approach, reproducible impedance characteristics of spheroids of the same age and seeding density were observed. In proof-of-concept studies, differences between several cell types, such as MCF-7 tumor spheroids, P19 embryonic bodies, and Cor.At cardiospheres, were demonstrated based on their altered dielectric structures. In addition, morphological changes upon exposure to invasive stimuli such as fixation, permeabilization, osmotic pressure, or hyperthermia have been studied.

II MICROFLUIDIC-BASED DEVICES

In addition to fundamental approaches, microfluidic-based devices in the form of microfluidic chips have been investigated that enable the retention, cultivation, and continuous analysis of spheroids. Due to the combination of all these processing steps from spheroid formation to analysis and stimulation, the development procedure of the assay is both challenging and time-consuming. However, based on fundamental approaches, certain principles can be implemented and optimized, as described in the following examples.

(I) The group of Olivier Frey develops impedance-based devices for spheroid analysis and has presented several concepts in recent years. For example, the researchers developed a microfluidic chip in which the spheroid could be loaded from the side and then trapped in the main channel at a central retention block (Schumacher et al., 2011; Fig. 1.6). For the

measurement, two planar platinum electrodes were placed close to the trap and two other electrodes further upstream. To increase the EIS resolution, hydrodynamic focusing was applied using three independent inlets upstream in the main channel. By using a conductive liquid in the center and two non-conductive liquids on the sides, a liquid sheet in the form of a vertical plane was created (Schumacher et al., 2011).

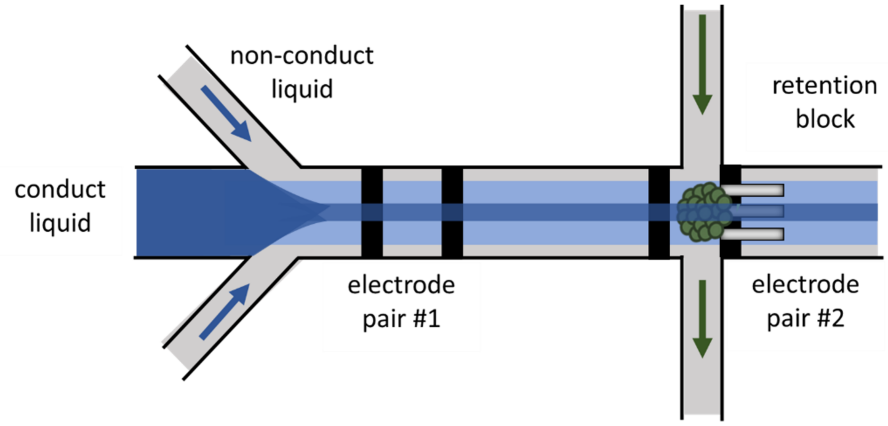

Fig. 1.6 Schematic illustration* of the microfluid-based device for impedance spheroid measurement developed by Schumacher et al. (Schumacher et al., 2011). The microfluid chip composes a main channel, which is connected to three independent addressable inlets used for generating hydrodynamic focusing and a tissue in- and outlet channel from the side. After spheroid trapping at the retention block, impedance measurements are performed in either reference mode (pair #1) or spheroid measurement mode (pair #2). By hydrodynamically focusing the conductive liquid in the center and two non-conductive liquids on the sides, tissue slices are generated during recording leading to spatial signal resolution.

*illustration is simplified and not to scale

(adapted from Schumacher et al., 2011)

In this way, impedance spectra of defined cross-sectional areas could be recorded by precisely scanning across the trapped spheroid. Using this approach, it was shown that a significant impedance increase could be measured after spheroid insertion compared to an empty device, that the positioning of the spheroids was reproducible, and that the sheath flow was adjustable. However, it was found that the system needed to be optimized, as a fraction of the conductive fluid was still flowing around the spheroid surface.

(II) In another measurement setup, an exchangeable EIS plug-in was integrated into a hanging drop device (Bürgel et al., 2015). The hanging drop network was produced by standard soft lithography and included eight separate drops connected via microchannels. Thus, spheroid formation, microfluidic cultivation, and impedance measurements were combined in one platform. The EIS plug-in was fabricated on a glass substrate with a set of integrated coplanar platinum microelectrodes patterned by lift-off lithography. By inserting the plug-in into a gap between the drop containing the spheroid and the glass substrate, the spheroid was

characterized by EIS and optically using an inverted microscope. In a proof-of-concept experiment, the beating of human cardiac spheroids was studied, revealing the possibility of modulating the beating frequency by varying the amplitude of the stimulation signal.

(III) A microfluidic-based device was developed by Luongo et al. using microelectromechanical systems techniques (Luongo et al., 2013). In this process, opposing electrodes were embedded on the top and bottom surfaces of a microfluidic channel made of Pyrex substrate, chromium gold, photoresist, and polydimethylsiloxane. To validate the novel design, the trapping of three-dimensional particles and multicellular spheroids was demonstrated, whereby spheroids in the range of 50 µm to 300 µm were positioned between the set of electrodes by trapping them at an array of pillars forming a horseshoe pattern around the electrodes. By using polystyrene beads and tumor spheroids of different diameters, the ability to detect conductivity changes between the electrodes was demonstrated.

III MULTIPLE SPHEROID MEASUREMENT DEVICES

Based on fundamental spheroid approaches, the next level is to perform multiple measurements simultaneously by constructing multiple spheroid measurement devices. Therefore, the basic principle used has to be reliable and easy to reproduce in a manufacturable way. Additionally, the measurement protocols have to be adapted to obtain reproducible results from all specific measurement units without complicating the handling procedures. In the following, examples of approaches are presented for the parallel measurement of multiple spheroids, which demonstrate the successful implementation of all these requirements.

(I) The vision outlined above was realized by the group of Andrea Robitzki with the development of a microcavity array for drug testing (Kloß et al., 2008a). This approach was an optimization of the planar gold electrode cavities array developed a few years earlier (see chapter I, example II). The new setup consisted of 15 square microcavities with a depth of 100 µm and different widths (200 µm, 300 µm, and 400 µm) for spheroids of different diameters (Fig. 1.7). Each side of a cavity contained a rectangular gold electrode, which enabled observations of impedance magnitude changes after spheroid positioning in each cavity. To insert the spheroids into the cavities, a micropipette or a micromanipulator was used while controlling the procedure with an optical microscope. It was shown that the use of this impedance-based setup facilitated the comparison of the impedance spectra of inorganic spherical models, such as zeolith and glass beads, as well as spheroids from five different cell types. In addition, the effect of different anti-tumor drugs on the spheroids was determined while the contraction of cardiomyocyte

spheroids was monitored by recording extracellular potentials, and the effect of an apoptosis-inducing compound on human melanoma spheroids was investigated (Kloß et al., 2008b).

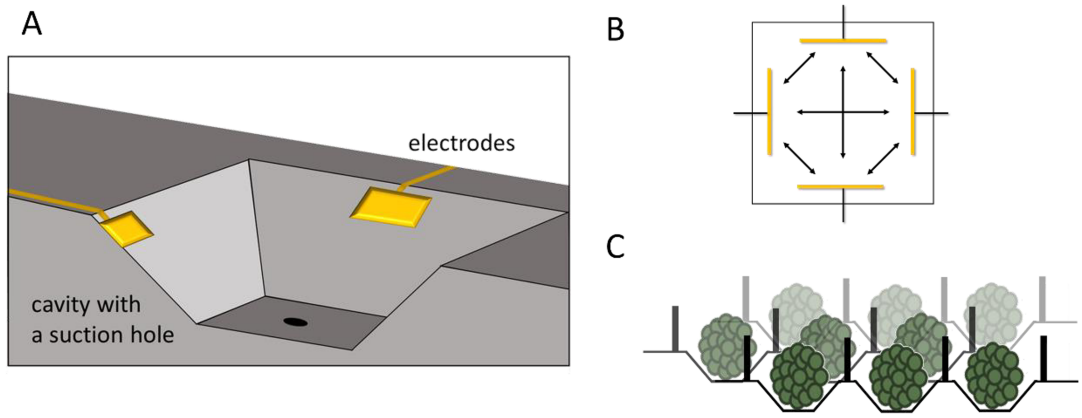

Fig. 1.7 Schematic illustration* of the multicavity chip for impedance spheroid measurement developed by Kloß et al. (Kloß et al., 2008a). The cavity (300 µm x 300 µm) is used for spheroid positioning and was further optimized by implementing a central suction hole (A; Jahnke et al., 2013). Each cavity has four electrodes for the spatial distribution of the impedance signals (B), whereby a total of up to 15 individual spheroids can be measured in parallel by the multicavity system (C).

*illustration is simplified and not to scale

(adapted from Kloß et al., 2008a)

Although the chip was applicable in principle, it had to deal with a low signal-to-noise ratio and a high impedance variance for spheroids of the same size. To improve the sensitivity of the chip, the setup was optimized by broadening the circuit paths, adding a thicker passivation layer, and increasing the electrode size (Krinke et al., 2010). Additional experimental optimization was achieved by incorporating a suction hole in the bottom of the cavity for automated positioning (Jahnke et al., 2013). As a result, the improved array setup was used to perform impedance measurements on brain tumor cultures in the context of drug efficacy testing (Eichler et al., 2015).

(II) Another device consisted of an automated EIS platform integrated into a microfluidic setup (Bürgel et al., 2016). On the chip, 15 separate chambers were constructed using electrodes and polymeric structures. Subsequently, the chip was placed in a standardized tray in conjunction with the EIS platform circuit board, mounted on a tilting stage, and sealed with a lid. For impedance measurements, a set of impedance measurement electrodes was placed in the center of the 580 µm x 700 µm channel while buffer reservoirs were mounted on the left and right sides of the channel. Additionally, supportive columns were positioned on both sides of the channel to keep the spheroid in place. By tilting the entire platform ± 30°, the spheroid passed over the electrodes and the impedance between the two electrodes changed. As

reported, this setup was used to monitor cardiac spheroids online and to study the effect of an anticancer drug on human cancer spheroids (Bürgel et al., 2016).

(III) A third EIS-based setup with multiple measurement slots was developed by the group of Michael Naumann (Valero et al., 2010). In this work, an impedimetric biosensor was established for online monitoring of neuronal differentiation in 3D matrices. The electrode array consists of 16 gold electrodes on a glass slide and was fabricated using a standard sputtering technique with a customized mask. On top of the gold electrodes, an adhesive silicone foil with circular wells (5 mm in diameter) was positioned to define the shape of the gel matrix. An additional thin sheet of stainless steel was placed on top to serve as a grounded reference electrode for impedance measurements, while several small holes were drilled to allow diffusion of medium into the gel. In this way, the gel films filled into each well were squeezed between the two electrodes to ensure proper electrical contact and a well-defined gel thickness. In addition, four microfluidic channels made of silicon foil allowed the perfusion of the cells with culture medium and different compound solutions. Finally, the stack of these specific layers was placed in a stainless-steel bioreactor with 16 pin connectors at the bottom and four inlets and four outlets at the top, which allowed the perfusion of the four chambers with different media. For impedance measurements, the cells were immobilized in the matrix on top of the gold electrodes, the gel was solidified in the incubator, and the stack of all specific layers was pressed for effective sealing. Several refinements for adjusting the cell density and gel composition were tested to demonstrate the neural differentiation of mouse neuroblast cells by increasing electrical impedance.

At present, only a few research groups are working on the development of novel and enhanced devices for the impedance-based analysis of multicellular spheroids. Since each measurement setup exhibits different advantages and disadvantages, the handling of the spheroid positioning and the securing of the spheroid trapping principle is crucial. In this context, the microfluidic-based hanging drop device of Bürgel et al. (Bürgel et al., 2015; chapter II, example II) offers an interesting approach to combine all processing steps from spheroid formation to analysis. In addition to the design and functionality of the device, its applicability is essential, as demonstrated in several reports studying the effects of different cell-stimulating compounds. Based on a well-characterized setup, the potential to scale up the measurement device is attainable, as shown by the microcavity array developed by Kloß et al. (Kloß et al., 2008a; chapter III, example I) as an optimization of the basic single-cavity setup.

CHAPTER 2

OBJECTIVES

The cultivation of organisms is characterized by complex biological, physical, and chemical interactions between a large number of cells and their microenvironment. In recent years, multicellular 3D tissue models have proven suitable for simulating the biological environment of real tissues and microtumors *in vitro*. Thus, three-dimensional culture systems, e.g., multicellular spheroids, are receiving increasing interest in numerous areas of biomedical research, including tissue engineering, the development of cancer therapies, and the improvement of medical diagnostics. Apart from the investigation of spheroid morphology and cellular integrity, several approaches for sensitive measurement of 3D tissue model alterations are required.

The objective of this thesis is to investigate a new measurement setup based on an existing flow channel device introduced by C. Hupf (Hupf, 2018). This system contributes to the technique of impedance-based analysis of 3D tissue models and enables the extraction of significant biological data while providing a time-resolved, non-invasive and label-free measurement of the spheroid response. Apart from sensitive data acquisition and quantification of the dielectric properties of the spheroids, the setup by Hupf requires a difficult handling procedure and lacks the ability to stimulate the spheroids trapped inside the measurement device. To overcome these issues, the orientation of a novel measurement setup should be shifted from a horizontal to an upright position facilitating easy handling and the simultaneous on-line stimulation of multiple spheroids. For this purpose, the choice of the fabrication material and the dimensions of the novel device in combination with an appropriate electrode layout will be adjusted to obtain optimal impedance signals from the measured tissue models. The novel setup should be characterized in detail impedimetrically with and without spheroids while establishing standardized experimental procedures and parameter settings.

Since the development of the new measurement setup should be accompanied by feasible experiments for the measurement and manipulation of spheroids, these test specimens should be characterized in detail. Therefore, key aspects of spheroid formation, proliferation, adhesion, and manipulation will be investigated using time-lapse imaging. The use of spheroids with different sizes or ages will identify the ideal tissue model conditions, which will be used for subsequent experiments, providing a standardized setting for repeatability and comparability of the measurements regardless of the different cell types used. In addition, well-defined variations of the sample in terms of spheroid size, spheroid age and pH should be used to investigate the influence on the impedimetric parameters as well as to validate the result interpretation of the new measurement setup.

To demonstrate the applicability of the novel impedance-based instrument for basic research on 3D tissue models and cytotoxicity assays, the responses of the spheroids to various stimuli with known effects will be tested. This will also demonstrate the key advantage of the newly developed setup, which

should allow direct compound addition during the measurement. The response of the spheroids to the different stimuli will be analyzed based on impedance measurements and correlated with complementary microscopic images, impedance measurements on cell monolayer cultures, or biochemical endpoint assays performed in the context of a defined model study. In this way, different perspectives will be considered, which will provide the framework for comprehensively validating the performance and applicability of the newly developed device.

CHAPTER 3

THEORETICAL BACKGROUND

3.1 ELECTROCHEMICAL IMPEDANCE SPECTROSCOPY 39

3.2 ELECTRICAL PROPERTIES OF TISSUE MODELS 49

3.3 ELECTRIC CELL-SUBSTRATE IMPEDANCE SENSING 55

The fundamental physical background of the impedance spectroscopy technique is essential for designing, optimizing, and applying the investigated measurement system. Thus, the use of appropriate electrical components reflecting the frequency-dependent properties of the system under investigation and the conversion of equivalent circuit diagrams into impedance spectra (and *vice versa*) are described in chapter 3.1. The link between theory and application in the field of tissue models is provided by the description of the equivalent circuit model for spheroids and by the illustration of simulated spectra in chapter 3.2. As a specific application, impedance spectroscopy is used commercially in conjunction with adherent cells in the form of electric cell-substrate impedance sensing, which is theoretically outlined in chapter 3.3.

The content of this chapter describes generally applicable principles, while the conceptual structure, description of the theoretical background, and formula provided in this chapter are adapted from and refer to the theses of Oberleitner (2017) and Hupf (2018).

3.1 ELECTROCHEMICAL IMPEDANCE SPECTROSCOPY

Impedance spectroscopy is used as a measurement principle to investigate the intrinsic electrical properties of a system and its interfaces based on the alternating current resistance, the so-called impedance (Wegener, 1998). Using this measurement technique the imaginary part of the electrical resistance, the impedance, is measured as a function of frequency in a distinct frequency range (e.g. 10^{-3} Hz–10^{8} Hz). To evaluate an impedance spectrum, equivalent circuits are modeled with suitable electrical components (resistor, capacitor, coil, etc.). By connecting these elements in series or parallel in a system-associated circuit model, they can be used to calculate the system-specific parameters by reflecting the frequency-dependent properties of the system under investigation. Impedance spectroscopy uses low-amplitude signals in combination with mainly high-time-resolution data acquisition, which makes the technique non-invasive and very informative for dynamic systems (Lvovich, 2012). In this work, impedance spectroscopy is used to study cells in the form of two-dimensional monolayer cultures and three-dimensional multicellular spheroids.

3.1.1 PHYSICAL BACKGROUND

Impedance is the complex resistance to alternating current (AC) that reflects the ability of an electrical system to resist current flow and store electrical energy. This is the case when an alternating current is applied to a circuit consisting of resistors, capacitors, and inductors. The mathematical description of the complex impedance is based on the resistance of an electrical circuit. According to Ohm´s law, the electrical resistance R is defined as the quotient of the voltage V and the current I when direct current or direct voltage is applied (Eq. 3.1).

$$R = \frac{V}{I} \qquad \textbf{Eq. 3.1}$$

Similarly, for alternating current, the impedance Z is given as the ratio of applied voltage $v(t)$ and resulting current $i(t)$ as a function of time (Eq. 3.2).

$$Z = \frac{v(t)}{i(t)} \qquad \textbf{Eq. 3.2}$$

The sinusoidal AC voltage $v(t)$ and the resulting sinusoidal AC current $i(t)$ are described by the amplitude $\hat{v}$ and $\hat{\imath}$, respectively, at a given time. In the presence of inductive or capacitive elements, the sinusoidal AC voltage induces a phase-shifted AC current with the same frequency; with Φ describing the phase

shift between the two quantities and ω being the angular frequency composed of the frequency *f* of the excitation signal multiplied by 2π (Eq. 3.3, Eq. 3.4; Fig. 3.1).

$$v(t) = \hat{v} \cdot sin(\omega t) = \hat{v} \cdot sin(2\pi f \cdot t) \quad \textbf{Eq. 3.3}$$

$$i(t) = \hat{\imath} \cdot sin(\omega t - \Phi) = \hat{\imath} \cdot sin(2\pi f \cdot t - \Phi) \quad \textbf{Eq. 3.4}$$

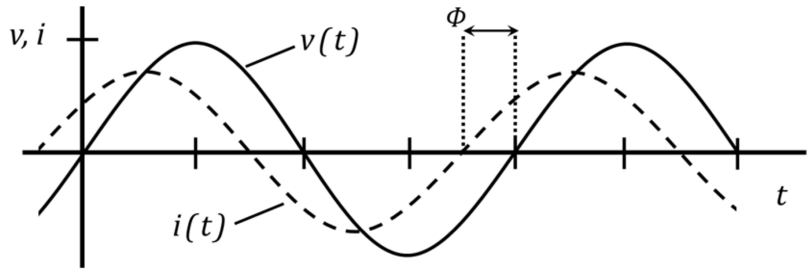

Fig. 3.1 Representation of the sinusoidal AC voltage *v(t)* and the resulting AC current *i(t)*, defined by the amplitude $\hat{v}$ or $\hat{\imath}$ and the phase ϕ. The influence of the coil and capacitor in a circuit results in a phase shift between the voltage and current of $\phi = \pm \pi/2$.

(adapted from Oberleitner, 2017)

Based on Eq. 3.3 and Eq. 3.4, the AC voltage *v(t)* and current $\underline{i}(t)$ are alternatively written as a combination of real and imaginary parts ($j = \sqrt{-1}$) in complex notation (Eq. 3.5, Eq. 3.6).

$$\underline{v}(t) = \hat{v} \cdot [cos(\omega t) + j \cdot sin(\omega t)] = \hat{v} \cdot e^{j(\omega t)} \quad \textbf{Eq. 3.5}$$

$$\underline{i}(t) = \hat{\imath} \cdot [cos(\omega t - \Phi) + j \cdot sin(\omega t - \Phi)] = \hat{\imath} \cdot e^{j(\omega t - \Phi)} \quad \textbf{Eq. 3.6}$$

Consequently, the equations Eq. 3.2, Eq. 3.5, and Eq. 3.6 are used to derive the complex impedance $\underline{Z}$ (Eq. 3.7).

$$\begin{aligned} \underline{Z} &= \frac{\underline{v}(t)}{\underline{i}(t)} = \frac{\hat{v}}{\hat{\imath}} \cdot e^{j\Phi} \\ &= |Z| \cdot e^{j\Phi} \\ &= |Z| \cdot [cos(\Phi) + j \cdot sin(\Phi)] \end{aligned} \quad \textbf{Eq. 3.7}$$

The complex impedance $\underline{Z}$ is described by the quantity $|Z|$ and the phase shift ϕ between the voltage and current whereby both quantities are displayed as functions of frequency in so-called Bode plots, $|Z|(f)$ and $\phi(f)$. According to equation Eq. 3.7, the complex impedance $\underline{Z}$ can be described by the sum of its real part $Re(\underline{Z})$ and imaginary part $Im(\underline{Z})$ (Eq. 3.8, Eq. 3.9).

$$\underline{Z} = |Z| \cdot [cos(\Phi) + j \cdot sin(\Phi)]$$

$$= |Z| \, cos(\Phi) + j \cdot |Z| \, sin(\Phi)$$

$$= Re(\underline{Z}) + j \cdot Im(\underline{Z}) \qquad \textbf{Eq. 3.8}$$

$$= R + j \cdot X \qquad \textbf{Eq. 3.9}$$

Thus, the real part $Re(\underline{Z})$ characterizes the frequency-independent ohmic or effective resistance R of the circuit, which represents the energy loss in the system. The imaginary part $Im(\underline{Z})$ expresses the energy storage in the system and is defined as the reactance X, which is composed of frequency-dependent inductive and capacitive components.

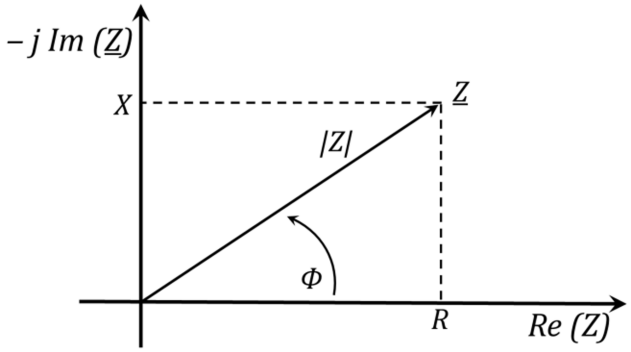

Fig. 3.2 Geometric representation of the impedance in the Gaussian plane in the form of a Nyquist diagram with the x-axis as the real part $Re(\underline{Z})$ and the y-axis as the imaginary part $Im(\underline{Z})$. Using Cartesian coordinates, the impedance is described by the resistance R and reactance X. In polar coordinates, the vector length defines the impedance magnitude $|Z|$ and the angle determines the phase shift ϕ.

(adapted from Oberleitner, 2017)

Apart from the Bode plots $|Z|(f)$ and $\phi(f)$, the complex impedance can also be represented in so-called Nyquist diagrams. Here, the relationship between the real and imaginary parts is displayed by a graphical representation of the complex impedance $\underline{Z}$ in the Gaussian plane (Fig. 3.2). The imaginary part $Im(\underline{Z})$ is plotted as a function of the real part $Re(\underline{Z})$ and the complex impedance $\underline{Z}$ is plotted as a vector in the plane, where its length corresponds to the magnitude of the impedance $|Z|$ and its angle to the phase ϕ of the impedance.

$$|Z| = \sqrt{Re(\underline{Z})^2 + Im(\underline{Z})^2} = \sqrt{R^2 + X^2} \qquad \textbf{Eq. 3.10}$$

$$\Phi = arctan\left[\frac{Im(\underline{Z})}{Re(\underline{Z})}\right] = arctan\left[\frac{X}{R}\right] \qquad \textbf{Eq. 3.11}$$

Using the equations Eq. 3.9, Eq. 3.10, and Eq. 3.11, both approaches for the representation in polar or Cartesian coordinates can be converted into each other. Thus, the four parameters $|Z|$, ϕ, R, and X can be calculated in dependence on each other and used individually for the analysis of an electrical system.

3.1.2 DATA ACQUISITION, REPRESENTATION, AND PROCESSING

The data acquisition methods used in this work, the fundamental ´Electric Impedance Sensing´ (EIS) and the ´Electric Cell-Substrate Impedance Sensing´ technique (ECIS™, see chapter 3.3), are based on the principle of impedance spectroscopy. Both measurement techniques are operated either in continuous wave mode to record the impedance as a function of the frequency from e.g. a trapped spheroid or cell-covered gold film electrodes or in single-frequency mode for recording minor cell shape fluctuations of adherently growing monolayer cells or within spheroids. Both methods use a small amplitude AC voltage so that impedance spectroscopy can be used as a non-invasive method for analyzing biological samples without affecting their electrochemical state (Ende and Mangold, 1993).

Two types of data representation are commonly used in the literature: the Bode plot and the Nyquist diagram as a complex plane plot. In Bode diagrams, the magnitude of the impedance and the phase shift are plotted as a function of the frequency on double- or semi-logarithmic scales, respectively, using a two-dimensional diagram with two y-axes. For complete impedance information, a 3D Bode diagram can be used with perpendicular axes for frequency (x-axis), impedance (y-axis), and phase shift (z-axis). For instance, Oberleitner used 3D Bode plots to display the correlation and time dependence of mechanical cell-substrate interactions and morphological/dielectric changes in a cell layer under study in more detail (Oberleitner, 2017). As another data representation type, a Nyquist plot shows the negative imaginary part of the impedance as a function of the real part on linearly scaled x- and y-axes. It is used to characterize the electrical structure of the system under study, e.g. a semicircle is plotted in the complex plane for a system with resistive and capacitive contributions using either a positive or negative frequency range. Since there is no direct information about the frequency dependence of the real and imaginary parts, an arrow in the direction of increasing frequency values is included in the plot. Compared to the 3D Bode plot, the Nyquist plot can also be combined with a third axis perpendicular to the complex plane for obtaining additional frequency information (Ende and Mangold, 1993).

After recording a series of impedance spectra by ECIS™ and EIS measurements during an experiment, the time-resolved data obtained were processed by *LabVIEW™*-based software (National Instruments™; Austin, Texas, USA) programmed by J. Wegener (Institute of Analytical Chemistry, Chemo- and Biosensors; University of Regensburg, Germany), which extracted the equivalent resistance and the equivalent capacitance value for each AC frequency. The frequency at which the

impedance/resistance/capacitance is most sensitive to the cell layer is obtained by dividing the impedance/resistance/capacitance spectra of a cell-covered electrode by the corresponding spectra of the identical cell-free electrode. These frequencies were used to plot the signal values obtained as a function of time. Furthermore, the time courses were set to a characteristic data point of each experiment, such as the time of cell seeding or cell stimulation, to visualize possible differences in the impedimetric signal amplitude and in the kinetics of value changes. Furthermore, the signal values were normalized with respect to their value of the data point at time zero whereby an absolute signal change was plotted as a percentage, which makes the data more comparable with that derived from other experiments. In general, experiments were repeated several times to form data packages, which were normalized and then averaged as well as statistically evaluated for identifying significant and reproducible effects of the monitored cell population.

3.1.3 IMPEDANCE ELEMENTS IN EQUIVALENT CIRCUITS

The fundamental objective of impedance spectroscopy studies on biological systems is to obtain electrical information that can be translated into specific physical or chemical properties of the system using an appropriate model. Therefore, the electrochemical systems are characterized in the form of equivalent circuit models using ideal and empirical circuit elements, which determine the current flow in an AC circuit and thus the complex impedance. For the three basic circuit elements, ohmic resistor R (I), capacitor C (II), and inductor L (III), an ideal electric behavior is assumed at all frequencies. However, the description of real biological systems requires additional empirical components, such as the constant phase element CPE and Warburg impedance σ (IV).

The individual impedance characteristics as single equivalent circuit elements are shown in Bode and Nyquist diagrams simulated by Oberleitner (Oberleitner, 2017).

I RESISTOR

The ohmic resistor R is considered to comprise the real part of the complex impedance and has no capacitive or inductive properties. Thus, the complex impedance of an ideal resistor $\underline{Z}_R$ has no imaginary component at all AC frequencies and is given by the resistance R. By calculating the impedance using the ratio of voltage and current magnitude, the transfer of Ohm´s law (Eq. 3.1) from DC circuits to AC circuits is reflected (Eq. 3.12).

$$\underline{Z}_R = Re(\underline{Z}) + j \cdot 0 = \frac{\hat{v}}{\hat{\imath}} = R \qquad \textbf{Eq. 3.12}$$

Without any imaginary impedance contribution, no phase shift occurs when using the AC voltage or current (Eq. 3.13).

$$\underline{Z} = R \cdot e^{j\Phi} \rightarrow \phi = \phi_v - \phi_i = 0 \qquad \textbf{Eq. 3.13}$$

The resistive impedance is frequency-independent and only affects the amplitude of the resulting current.

II CAPACITOR

An electrical circuit consisting of an ideal capacitor is free from any resistive influence. In contrast to Ohm´s law for resistors, for capacitors, the resulting current is directly proportional to the voltage change over time (Eq. 3.14). Consequently, the capacitive impedance $\underline{Z}_R$ decreases with increasing frequency and capacitance values (Eq. 3.15).

$$\underline{i} = C \cdot \frac{d\underline{v}}{dt} = C \cdot \underline{v} \cdot j\omega \qquad \textbf{Eq. 3.14}$$

$$\underline{Z}_C = \frac{\underline{v}}{\underline{i}} = \frac{1}{j\omega C} = -j\frac{1}{\omega C} \qquad \textbf{Eq. 3.15}$$

The phase of the capacitive current shifts –90° in relation to the voltage (Eq. 3.16).

$$\phi = \phi_v - \phi_i = -\frac{\pi}{2} \qquad \textbf{Eq. 3.16}$$

In the Nyquist plot, the impedance vector of an ideal capacitor is represented as a straight line along the negative reactance-axis.

III INDUCTOR

Like capacitors, ideal inductors also only possess an imaginary component without any resistance contribution to the impedance. For inductors, the driving voltage is proportional to the current change with time (Eq. 3.17). Thus, the inductive impedance $\underline{Z}_L$ is directly proportional to the frequency (Eq. 3.18) and likewise increases.

$$\underline{v} = L \cdot \frac{d\underline{i}}{dt} = L \cdot \underline{i} \cdot j\omega \qquad \textbf{Eq. 3.17}$$

$$\underline{Z}_L = \frac{\underline{v}}{\underline{i}} = j \cdot \omega L \qquad \textbf{Eq. 3.18}$$

The phase of the inductive current causes a phase shift of 90° with respect to the voltage (Eq. 3.19).

$$\phi = \phi_v - \phi_i = \frac{\pi}{2} \qquad \textbf{Eq. 3.19}$$

The typical Nyquist plot represents the inductive impedance contribution as a straight line along the positive reactance-axis. As an impedance element, the inductor is necessary to describe the piezoelectric properties of an oscillating system with electric equivalents, e.g. in the ´Quartz crystal microbalance´ technique (for more information, also see Oberleitner, 2017).

IV CONSTANT PHASE ELEMENT AND WARBURG IMPEDANCE

The CPE and Warburg impedance elements are empirically determined, non-ideal electrical components in the equivalent circuit. Both elements are often required for modeling the impedance characteristics of real systems to fit the transfer function determined on the basis of the equivalent circuit to the measured data. For example, dielectric inhomogeneity or roughness of the electrodes is considered non-ideal behavior (Lvovich, 2012). The Warburg impedance is used to model the impedance of systems with diffusion limitations of electrochemical reactions (Warburg, 1901). The CPE aims to describe the interfacial impedance of cell membranes as well as systems consisting of electrodes in contact with an electrolyte. Its interface impedance $\underline{Z}_{CPE}$ consists of the frequency-independent parameters A and n (Eq. 3.20).

$$\underline{Z}_{CPE} = \frac{1}{A \cdot (j\omega)^n}, \text{with } n = [0,1] \qquad \textbf{Eq. 3.20}$$

By definition, the phase angle of the CPE is independent of the frequency and thus the phase shift angle between the AC voltage and current varies between 0 and –90° (Eq. 3.21).

$$\phi = -n \cdot \frac{\pi}{2} \qquad \textbf{Eq. 3.21}$$

Concerning the electrical behavior of the CPE, three cases are observed (Lvovich, 2012; Barsoukov and Macdonald, 2005).

- $n = 0$ the CPE describes an ideal resistor
- $n = 1$ the CPE describes an ideal capacitor

- $n =]0,1[$ the CPE displays mixed electrical properties with dominating resistive characteristics for $n < 0.5$ and dominating capacitive characteristics for $n > 0.5$

The CPE is an important component in EIS for developing the equivalent circuit model of biological systems. It adequately describes the non-ideal capacitive characteristics of the electrode-electrolyte interface of metal electrodes covered with physiological buffers or cell culture medium. As summarized by Cole, the phase-constant behavior may be related to the electrolytic behavior of ions in or near cell membranes (Cole, 1972). For $n = 1$, the membrane is considered as a perfect capacitor, whereby the membrane is completely impermeable to ions. For $n = 0$, the CPE represents an ideal resistor, and between these two extrema, the CPE exhibits resistive and capacitive behavior.

3.1.4 EQUIVALENT CIRCUIT MODELS

Equivalent circuit models are used for impedance spectroscopy to obtain electrical information from the system of interest by describing each impedance contribution using a basic circuit element. The theoretical impedance of the entire circuit is expressed mathematically by integrating the impedance contribution of all individual impedance elements used. By applying the resulting algorithmic transfer function, the experimental impedance data are fitted to translate the electrical information of each circuit element into the physical or chemical properties of the corresponding structural component.

To maintain the simplicity of the corresponding equivalent circuit model of complex composed or structured systems, e.g. whole cell biosensors, suitable assumptions are used to model only the part of interest. Thus, simplified models such as the combination of a resistor and a capacitor are applied to either reflect an electrode-electrolyte interface using a serial connection, or to model a cell membrane by connecting both elements in parallel.

The effect of connecting one or two resistors with one capacitor in various combinations on the impedance spectra as well as on the resistance and reactance values are described in the following. Thereby ideal conditions are assumed. For illustration purposes, Oberleitner gives an overview of typical impedance spectra of these basic equivalent circuit models using Bode and Nyquist diagrams (Oberleitner, 2017).

I RESISTOR – CAPACITOR CIRCUIT

An equivalent circuit established for modeling the impedance of an electrode-electrolyte interface is the combination of an ideal resistor and an ideal capacitor connected in series. In this RC model, the

current follows a single pathway and is affected by the resistance contributions of the resistor as well as by the reactance behavior of the capacitor (Eq. 3.22).

$$\underline{Z}_{R-C} = R - j\frac{1}{\omega C} \qquad \textbf{Eq. 3.22}$$

Thereby, the impedance signal is influenced by the capacitance at low frequencies, which is indicated by a negative slope and a phase shift of –90° in the Bode plot. At high frequencies, the ohmic contribution dominates and is indicated by a frequency-independent magnitude and a phase shift of 0°. The corresponding Nyquist diagram of the RC model displays a frequency-independent real part and a frequency-dependent imaginary part shown by a straight line at the value of the resistance R, parallel to the y-axis. In this plot, the increasing influence of the resistance on the total impedance signal with increasing frequency is indicated by an arrow.

II RESISTOR || CAPACITOR CIRCUIT

The impedance contribution of a cell layer is represented by the parallel connection of resistance and capacitance in an equivalent circuit model (Eq. 3.23).

$$\underline{Z}_{R||C} = \frac{1}{\frac{1}{R} + j\omega C} \qquad \textbf{Eq. 3.23}$$

In general, intracellular fluids behave resistively by containing ions capable of conducting current and contributing to power losses at higher frequencies, whereas cell membranes behave like capacitors due to their structure as dielectric materials between two current conducting electrolytes. In this way, two frequency-dependent current pathways are indicated. At lower frequencies, the impedance signal is dominated by the resistance, which reflects the paracellular route along the intercellular gap and across the tight junctions of adherent cells. As the frequency increases, the transcellular current pathway becomes predominant reflecting the entire capacitive contribution of the system. The typical impedance signal in the Nyquist plot forms a semicircle in the complex plane.

III RESISTOR – (RESISTOR || CAPACITOR) CIRCUIT

Upon the combination of more than two electrical circuit elements within an equivalent circuit model, more complex systems can be described. One possible combination of resistor and capacitor elements is the connection of a parallel RC circuit (R_1 and C) with a second resistor R_2 in series (Eq. 3.24).

$$\underline{Z}_{R_2-R_1||C} = R_2 + \frac{1}{\frac{1}{R_1} + j\omega C} \qquad \textbf{Eq. 3.24}$$

This circuit could be used for describing the electrical situation of a cell membrane in contact with an electrolyte, where R_2 represents the resistance of the suspending medium, R_1 characterizes the resistance of cell interiors, and C signifies the cell membrane capacitance. In contrast to the two-component equivalent circuits, the impedance converges in this model at low as well as at elevated frequency levels. At low frequencies, the current flows around the cellular bodies, and the impedance magnitude is determined by the sum of R_1 and R_2 values. In the case of high frequencies, the current passes through the membrane and the impedance is defined by the intracellular fluid resistance R_2. The transition region between these two extremes is dominated by the capacitive properties of the membrane. The Nyquist diagram of the Lapicque-model displays a semicircle signal similar to the parallel RC circuit with an additional fixed ohmic contribution, originating from the second resistor R_2. This results in the impedance not becoming purely imaginary at any frequency.

3.2 ELECTRICAL PROPERTIES OF TISSUE MODELS

The electrical properties of biological tissue models are essential for accurately modeling the interaction of animal or human tissue with electric current. By applying an electrical stimulus, the resulting current densities and pathways are determined by the relative permittivity and specific conductivity of the biological tissue. Thus, the electrical properties are vital for the analysis of a variety of biomedical applications, e.g. functional electrical stimulation, diagnosis, and treatment of various physiological conditions with weak electrical currents, radiofrequency hyperthermia, electrocardiography, and body composition (Abdalla et al., 2010; Miklavčič et al., 2006). Knowledge of these electrical properties enables an understanding of underlying biological processes, as they relate to tissue damage, temperature, blood flow as well as blood vessels. Thus, the electrical properties of tissues have been extensively studied and characterized by researchers (McAdams and Jossinet, 1995). Based on the assumption that the basic properties are also valid for 3D tissue models, the electrical characterization of spheroids is described in this chapter. The scientific findings on this subject were used to derive an equivalent circuit and the corresponding transfer function by adapting the circuit model of two-dimensional cell structures to the electrical properties inside a spheroid.

3.2.1 EQUIVALENT CIRCUIT MODEL FOR SPHEROIDS

As described in chapter 1.2, spheroids are cell aggregates consisting of several hundred to thousands of individual cells connected via cell-cell junctions. The general internal architecture of a spheroid comprises different cell layers in the form of concentric zones with their own microenvironment due to non-existent vascularity (Fig. 3.3).

In terms of electrical properties, Grimnes and Martinsen defined spheroids as a composition of intracellular and extracellular electrolytes separated by the insulating cell membranes (Grimnes and Martinsen, 2008). Thus, the application of an external electric field results in a frequency-dependent current flow through the spheroid, as through a cell monolayer. At low frequencies, the current is forced to flow paracellularly around the individual cell bodies, while it is able to capacitively couple across the cell membranes and flow in a transcellular way at high frequencies (Fig. 3.3).

For describing the electric structure of spheroids with an equivalent circuit, the structural components of the spheroid are associated with resistive and capacitive impedance contributions. The resistive contribution within a spheroid is composed of the intracellular resistance R_{int}, which correlates to the resistance of the cytoplasm, and the extracellular resistance R_{ext}, which reflects the resistance induced

by the current flow through intercellular spaces and the ECM. The total capacitance of the cell membrane A_{sph} corresponds to the non-ideal spheroid capacitance. However, since typical n-values for tissues range from 0.5 to 0.8 (Kyle et al., 1999), the spheroid capacitance is modelled using a constant phase element to adequately characterize it as a biological sample.

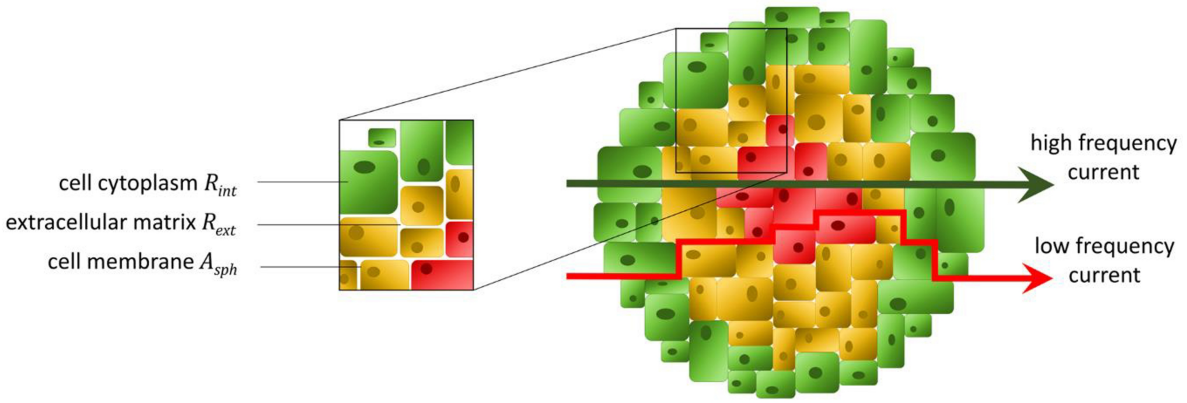

Fig. 3.3 Illustration* of the internal structure of a spheroid in cross-section showing the cellular distribution, the resulting spheroidal microenvironment visualized by color-coding single cells according to their viability (green: viable, yellow: viable/quiescent, red: dead cells), and the frequency-dependent current pathways. The applied current is affected by the impedance contribution within the spheroid as it has to overcome the resistive and capacitive components of the cell membranes (A_{sph}), cell cytoplasm (R_{int}), and extracellular matrix (R_{ext}) of several cells. This leads to a frequency dependence, where the current either flows paracellularly through the spheroid at low frequencies (red arrow) or trans- and paracellularly at high frequencies (green arrow).

*illustration is simplified and not to scale

(adapted in parts from Hupf, 2018)

The equivalent circuit model for describing spheroids was created by adapting the circuit model of Fricke and Morse, which represents the electrical properties of cell suspensions (Fricke and Morse, 1925). By transferring this model to the electric structure of a spheroid and adding a resistor and a capacitance element to describe the surrounding system, the entire experimental measurement setup can be represented (Fig. 3.4; Kyle et al., 1999; Thielecke et al., 2001; Kyle et al., 2004). Accordingly, the equivalent model is based on a serially connected RC circuit consisting of the parameters R_{int} and A_{sph}, which is linked to a second resistor R_{ext}. Additional components such as the electrode capacitance described by a constant phase element A_{el} and the resistance of the surrounding bulk medium R_{bulk} have to be connected in series. To consider the arising parasitic contributions of the electronic readout systems and cables that are used, the constant phase element A_{para} is inserted into the model in parallel to the other elements. The final equivalent circuit was used for fitting the impedance measurement data of the developed spheroid setup.

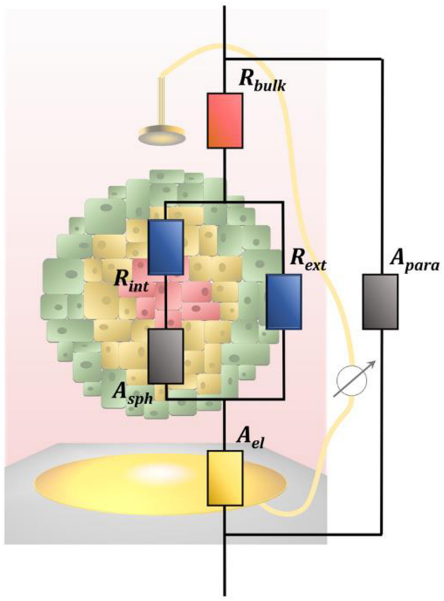

Fig. 3.4 Illustration* of the equivalent circuit model for spheroids in the novel measurement setup for EIS analysis. The impedance contribution of the spheroid is represented by the spheroid capacitance A_{sph} and n_{sph}, the intracellular resistance R_{int}, and the extracellular resistance R_{ext}. Additional circuit elements represent the bulk medium resistance R_{bulk}, the capacitive contribution of the electrode-electrolyte interface A_{el} and n_{el}, and the parasitic contribution A_{para} and n_{para}. The circuit elements can be assigned to the corresponding measurement components based on the underlying figure.

*illustration is simplified and not to scale
(adapted in parts from Hupf, 2018)

3.2.2 DERIVATION OF THE TRANSFER FUNCTION

For the determination of the three spheroid parameters $R_{int} \mid R_{ext} \mid A_{sph}$, the transfer function of the equivalent circuit model has to be fitted to the experimental data obtained. Therefore, the transfer function can be calculated by the stepwise derivation of the single cell impedance to the spheroid impedance in the context of the EIS measurement using Kirchhoff´s law.

First, the impedance of a single cell Z_{cell} is expressed as the sum of its intracellular resistance and membrane capacitance, which is given by the CPE terms A_{mem} and n_{mem} (Eq. 3.25).

$$Z_{cell} = R_{int} + \frac{1}{(i\omega)^{n_{mem}} \cdot A_{mem}} \qquad \textbf{Eq. 3.25}$$

Then, the total impedance of a spheroid Z_{total} can be calculated by composing the total impedance of the cells within the spheroid Z_{sph} and the extracellular resistance along the current pathway (Eq. 3.26).

$$Z_{total} = \left(\frac{1}{Z_{sph}} + \frac{1}{R_{ext}}\right)^{-1} \qquad \textbf{Eq. 3.26}$$

Both equations are combined and subsequently converted, whereby A_{mem} and n_{mem} are replaced by the terms A_{sph} and n_{sph} to represent the total capacitance contribution of the spheroid (Eq. 3.27).

$$Z_{total} = \frac{R_{ext} \cdot \left[R_{int} \cdot (i\omega)^{n_{sph}} \cdot A_{sph} + 1\right]}{(R_{ext} + R_{int}) \cdot (i\omega)^{n_{sph}} \cdot A_{sph} + 1} \qquad \textbf{Eq. 3.27}$$

The electrode capacitance and parasitic contributions of the measurement setup used are considered using constant phase elements, which are added to the equation with the corresponding terms A_{para}, n_{para} and A_{el}, n_{el} (Eq. 3.28).

$$Z_{total} = \left[\frac{1}{Z_{sph} + R_{bulk} + \frac{1}{(i\omega)^{n_{el}} \cdot A_{el}}} + (i\omega)^{n_{para}} \cdot A_{para}\right]^{-1} \qquad \textbf{Eq. 3.28}$$

Finally, the three spheroid parameters can be determined by fitting the transfer function (Eq. 3.28) to the experimental data.

3.2.3 SIMULATED SPECTRA OF SPHEROID PARAMETERS

For illustrating the influence of the spheroid parameters R_{int} | R_{ext} | A_{sph} on the impedance spectra, as well as on their real and imaginary parts in detail, simulations based on the equivalent circuit for spheroids were performed (Tab. 3.1). To this end, the values of these parameters were varied stepwise within a distinct range, while the underlying system parameters, such as the capacitive values of the electrodes or the resistance value of the bulk medium, were kept constant. The values variations were applied using a *LabVIEW™*-based software (National Instruments™; Austin, Texas, USA) programmed by J. Wegener (Institute of Analytical Chemistry, Chemo- and Biosensors; University of Regensburg, Germany) and subsequently processed to visualize the changes in impedance upon variation of the respective spheroid parameter.

The variation of the first parameter R_{ext} affects the impedance as well as the resistance signal magnitude at low frequencies by causing a level increase of the first plateau with increasing extracellular resistance values (Tab. 3.1, A). Since the reactance of the measurement setup without a spheroid is represented monotonically as a linearly decreasing slope, it becomes biphasic with local extrema in the presence of a spheroid. In relation to increasing values of R_{ext}, the reactance curve's minimum and maximum values are shifted to higher signal values and lower frequencies.

Tab. 3.1 Simulated spectra of frequency-dependent impedance $|Z|$, resistance R, and reactance X for the spheroid measurement setup under variation of the parameters R_{int} | R_{ext} | A_{sph}. The data simulation was obtained using the model proposed by Kyle and Thielecke (Kyle et al., 1999; Kyle et al., 2004; Thielecke et al., 2001). Spectra are shown for the spheroid-free setup (w/o spheroid, dashed line) and the spheroid-containing setup (w/ spheroid, solid line). For the simulation, one of the parameters R_{int} | R_{ext} | A_{sph} was varied stepwise, while the other two parameters were kept constant. The default values of the system parameter were chosen as R_{bulk} = 5,400 Ω, A_{el} = 10·10^{-6} Fs^{n-1}cm^{-2}, and n_{el} = 0.90 with an electrode area of 0.2 cm². The standard values of the parameters shown as dashed lines were set as R_{ext} = 50 kΩ, R_{int} = 500 Ω, A_{sph} = 2·10^{-9} Fs^{n-1}cm^{-2}, and n_{sph} = 0.75. The following parameter value ranges shown as solid lines were applied: R_{ext} = 10–100 kΩ, R_{int} = 10–5,000 Ω, and A_{sph} = 20–0.2·10^{-9} Fs^{n-1}cm^{-2}. The direction of the increasing parameter values is indicated using arrows.

(adapted from Hupf, 2018)

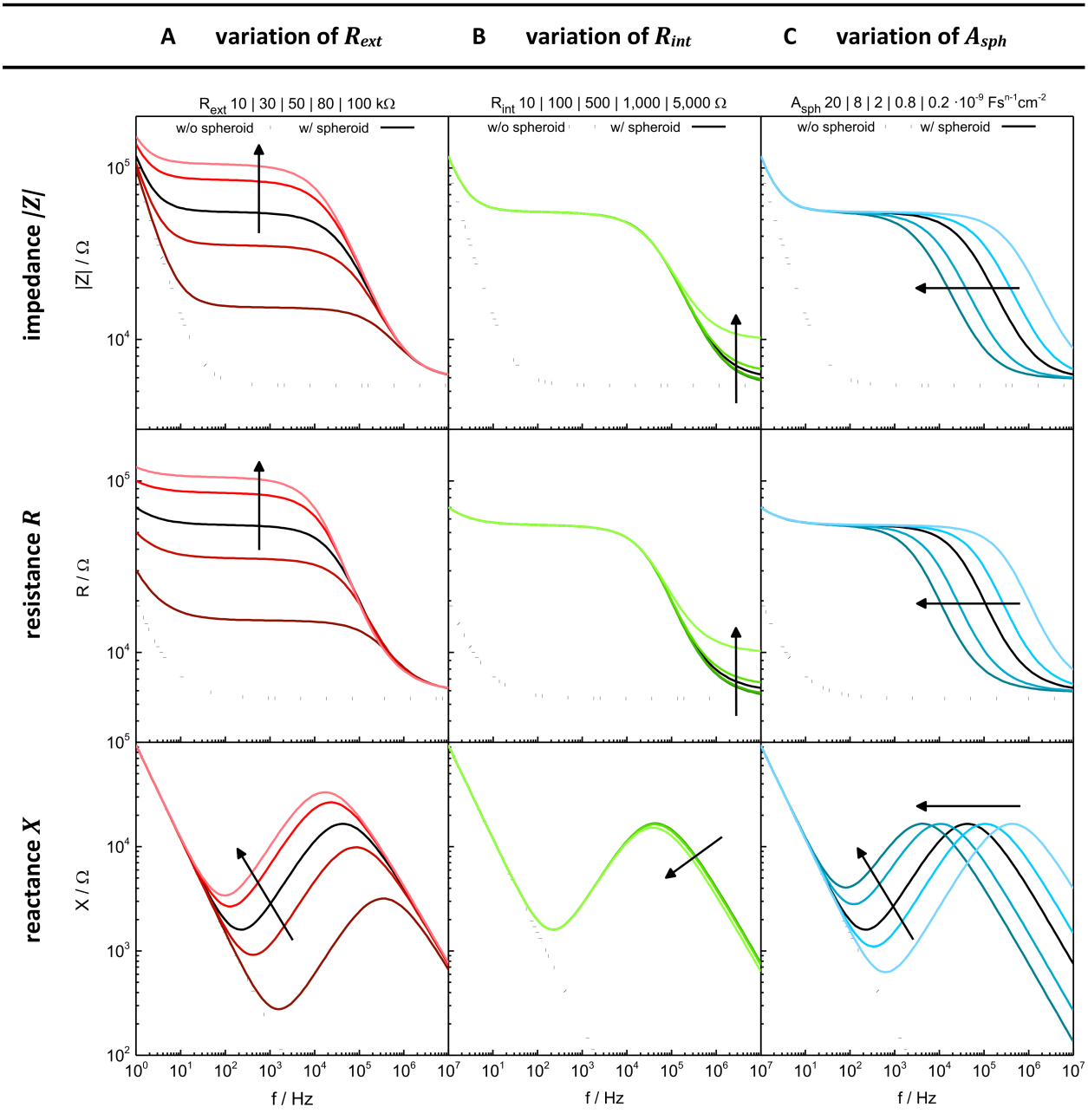

In contrast to the extracellular resistance R_{ext}, the intracellular resistance R_{int} influences the impedance and resistance at very high frequencies (Tab. 3.1, B). An increase in the intracellular resistance values leads to a slight increase in the signal amplitudes of the second plateau, while a steep change can be simulated for values of 5,000 kΩ. The resulting variations in reactance upon increasing R_{int} values are also marginal in the high-frequency range for values between 10–1,000 kΩ. A significant shift of the reactance curve to smaller signal amplitudes and frequencies is obtained by applying the highest value of intracellular resistance.

To simulate the dependence of the impedance spectra on the non-ideal spheroid capacitance A_{sph}, the values of this parameter were varied with a constant n_{sph} value (Tab. 3.1, C). An increase of the capacitance results in a frequency shift of the second linear slope of the impedance as well as resistance signals to lower values and a decrease of the first signal plateau range. The reactance curve is affected by increasing A_{sph} values with a stepwise shift of the minimum and maximum to lower frequencies, while the signal level of the minimum increases.

Based on the simulated data, a detailed overview of the influence of the spheroid's microstructure on the impedance measurements is given, which also provides information on the expected results and facilitates troubleshooting during the development of a new measurement setup.

3.3 ELECTRIC CELL-SUBSTRATE IMPEDANCE SENSING

The ECIS™ principle serves as a label-free and non-invasive measurement technique, which was invented by Giaever and Keese in 1984 and further developed in recent decades (Giaever and Keese, 1984; Wegener et al., 2000b; Lukic and Wegener, 2015). This technique has been widely used as a 'morphological biosensor for mammalian cells' (Giaever and Keese, 1993) in a variety of cell-based applications to study e.g. cell growth, movement, and death. Since it is a very sensitive technique to monitor the barrier functionality changes of adherent cell monolayers, it can be applied for the analysis of different kinds of stimuli, e.g. cytotoxic reagents (Arndt et al., 2004; Campbell et al., 2007; Stolwijk et al., 2012). Therefore, cellular motility such as micromotion can also be analyzed by performing time-resolved readings of impedance fluctuations (Giaever and Keese, 1991; Lo et al., 1993; Tarantola et al., 2010). By utilizing the gold electrodes required for detection, the cultivated cell layers on top can further be actively manipulated and wounded by applying an electrical field. The so-called electroporation can be categorized into the non-destructive and reversible short-term permeabilization and the irreversible damaging of the attached cells on the ECIS™ working electrode(s), depending on the frequency, duration, and magnitude of the applied electrical pulses (Stolwijk, 2011). Thus, a diffusion-driven transfer of cell membrane-impermeable molecules into the cytoplasm can be enabled by a short-term opening of the cellular membranes or a reproducible, well-defined wound is generated for various wound healing assays which are subsequently monitored by ECIS™ (Keese et al., 2004; Wegener et al., 2002; Stolwijk et al., 2011). In combination with other label-free sensing techniques, the ECIS™-like measurements enable further developments: impedance and shear wave resonance analysis of ligand-receptors (Steinem et al., 1997); quartz crystal microbalance in cell biology (Heitmann et al., 2007); multiparametric cell profiling by combining impedance analysis with surface plasmon resonance (Michaelis et al., 2013) or with quartz crystal microbalance (Oberleitner, 2017).

3.3.1 BASIC PRINCIPLES OF ECIS™ MEASUREMENTS

The measurement principle is based on impedance spectroscopy, and the determination of the AC resistance as a function of frequency (see chapter 3.1). For this purpose, a coplanar electrode arrangement with two gold film electrodes is used, which are located on the bottom of the culture substrate and on which the adherent cells are cultivated. A weak and non-invasive AC voltage is applied between the gold electrodes, which are conductively connected via cell culture medium or buffer, and the resulting AC current flow is measured (Fig. 3.5). Thus, the gold surfaces of the working and counter electrode both serve as growth substrates for cells as well as measuring electrodes for determining the complex impedance of the entire system.

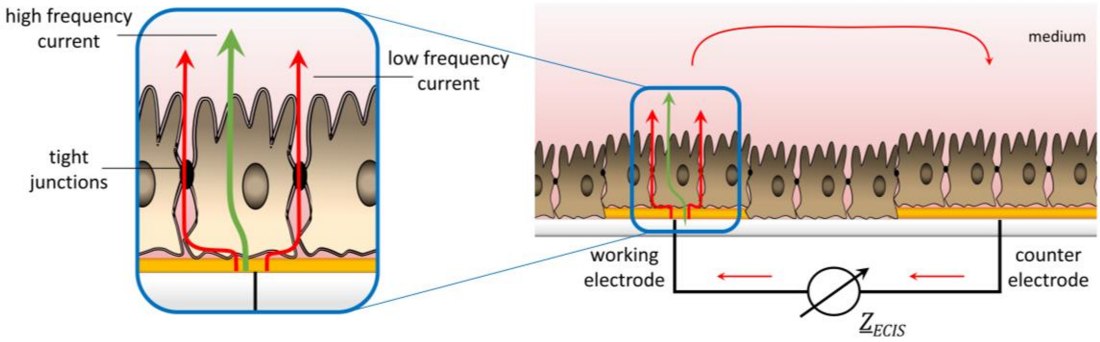

Fig. 3.5 Illustration* of the ECIS™ measurement principle. A counter electrode and a 500–1,000 times smaller working electrode are conductively connected with a buffer or cell culture medium and are used as a culture substrate for adherent cells. By applying an AC voltage to the cell-covered gold electrodes, the resulting current flows in a frequency-dependent manner between the electrodes and across the cell layer. The current either passes through the cells via transcellular pathways at high frequencies (green arrow) or flows beneath and between the cells via paracellular pathways at low frequencies (red arrows) whereby information about their morphological properties is provided by recording the frequency spectra.

*illustration is simplified and not to scale

(adapted from Lukic and Wegener, 2015; Oberleitner, 2017)

By recording the impedance spectroscopically in a wide frequency range, the impedimetric contribution of the system is reflected. Before cell seeding, the impedance spectrum is determined by the bulk resistance of the medium at high frequencies and by the interfacial impedance of the electrodes in the low-frequency range. After cell seeding, the impedance increases with the degree of electrode coverage by the cells, since the cellular bodies act as insulating particles and provide an additional impedance contribution. Like in tissue models, the current pathway across the cell monolayer is determined by the frequency of the applied AC voltage. Thus, the impedance contribution at low frequencies depends on the paracellular pathway, which reflects the electrical properties of the cell-substrate and cell-cell contacts (Fig. 3.5, red arrows) whereas in the higher frequency range, the entire transcellular impedance of the cell monolayer is determined (Fig. 3.5, green arrow).

The ECIS™ technique is very sensitive to cellular processes occurring at the small working electrode due to the proximity of the electrodes to the cells and the size difference between the electrodes themselves. Since the working electrode is approximately 500–1,000 times smaller than the counter electrode, the impedance of the system is not dominated by the bulk resistance of the electrolyte between the electrodes. Also, the impedance contribution from the counter electrode can be neglected and the interfacial impedance between the working electrode and the electrolyte determined, which is influenced by the electrical properties of the attached cells (Lukic and Wegener, 2015). The impedance sensitivity increases with decreasing size of the working electrode, which defines the number of cells measured. Since the electrical properties of only a few cells may not be representative of the whole cell

layer, the electrode size must be adapted to the individual requirements of the experiment by using different types of commercially available ECIS™ arrays (Applied BioPhysics, Inc. (Troy, USA)).

3.3.2 EQUIVALENT CIRCUIT MODEL OF CELL MONOLAYERS

The measurement system of a cell-covered gold electrode is characterized by a corresponding ECIS™ model, which was first introduced by Giaever and Keese in 1991 (Fig. 3.6; Giaever and Keese, 1991).

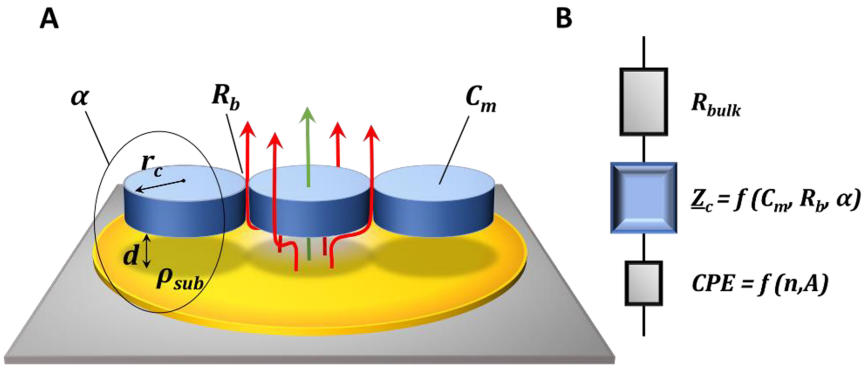

Fig. 3.6 Illustration* of the ECIS™ model (A) and the resulting equivalent circuit diagram (B) for a cell-covered gold electrode. The impedance of the system is composed of the ohmic resistance of the solution R_{bulk}, the impedance of the cell layer Z_c, and the capacitance of the electrode-electrolyte interface CPE, which are connected in series as impedance elements. In the ECIS™ model, the cells are considered cylindrical disks with a uniform height, radius r_c, and distance d from the electrode. The additional impedance contribution of the cell layer is characterized using the parameters C_m (contribution of the cell membrane capacitance), R_b (contribution of the paracellular barrier resistance), and α (contribution of the cell-substrate contact).

*illustration is simplified and not to scale

(modified after Giaever and Keese, 1991; Oberleitner, 2017)

In the ECIS™ model, the cells are approximated as cylindrical bodies of uniform size and radius r_c, located at a certain distance d from the electrode surface. At frequencies above 10 kHz, parts of the current flow in a transcellular way through the cell layer. The cell membrane exhibits dielectric properties depending on the morphology of the plasma membrane and therefore provides a capacitive contribution C_m to the impedance of the cell layer. Below 10 kHz, the current flows paracellularly between the cell-cell contacts and along the gap between the cell layer and the electrode surface. Here, the resistance of the cell-cell contact R_b increases for strongly barrier-forming cell types and the impedance contribution of the cell-substrate contact α increases with decreasing distance of the cell layer from the surface.

Based on the ECIS™ model, the equivalent circuit was developed considering the electric properties of the cell-electrode interface and structural elements of an adherent cell monolayer. The impedance spectrum of a cell-free electrode can be described with an RC equivalent circuit, where the capacitor

represents the capacitance of the electrode, and the resistor characterizes the bulk resistance of the electrolyte. To reflect the non-ideal behavior of the electrode, the capacitance was substituted by a CPE element according to the proposal of Wegener et al. (Wegener et al., 2000a). After cell seeding, the impedance of the entire system increases due to an insulating effect of the cell monolayer upon the electrode surface. Therefore, an additional impedance contribution Z_C has to be considered in the equivalent circuit depending on the three characteristic parameters C_m, R_b, and α arising from the cell layer. The electrical properties of the cell-substrate contact α are defined as a function of the average cell radius r_c, the specific resistivity of the subcellular electrolyte ρ_{sub}, and the cell-electrode distance d (Eq. 3.29).

$$\alpha = r_c \cdot \sqrt{\frac{\rho_{sub}}{d}} \qquad \textbf{Eq. 3.29}$$

The total impedance of the cell-covered electrode is composed of six parameters (α, R_b, C_m, n, A_{CPE}, and R_{bulk}) and Bessel functions of the first kind of order 0 and 1, which are solutions of Bessel´s differential equation and are used for solving problems in cylindrical coordinate systems (Giaever and Keese, 1991). The values of these certain parameters are determined by recording the impedance spectra of the cell-free and cell-covered electrodes over a distinct frequency range and fitting the ECIS™ model to the experimental data.

Simulations were performed by Stolwijk to demonstrate the individual influence of the three cell-related parameters on the shape of the impedance spectra of a cell-covered electrode (Stolwijk, 2012). Thus, the model is utilized to differentiate between the individual contributions of the cell-cell and cell-substrate contacts, and the plasma membrane. Using this approach, Reiß characterized the behavior and morphology of different cell types depending on the determined values of the distinctive cell-related parameters (Reiß, 2004).

CHAPTER 4

MATERIALS AND METHODS

4.1 CELL CULTURE TECHNIQUES 61

4.2 MICROSCOPIC TECHNIQUES 70

4.3 IMPEDANCE ANALYSIS: MEASUREMENT MODES AND DEVICES 77

In this chapter, a detailed overview of each preparation and manufacturing step is given by specifying the materials used (e.g. cell lines, chemicals, instrumental equipment) as well as the applied methods (e.g. manufacturing protocols, technical settings).

This chapter describes general protocols and performance strategies based on the scripts utilized in the research group of Prof. Wegener (Institute of Analytical Chemistry, Chemo- and Biosensors; University of Regensburg, Germany).

4.1 CELL CULTURE TECHNIQUES

For the experiments included in this thesis, two different cell lines were chosen with which multicellular spheroids could be formed. Both cell lines exhibit different characteristics and have distinct subcultivation protocols. In this context, spheroid formation in general, modified spheroids, and cell-manipulating substances are described.

4.1.1 CELL LINES

In this thesis, two different types of multicellular spheroids were formed and analyzed using the U-373 MG (*Uppsala*) and MCF-7 (*Michigan Cancer Foundation-7*) cell lines.

U-373 MG cells were isolated by J. Pontén and associates in 1966 from the malignant human brain tumor (glioblastoma-astrocytoma) of a 50-year-old Caucasian man using the explant technique. The cell line displays pleomorphic characteristics with small, accumulated cells and large flat cells forming a prominent glial pattern on an adhesive surface (Bigner et al., 1981), while building tightly packed, rounded spheroids in 3D. By endogenously expressing the human histamine 1 receptor (hH1R; Arias-Montaño et al., 1994), U-373 MG cells can be used for research on g-protein-coupled receptors (GPCRs). The U-373 MG cells used in this thesis were kindly provided by the research group of Prof. Buschauer (University of Regensburg, Germany).

MCF-7 cells are human breast adenocarcinoma cells isolated from the pleural effusion of a 69-year-old Caucasian woman with metastatic disease. This epithelial cell line was established in 1973 by H. Soule and colleagues as the first stable mammary cell line with adherent growth behavior (Soule et al., 1973). These cells express the adhesion molecule E-cadherin and grow with a polygonal morphology while also forming tightly packed, rounded spheroids (Lee et al., 2010). The cell line is mainly used for the *in vitro* investigations of breast cancer therapy and estrogen response regarding their characteristic expression of estrogen receptors (Levenson and Jordan, 1997; Comşa et al., 2015). The MCF-7 cells were kindly provided by Prof. Göpferich (University of Regensburg, Germany).

4.1.2 GENERAL CULTURE CONDITIONS

According to the general requirements, the cell culture work was performed under sterile conditions in a laminar flow hood (HERAsafe, Thermo Fisher Scientific). All consumables, cell media, and other solutions were purchased sterile, autoclaved (120 °C, 20 min; autoclave DX-45, Systec GmbH & Co. KG), or passed through a sterile filter with a pore diameter of 0.2 µm (Techno Plastic Products AG). The cell

lines were cultured on the bottom of sterile polystyrene culture flasks (25 cm^2 + 4 mL medium or 75 cm^2 + 12 mL medium; Sarstedt AG & Co. KG) and kept in cell culture incubators (Heraeus Function Line, Thermo Fisher Scientific) at 37 °C and 5 % CO_2 in a humidified atmosphere. The cell culture medium (see Tab. 4.1 for the composition) was exchanged at least every third day.

Tab. 4.1 Cell culture medium composition for the U-373 MG and MCF-7 cell lines.

cell line	**culture medium composition**	**cell line**	**culture medium composition**
U-373 MG cell line	MEM-Eagle incl. 1 g/L glucose incl. 2.2 g/L $NaHCO_3$ + 5 % (v/v) FCS + 100 μg/mL penicillin + 100 μg/mL streptomycin + 2 mM L-glutamine	MCF-7 cell line	MEM-Eagle incl. 1 g/L glucose incl. 2.2 g/L $NaHCO_3$ + 10 % (v/v) FCS + 100 μg/mL penicillin + 100 μg/mL streptomycin + 2 mM L-glutamine + 1 mM pyruvate

4.1.3 SUBCULTIVATION

The subcultivation of the U-373 MG and MCF-7 cell lines was performed once weekly according to individual subculturing protocols and general cell culture work conditions. All physiological buffers, solutions, and culture media were pre-warmed to 37 °C in a water bath (water bath TW12, Julabo GmbH) before they were added to the cells (see Tab. 4.2 for the composition).

Tab. 4.2 Composition of the subcultivation solutions.

solution	**composition**
Dulbecco´s Phosphate Buffered Saline (PBS^{--})	0.2 g/L KCl 0.2 g/L KH_2PO_4 8.0 g/L NaCl 1.15 g/L Na_2HPO_4
ethylenediaminetetraacetic acid (EDTA) solution	1 mM EDTA in PBS^{--}
trypsin solution	0.025 % (w/v) trypsin in EDTA solution

To detach the cells from the culture substrate, the cell monolayer was washed twice with phosphate-buffered saline solution (Dulbecco´s Phosphate Buffered Saline without Mg^{2+} or Ca^{2+} ions, PBS^{--}; Sigma-

Aldrich Chemie GmbH) which was subsequently followed by enzymatic digestion with trypsin at 37 °C (U-373 MG: 3–5 min; MCF-7: 5–7 min; Sigma-Aldrich Chemie GmbH). The digestion process was stopped by the addition of the culture medium in ten-fold excess. The cell suspension was transferred into a centrifuge tube (centrifuge tube CELLSTAR®; Greiner Bio-One GmbH) and centrifugated at room temperature (U-373 MG: 10 min, 110 x g; MCF-7: 5 min, 200 x g; centrifuge Heraeus Multifuge 1 S-R, Thermo Fisher Scientific). After discarding the supernatant, the cell pellet was resuspended in a fresh culture medium. The cell suspension was transferred to fresh culture flasks and diluted with a ratio of 1:10 (U-373 MG) or 1:20 (MCF-7) in the culture medium relative to the original cell density per cm^2.

To generate multicellular spheroids or to cultivate cells on culture substrates for further measurements, cells were seeded in defined cell numbers for which a haemocytometer (Bürker, Paul Marienfeld GmbH & Co. KG) was used to count the suspended cells during the course of the subcultivation. Consequently, the cell suspension was diluted respectively to the required cell density and either seeded onto non-adhesive surfaces to form spheroids (chapter 4.1.5) or on culture substrates with integrated electrodes (chapter 4.3.5).

4.1.4 CRYOPRESERVATION

The cryopreservation of adherently growing U-373 MG or MCF-7 cells was performed according to a standardized protocol. After detaching the cells from standard culture flasks and centrifugation according to the respective subculture protocol (chapter 4.1.3), the cell pellet was resuspended in a cryoprotective solution consisting of 90 % (v/v) fetal calf serum (FCS; Sigma-Aldrich Chemie GmbH; Biochrom AG) and 10 % (v/v) dimethyl sulfoxide (DMSO*;* Carl Roth GmbH & Co KG). The cell suspension was aliquoted into cryovials (1.5–2 mL; Techno Plastic Products AG), followed by a slow cooling phase (1 °C/min) at –70 °C using an isopropanol bath (Nalgene® CryoBox™, Sigma-Aldrich Chemie GmbH). Afterwards, the cryovials were transferred into a liquid nitrogen tank (GC-BR2150 M, Jutta Ohst german-cryo GmbH) for long-term storage.

To recultivate the frozen cells, the respective cryovial was kept at –20 °C for 1–2 h and subsequently subjected to rapid thawing in a water bath at 37 °C. The cell suspension was transferred into a centrifugation tube and pre-warmed culture medium was added dropwise to a ten-fold excess. After centrifugation, the cell pellet was resuspended in fresh culture medium and cells were seeded in culture flasks at different ratios of 1:2, 1:4, 1:8, and 1:10 relative to the growth area prior to freezing. Twenty-four hours after cell thawing, the culture medium was exchanged, and the cells were incubated until they reached ~90 % confluence after which subcultivation was performed according to the respective protocol (chapter 4.1.3).

4.1.5 FORMATION OF SPHEROIDS

The formation of multicellular spheroids of U-373 MG and MCF-7 cells was achieved by applying the commonly used technique of cell seeding onto ultra-low attachment plates. Hence, standard cell culture plates (96-well plate; Sarstedt AG & Co. KG) were coated with heated 1.5 % agarose solution (50 µL/well, solution in respective serum-free culture medium; Sigma-Aldrich Chemie GmbH) directly before cell subcultivation. After the cell subcultivation process following the respective protocol (chapter 4.1.3) and cell counting, the cell suspension was diluted to specific cell densities using fresh culture medium supplemented with HEPES (4-(2-hydroxyethyl)-1-piperazineethane-sulfonic acid) buffer (20 mM; Carl Roth GmbH & Co. KG). This supplement was necessary because the seeded cells were kept in an incubator without CO_2 during the first day of the spheroid-formation process. The diluted cell suspension was transferred into the wells of the prepared non-adhesive 96-well plate (200 µL/well), which were sealed with Parafilm® (Pechiney Plastic Packaging) and kept in an incubator at 37 °C without CO_2. To enhance the cell aggregation, the plate was rotated directly after cell seeding using an orbital shaker (4 h at 120 rpm; overnight at 50 rpm; orbital shaker KM-2 AKKU, Edmund Bühler GmbH). Afterwards, the 96-well spheroid plate was incubated in a standard cell culture incubator at 37 °C and 5 % CO_2 for at least five days.
In the following, spheroids are clearly defined by their cell type, seeding density per well (abbreviated as "c/well") and duration of incubation from cell seeding or spheroid formation, respectively.

4.1.6 GROWTH STUDIES OF SPHEROIDS

Different growth studies were performed for the U-373 MG and MCF-7 cell lines by generating spheroids containing various cell numbers, using different serum concentrations or pH values, or as co-culture spheroids (Tab. 4.3). The spheroid formation process was performed in agarose-coated 96-well plates following the spheroid formation protocol (chapter 4.1.5). For monitoring the growth behavior, the individual spheroid models were documented for eight days using a phase contrast microscope (Nikon Diaphot, Nikon Instruments Inc.) with an attached digital camera. The evaluation of the spheroid diameters and other parameters was achieved by applying *ImageJ* software (Rasband, W.S., National Institutes of Health, USA).

I SPHEROIDS FORMED WITH DIFFERENT CELL NUMBERS

Spheroids with different cell numbers were generated by diluting the respective cell suspension to appropriate cell densities using a culture medium supplemented with HEPES buffer. Distinct cell

numbers in an individual concentration range were taken (U-373 MG: 18,000–45,000 c/well; MCF-7: 4,000–20,000 c/well; Tab. 4.3).

Tab. 4.3 Overview of the different U-373 MG and MCF-7 spheroid models.

	spheroid models	U-373 MG cell line	MCF-7 cell line
I	spheroids formed with different cell numbers [$\cdot 10^3$ c/well]	18 | 20 | 25 | 30 | 35 | 40 | 45	4 | 10 | 12 | 14 | 16 | 18 | 20
II	spheroids exposed to different serum concentrations [% (v/v)]	0 | 2.5 | 5.0 | 10.0	—
III	spheroids exposed to different pH values	6.6 | 6.8 | 7.0 | 7.2 | 7.4 | 7.6 | 7.8	—
IV	co-cultured spheroids [ratio of U-373 MG to MCF-7 cells]	5:1 | 3:1 | 1:1 | 1:3 | 1:5	

II SPHEROIDS EXPOSED TO DIFFERENT SERUM CONCENTRATIONS

U-373 MG spheroids were prepared with similar cell numbers and various serum concentrations. The cell suspension was diluted to 30,000 c/well using a culture medium supplemented with HEPES buffer (20 mM; Carl Roth GmbH & Co. KG) and specific concentrations of FCS (0–10.0 % (v/v)).

III SPHEROIDS EXPOSED TO DIFFERENT PH VALUES

To form and incubate spheroids with similar cell numbers and different pH values, the cell suspension was diluted to 30,000 c/well (U-373 MG cells) using a culture medium supplemented with HEPES buffer (20 mM; Carl Roth GmbH & Co. KG) and distinct pH values (pH 6.6–7.8).

IV CO-CULTURED SPHEROIDS

Co-cultured spheroids were prepared with a total cell number of 24,000 c/well and different ratios of U-373 MG to MCF-7 cells (5:1–1:5). The cell suspensions of each cell line were diluted respectively using the required culture medium supplemented with HEPES buffer (20 mM; Carl Roth GmbH & Co. KG). After combining both cell suspensions, the mixed cells were seeded into the non-adhesive wells.

4.1.7 PREPARATION OF BUFFERS AND SOLUTIONS

In addition to specific solutions for cell subcultivation, other chemical solutions were used to perform manipulating model studies or to stain cells. An overview of these distinct substance solutions and their stock concentrations and applications are shown in Tab. 4.4.

Tab. 4.4 Overview of the substances used, the respective solvent with which the stock solution was diluted and applications in this thesis.

substance	supplier	stock solution	application
bovine serum albumin (BSA)	Sigma-Aldrich Chemie GmbH	diluted with PBS^{++}/glc or L-15	cell adhesion inhibitor: impedance model studies
cytochalasin D	Sigma-Aldrich Chemie GmbH	diluted with DMSO	actin polymerization inhibitor: impedance model studies, time-lapse microscopy
glutaraldehyde (GA)	Sigma-Aldrich Chemie GmbH	diluted with PBS^{++}/glc	cell fixation: impedance model studies
saponin	Sigma-Aldrich Chemie GmbH	diluted with PBS^{++}/glc	cell permeabilization: impedance model studies, time-lapse microscopy, viability assay
Triton™ X-100	Sigma-Aldrich Chemie GmbH	diluted with PBS^{++}/glc	cell permeabilization: viability assay
Alexa Fluor™ 488 phalloidin	Invitrogen™, Thermo Fisher Scientific	diluted with PBS^{++}/glc	cell staining: cytoskeleton (actin filaments)
calcein acetoxy-methyl ester (CaAM) and	LIVE/DEAD™ Viability/ Cytotoxicity Kit; Invitrogen™, Thermo Fisher Scientific	diluted with PBS^{++}/glc	cell staining: viability (vital cells)
ethidium homo-dimer-1 (EthD-1)		diluted with PBS^{++}/glc	cell staining: viability (dead cells)

The effect of osmotic pressure on spheroids and cell monolayer culture was studied using hyperosmotic buffer solutions with varying osmolality levels in contrast to physiological isotonic osmolality in the

range of 260–320 mosmol/kg (Freshney, 2010). Therefore, buffer solutions with different concentrations of sucrose solutions were prepared using the standard buffer PBS^{++} supplemented with D-glucose (1 g/L; PBS^{++}/glc; Merck KGaA). To obtain the same baseline impedance values in EIS measurements, the conductivity of each sucrose buffer solution was adjusted to 15.85 mS/cm of the isoosmotic buffer (298.7 ± 0.6 mosmol/kg, without sucrose). The measurements were performed with an electrical conductivity meter (inoLab Multi 720, WTW Weilheim) at 25 °C, while adding various quantities of sodium chloride solution (1.5 M in PBS^{++}/glc; Merck KGaA) until the specific conductivity reached a value close to that of the corresponding isotonic solution. As the final differences in conductivity measured were very small, no effect in terms of specific conductivity on cellular behavior was expected. For cell manipulation, the working concentrations of the sucrose buffer solutions had to be adjusted to the given experimental setup to obtain the similar final osmolality values after compound addition (see Tab. 4.5). Therefore, two- and fivefold higher concentrated sucrose buffer solutions were prepared, which were diluted during the compound addition to the cell models with the following dilution factors respectively: ECIS™-based measurement setup: 1:2; time-lapse microscopy: 1:2; funnel-based measurement setup: 1:5. The hyperosmotic buffer solutions that were prepared were passed through a sterile filter with a pore diameter of 0.2 µm (Techno Plastic Products AG) and stored at 4 °C.

Tab. 4.5 Measured osmolality values of the prepared hyperosmotic buffers with various sucrose concentrations (mean ± SD, n = 3). The conductivity was adjusted to 15.85 mS/cm of the isoosmotic buffer. Buffers were used in distinct mixture ratios to obtain similar final values for the specific requirements (ECIS™-based measurement setup: 1:2; time-lapse microscopy: 1:2; funnel-based measurement setup: 1:5).

final sucrose concentration	**osmolality pure**	**sucrose concentration used**	**osmolality 1:2**	**sucrose concentration used**	**osmolality 1:5**
[mM]	[mosmol/kg]	[mM]	[mosmol/kg]	[mM]	[mosmol/kg]
20	318 ± 1	40	324 ± 3	100	319 ± 3
50	348 ± 3	100	354 ± 4	—	—
100	404 ± 4	200	411 ± 4	500	414 ± 6
200	524 ± 5	400	522 ± 7	1000	520 ± 10
300	650 ± 10	600	650 ± 10	—	—
400	780 ± 10	800	770 ± 20	—	—
500	910 ± 20	1000	900 ± 30	—	—

For verifying the similar final osmolality values after applying the respective dilution factor in dependence of the respective measurement setup, the osmolality values after diluting the two- or

fivefold higher concentrated sucrose buffer solutions were determined (Tab. 4.5) using a cryoscopic osmometer (Osmomat™ 030, Gonotec Meß- und Regeltechnik GmbH).

4.1.8 CELL VIABILITY ASSAY FOR 2D AND 3D TISSUE MODELS

For the determination of the metabolic activity of spheroids and 2D cell culture, the PrestoBlue™ cell viability assay (Invitrogen™, Thermo Fisher Scientific) was applied. It is based on the cell membrane-permeable and non-fluorescent redox indicator resazurin. In contact with vital cells, the compound is reduced within the cytoplasm to pink resorufin with a strong fluorescence ($\lambda_{exc} \approx 535$ nm, $\lambda_{em} \approx 615$ nm) whereby the detected fluorescence intensity directly correlates with the amount of vital and metabolically active cells within a spheroid or cell monolayer.

In this thesis, the PrestoBlue™ HS Cell Viability Reagent was used to determine the effect of saponin on U-373 MG and MCF-7 spheroids as well as on cell monolayer viability, respectively. The assay was performed in combination with 2D cell culture by seeding U-373 MG (100,000 c/cm², 200 µL/well) or MCF-7 (100,000 c/cm², 200 µL/well) cells into columns 1–11 of a 96-well plate (Sarstedt AG & Co. KG). Correspondingly, an agarose-coated 96-well plate loaded with five- to six-day-old U-373 MG (18,000 c/well) or MCF-7 (4,000 c/well) spheroids in columns 1–11 was used. One day before the experiment, the medium in each well was exchanged for fresh cell culture medium (200 µL/well). To adapt the cells or spheroids to the solutions buffer, the medium was replaced by PBS^{++}/glc (200 µL/well) three hours prior to exposure to saponin.

Tab. 4.6 Pipetting scheme for a 96-well plate with (w/) and without (w/o) cells (2D) or spheroids (3D) incubated with saponin (diluted with PBS^{++}/glc), Triton™ X-100 (diluted with PBS^{++}/glc), or PBS^{++}/glc.

column	well content 2D | 3D		column	well content 2D | 3D	
1	0.3 | 3 mg/mL saponin	w/	7	0.005 | 0.05 mg/mL saponin	w/
2	0.1 | 1 mg/mL saponin	w/	8	0.003 | 0.01 mg/mL saponin	w/
3	0.07 | 0.5 mg/mL saponin	w/	9	0.001 | 0.005 mg/mL saponin	w/
4	0.05 | 0.3 mg/mL saponin	w/	10	0.5 | 2 % (v/v) Triton™ X-100	w/
5	0.03 | 0.2 mg/mL saponin	w/	11	PBS^{++}/glc	w/
6	0.01 | 0.1 mg/mL saponin	w/	12	PBS^{++}/glc	w/o

For the experiment, the buffer was exchanged by transferring saponin, Triton™ X-100 (positive control), and buffer solution (PBS^{++}/glc; negative control) into the wells (200 µL/well; in PBS^{++}/glc; Tab. 4.6). The

plate was incubated for five hours at 37 °C and 0 % CO_2. After completion of the incubation, the supernatant in each well was carefully removed and the wells containing spheroids or cell monolayers were washed with PBS^{++}/glc (200 µL/well). Subsequently, the PrestoBlue™ HS Cell Viability Reagent was added in each well (150 µL/well, diluted 1:10 [cell monolayer] or 1:8 [spheroid] with PBS^{++}/glc) and incubated for one hour (cell monolayer) or one day (spheroid) at 37 °C and 0 % CO_2. The fluorescence was measured using a microplate reader (GENios™, Tecan Group Ltd.) in top read mode ($\lambda_{exc} \approx 532$ nm, $\lambda_{em} \approx 600$ nm).

In a proof-of-principle study, the invasiveness of cytochalasin D on the metabolic activity of MCF-7 spheroids was investigated. The PrestoBlue™ cell viability assay was conducted on the basic protocol described either five hours or ten hours after the addition of cytochalasin D solutions at different concentrations (0.02–5 µM; see the pipetting scheme Tab. A-4.1).

In the case of saponin treatment, the experiments described were repeated three times in combination with cell monolayers or spheroids of every cell line and every experiment was evaluated individually for the data analysis. For the concept study of cytochalasin D the spheroids were incubated with different concentrations of the compound for either five or ten hours, respectively, and the measured fluorescence intensities were evaluated individually. Therefore, the measured fluorescence intensities of each column were verified by applying the Grubbs´ test for outliers (confidence level: 90 %), averaged, and then corrected by the averaged value of wells without cells or spheroids. The cytotoxicity index (CI) reflects the viability of cells or spheroids after the treatment. This index was calculated for every concentration (Eq. 4.1) using the corrected average intensity of treated cells I_{sample} while the corrected average intensity of non-treated cells served as a negative control $I_{control}$.

$$CI\ [\%] = \left(1 - \frac{I_{sample}}{I_{control}}\right) \cdot 100 \qquad \textbf{Eq. 4.1}$$

For evaluating the concentration of the half-maximum response EC_{50}, the CI values were plotted as a function of the logarithmic saponin concentrations and fitted by applying the dose-response sigmoidal Boltzmann transfer function (Eq. 4.2). The fitting parameters describe the signal response y at a given concentration x with a minimal response A_1, a maximal response A_2, point of inflection x_o (as EC_{50}), and the slope dx indicating the range in which the transition between top and bottom occurs.

$$y = A_2 + \frac{A_1 - A_2}{1 + e^{(x - x_0)/dx}} \qquad \textbf{Eq. 4.2}$$

The resulting EC_{50} values of all three individual experiments were combined by calculating the weighted arithmetic mean.

4.2 MICROSCOPIC TECHNIQUES

Several microscopes with different microscopic modes were applied for distinct purposes. In addition to laboratory routine analysis for monitoring the growth behavior of spheroids or spheroid placement for EIS measurements, they were also used for live cell imaging of the spheroid treatment with different stimuli. By performing cytochemical staining, individual cellular regions or cell viability were observed using fluorescence microscopy.

4.2.1 MICROSCOPES

An overview of all utilized microscopes with their specifications is provided in Tab. 4.7.

Tab. 4.7 Overview of microscopes used with their respective manufacturers and specifications (microscopy mode, setup, and objectives/magnification).

	microscope	manufacturer	mode	setup	objectives/ magnification
I	Nikon Eclipse 90i	Nikon Instruments Inc.	confocal laser scanning microscopy	upright	plan, 10x/0.25
II	Nikon Diaphot	Nikon Instruments Inc.	phase contrast microscopy	inverted	plan, 4x/0.13
III	Nikon SMZ 1500	Nikon Instruments Inc.	stereomicroscopy	upright	0.75x–1.25x
IV	Digital USB	Shenzhen Supereyes Technology Co. Ltd	digital microscopy, portable	optional	10x–500x
V	zenCELL owl	innoME GmbH	digital microscopy	upright	10x

I CONFOCAL LASER SCANNING MICROSCOPY

The Nikon Eclipse 90i microscope was required for visualizing the fluorescence of cytochemical stained spheroids and is based on the principle of confocal laser scanning microscopy (CLSM, Fig. 4.1). Using this technique, three-dimensional images of spheroids could be modelled by recording a set of confocal images from the specimen with a high resolution along the optical axis (z-stack). Three lasers with monochromatic light for fluorophore excitation at 408 nm, 488 nm, and 543 nm as well as three detectors at 450/35 nm (bandpass), 515/30 nm (bandpass), and 650 nm (longpass) are installed. The

microscope is connected to an ordinary computer for image acquisition and data storage controlled by the *EZ-C1* software (Nikon Instruments Inc.).

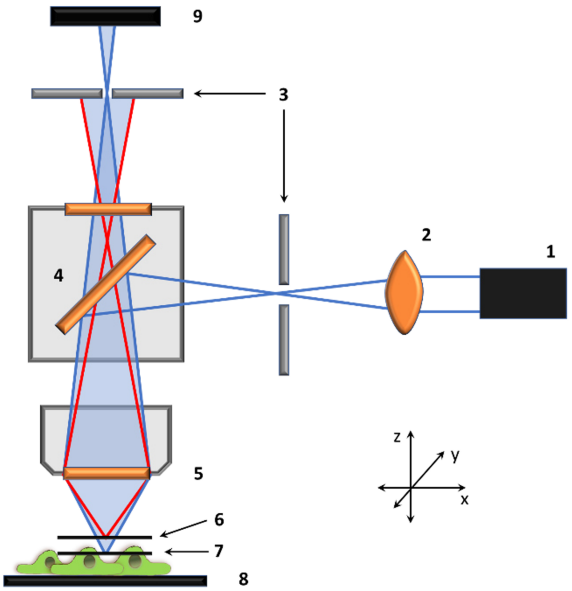

Fig. 4.1 Illustration* of a confocal laser scanning microscope. The excitation light of the laser (1) is directed by using a converging lens (2) through the illumination pinhole (3) to a dichroic mirror (4) and deflected as well as focused via an objective (5) on the specimen on the microscope stage (8). The emitted light from the focal plane (7) passes the dichroic mirror and the variable detection pinhole (3) up to the detection via a photomultiplier (9). Due to the optical connection of the two pinholes (3) with the focal plane and the point-by-point scans of the sample by the laser beam, the scattered light above (6) and below the focal plane is masked to increase the lateral resolution.

*illustration is simplified and not to scale
(modified according to Carlsson et al., 1985)

II PHASE CONTRAST MICROSCOPY

The laboratory routine was performed using the phase contrast microscope Nikon Diaphot, i.e. for controlling the cellular cultures or confirming the formation of spheroids. The microscope is connected to a digital camera (Nikon Instruments Inc.), which was used for image acquisition in terms of monitoring the spheroids' growth behavior.

III STEREOMICROSCOPY

To obtain images of the developed measurement funnels with a spatial impression, the Nikon SMZ 1500 stereomicroscope was applied. It is based on the principle of a telescope system and enables zooming in without interrupting the observation. The microscope consists of a two-stage magnification through changeable objectives and an eyepiece as well as a transmitted light illumination in the stand base. By connecting the stereomicroscope to a digital camera (Nikon Instruments Inc.), image acquisition and data storage via memory card were performed.

IV DIGITAL MICROSCOPY (PORTABLE)

For observing the placement and behavior of spheroids during impedimetric measurements, the handheld USB Digital Microscope was installed on a stand next to the experimental setup. This small and portable microscope contains a macro lens, a charge-coupled device (CCD) camera, and a ring of LED lights around the camera for illumination of the sample. The microscope is connected via USB to an ordinary computer and controlled by the *supereyes 3.54* software, which enables live imaging of the spheroids, image acquisition, and video recording.

V DIGITAL MICROSCOPY (ZENCELL OWL)

The digital microscope zenCELL owl was applied to perform microscopic investigations of multicellular spheroids on different surfaces or in the presence of various stimuli (Fig. 4.2). The microscope is equipped with 24 independent cameras with integrated LED lights for the illumination of the samples, which enables automatic brightfield scans of up to 24 wells in parallel. Due to its small footprint and an operating environment of 20–45 °C and 20–95 % humidity, it can be used as an incubator microscope. The microscope is connected via USB 3.0 to an ordinary computer and controlled by the *zencell-owl v2.0* software (innoME GmbH), which enables the image acquisition, data storage, and determination of various parameters, e.g. area coverage or cell counting, by using individual algorithms.

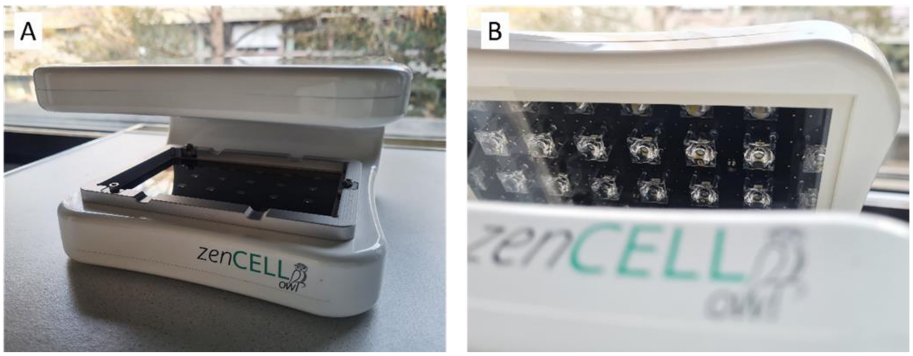

Fig. 4.2 Picture of the digital microscope zenCELL owl (A) with a detailed view of the 24 individual cameras (B).

4.2.2 TIME-LAPSE MICROSCOPY

To perform time-lapse microscopy measurements, the zenCELL owl microscope was applied to facilitate the continuous observation of various effects on multicellular spheroids: the spheroid formation (I), their growth kinetic (II), spheroid adhesion onto cell substrate (III) as well as manipulation (IV). The microscope was installed inside an incubator and was used in combination with 24-well plates (Eppendorf SE). For all experimental assays, the adjustable recording time was set to ten minutes and all 24 wells were monitored in parallel. The recorded images of each experiment were processed and

analyzed using the *zencell-owl v2.0* (innoME GmbH) and *ImageJ* software (Rasband, W.S., National Institutes of Health, USA).

I FORMATION OF SPHEROIDS

The formation of spheroids was observed by using non-adhesive surfaces, which were prepared by coating the 24-well plate with heated 1.5 % (w/v) agarose solution (150 µL/well; in respective serum-free culture medium). For cell seeding, the cell suspension with the respective cell density (U-373 MG: 18,000 c/well; MCF-7: 4,000 c/well) was transferred into the wells of the prepared non-adhesive 24-well plate (1 mL/well). Afterwards, the plate was placed onto the zenCELL owl microscope inside an incubator at 37 °C and 5 % CO_2. To enhance the cell aggregation, the whole microscope included the plate was rotated directly after cell seeding using an orbital shaker (4 h at 120 rpm; overnight at 50 rpm; orbital shaker KM-2 AKKU, Edmund Bühler GmbH). The formation process was continuously observed over 24 h after cell seeding using the following settings: *Total Time-Lapse Imaging*: 24 h, *Interval*: 10 min, *Focus*: 50–100, *Exposure*: –7, *Illumination*: 30, *Brightness*: 16.

II GROWTH KINETIC OF SPHEROIDS

To monitor their growth behavior, spheroids (one day old, U-373 MG: 18,000 c/well; MCF-7: 4,000 c/well) were placed in their respective cell culture medium (1 mL/well) in the wells of an agarose-coated 24-well plate (1.5 % [w/v], 150 µL/well; in the respective serum-free culture medium) to prevent adhesion of the spheroids. The plate was placed onto the zenCELL owl microscope inside an incubator at 37 °C and 5 % CO_2 and the spheroids´ growth kinetic was observed over four days using the following settings: *Total Time-Lapse Imaging*: 96 h, *Interval*: 10 min, *Focus*: ~500–600, *Exposure*: –7, *Illumination*: 30, *Brightness*: 16.

III ADHESION OF SPHEROIDS

The adhesion of the spheroids was studied by positioning spheroids (five days old, U-373 MG: 18,000 c/well; MCF-7: 4,000 c/well) in the wells of an uncoated, thus adhesive, 24-well plate in respective cell culture medium (1 mL/well). To hit the field of view of the individual cameras, specialized positioning disks made of LEXAN® solid sheet (thickness: 1.0 mm; Feinmechanik-Werkstatt, University of Regensburg, Germany) were used to ensure the central placement of the spheroids (Fig. 4.3). The plate was placed onto the zenCELL owl microscope inside an incubator at 37 °C and 5 % CO_2 and the spheroids´ adhesion was observed by the zenCELL owl with the following settings: *Total Time-Lapse Imaging*: 48 h, *Interval*: 10 min, *Focus*: ~400–500, *Exposure*: –7, *Illumination*: 30, *Brightness*: 26.

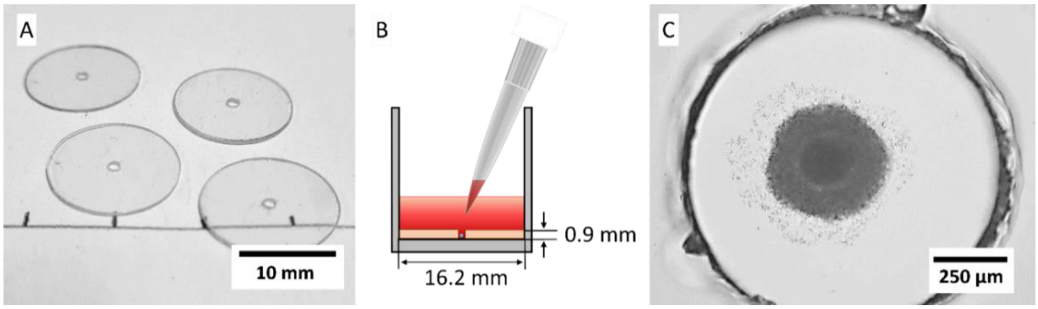

Fig. 4.3 Picture of the positioning disks made of LEXAN® solid sheet (thickness: 1.0 mm, Feinmechanik-Werkstatt, University of Regensburg, Germany) with an outer diameter of 16.2 mm and a central hole with 1.2 mm in diameter (A). The positioning disks were used in the wells of a 24-well plate (B*) for central placement of the spheroids in case of time-lapse measurements with the zenCELL owl microscope. Phase contrast image of an adhered MCF-7 spheroid (seven days old, 4,000 c/well) placed in the cavity of a positioning disk (C).

*illustration is simplified and not to scale

IV MODEL STUDIES WITH SPHEROIDS

Adhered spheroids were used for the spheroid model studies concerning permeabilization, cytotoxic effects, or osmotic stress (Tab. 4.8).

Tab. 4.8 Overview of time-lapse measurements for different spheroid model studies using the zenCELL owl microscope. The different solutions were added to the spheroids in a two-fold concentration (500 µL/well) to obtain the listed final concentrations with a 1:2 mixture ratio. The individual durations of time-lapse imaging were applied with a distinct interval of 10 min.

model studies	substance	final concentration	duration
response to permeabilization	saponin solution diluted with PBS^{++}/glc	0.3 | 1 | 3 [mg/mL]	24 h
response to cytotoxicity*	cytochalasin D solution diluted with DMSO	1 | 5 | 10 [µM]	48 h
response to osmotic pressure	hyperosmotic buffer solution diluted with PBS^{++}/glc	20 | 100 | 200 | 300| 400 [mM]	1.5 h

*only MCF-7 spheroids model study

Therefore, spheroids (five days old, U-373 MG: 18,000 c/well; MCF-7: 4,000 c/well) were placed in the wells of an uncoated 24-well plate in respective cell culture medium (1 mL/well) using positioning disks and kept in an incubator for 48 h (37 °C, 5 % CO_2). The medium was exchanged for fresh cell culture medium (1 mL/well) one day after positioning. To adapt the spheroids to the solutions buffer, the medium was replaced by PBS^{++}/glc (500 µL/well) three hours prior to exposure to the experimental substances. It should be noted that the age of the spheroids at the time point of the simulation is altered to day 7 due to the required adhesion procedure onto the substrate surface in comparison to the

manipulation studies performed using the funnel-based measurement setup in combination with spheroids at day 5 and day 6 after spheroid generation, respectively.

For the model studies, the double-concentrated substances were added to the spheroids (500 µL/well) under sterile conditions. The plate was placed onto the zenCELL owl microscope inside an incubator at 37 °C and 0 % CO_2 and the spheroids´ responses were observed over individual durations using the following settings: *Total Time-Lapse Imaging*: 3–24 h, *Interval*: 10 min, *Focus*: ~100–150, *Exposure*: –7, *Illumination*: 30, *Brightness*: 26.

4.2.3 CYTOCHEMICAL STAINING

Cytochemical staining was used for investigating the cellular viability of the spheroids (I) and for determining the spheroids´ shape after EIS measurements by fluorescently labelling the cytoskeleton (II). The staining procedure for a cell monolayer was thus adapted to three-dimensional tissue models by increasing the fluorophore concentration and incubation time. The fluorescence of the stained spheroids was visualized and documented using the Nikon Eclipse 90i fluorescence microscope (Nikon Instruments Inc., see chapter 4.2.1). A compilation of recorded images taken at a set interval between the first and last planes of focus of the specimen was modelled in the form of z-stacks and analyzed using *EZ-C1* (Nikon Instruments Inc.) and *ImageJ* software (Rasband, W.S., National Institutes of Health, USA).

I VIABILITY STAINING OF SPHEROIDS

The viability characterization of the spheroid-forming cells was performed by simultaneous staining of live and dead cells with calcein acetoxymethyl ester (CaAM) and ethidium homodimer-1 (EthD-1; LIVE/DEAD™ Viability/Cytotoxicity Kit; Invitrogen™, Thermo Fisher Scientific). The membrane-permeable, non-fluorescent CaAM which can permeate the intact cell membrane was used for labelling vital cells. By hydrolyzing the ester groups of the probe due to intact esterase activity, the green fluorescent dye calcein (λ_{ex} = 494 nm, λ_{em} = 517 nm) is generated in the cytoplasm of the cells. This generated polyanionic dye does not pass through the membrane and is therefore accumulated in the cytoplasm of cells with an intact membrane. For identifying dead cells, EthD-1 as a non-membrane-permeable marker was applied. This probe can only enter cells with damaged membranes and emits a 40-fold enhanced red fluorescence intensity (λ_{ex} = 528 nm, λ_{em} = 617 nm) upon intercalation with nucleic acids. Consequently, the cytosol of viable cells emits a green fluorescence and the cell nuclei of dead cells appear red after excitation of the applied probes.

The viability of U-373 MG and MCF-7 spheroids were investigated either after fixation and permeabilization or only permeabilization treatment as well as in the presence of a hyperosmotic buffer solution. Therefore, the spheroids were transferred onto coverslips (d = 15 mm, Paul Marienfeld GmbH & Co. KG) and directly incubated with GA solution (0.03 % [v/v], in PBS^{++}/glc) followed by saponin solution (3 mg/mL, in PBS^{++}/glc), only with saponin solution (3 mg/mL, in PBS^{++}/glc), with hyperosmotic buffer solution (1000 mM), or with buffer solution (PBS^{++}/glc) as a control (ctrl). After the treatment, the spheroids were washed once with PBS^{++}/glc and incubated with the staining solution (2.5 µM CaAM, 5 µM EthD-1, in PBS^{++}/glc) in the dark under gentle shaking (3 h, 37 °C, 0 % CO_2). The stained spheroids were imaged using a confocal laser scanning microscope (Nikon Instruments Inc.) and the following parameters: CaAM 488 nm|515/30 nm bandpass; EthD-1 543 nm|650 nm longpass.

II CYTOSKELETON STAINING OF SPHEROIDS

The cytoskeleton of spheroids was stained by applying the green-fluorescent dye Alexa Fluor™ 488 phalloidin (Invitrogen™, Thermo Fisher Scientific). This probe is a conjugate of the toxin phalloidin from the tuberous leaf fungus (*lat.: Amanita phalloides*) and specifically binds to the actin filaments of cells. It stabilizes these filaments and prevents their dynamic polymerization/depolymerization equilibrium by inhibiting the depolymerization of actin monomers. Thus, the cells are damaged regarding any dynamic vital processes. By covalently linking phalloidin to a fluorophore, the property of specific binding is used to stain the actin cytoskeleton and visualize cellular structures. To facilitate the entry of the non-membrane-permeable probe into the cytoplasm, the cell membrane has to be permeabilized before staining.

For the determination of the U-373 MG and MCF-7 spheroids´ shape inside the funnel-based measurement setup, already fixed and permeabilized spheroids were used, which were analyzed in the context of the respective model study (chapter 4.3.5). The prepared spheroids were transferred onto coverslips (d = 15 mm, Paul Marienfeld GmbH & Co. KG) and incubated with the staining solution (Alexa Fluor™ 488 phalloidin solution, 1:80, in PBS^{++}/glc) in the dark while undergoing gentle shaking (2 h, 37 °C, 0 % CO_2). The stained spheroids were imaged using the Nikon Eclipse 90i fluorescence microscope (Nikon Instruments Inc.) under the following parameters: phalloidin 488 nm|515/30 nm bandpass.

4.3 IMPEDANCE ANALYSIS: MEASUREMENT MODES AND DEVICES

The impedance analysis was the method of choice for performing label-free and non-invasive investigations of monolayer cells and tissue models. A novel measurement setup was developed for the impedimetric study of multicellular spheroids. Based on the flow channel-based measurement setup, the established funnel-based device provides cellular manipulations during the impedance recording. Thus, a variety of model studies was accomplished using the detergent saponin, the actin polymerization inhibitor cytochalasin D, or buffers with different osmolalities. The influence of the chemical stimuli was investigated comparatively on spheroids and 2D cell culture using the standardized ECIS™ technique.

4.3.1 IMPEDANCE MEASUREMENT MODES

Two different measurement modes were applied to either determine the electrical properties of spheroids or monitor cellular micromotion. This approach enabled the comprehensive determination of the cellular system by varying both types during a measurement sequence. For the parameter setting and control of the distinct measurement modes, the corresponding *LabVIEW™*-based software (National Instruments™) programmed by J. Wegener (Institute of Analytical Chemistry, Chemo- and Biosensors; University of Regensburg, Germany) was used.

I MULTI FREQUENCY/TIME (MFT)

The MFT mode provides the recording of impedance spectra as a function of time by measuring the impedance at distinct frequencies within a certain frequency range. The resulting impedance spectra enable the characterization of the electrical properties of the measured spheroid. Thus, the spheroid parameters $R_{ext} \mid R_{int} \mid A_{sph}$ were determined by fitting the elements of an equivalent circuit to the recorded impedance spectra using a *LabVIEW™*-based software (National Instruments™) programmed by J. Wegener (Institute of Analytical Chemistry, Chemo- and Biosensors; University of Regensburg, Germany). With this software, an automated data fitting was performed by applying a numerical non-linear least-square approach. Therefore, values of the parameters $R_{bulk} \mid A_{el} \mid n_{el} \mid A_{para} \mid n_{para}$ were defined by analyzing the impedance spectra of a spheroid-free measurement setup. While the value for the electrode area was set constantly to 1.0 cm², the other values can slightly differ depending on temperature fluctuations and minor changes in the medium conductivity. The individually applied parameter values are provided in the headings of the result tables. After setting these values, the starting values of the spheroid parameters $R_{ext} \mid R_{int} \mid A_{sph}$ were specified by automatically fitting the elements of an equivalent circuit to the imported impedance spectra. Afterwards, the analysis of the

repeatedly measured impedance spectra was executed with dynamic starting values by applying the best fit results for spectrum (i) as initial values for spectrum (i + 1).

In this thesis, MFT measurements were performed in a frequency range of 1 Hz–10^6 Hz at 61 definite frequencies using an alternating voltage with an amplitude of 50 mV. When ECIS™ measurements or multiple funnel-based measurements were performed in parallel, a smaller frequency range of 10^2 Hz–10^5 Hz with 31 distinct frequencies was applied according to a better time resolution. For the data analysis, the recorded impedance spectra were either fitted as described previously or processed using the corresponding *LabVIEW™*-based software (National Instruments™) programmed by J. Wegener (Institute of Analytical Chemistry, Chemo- and Biosensors; University of Regensburg, Germany) to obtain impedance values over time at a distinct frequency.

II RAPID TIME COLLECT (RTC)

The RTC measurement mode was initially developed in the early 1990s by Giaever and Keese (Giaever and Keese, 1991) in cooperation with Lo (Lo et al., 1993), who used this method to electrically record minor cell shape fluctuations of adherently growing monolayer cells. This method was transferred to tissue models by monitoring cellular micromotion within spheroids, as established by Hupf (Hupf, 2018). In the RTC mode, time series measurements were performed at a single frequency with a high time resolution whereby small spheroid shape fluctuations and spheroids´ movements in the nanometer range can be detected electrically as rapid impedance fluctuations. By correlating micromotion with dynamic cellular processes such as cytoskeleton integrity and metabolic activity, the impedance fluctuations are an indicator of cell viability.

In this thesis, the RTC mode was used in the impedimetric model studies of different types of spheroids and for cell monolayer measurements to derive additional information about cellular viability. Thus, micromotion data were recorded at strategic time points during the multiple frequency scans using the respective *LabVIEW™*-based software (National Instruments™) programmed by J. Wegener (Institute of Analytical Chemistry, Chemo- and Biosensors; University of Regensburg, Germany). RTC measurements were performed with a time resolution of 0.5 s over 5 min using an alternating voltage with an amplitude of 50 mV at a single frequency of 200 Hz with spheroids and at a frequency of 4,000 Hz with cell monolayers, respectively. For the data analysis, the recorded impedance values were either linearly detrended and plotted as RTC time courses or processed using the corresponding *LabVIEW™*-based software (National Instruments™) programmed by J. Wegener (Institute of Analytical Chemistry, Chemo- and Biosensors; University of Regensburg, Germany) to calculate the variance of increments for the 32 s data packages after segmented detrending.

4.3.2 FLOW CHANNEL-BASED MEASUREMENT SETUP

The flow channel-based measurement setup was developed by C. Hupf (Hupf, 2018). This system features a flow channel with two buffer reservoirs and a central aperture, which was individually fabricated by ibidi GmbH. After positioning the flow channel onto two planar self-made electrodes, spheroids were subjected to impedimetric monitoring by trapping one spheroid in the central restriction area. A detailed description of the flow channel development, characterization and measurement procedure are given in the thesis of C. Hupf (Hupf, 2018).

In this thesis, the flow channel-based measurement setup was used for initial measurements based on the experiments of C. Hupf (Hupf, 2018) studying the general handling, positioning of spheroids, measurement procedure, and software settings. Based on this, further investigations regarding the novel micro-trap device were established. To validate the evolutionary steps and to compare the measurement results between the flow channel and the funnel-based setup, several findings of C. Hupf were referred to and discussed in the respective chapters.

4.3.3 FUNNEL-BASED MEASUREMENT SETUP

The funnel-based measurement setup was established based on the flow-channel system. This device was individually fabricated according to customer specifications by the Feinmechanik-Werkstatt (University of Regensburg, Germany). It consists of an upper compartment with a funnel-like shape, which is connected to a lower compartment via a central opening. Spheroids were subjected to impedimetric monitoring after trapping one spheroid in the central restriction.

I LAYOUT OF THE FUNNEL

The details of the investigation process regarding the funnel layout are described in chapter 5. Different prototypes with varying dimensions and materials were fabricated to gain the highest sensitivity of impedance signaling and reproducibility in the measurement procedures. In this thesis, the final prototype of the funnel design was used, which features optimal dimensions for the spheroids´ positioning, ideal working volumes in the upper and lower compartments, and a funnel resistance of ~6 kΩ. The final layout comprises an 18.3 mm long funnel-shaped upper compartment with a 10 mm inner diameter, a 116.50° gradient of the inlet zone towards the central opening with 250 µm in diameter, and a total aperture height of 0.4 mm (Fig. 4.4).

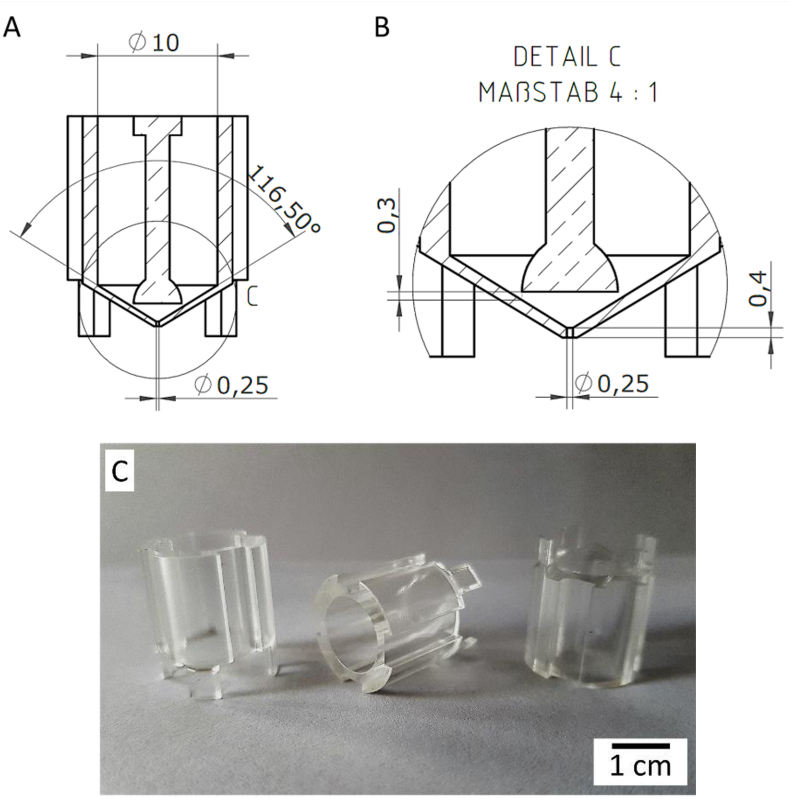

Fig. 4.4 Technical drawings (A, B) and photograph (C) of the funnel-based measurement device that was developed. The technical drawings illustrate the dimensions of the final micro-trap prototype in combination with a central dipping electrode in full-view (A) and the central aperture in detail (B). The funnel-shaped micro-trap prototypes were manufactured based on the fabrication template, and the final measurement devices are shown in picture (C) from different perspectives.

II MEASUREMENT PRINCIPLE AND PROCEDURE

For impedance measurements with the funnel system, the commercially available ECIS™ Trans Filter Adapter device from Applied BioPhysics, Inc. (Troy, USA) was used. This adapter array is comprised of three parts: the base with contact pads and eight individually addressable gold electrodes, the gold-plated stainless-steel dipping electrodes, and a lid (Fig. 4.5).

Thus, the layout dimensions of the funnel were adjusted to the adapter dimensions whereby the dipping electrode assembly was inserted into the funnel inserts and magnetically forced to rest on three gold pins that stick out of the base to facilitate the electrical connection. Ensuring the sterile and physiological conditions, the wells were covered with the lid and the adapter array was placed inside an incubator at 37 °C and 0 % CO_2. Overall, a total of up to eight spheroids respectively experiments can be performed in parallel (Fig. 4.6).

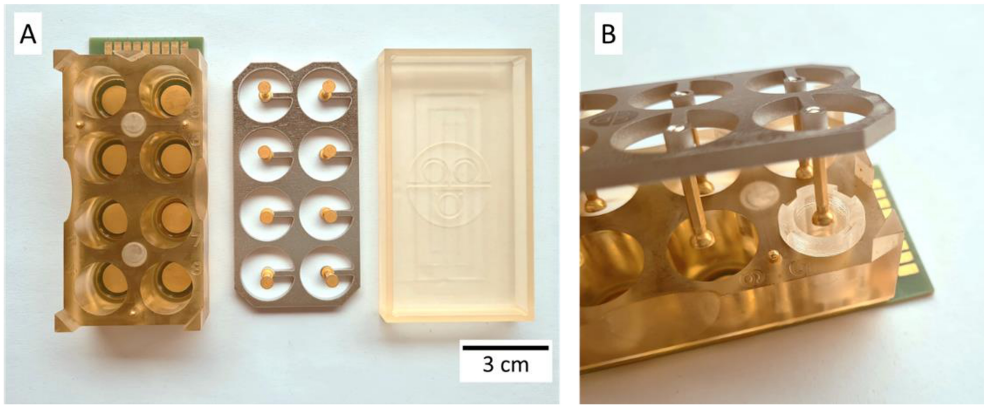

Fig. 4.5 Picture of the ECIS™ Trans Filter Adapter device (Applied BioPhysics, Inc.) comprised of the base part with eight bottom electrodes, the dipping electrodes array, and the lid (A). Detailed view of the setup assembling step by funnel insertion into one well of the array and placement of the dipping electrodes (B).

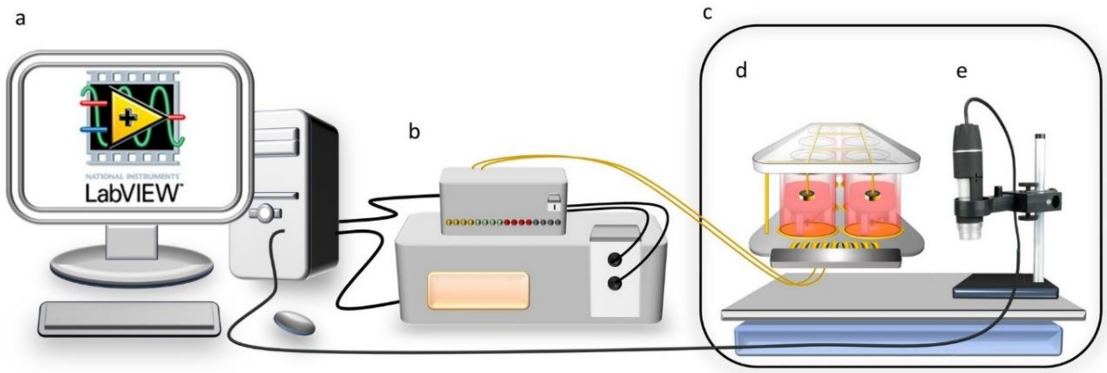

Fig. 4.6 Illustration* of the experimental funnel-based measurement setup for spheroids. Up to eight measurement micro-trap devices (d) were placed into the ECIS™ Trans Filter Adapter device (Applied BioPhysics, Inc.), which were mounted in an incubator for cell experiments (c; 37 °C, 5 % CO_2), with the wiring brought to the outside to connect them to the impedance analyzer via a relay (b). The impedance analyzer was linked to an ordinary computer (a) for data storage and measurement control by using the appropriate *LabVIEW™*-based software (National Instruments™) programmed by J. Wegener (Institute of Analytical Chemistry, Chemo- and Biosensors; University of Regensburg, Germany) for the RTC and MFT measurements. For live spheroid observation and image acquisition before and after the measurements, a portable digital microscope (e; Shenzhen Supereyes Technology Co. Ltd) was mounted inside the incubator and controlled by the *supereyes 3.54* software.
*illustration is simplified and not to scale

For spheroid measurement, the adapter array was linked to an impedance analyzer (SI-1260; Solartron Instruments) via a relay by electrically connecting the contact pads using an eight-well array holder. To individually address the electrodes for measurement control and data storage, the impedance analyzer was linked to an ordinary computer with the appropriate *LabVIEW™*-based software (National Instruments™) programmed by J. Wegener (Institute of Analytical Chemistry, Chemo- and Biosensors; University of Regensburg, Germany) for the RTC and MFT measurements. A portable digital microscope (Shenzhen Supereyes Technology Co. Ltd) was used to capture observations before and after the measurements.

Before the measurement setup was assembled, the pre-warmed funnel inserts and adapter array were sterilized and hydrophilized using argon plasma (30 s; Argon Plasma Cleaner PDC 32G-2, Harrick Plasma Inc.). The wells of the adapter array were filled with physiological buffer solution (PBS^{++}, 1 mL; supplemented with BSA [1 % (v/v)]; Sigma-Aldrich Chemie GmbH) as a conductive solution, the inserts were carefully placed into the wells, and the upper compartment was also filled with buffer solution (1 mL). Thus, the current flow through the funnel insert was obtained by applying an alternating voltage between the bottom electrode and the dipping electrode above. After assembling the measurement setup, the baseline recording was started in MFT mode while addressing the electrodes individually one after the other. The measurement device was warmed up for three hours. In the recorded impedance spectra of the spheroid-free system, the bulk resistance of the conductive solution R_{bulk} and the non-ideal electrode capacitance CPE are indicated. The measurement was paused during the spheroids´ positioning into the upper compartment of the funnel inserts. One spheroid per well was placed directly above the central aperture and was also pushed partly inside the narrowing caused by gravitational force. Due to funnel sealing, the medium and current flow between the electrodes was inhibited, whereas the current was directed through the spheroid´s body instead. This caused higher resistance and significantly increased the impedance values. Consequently, the impedance contribution inside the spheroid could be illustrated using the recorded impedance spectra. By applying the data analysis for the MFT measurements, the electrical properties of the spheroids were characterized. After every experiment, the spheroid was manually removed from the central aperture by gently sucking it out with a pipette. Subsequently, the funnel inserts and the adapter array were washed with ultrapure water, isopropanol (70 % [v/v]; Merck KGaA) and ethanol solution (70 % [v/v]; Merck KGaA). The adapter array was dried and the funnel inserts were incubated for two hours in a detergent solution (5 % [v/v], 70 °C, Elma Clean 10 solution, Elma Schmidbauer GmbH). Then, the micro-trap devices were washed several times with ultrapure water, dried, and stored until they had been re-used several times.

III MODEL STUDIES

The funnel-based measurement setup was used for fundamental measurements with different types of spheroids, which are listed in Tab. 4.9, and for further model studies regarding spheroids´ manipulation, which are described in chapter 4.3.5. The specific spheroid models were generated by applying the distinct protocol in chapter 4.1.5.

For the characterization of the influence of spheroid size on the recorded impedance signal, spheroids with different cell seeding concentrations and equal incubation age were measured. Therefore, U-373 MG spheroids with 20,000–40,000 c/well and MCF-7 spheroids with 8,000–18,000 c/well were positioned in the funnel insert. The spheroids´ settling into the central aperture was recorded in MFT

mode for a minimum of three hours until the constant impedance values were reached, followed by RTC measurements. To investigate the dependency of cell viability on the spheroids' age, spheroids with the same cell seeding concentration and different incubation times were studied. Impedance measurements in RTC were recorded three hours after the spheroids´ placement of five- to eight-day-old U-373 MG spheroids and MCF-7 spheroids into the funnel insert.

Tab. 4.9 Overview of different spheroid model studies using the funnel-based measurement setup.

model studies	**spheroids´ specification**	**measurement mode**
influence of spheroids´ size on the impedance signal	age: 5 | 6 [days] U-373 MG: 20 | 30 | 40 [·10^3 c/well] MCF-7: 8 | 12 | 18 [·10^3 c/well] pH: 7.2	3 h MFT
cell viability of spheroids with different ages	age: 5 | 6 | 7 | 8 [days] U-373 MG: 30 [·10^3 c/well] MCF-7: 12 [·10^3 c/well] pH: 7.2	RTC 3 h after spheroid placement
cell viability of spheroids with different pH values	age: 5 | 6 [days] U-373 MG: 30 [·10^3 c/well] pH: 6.8 | 7.0 | 7.4 | 7.6	RTC 3 h after spheroid placement

The cell viability according to the pH value during the spheroid formation process was studied by measuring spheroids with identical cell seeding concentrations and various pH values. Thus, U-373 MG spheroids, which were generated using pH values of pH 6.8 to 7.6, were positioned into the funnel inserts. Three hours after the spheroids´ placement into the funnel insert the impedance was measured using the RTC mode.

4.3.4 ECIS™-BASED MEASUREMENT SETUP

The experiments with monolayer cells were performed using the commercially available ECIS™ device setup from Applied BioPhysics, Inc. (Troy, USA). This system is based on the ECIS™ technique as described in chapter 3.3.

I ELECTRODE LAYOUT

Commercially available 8W10E electrode arrays from Applied BioPhysics, Inc. (Troy, USA) were used in this work (Fig. 4.7). Each of the eight wells covered a substrate area of 0.75 cm² and contained a set of ten circular working electrodes (250 µm diameter) on a polyethylene terephthalate foil (PET). The

electrodes were connected in parallel on a gold pad against one common counter electrode. Thus, eight individual measurement chambers per array were available.

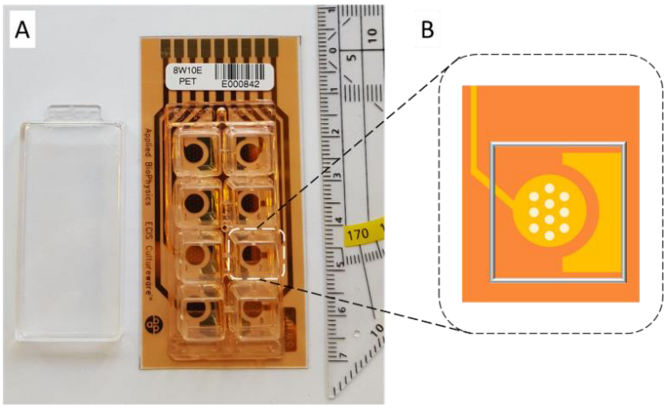

Fig. 4.7 Picture (A) and schematic illustration (B) of the 8W10E array (Applied BioPhysics, Inc.) used for the ECIS™ measurements. The array is connected to the impedance measurement system via the gold leads using a holder, whereby ten small working electrodes are coupled to one large counter electrode per well. Cells were incubated in the eight wells for 48 h after seeding and then manipulated by adding certain substance solutions to represent different model studies.

II MEASUREMENT PRINCIPLE AND PROCEDURE

Before the array was used for the first time, it was pulsed to clean and activate the substrate surface to enhance the reproducibility of the electrode/electrolyte interface impedance (Wegener et al., 2000b). Therefore, the array was sterilized using argon plasma (30 s; Argon Plasma Cleaner PDC 32G-2, Harrick Plasma Inc.) and the wells were filled with cysteine solution (200 µL/well, 10 mM in water, supplemented with 150 mM sodium chloride; Sigma-Aldrich Chemie GmbH). It was connected to the commercial ECIS™ measurement device (Applied BioPhysics, Inc.) via the contact pads using an array holder, which could address two arrays and thus sixteen different measurement chambers in parallel (Fig. 4.8). The ECIS™ measurement device was connected to an ordinary computer with the commercial *ECIS™* software for measurement control, data acquisition, and storage. After recording three impedance spectra of each electrode, the pulse was applied for 30 s (1,500 Hz, 1,000 µA) successively to each well. Subsequently, the wells were washed five times with ultrapure water and dried under sterile conditions. For cell seeding of U-373 MG or MCF-7 cells, the wells were filled with the respective cell culture medium (400 µL/well) and incubated (1 h, 37 °C, 5 % CO_2). After cell subcultivation, the cell suspension was transferred into the wells (400 µL/well) with the respective seeding density (U-373 MG: 100,000 c/cm²; MCF-7: 100,000 c/cm²) and incubated at 37 °C with 5 % CO_2. When the model studies were finished, the array was disconnected from the ECIS™ measurement device and the cell monolayer was detached from the substrate by enzymatic digestion using trypsin solution (400 µL/well, 0.025 %

[w/v] in EDTA solution; 1 h at 37 °C). The wells were washed five times with ultrapure water, dried under sterile conditions, and re-used up to three times.

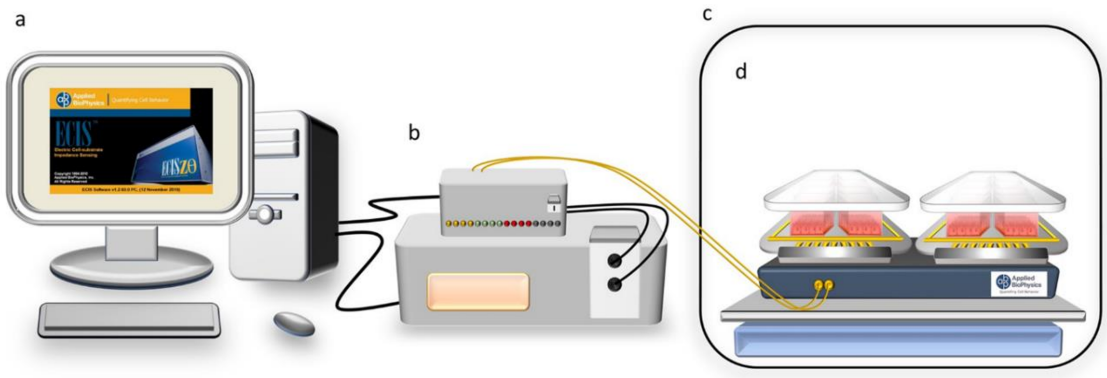

Fig. 4.8 Illustration* of the experimental ECIS™-based measurement setup for cell monolayers. Up to two electrode arrays (d; Applied BioPhysics, Inc.), each consisting of eight individual measurement chambers, were mounted onto an ECIS™ array holder (Applied BioPhysics, Inc.) in an incubator for cell experiments (c; 37 °C, 5 % CO_2), with the wiring brought to the outside to connect them to the impedance analyzer via a relay (b). The impedance analyzer was linked to an ordinary computer (a) for data storage and measurement control by using the commercial *ECIS™* software (Applied BioPhysics, Inc.) for RTC and MFT measurements.

*illustration is simplified and not to scale

III MODEL STUDIES

The model studies with 2D cell monolayers were performed in comparison to the model studies using spheroids and are described in detail in chapter 4.3.5. One day after cell seeding, the medium in each well was exchanged with fresh cell culture medium (400 µL/well) and the model experiments were performed 48 hours after cell seeding.

4.3.5 IMPEDIMETRIC MODEL STUDIES

Identical impedimetric model studies were performed to compare the cellular behavior as two-dimensional cell monolayers or as three-dimensionally formed spheroids. Therefore, two-dimensional cell monolayers of MCF-7 cells (100,000 c/cm²) and U-373 MG cells (100,000 c/cm²) as well as MCF-7 spheroids (12,000 c/well) and U-373 MG spheroids (30,000 c/well) were used. In total, three different manipulating approaches such as the permeabilization with saponin, the cytotoxicity reaction induced by cytochalasin D, or the stimulation regarding osmotic stress were applied. The final concentration values of the individual substance solutions were adjusted depending on the dimensionality of the cellular structure. For instance, standard concentration values for saponin solutions were used for cell monolayer experiments, which were multiplied ten times regarding spheroids. The cellular response was monitored using the ECIS™-based and the funnel-based measurement setup in the MFT and RTC modes (Tab. 4.10).

Tab. 4.10 Overview of different model studies for two-dimensional cell monolayers or as three-dimensionally formed spheroids in comparison using the ECIS™-based and the funnel-based measurement setup in the MFT and RTC modes. In this table, the final concentrations of the respective substance solutions are given, which were obtained by using either a twofold (for experiments on 2D cell models) or a fivefold (for experiments on 3D cell models) higher working concentration, depending on the experimental setup.

model studies	**substance solutions**	**measurement mode and duration**
response to permeabilization	saponin solution diluted with PBS^{++}/glc 2D: 0.003 | 0.005 | 0.01 | 0.03 | 0.05 | 0.1 | 0.3 [mg/mL] 3D: 0.3 | 1 | 3 [mg/mL]	2D: RTC + 5 h MFT + RTC 3D: RTC + 15 h MFT + RTC
response to cytotoxicity	cytochalasin D solution diluted with DMSO 2D: 0.3 | 0.5 | 1 | 2 | 3 | 4 | 5 [µM] 3D: 5 [µM]	2D / 3D: RTC + 15 h MFT + RTC
response to osmotic stress	hyperosmotic buffer solution diluted with PBS^{++}/glc 2D: 20 | 50 | 100 | 200 | 300 | 400 | 500 [mM] 3D: 20 | 100 | 200 [mM]	2D / 3D: RTC + 1.5 h MFT + RTC

Three hours before the substance exposure, the cells grown as cell monolayer were adapted to the respective solution buffers by replacing the medium in the wells with Leibovitz Medium (Sigma-Aldrich Chemie GmbH) or PBS^{++}/glc solution (200 µL/well). Corresponding to the funnel measurements, the spheroids were already incubated with the respective buffer during the baseline recording three hours prior to stimulation. Before and after each experiment, RTC measurements were applied to determine the relative cellular response. For cell manipulation, the working concentrations of the different substances had to be adjusted to the given experimental setup to obtain the final substance concentrations listed in the table (Tab. 4.10). The stimulation of cell monolayers was performed by mixing double-concentrated substance solutions directly in the wells of the ECIS™ array (200 µL/well). For model studies on 3D cell models, substance solutions were directly transferred into the micro-traps to the spheroids by removing 200 µL of buffer solution and adding 200 µL substance solution in parallel using fivefold concentration values. The respective solutions with which the substances were diluted were added for the control condition (ctrl). After the addition of the substance solution, the impedance was recorded in the MFT mode for a period of time depending on the individual induced signal change. Subsequently, RTC measurements were applied, and the experiments were completed.

The results of the impedimetric model studies are combined with the results of the cell viability (chapter 4.1.8), and microscopic model studies (chapter 4.2.2) of each cellular manipulation to provide a comprehensive overview of the cellular response to each compound from different perspectives.

CHAPTER 5

SETUP DEVELOPMENT AND CHARACTERIZATION

5.1 THE MEASUREMENT SETUP 89

5.2 EVOLUTION OF THE FUNNEL DESIGN 102

5.3 DISCUSSION: COMPARISON TO ALTERNATIVE SYSTEMS 114

5.4 SUMMARY AND OUTLOOK 116

The development of the novel impedimetric measurement system for spheroids was based on the flow channel developed by C. Hupf, University of Regensburg (Hupf, 2018). Since the measurement principle of the two setups is similar, the micro-trap design has to be systematically adapted to novel conditions. In this chapter, the basic considerations for the setup development are provided by describing the main features of the measurement funnel such as the fabrication material and the dimensions of the aperture. The setup evolution of the funnel was verified in accordance with the measurement principle by recording impedance spectra with and without spheroids. In addition, the influence of parasitic impedance contributions was investigated.

5.1 THE MEASUREMENT SETUP

The measurement setup using impedance spectroscopy was developed for studying spheroids by physical means. Hence, the construction of a micro-device was required for a sufficient fixation and coupling of biological objects to a physical transducer. In cooperation with the Feinmechanik-Werkstatt at the University of Regensburg (Regensburg, Germany), a three-dimensional miniaturized funnel, also called ´micro-trap´, was designed to hold a spheroid, thereby making it accessible for impedance analysis. The funnel was individually fabricated from a biocompatible material by micro-milling according to customer requirements and allows a spheroid to come to rest by gravity alone. Technical drawings were used to design the dimensions of the funnel precisely and as construction templates, which also serve for visualization in this chapter. The final micro-device was placed between two electrodes, which forces the current to flow through the spheroid for performing impedance-based monitoring.

5.1.1 MEASUREMENT PRINCIPLE

As a fundamental measurement principle for the impedimetric monitoring of spheroids, the spheroids have to be trapped e.g. at a central restriction point (Fig. 5.1, A). With the use of the funnel-like shape of the micro-trap device, the gravitational force and hydrodynamic pressure, the spheroid will be kept at the central opening. The measurement well chamber with a bottom electrode is filled with a conductive solution such as a physiological buffer or cell culture medium, and the micro-trap device is placed into the chamber and is filled with the identical conductive solution. After connecting the measurement chamber and inserting the dipping electrode into the micro-trap from above, the applied current can flow freely through the funnel between the two electrodes.

The measurement setup was validated in a proof-of-principle experiment in which impedance measurements were performed on a pure measurement chamber filled with medium and on an inserted micro-trap device with and without a central opening (Fig. 5.1). As the comparison of the resulting spectra shows, the pure measurement chamber filled with medium and without the micro-trap has the lowest impedance as it allows the current to flow in an undirected and unimpeded fashion (see Fig. 5.1, B: w/o micro-trap). Thus, the impedance value that was measured comprises the contribution of the non-ideal electrode capacitance and the bulk resistance of the medium. By using the developed micro-trap without a hole the resistance and consequently the impedance increase to a maximum as well as displaying a steep signal decline resulting from high parasitic capacitances originating from wiring and the experimental setup (see Fig. 5.1, B: w/ micro-trap (w/o hole)). In contrast, the impedance

decreases upon the usage of the micro-trap with a central opening (see Fig. 5.1, B: w/ micro-trap (w/ hole)). The impedance spectrum of this system arises from the bulk resistance of the conductive solution R_{bulk} in composition with the resistance of the central opening of the micro-trap, the non-ideal electrode capacitance CPE, and stray capacitances due to the wiring.

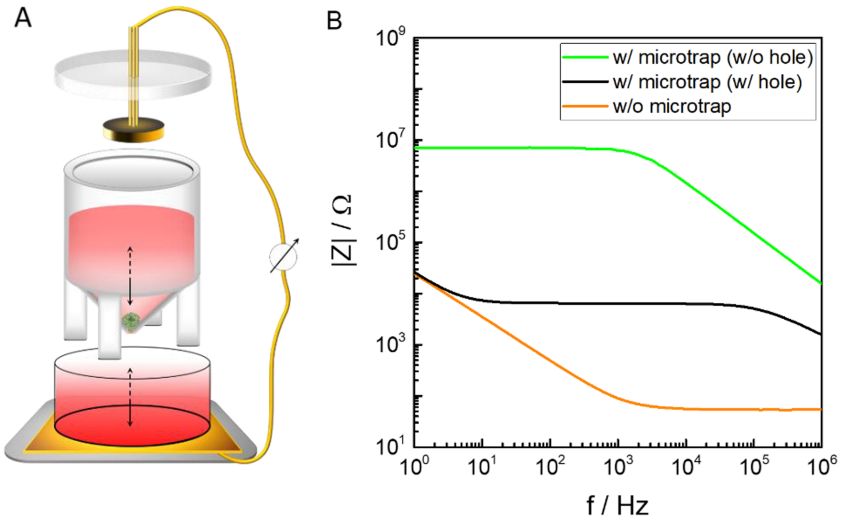

Fig. 5.1 Illustration of the core components of the funnel-based measurement setup as explosion drawing (A; illustration not to scale) and impedance spectra (B) of a measurement chamber filled with medium in the presence and absence of a micro-trap (w/ or w/o micro-trap), which either contains or does not contain a central opening (w/ or w/o hole). The impedance values increase upon the insertion of a micro-trap. When using the micro-trap without a hole, the impedance displays the highest values indicated by the blockage of the current path between the two electrodes. When using the micro-trap with a hole, the current is conducted through the constriction and the impedance decreases. This experiment provided a proof of principle for the spheroid measurements by confirming the current pathway through the central hole. Experiments were performed in a standard cell culture incubator at 37 °C and 5 % CO_2.

Thus, it has been demonstrated that the current flow can be directed vertically through the aperture while it would be blocked to flow directly between the bottom and the dipping electrode without a hole. This fact was essential for performing impedance measurements of spheroids to ensure the current flow path through the tissue model trapped at the restriction.

A spheroid is positioned onto the central opening of the funnel-shaped micro-trap by gravitation and minimal top fluid flow. The spherical tissue model is held back at the restriction and subsequently partly adapts to the form of the aperture due to hydrodynamic pressure as documented via fluorescence microscopy images (Fig. 5.2). Since the spheroid thus seals the opening by itself, the fluid and current flow through the micro-trap is significantly inhibited. As a result, the applied current is forced to flow through the cellular aggregate, which enables the monitoring of the impedance contribution originating from the spheroid body. The resulting significant impedance increase is composed of the intra- and extracellular resistance R_{int} and R_{ext}, as well as the non-ideal spheroid capacitance A_{sph}.

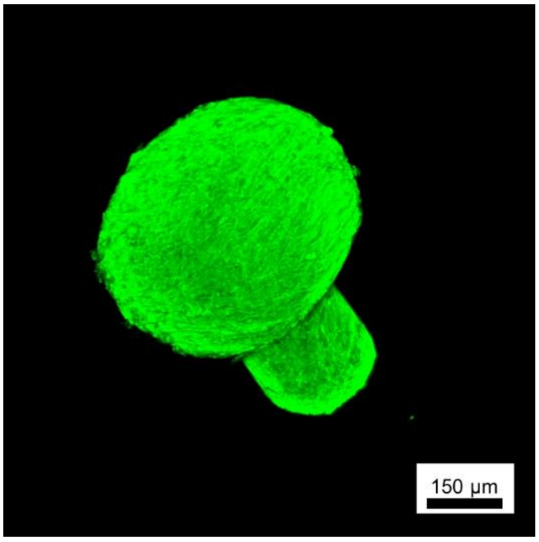

Fig. 5.2 Confocal microscopy image of an MCF-7 spheroid, which was positioned in the funnel-based micro-trap. Three hours after placement, the spheroid structure had adapted to the funnel constriction hole and was fixed in its position by adding glutaraldehyde to the micro-trap. For fluorescence microscopy, the spheroid body was prepared using the cytoskeleton staining protocol for spheroids (see chapter 4.2.3). Using fluorescence microscopy with z-stack imaging, an xyz image has been rendered.

5.1.2 FREQUENCY DEPENDENT IMPEDANCE

Data collection was performed using multifrequency impedance recordings over a period of time for the development of the setup, investigation, and spheroid measurements. Typical impedance spectra of the buffer-filled micro-trap illustrate the influence of a spheroid in comparison with a spectrum without spheroid (Fig. 5.3, A). In the case of the micro-trap without a spheroid, the spectrum displays a linear decrease in the frequency range of 1–10 Hz resulting from the non-ideal electrode capacitance and remains constant between 10–10^5 Hz due to the electrolyte resistance R_{bulk}. In the higher frequency range beyond approximately 10^5 Hz the measured impedance is dominated by the parasitic capacitance originating from the experimental setup including wiring and contacting contributions.

After inserting and sealing the central opening of the micro-trap using a spheroid, the spectrum shifts towards higher impedance values (Fig. 5.3, A). In this case, the averaged spectrum with a U-373 MG spheroid shows a linear decrease of the electrode capacitance at very low frequencies from 1 Hz to 3 Hz compared to the spectrum of the micro-trap without spheroid. The resistive contributions of the cell bodies are reflected by a frequency-independent plateau at frequencies between 3 Hz and 200 Hz. This is related to the current pathways around the insulating cell bodies flowing through cell-cell contacts. In contrast, the capacitive contributions of the spheroid are represented in the kHz frequency range by a slight impedance decrease from $2 \cdot 10^2$ Hz to 10^5 Hz, which turns into a steep linear drop beyond approximately 10^5 Hz reflecting stray capacitances from the experimental setup.

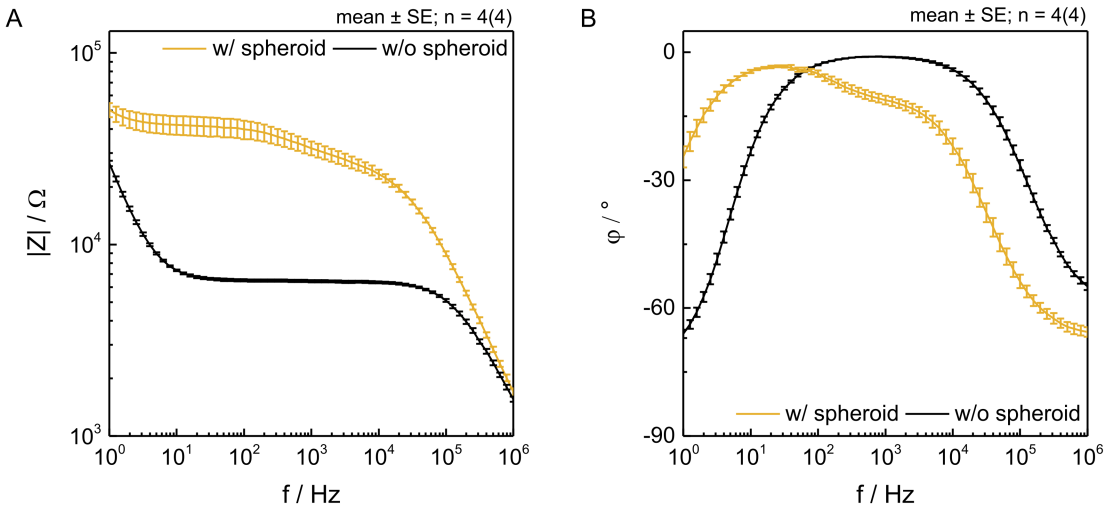

Fig. 5.3 Frequency-dependent impedance spectra of the funnel-shaped micro-trap device in the form of Bode plots. Spectra with and without U-373 MG spheroids positioned at the aperture of the medium-filled micro-trap are shown for the magnitude $|Z|$ (A) as well as the phase shift angle φ (B). Experiments were performed in a standard cell culture incubator at 37 °C and 5 % CO_2. Data sets were averaged, mean ± SE; n = 4(4).

Additionally, the phase spectra with and without a spheroid illustrate the cellular influence on the impedimetric measurement system (Fig. 5.3, B). The spectrum of the micro-trap without spheroid indicates capacitive contributions from the CPE element at low as well as from parasitic stray capacitances at high frequencies with a shift of approximately –60°. In the medium frequency range a purely resistive influence due to the electrolyte resistance is reflected by the absence of a phase shift. After spheroid insertion, the corresponding phase shift at lower frequencies increases and approximates the value of the cell-free system shifted to lower frequency values. At frequencies between 10 Hz and 10^4 Hz the resistive as well as capacitive contribution originating from the spheroid is reflected as the phase shift decreases progressively by displaying a plateau at approximately $2 \cdot 10^3$ Hz. The maximum phase shift is shown in the MHz region resulting from high parasitic capacitances originating from the wiring and experimental setup.

The impedance and the phase spectra show a characteristic frequency dependency, the so-called dielectric dispersion phenomenon, between 200–$5 \cdot 10^4$ Hz after inserting a spheroid. The dispersion represents the dependence of the permittivity of a dielectric material on the frequency of an applied electric field. In general, dispersions are related to the orientation of the dipoles and the motion of the charge carriers (Miklavčič et al., 2006). At low frequencies, the dipoles align with the change of the applied field and the permittivity is relatively high while the conductivity is relatively low. As the frequency increases, the dipoles become less able to follow the changes in the applied electric field, and the corresponding polarization disappears. In addition, the dielectric constant decreases and the conductivity increases.

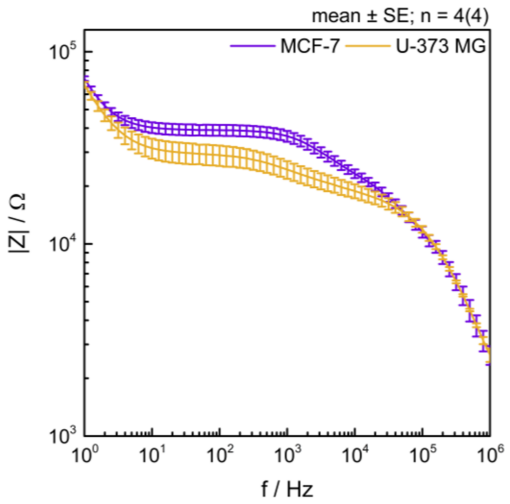

Fig. 5.4 Impedance spectra of the funnel-shaped micro-trap device with MCF-7 and U-373 MG spheroids positioned at the aperture of the micro-trap. Cell type-specific differences of *beta* dispersion profiles differing in the frequency range are displayed (U-373 MG: 200–5·10^4 Hz; MCF-7: 1·10^3–5·10^4 Hz). Data sets of spheroids with similar impedance magnitude of both cell types used were averaged, mean ± SE, n = 4(4).

Since biological tissue is a highly inhomogeneous material, it exhibits several different dispersions over a wide range of frequencies. In accordance with Schwan, three discrete frequency regions of dispersion are characterized (Schwan, 1957). At low frequencies (10 Hz to a few kHz), cells in suspension can be considered as insulating bodies in a conducting fluid, and the *alpha* dispersion is associated with counterion polarization along cell membranes. In the MHz range (1 kHz to several MHz), the external electric field begins to penetrate the cell interior, and capacitive coupling across the cell membrane becomes relevant. Consequently, the *beta* dispersion results from the interfacial polarization of the cell membranes, while additional dispersive properties of the extracellular matrix, cytosol, proteins and other organic macromolecules have to be considered. In the GHz range (>10 GHz), the *gamma* dispersion reflects the polarization of water molecules. As reviewed by Foster and Schwan, mainly the two distinctly different dispersions, the *alpha* and *beta* dispersion, are reported in biological tissues (Foster and Schwan, 1989). In the impedance spectra of the funnel-shaped micro-trap, the *beta* dispersion is dominant and reflects the capacitive contribution of multiple cell membranes as well as the extracellular matrix on the current path through the spheroid body at medium frequencies. In dependence on the cell type used for spheroid formation, MCF-7 and U-373 MG spheroids exhibit characteristic *beta* dispersion profiles differing in the frequency range. The impedance spectra of U-373 MG spheroids display the dispersion region between 200–5·10^4 Hz, whereas MCF-7 spheroids demonstrate a reduced range of 1·10^3–5·10^4 Hz (Fig. 5.4). Thus, the individual resistive and capacitive contribution of the cell type on the impedance signaling is reflected. Since U-373 MG spheroids are composed of approximately two to five times more individual cells, the multiplicity of cell membranes has to be considered in terms of enhanced A_{sph} values, whereas MCF-7 spheroids obtain enhanced

resistance values R_{ext} as a result of the more pronounced cell-cell conjunctions. These cell type-specific differences are represented in the dispersion pattern and also quantified in the spheroid parameters extracted from the impedance spectra (see for example chapter 7.1).

In addition, Nyquist plots of a medium-filled micro-trap with and without a spheroid are given, in which the imaginary part is represented as a function of the real part of the complex impedance (Fig. 5.5). The Nyquist plot of the micro-trap without spheroid displays at low frequencies, respectively at the upper real part of the impedance, a linear signal decline, which reflects the diffusion-restricting region of the electrolyte-electrode interfaces (Fig. 5.5, A). As the decline exhibits a steeper slope than the characteristic phase angle of the Warburg impedance of 45°, it corresponds to the CPE component A_{el} describing the electrolyte-electrode interfaces. At the signal minimum, the bulk resistance is represented by the axis of the real part of the impedance with approximately 5 kΩ. The small signal increase at higher frequencies reflects the parasitic contributions of the measurement setup, which represent a marginal part of the overall signal profile, since the influence of the CPE is dominating.

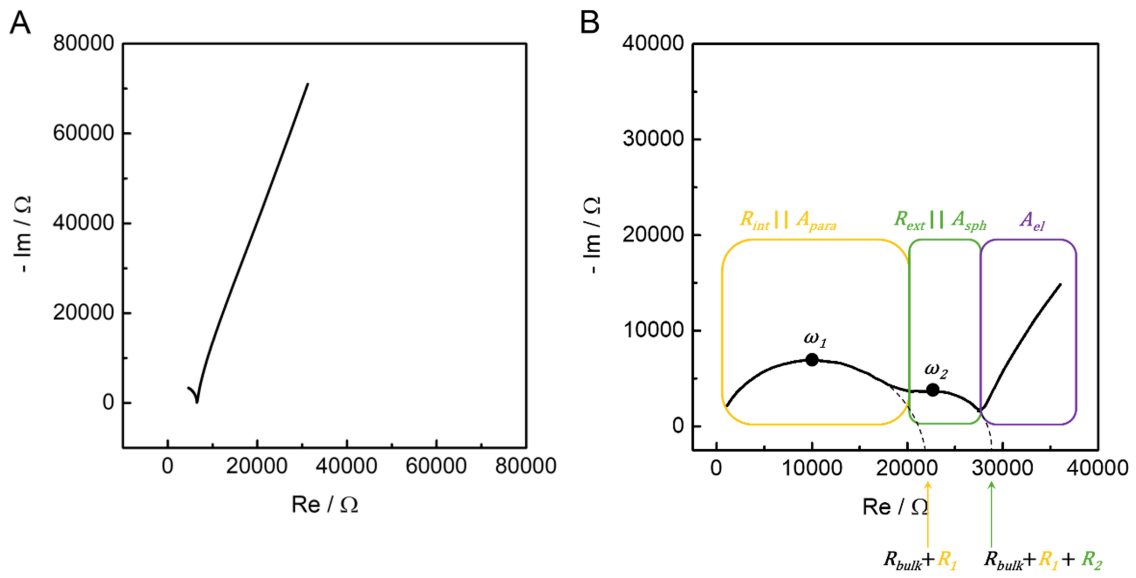

Fig. 5.5 Examples of a Nyquist plot of a medium-filled micro-trap without (A) and with a U-373 MG spheroid (B) are shown; the imaginary part was calculated based on the measured impedimetric data and characteristic parameters are marked within the plot, which are further explained in the text (B). Experiments were performed in a standard cell culture incubator at 37 °C and 5 % CO_2.

The Nyquist plot of the micro-trap with a spheroid is segmented into three parts reflecting the impedimetric contribution of the system in accordance with increasing frequency (Fig. 5.5, B). At low frequencies, the diffusion-restricting region of the electrolyte-electrode interfaces is displayed as explained for the plot of the micro-trap without spheroid. In the region at medium and high frequencies, the frequency-dependent curve consists of two semicircles. As the number of semicircles describes the number of occurring time constants of the system, the Nyquist plot illustrates two parallel R||C circuit

components. Since the two semicircles are not clearly separated, the time constants are not high significantly different either, which makes the two RC-terms less distinguishable. Thus, two closely linked electrochemical processes with different associated R and C values are reflected, which originate either from the heterogeneity of structural properties within the spheroid or from the transition between two structural properties (Huang et al., 2006). With the Nyquist plot showing depressed semicircles with centers shifted below the real axis, a non-ideal capacitive contribution is indicated, and the two parallel R||C circuits have to be composed of R and CPE elements (Instruments, 2007).

Following the frequency course, the semicircle in the lower frequency range represents the paracellular current pathway through the spheroid body when the external electric field begins to penetrate the cell interior showing *beta* dispersion (Foster and Schwan, 1989). In this case, the extracellular resistance R_{ext} as well as the capacitive contribution of the spheroid A_{sph} has to be considered. In contrast, the first semicircle in the high frequency range illustrates the parallel R||C circuit of the intracellular resistance R_{int} as referred to the transcellular current pathway in combination with the parasitic impedance contribution A_{para}. Both parameters are evident in the impedance spectra at frequencies above approximately 10^5 Hz (compare chapter 3.2.3; Tab. 3.1; Fig. 5.11).

The time constant τ of an RC-element is a measure of how quickly a system reacts to a change and is calculated from the product of associated R and C values. In general, the Nyquist plot is composed of semicircles with increasing time constants according to the reciprocal relationship of the time constant to the transition frequency ω at which the imaginary part within a semicircle is maximal. As displayed in Fig. 5.5 (B), the time constants are inverted and the first semicircle describes a process dominating the dynamics of the system. In this case, the calculation of the time constants provides no direct correlation to the displayed RC-terms. Further, as revealed by experiments with U-373 MG and MCF-7 spheroids, the resistance of the cell interior is smaller than the extracellular resistance, differing by a factor of 5 (U-373 MG; 30,000 c/well; compare chapter 7.1.1; Tab. 7.2) or 60 (MCF-7; 12,000 c/well; compare chapter 7.1.1; Tab. 7.1). Thus, the time constant and therefore the diameter of the first semicircle should be smaller than that of the second semicircle. However, the exact composition of capacitive contribution of the spheroid and the parasitic contribution can strongly influence the diameter ratios. In general, the time constant reflects the velocity of the occurring electrochemical reactions, i.e. the system reacts more slowly to changes showing a higher time constant (Black and Andreas, 2009). In the first semicircle, the transfer of electrical potential is hindered by the parasitic impedance contribution of the measurement setup compromising non-ideal capacitive characteristics. At frequencies above 10^5 Hz, additional resistive and inductive contributions may lead to delayed charge carrier movements and thus delayed response dominating the entire measurement in the high

frequency range. The second semicircle describes processes that are faster than those represented in the first semicircle, e.g. diffusion processes within the spheroid occur very quickly in the lower frequency range, e.g. around 10^3 to 10^5 Hz. Since the two semicircles are not clearly separated on the x-axis, the associated processes are less distinct and may merge.

In the ohmic region of the Nyquist plot, the bulk resistance is represented by the axis of the real part of the impedance (compare Fig. 5.5, B). The point of intersection between the two semicircles describes the sum of R_{bulk} with the first R component (~22,000 Ω; R_{bulk}+R_1), which in the impedance spectrum corresponds to the inflection point between the slope representing the capacitive influence and R_{int}. Thus, an indication for the combination of R_{int} and A_{para} is given. The minimum between the second semicircle and the linear signal increase describes the sum of the resistance values of the measurement setup and the spheroid (~29,000 Ω; R_{bulk}+R_1+R_2), respectively the value of R_{ext}, in correspondence to the impedance value in the low kHz region. In addition, the transfer frequency of each semicircle determines the frequency at which the impedance of the capacitor equals the resistance of the respective RC-term and thus reflects the transition between the low to high frequency behavior. In the case of U-373 MG spheroids, the transition frequencies are given as ω_1 with 63.000 Hz and ω_2 with 1.000 Hz. These frequencies represent the inflection points of the respective RC-terms in the corresponding Bode plot (compare Fig. 5.4) and are thus an additional proof of the parallel circuits between R_{int} and A_{para} as well as R_{ext} and A_{sph}.

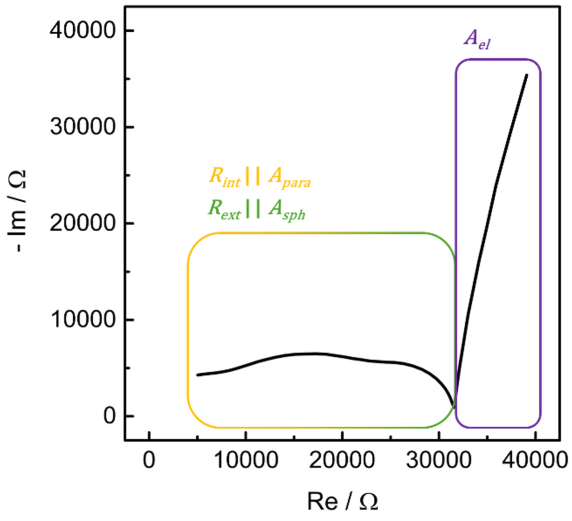

Fig. 5.6 Example of a Nyquist plot of a medium-filled micro-trap with an MCF-7 spheroid is shown; the imaginary part was calculated based on the measured impedimetric data. Experiment was performed in a standard cell culture incubator at 37 °C and 5 % CO_2.

In this context, also the Nyquist plot of an MCF-7 spheroid is considered. The frequency course shows a similar linear signal decrease at low frequencies as for the U-373 MG spheroids, which turns into a two-semicircular-like profile (Fig. 5.6). In this example, several processes with very similar time constants are

running simultaneously, resulting in two overlapping non-distinguishable semicircles. In the case of MCF-7 spheroids, and barrier cultures in general, the extracellular resistance is dominant upon the multiple tight junctions and distorts other resistive as well as capacitive contributions (Gerasimenko et al., 2020).

As a result of the interpretation of the Bode and Nyquist plots, several circuit models correspond to the two time constant spectrum representing two parallel R||C circuits of R_{int} and A_{para} as well as R_{ext} and A_{sph} (Fig. 5.7; Instruments, 2007). These models are similar to the equivalent circuit model for spheroids utilized in this work by taking into account the CPE component of the parasitic contribution in a different arrangement, which would lead to a different transfer function for data fitting.

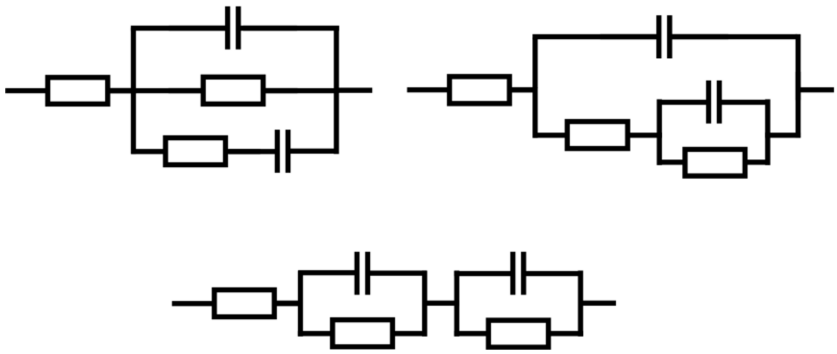

Fig. 5.7 Different equivalent circuit models composed of two parallel R||C circuits reflecting two time constants (Instruments, 2007).

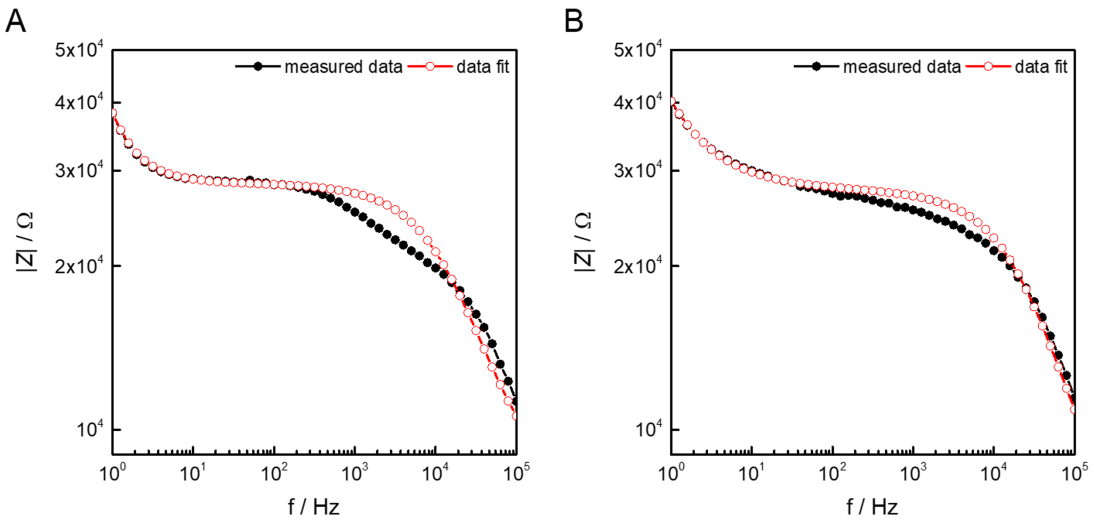

Fig. 5.8 Exemplary impedance spectra of U-373 MG (A) and MCF-7 spheroids (B) in combination with the respective data fit, which was obtained by applying the equivalent circuit model (compare Fig. 3.4). The quality of the fit is given by R^2 of 0.95 (U-373 MG; A) and 0.98 (MCF-7; B).

Since the verification of the exact model is difficult due to the high similarity of the model performance, the initial equivalent circuit model has been applied for data fitting (see Fig. 3.4). The equivalent circuit

model provides a sufficient fit to the measured data, as the coefficient of determination was obtained with R^2 values of 0.95 for U-373 MG spheroids and 0.98 for MCF-7 spheroids (Fig. 5.8). Thereby, the averaging of the capacitance contributions of the *beta* dispersion with only one parameter as A_{sph} was taken into consideration. Based on this, it is stated, that there may be considerable differences between different cells and tissues, which complicate the interpretation and thus the determination of the exact equivalent circuit model, while the elements R_{int}, R_{ext} and A_{sph} are sufficient for representing the tissue model in the simplest way.

To determine the frequency at which the impedance changes associated with the spheroid could be recorded with the highest sensitivity, the relative impedance was calculated (Fig. 5.9). The relative impedance values indicate that the measurement setup exhibits a sensitivity of 500 % for monitoring spheroids over a frequency range from $5 \cdot 10^0$ Hz to 10^3 Hz. Based on this, the frequency of 200 Hz was chosen as the monitoring frequency for data evaluation and presentation of all time courses of impedance in this thesis, also in comparison to the monitoring frequency of the flow channel measurement setup (Hupf, 2018).

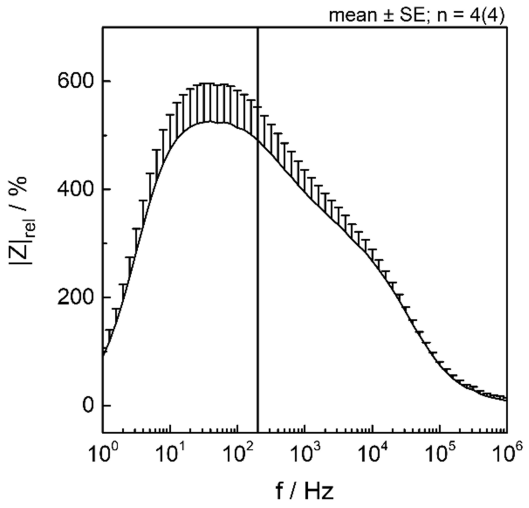

Fig. 5.9 The sampling frequency for the time-resolved experiments was determined as 200 Hz by plotting the relative impedance as a function of frequency (D). Data sets were averaged, mean ± SE; n = 4(4).

For visualization, the time- and frequency-dependent changes of the micro-trap impedance during the insertion of a spheroid are illustrated as a 3D surface plot (Fig. 5.10, A). The typical time course of impedance at the monitoring frequency of 200 Hz is marked in the 3D surface plot and is also plotted individually (Fig. 5.10, B). Before spheroid positioning, the impedance time course displays the medium-filled micro-trap profile with a constant impedance value of approximately 5.4 kΩ. When a spheroid is inserted into the micro-trap funnel, an immediate and steep increase of the impedance value at the monitoring frequency of 200 Hz is measured, accompanied by a characteristic change in the entire

impedance spectrum. In this example, a constant impedance value of 28 kΩ is reached within approximately 1.0 h at the monitoring frequency of 200 Hz.

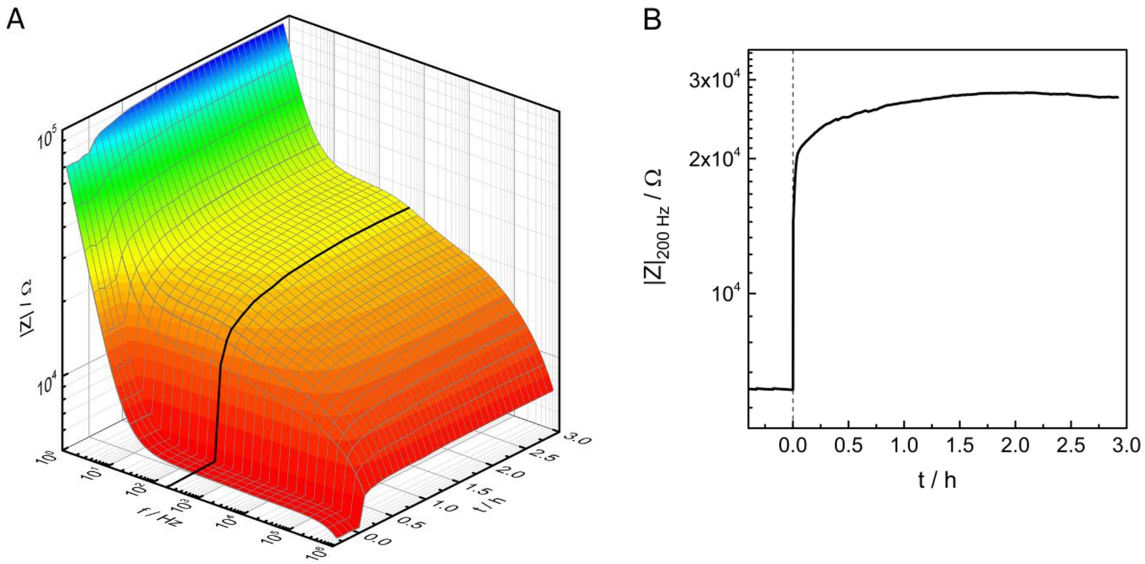

Fig. 5.10 Typical time course of the impedance magnitude of the micro-trap measurement setup during spheroid positioning in the form of a 3D surface plot showing the time and frequency dependence (A) and at the monitoring frequency of 200 Hz (B) which is also marked as a black line in the 3D plot. Experiment was performed in a standard cell culture incubator at 37 °C and 5 % CO_2.

Using this time course, the spheroid behavior after its positioning at the aperture of the micro-trap can be investigated. The spheroid initially comes to rest on the opening as the impedance increases rapidly. Then, the spheroid body adapts accordingly to the successive impedimetric increase stepwise to the central hole by deformation of its spherical structure, until the tissue model finally seals the aperture, and the impedance stagnates.

5.1.3 PARASITIC IMPEDANCE CONTRIBUTION

In addition to the capacitive and resistive impedance contributions originating from the measurement setup, e.g. the electrolyte, electrodes, and spheroid, contributions originating from the electronics and connecting electric wires also arise. These parasitic contributions comprise capacitive, resistive, and inductive components. For representation in the equivalent circuit, a constant phase element (A_{para}, n_{para}) is used, which is positioned in parallel to the remaining part of the equivalent circuit, thereby assuming a non-ideal capacitive character.

To determine the parasitic contribution of the electronic equipment used for impedance measurements, four micro-trap devices with different hole diameters (100 µm, 250 µm, 400 µm, and 500 µm) were fabricated. Thus, a defined resistance component is inserted into the electric circuit

by forcing the current flow through a smaller opening, which also represents the overall measurement procedure. By recording the impedance magnitude of the micro-traps filled with buffer, the influence of the parasitic contribution on the shape of the impedance spectrum is characterized (Fig. 5.11).

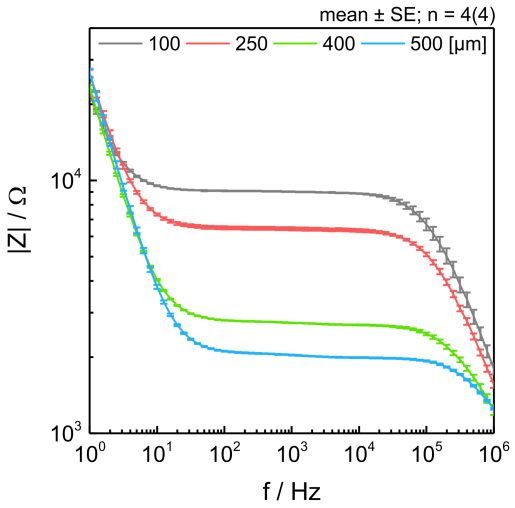

Fig. 5.11 Recorded impedance spectra of funnel-shaped micro-trap prototypes with different hole diameters of 100 µm, 250 µm, 400 µm, and 500 µm, which were filled with buffer and measured without a spheroid using the final measurement setup. Experiments were performed in a standard cell culture incubator at 37 °C and 0 % CO_2. Data sets were averaged, mean ± SE; n = 4(4).

The impedance spectra of the four micro-trap devices illustrate the typical impedance decrease at low frequencies and the horizontal, frequency-independent section at high frequencies (detailed discussion see chapter 5.2). At frequencies above 10^5 Hz, a second impedance decline can be recorded, which represents the parasitic influence of the electronics. This influence is illustrated by increasing resistance since the micro-trap device with the smallest diameter displays the earliest and most significant drop in impedance values.

Tab. 5.1 Calculated values of A_{para} and n_{para} as CPE terms reflecting the parasitic contribution of the electronic equipment in dependence on four different hole diameters of the micro-trap prototypes used. The values were determined by fitting each measured impedance spectrum of the different prototypes using a *LabVIEW™*-based software (written by J. Wegener, University of Regensburg). Data sets were averaged after fitting, mean ± SE; n = 4(4).

	d_{hole} [µm]			
	100	250	400	500
A_{para} [$Fs^{n-1}cm^{-2}$]	$2.0 \cdot 10^{-10}$	$2.4 \cdot 10^{-10}$	$1.8 \cdot 10^{-10}$	$2.2 \cdot 10^{-10}$
n_{para}	0.95	0.95	0.95	0.95
n	4(4)	4(4)	4(4)	4(4)

Furthermore, the amount of A_{para} and n_{para} from the CPE element can be calculated by fitting each spectrum using a *LabVIEW™*-based software (written by J. Wegener, University of Regensburg). The resulting values for the CPE element imply an independency of the parasitic capacitance contribution regarding the increasing resistance, which was modulated using a decreasing prototype hole diameter, as the values of A_{para} fluctuate between $1.8 \cdot 10^{-10}$ $Fs^{n-1}cm^{-2}$ and $2.4 \cdot 10^{-10}$ $Fs^{n-1}cm^{-2}$ with constant n_{para} values of 0.95 (Tab. 5.1).

It can be summarized that the experimental setup contains a measurable contribution of the parasitic impedance, which is evident in the impedance spectra at frequencies above 10^5 Hz. As the alterations of R_{int} are also only observed in this frequency range, the impedance spectra had to be corrected by the CPE impact before being fitted to determine the spheroidal parameters R_{ext}, R_{int}, and A_{sph}. Therefore, the values of A_{para} and n_{para} were used, which were quantified by pre-analysis of the spectra.

5.2 EVOLUTION OF THE FUNNEL DESIGN

To achieve the highest sensitivity of impedance signaling and reproducibility of measurement procedures, several micro-trap prototypes with different dimensions and materials were manufactured and tested.

Based on the measurement setup of the flow channel, the focus for the development of the novel micro-trap design was to change the orientation of the fluid flow from horizontal to vertical. This innovation required an impedimetric electrode setup containing an upper and a lower electrode. Therefore, the commercially available electrode arrangement for transwell experiments, the ECIS™ Trans Filter Adapter device from Applied BioPhysics, Inc. (Troy, USA), was chosen as the fundamental measurement arrangement. The adapter consists of individually addressable gold electrodes at the bottom with corresponding dipping electrodes. Thus, the designed spheroid micro-trap can be placed as the central component between a pair of electrodes by inserting the funnel into the fabricated cavity (see Fig. 4.5). Therefore, the general micro-trap proportions had to be designed to fit the given measurement adapter and electrode dimensions.

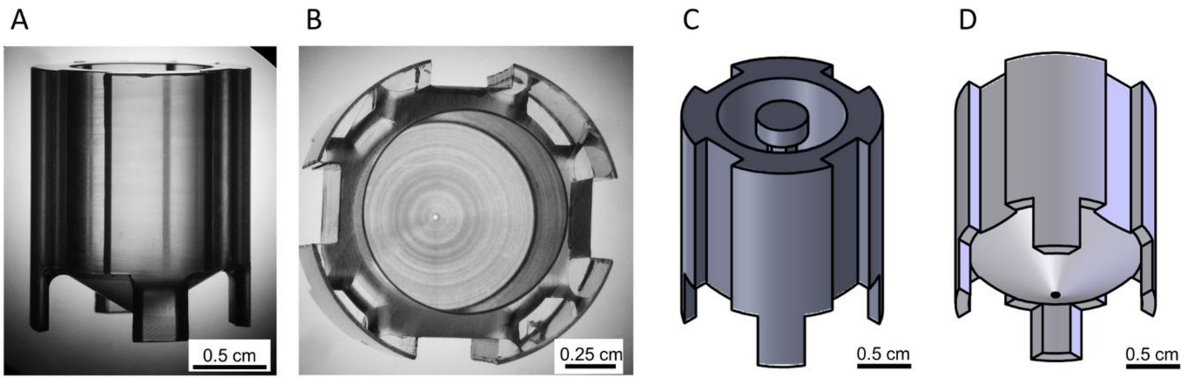

Fig. 5.12 Stereo microscopic pictures (A, B) and technical drawings (C, D). Shown is the micro-trap fabricated using Plexiglas® in a side view (A) and from the top (B). The technical drawings illustrate the micro-trap as a volume rendering in side view with a centrally placed dipping electrode (C) and in bottom view (D). For demonstration purposes, the dipping electrode is only shown from the level inside the micro-trap (C).

In general, the spheroid micro-trap consists of an upper, funnel-shaped compartment connected to a lower compartment via a central opening (Fig. 5.12). The technical drawing of the fundamental prototype features a cylindrical device with a radius of 15.5 mm, a height of 18.3 mm, and a central aperture of 0.4 mm height and 0.25 mm width. The total internal volume was calculated to be 1188 mm^3 including the central aperture. By gradually narrowing the upper section in the form of a funnel with the greatest possible slope, a spheroid can easily be forced to reach the aperture by gravity. For easier device handling, flow paths were created on the outside of the measurement micro-trap by milling them

into the funnel wall. Thus, the determined flow behavior was improved by facilitating the removal of stuck air bubbles towards the top. Additional variations of the funnel hole diameter, length, and inlet zone were created individually by developing further prototypes based on the fundamental shape.

5.2.1 VARIATION OF THE FUNNEL HOLE DIAMETER

Regarding the central aperture dimensions, the hole diameter was varied systematically to minimize the resistance contribution of the micro-trap itself while ensuring the retention of the spheroid at the opening. To this end, individual prototypes of the micro-trap made of Plexiglas® were fabricated with hole diameters of 100 µm, 250 µm, 400 µm, and 500 µm (Fig. 5.13).

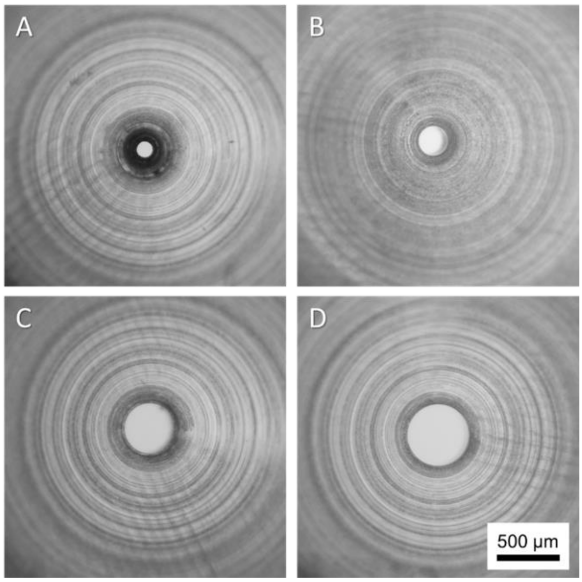

Fig. 5.13 Stereomicroscopic pictures of the central borehole of the funnel-based micro-trap device shown for varying diameters of 100 µm (A), 250 µm (B), 400 µm (C), and 500 µm (D).

Tab. 5.2 Dimensions and calculated electrical resistance of each prototype with a variable hole diameter whereby the length and the cross-sectional area of the central opening based on its radius are shown. The resistance contribution of the funnel hole was calculated from this data using Eq. 5.1 with ρ = 60 Ω·cm.

	d_{hole} [µm]			
	100	250	400	500
L_{hole} [mm]	0.4	0.4	0.4	0.4
A_{hole} [mm²]	0.01	0.05	0.13	0.20
R_{hole} [kΩ]	30.6	4.89	1.91	1.22

The resistance contribution of the aperture was calculated in dependence on the hole dimensions by determination of the electrical resistance of the conducting buffer inside the micro-trap device

(Tab. 5.2), whereby a constant current density distribution over the conductor's cross-section was assumed. As the dimensions of the upper compartment were identical, the calculation only comprises the resistance contribution of the varying central opening. The resistance R_i was calculated individually using the specific resistivity of the buffer medium (ρ = 60 Ω·cm) the length L_i, and the cross-sectional circular area A_i (Eq. 5.1).

$$R_i = \frac{\rho \cdot L_i}{A_i} \qquad \textbf{Eq. 5.1}$$

The electrical resistance values calculated for the four prototypes indicate the impedimetric contribution dependent on the hole diameter. By increasing the diameter of the central opening from 100 µm to 500 µm, the overall resistance contribution is reduced from 30.6 kΩ to 1.22 kΩ.

Tab. 5.3 Comparison of the calculated electrical resistance and the measured impedance values of each prototype at the monitoring frequency of 200 Hz depending on the various hole diameters. Data sets were averaged, mean ± SE; n = 4(4).

	d_{hole} [µm]			
	100	250	400	500
R_{hole} [kΩ]	30.6	4.89	1.91	1.22
$\lvert Z \rvert_{200\,Hz}$ [kΩ]	9.08 ± 0.03	6.48 ± 0.09	2.775 ± 0.008	2.080 ± 0.008
n	4(4)	4(4)	4(4)	4(4)

This trend was also demonstrated by the impedance measurements of the prototypes without a spheroid (compare Fig. 5.11). The spectra of the medium-filled micro-trap devices show the resistance contribution of the prototypes depending on the funnel hole diameter. While the prototype with a central opening of 100 µm displays the highest impedance value of 9.08 (± 0.03) kΩ at the monitoring frequency of 200 Hz, the impedance values systematically decrease to around 2 kΩ (Tab. 5.3). Based on these values, the fivefold increase in hole diameter results in a 25-fold reduction in resistance contribution and a fourfold reduction in total impedance when comparing the results of the 100 µm hole diameter prototype to the 500 µm hole diameter prototype.

Since the frequency-independent range between 10^1–10^5 Hz characterizes the ohmic resistance contribution of the entire system, the impedance values that are derived can be compared to the calculated electrical resistance values of the central opening itself by assuming a constant resistance contribution of the remaining measurement setup. In the case of the 250 µm-, 400 µm- and 500 µm-prototypes, the calculated electrical resistance is lower than the measured impedance

indicating a difference of 900–1,600 Ω, which reflects the contribution of the remaining measurement system to the impedance magnitude despite the aperture hole. The 100 µm-prototype shows the opposite effect, with a resistance three times higher than the impedance value; no explanation could be provided for this discrepancy.

To investigate the effects of the hole diameter on the spheroids' behavior at the central aperture and to confirm the sensitivity of the impedimetric signal, equally sized U-373 MG spheroids of the same batch with a diameter of approximately 700 µm were measured using the different funnel hole prototypes. Figure 5.14 shows the impedance spectra of the four buffer-filled micro-trap prototypes with spheroids recorded three hours after positioning and without spheroids, each paired according to the hole diameter (Fig. 5.14; see Fig. A-5.1 for the corresponding phase spectra).

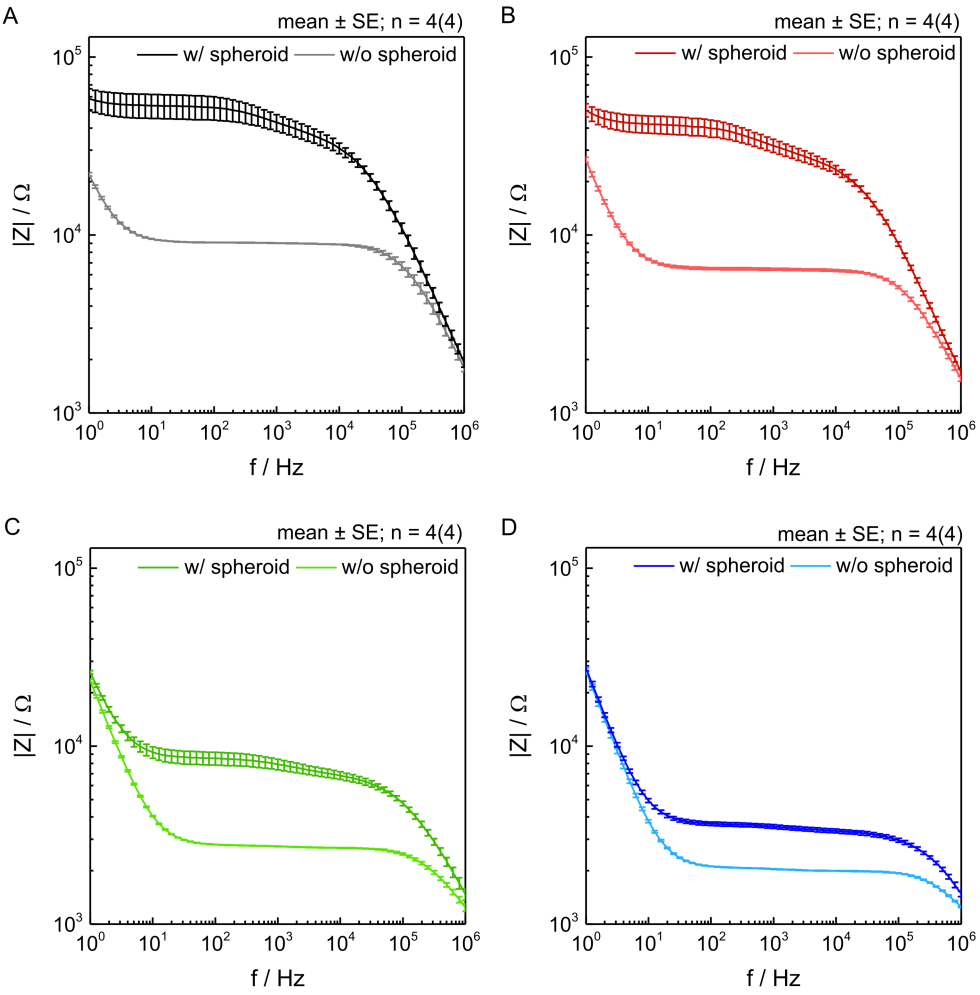

Fig. 5.14 Recorded impedance spectra of the funnel-shaped micro-trap prototypes with different hole diameters of 100 µm (A), 250 µm (B), 400 µm (C), and 500 µm (D), which were filled with buffer and measured with U-373 MG spheroids (w/; recorded three hours after positioning) and without (w/o) a spheroid using the final measurement setup. Experiments were performed in a standard cell culture incubator at 37 °C and 0 % CO_2. Data sets were averaged, mean ± SE; n = 4(4).

As discussed previously, all graphs display the typical impedance behavior with the medium-filled micro-trap and in the presence of a spheroid (see chapter 5.1.2). In comparison, the spectra pairs indicate the decreasing ohmic resistance contribution due to the increasing hole diameter of the aperture, as shown in Fig. 5.11, as well as a decrease in the relative spheroid signaling magnitude.

This signal reduction can be associated with a decreasing measurement sensitivity concerning the increasing bulk resistance. This fact was verified by calculating the relative impedance of each prototype based on the measured spectra (Fig. 5.15). The relative impedance plot for the prototypes containing a hole diameter of 100 µm and 250 µm displays a broad peak maximum in the range of 10^1–$2{\cdot}10^2$ Hz and high impedance sensitivities of approximately 500 % at 200 Hz. In contrast, the prototypes consisting of a 400 µm and 500 µm aperture show significantly lower sensitivities across a larger frequency range between $2{\cdot}10^1$–10^5 Hz.

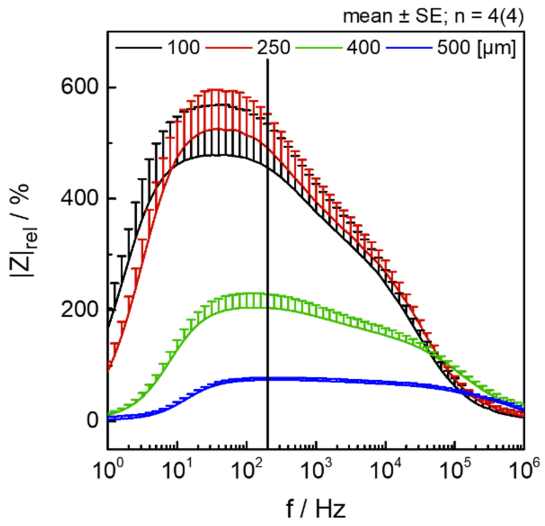

Fig. 5.15 Relative impedance (A) based on recorded spectra of funnel-shaped micro-trap prototypes with different hole diameters of 100 µm, 250 µm, 400 µm, and 500 µm, which were measured with a spheroid (recorded three hours after positioning) and without a spheroid. The monitoring frequency is marked at 200 Hz. Experiments were performed in a standard cell culture incubator at 37 °C and 0 % CO_2. Data sets were averaged, mean ± SE; n = 4(4).

This fact is also reflected by respective differences of the calculated electrical spheroid parameters (Tab. 5.4). Here, the external and internal resistance values of the spheroids are decreasing with increasing funnel hole diameters. A significant resistance drop is shown between the 250 µm (R_{ext} = 28 (± 2) kΩ; R_{int} = 3.0 (± 0.9) kΩ) and 400 µm funnel hole (R_{ext} = 6 (± 1) kΩ; R_{int} =0.8 (± 0.1) kΩ), which may highlight the associated loss in sensitivity when measuring the identical spheroid body with different hole diameters. The non-ideal membrane capacity values of the spheroids A_{sph} increase with increasing hole diameters, indicating a less dense and more perforated, flexible cell structure within the measured tissue model, as the spheroids were not forced into the hole as much as using smaller hole diameters. In addition, leakage currents between the spheroids and the central aperture may be

considered in the case of the two larger apertures, resulting in reduced resistive and capacitive spheroid contributions.

Tab. 5.4 Calculated values of R_{ext}, R_{int} and A_{sph} reflecting the electric structure of U-373 MG spheroids as a function of four different hole diameters of the micro-trap prototypes used. The values were determined by fitting each measured impedance spectrum three hours after spheroid insertion using a *LabVIEW™*-based software (written by J. Wegener, University of Regensburg) and the following parameter values: A_{el} = 12 (± 2) | 10 (± 1) | 8.7 (± 0.5) | 6.8 (± 0.5) ·10^{-6} $Fs^{n-1}cm^{-2}$; n_{el} = 0.87 (± 0.03) | 0.88 (± 0.02) | 0.89 (± 0.02) | 0.92 (± 0.02); A_{para} = 2.0 | 2.4 | 1.8 | 2.2 ·10^{-10} $Fs^{n-1}cm^{-2}$; n_{para} = 0.9; n_{sph} = 0.75. Data sets were averaged after fitting, mean ± SE; n = 4(4).

	d_{hole} [µm]			
	100	250	400	500
R_{ext} [kΩ]	34 ± 6	28 ± 2	6 ± 1	4.4 ± 0.8
R_{int} [kΩ]	4.7 ± 0.5	3.0 ± 0.9	0.8 ± 0.1	0.37 ± 0.05
A_{sph} [10^{-9} $Fs^{n-1}cm^{-2}$]	4.6 ± 0.7	8 ± 1	14 ± 1	22 ± 2
R_{bulk} [Ω]	8,630	5,400	2,600	1,980
n	4(4)	4(4)	4(4)	4(4)

In addition to the lower sensitivity, another disadvantage of the 500 µm prototype occurred by measuring spheroids for three hours after set up as the spheroids slid through the hole into the lower chamber. Although the chosen diameter of the spheroids was deemed to be large enough for this experiment to prevent them from slipping through the largest hole, the cell aggregates quickly adapt to the constriction due to the force of gravity. Thus, the use of smaller apertures can ensure that the spheroid will be kept in position for a longer period of time to perform ongoing experiments with it.

As a consequence, the micro-trap prototype combining the benefits of easier handling and the highest sensitivity resulting in the most significant impedance signal changes was used for the spheroid measurements. While the sensitivities of the 100 µm- and 250 µm-prototypes are similar, the impedance signal of the smallest aperture shows larger fluctuations, as can be seen from the height of the error bars during spheroid positioning. For example, the normalized impedance values 60 min after spheroid insertion are given as 580 (± 50) % for the aperture of 100 µm and 570 (± 30) % for the 250 µm diameter hole. Considering these results, and based on the previous work of Hupf using the flow channel with a narrow opening of 250 µm, a funnel hole diameter of 250 µm was also chosen for spheroid measurements (Hupf, 2018).

5.2.2 VARIATION OF THE FUNNEL APERTURE LENGTH AND INLET ZONE

Apart from refining the diameter of the hole, a further step in developing the measurement setup was to adapt the length of the opening to the lower compartment and to optimize the inlet zone, where the spheroid is positioned. Individual prototypes of the micro-trap made of Makrolon® were fabricated with an identical hole diameter of 300 µm and varying aperture lengths of 0.5 mm, 1.0 mm, and 1.5 mm or varying angles of the funnel inlet zone.

Regarding the different aperture lengths, the variations have to be chosen to place the micro-trap hole into the 2.7 mm gap between the lower and upper electrodes without contacting them. Thus, it was possible to systematically extend the length of the aperture hole by doubling and tripling the original dimension starting from 0.5 mm. As a result of varying hole dimensions, the resistance contribution of the measurement setup increases due to an enlargement of the aperture length. The resistance contribution of the aperture was calculated using Eq. 5.1 and also determined by impedance measurements in a similar approach to that of the experiment concerning the different hole diameters (see chapter 5.2.1). In Tab. 5.5, the calculated and measured results depending on the funnel aperture length that was used are listed.

Tab. 5.5 Dimensions and calculated electrical resistance of each prototype with a variable aperture length. The length and the cross-sectional area of the central opening based on its radius are provided. From this data, the resistance contribution of the funnel hole was calculated using Eq. 5.1 with ρ = 60 Ω·cm. For comparison, the measured impedance values of each prototype at the monitoring frequency of 200 Hz depending on the various aperture lengths are noted. Data sets were averaged, mean ± SE; n ≥ 3(3).

	L_{hole} [mm]		
	0.5	1.0	1.5
A_{hole} [mm²]	0.94	0.94	0.94
R_{hole} [kΩ]	4.2	8.5	12.7
$\lvert Z\rvert_{200\ Hz}$ [kΩ]	8.7 ± 0.4	11.2 ± 0.5	14.8 ± 0.4
n	4(4)	3(3)	4(4)

The results of the calculated resistance and the measured impedance values at the monitoring frequency of 200 Hz show that the basic resistance of the funnel micro-trap increases according to the aperture length. As the funnel aperture length is extended by a factor of three from 0.5 mm to 1.5 mm, the calculated resistance values are also systematically triplicated. In comparison, the experimentally

determined impedance values display a linear increase of approximately 3 kΩ concerning the elongation of 0.5 mm per step. Thus, the impedance signal magnitude caused by spheroid insertion would be diminished when the length of the funnel hole increases as the base resistance rises. Consequently, the wall thickness and thus the length of the funnel hole was minimized as much as possible determined by the fabrication process, resulting in the final micro-trap design with a funnel aperture length of 0.4 mm. The hole was located at the maximum distance between the dipping and the bottom electrode to avoid interference with the material (compare Fig. 4.4, B).

The angle of the funnel inlet was optimized by choosing the largest possible slope. However, this was limited by the dimensions of the drilling head used to manufacture the micro-trap. The initial prototypes, e.g. with different funnel hole diameters or manufactured using different fabrication materials, yielded an angle of 134°. Finally, the best solution was achieved by filing the drill head to an appropriate angle before use. Thus, the smallest possible angle of 116.5° could be achieved for the inlet zone, thereby enabling the most efficient use of gravity for positioning the spheroid by physical means. In terms of practical handling, the minimal angle also facilitated the removal of air bubbles sitting in the lower compartment underneath the inlet zone that impeded good microscopy pictures of the spheroid positioned in the micro-trap being taken.

5.2.3 MATERIALS FOR THE FUNNEL FABRICATION

Apart from the optimal funnel micro-trap design and dimensions, the fabrication material that is used is also essential. Three different materials, namely Teflon®, Makrolon®, and Plexiglas® were investigated by manufacturing individual prototypes of the micro-trap from scratch. A brief overview of the material properties relevant to this thesis is given in Tab. 5.6.

Each material type was easy processable, and hence the funnel micro-trap could be milled from a respective solid chunk using similar machine settings. While polycarbonate (Makrolon®) and polymethyl methacrylate (Plexiglas®) are strong and stiff thermoplastic materials showing excellent dimensional stability, polytetrafluoroethylene (Teflon®) features elastic and thus deformable characteristics. This fact was evident from the hole drilling of the funnel, as the hole roundness of the Teflon® prototype was twisted and out of shape half a year after processing (Fig. 5.16).

Since the reproducibility of the experiments depends on the stability of the measurement setup and especially on the durability of the micro-trap in detail, Teflon® was a less suitable material for this purpose. Another disadvantage of Teflon® with respect to its use in this work was that it is a white, opaque material. Thus, it was not possible to see the spheroid during the insertion into the micro-trap

funnel or to take pictures with the microscope camera. Instead, Plexiglas® and Makrolon® as amorphous polymers have a clear and highly transparent appearance, which made them more suitable for handling during the whole measurement procedure (compare Fig. 5.16).

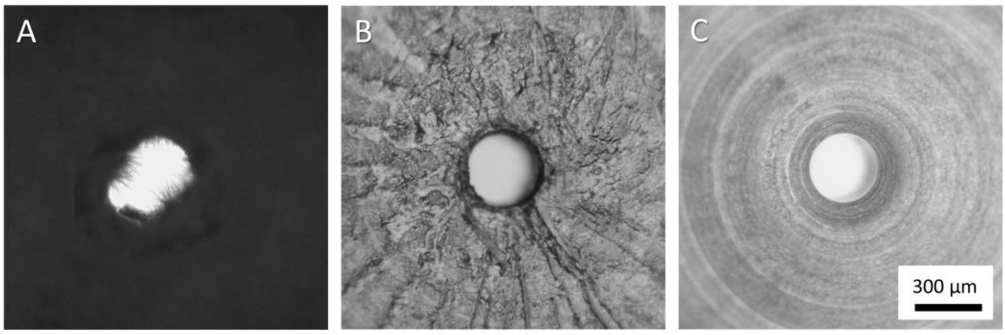

Fig. 5.16 Stereomicroscopic pictures of the central borehole of the funnel-based micro-trap device shown for the tested materials Teflon® (A), Makrolon® (B), and Plexiglas® (C).

Tab. 5.6 Overview of the material properties of the three different materials Teflon®, Makrolon®, and Plexiglas® used for the fabrication of the funnel-based micro-trap (see https://omnexus.specialchem.com; https://www.vanderveerplastics.com).

	Teflon®	**Makrolon®**	**Plexiglas®**
name	polytetrafluoro-ethylene	polycarbonate	polymethyl methacrylate
acronym	PTFE	PC	PMMA
formula	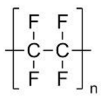	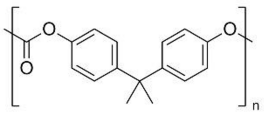	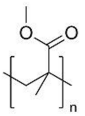
description	non-transparent, elastic thermoplastic material	transparent, strong and stiff thermoplastic material	transparent, strong and stiff thermoplastic material
water absorption, 24 h immersion ISO 62 [%]	0.005–0.01	0.2–0.3	0.2–0.4
chemical resistance	very good	poor	poor

Since the sensitivity of the entire measurement setup relies on minimizing the intrinsic resistance of the funnel, it was fundamental that – despite the constriction – no excessive resistances were generated. The water absorption rate or the contact angle with water indicated the wettability of the three

materials and thus the effective diameter of the funnel hole. Teflon® is considered to be extremely difficult to wet because it provides a very low surface tension and has a contact angle of 118° (Zhang et al., 2004). In contrast, the water absorption rates of Makrolon® and Plexiglas® in the range of 0.2–0.4 % are ten times higher than the rate of Teflon®. In comparison, the use of Teflon® causes an increase in the existing constriction resistance due to lower wettability by artificially narrowing the hole diameter. This fact is also confirmed by the measured impedance spectra of the funnel filled with buffer, where the resistance values differ in relation to the prototype material used. The effective hole diameter was determined based on Eq. 5.1 for calculating the resistance contribution depending on the impedimetrically measured buffer resistivity and the aperture length (Tab. 5.7).

Tab. 5.7 Dimensions, electrical resistance and the calculated aperture diameter of each prototype with variable fabrication material are summarized. Based on the length and the impedimetrically measured resistance, the diameter of the funnel hole was calculated using Eq. 5.1 with ρ = 60 Ω·cm.

	Plexiglas®	Makrolon®	Teflon®
L_{hole} [mm]	0.5	0.5	0.5
R_{hole} [kΩ]	5.1	8.7	400
d_{hole} [µm] (calculated)	270	210	30

By using the measured resistance values at the monitoring frequency of 200 Hz, the actual diameters of the respective funnel holes were calculated as approximately 270 µm for Plexiglas®, 210 µm for Makrolon®, and 30 µm for Teflon®. The calculated diameter of the Teflon® prototype appears to be ten times smaller than the original milled one with 300 µm in diameter. Thus, the results show that the resulting hole diameter is dependent on the material and its wettability, although the prototypes were manufactured with identical dimensions.

As another factor, the durability of the material used on exposure to different solvents and substances is significant for the funnel micro-trap use and cleaning procedure. Due to a low water absorption rate and a strong chemical bonding between carbon and fluor atoms, Teflon® is very robust and less reactive towards chemicals. Polycarbonate has high fracture resistance, while Plexiglas® has a hard and highly scratch-resistant surface but is susceptible to breakage due to the brittleness of the plastic. One disadvantage of their use relates to the fact that both materials, Makrolon® and Plexiglas®, have poor chemical resistance and should not be cleaned with alcohol or solvents, as this leads to stress corrosion and cracking of the material.

Considering the material characteristics discussed, Plexiglas® was chosen as the manufacturing material for the funnel micro-trap. Next to material transparency, good processability, and dimensional stability, the most important decision criterion was the water absorption rate. Compared to Makrolon®, Plexiglas® exhibited better material wettability and was thus the most suitable material for the application, since the effective hole diameter is the main feature of the entire measurement setup. Therefore, it was accepted that the material would be affected by long-term use due to the applied chemical treatments of the spheroids and the repeated cleaning procedures after each measurement.

5.2.4 DETERMINATION OF THE FUNNEL FLOW BEHAVIOR

The funnel flow behavior was determined to ensure either a proper sealing of the aperture in the presence of a spheroid and a balanced fluid exchange between the upper and lower compartments in the absence of a spheroid, which enables the insertion of the micro-trap into the fluid-filled wells of the measurement array for the measurement setup without creating air bubbles.

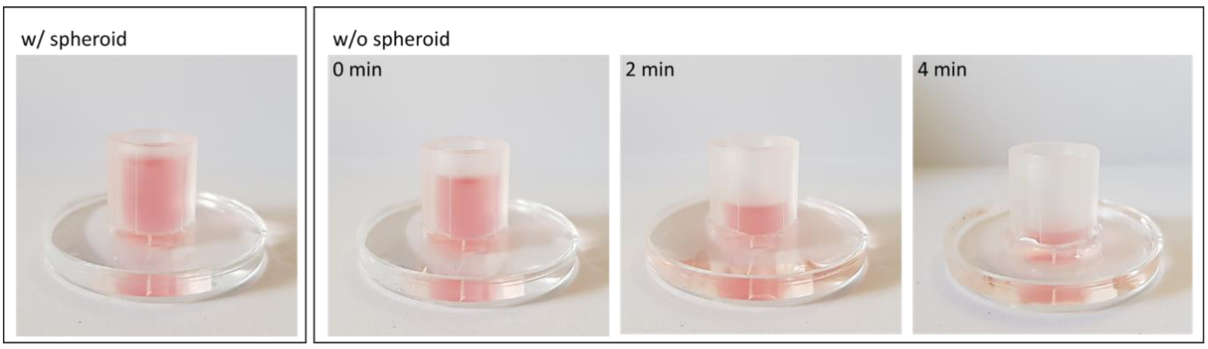

Fig. 5.17 Photographs of the determination of the flow behavior of the funnel by recording the fluid level of the red-colored culture medium in the presence of a spheroid and at specific time points (0 min, 2 min, 4 min) after removing the spheroid from the aperture. In the presence of a spheroid, the central opening was sealed and medium exchange is prohibited, while in the absence of a spheroid, the fluid rinse from the upper to the lower compartments occurs within four minutes. Experiment was performed at room temperature for visualization purposes.

The micro-trap was thus filled with red-colored cell culture medium and a spheroid was inserted into the funnel at the aperture (Fig. 5.17). To represent the situation in the measurement chamber, and for potential fluid exchange, the funnel was subsequently placed into a Petri dish filled with buffer. In the presence of a spheroid, no fluid flow from the upper to the lower compartments was observed for one hour. After removing the spheroid by gently sucking it up with a pipette, a significant fluid exchange occurred as indicated by a decreasing fluid level within four minutes, corresponding to a flow rate of approximately 0.3 mL/min.

The experiment showed that a spheroid positioned at the aperture effectively seals the constriction and prevents fluid exchange through the funnel hole. This is an important requirement for the measurement

of the spheroid impedance. However, sealing also represents a challenge regarding the homogeneous distribution of chemical substances that are used for manipulating the spheroid within the micro-trap. Thus, a special pipetting procedure for adding solutions was investigated by which a certain mixing ratio and thus an appropriate distribution within the upper compartment was achieved (see chapter 4.3.5).

On the other hand, a continuous fluid exchange is important for preventing air bubbles within the micro-trap, especially inside the funnel hole. To improve this process, additional flow paths were milled at the outside of the micro-trap device for optimal fluidal circulation between the measurement chamber wall of the ECIS™ Trans Filter Adapter device (Applied BioPhysics, Inc.) and the micro-trap (see Fig. 5.12).

5.3 DISCUSSION: COMPARISON TO ALTERNATIVE SYSTEMS

The newly developed impedance-based measurement setup can be compared to different systems, e.g. the flow channel (Hupf, 2018), the microcavity array (Krinke et al., 2010), and the capillary setup (Thielecke et al., 2001), which were presented in chapter 1.3.

Since the new funnel-based design is an evolution of the flow-channel setup, certain similarities are apparent (Hupf, 2018). The constriction for spheroid trapping is located in the center of both measurement setups between a pair of electrodes on the left and right or up- and downwards. Their aperture has an identical diameter of 250 µm at which spheroids were positioned by using hydrodynamic pressure either from the side of the respective buffer reservoir or the upper fluid compartment. In both cases, impedance signal changes of up to 600 % or 800 % could be reached using MCF-7 spheroids, making the measurement setups highly sensitive. Upon the new orientation of the setup from horizontal to vertical, the microscopic observation of a trapped spheroid during the experiment is impossible using the funnel-based micro-trap. Here, pictures of the spheroid inside the micro-trap can only be taken if the circuit and thus the measurement is interrupted, e.g. before and after a single experiment. However, the new alignment has the crucial advantage of enabling the user to perform stimulation studies during an impedance measurement. The respective compound solution can be added via the upper compartment to induce cellular reactions without removing the spheroid from the trap. In the case of using the horizontal micro-trap device, the spheroid has to be pulled back from the aperture, submerged in the respective substance solution, and replaced into the flow channel for ongoing impedance measurements. Thus, an identical positioning of the spheroid is not possible. As another advantage, the new measurement setup is used in combination with an electrode array, which is composed of robust materials and provides parallel measurements of up to eight spheroids. In comparison, the predecessor model works in a single-spheroid mode using self-made ITO electrodes, which are susceptible to scratches and solvents. As a result, the area-wide conductivity of the electrode pads will be diminished over time and the assembly has to be renewed. Overall, the funnel-based micro-trap offers additional advantages as it was developed to further improve the flow-based measurement setup.

When comparing the developed micro-trap with the microcavity array, the aspects of spheroid positioning, intrinsic parasitic contributions, and application can be considered. The microcavity array chip, which was described by Kloß et al. and Krinke et al., allows simultaneous measurements on fifteen spheroids using cavities with an edge length between 200 µm and 400 µm (Kloß et al., 2008; Krinke et al., 2010). Here, spheroid positioning requires a pipette, light microscope, and good handling practice,

making the procedure more challenging compared to the new micro-trap setup. Using their setup, they achieved a mean relative spheroid impedance of approximately 50 % for spheroids derived from a neuroblastoma cell line. To compare, the new developed EIS measurement setup exhibits a ten-fold higher relative sensitivity of 500 % and allows spheroid monitoring over a wide, sensitive frequency range from $5 \cdot 10^0$ Hz to 10^3 Hz. Using the microcavity array, the group was able to detect specific neurodegenerative processes based on distinguishing the impedance signals of cells expressing a microtubule-associated protein as wild-type or mutant. Likewise, the use of the funnel-shaped micro-trap allows differentiation of physiologically distinct spheroids in terms of age, size, or e.g. pH-value by performing RTC measurements (see chapter 7.1), although experiments with wild-type and mutant cells have not yet been tested.

The basic idea and setup of the capillary setup presented in the paper of Thielecke et al. is similar to the flow channel measurement setup developed by Hupf as the spheroid is placed at a restrictive area applying hydrodynamic force (Thielecke et al., 2001; Hupf, 2018). Either a pumping system is required to position the spheroids, or different fluid levels of associated reservoirs can be used, whereby positioning of a spheroid in the funnel-shaped micro-trap is accomplished by utilizing gravity, eliminating the need for additional equipment. However, Thielecke et al. noted that an influence of the measurement procedure on the intrinsic cellular structure, due to compressing the spheroid body into the glass capillary with a diameter of 300 µm, would be possible. The corresponding equivalent circuit model of the capillary system equals the model of the funnel-based system comprising the parameters R_{ext}, R_{int}, and C_{mem} (equally A_{sph}). In the report, the capillary system was applied to distinguish e.g. healthy and gene-manipulated T47D human breast carcinoma spheroids based on the respective R_{ext} values calculated using an equivalent circuit model from Fricke and Morse for fitting the measured impedance data. Apart from detecting R_{ext} values in a similar range, the new EIS instrument displays low parasitic contributions enabling spheroid characterization.

As a result, the novel impedimetric measurement setup for spheroid analysis provides an easy handling procedure due to simple spheroid positioning and manipulation strategies compared to other measurement setups. An optimized low resistance contribution of the funnel-based micro-trap device enables signal sensitivity over a wide frequency range. In combination with adjustable measurement settings, data can be recorded in multi-frequency or rapid time collection mode with variable time resolution adapted to the experimental process studied. In addition, the ability of conducting up to eight experiments in parallel making the developed EIS measurement setup a useful system for spheroid analysis.

5.4 SUMMARY AND OUTLOOK

The novel impedimetric device is an upright funnel-shaped micro-trap with a central opening located between two electrodes. When a spheroid is inserted into the measurement device, it is held back at the aperture and partially forced into the funnel hole due to hydrodynamic pressure and gravity. The spheroid thus seals the opening by adapting to the smaller diameter of the funnel hole, thereby enabling impedimetric analysis.

The measurement principle was evaluated by performing a proof-of-principle experiment in which the impedance spectra of the empty buffer-filled measurement chamber, initial funnel prototype, and a trapped spheroid were recorded. By determination of the relative impedance from the spectra of a spheroid-free and a spheroid-loaded micro-trap, values up to 500 % were obtained, which indicate that signal changes resulting from the sealing of the central constriction by a spheroid can be detected sensitively. While performing the spheroid experiments in multi-frequency mode, the time course of the impedance values is extracted from the spectra at the monitoring frequency of 200 Hz. In addition to signal intensities, the shape of the impedance spectrum is defined by the influence of the three spheroid parameters as illustrated using simulated spectra (chapter 3.2.3). In this context, the phenomenon of the dielectric dispersion and the Nyquist plot demonstrating two time constant spectra have been discussed. In the high-frequency range of the spectral curve, the parasitic impedance contribution of the electronic equipment is evident and was determined for the final micro-trap device as $2.4 \cdot 10^{-10}$ $Fs^{n-1}cm^{-2}$ (with $n_{para} = 0.95$).

Based on the micro-trap prototype, further evolution steps have been performed to achieve the highest sensitivity of impedance signaling and reproducibility of measurement procedures. Therefore, several micro-trap prototypes with different dimensions and materials were manufactured and tested. Finally, the new instrument for spheroid analysis was successfully developed comprising the transparent funnel-based micro-trap, which was adapted to the selected electrode arrangement. All refinements were investigated based on the impedance measurements conducted, thereby leading to the final layout details. In this way, several micro-traps were fabricated so that different spheroid experiments could be performed simultaneously. The EIS measurements for analyzing the impedance contribution of one spheroid per micro-trap could be performed in a sensitive and cost-efficient way by reusing the manufactured devices.

For the measurement procedure, the commercially available ECIS™ Trans Filter Adapter device from Applied BioPhysics, Inc. (Troy, USA) was utilized, which enables the performance of up to eight spheroids

respectively experiments in parallel (see chapter 4.3.3). This throughput was sufficient for the experiments performed in this work.

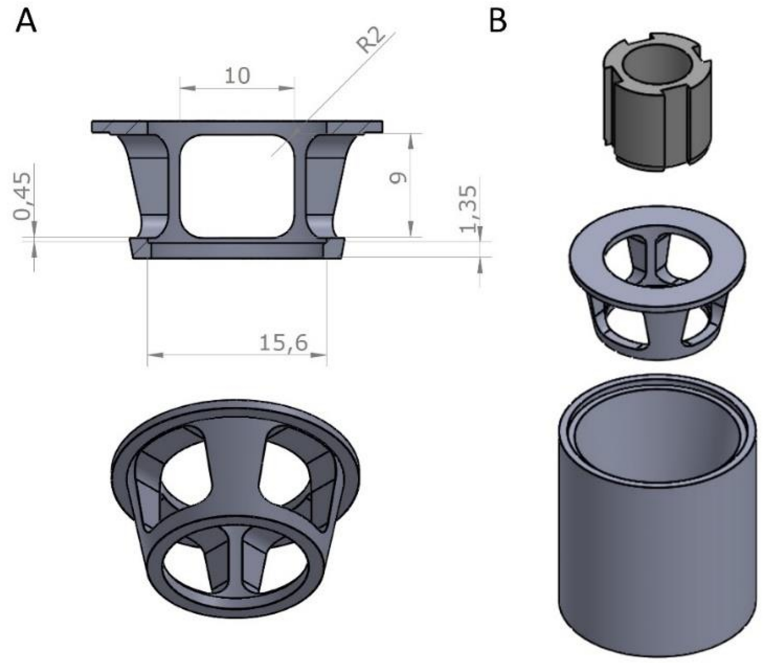

Fig. 5.18 Technical drawings of the adapter tool developed for positioning funnel micro-trap devices into the wells of the cellZscope® measurement setup (A). By inserting the micro-trap into the adapter tool, the assembly is mounted into the pots as shown in the explosion drawing (B).

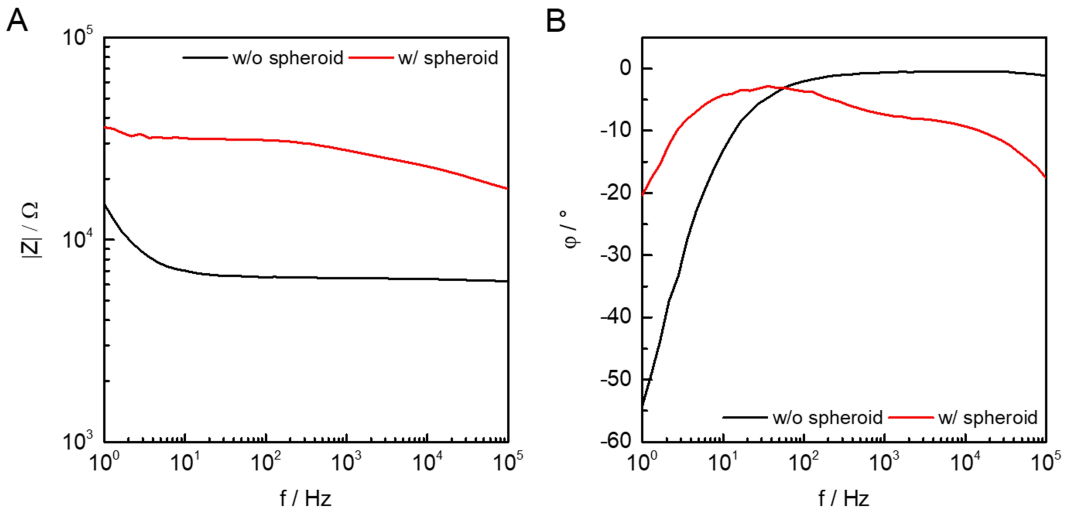

Fig. 5.19 Frequency-dependent impedance spectra of the funnel-shaped micro-trap device in the form of Bode plots. Spectra with and without a spheroid positioned at the aperture of the micro-trap are shown for the magnitude $|Z|$ (A) as well as the phase shift angle φ (B). This experiment provided a proof of principle for the spheroid measurements using the cellZscope® device by confirming the similar sensitivity of impedance signaling with identical result output compared to the ECIS™ Trans Filter Adapter device. Experiments were performed in a standard cell culture incubator at 37 °C and 0 % CO_2.

However, the applicability of the measurement principle as well as the optimized micro-trap setup was evaluated using the cellZscope® device, which is commercially available from nanoAnalytics GmbH (Münster, Germany). The cellZscope® system is typically used for the analysis of the transepithelial electrical resistance of cell layers and provides the measurement of 24 individual wells. For adjusting the developed micro-trap device to the pots of the measurement system, an adapter tool compromising the dimensions of the measurement chamber pots in combination with the micro-trap funnel device has been designed (Fig. 5.18). This adapter tool uses the groove of the pots for positioning the cell culture inserts into the wells and thus enables a similar mounting of the funnel-adapter assembly as indicated in the explosion drawing (Fig. 5.18, B).

In a proof-of-principle experiment, the applicability of the measurement system was confirmed, providing similar sensitivity of impedance signaling with identical result output compared to the ECIS™ Trans Filter Adapter device used in this work, while enabling a 24-fold approach (Fig. 5.19).

CHAPTER 6

CHARACTERISTICS OF MCF-7 AND U-373 MG SPHEROIDS

6.1 SPHEROID FORMATION 121

6.2 SPHEROID GROWTH KINETICS 123

6.3 SPHEROID ADHESION 134

6.4 DISCUSSION 137

6.5 SUMMARY AND OUTLOOK 148

Since the new measurement setup is validated by the measurement and manipulation of spheroids, the measurement specimens are characterized in this chapter. Therefore, the three key aspects of spheroid formation, proliferation, and adhesion were investigated by performing time-lapse imaging (Fig. 6.1).

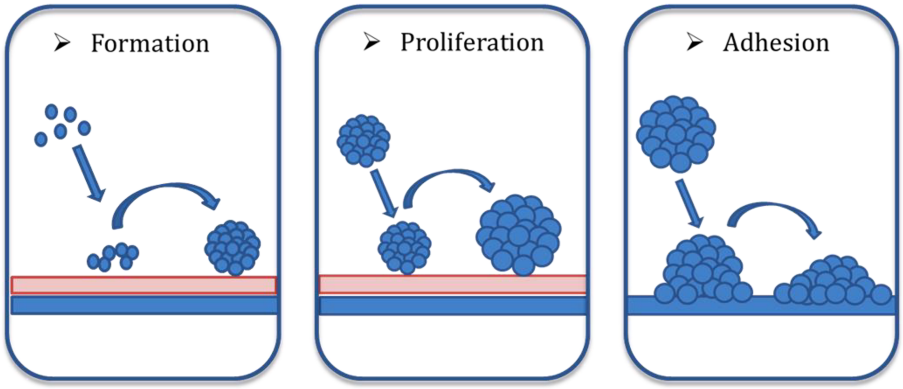

Fig. 6.1 Illustration* of the three key aspects of spheroid characterization studies.

*illustration is simplified and not to scale

First, spheroids were formed using the liquid overlay culture technique, followed by the observation of the spheroid's growth behavior and the spheroid's adhesion onto an adhesive surface. In this context, the use of varying cell concentrations, the influence of different serum concentrations, and the alteration of the pH value of the cell culture medium were analyzed. The results were compared concerning the characteristics of the U-373 MG and MCF-7 cell lines.

6.1 SPHEROID FORMATION

All spheroids that were used in the experiments presented in this thesis were prepared by seeding cells onto an agarose-coated surface of 96-well plates (see also the protocol in chapter 4.1.5). Using this approach, cell aggregates were formed by preventing the cells from attaching to the culture substrate, while the aggregation step was enhanced by applying orbital shaking after cell seeding. With the zenCELL owl digital microscope, the formation processes of U-373 MG (Fig. 6.2) and MCF-7 spheroids (Fig. A-6.1) were documented for 24 hours after cell seeding using compatible 24-well plates.

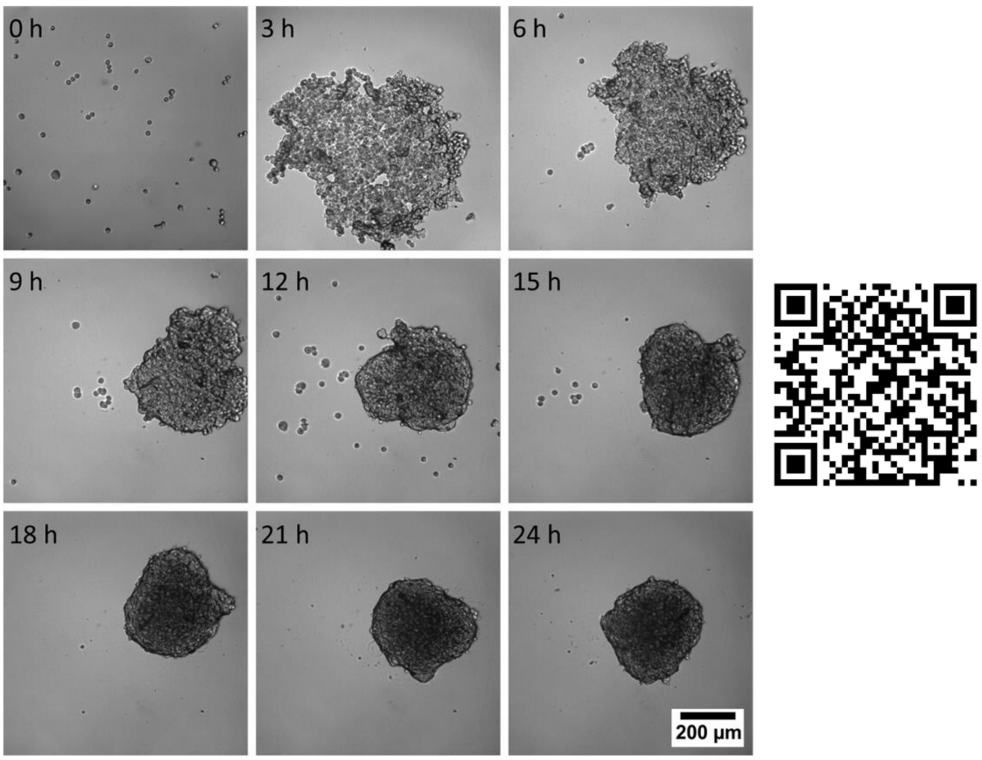

Fig. 6.2 Time-resolved micrographs of the spheroid formation process of U-373 MG cells (seeding density: 18,000 c/well) documented for 24 hours using the zenCELL owl digital microscope. Experiment was performed in a standard cell culture incubator at 37 °C and 5 % CO_2. The full time-lapse clip is available by scanning the QR code (see chapter 11.1, Tab. A-6.2 for the password).

The time-lapse images show the three steps of the spheroid formation mechanism (compare chapter 1.2.2; Lin et al., 2006). In the first phase, mono-dispersed cells form a loose aggregate, as shown within the first three hours after cell seeding. Here, the image section at the time of seeding only shows a certain number of the 18,000 cells in total that were seeded per well. A loose aggregate is subsequently assembled by the attachment of neighboring, suspended single cells, which is promoted by the secretion of extracellular matrix fibers such as collagen or fibronectin and a high expression of integrins leading to subsequent integrin-ECM adhesion (Robinson et al., 2004). This phase is followed by a lag phase, in which no morphological changes are observed (Lin et al., 2006). It may be assigned to the period from

three to nine hours in the present micrographs which, however, merges into the last phase, as the third step comprises the compaction of the cell aggregate to a spheroid. The spheroid compaction is proceeded by the formation of strong cell-cell contacts, which leads to a tightly packed spheroid 18 hours after seeding. For surface area minimization, the spheroid shape becomes round, and the cells of the outer spheroid shell differentiate into polarized cells acting like a physical barrier (O´Brien et al., 2002). Finally, a single spheroid is generated in each well, while no single cell can be seen outside the aggregate. After spheroid formation, orbital shaking is stopped, and the spheroids undergo growth processes by further cultivation.

In contrast to the usual spheroid production approach outlined in this thesis, compatible 24-well plates were used when taking time-lapse images with the zenCELL owl digital microscope. Since the preparation of spheroids in coated 96-well plates results in spheroids with a defined cell number and reproducible size, with one spheroid formed per well, the formation using other plate formats with larger well sizes typically leads to spheroids with an irregular shape and a broad size distribution. Therefore, the spheroids that are produced to document the entire formation process by time-lapse imaging will not exactly represent the standardized spheroids as used in further spheroid characterization studies.

6.2 SPHEROID GROWTH KINETICS

After the formation process, the freshly generated spheroids can be further incubated to achieve the required size and to strengthen the cell-cell and cell-ECM contacts. As growth progresses, the number of proliferating cells decreases and the proportion of non-proliferating, quiescent cells increases. Upon depletion of oxygen, glucose, and other substrates in conjunction with the accumulation of toxic metabolic waste products, cell death and necrosis occur in the spheroid centers (Sutherland, 1988; Costa et al., 2016; see also chapter 1.1.3). The spheroid growth behavior is specific for every cell line and depends on multiple factors such as the number of cells assembled in one spheroid, the nutrient concentrations in the growth media, the cellular nutrients consumption rates, and cell packing densities. In addition, different cell types vary in their spheroid shape as well as size despite using the same seeding density. For example, while tumor cell spheroids mostly show a linear growth behavior over time (Landry et al., 1982), spheroids of other cell types exhibit a sigmoidal growth curve (Gompertz, 1825) or become more compact by reducing their diameter, as discovered in this thesis in the case of U-373 MG spheroids.

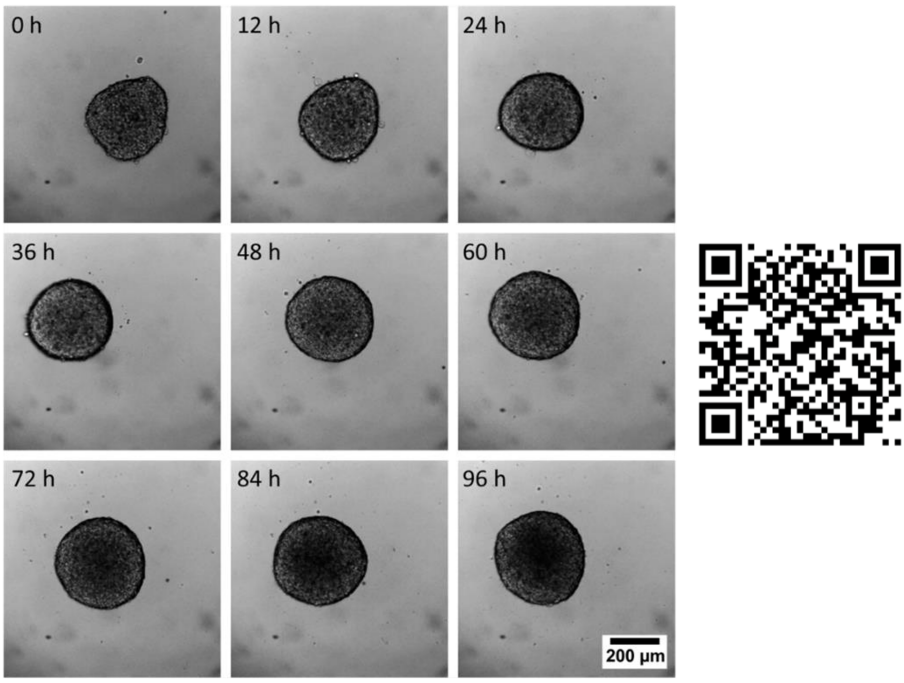

Fig. 6.3 Time-resolved micrographs of the spheroid growth process of an MCF-7 spheroid (1 d, 4,000 c/well) documented for 96 hours using the zenCELL owl digital microscope. Experiment was performed in a standard cell culture incubator at 37 °C and 5 % CO_2. The full time-lapse clip is available by scanning the QR code (see chapter 11.1, Tab. A-6.2 for the password).

In this work, the kinetics of the spheroid growth of MCF-7 (Fig. 6.3) and U-373 MG spheroids (Fig. A-6.2) were studied by recording time-resolved images over eight days, either automatically for microfilming

using the zenCELL owl digital microscope or manually by taking microscopic images each day. The micrographs showing the growth behavior of a one-day-old MCF-7 spheroid illustrate the constant increase in spheroid diameter in accordance with a more smooth and round shape over 96 hours (Fig. 6.3). During incubation, the darker area in the center of the spheroid body also increases in size with time. This denser area may indicate the zone of the most stratified cell structures, while it does not provide evidence for the region of the necrotic core (Hari et al., 2019; Petry and Salzig, 2022), as this could not be verified in this work. The growth of the spheroid is primarily driven by cell proliferation at the outer shell while the spheroid shape becomes round due to surface area minimization (Ruckdäschel et al., 2020). During this process, the spheroid moves randomly across the surface, making it difficult to monitor the growth kinetics within the given field of view.

When comparing the two types of cell lines used, it is observed that the kinetics of U-373 MG spheroids differ significantly from those derived of MCF-7 cells. In the case of the U-373 MG cells, the size of the derived spheroids decreases, and the body becomes more compact over time. Within 96 hours, the original diameter of the monitored spheroid aggregate shown in the micrographs is diminished from 830 µm to 500 µm while moving over the non-adherent surface (Fig. 6.4).

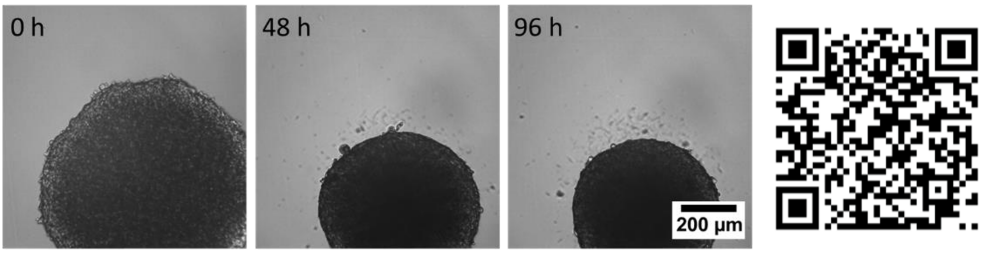

Fig. 6.4 Time-resolved micrographs of the spheroid growth process of a U-373 MG spheroid (1 d, 18,000 c/well) documented for 96 hours using the zenCELL owl digital microscope; see also Fig. A-6.2 for a detailed time resolution. Experiment was performed in a standard cell culture incubator at 37 °C and 5 % CO_2. The full time-lapse clip is available by scanning the QR code (see chapter 11.1, Tab. A-6.2 for the password).

The described phenomenon of spheroid compaction in relation to the kinetics of volume growth is further discussed by comparing the growth kinetics of MCF-7 and U-373 MG spheroids at different cell numbers seeded in chapter 6.4.2.

6.2.1 SPHEROIDS FORMED WITH DIFFERENT CELL NUMBERS

To investigate the influence of growth time, initial cell number, and cell type, spheroids with different cell numbers were prepared and incubated over eight days. In principle, the number of proliferating cells in the outer shell depends on the initial seeding cell number and the duration of incubation after spheroid formation. Thus, for each initial cell number and specific growth time, spheroids with individual

diameters are formed. On condition of reproducibility, the size of the spheroids can be controlled by adjusting the initial cell number and the incubation time to the requirements of the experiment.

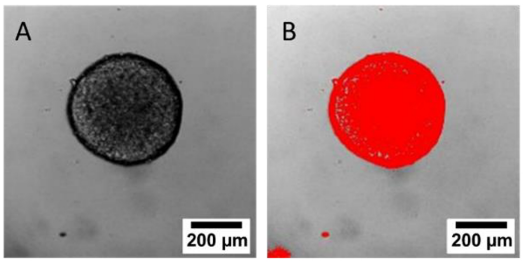

Fig. 6.5 Original (A) and processed (B) image of an MCF-7 spheroid captured using *ImageJ* software. The microscopic picture was taken 48 hours after placing one MCF-7 spheroid (one-day-old; 4,000 c/well) onto a non-adhesive surface by performing time-lapse imaging with the zenCELL owl digital microscope. After applying contrast and image thresholds, the software automatically detects the outline of the spheroid and measures the framed area, which is depicted as a red-colored zone in the exemplary image.

The statistical analysis was performed by obtaining a quantitative description of the spheroids by measuring various parameters such as the area of the spheroid, its diameter, and its roundness using *ImageJ* software (Rasband, W.S., National Institutes of Health, USA; Fig. 6.5). In this way, more than 40 spheroids per seeding density and day were analyzed. To enhance the comprehensibility of the findings, only the time dependence of the spheroid diameter is plotted in the following.

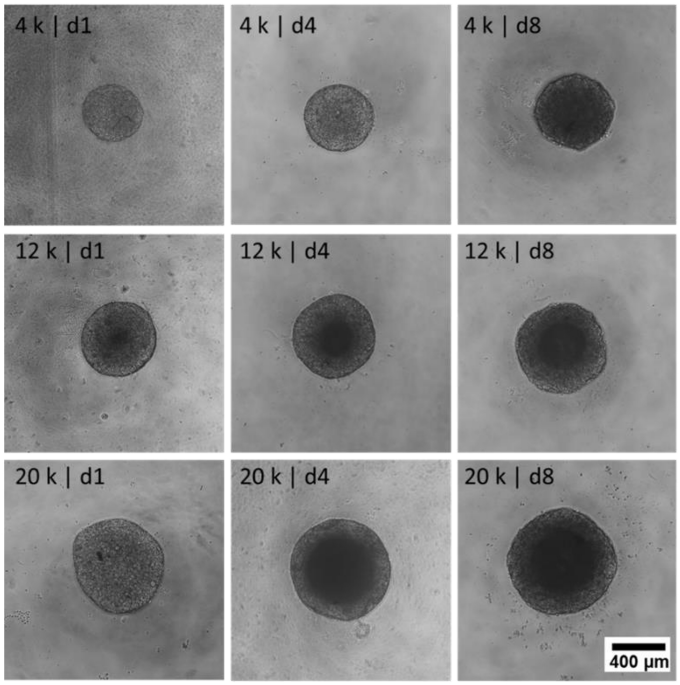

Fig. 6.6 Micrographs of the spheroid growth process of three MCF-7 spheroids, which were seeded with different cell concentrations (first row: 4,000 c/well; second row: 12,000 c/well; third row; 20,000 c/well) and documented at day 1, day 4, and day 8 after spheroid formation using a phase contrast microscope. Experiment was performed in a standard cell culture incubator at 37 °C and 5 % CO_2.

In general, MCF-7 and U-373 MG spheroids can easily be prepared in various defined sizes according to the protocol in chapter 4.1.5. To be suitable for the novel setup, the spheroids must be large enough to be held at the central opening. Hence, to determine the optimal seeding density and incubation period, the spheroids were grown using different initial cell numbers dependent on the cell type ranging from 4,000–20,000 c/well for MCF-7 cells and 20,000–45,000 c/well for U-373 MG cells. Their growth was documented over eight days using phase-contrast imaging. As illustrated in Fig. 6.6, MCF-7 spheroids exhibit a round, smooth shape on the first day after seeding and continuously grow during incubation. Here, a clear dependency of the seeding density and the incubation time can be seen, as the diameter of the spheroids increases in proportion to both factors. For the analysis, the diameter of over 40 individual MCF-7 spheroids per seeding density and day was determined (Fig. 6.7).

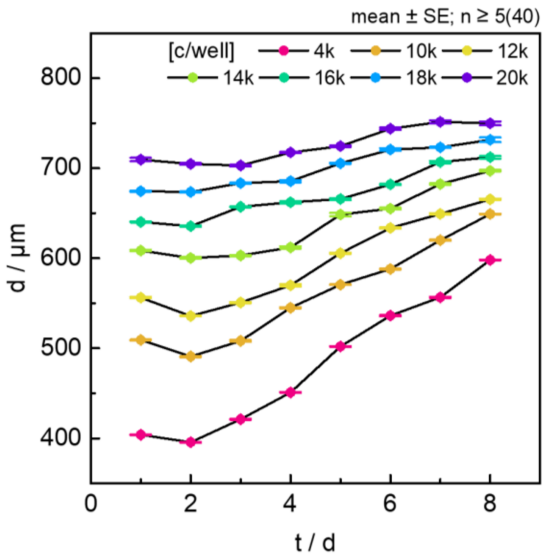

Fig. 6.7 Kinetic growth study of MCF-7 spheroids from different seeding densities (4,000–20,000 c/well) documented over eight days. Experiments were performed in a standard cell culture incubator at 37 °C and 5 % CO_2. Data sets were averaged, mean ± SE; n ≥ 5(40).

After spheroid aggregation, the diameter decreases slightly from day 1 to day 2, regardless of the initial cell number, due to cell reorganization and rearrangement within the spheroid. From the second to the eighth day, spheroids of each seeding density exhibit reproducible, linear growth behavior, resulting in spheroids with characteristic diameters at each seeding density and day in a total range of 400–750 µm. In addition, the spheroid roundness increases from 0,907 at day 1 to 0,959 at day 3 after spheroid formation (Ruckdäschel et al., 2020).

To analyze the growth kinetics of MCF-7 spheroids, the growth curves were normalized to day 2 after spheroid formation (Fig. 6.8, A). Since growth starts on day 2, while the diameter of the spheroids initially decreases between day 1 and day 2 due to the strengthening of cell-cell contacts, day 1 is not included in the mathematical evaluation. Using normalization, a clear dependence of the kinetics on the

seeding density can be illustrated by a decreasing growth rate due to a higher cell concentration. Additionally, a linear growth curve was fitted to the averaged data of each seeding density in the time range from day 2 to day 8 (Fig. 6.8, B).

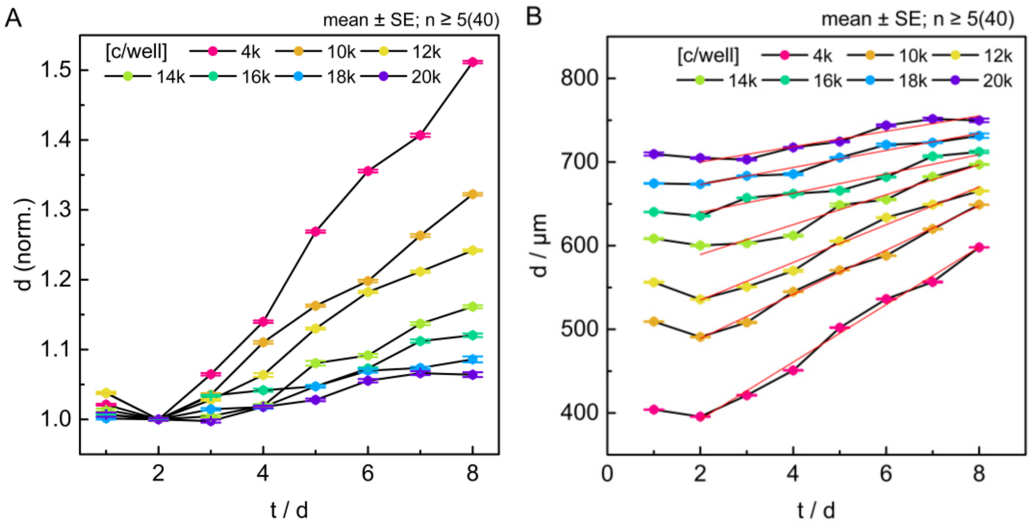

Fig. 6.8 Kinetic growth study of MCF-7 spheroids from different seeding densities (4,000–20,000 c/well) documented over eight days (mean ± SE; n ≥ 5(40)). After averaging, data sets were either normalized to day 2 after spheroid formation (A) or linearly fitted (B). The resulting values of the calculated linear equations, intercept and slope, are provided in chapter 11.1 (Tab. A 6.1).

The resulting values of the calculated linear equations are provided in chapter 11.1 (Tab. A-6.1), whereby the slope values of the linear regression represent each change in diameter per day and were plotted against the respective seeding density (Fig. 6.9). The change in diameter per day linearly decreases for seeding densities between 4,000 c/well (daily growth of 34 (± 1) µm/d) and 16,000 c/well (12 (± 1) µm/d) but becomes more constant at higher seeding densities (18,000 c/well: 10.2 (± 0.6) µm/d; 20,000 c/well: 9 (± 1) µm/d).

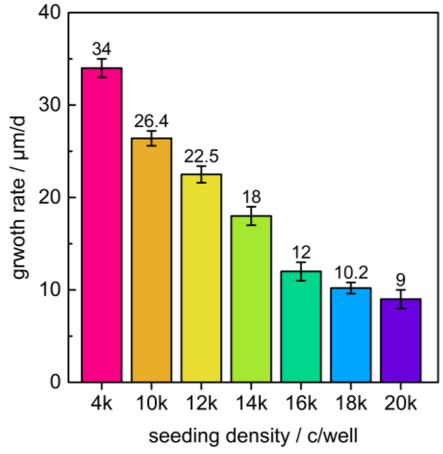

Fig. 6.9 Growth rate based on the kinetic growth study of MCF-7 spheroids from different seeding densities (4,000–20,000 c/well). The spheroid growth per day was determined for every seeding density using linear regression and plotting the calculated slope values with respect to the seeding density.

To compare the findings, the growth kinetics of U-373 MG spheroids were studied using a similar approach over eight days. These spheroids also form a round, smooth aggregate on the first day after cell seeding, like the MCF-7 spheroids, and exhibit a characteristic size distribution per seeding density and day in a reproducible manner. As previously shown in Fig. 6.4, the U-373 MG spheroids undergo compaction associated with a decrease in diameter. This phenomenon was determined by analyzing 40 individual U-373 MG spheroids per seeding density per day (Fig. 6.10). While in the period between the first and third day after spheroid formation, the total size decreases by more than 30 % e.g., from 1,000 µm to 700 µm diameter at an initial cell count of 45,000 c/well, the compaction process is more gradual in the second part of the documentation.

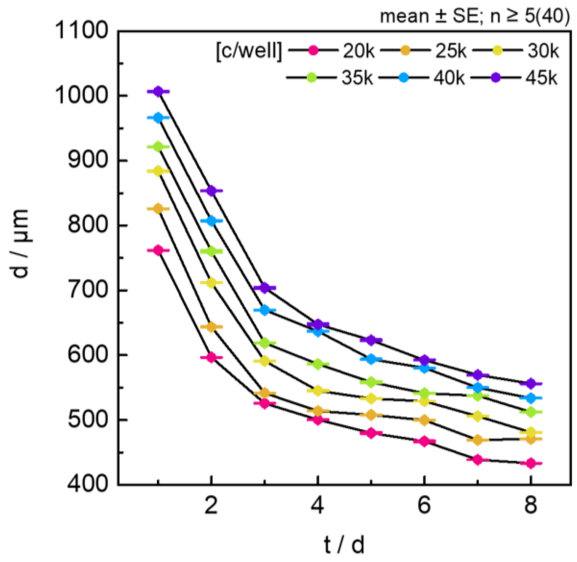

Fig. 6.10 Kinetic growth study of U-373 MG spheroids from different seeding densities (20,000–45,000 c/well) documented over eight days. Experiments were performed in a standard cell culture incubator at 37 °C and 5 % CO_2. Data sets were averaged, mean ± SE; n ≥ 5(40)).

To investigate any kinetic context for this phenomenon, the growth curves were normalized to day 1 after spheroid formation (Fig. 6.11, A). The normalization reveals that the shape of the growth curves is almost identical and that there is no correlation of the kinetics due to different seeding concentrations. Thus, the curves can be averaged (Fig. 6.11, B) and mathematically described by an exponential fit (Eq. 6.1) with the offset y_0 (here: 0.55 (± 0.02)); the initial value A (here: 0.6 (± 0.1)), and the exponential rate R_0 (-0.4 (± 0.1)).

$$y = y_0 + A \cdot exp^{R_0 x} \qquad \textbf{Eq. 6.1}$$

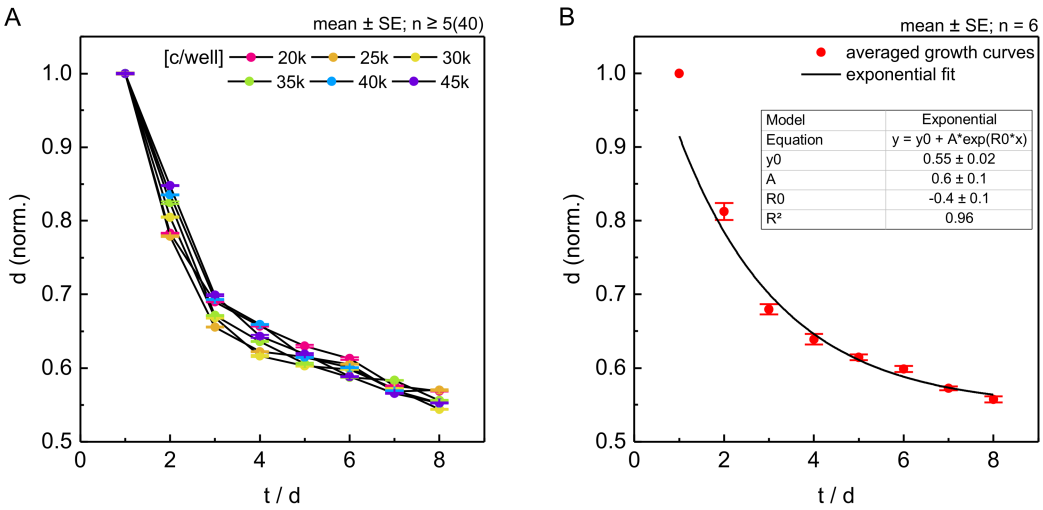

Fig. 6.11 Kinetic growth study of U-373 MG spheroids from different seeding densities (20,000–45,000 c/well) documented over eight days (A; mean ± SE; n ≥ 5(40)). After averaging, data sets were normalized to day 1 after spheroid formation (A) and exponentially fitted (B; Eq. 6.1; mean ± SE; n = 6).

6.2.2 SPHEROIDS EXPOSED TO DIFFERENT SERUM CONCENTRATIONS

To examine the influence of FCS concentration on spheroid formation and growth behavior, spheroids with similar cell seeding density were exposed to different serum concentrations. For this purpose, U-373 MG spheroids (30,000 c/well) were prepared using cell culture media supplemented with specific FCS concentrations that varied between 0 % (v/v) and 10 % (v/v), whereas 5 % (v/v) was used for U-373 MG cells standardized during cell cultivation. Their growth was documented over eight days using phase-contrast imaging (Fig. 6.12).

The analysis of more than 25 individual spheroids per FCS concentration and day demonstrates that spheroids can also be formed using different FCS concentrations, as well as no serum addition. The kinetic growth study shows the identical growth behavior of U-373 MG spheroids in general by forming cell aggregates with distinct diameters for a given growth time and a clear compaction process during incubation. Depending on the FCS concentration, the diameter of the spheroids increases with higher serum concentration. On the first day, the diameter varies in a range of 90–110 % with respect to the normal FCS concentration of 5 % (v/v), while for example on the fifth day, the absolute diameter differs by approximately 20 µm per FCS concentration level. This slight size difference is hardly noticeable in the exemplary phase-contrast images (Fig. 6.13, A). Consistent with the U-373 MG spheroid growth study using different seeding densities, normalization of the growth curves in the context of different serum concentrations presents no difference in growth kinetics for 0 %, 2.5 %, and the standardized 5 % (v/v) (Fig. 6.13, B).

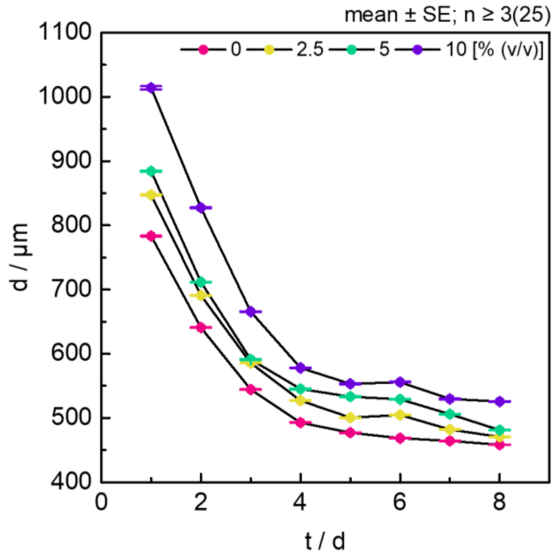

Fig. 6.12 Kinetic growth study of U-373 MG spheroids (30,000 c/well) incubated with cell culture medium containing various serum concentrations (0–10 % (v/v)), documented over eight days. Experiments were performed in a standard cell culture incubator at 37 °C and 5 % CO_2. Data sets were averaged, mean ± SE; n ≥ 3(25).

Thus, the normalized growth curves can also be described by the calculated exponential fit for U-373 MG spheroids investigated in chapter 6.2.1 (Eq. 6.1). However, for spheroids formed in 10 % (v/v) FCS-supplemented cell medium, significantly altered kinetics were observed as the normalized curve decreases by approximately 50 % within seven days.

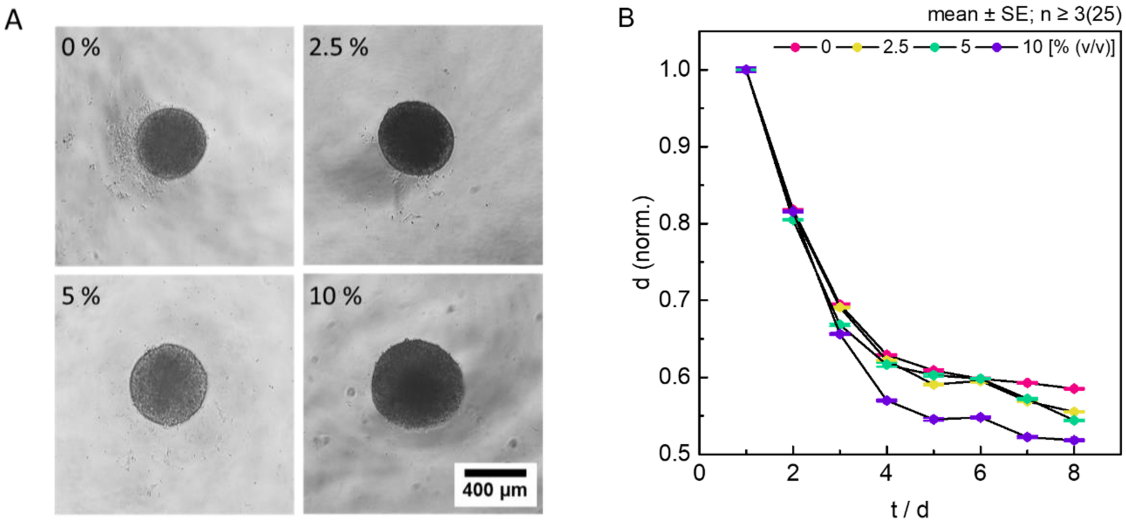

Fig. 6.13 Micrographs on day 8 after spheroid formation (A) and normalized growth curve (B) based on the kinetic growth study of U-373 MG spheroids (30,000 c/well) incubated with cell culture medium containing various serum concentrations (0–10 % (v/v)), documented over eight days (mean ± SE; n ≥ 3(25)). Experiments were performed in a standard cell culture incubator at 37 °C and 5 % CO_2. After averaging, data sets were normalized to day 1 after spheroid formation (B).

6.2.3 SPHEROIDS EXPOSED TO DIFFERENT PH VALUES

In addition to spheroids produced from different serum concentrations, spheroids prepared with varying medium pH values were also characterized. In this instance, the cell suspension was diluted to 30,000 c/well (U-373 MG cells) using a culture medium with distinct pH values (pH 6.6–7.8). The spheroids' growth behavior was documented over eight days using phase-contrast imaging.

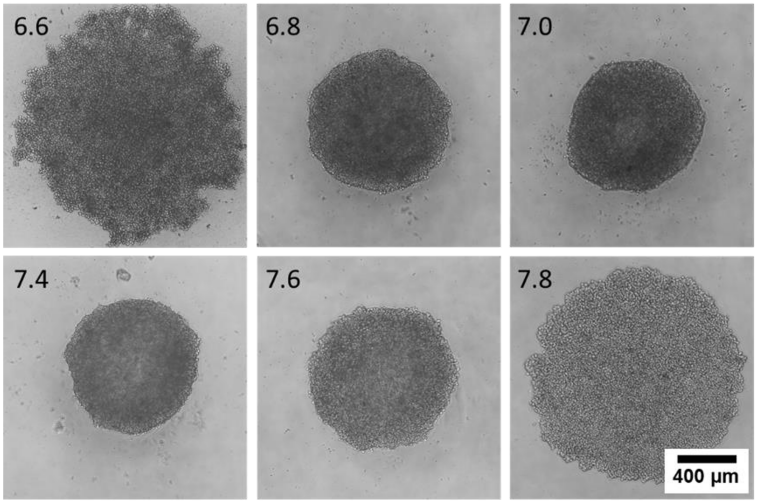

Fig. 6.14 Micrographs of U-373 MG spheroids (30,000 c/well), which were seeded using a culture medium with distinct pH values (pH 6.6–7.8) and documented at day 1 after spheroid formation using a phase contrast microscope. Experiments were performed in a standard cell culture incubator at 37 °C and 5 % CO_2.

For this experiment, the pH value of the nutrient medium was both increased and decreased, starting from the physiological pH value of pH 7.2 used as a standard. The size measurements were evaluated in the range of pH 6.6 to 7.8 since no spheroids were formed at pH values below or above this as only shapeless, inhomogeneous cell aggregates and cell death were observed. At these pH extrema, destruction of the agarose coating could be noticed, representing an additional mechanical impact factor apart from the dysregulation of the cellular processes for spheroid formation. Within the pH range of pH 6.6–7.8 spheroids or spheroid-like cell aggregates were formed, while the typical spheroid structure was found between pH 6.8 and 7.6 (Fig. 6.14).

The kinetic growth study of more than 25 individual spheroids per pH value and day indicates the further growth behavior of U-373 MG spheroids (Fig. 6.15). As already discussed in chapter 6.2.1, at the physiological pH of 7.2, the expected process of spheroid compaction and diameter stagnation is shown. Furthermore, the growth study indicates that the spheroid sizes in the range of pH 7.0–7.6 are independent of the adjusted pH value of the cell medium used and represent identical kinetics. At pH 7.8, the influence of the pH is visible, as an identical size profile was analyzed for U-373 MG spheroids, whereby the investigated spheroids exhibit a larger diameter by a factor of approximately

1.5 compared to the physiological spheroids with identical cell numbers. On the other extrema, at pH 6.6 and pH 6.8, the spheroids differ in size and growth kinetics. Here, the phase-contrast images show a loose, spherical aggregate that maintains the same shape during the incubation period studied, whereby size fluctuations are due to difficulties in data evaluation by optical means.

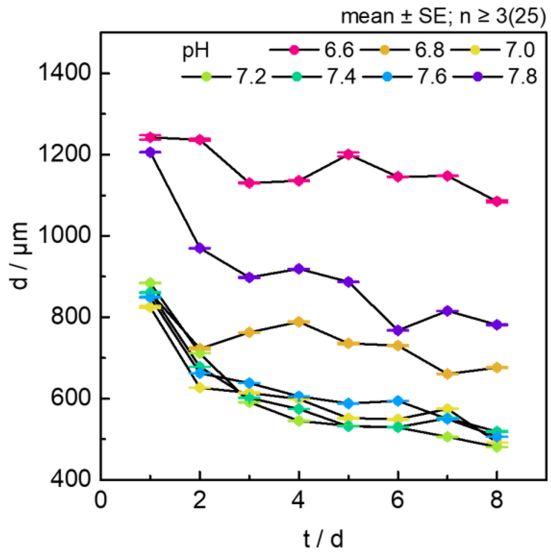

Fig. 6.15 Kinetic growth study of U-373 MG spheroids (30,000 c/well) incubated with cell culture medium at different pH values (pH 6.6–7.8), documented over eight days. Experiments were performed in a standard cell culture incubator at 37 °C and 5 % CO_2. Data sets were averaged, mean ± SE; n ≥ 3(25).

The spheroid growth kinetics is exemplarily displayed for spheroids formed and incubated at the two pH extremes of pH 6.6 and pH 7.8 shown on day 1 and day 8 after formation (Fig. 6.16, A).

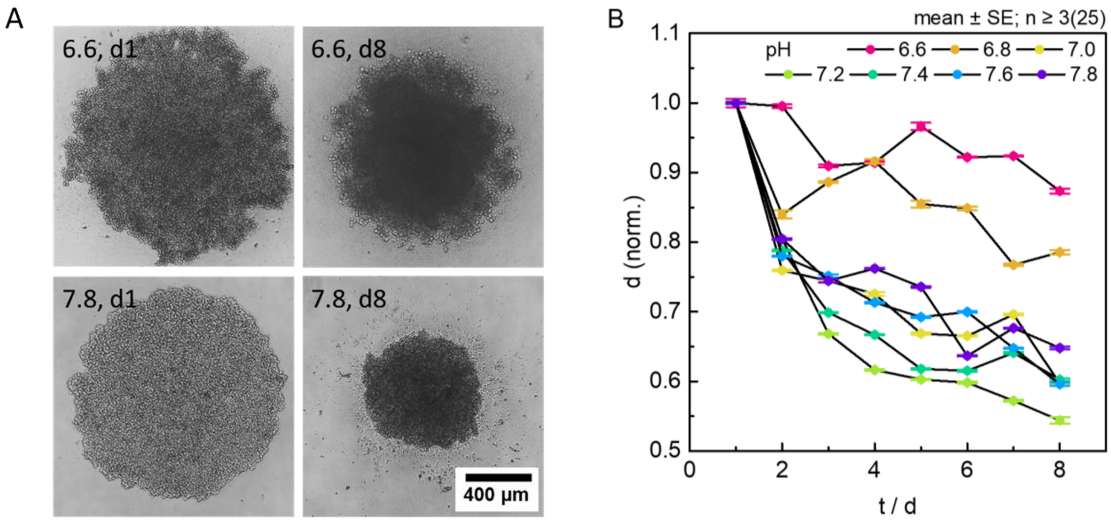

Fig. 6.16 Micrographs on day 1 and day 8 after spheroid formation (A) of U-373 MG spheroids (30,000 c/well) incubated with cell culture medium at different pH values (pH 6.6 and pH 7.8). Normalized growth curve (B) based on the kinetic growth study of U-373 MG spheroids (30,000 c/well) incubated with cell culture medium at different pH values (pH 6.6–7.8), documented over eight days (mean ± SE; n ≥ 3(25)). Experiments were performed in a standard cell culture incubator at 37 °C and 5 % CO_2. After averaging, data sets were normalized to day 1 after spheroid formation (B).

The micrographs demonstrate the size reduction of the spherical body starting from a similar diameter of approximately 1,400 µm in both cases, with the final size of 1,100 µm (pH 6.6) and 750 µm (pH 7.8). Thus, a significant difference in growth kinetics depending on the pH value is detected, which is also reflected after normalization of the investigated growth curves in the context of different pH values (Fig. 6.16, B). An equivalent growth kinetic to the physiological pH of 7.2 is likely to be found for more alkaline pH values of pH 7.4, 7.6, and 7.8, whereas acidification of the cell culture medium results in an atypical growth course found at pH 6.6 and pH 6.8. At these pH values, the spheroids undergo even less compaction, decreasing in diameter by only 10 % to 20 % compared to the more typical reduction by almost 50 %.

6.3 SPHEROID ADHESION

For a complete spheroid characterization, the adhesion process of U-373 MG and MCF-7 spheroids was analyzed. Although the adhesion process was not necessary for the impedance measurements of trapped spheroids, the information on adhesion kinetics and the practice of proper handling was crucial for setting up the time-lapse stimulation experiments using adherent spheroids.

The adhesion and outgrowth of spheroids on a tissue culture-treated surface were observed by time-lapse imaging with the zenCELL owl digital microscope (Fig. 6.17 [U-373 MG spheroid]; see chapter 11.1, Fig. A-6.3 [MCF-7 spheroid with full time-lapse clip]; also see *Application Note*: Ruckdäschel et al., 2020, InnoME GmbH). As spheroids settle into the pre-treated wells, cells adhere to the surface and begin to grow. Initially, cells of the outer shell attach to the surface and form cell surface contacts mediated by the ECM. The spheroid flattens, and within 12 hours after the spheroid is placed in the well, additional cells migrate out of the initial contact zone. This outgrowth of the spheroid initially starts in one direction, then gradually increases around the spheroid, and finally results in a centrosymmetric seam of spread cells. After 48 hours, the adherent spheroid consists of a hemispherical three-dimensional part and a surrounding monolayer of cells (compare *Application Note*: Ruckdäschel et al., 2020, InnoME GmbH).

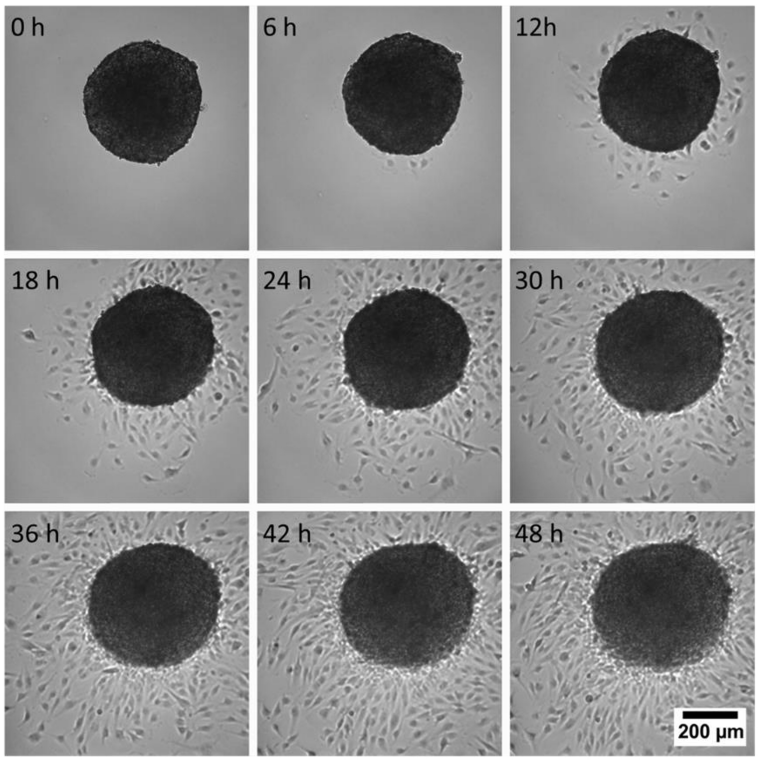

Fig. 6.17 Time-resolved micrographs of the spheroid adhesion process of a U-373 MG spheroid (5 d; 18,000 c/well) documented for 48 hours using the zenCELL owl digital microscope. Experiment was performed in a standard cell culture incubator at 37 °C and 5 % CO_2.

Adhesion kinetics were quantified using microscopic time-lapse images of the zenCELL owl digital microscope, which were processed with *ImageJ* software (Rasband, W.S., National Institutes of Health, USA). The spheroid growth was calculated by measuring the area covered by migrating cells over 48 hours and normalizing to the initial spheroid size at time point zero. In this way, the adhesion and outgrowth of MCF-7 and U-373 MG spheroids can be compared over time (Fig. 6.18).

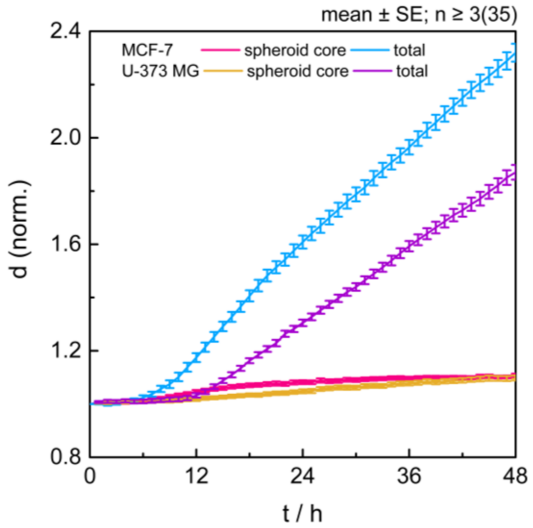

Fig. 6.18 Adhesion kinetic study of MCF-7 and U-373 MG spheroids documented for 48 hours using the zenCELL owl digital microscope. Apart from the quantification of the diameter changes of the spheroid core itself, the total area covered by the outgrown cells building a monolayer was measured. Experiments were performed in a standard cell culture incubator at 37 °C and 5 % CO_2. Data sets were averaged after normalization to the initial spheroid size at time point zero, mean ± SE; n ≥ 3(35).

After placement of the spheroid at time point zero, the core body remains in its position during the adhesion while losing height and gradually increasing its diameter. Regardless of the cell type tested, i.e., MCF-7 or U-373 MG, an increase in the spheroid core body of 0.21 (± 0.01) %/h was determined by linear regression of the normalized “spheroid core” diameter curve. The outgrowth of single cells of the spheroid starts, in the case of MCF-7 spheroids, at 7.34 (± 0.05) h and for U-373 MG spheroids at 12.22 (± 0.04) h after deposition on the adhesive substrate. This time point is marked by the significant increase in the monolayer diameter curve plotted against time. For both cell types, the “total” spheroid diameter with the area of the cell monolayer included increases almost linearly, with a higher outgrowth rate of 3.24 (± 0.03) %/h for MCF-7 cells compared to 2.357 (± 0.008) %/h for U-373 MG cells.

In spheroid adhesion, the spheroid settles on the adhesive surfaces due to gravity and gradually adheres, while its three-dimensional spheroid structure collapses over time. In contrast to the repulsive effect of agarose-coated surfaces, the cells of the outer spheroid layer, which are located on the contact side to the surface, form adhesion points and start to migrate. Thus, the entire spheroid body slowly settles, loses height, and dissolves by creating an increasing cell monolayer that spreads two-

dimensionally on the surface. This spheroid outgrowth was documented on live/dead stained MCF-7 spheroids adhered to a Petri dish for 24 hours and 48 hours using fluorescence microscopy with z-stack imaging (Fig. 6.19).

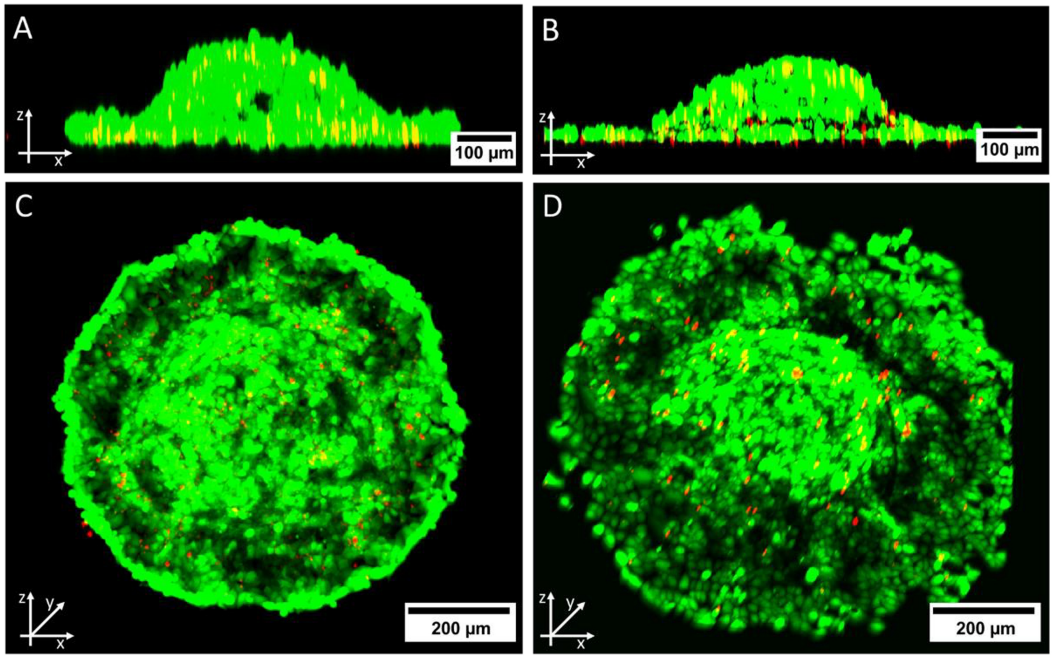

Fig. 6.19 Microscopic images of live/dead stained MCF-7 spheroids using fluorescence microscopy with z-stack imaging. The rendered xyz images show the side (A, B) and tilted top view (C, D) of the individual spheroid under study adhered to a Petri dish for 24 hours (A, C) and 48 hours (B, D). Experiments were performed in a standard cell culture incubator at 37 °C and 5 % CO_2 for spheroid adhesion procedure, whereas the viability staining was performed at 37 °C and 0 % CO_2.

The rendered xyz images display the top and side view of the individual spheroid under study and also show the viability of the spheroid-building cells via immunofluorescence staining. In general, the side view (Fig. 6.19, A and B) shows the hemispherical three-dimensional part of the spheroid, while the tilted top view (Fig. 6.19, C and D) displays the centrosymmetric seam of spread cells around the core spheroid. After 24 hours incubation, the spheroid has effectively adhered to the surface by building a monolayer of outgrown cells of approximately 800 µm in diameter around the centric body (Fig. 6.19, C). Through further cellular outgrowth, the seam of spread cells increases to approximately 930 µm in diameter 48 hours after spheroid placement (Fig. 6.19, D). Meanwhile, the total height of the spheroid body decreases from 210 µm to 170 µm as shown in the side view (Fig. 6.19, A and B), indicating a disruption of the entire three-dimensional structure during the adhesion process. The viability of the cells is largely maintained during the process, and only isolated red spots indicating dead cells are visible in the CLSM z-stack images taken 48 hours after spheroid placement.

6.4 DISCUSSION

As described in the previous chapters, differences between the two cell types used can be observed in terms of their spheroid formation, proliferation, and adhesion. These characteristics are presented and discussed in the following.

6.4.1 COMPARISON OF SPHEROID FORMATION

In chapter 6.1, the process of spheroid formation was described, whereby a loose aggregate is formed, and cell-cell contacts are established, followed by their amplification. These steps describe the respective stages of spheroid formation and are dependent on each other. The length of each phase and whether spheroids are formed or not are determined by physiological and environmental conditions.

At the physiological level, the genetic disposition and thus expression levels of certain protein molecules to form cell-cell respectively cell-ECM contacts is crucial for the formation of tissue models. Next to integrin-mediated attachment to ECM molecules promoting the initial aggregation of spheroid cells (Casey et al., 2001; Ivascu and Kubbies, 2007), actomyosin-mediated contractility promotes the formation of compact 3D spheroids (Tzanakakis et al., 2001; Napolitano et al., 2007). Thus, the ability of cells to form spheroids differs depending on the individual cell type and does not necessarily correlate with the tissue origin of the cells (Carlsson et al., 1983; Ivascu and Kubbies, 2006). For instance, some breast cancer cell lines are able to build spheroids (e.g., MCF-7, as used in this thesis), while different breast cancer cell lines form disordered cellular aggregates consisting of loosely packed cells (e.g., MDA-MB-231, MDA-MB-468; Ivascu and Kubbies, 2006). A fundamental study from 1978 that involved testing the spheroid formation ability of 14 breast cancer lines derived from humans, rats, and mice observed that only cell lines obtained from solid growths (primaries or metastases) formed multicellular spheroids and hence the source of the original tumor cells is the key factor in this context (Yuhas et al., 1978). Carlsson et al. studied the spheroid formation ability of 39 different human cell lines (malignant and normal), which normally grow in a monolayer or suspension (Carlsson et al., 1983). The authors found that ten out of 12 normal cells and 16 out of 27 cancer cells were able to form spheroids using the fluid overlay technique. However, the other cell lines remained as single cells or formed flat cell aggregates and large, disordered aggregates. The difference between these individual cell types is the expression level of binding proteins, which are mainly responsible for cell-cell and cell-ECM contacts within the 3D microstructure. In spheroids, the expression of E-cadherin on the cell surface is increased

up to threefold compared to monolayer cultures. Therefore, E-cadherin-expressing cell lines, such as MCF-7 cells, spontaneously form spheroids *in vitro* (Ivascu and Kubbies, 2007).

Concerning the influence of environmental conditions on spheroid formation, external factors such as the cultivation temperature and the use of an appropriate cell medium with the required pH are important (see discussion in chapter 6.4.4). The selection of the correct culture surface and shape, the adequate biomaterials used in the plate-coating procedure, and the setting of the rotation frequency should also be considered. The literature indicates that the use of concave low attachment surfaces usually leads to the formation of cellular aggregates with a more defined spherical shape (Costa et al., 2014; Gaskell et al., 2016). This concave shape is also used for the spheroid formation in this thesis (see protocol in chapter 4.1.5), where a distinct volume of non-adherent biomaterial solution (e.g., agarose) was added to a flat bottom well giving it a U-shape design. Recent studies have compared the spheroid formation between flat surfaces and 96-well plates (Gaskell et al., 2016), 24-well plates (Costa et al., 2014), and even Cellstar® V-shaped 96-well plates (Froehlich et al., 2016), which all yield an irregular, non-spherical or spherical-like structure with a poorly defined outer perimeter. In this context, it is also clarified that the spheroid formation in the 24-well plates used for the time-lapse images does not yield exactly the same kind of spheroids as those routinely produced in the 96-well plates and is merely used for illustrative purposes.

Overall, the importance of appropriate cell physiology and environmental conditions was considered, and the two cell lines used were selected to represent two different tumor entities that are often studied in the literature as non-vascularized tumor models. The differences in their physiological levels are crucial for the individual cell behavior, especially spheroid formation in this context, as the environmental conditions are identical. Nevertheless, some cell culture medium additives can also be used to facilitate cell aggregation through the liquid overlay technique and a troubleshooting guide for the main issues related to spheroid production is provided by Costa et al. (Costa et al., 2018).

To examine the spheroid formation of U-373 MG and MCF-7 cells, the time-resolved images from the zenCELL owl digital microscope were compared at the individual time points of 3 h, 12 h, and 24 h (Fig. 6.20). The described phases of spheroid formation using the example of U-373 MG cells in chapter 6.1 can also be applied to the preparation of spheroids using MCF-7 cells. As the micrographs show, only the time intervals of the individual phases are time-shifted compared to the U-373 MG spheroids. Here, at time point three hours after cell seeding, the U-373 MG cells agglomerate significantly earlier to a loose, but already roundish structure, whereas the microscopic picture of the MCF-7 cells indicates the formation of only a few small clusters and mainly shows suspended cells.

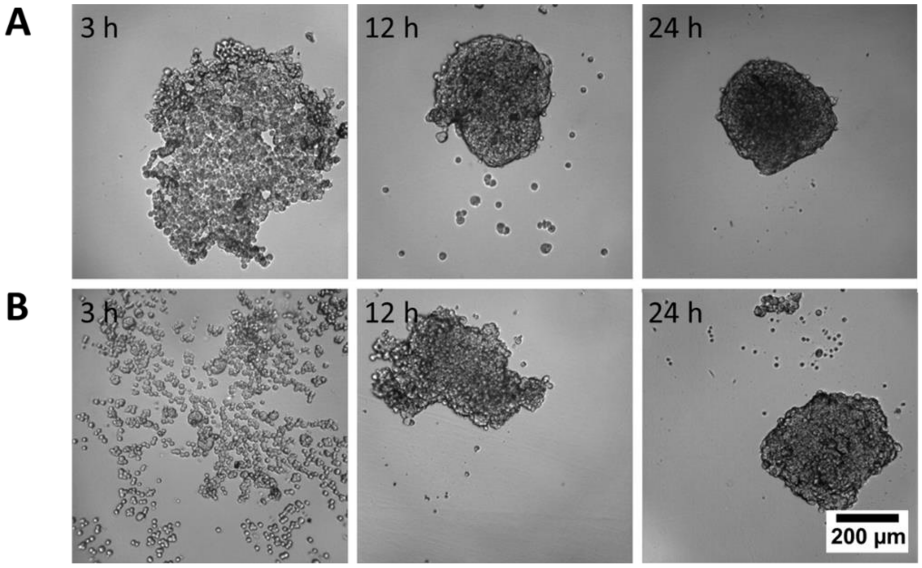

Fig. 6.20 Time-resolved micrographs of the spheroid formation process of U-373 MG cells (A; 18,000 c/well) and MCF-7 cells (B; 4,000 c/well) documented for 24 hours using the zenCELL owl digital microscope. Experiments were performed in a standard cell culture incubator at 37 °C and 5 % CO_2.

For comparison, the formation of the cell aggregate takes six hours using the MCF-7 cells (see Fig. A-6.1) and only three hours using the U-373 MG cells. Thus, a spheroid body is visible in both cases after 12 hours, whereby the structure of the newly formed U-373 MG spheroid already appears spherical in contrast to the MCF-7 spheroid. This trend continues with further incubation, while spheroid compaction already starts after nine hours in the case of the U-373 MG spheroid and only begins after approximately 15 hours for the MCF-7 spheroid. Finally, after 24 hours of spheroid formation, a single, dense-packed spheroid is produced for both cell types.

6.4.2 COMPARISON OF GROWTH KINETICS

In general, three distinct phases have been described for these three-dimensional structures, as already reviewed by Landry, Freyer and Sutherland (Landry et al., 1982) and described in chapter 1.2. The first phase, namely the initiation period, is characterized by the aggregation of individual cells into small clumps and their quasi-exponential growth until a critical volume is reached. At this point, the cell cycle distribution within the spheroids changes, resulting in an accumulation of G1-like cells in the center and a deposition of proliferating cells at the periphery. This leads to a progressive decrease in growth and a second growth phase characterized by a linear increase in spheroid diameter with time. Finally, as the spheroids continue to grow, their growth slows progressively, thereby achieving a maximum diameter.

The kinetics of spheroid growth can be described by applying growth curves, which can be used to determine the spheroid size for a specific growth period. For this purpose, the geometric mean diameter

of the individual spheroids must be analyzed by microscopic techniques within a defined incubation period. From such measurements, the spheroid volumes can be calculated and, in the case of spheroids derived from cell types that can easily be separated into single-cell suspensions, the number of cells per spheroid can also be determined. The resulting spheroid growth curves were analyzed theoretically and various models concerning the growth kinetics were developed.

- The Gompertzian growth curve model represents the complex pattern of almost every tumor's growth (Gompertz, 1825). This model describes a sigmoid function, where $\mu(x)$ denotes the mortality rate at age x, and α and β are constants, indicating that growth is slowest at the beginning and end of a given period (Eq. 6.2; Greenwood, 1928)

  $$\mu(x) = a \cdot e^{\beta x} \qquad \textbf{Eq. 6.2}$$

  With this, the retarded phases, such as the stepwise formation of cell aggregates from single cells and the formation of a maximum spheroid diameter due to the limited availability of nutrients, are considered by including a plateau phase.

- Düchting and Vogelsaenger developed the cubic vascularized tissue model to study the influence of different effects on spheroid growth by computer simulation (Düchting and Vogelsaenger, 1981). The model contains a static capillary network in which normal cells are distributed using uniform random variables while addressing different cell cycle durations. Therefore, certain assumptions have been applied, for example, a cell can be placed in any position within the cubic space at any time during any cell phase, cell multiplication can only take place if the distance between the medium and the dividing cell does not exceed two tumor cell layers, and cells can die at any time interval with a probability of 50% starting with it a certain moment after setup, which can be varied by the simulation (Düchting and Vogelsaenger, 1981).

- The model of Landry et al. considers the properties of single cells and the spheroid structure, e.g., the cell doubling time in the monolayer, the rate of cell detachment from the spheroid, and the thickness of the outer shell consisting of proliferating cells (Landry et al., 1982). Landry and colleagues derived a mathematical equation that relates the growth rate of multicellular spheroids to some easily measurable parameters and predicts a linear increase of the spheroid diameter with time. The spheroid growth rate D is described by the cell doubling time in monolayer culture T, the dividing shell depth r, the shedding factor $\beta\vartheta$, packing factor p expressing the fraction of the cellular region which is actually composed of intact cells, and

distinct factors F_1 and F_2 depending on the radius shedding starts as well as the spheroid radius (Eq. 6.3).

$$D = \frac{ln2}{T} F_1 \cdot r - F_2 \cdot \beta \frac{\vartheta}{p} \quad \textbf{Eq. 6.3}$$

In this way, the model provides a simple and practical view of growth control in spheroids and can be further adapted to include more parameters (Landry et al., 1982).

According to Düchting and Vogelsaenger, spheroid growth is limited to a maximum volume in a range of 3–4 mm in diameter, beyond which no further expansion can be achieved, regardless of how often the medium is renewed (Düchting and Vogelsaenger, 1984). This behavior can be explained by the relationship between the surface area and volume in a spheroid, as there is a decrease of $\frac{O}{V}$ when the diameter d rises (Eq. 6.4). Hence, oxygen flow, nutrient supply, and toxic waste removal are only guaranteed up to the critical diameter of 3–4 mm. In this context, it has to be noted that this critical diameter was not reached by the spheroids used in this thesis.

$$\frac{O}{V} = \frac{4\pi r^2}{\frac{4}{3}\pi r^3} = \frac{3}{r} = \frac{6}{d} \quad \textbf{Eq. 6.4}$$

The growth kinetics of MCF-7 spheroids correspond in general to the linear growth behavior postulated by Landry and coworkers (Landry et al., 1982). Upon linear regression, the change in diameter per day was calculated and demonstrated that smaller spheroids grow faster than larger ones. The diameter change linearly decreases for seeding densities up to 16,000 c/well but becomes more constant at higher seeding densities. Thus, the spheroid microenvironment affects growth kinetics, as growth is subsequently reduced when the maximum capacity of relevant metabolic processes becomes limited by diffusion gradients into or out of the spheroids body according to Düchting and Vogelsaenger (1984). In comparison, Hupf analyzed the growth kinetics of MCF-7 spheroids with a cell seeding density between 1,000 and 6,000 c/well and also stated that smaller spheroids grow faster than bigger spheroids (Hupf, 2018). However, the results obtained by Hupf are not consistent with the values calculated in this study, since Hupf includes the first day after spheroid aggregation in the linear regression, and thus the value for the concentration of, for instance, 4,000 c/well differs by approximately 80 % (Hupf, 2018). Despite this discrepancy, in general, it can be stated that the trend of decreasing growth rates continues with increased cell concentrations.

In contrast, the growth kinetics of U-373 MG spheroids are related to the special effect of spheroid compaction. The growth curves displayed an identical exponential diameter decrease of approximately

40 % for the different seeding concentrations between 20,000–45,000 c/well during spheroid incubation. In literature, similar spheroid compaction rates are reported for spheroids derived from human breast cancer cells (approx. 50 % for the MDA-MB-231 or MDA-MB-157 cell line; Devanny et al., 2021), or human liver cancer cells (approx. 60 % for the HepG2 cell line; Lin et al., 2005).

Hoyer and colleagues discussed the controversial situation of spheroids shrinking in size while cells are producing substantial amounts of ECM and expressing the typical ECM components (Hoyer et al., 2015). In the case of U-373 MG spheroids, the compaction phenomenon could not be related to their origin as a highly invasive brain tumor cell type and might represent an *in vitro* artifact. Some potential explanations for this growth kinetics might be an increased cell death rate leading to a loss of the cells involved within the spheroid, shrinkage of the spheroid due to more intense cell-cell contacts, or the occurrence of retraction forces of the cells on the ECM fibrils (Hoyer et al., 2015). Additionally, enhanced decomposition of the ECM through the release of degradative enzymes or some leaching of ECM components by the culture medium could also contribute to the effect.

To analyze the compaction process, the concentration of certain mediators on the biochemical level was studied (e.g., the expression level of collagens IV (Mammoto et al., 2013; Rape et al., 2014); amount of glycosaminoglycans (Zahn et al., 2021); release of degrading enzymes (Hoyer et al., 2015)). Further, different engineering strategies for modulating the glioblastoma environment, except for angiogenesis, were considered by physically forcing the spheroid compaction. For example, certain soluble molecules such as methylcellulose were added to increase the viscosity of the cell medium (Zahn et al., 2021) and, in another study, microcontact printing of adhesive fibronectin islands was used to simulate the physical compaction (Rape et al., 2014). However, the role of the physical properties of the tumor microenvironment in the angiogenesis and progression of brain tumors has not been sufficiently elucidated.

6.4.3 COMPARISON OF SIZE DISTRIBUTION

In most studies, it is important to achieve a homogeneous and reproducible size of the spheroids in culture. Therefore, it is important to optimize and standardize the growth conditions for different cell types and research objectives, as Sutherland and Durand already emphasized in the context of multicellular spheroid culture methods (Sutherland and Durand, 1984). These conditions include the consistency of spheroid cellular metabolism and the macroenvironment during the culture period, as they largely determine the kinetics of spheroid growth, cellular properties, and microenvironment. In the context of producing spheroids with a defined size, Costa discussed the influence of fine-tuning the initial number of cells (Costa et al., 2018).

The approach of varying the cell seeding density was also applied in the investigations outlined in this thesis. To this end, the spheroid sizes were optimized by modulating the initial number of cells seeded on the non-adherent surfaces to ensure that the diameters of the generated spheroids are suitable to fit into the funnel-based measurement setup without slipping through the opening and are also similar between both cell types used. For this purpose, kinetic studies were performed on spheroids with different cell concentrations and ages, including the test of different spheroid sizes inserted into the measurement setup by considering the following basic properties.

- ➔ To ensure that the spheroids can tightly seal the opening of the funnel-based measurement setup without slipping through, a lower cut-off limit of approximately 400 µm must be reached.
- ➔ The ratio of surface area to spheroid volume has to be suitable for the individual cell type regarding the formation of a single aggregate.
- ➔ To prevent spheroid disruption due to the retention forces occurring at the measurement opening, the cell-cell connections within the spheroid must be strong enough to withstand these tensions.
- ➔ The minimum age is set at five days as used in the experiments for studying the cellular micromotion in dependence of the spheroid age, thereby ensuring that the reorganization of the cells within the spheroid is completed.
- ➔ The maximum age is set at eight days as used in the experiments for studying the cellular micromotion in dependence on the spheroid age, as a rapid decrease of spheroids´ dynamic after six days has been determined.
- ➔ For research purposes, a sufficient size difference between small, medium, and large spheroids should be achieved to generate significantly different impedance signals.
- ➔ A similar size distribution between MCF-7 and U-373 MG spheroids must be achieved to compare the recorded measurement signals.

In addition to all these requirements, the different growth kinetics of the spheroid types must be considered. For a practical comparison of the total number of spheroids generated, their individual diameter ranges from smallest to largest spheroid per day and cell type was plotted in a simplified way (Fig. 6.21).

Thus, the period in which spheroids with the same diameter can be determined ranges from the second to the seventh day of incubation, in addition to the characteristic kinetics of both cell types. For example, a U-373 MG spheroid with a diameter of 500 µm on day 5 is prepared by using a cell seeding density of 20,000 c/well, whereas generating an MCF-7 spheroid with the identical diameter of 500 µm requires a fivefold lower initial cell number of 4,000 c/well.

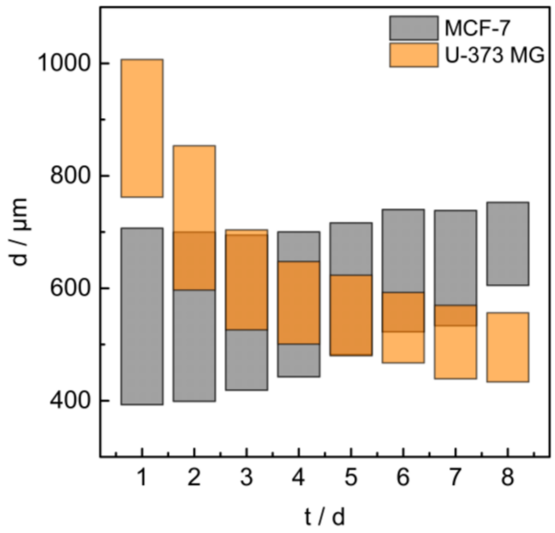

Fig. 6.21 Comparison of the spheroid growth studies of MCF-7 and U-373 MG spheroids presented in a simplified manner by plotting their individual diameter range from smallest to largest spheroid per day and cell type. For a detailed view, also see Fig. 6.7 and Fig. 6.10.

Overall, it can be stated that the individual cell seeding densities were successfully fine-tuned to fulfill all the requirements for the research presented in this work.

6.4.4 COMPARISON OF MICROENVIRONMENTAL CHANGES

For a complete characterization of spheroids, microenvironmental aspects were also investigated. Therefore, alterations of the serum concentration (see chapter 6.2.2) and the variation of extracellular pH values (see chapter 6.2.3) could easily be performed by distinct adjustments of the cell culture medium. Apart from the individual serum amount required to regulate the physiological state of cells and tissues, homeostasis of intracellular and extracellular pH is crucial for normal cell function.

In general, FCS is a universal growth supplement for cell and tissue culture media consisting of a natural cocktail of most factors required for cell attachment, growth, and proliferation (Gstraunthaler et al., 2013; Puri et al., 2015). The serum provides attachment factors, nutrients, and hormones for mammalian cells and serves as a buffer against disturbances such as pH changes and the buildup of endotoxins. Additionally, a high concentration of growth-promoting factors is provided such as carrier proteins and macromolecular proteins, while FCS also contains small amounts of antibodies. Overall, serum supplementation is essential for the growth and maintenance of cells, both *in vivo* and in culture.

As investigated by growth studies using different FCS concentrations between 0 % and 10 % (v/v), the FCS concentration does not affect the spheroid formation of U-373 MG cells, as spheroids are formed in the absence of serum, rather than growth or the typical U-373 MG compaction process. The growth curves indicate a clear dependency of the generated spheroid size on the serum concentration by means

of increasing spheroid diameters in accordance with rising FCS concentrations. Thus, the FCS concentration only influences the size of spheroids by improving the supply of growth factors, nutrients, and other important proteins, which leads to the production of, for instance, an extracellular matrix with higher fibronectin content, resulting in greater cell volume, as well as stronger cell-cell contact interactions and less cell death (Swisher and Rannels, 1997). During incubation, no difference in growth kinetics for 0–5 % (v/v) was observed, while significantly altered kinetics were observed for spheroids formed in 10 % (v/v) FCS-supplemented cell medium. At this concentration, a rough compaction process of minimizing the diameter by almost 50 % during spheroid incubation was indicated. This may be a result of overstimulated cell-cell binding due to the enhanced FCS concentration and its adhesion-promoting properties (Hayman et al., 1985).

As another microenvironmental aspect, the cellular pH level was influenced by performing spheroid formation and incubation in cell media with different pH values. Typically, pH levels are highly regulated in extracellular and intracellular environments. The extracellular pH value pH_e of normal cells ranges from pH 7.3 to pH 7.4, while their intracellular pH value pH_i is generally lower. The pH_i remains around pH 7.2 (Webb et al., 2011) and tends to become acidic as a result of metabolic activity. Thus, cells express Na^+-driven ion carriers, specifically Na^+-H^+ exchangers and Na^+-HCO_3^- co-transporters, which are located in the plasma membrane and pump protons into the extracellular space to prevent acidosis and maintain cellular functions (Casey et al., 2010). In contrast, most malignant cells exhibit a pH gradient inversion, with an acidification of pH_e and an alkalization of pH_i (Sharma et al., 2015). This reversed pH gradient is observed in the initial phases of tumorigenesis and is crucial for tumor evolution and proliferation, regardless of the pathology, genetics, or origin (Zagaynova et al., 2017). In addition, this microenvironment is essential for the prevention of apoptosis and contributes to drug resistance in cancer.

In the experiments performed, the extracellular pH level was either acidified or alkalized by adjusting the cell media used for incubation to distinct pH values in a range between pH 6.6 to pH 7.8. As shown in chapter 6.2.3, a single spheroid was formed at each pH value followed by the typical compaction process of U-373 MG spheroids.

In the case of acidification, the already acidic pH value of the extracellular environment is further reduced with the addition of an acidic culture medium, causing further enhancement of the inverse pH gradient and thus acidification of the normally alkaline pH_i. The environmental acidification enhances the motility of the cells inside the spheroids and also promotes their body expansion (Ralph et al., 2020). This leads to a twofold increase in the growth of U-373 MG spheroids as investigated at pH 6.6 and likewise at pH 6.8, by making the cell aggregate more diffuse and the cell-cell bonds weaker. In addition,

the dysregulation of the inverse pH gradient affects the integrin-ECM interactions and could slow the rate of adhesion and migration (Stock and Schwab, 2006). For example, the addition of an acidic culture medium could cause a rapid equilibrium imbalance and thus activity decrease of the NHE1 antiporter, which operates as a membrane protein for transporting Na^+-ions into the cell and H^+-ions out of the cell. This results in an acidification of the normally alkaline pH_e and a drastic reduction in proliferation, meaning a reduced compaction procedure due to decreased adhesion activity in the case of U-373 MG spheroids.

In contrast, cellular alkalinization has been reported to induce increased cell proliferation by stimulating the synthesis of proteins, DNA, and RNA, resulting in highly dense and disorganized cell masses (Madhus et al., 1988; Koliakos et al., 2008). Thus, the kinetics of spheroid growth at pH 7.4, pH 7.6 as well as pH 7.8 is accompanied by an even stronger upregulation of metabolic processes, causing an increase in cell proliferation and a larger diameter compared to spheroids at pH 7.2.

Overall, the results of this study indicate that appropriate microenvironmental conditions are essential for intercellular architecture, providing integrin-ECM interactions, as well as cellular balancing of intracellular and extracellular pH values, pH_i and pH_e (Stock and Schwab, 2006).

6.4.5 COMPARISON OF ADHESION KINETICS

The complex interactions of cells with an adhesive surface or substrate in combination with the secreted ECM play a critical role in mediating and regulating numerous processes, including cell adhesion, migration, and signal transduction during morphogenesis, tissue homeostasis, wound healing, and tumorigenesis (Berrier and Yamada, 2007).

In general, the kinetics and mechanics of cell adhesion are linked, affecting the receptor-ligand bond formation and dissociation in terms of how likely, how fast, and how strongly cells bind and how long they remain bound (Zhu, 2000). Regarding the biochemical aspect, cell adhesion is mediated by a specific interaction between receptors and ligands. Many of these interactions involve focal adhesions, which are responsible for the intensive adhesion of cells to a surface. Focal adhesions are multi-protein structures that form mechanical links between intracellular actin bundles and the ECM or substrate via transmembrane integrins (Owen et al., 2005). Using bi-directional signaling, cells can sense their environment by recognizing the chemical and physical properties of the matrix and translating these extracellular signals into intracellular signals (Hayes et al., 2012). This dynamic cross-talk provides an interactive interface that influences global cell physiology, functional changes at the cell surface, and the molecular scaffold of adhesion sites (Geiger and Yamada, 2011).

In this work, the adhesion process and spheroid outgrowth were analyzed to fully characterize the spheroid types studied. Regardless of the cell type tested, i.e., MCF-7 or U-373 MG, a similar increase in the spheroid core body was observed, while the outgrowth of single cells of the spheroid started differently, indicating a delay time of approximately five hours in the case of U-373 MG spheroids compared to MCF-7 spheroids. This significantly different starting times until a cell seam is formed around the spheroid, indicates a stronger adhesive force related to strong cell-surface contacts of the MCF-7 cells. On the other hand, this may also be an indication of more intense cell-cell contacts of U-373 MG cells within the spheroid, or the occurrence of retraction forces of the cells on the ECM fibrils (Hoyer et al., 2015), which was already mentioned concerning the phenomenon of spheroid body compaction (see chapter 6.4.2). This fact is also accompanied with the different outgrowth rates as for MCF-7 spheroids an enhanced rate was calculated.

The changes in the spheroid diameter and migration distance of cells after seeding on the substrate can be used as parameters to quantitatively evaluate cell-surface interactions or identify differences between cell types. A comparison of which spheroid cell type loses height and collapses faster due to spheroid adhesion was not possible since the resolution of the confocal laser microscope used was not sufficient (see Fig. 6.19). Overall, it must be considered that the time course depends on several factors and can differ significantly depending on the cell type, cell number, spheroid age, and culture conditions.

6.5 SUMMARY AND OUTLOOK

In this chapter, several aspects of spheroid characteristics were described and discussed for both cell types used, namely MCF-7 and U-373 MG spheroids. In the following, an overview of the main topics is outlined (Fig. 6.22).

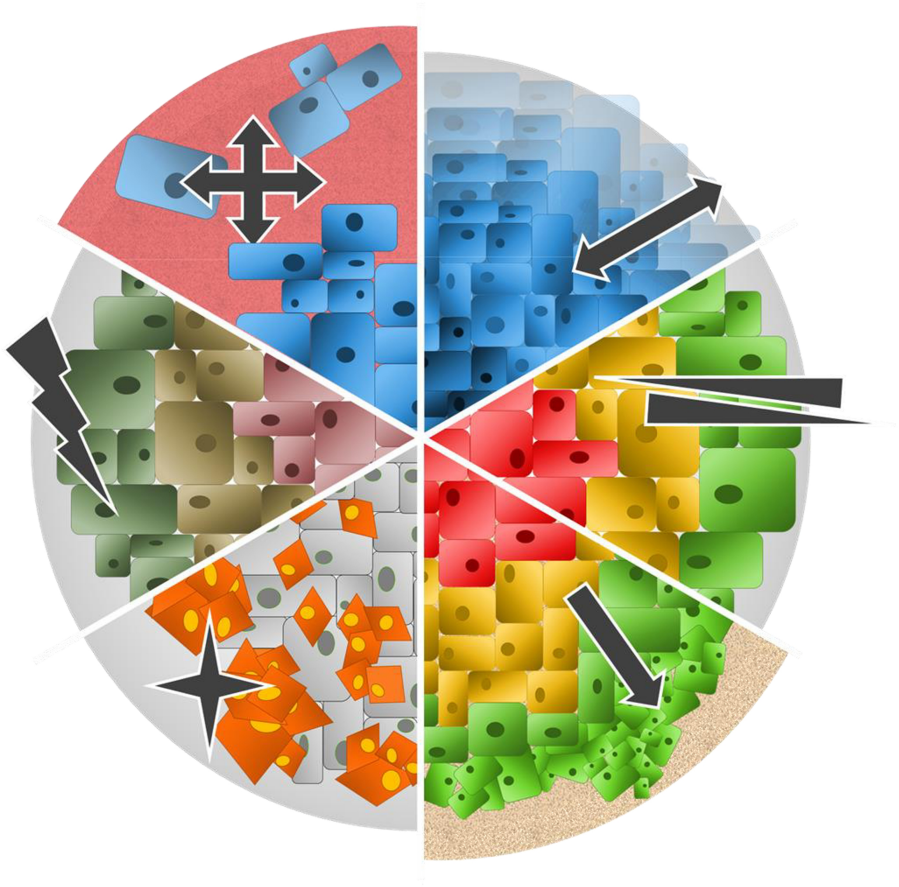

Fig. 6.22 Illustration* of different spheroid characteristics: Spheroid formation; Spheroid growth kinetics; Spheroid microenvironment; Spheroid adhesion; Spheroid co-culture; Spheroid manipulation.

*illustration is simplified and not to scale

Spheroid formation

The spheroid formation is crucial for any further investigations using three-dimensional tissue models. Apart from the requirement of spheroid-forming cell types, the formation is also the key step that determines the morphology, size, and shape of the spheroids. Therefore, the choice of the formation technique in combination with the number of spheroids per batch, the fine-tuning of the individual cell-type parameters such as the seeding cell number and the incubation period after formation, and the variation of cell culture medium ingredients, e.g., the pH value, are some of the most important factors

discussed in this thesis. After defining all these factors, the individual spheroid formation has to be standardized by controlling the spheroid size and morphology in a reproducible manner. Such fine-tuning is essential to determine all spheroid characteristics and to produce suitable test specimens e.g., newly developed measurement setups. After the investigation of the cell type-specific spheroid formation protocols, the formation process was documented by using time-lapse microscopy and analyzed in detail. Based on this assay, further spheroid formation studies can be performed using different cell types.

Spheroid growth kinetics 

The spheroid formation process is followed by spheroid growth kinetics. During the incubation period, the morphology of the spheroids is refined and the whole body varies in shape and size. Inside the spheroid, cell-cell and cell-matrix junctions are established and strengthened as the cells begin to proliferate. Within a three-dimensional structure, doubling times in the exponential growth phase are significantly longer than in monolayer cultures, mimicking the growth rates of the same cell types as tumors *in vivo* (Yuhas et al., 1977). Changes in surface area and membrane properties may be involved in this phenomenon and are also decisive in defining the individual spheroid growth kinetics. In addition to the typical increase in size of MCF-7 spheroids, spheroids derived from U-373 MG cells show the opposite growth behavior of compaction. Therefore, spheroid growth is specific to each cell type used and has to be adjusted individually, since the same number of seeded cells and incubation time will not produce the same size of spheroids. In this work, different cell numbers and spheroid diameters were investigated as a function of cultivation time and compared for the individual cell types. For example, by changing the serum concentration of the cell culture medium, the spheroid size changes in proportion to the FCS concentration as a result of the growth factors contained.

Spheroid microenvironment 

While the cell-cell and cell-matrix bonds are strengthened and formed, the cells within the spheroid are rearranged creating the typical spheroid microenvironment (compare chapter 1.2.3). Due to the lack of vascularity, microenvironmental changes occur within the spheroids. As a result, gradients of key metabolites such as oxygen, lactate, and other nutrients can be observed. The spheroid lacks these substances because they cannot penetrate the center and, instead, toxic metabolites such as CO_2 or waste accumulate inside the spheroid. This leads to the formation of concentric zones with their own environment. Along the periphery of the spheroid proliferating, viable cells are found, while in an intermediate zone, viable but quiescent cells are present followed by necrotic cells in the core. The

thickness of all three zones can vary with different cell lines, seeding densities, and growth conditions. For the determination of this microenvironment, basic studies were performed, such as the development and application of oxygen and pH value-sensitive sensor foils purchased from PreSens Precision Sensing GmbH Regensburg (Schmittlein, 2018; Pütz, 2021). In addition, specific staining procedures can be performed to fluorescently label viable versus dead cells of the outer spheroid shell, including during spheroid adhesion or spheroid disruption.

Spheroid adhesion

When spheroids are allowed to settle onto the surface, the cells adhere to the surface, and they start to grow out (compare *Application Note*: Ruckdäschel et al., 2020, InnoME GmbH). First, cells from the outer shell attach to the surface and form cell-surface contacts mediated by the ECM. The spheroid flattens and more cells migrate out of the initial contact zone within 12 hours. This outgrowth of the spheroid initially starts in one direction, gradually increases all around the spheroid, and finally leads to a circular/round seam of spread cells. After 48 hours, the adhered spheroid consists of a semispherical three-dimensional part and a surrounding cell monolayer. The process of spheroid adhesion was documented in this work with the help of time-lapse recordings, which allow an accurate quantitative calculation of cell growth and spheroid destruction over time. Based on this, cell type-specific differences were observed between U-373 MG and MCF-7 spheroids. In further studies, the effect of cell adhesion-inhibiting substances could be investigated based on this assay.

Spheroid co-culture

It is also possible to generate spheroids from two different cell lines as co-cultured assemblies within one array well to imitate the heterogeneity of tumors.

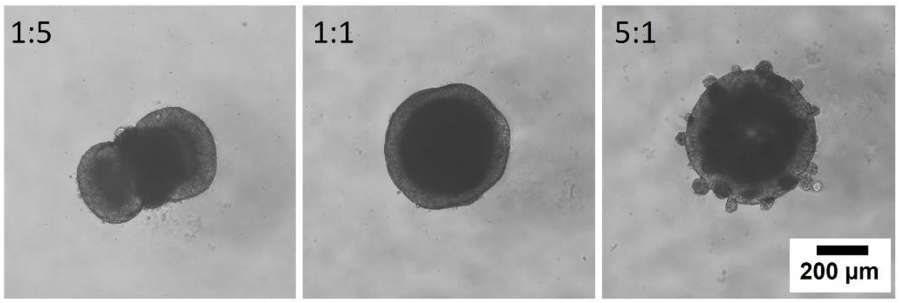

Fig. 6.23 Micrographs on day 5 after the spheroid formation of co-cultured spheroids resulting from mixing the two cell types of MCF-7 and U-373 MG cells with different ratios of 1:5/1:1/5:1 within one array well (total cell seeding concentration: 24,000 c/well). The pictures were taken using phase contrast microscopy. Experiments were performed in a standard cell culture incubator at 37 °C and 5 % CO_2.

In this context, a proof-of-principle experiment was performed in which U-373 MG and MCF-7 cells were mixed and cultured simultaneously in different ratios using the standardized spheroid formation protocol. Here, the 1:1 ratio and the two extremes with the 1:5 and 5:1 ratios of the different seeding combinations tested are shown (Fig. 6.23; see chapter 4.1.6, IV). While using the identical concentration of both cell types creates a homogeneous, co-cultured spheroid, the two extreme ratios of the batches show a different spatial organization of the two cell types within the three-dimensional body. The mixing ratio of MCF-7 to U-373 MG cells of 1:5 results in a three-dimensional body in which the cell types separate from each other during the incubation period, leading to a bispherical structure. In contrast, the reverse mixing ratio of 5:1 produces an MCF-7 spheroid that is spiked with individual, significantly smaller U-373 MG spheroids sitting on the outer shell. In this case, identification was based on cell number and documentation of spheroid growth, with the attached small spheroids showing the typical compaction effect of U-373 MG spheroids, while the diameter of the main spheroid increases according to the MCF-7 spheroid growth kinetics (data sets not shown in this thesis). Concerning this concept study, the rapid and simple mixing test can be used to further fundamentally investigate the heterogeneity of tumors.

Spheroid manipulation 

Spheroids are a tool for assessing the realistic long-term effects of mixtures of, among others, pollutants, nanomaterials, or chemicals. Their use as *in vitro* approaches can provide essential information on the mechanisms underlying the toxicity of very low, environmentally realistic concentrations of substances that cause effects only after long periods of exposure (see https://cordis.europa.eu). As outlined in this thesis, various experiments on spheroid manipulation are possible (see chapter 7.2; chapter 7.3; chapter 7.4). Therefore, the spheroid model studies were processed using concentrations that induce cellular reactions within at least 48 hours of signal measurement. Apart from evaluating the response of the spheroids to osmotic stress, concentration studies were also conducted using fixatives or permeabilizing substances, while the response of the spheroids was recorded impedimetrically (using the newly developed device) and microscopically. According to this, it is evident that a detailed study of the growth behavior of both spheroid cell types was crucial for ongoing experiments. The exact sizes and types of spheroids and the age of the spheroids used for further experiments can be found in the corresponding protocols or the descriptions of the respective measurement results.

CHAPTER 7

MODEL STUDIES WITH MCF-7 AND U-373 MG TISSUE MODELS

7.1	MODEL STUDY: THE NOVEL MEASUREMENT SETUP	155
7.2	MODEL STUDY: CELLULAR RESPONSE TO PERMEABILIZATION	172
7.3	MODEL STUDY: CELLULAR RESPONSE TO ACTIN CYTOSKELETON DEGRADATION	212
7.4	MODEL STUDY: CELLULAR RESPONSE TO OSMOTIC PRESSURE	233
7.5	SUMMARY	270
7.6	OUTLOOK	275

In general, it is important to investigate the growth and cellular characteristics of spheroids, not only because of the information that this model system may provide about the development of cellular regions and their microenvironment but also to determine the responses to different tumor therapy modalities. Thus, based on the detailed spheroid characterization (chapter 6), various spheroid model studies were performed in a highly controlled manner and the cellular response to different stimuli was studied. As a versatile tool for the sensitive detection of morphological changes in cells upon exposure to external stimuli, the value of impedance spectroscopy has been proven, especially for 2D monolayer cells (Wegener et al., 2000b; Stolwijk et al., 2011; Lieb et al., 2016) and has also been investigated for 3D assays (Hupf, 2018). In this thesis, a novel impedance-based device was introduced (chapter 5), which enables the characterization of cellular micromotion, the direct stimulation of spheroids during the measurement, and the study of the induced electrophysiological and morphological alterations. Apart from the characterization of the impedance signal in combination with spheroids of different seeding densities and investigating cellular micromotion as a function of spheroid age as well as pH-value, the responses of spheroids U-373 MG and MCF-7 to different stimuli with known effects were tested. For model studies, stimulation reagents such as a chemical cross-linker (chapter 7.2), a detergent (chapter 7.2), an actin filament polymerization inhibitor (chapter 7.3), or buffers with different osmolalities (chapter 7.4) were used. The response of the spheroids to the different stimuli was analyzed on the basis of impedance measurements and complementary microscopic images, impedance measurements on cell monolayer culture, or biochemical endpoint assays such as the PrestoBlue™ assay. By comparing the results of these additional methods, the sensitivity and applicability of the newly developed device were evaluated.

7.1 MODEL STUDY: THE NOVEL MEASUREMENT SETUP

To characterize the impedance signaling of the newly developed funnel-based measurement device in dependence on basic spheroids features, fundamental model studies were performed. For this purpose, elementary spheroid properties such as the spheroid size, the spheroid age, and the pH value used for spheroid formation were varied and the generated spheroids measured. The impedance measurements in MFT and RTC mode were analyzed and used to determine the ideal tissue model conditions for subsequent experiments.

7.1.1 INFLUENCE OF SPHEROID SIZE ON THE IMPEDANCE SIGNAL

Based on the studies of spheroid growth kinetics, the influence of spheroids with various diameters on the impedance signal was investigated. To this end, small, medium, and large-sized tissue models were placed into the measurement chamber and the impedance signal was recorded for three hours following the protocol presented in chapter 4.3.3.

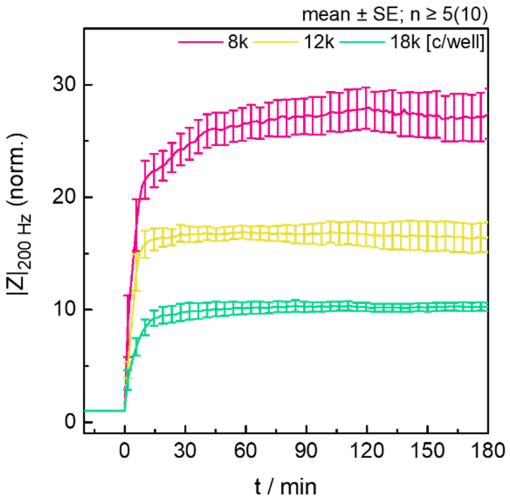

Fig. 7.1 Time course of the normalized impedance magnitude at 200 Hz of MCF-7 spheroids with different diameters (8,000, 12,000, and 18,000 c/well; day 5 and/or day 6 after spheroid generation). Time courses were normalized with respect to the last data point before spheroid placement at time point zero. Experiments were performed in a standard cell culture incubator at 37 °C and 0 % CO_2. Data sets were averaged after normalization, mean ± SE; n ≥ 5(10).

In the case of MCF-7 spheroids, the spheroid concentrations of 8,000, 12,000, and 18,000 c/well were analyzed. The time course of the normalized impedance magnitude at 200 Hz displays the typical impedance increase upon spheroid placement (Fig. 7.1). Here, a clear dependency of spheroid size and the height of the detected impedance signal is shown. After equilibration, the smallest spheroid generated a relative signal increase of 2,700 (± 200) %, the medium-sized spheroid of 1,600 (± 100) %,

and the biggest spheroid of 1,020 (± 40) %. Thus, the amplitude of the impedance increases with decreasing spheroid diameter, while significant signal differences can be observed between the three spheroid sizes.

An evaluation of the three spheroid parameters based on the recorded data shows a constant decrease of R_{ext} and R_{int} values for increasing spheroid cell concentration, respectively spheroid diameter (Tab. 7.1). The extracellular resistance is reduced from 180 (± 20) kΩ (8,000 c/well) to 66 (± 9) kΩ (18,000 c/well), while the intracellular resistance decreases in a range from 2.6 (± 0.2) kΩ (8,000 c/well) to 1.6 (± 0.6) kΩ (18,000 c/well). The non-ideal spheroid capacitance A_{sph} reacts in reverse and increases slightly with spheroid diameter.

Tab. 7.1 Calculated values of R_{ext}, R_{int}, and A_{sph} reflecting the dielectric structure of MCF-7 spheroids as a function of different cell seeding densities (8,000, 12,000, and 18,000 c/well; day 5 and/or day 6 after spheroid generation). The values were determined by fitting each measured impedance spectrum three hours after spheroid insertion using a *LabVIEW™*-based software (written by J. Wegener, University of Regensburg) and the following parameter values: A_{el} = 13 (± 1) | 12 (± 1) | 12 (± 1) ·10^{-6} $Fs^{n-1}cm^{-2}$; n_{el} = 0.82 (± 0.03) | 0.86 (± 0.02) | 0.87 (± 0.01); R_{bulk} = 5,400 Ω; A_{para} = 2.4 ·10^{-10} $Fs^{n-1}cm^{-2}$; n_{para} = 0.9; n_{sph} = 0.75. Data sets were averaged after fitting, mean ± SE; see the table for the respective number of experiments.

	spheroid size [c/well]		
	8,000	12,000	18,000
R_{ext} [kΩ]	180 ± 20	120 ± 8	66 ± 9
R_{int} [kΩ]	2.6 ± 0.2	2.0 ± 0.4	1.6 ± 0.6
A_{sph} [10^{-9} $Fs^{n-1}cm^{-2}$]	2.9 ± 0.2	3.2 ± 0.2	3.3 ± 0.3
n	4(6)	4(7)	4(8)

For comparison, the identical model study was performed using U-373 MG spheroids with three significantly different diameters based on the cellular concentrations of 20,000, 30,000, and 40,000 c/well. The typical time course of spheroid positioning in the micro-trap is shown by the recorded impedance signal (Fig. 7.2).

In this study, the normalized impedance magnitude also increases instantly as the funnel hole is sealed, showing a clear signal change in relation to the cell seeding density. With decreasing spheroid diameter, and respective cell concentration, the impedance signal increases and differs significantly between the three cell seeding densities studied. Three hours after spheroid positioning, the small spheroids gained a relative impedance increase of 900 (± 10) %, the medium spheroids of 740 (± 20) %, and the large

spheroids of 540 (± 30) %. In addition, the time courses of the U-373 MG spheroids do not reveal equilibrium after 180 minutes, as a gradual signal increase was recorded. The slope of each time course was calculated by linear regression showing rising values with shrinking spheroid sizes, and respective cell concentrations from 0.509 ± (0.006) %/min (40,000 c/well) to 1.47 ± (0.01) %/min (20,000 c/well).

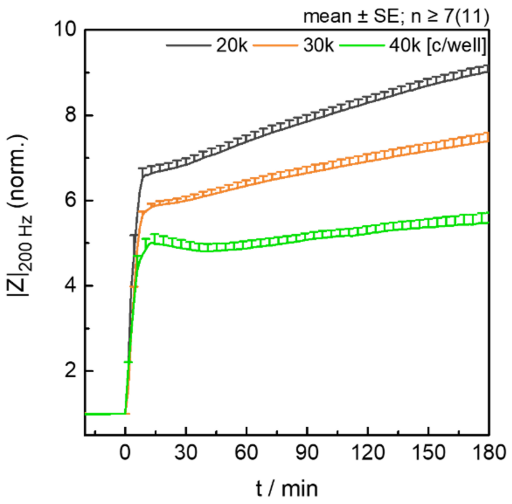

Fig. 7.2 Time course of normalized impedance magnitude at 200 Hz of U-373 MG spheroids with different cell seeding densities (20,000, 30,000, and 40,000 c/well; day 5 and/or day 6 after spheroid generation). Time courses were normalized with respect to the last data point before spheroid placement at time point zero. Experiments were performed in a standard cell culture incubator at 37 °C and 0 % CO_2. Data sets were averaged after normalization, mean ± SE; n ≥ 7(11).

Tab. 7.2 Calculated values of R_{ext}, R_{int}, and A_{sph} reflecting the dielectric structure of U-373 MG spheroids as a function of different cell seeding densities (20,000, 30,000, 40,000 and 60,000 c/well; day 5 and/or day 6 after spheroid generation). The values were determined by fitting each measured impedance spectrum three hours after spheroid insertion using a *LabVIEW™*-based software (written by J. Wegener, University of Regensburg) and the following parameter values: A_{el} = 12 (± 1) | 11.5 (± 0.4) | 11.2 (± 0.8) | 10 (± 1) ·10^{-6} $Fs^{n-1}cm^{-2}$; n_{el} = 0.86 (± 0.01) | 0.862 (± 0.004) | 0.875 (± 0.008) | 0.88 (± 0.02); R_{bulk} = 5,400 Ω; A_{para} = 2.4 ·10^{-10} $Fs^{n-1}cm^{-2}$; n_{para} = 0.9; n_{sph} = 0.75. Data sets were averaged after fitting, mean ± SE; see the table for the respective number of experiments.

	spheroid size [c/well]			
	20,000	30,000	40,000	60,000
R_{ext} [kΩ]	43 ± 1	38 ± 1	30 ± 2	28 ± 2
R_{int} [kΩ]	15 ± 1	7.6 ± 0.5	5 ± 1	3.0 ± 0.9
A_{sph} [10^{-9} $Fs^{n-1}cm^{-2}$]	9.8 ± 0.8	9.1 ± 03	8.9 ± 0.6	8 ± 1
n	6(10)	15(27)	6(11)	4(4)

The calculated values of the parameters reflecting the spheroid dielectric structure show a decrease in both the extracellular (R_{ext}) and intracellular (R_{int}) resistance values with increasing seeding density and

spheroid size, respectively (Tab. 7.2). While the extracellular resistance decreases in a range from 43 (± 1) kΩ (20,000 c/well) to 28 (± 2) kΩ (60,000 c/well), the intracellular resistance is reduced from 15 (± 1) kΩ to 3.0 (± 0.9) kΩ. The same trend of decline is reflected by the values of the non-ideal spheroid capacitance A_{sph}. These values decrease slightly with increasing cell seeding density beginning from 9.8 (± 0.8) $\cdot 10^{-9}$ $Fs^{n-1}cm^{-2}$ (20,000 c/well) down to 8 (± 1) $\cdot 10^{-9}$ $Fs^{n-1}cm^{-2}$ (60,000 c/well).

The impedimetric model study demonstrates that the magnitude of spheroid impedance signaling and the tendency of the spheroid to migrate into the funnel opening is dependent on the tissue model size. Therefore, experiments were performed with spheroids of equivalent size for purposes of comparison. In the following, MCF-7 spheroids with a seeding density of 12,000 c/well and U-373 MG spheroids with a seeding density of 30,000 c/well were generally used for further impedance measurements, corresponding to spheroids with an average diameter of 550–600 µm at day 5 and day 6 after spheroid generation.

7.1.2 INFLUENCE OF AGE ON THE SPHEROID CELL DYNAMIC

In addition to the model study of different spheroid sizes, the influence of spheroid age on cell dynamic was investigated. Spheroids generated with the same seeding cell concentration were measured after different incubation times between day 5 and day 8. The cellular micromotion and dielectric spheroid parameters were determined by measuring RTC and MFT spectra three hours after spheroid placement according to the protocol in chapter 4.3.3.

The high time resolution measurements were analyzed to investigate whether different periods of spheroid incubation affect the internal micromotion of the tissue models. The detrended RTC data for each condition show a clear dependence of cellular micromotion on spheroid age as the cell fluctuations within the spheroids were reduced with increasing incubation time (Fig. 7.3). In the case of MCF-7 spheroids, fluctuations in resistance values start from a range of -200–200 Ω on day 5 and decrease to -50–50 Ω on day 8. For U-373 MG spheroids, the values start in a range of -10–10 Ω on day 5 and decrease steadily to -2.5–2.5 Ω on day 8 (see chapter 11.1, Fig. A-7.1).

Based on the measured RTC data, an analysis of the variance of increments was performed after segmented detrending for all conditions using a time interval of 32 s. The analysis shows a generally decreasing trend for the variance of increments for spheroids with increasing incubation time (Fig. 7.4). On day 5, the variance of increments of MCF-7 spheroids was calculated as 4,100 (± 800) Ω^2 while the values decreased linearly to 630 (± 30) Ω^2 on day 8.

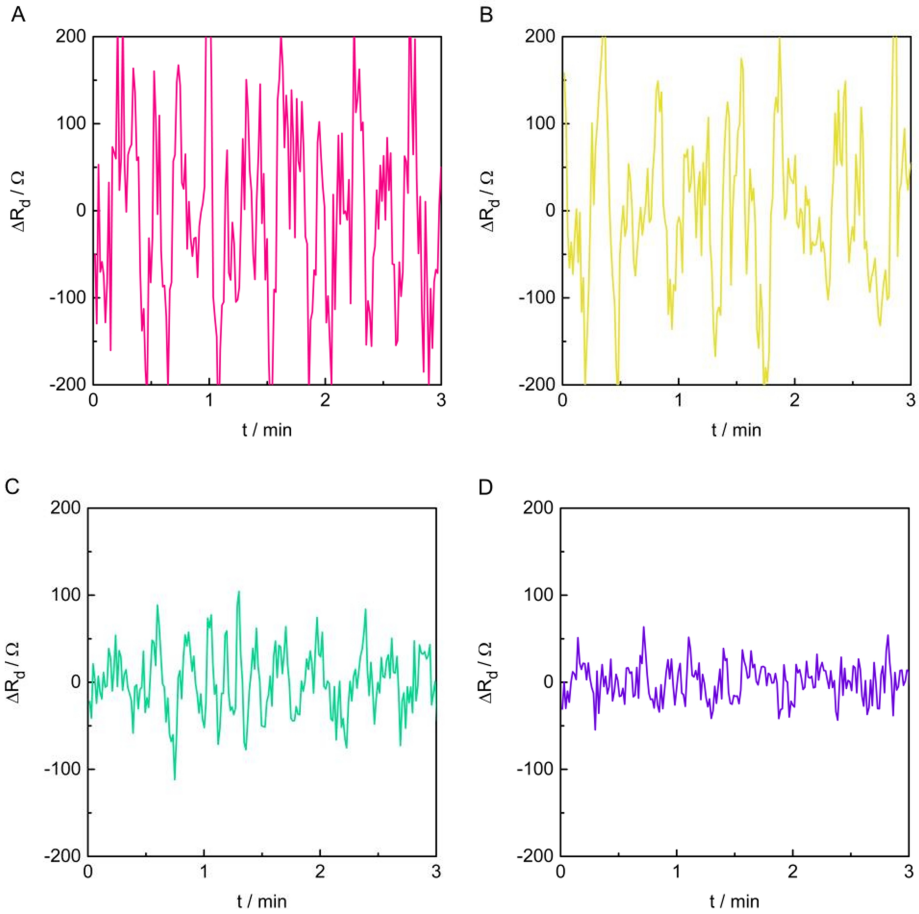

Fig. 7.3 Detrended RTC data at 200 Hz three hours after positioning of MCF-7 spheroids (12,000 c/well) at different ages of five (A), six (B), seven (C), and eight (D) days after spheroid formation. Experiments were performed in a standard cell culture incubator at 37 °C and 0 % CO_2.

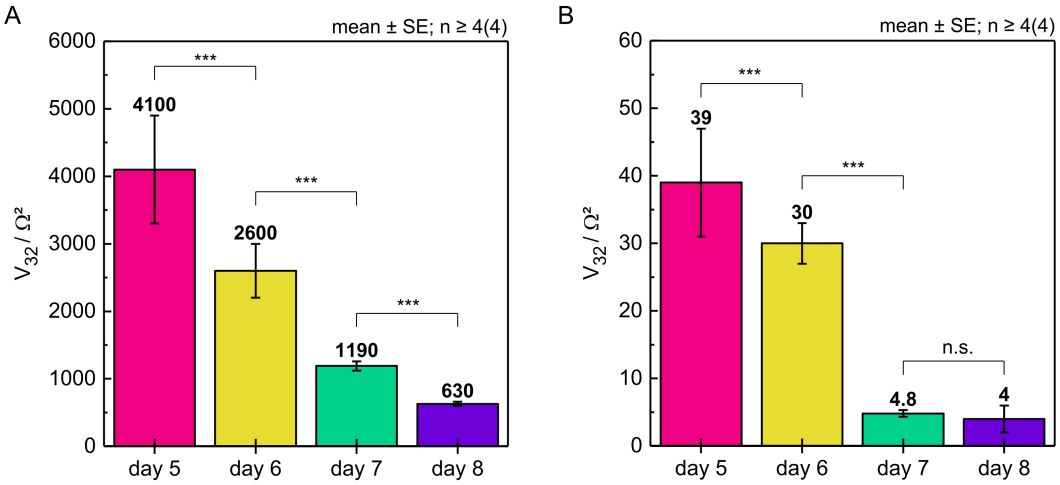

Fig. 7.4 Variance of increments of impedance fluctuations after segmented detrending measured three hours after spheroid placement of MCF-7 (A; 12,000 c/well) and U-373 MG spheroids (B; 30,000 c/well) at different ages (from day 5 to day 8 after incubation). Significance was determined by a two-sample t-test using a significance level of 0.1 (*), 0.05 (**), and 0.01 (***). Data sets were averaged after segmented detrending, mean ± SE; n ≥ 4(4).

A two-sample t-test demonstrates that there is a significant difference between each of the spheroid ages studied. In contrast, the U-373 MG spheroids showed the highest variance of increments of 39 (± 8) Ω² at the shortest incubation time of five days, which decreased to 30 (± 3) Ω² on day 6, while it rapidly dropped to 4.8 (± 0.5) Ω² and 4 (± 2) Ω² on day 7 and day 8 after spheroid generation. While the variance of increments varied significantly on the fifth and sixth days and between the last two days, no significance was observed between the seventh and eighth day when applying a two-sample t-test.

In the case of MCF-7 spheroids, an evaluation of the three spheroid parameters, based on the recorded data, displays a constant decrease of R_{ext} and R_{int} values for increasing spheroid incubation time, respectively spheroid age (Tab. 7.3). The extracellular resistance decreases from 130 (± 10) kΩ (day 5) to 80 (± 20) kΩ (day 8) and the intracellular resistance is reduced from 3 (± 1) kΩ (day 5) to 0.17 (± 0.03) kΩ (day 8), whereas the non-ideal spheroid capacitance A_{sph} remains in a range of 3.2–3.4 $\cdot 10^{-9}$ $Fs^{n-1}cm^{-2}$ (day 5 to day 8) with a slight increase related to spheroid age.

Tab. 7.3 Calculated values of R_{ext}, R_{int}, and A_{sph} reflecting the dielectric structure of MCF-7 spheroids as a function of different spheroid ages (day 5 | day 6 | day 7 | day 8; 12,000 c/well). The values were determined by fitting each measured impedance spectrum three hours after spheroid insertion using a *LabVIEW™*-based software (written by J. Wegener, University of Regensburg) and the following parameter values: A_{el} = 12.3 (± 0.6) | 12.0 (± 0.5) | 11.9 (± 0.9) | 12 (± 2) $\cdot 10^{-6}$ $Fs^{n-1}cm^{-2}$; n_{el} = 0.85 (± 0.01) | 0.86 (± 0.01) | 0.84 (± 0.01) | 0.85 (± 0.02); R_{bulk} = 5,400 Ω; A_{para} = 2.4 $\cdot 10^{-10}$ $Fs^{n-1}cm^{-2}$; n_{para} = 0.9; n_{sph} = 0.75. Data sets were averaged after fitting, mean ± SE; see the table for the respective number of experiments.

	spheroid age			
	day 5	day 6	day 7	day 8
R_{ext} [kΩ]	130 ± 10	110 ± 10	100 ± 20	80 ± 20
R_{int} [kΩ]	3 ± 1	1.0 ± 0.3	0.25 ± 0.05	0.17 ± 0.03
A_{sph} [10^{-9} $Fs^{n-1}cm^{-2}$]	3.2 ± 0.2	3.3 ± 0.2	3.4 ± 0.4	3.4 ± 0.4
n	9(26)	7(17)	4(8)	3(3)

For U-373 MG spheroids, the calculated values of the dielectric spheroid parameters show similar parametric trends (see chapter 11.1, Tab. A-7.1). With increasing spheroid age, the values of extracellular and intracellular resistance are constantly decreasing. While the extracellular resistance decreases in a range from 41 (± 2) kΩ (day 5) to 27 (± 1) kΩ (day 8), the intracellular resistance is reduced from 8.0 (± 0.5) kΩ to 2.6 (± 0.4) kΩ. An inverse trend concerning increasing values is reflected by the values of the non-ideal spheroid capacitance A_{sph} that constantly increase with increasing spheroid incubation time from 8.9 (± 0.5) $\cdot 10^{-9}$ $Fs^{n-1}cm^{-2}$ (day 5) up to 13 (± 2) $\cdot 10^{-9}$ $Fs^{n-1}cm^{-2}$ (day 8).

The analysis of the spheroid micromotion, the calculated variance of increments, and the dielectric spheroid parameters demonstrate a clear dependence on the spheroid age. Based on these impedimetric model studies of U-373 MG and MCF-7 spheroids, the use of tissue models for further measurements should be linked to their previous incubation period. To ensure reproducible impedance signals and comparability of subsequent experiments, five- or six-days-old spheroids were generally used.

7.1.3 INFLUENCE OF PH ON THE SPHEROID CELL DYNAMIC

Another aspect in the fundamental characterization of the tissue models was the influence of the pH value used for spheroid generation on cell dynamic. Therefore, U-373 MG spheroids were generated with identical seeding concentrations and different pH values ranging from pH 6.8 to pH 7.6. The cellular micromotion and dielectric spheroid parameters were determined by measuring RTC and MFT spectra three hours after spheroid placement according to the protocol in chapter 4.3.3.

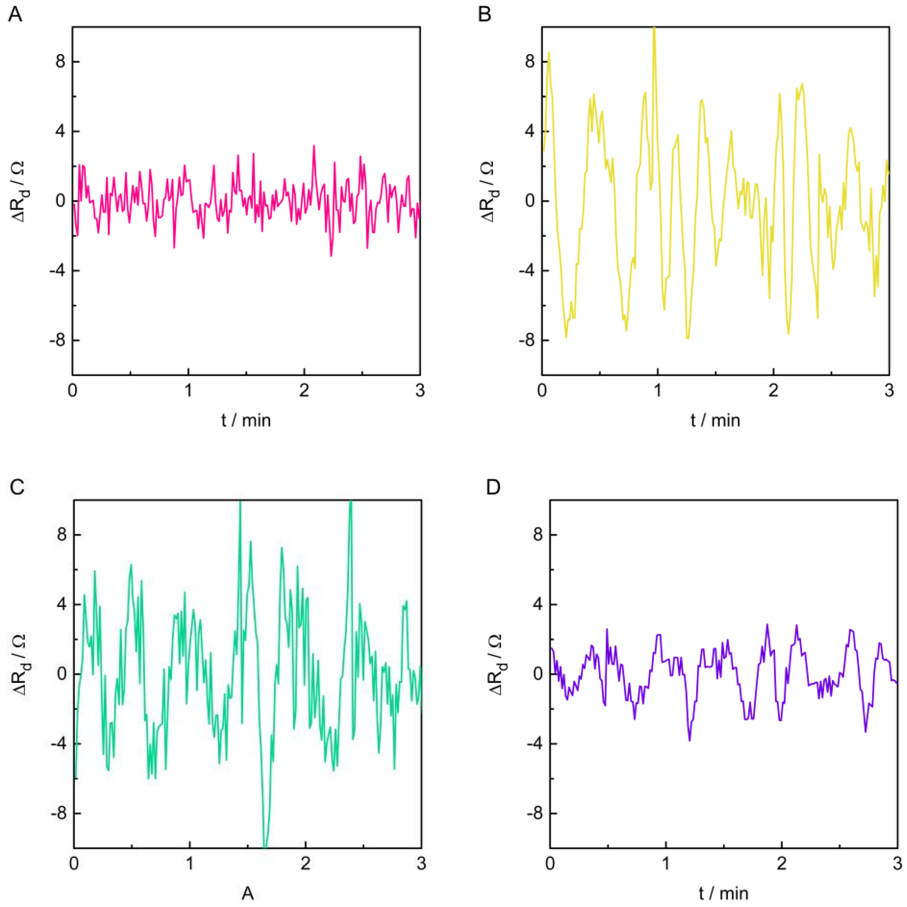

Fig. 7.5 Detrended RTC data at 200 Hz three hours after positioning of U-373 MG spheroids (30,000 c/well) generated using different pH values of pH 6.8 (A), pH 7.0 (B), pH 7.4 (C), and pH 7.6 (D). Experiments were performed in a standard cell culture incubator at 37 °C and 0 % CO_2.

To investigate whether different pH values of the cell culture medium affect the internal micromotion of the generated spheroids, the high time resolution measurements were analyzed (Fig. 7.5). The time courses of detrended RTC data display a slightly increasing fluctuation of signal amplitude from pH 6.8 (-3–3 Ω) to pH 7.4 (-10–10 Ω), whereas the cellular micromotion is markedly reduced at pH 7.6 (-3–3 Ω). For reference, the results of the RTC measurements at pH 7.2 are presented in Fig. A-7.1 (see chapter 11.1) for the fifth (A) and sixth (B) day of the spheroid aging model study, showing a similar signal amplitude of approximately -12–12 Ω towards pH 7.0.

After performing segmented detrending on the measured RTC data, the variance of increments of each pH was obtained using a time interval of 32 s (Fig. 7.6). The analysis shows a significant increase in values at pH 7.0 (43 (± 8) Ω²) and pH 7.4 (35 (± 9) Ω²) in relation to the results of pH 6.8 and pH 7.6. The result at pH 7.2 of 39 (± 8) Ω² on day 5 is similar to pH 7.0 and pH 7.4 (see Fig. 7.4). At the extreme pH values of pH 6.8 and pH 7.6, the variance of increments is significantly reduced and exhibits a range of 5–13 Ω². A two-sample t-test confirmed the significance of the calculated values for each pH value studied, with the exception that no significance was found in the range of pH 7.0–7.4 (including pH 7.2).

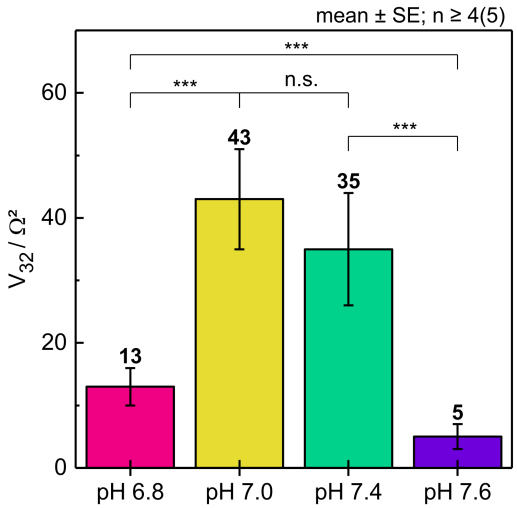

Fig. 7.6 Variance of increments of impedance fluctuations after segmented detrending measured three hours after spheroid placement of U-373 MG spheroids (30,000 c/well) generated using different pH values (pH 6.8 to pH 7.6). Significance was determined by a two-sample t-test using a significance level of 0.1 (*), 0.05 (**), and 0.01 (***). Data sets were averaged after segmented detrending, mean ± SE; n ≥ 4(5).

The evaluation of the three spheroid parameters based on the recorded data reveals an ascending pattern from pH 6.8 to pH 7.2, followed by a descending trend from pH 7.2 to pH 7.6 for each parameter (Tab. 7.4). For the extracellular and intracellular resistances, the tendencies with increasing pH are contrary. In the case of R_{ext}, the values increase from 28 (± 3) kΩ (pH 6.8) to 38 (± 1) kΩ (pH 7.2) and decrease towards 33 (± 2) kΩ (pH 7.6). In contrast, the intracellular resistance shows the highest values in the extreme pH areas of pH 6.8 (11 (± 3) kΩ) and pH 7.6 (12 (± 5) kΩ), while the values in between

vary in a range of 6–7.6 kΩ. The non-ideal spheroid capacitance A_{sph} fluctuates down- and upwards, exhibiting the maximum value at pH 6.8 (13 (± 3) ·10^{-9} $Fs^{n-1}cm^{-2}$) and a second maximum at pH 7.2 (9.1 (± 0.3) ·10^{-9} $Fs^{n-1}cm^{-2}$).

Tab. 7.4 Calculated values of R_{ext}, R_{int}, and A_{sph} reflecting the dielectric structure of U-373 MG spheroids (30,000 c/well) as a function of different pH values used for spheroid generation (pH 6.8 | 7.0 | 7.2 | 7.4 | 7.6). The values were determined by fitting each measured impedance spectrum three hours after spheroid insertion using a *LabVIEW™*-based software (written by J. Wegener, University of Regensburg) and the following parameter values: A_{el} = 17 (± 2) | 11.7 (± 0.9) | 11.5 (± 0.4) | 11 (± 2) | 14 (± 2) ·10^{-6} $Fs^{n-1}cm^{-2}$; n_{el} = 0.71 (± 0.05) | 0.845 (± 0.008) | 0.862 (± 0.004) | 0.86 (± 0.02) | 0.74 (± 0.05); R_{bulk} = 5,400 Ω; A_{para} = 2.4 ·10^{-10} $Fs^{n-1}cm^{-2}$; n_{para} = 0.9; n_{sph} = 0.75. Data sets were averaged after fitting, mean ± SE; see the table for the respective number of experiments.

	pH value				
	pH 6.8	pH 7.0	pH 7.2	pH 7.4	pH 7.6
R_{ext} [kΩ]	28 ± 3	33 ± 3	38 ± 1	35 ± 1	33 ± 2
R_{int} [kΩ]	11 ± 3	7 ± 3	7.6 ± 0.5	6 ± 2	12 ± 5
A_{sph} [10^{-9} $Fs^{n-1}cm^{-2}$]	13 ± 3	7.9 ± 0.9	9.1 ± 0.3	7.8 ± 0.5	8 ± 2
n	5(5)	4(4)	15(27)	5(5)	5(5)

Overall, the analysis of the spheroid micromotion, the calculated variance of increments, and the dielectric spheroid parameters demonstrate a clear dependence on the spheroid pH value. Starting from pH 7.2, the assessed cell micromotion decreases towards the two extremes in both the acidic and alkaline ranges. Thus, the physiological pH acts as a tilting point with optimal conditions for cell dynamic. Based on this impedimetric model study of U-373 MG spheroids, tissue models with a standardized cell culture medium with a pH value of pH 7.2 were used for further measurements and experiments with MCF-7 as well as U-373 MG spheroids.

7.1.4 DISCUSSION: INFLUENCE OF TISSUE MODEL CONDITIONS

To define the ideal tissue model conditions for subsequent experiments, basic model studies were performed. This involved varying the fundamental spheroid properties such as spheroid size -respective cell seeding density-, spheroid age -respective incubation period-, and the pH used for spheroid formation, and analyzing the recorded data.

Apart from the tissue model condition dependencies, the raw data values of impedance magnitude as well as the three spheroid parameters reflect the cell type specific structure of the derived spheroids,

as discussed in chapter 6.4. As a result of an assumed higher number of cell-cell junctions within MCF-7 spheroids, the extracellular resistance is increased in combination with higher impedance magnitudes compared to U-373 MG spheroids. In contrast, U-373 MG spheroids exhibiting a similar spheroid diameter as MCF-7 spheroids are composed of up to five times higher number of cells due to the subsequent cell type specific compaction process. Thus, an enhanced number of cells results in amplified values of A_{sph} indicating a lower ratio of live to dead cells compared to MCF-7 spheroids and in increased R_{int} values based on internal cell body resistance.

I INFLUENCE OF SPHEROID SIZE

The influence of the cell seeding density and thus spheroid size on the impedance signal was evaluated. Since the size of a spheroid can be controlled by cell number and growth time prior to use (compare chapter 6.2.1), experiments were performed with three different-sized spheroids of each cell type with a similar incubation period of five to six days. As stated in chapter 7.1.1, the impedance is size-dependent and yields significant signal differences for small, medium, and large-sized tissue models.

- ➔ As the spheroid size increases, the impedance decreases.
- ➔ As the spheroid size increases, R_{ext} and R_{int} decrease.
- ➔ As the spheroid size increases A_{sph} increases in the case of MCF-7 spheroids or decreases in the case of U-373 MG spheroids.

The impedimetric results are considered contrary to the expectation that spheroids with the highest seeding density tested would have the highest impedance and extra- as well as intracellular resistance values. This has been reported, for example, in the work of Thielecke and coworkers who performed EIS measurements in a capillary system with T47D human breast cancer spheroids (Thielecke et al., 2001). They determined the R_{ext} value using a non-linear least-squares fitting technique and calculated a R_{ext} value of 92 kΩ for larger spheroids (600–700 µm diameter) and a R_{ext} value of only 18 kΩ for smaller spheroids (400–500 µm diameter). The researchers explained this finding by stating that the path of the current through the larger spheroid is longer and it has to cross more layers of cells, so it has a higher resistance than the smaller spheroid (Thielecke et al., 2001).

In accordance with this, Hupf investigated the translocation of spheroids within the constriction of the channel-based measurement setup by performing a microscopic study (Hupf, 2018). This was done by analyzing images of three different-sized MCF-7 spheroids placed in the channel to calculate the area occupied by the spheroid. The results reveal that the percentage of the occupied total internal volume of the central restriction is highest for small spheroids at 56 (± 6) % (1,000 c/well) and decreases steadily

for large spheroids to 38 (± 4) % (6,000 c/well; Hupf, 2018). Since the channel- and the funnel-based measurement system are similar setups concerning the identical diameter of the central opening, this finding can be transferred to the micro-trap device.

The results of the impedimetric study in combination with those of the microscopic study by Hupf prove that the spheroid size dependence of the impedance signal is related to the tendency of the spheroid to migrate into the aperture. In the case of small spheroids, a large proportion of the spheroid body covers the funnel aperture due to its ability to adapt to the narrow aperture more easily than larger spheroids. Thus, a longer effective length of the spheroid had to be overcome by the current flow, resulting in a greater resistive effect on the impedance signal. In addition, the efficient physical blocking of the micro-trap constriction results in smaller extracellular spaces and higher extracellular and intracellular resistance. In contrast, the fraction of the larger species within the micro-trap hole was significantly smaller, providing more extracellular space for the current to pass through the spheroid body leading to lower parametric values. Another explanation for the lower R_{ext} value of the larger spheroids could be that they potentially contain more dead cells than the small spheroids due to accelerated nutrient and waste gradients in larger spheroids (Hupf, 2018). By investigating the specific albumin secretion rate as a function of spheroid size, Glicklis et al. noted that cellular micromotion decreases with increasing spheroid size, while the magnitude of change depends on the surface-to-volume ratio of the spheroid (Glicklis et al., 2014). As spheroids become larger, the surface-to-volume ratio and the ratio between the volume of viable cells to the whole spheroid decreases, which is generally associated with a decrease in R_{ext} values (Thielecke et al., 2001).

A comparison of the investigated signal trends between MCF-7 and U-373 MG spheroids shows that the size dependence, and thus the cell seeding density, has an identical effect on all parameters regardless of the cell type, with the exception of the spheroid capacitance A_{sph}. The trends of the impedance signal as well as extracellular and intracellular resistance regarding the size dependency, are generally based on the explanations discussed in this chapter. Concerning the effect of the spheroid size on A_{sph} values, the increase in the parameter values in the case of MCF-7 spheroids implies an increasing permeability of cell membranes or respectively a higher number of dead cells in the spheroids with highest cell seeding density, whereas a decreasing trend in the case of U-373 MG spheroids reflects their typical morphological architecture of spheroid compaction (see chapter 6.4.2). The spheroid size does not increase in proportion to the cell concentration used, but the ratio of live to dead cells becomes higher within an almost similar body volume. Consequently, the capacitance decreases due to the rising amount of intact cell membranes within the U-373 MG spheroid.

In a detailed view of the MCF-7 model study, an increase in data errors with decreasing cell seeding density was observed, as shown by the recorded relative impedance values of 1,020 (± 40) % for spheroids with a concentration of 18,000 c/well and 2,700 (± 200) % with a concentration of 8,000 c/well three hours after spheroid positioning. These data indicate that the smaller MCF-7 spheroid adapts more flexibly to the opening into which it is pushed by gravity than a larger spheroid, which remains in position recording more reproducible time curves and thus fewer errors bars. For U-373 MG spheroids, the errors in the impedance data are similar between the three different seeding densities, indicating that the reproducibility of spheroid placement is not size-dependent in this case. However, a different size dependence was investigated in the U-373 MG model study, relating to the increasing slope value at which impedance increased steadily over three hours with decreasing spheroid size. Here, it can be assumed that the constriction is progressively filled by the spheroid's body, causing a constant increase in resistance, which is more apparent for the smaller than for the larger spheroids. This observation provided evidence to support the previously mentioned hypothesis of physical adaptation of the spheroids to the funnel hole, with the smaller bodies being more adaptable than the larger ones. In terms of determining the signal changes induced by different model study experiments, the results are not affected by slight spheroid adaption since a control reaction was always being monitored in parallel.

The comparison of the size dependencies investigated in this thesis with the spheroid study of Hupf is only possible in a qualitative way and not in terms of absolute values as the basic system parameters are different (Hupf, 2018). However, both model studies were performed using MCF-7 spheroids and displayed identical size-dependent trends for the system-related parameters.

II INFLUENCE OF SPHEROID AGE

In accordance with the spheroid size, the influence of the incubation time, and thus the age of the spheroids on the cellular micromotion, was investigated. Spheroids of identical seeding density were used after five to eight days of cultivation. The RTC measurements and the calculated variance of increments, as well as the three impedimetric parameters of the spheroids, show clear variations depending on the cultivation time of the tissue model used, as described in chapter 7.1.2.

- ➔ As the spheroid age increases, the variance of increments decreases.
- ➔ As the spheroid age increases, R_{ext} and R_{int} decrease, and A_{sph} increases.

As there is a direct correlation between a spheroid's size and its incubation time, it should be noted that the spheroid diameter may change with increasing spheroid age in this model study. In particular, in the

case of MCF-7 cells, the spheroid diameter increases by a total of approximately 60 µm between day 5 and day 8, whereas for U-373 MG spheroids it decreases by a total of approximately 50 µm. Thus, it cannot be guaranteed that this fact does not influence the results discussed for spheroid age. However, by comparing the determined values of e.g., the intracellular resistance in dependence of the spheroid size, the values decrease by 20 % when the spheroid diameter differs by 100 µm in diameter in case of MCF-7 spheroids (compare Tab. 7.1), while the signal decreases by 90 % regarding the spheroid age between day 5 and day 8 with a total diameter increase of 60 µm. Based on this, the results are considered to be more sensitive to changes in spheroid age than to changes in spheroid size, at least within the age and size intervals investigated in this thesis.

The study of cell micromotion in terms of spheroid age is focused on the internal dynamic of the spheroid. Several biological phenomena are affected by the cultivation time, such as the restriction of proliferation to the outer rim of the spheroid (also known as the constant crust model), the formation and influence of a necrotic center, the availability and transport of nutrients, the changing growth status of the cells, and even the possibility of cell migration (Nirmala et al., 2001). Consistent with the theory of three distinct spheroid zones, it is evident that internal cellular activities and cellular micromotion decrease with increasing spheroid cultivation time. For example, a long-term experiment performed by Nirmala and colleagues using a glioblastoma cell line (SNB19) and MIB-1 staining revealed that the density of proliferating cells at the spheroid rim decreases after at least three weeks and the proliferation in the center seemed to stop after more than two weeks (Nirmala et al., 2001).

Consequently, the tendencies of the signal values determined for the variance of increments and dielectric spheroid parameters display the expected behavior with increasing spheroid age. The decreasing variance of increments indicates a reduced cellular micromotion within the spheroid and thus less cell dynamic. In conjunction with a reduced cellular micromotion, the proportion of quiescent and dead cells must increase. This assumption is reinforced by the fact that the signal decreases for both R_{ext} and R_{int} values, which is associated with loss of cell barrier function, allowing the current to flow with less resistance. In addition, the increase in signal from A_{sph} indicates increasing permeability within the spheroid body. The combination of all three signal trends reveals the gradual disintegration of the cell membrane with increasing spheroid age. A comparison of the investigated signal trends between MCF-7 and U-373 MG spheroids shows that the spheroid age has an identical effect on all parameters regardless of the cell type, thereby emphasizing cell aging as a fundamental effect.

A detailed examination of each parameter, which reflects the dielectric structure of the spheroid, reveals a drastic decline between day 6 and day 7 of cultivation. This marked contrast cannot be explained by progressive cell death on a physiological level due to increasing incubation time and cell

aging since it may be related to the overall environmental effect of the multicellular spheroid. In general, concentration gradients of nutrients and waste products are formed within the spheroid that are further enhanced with increasing cultivation time. The restricted availability of nutrients and the increased levels of catabolites in the spheroid center are the controlling factors for cell division and dynamic, while limited access to oxygen is the most critical metabolic pathway. Oxygenation decreases progressively from the outer layers to the center with an oxygen partial pressure below 10 torr (Mueller-Klieser and Sutherland 1982). Franko and Sutherland's observations showed a clear correlation between the calculated theoretical oxygen penetration distance and the thickness of the resulting viable rim of V79 spheroids by artificially regulating the external oxygen concentration down to 50 torr (Franko and Sutherland, 1979). A mathematical model developed by Glicklis et al. predicts the distribution profiles of oxygen and viable cells in spheroids of different sizes and mentions that no oxygen limitation occurs in spheroids up to 100 µm in diameter (Glicklis et al., 2004). Using a novel imaging setup, Schmittlein monitored oxygen gradients within spheroids and studied age-related differences in oxygen partial pressure distribution using seven- to nine-days-old MCF-7 spheroids (Schmittlein, 2017). The recorded time-lapse images showed an initial steep drop in oxygen levels from the normoxic values of the surrounding medium at the spheroid edge, reaching stable values below 40 torr at the spheroid center. Based on the analysis of three individual samples for each spheroid age, Schmittlein found that the area size of the minimum oxygen partial pressure did not significantly increase with age but was highly dependent on the cell batch and passage number (Schmittlein, 2017). However, this result can be compared with the result of the steep decrease of the system-related impedimetric parameters between day 6 and day 7 observed in this chapter, as no further significant changes of the oxygenation within the spheroid could be detected from day 7 to day 9. Thus, this is an indicator for the assumption that gradient-induced spheroid aging is a phenomenon related to the overall environmental effect of multicellular spheroids. Despite the fact that nothing conclusive is known about age-dependent oxygenation in spheroids, the results from the literature indicate that oxygen levels in spheroids are strongly dependent on the cell type, spheroid size, ambient oxygen levels, and culture conditions (Schmittlein, 2017).

III INFLUENCE OF SPHEROID PH

As a third environmental aspect of investigating optimal settings for spheroid culture conditions, the influence of the pH value on cellular micromotion was studied. Spheroids with identical seeding densities but different pH values of the cell culture medium used for generation were analyzed. The analysis of the spheroid micromotion, the calculated variance of increments, and the dielectric spheroid

parameters show clear variations depending on the pH of the tissue model used, as described in chapter 7.1.3.

- ➔ As the spheroid pH value increases, the variance of increments and R_{ext} initial increases, and subsequently decreases above pH 7.2.
- ➔ As the spheroid pH value increases, R_{int} and A_{sph} decrease and increase, while A_{sph} additionally declines at the highest pH value.

The pH value is one of the key factors controlling metabolic activity in the extracellular environment and in the intracellular compartments of living cells. In addition to providing an optimal chemical environment for proteins, ensuring ion transports and enzyme activities, and defining the charge of biological surfaces, maintaining specific pH values is crucial for all cell functions and thus cell viability. Although small variations in pH can be compensated by cells due to the buffering capacity of various weak acids and bases, such as phosphate groups and certain amino acid side chains (Roos and Boron, 1981), larger variations in pH lead to decreasing cell activity and cell death, whereby the range of tolerance may vary depending on the age and type of cell. Applying a novel sensor foil-based imaging setup, Pütz recorded the oxygen consumption of spheroids derived from a melanoma cell line (SK-MEL-28) to investigate the pH dependence of respiratory activity (Pütz, 2022). The analysis of the time-lapse images showed that the spheroids exposed to an acidic environment respirated less oxygen compared to the spheroids under more physiological or even alkaline conditions (Pütz, 2022). Furthermore, von Euler et al. indicated that an acidic environment leads to either necrosis or apoptosis, whereas an alkaline milieu causes cell necrosis (von Euler et al., 2002).

The impedimetric results suggest that cell viability, and therefore the optimal pH environment, is set at the physiological pH of 7.2. Based on this, the micromotion decreases in both the alkaline and acidic pH ranges, as reflected in the calculated variance of increments. In addition, the extracellular resistance also tends to decrease in both directions, mimicking the morphology of the U-373 MG spheroid at higher or lower pH values. As discussed in chapter 6.4.4, the spheroid shape varies in diameter and growth kinetics within the investigated pH range of pH 6.6 to pH 7.8, whereby the spheroid exhibited a significantly larger overall diameter with decreasing or increasing pH value. While an equivalent growth kinetic to the standardized pH 7.2 was found between pH 7.0 and pH 7.8, the spheroids displayed a less typical compaction behavior in the acidic environment. In this context, the extracellular resistance also displays lower values in the extreme pH regions, indicating unhindered current flow through the less dense spheroid body. The trends in the intracellular resistance parameter appear counterintuitive as an increase in signal along with R_{ext} was expected. An explanation for the signal decrease toward pH 7.2 can be found in the fact that cells contain a certain intracellular ion concentration that influences

intracellular resistance (Sasser et al., 1993). As the cell shrinks due to a higher compaction level at pH 7.2, water efflux leads to an increase in ion concentration and consequently a decrease in R_{int} values due to improved conductance. The fluctuation of the capacitive parameter A_{sph} indicates an up-and-down regulation of the permeability of the whole spheroid body structure according to the cell type-specific spheroid growth kinetics. The maximum value was found at pH 6.8, indicating the highest permeability and less dense spheroid structure within the pH range. However, there is no explanation for the varying values and the remarkably low value at pH 7.6 compared to pH 7.2.

Overall, the results indicate optimal environmental conditions when using the physiological pH of 7.2. Although the experiment on cell dynamic as a function of pH was only performed with U-373 MG spheroids, the results are also applicable to MCF-7 spheroids.

7.1.5 SUMMARY OF IDEAL TISSUE MODEL CONDITIONS

Living organisms are highly dependent on precisely regulated environmental conditions. In this chapter, the three different aspects of tissue model conditions concerning spheroid size, spheroid age, and pH, were studied by analyzing their influence on the impedimetric parameters.

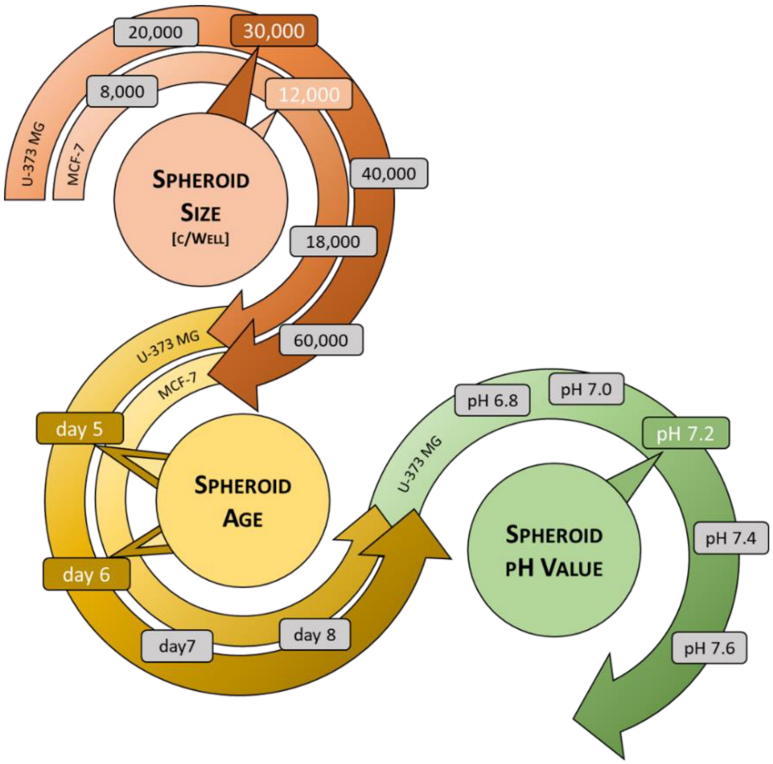

Fig. 7.7 Overview of the tissue model conditions tested using funnel-based impedance measurements. By varying the spheroid size, spheroid age, and spheroid pH, the ideal conditions for each cell type were obtained, as highlighted in the figure. The cogwheel-like pattern of each category demonstrates the progression and interaction of each factor.

These three key factors were altered in their individual system-relevant range as described in the respective protocols. The combination of all three ideally adjusted factors provides the best possible setting for tissue model conditions in the context of this thesis (Fig. 7.7).

In summary, the variability in spheroid impedance is likely to be due to small differences in spheroid structure resulting from internal or external environmental influences. Although spheroids are derived from the same initial cell concentration and measured at the same age, they differ slightly in size, morphology, and internal structure (ratio of cell mass to extracellular matrix; proportion of viable and dead cells), according to Hupf (Hupf, 2018). Since no two spheroids are identical, their impedance measurements will differ to a certain degree.

7.2 MODEL STUDY: CELLULAR RESPONSE TO PERMEABILIZATION

In this model study, the measurement signals of spheroids were characterized upon their response to either fixation and/or permeabilization processes. For fixation, the aldehydes glutaraldehyde (GA) and paraformaldehyde (PFA) were tested, which caused the cross-linking of proteins in the biological sample, thereby preserving cellular structures and terminating cell viability (compare chapter 7.2.6). To analyze the effect of membrane permeabilization, the spheroids were exposed to different concentrations of the detergent saponin. This compound is used in standard cytochemical experiments as a non-ionic surfactant that selectively interacts with membrane cholesterols and/or removes cholesterols leading to the formation of cell membrane pores (compare chapter 7.2.7; Lacaille-Dubois and Wagner, 1996).

The fixation procedure was only performed in conjunction with impedimetric analysis of the spheroids, as it was required for measurements using the newly developed funnel-based measurement setup to prevent the spheroids from slipping through the aperture after permeabilization. The determination of cell toxicity and the influence of different detergent concentrations on cellular micromotion was performed in both 2D and 3D tissue models. In addition, time-resolved microscopy studies were conducted to correlate the results with visual observations.

7.2.1 VIABILITY ANALYSIS OF THE SPHEROID AND CELL MONOLAYER

The PrestoBlue™ cell viability assay (Invitrogen™, Thermo Fisher Scientific) was used to determine the invasiveness of different saponin concentrations on the metabolic activity of spheroids and 2D cell culture. The experiments were repeated three times for each cell line, U-373 MG and MCF-7 cells, and the results of the measured fluorescence intensities were evaluated individually according to the protocol described in chapter 4.1.8.

For the data analysis, the calculated CI values were plotted as a function of the logarithmic saponin concentration and fitted using the sigmoidal dose-response Boltzmann transfer function (chapter 4.1.8, Eq. 4.2). This is shown exemplarily for MCF-7 cells as a cell monolayer and a spheroid model (Fig. 7.8). An identical comparison of the results with respect to the cell dimensionality for U-373 MG cells is shown in chapter 11.1 (see chapter 11.1, Fig. A-7.2) and the respective replicates (see chapter 11.1, MCF-7: Fig. A-7.3 and Fig. A-7.4; U-373 MG: Fig. A-7.5 and Fig. A-7.6).

At the inflection point x_o, the EC_{50} value was determined, which corresponds to the concentration of a tested substance causing 50 % changes in response or, in this case, a 50 % reduction in cell viability. In

summary, the calculated values were listed individually for each experiment and in relation to the cell monolayer and spheroid models tested (Tab. 7.5).

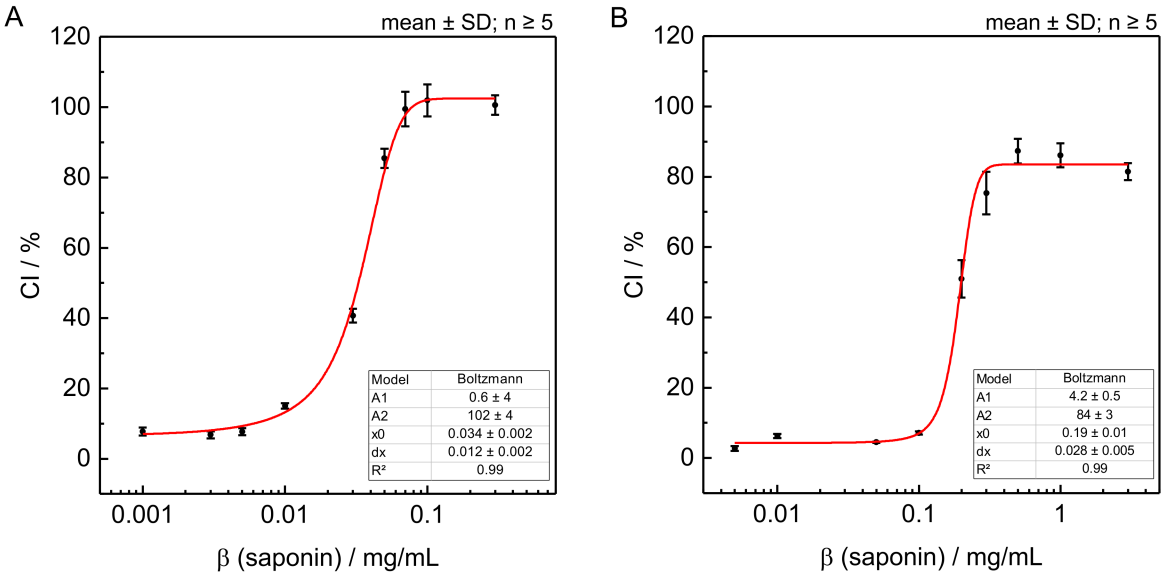

Fig. 7.8 Dose-response curve of the cytotoxicity index CI as a function of the saponin concentration used to determine the effect of permeabilization on MCF-7 cell monolayer culture (A) and spheroid (B) viability. One of three independent experiments is shown for each cell dimensionality, respectively. The PrestoBlue™ cell viability assay was performed five hours after the addition of saponin solution at different concentrations (2D: 0.001–0.3 mg/mL; 3D: 0.005–3 mg/mL). Experiments were performed in a standard cell culture incubator at 37 °C and 0 % CO_2. The results were fitted by the sigmoidal Boltzmann equation and the overall EC_{50} value was determined. Data sets of respectively one experiment were averaged, mean ± SD, A and B: n ≥ 5.

Tab. 7.5 Overview of the EC_{50} values of saponin treatment determined using the PrestoBlue™ cell viability assay for MCF-7 and U-373 MG cell monolayers (2D) and spheroids (3D); the coefficient of determination is given in the table respectively for each experiment. Three individual experiments were combined by calculating the weighted arithmetic mean for each cell dimensionality, respectively; mean ± SE, n = 3. Significance was determined between the identical cell dimensionalities by a two-sample t-test using a significance level of 0.1 (*), 0.05 (**), and 0.01 (***).

	MCF-7		U-373 MG	
EC_{50} [mg/mL]	2D	3D	2D	3D
experiment #1	0.04 ± 0.01 (R^2 = 0.80)	0.2 ± 0.1 (R^2 = 0.93)	0.034 ± 0.001 (R^2 = 0.99)	0.14 ± 0.04 (R^2 = 0.70)
experiment #2	0.04 ± 0.01 (R^2 = 0.70)	0.19 ± 0.01 (R^2 = 0.99)	0.026 ± 0.004 (R^2 = 0.98)	0.168 ± 0.009 (R^2 = 1.00)
experiment #3	0.034 ± 0.002 (R^2 = 0.99)	0.20 ± 0.02 (R^2 = 0.98)	0.03 ± 0.01 (R^2 = 0.89)	0.14 ± 0.03 (R^2 = 1.00)
mean value (mean ± SE; n = 3)	0.034 ± 0.002$^{n.s.}$	0.192 ± 0.009**	0.033 ± 0.001$^{n.s.}$	0.165 ± 0.008**

In general, a higher EC_{50} value was obtained in case of using spheroids compared to cell monolayer culture regardless of the cell type. In the case of MCF-7 cells, the mean values of the EC_{50} were calculated as 0.034 (± 0.002) mg/mL (cell monolayer) and 0.192 (± 0.009) mg/mL (spheroid). In contrast, for U-373 MG cells, the mean values of the EC_{50} were calculated as 0.033 (± 0.001) mg/mL (cell monolayer) and 0.165 (± 0.008) mg/mL (spheroid). The significance for each dimensionality of both cell types was determined by a two-sample t-test, which showed no significance ($^{n.s.}$) for the cell monolayer results and a significance level of 0.05 (**) for the two calculated EC_{50} values for spheroids.

7.2.2 IMPEDIMETRIC ANALYSIS OF THE CELL MONOLAYER

In order to compare the cellular response depending on the dimensionality of the *in vitro* model, the influence of permeabilization was analyzed by performing ECIS™ measurements on cell monolayer cultures derived from MCF-7 and U-373 MG cells. For these experiments, saponin was used in a lower concentration range of 0.003–0.3 mg/mL compared to the spheroid model studies. The cellular behavior was recorded during the addition of the detergent solution at different concentrations by measurements in MFT as well as RTC mode.

The measurements in MFT mode were recorded over a period of five hours, whereas the time course of the normalized impedance magnitude at 4,000 Hz is shown for three hours after compound addition (Fig. 7.9). With decreasing signal values, an increasing cell monolayer permeability is indicated and a clear dose-response dependence of saponin on the permeabilization kinetics is observed for both MCF-7 and U-373 MG cell monolayer cultures. In the case of MCF-7 cells (Fig. 7.9, A), the responses of the control and the two lowest concentrations of 0.003 mg/mL and 0.005 mg/mL display an identical, unaffected signal course, resulting in 93 (± 2) % (ctrl) after three hours incubation. The impedance of the 0.01 mg/mL saponin solution displays an initial signal increase after substance addition, followed by a constant baseline at 102.0 (± 0.8) %. A reproducible biphasic response was observed for the concentrations of 0.03 mg/mL and 0.05 mg/mL, exhibiting an initial signal decrease followed by an increase to 91 (± 9) % and 60 (± 10) % of the normalized impedance magnitude measured after three hours. In contrast, the two highest detergent concentrations of 0.1 mg/mL and 0.3 mg/mL caused a decline in the impedance signal directly after the compound addition, mimicking a cell-free setup signal of 24 (± 4) % for the highest concentration within three hours. As a result, the signal decays more rapidly with increasing compound concentration, indicating a faster permeabilizing effect during incubation.

In comparison, a similar impedance time course was found for U-373 MG cell monolayers (Fig. 7.9, B). The signal from the control cells is identical to the two lowest concentrations of 0.003 mg/mL and 0.005 mg/mL, yielding a final signal of 95 (± 1) % (ctrl) after three hours of incubation. For the

0.01 mg/mL saponin concentration, the impedance initially displays a signal increase after the addition of the compound, which is followed by a steady decline resulting in 100 (± 1) %. After applying saponin concentrations in the range of 0.03–0.3 mg/mL to the cell monolayer, a direct signal decrease was observed, reaching a cell-free level of approximately 77 (± 1) % (0.3 mg/mL) roughly one hour after the addition.

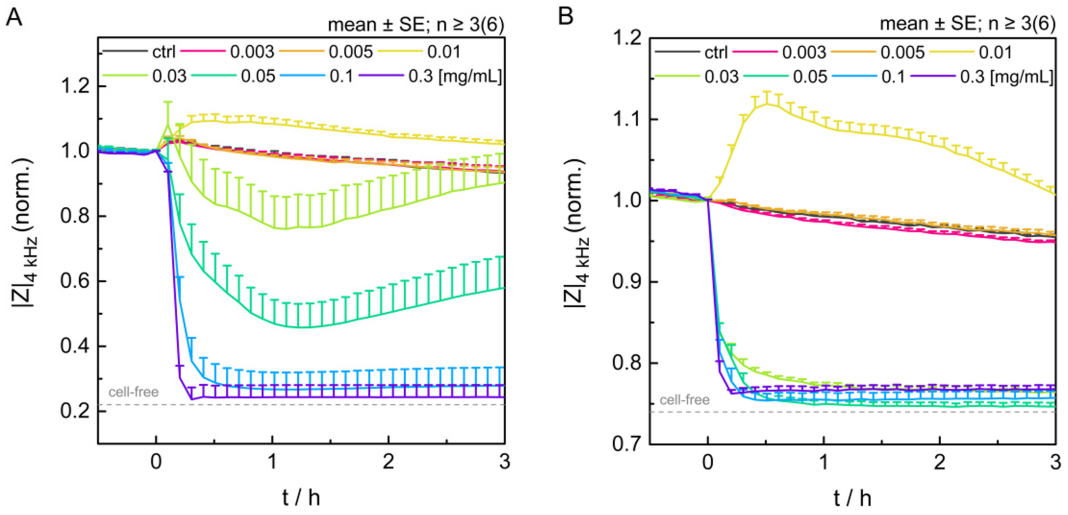

Fig. 7.9 Time course of normalized impedance magnitude at 4,000 Hz of MCF-7 (A) and U-373 MG (B) cell monolayer culture after the addition of saponin solutions with different concentrations in a range of 0.003–0.3 mg/mL. Time courses were normalized with respect to the last data point before compound addition at time point zero. Grey horizontal lines in A and B indicate mean values of cell-free sensors. Experiments were performed in a standard cell culture incubator at 37 °C and 0 % CO_2 using 8W10E arrays. Data sets were averaged after normalization, mean ± SE; n ≥ 3(6).

As a result, significant signal variations were observed as a function of compound concentration, representing different levels of cell monolayer permeability. When MCF-7 cells were used, a clear distribution between substance concentrations was observed, whereas U-373 MG cells were either unaffected or completely permeabilized. The difference in the relative impedance values between the two cell types is caused by the low sensitivity of the ECIS™ measurements to U-373 MG cells since the standardized monitoring frequency of 4,000 Hz was used for comparison. In addition, it should be noted that the time course of the capacitance for the highest concentrations displays a cell disruption from the electrode surface instantly after detergent exposure, regardless of the cell type used (data sets not shown in this thesis).

Based on RTC measurements five hours after detergent addition (data sets not shown), the variance of increments was calculated after performing segmented detrending for all concentrations using a time interval of 32 s. The results for both cell types were normalized to the control condition and show a general increase in the variance of increments for the cell monolayer without a proportional dose-response dependence (Fig. 7.10). Initially, the results increase stepwise with a maximum value of

400 (± 100) % at a concentration of 0.01 mg/mL for MCF-7 cells and 114 (± 9) % for U-373 MG cells at a concentration of 0.03 mg/mL. At higher concentrations, the variance of increments is diminished, demonstrating relative values of 240 (± 30) % (MCF-7) and 106 (± 8) % (U-373 MG) at a saponin concentration of 0.3 mg/mL. A two-sample t-test reveals that there is a high significance for all results above a concentration of 0.01 mg/mL determined for the MCF-7 cell monolayer, whereas, in the case of U-373 MG cells, only the maximum is highly significant towards the control condition. Significance values between the concentration levels were not calculated.

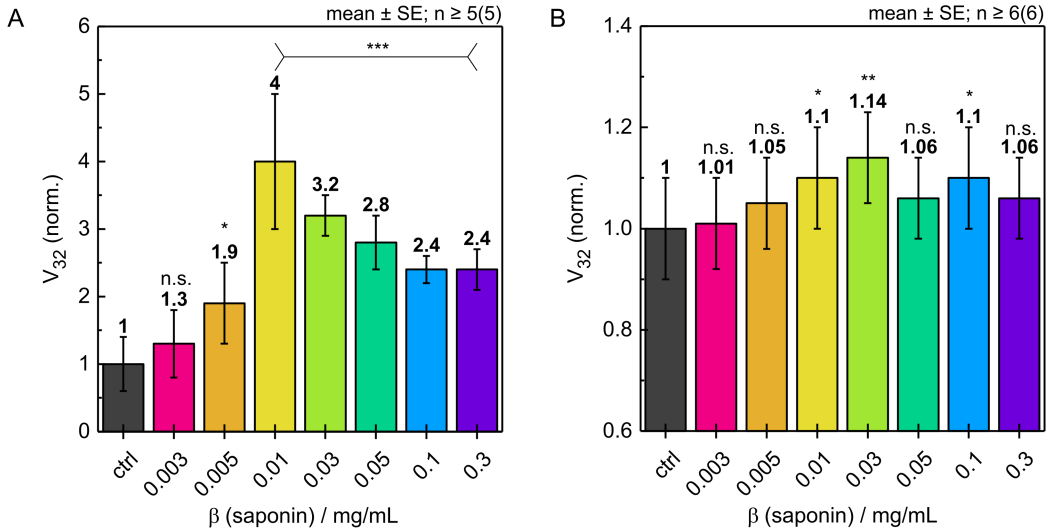

Fig. 7.10 Normalized variance of increments of impedance fluctuations after segmented detrending measured five hours after the addition of saponin solution with different concentrations in a range of 0.003–0.3 mg/mL to MCF-7 (A) and U-373 MG (B) cell monolayer culture. Significance was determined relative to the control condition by a two-sample t-test using a significance level of 0.1 (*), 0.05 (**), and 0.01 (***). Data sets were averaged after segmented detrending, mean ± SE; A: n ≥ 5(5); B: n ≥ 6(6).

In general, the ECIS™-based measurements revealed an increase in cell monolayer permeability as a function of saponin concentration represented by decreasing impedance values. However, no clear dose-response relationship can be identified from the variance of increments and only a trend may be indicated. It should be noted that due to the large electrode area, the analysis of cellular micromotion is less sensitive when using 8W10E electrode arrays.

7.2.3 IMPEDIMETRIC ANALYSIS OF THE SPHEROID DURING FIXATION

To measure the spheroid response during permeabilization impedimetrically using the funnel-based device, a two-step process was required. Prior to permeabilization, the entire spheroid body has to be fixed in its position to prevent the spheroid from sliding through the opening of the measurement device due to disintegrating effects induced by the detergent. The detergent can then be applied to the prepared spheroid and the impedance changes during the permeabilization process were recorded (see

chapter 7.2.4). In addition to time course measurements in MFT mode, cellular micromotion was measured after the fixation in RTC mode, and the parameters describing the intrinsic dielectric spheroid structure were calculated.

The cross-linking or fixation of cells and tissues is a standard cytochemical technique for the preservation of cell morphology e.g., subsequent fluorescent staining or as a type of histochemical preparation. During the process of fixation, the internal structure of the specimen is preserved and current biochemical reactions are stopped (Ganjali and Ganjali, 2013). In this way, cellular micromotion is inhibited, but the morphological structure of the tissue is fixated, providing a snapshot of the entire environment at the point of fixation (Ganjali and Ganjali, 2013).

A detailed discussion on choosing the appropriate reagent between GA and PFA for the intended application is provided in chapter 7.2.6. To determine the appropriate concentration of fixative to sufficiently secure the spheroid in the measurement device, different concentrations of fixative were applied. For these experiments, GA was used as the standard chemical compound for fixation in a concentration range of 0.03–0.3 % (v/v), generating spheroids at different stages of fixation. The fixation process was recorded impedimetrically and cell micromotion was analyzed using high time resolution measurements.

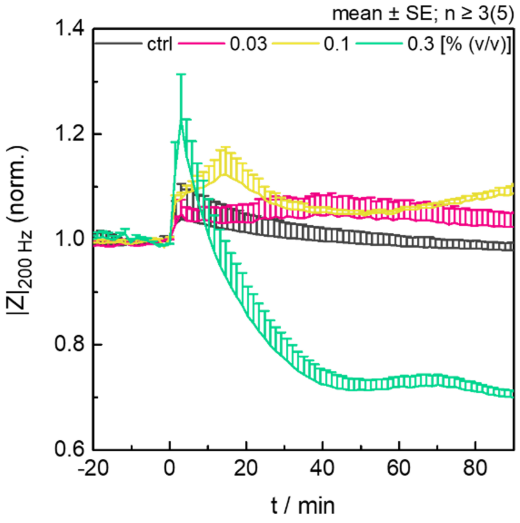

Fig. 7.11 Time course of normalized impedance magnitude at 200 Hz of U-373 MG spheroids after the addition of GA solutions with different concentrations (ctrl | 0.03 | 0.1 | 0.3 % (v/v)). Time courses were normalized with respect to the last data point before compound addition at time point zero. Experiments were performed in a standard cell culture incubator at 37 °C and 0 % CO_2. Data sets were averaged after normalization, mean ± SE; n ≥ 3(5).

The time course of the normalized impedance magnitude at 200 Hz displays different signals upon incubation with different fixative concentrations (Fig. 7.11). At the highest concentration of 0.3 % (v/v), the impedance initially increases by 120 % at time point zero and continuously decreases to 70 % one

hour after substance addition. After the addition of 0.1 % (v/v) GA solution to the spheroids, a biphasic course is exhibited within 90 minutes of recording. The lowest fixative concentration of 0.03 % (v/v) causes a slight increase of the signal to 105 % and the control spheroids show no alterations as the signal remains at baseline level after an initial signal increase due to the addition of substance. Thus, significant signal variations as a function of compound concentration can be observed, representing different grades of spheroid fixation.

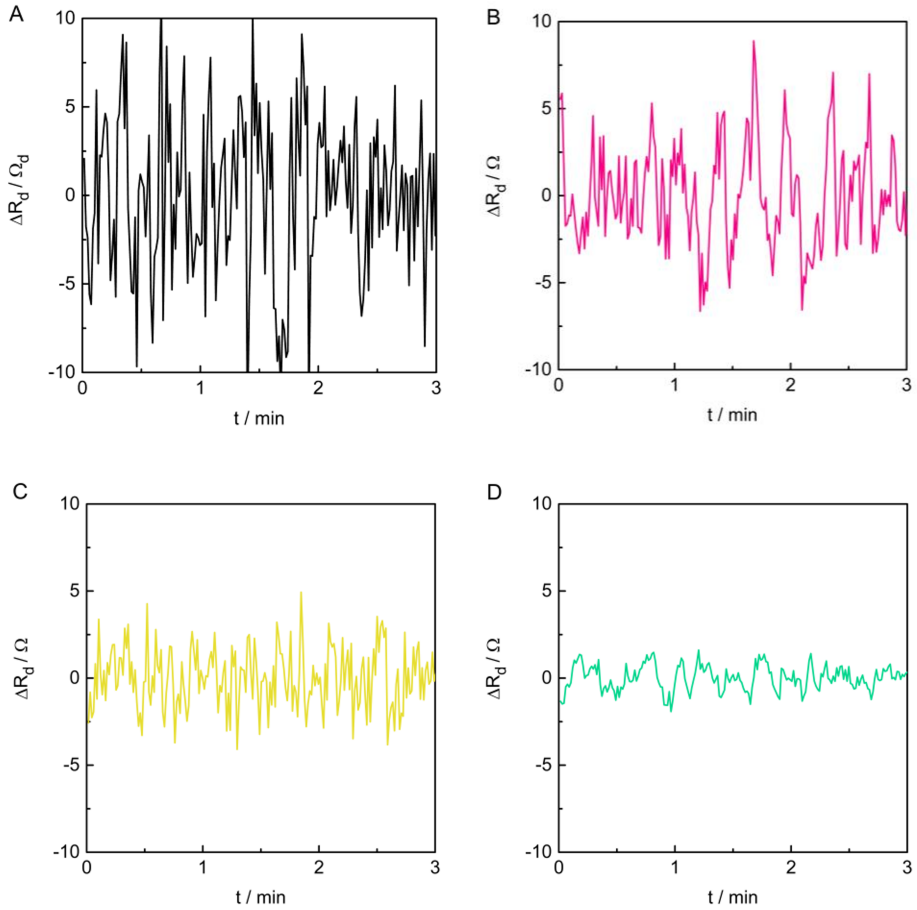

Fig. 7.12 Detrended RTC data at 200 Hz two hours after the addition of GA solution with different concentrations to U-373 MG spheroids (ctrl (A) | 0.03 (B) | 0.1 (C) | 0.3 (D) % (v/v)). Experiments were performed in a standard cell culture incubator at 37 °C and 0 % CO_2.

To analyze the influence of cross-linking on cellular micromotion, RTC measurements were performed for each GA concentration including the control sample (Fig. 7.12). The montage shows a clear dependence of the fluctuation on the compound concentration, as the amplitude decreases with increasing fixation level. The fluctuation amplitudes of the resistance values start in a range of -10–10 Ω for intact vital spheroids and are diminished to -7.5–7.5 Ω at the minimum concentration of 0.03 % (v/v), while no significant fluctuation is observed at the highest concentration of 0.3 % (v/v), where the signal oscillates around the zero point.

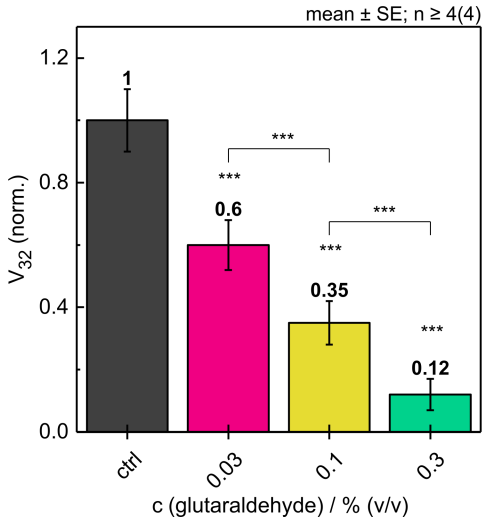

Fig. 7.13 Normalized variance of increments of impedance fluctuations after segmented detrending measured two hours after the addition of GA solution with different concentrations (ctrl | 0.03 | 0.1 | 0.3 % (v/v)) to U-373 MG spheroids. The significance was determined relative to the control condition and between the different concentrations by a two-sample t-test using a significance level of 0.1 (*), 0.05 (**), and 0.01 (***). Data sets were averaged after segmented detrending, mean ± SE; n ≥ 4(4).

Tab. 7.6 Calculated values of R_{ext}, R_{int}, and A_{sph} reflecting the dielectric structure of U-373 MG spheroids as a function of different GA concentrations (ctrl | 0.03 | 0.1 | 0.3 % (v/v); 30,000 c/well) used for fixation. The values were determined by fitting each measured impedance spectrum two hours after GA addition using a *LabVIEW™*-based software (written by J. Wegener, University of Regensburg) and the following parameter values: A_{el} = 11.0 (± 0.6) | 10.6 (± 0.5) | 10.3 (± 0.4) | 9.9 (± 0.3) $\cdot 10^{-6}$ $Fs^{n-1}cm^{-2}$; n_{el} = 0.85 (± 0.01) | 0.885 (± 0.005) | 0.869 (± 0.002) | 0.884 (± 0.006); R_{bulk} = 5,400 Ω; A_{para} = 2.4 $\cdot 10^{-10}$ $Fs^{n-1}cm^{-2}$; n_{para} = 0.9; n_{sph} = 0.75. Data sets were averaged after fitting, mean ± SE; see the table for the respective number of experiments.

	$concentration$ [% (v/v)]			
	ctrl	0.03	0.1	0.3
R_{ext} [kΩ]	37 ± 2	31 ± 1	26 ± 3	19 ± 2
R_{int} [kΩ]	8 ± 2	7.3 ± 0.2	4.9 ± 0.3	4.1 ± 0.7
A_{sph} [10^{-9} $Fs^{n-1}cm^{-2}$]	10 ± 1	8.0 ± 0.7	6.6 ± 0.2	5.2 ± 0.5
n	3(4)	8(15)	3(3)	3(4)

Based on the RTC measurements, the variance of increments of each compound concentration was calculated after performing segmented detrending using a time interval of 32 s and normalized to the control (Fig. 7.13). The analysis shows a significant stepwise decrease of the results from 60 (± 8) % (0.03 % (v/v)) down to 12 (± 5) % (0.3 % (v/v)) in relation to the standardized value of the control spheroids. Thus, a definite dose-dependent effect is displayed with increasing compound concentrations resulting in varying degrees of spheroid fixation. A two-sample t-test confirmed the

significance of the calculated variance of increments for each concentration studied, indicating a high level of significance relative to the control condition and between each concentration step.

An evaluation of the three spheroid parameters based on the recorded data displays a constant decrease of resistance and capacitive values for increasing fixative concentration in comparison to the control (Tab. 7.6). The extracellular resistance decreases from 37 (± 2) kΩ (ctrl) to 19 (± 2) kΩ (0.3 % (v/v)) and the intracellular resistance is reduced from 8 (± 2) kΩ (ctrl) to 4.1 (± 0.7) kΩ (0.3 % (v/v)). The same trend of decline is reflected by the values of the non-ideal spheroid capacitance A_{sph} decreasing slightly with increasing concentration starting with 10 (± 1) $\cdot 10^{-9}$ $Fs^{n-1}cm^{-2}$ (ctrl) and going down to 5.2 (± 0.5) $\cdot 10^{-9}$ $Fs^{n-1}cm^{-2}$ (0.3 % (v/v)).

Overall, the impedance time course, spheroid micromotion analysis, and spheroid dielectric parameters show a clear dependence on fixative concentration. The results indicate different dose-dependent fixation levels of the test spheroids. Since it was assumed that the fixation should only prevent the spheroids from slipping through the central opening of the funnel device while keeping the cellular dynamic as high as possible, the lowest concentration of GA with 0.03 % (v/v) was applied before the permeabilization step, regardless of whether MCF-7 or U-373 MG spheroids were used.

7.2.4 IMPEDIMETRIC ANALYSIS OF THE SPHEROID DURING PERMEABILIZATION

The influence of the degradation of the cell membranes within the spheroids was measured with the funnel-based measurement setup. After fixation of the spheroids in the micro-trap to prevent the tissue model from slipping through, the response to cell membrane permeabilization was investigated by performing a complete spheroid positioning-fixation-permeabilization assay. For these experiments, saponin solution was used in a concentration range of 0.3–3 mg/mL, generating spheroids (either U-373 MG or MCF-7 spheroids) at different stages of permeabilization. The spheroid response was recorded impedimetrically using both MFT and RTC mode measurements to record time-resolved signal changes, to detect changes in cellular micromotion, and to calculate the dielectric spheroid properties.

The measurements in MFT mode show the time course of the normalized impedance magnitude at 200 Hz over 15 hours after compound addition (Fig. 7.14). A clear dependence of the saponin concentration on the permeabilization kinetics is shown for both MCF-7 and U-373 MG spheroids. With a decreasing signal value, an increasing spheroid body permeability is indicated. In the case of MCF-7 spheroids (Fig. 7.14, A), the control curve shows an initial signal increase due to substance addition followed by a downward sloping curve resulting in 87 (± 4) % after 15 hours. In contrast, the highest concentration of 3 mg/mL caused a drop in the impedance signal directly after the compound addition,

mimicking a cell-free setup signal within three hours. For saponin concentrations of 1 mg/mL and 0.3 mg/mL, similar signal curves were observed with a slower rate of decrease, reaching the cell-free level at the time points of 8 h (1 mg/mL) and approximately 14 h (0.3 mg/mL) after compound addition. As a result, the signal decays more rapidly with increasing compound concentration, indicating faster permeabilization effects within the spheroid body.

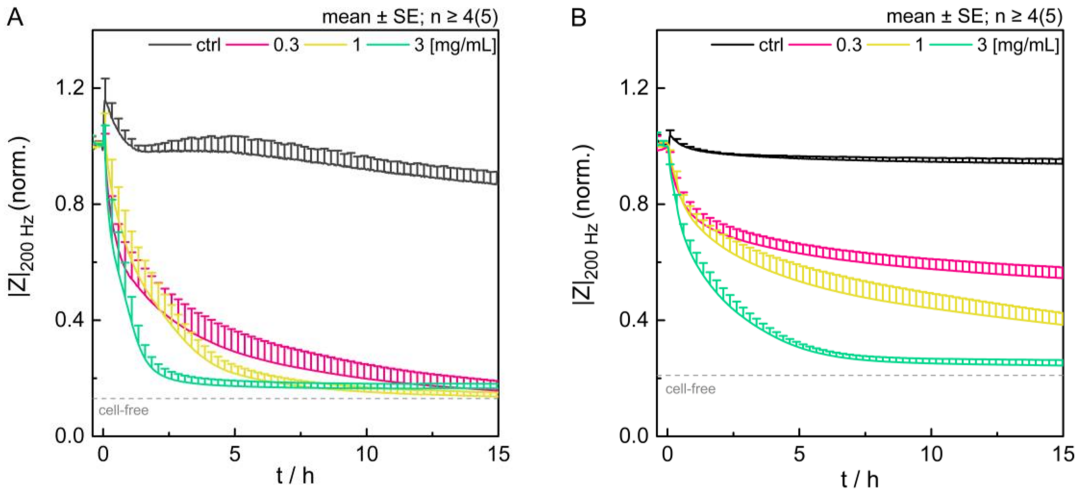

Fig. 7.14 Time course of normalized impedance magnitude at 200 Hz with GA (0.03 % (v/v)) pre-fixed MCF-7 spheroids (A) and U-373 MG spheroids (B) after the addition of saponin solutions with different concentrations (ctrl | 0.3 | 1 | 3 mg/mL). Time courses were normalized with respect to the last data point before compound addition at time point zero. Grey horizontal lines in A and B indicate mean values of spheroid-free micro-traps. Experiments were performed in a standard cell culture incubator at 37 °C and 0 % CO_2. Data sets were averaged after normalization, mean ± SE; n ≥ 4(5).

In comparison, a similar impedance time course was found for U-373 MG spheroids (Fig. 7.14, B). While the signal from the control spheroids is almost constant with a relative response of 94 (± 2) % at 15 h, the influence of different saponin concentrations on the spheroids and thus on the detected impedance is significant. After the addition of 0.3 mg/mL or 1 mg/mL saponin solution, an exponential signal decrease was recorded, reaching relative impedance levels of 55 (± 3) % and 38 (± 4) % within 15 hours. Additionally, by using the highest concentration, an exponential signal decrease was observed with a higher degrading degree approximating a cell-free level seven hours after the compound addition. Thus, significant signal variations as a function of compound concentration can be observed, representing different grades of spheroid permeabilization.

The slope values of the time course were determined within two hours after compound addition, indicating the rate of permeabilization (Tab. 7.7). Fundamentally, the control condition reflects the initial influence of the compound addition procedure, which is more pronounced when using MCF-7 spheroids. With increasing saponin concentration, the slope values rapidly increase in accordance with an enhanced spheroid degradation process in a range from -24 (± 1) % to -36 (± 1) % per hour for MCF-7

cells and, in the case of U-373 MG cells, from -12.5 (± 0.6) % to -22.8 (± 0.8) % per hour. As shown by the recorded time courses, the slope values also reflect the greater effect on MCF-7 spheroids, which show a steeper decline in values and significantly higher values at each concentration in contrast to U-373 MG spheroids.

Tab. 7.7 Overview of the slope values as a function of the saponin concentration applied, calculated from the impedance time course (Fig. 7.14). The slope was determined within two hours after saponin addition to MCF-7 and U-373 MG spheroids using the averaged data; high slope values correlate with a more rapid cell permeabilization progression.

	concentration [mg/mL]			
	ctrl	0.3	1	3
slope (MCF-7) [%/h]	-8.3 ± 0.5	-24 ± 1	-27.7 ± 0.8	-36 ± 1
slope (U-373 MG) [%/h]	-2.6 ± 0.1	-12.5 ± 0.6	-15.7 ± 0.6	-22.8 ± 0.8

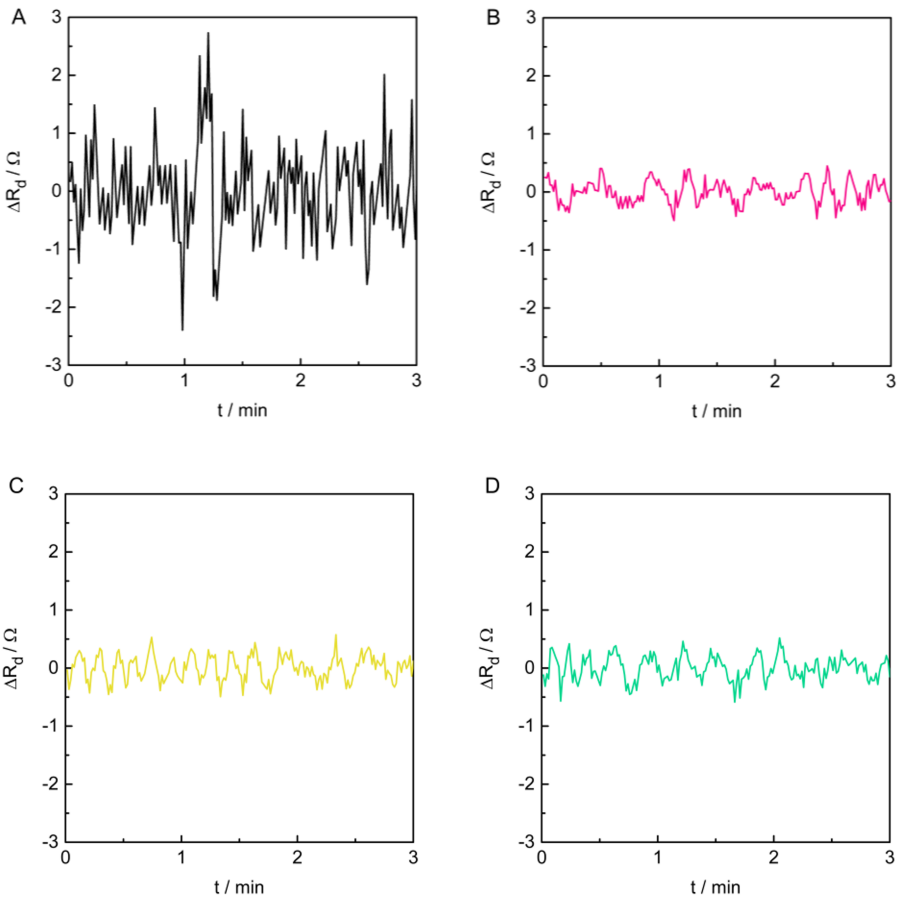

Fig. 7.15 Detrended RTC data at 200 Hz, 15 hours after the addition of saponin solution with different concentrations (ctrl (A) | 0.3 (B) | 1 (C) | 3 (D) mg/mL) to GA (0.03 % (v/v)) pre-fixed MCF-7 spheroids. Experiments were performed in a standard cell culture incubator at 37 °C and 0 % CO_2.

To investigate the influence of spheroid permeabilization on cellular micromotion, the high time resolution measurements were analyzed. The montages of each saponin concentration indicate a clear dose-response effect, as the cell fluctuations in MCF-7 spheroids (Fig. 7.15) and U-373 MG spheroids (see chapter 11.1, Fig. A-7.7) were reduced with an increase in permeability. For both types of cells, the control spheroids that were fixed but not permeabilized show distinct fluctuations. As the saponin concentration increases, the amplitudes of fluctuation of resistance values decrease significantly. At a concentration of 1 mg/mL and the highest concentration of 3 mg/mL saponin, no significant fluctuation is observed, which could relate to cellular micromotion, as the RTC signal oscillates around the zero point.

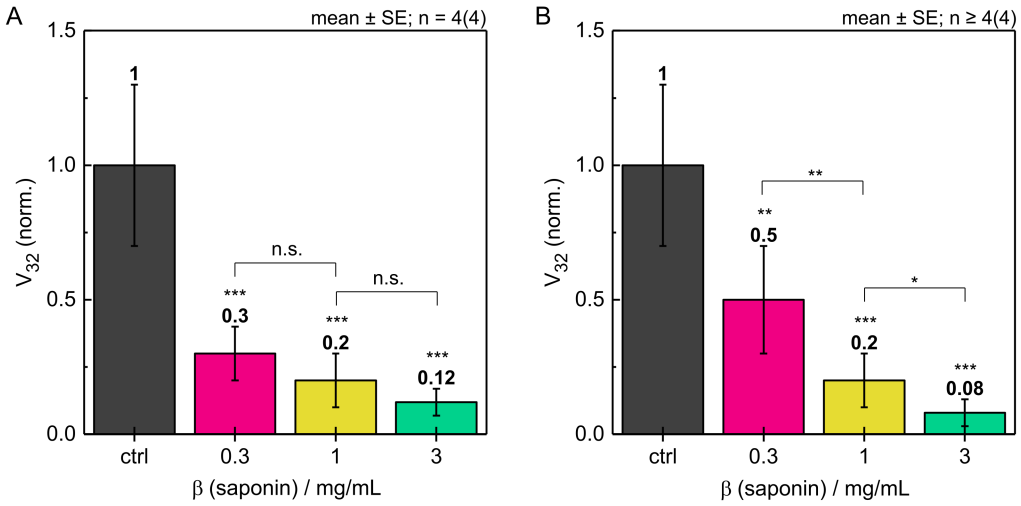

Fig. 7.16 Normalized variance of increments of impedance fluctuations after segmented detrending measured 15 hours after the addition of saponin solution with different concentrations (ctrl | 0.3 | 1 | 3 mg/mL) to GA (0.03 % (v/v)) pre-fixed MCF-7 spheroids (A) and U-373 MG spheroids (B). Significance was determined relative to the control condition and between the different concentrations by a two-sample t-test using a significance level of 0.1 (*), 0.05 (**), and 0.01 (***). Data sets were averaged after segmented detrending, mean ± SE; n ≥ 4(4).

An analysis of the variance of increments was conducted on the measured RTC data after segmented detrending for all conditions using a time interval of 32 s. The values for both cell types were normalized to the control condition, and the results indicate a general decrease for spheroids with increasing compound concentration (Fig. 7.16). For the lowest compound concentration, the normalized variance of increments was calculated to 30 (± 10) % (MCF-7) and 50 (± 20) % (U-373 MG) relative to the control condition. When the concentration was increased to 1 mg/mL, the values further decreased to 20 (± 10) % (MCF-7; U-373 MG), respectively, and at the highest concentration, a value of approximately zero was calculated. Thus, very distinct, dose-dependent value ranges were found with mainly high significance for each condition relative to the control condition and between the concentration levels as observed using a two-sample t-test (except in the case of MCF-7 spheroids no significance was determined between the different saponin concentrations).

An evaluation of the dielectric spheroid structure based on the recorded data indicates, for MCF-7 spheroids, a rapid decrease in R_{ext} and R_{int} values with increasing saponin concentration (Tab. 7.8). In particular, the extracellular resistance drops from 93 (± 6) kΩ after fixation to 79 (± 4) kΩ (ctrl) after 15 hours, down to values in the range of 4.1–2.9 kΩ. The intracellular resistance decreases from 1.8 (± 0.2) kΩ calculated after fixation to 0.8 (± 0.2) kΩ (ctrl), which is further reduced to 0.0018 (± 0.0003) kΩ (3 mg/mL) with increasing compound concentration. The capacitance of the non-ideal spheroids A_{sph} increases contrary starting at 2.7 (± 0.2) ·10^{-9} $Fs^{n-1}cm^{-2}$ after fixation with a slight increase to 5 (± 2) ·10^{-9} $Fs^{n-1}cm^{-2}$ (ctrl) after 15 hours, up to values of approximately 30 (± 4) ·10^{-9} $Fs^{n-1}cm^{-2}$ (1 mg/mL).

Tab. 7.8 Calculated values of R_{ext}, R_{int}, and A_{sph} reflecting the dielectric structure of MCF-7 spheroids as a function of different saponin concentrations (ctrl | 0.3 | 1 | 3 mg/mL; 12,000 c/well) used for permeabilization. The values were determined by fitting each measured impedance spectrum three hours after spheroid fixation with GA (0.03 % (v/v)) and impedance spectrum 15 hours after the addition of saponin solution respective 18 hours after spheroid fixation using a *LabVIEW™*-based software (written by J. Wegener, University of Regensburg) and the following parameter values: A_{el} = 11.0 (± 0.6) | 10.7 (± 0.5) | 12 (± 1) | 12.2 (± 0.9) | 13.5 (± 0.3) ·10^{-6} $Fs^{n-1}cm^{-2}$; n_{el} = 0.879 (± 0.009) | 0.83 (± 0.04) | 0.88 (± 0.01) | 0.87 (± 0.02) | 0.88 (± 0.02); R_{bulk} = 5,400 Ω; A_{para} = 2.4 ·10^{-10} $Fs^{n-1}cm^{-2}$; n_{para} = 0.9; n_{sph} = 0.75. Data sets were averaged after fitting, mean ± SE; see the table for the respective number of experiments.

		$concentration$ [mg/mL]			
	after fixation	ctrl	0.3	1	3
R_{ext} [kΩ]	93 ± 6	79 ± 4	4.1 ± 0.3	3.1 ± 0.3	2.9 ± 0.4
R_{int} [kΩ]	1.8 ± 0.2	0.8 ± 0.2	0.027 ± 0.008	0.0030 ± 0.0003	0.0018 ± 0.0003
A_{sph} [10^{-9} $Fs^{n-1}cm^{-2}$]	2.7 ± 0.2	5 ± 2	15 ± 4	30 ± 4	28 ± 4
n	8(15)	4(4)	4(5)	5(5)	5(5)

For U-373 MG spheroids, the determined dielectric parameter values display similar trends (see chapter 11.1, Tab. A-7.2). As the compound concentration increases, both the extracellular and intracellular resistance values drop significantly compared to control condition. The extracellular resistance decreases from 27 (± 1) kΩ (ctrl) to 2.3 (± 0.3) kΩ (3 mg/mL), whereas the intracellular resistance is reduced from 4 (± 1) kΩ (ctrl) to 0.002 (± 0.001) kΩ (3 mg/mL) with increasing saponin concentrations. Identical to the MCF-7 experiments, an inverse trend due to increasing values is reflected by the non-ideal spheroid capacitance A_{sph}. The capacitance values increase constantly with

increasing compound concentration from 11 (± 2) $\cdot 10^{-9}$ $Fs^{n-1}cm^{-2}$ (ctrl) to 30 (± 4) $\cdot 10^{-9}$ $Fs^{n-1}cm^{-2}$ (3 mg/mL). Following the analysis of the dielectric characteristics of MCF-7 and U-373 MG spheroids using varying detergent concentrations, a noticeable divergence between the control and induced permeabilized stages was observed.

The results of impedance time response, spheroid micromotion analysis, and spheroid dielectric properties demonstrate a clear dependence on detergent concentration. These findings indicate that the amount of detergent used determines the permeability of the spheroids in a dose-dependent manner and that even at low concentrations the detergent has a strong influence on the spheroid morphology, regardless of whether it was derived from MCF-7 or U-373 MG cells.

7.2.5 TIME-LAPSE MICROSCOPY ANALYSIS OF THE SPHEROID

For a complete characterization of the influence of permeabilization on spheroids, the impact of saponin on cellular morphology was observed by time-lapse imaging with the zenCELL owl digital microscope.

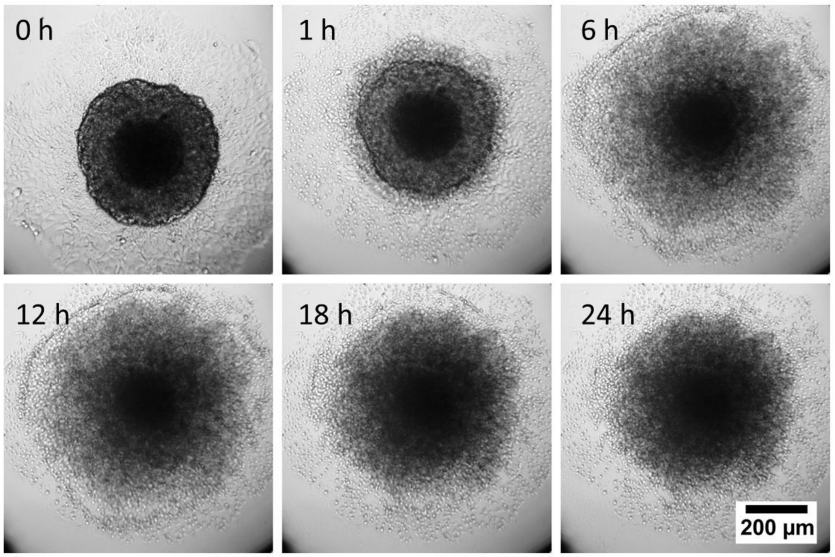

Fig. 7.17 Time-resolved micrographs of the spheroid permeabilization process after the addition of saponin solution (3 mg/mL) to MCF-7 spheroid (7 d, 4,000 c/well). Compound addition was performed at time point zero and the process was documented for 24 hours using the zenCELL owl digital microscope. Experiments were performed in a standard cell culture incubator at 37 °C and 0 % CO_2. The full time-lapse clip is available by scanning the QR code (see Tab. A-6.2 for the password).

To this end, spheroids derived from MCF-7 and U-373 MG cells were adhered to the adhesive surface and exposed to saponin solution with different concentrations. The response of the spheroids was monitored by taking microscopic images at regular 10-minute intervals over 24 hours. In this study, similar observations were made for both cell types used. The time-resolved images of MCF-7 spheroids show the overall process of permeabilization using saponin solution with a concentration of 3 mg/mL

(Fig. 7.17). After the addition of saponin, the detergent diffuses into the cell membrane by complexing with cholesterol molecules and causing the formation of pores (see chapter 7.2.7, Fig. 7.25). Thus, the entire spheroid structure is disrupted as the spheroid body disintegrates, thereby exhibiting an increased diameter with the loss of the outer rim within the first six hours. Additionally, the cell monolayer is affected, as shown by the increasing number of single cells surrounding the spheroid core after cell-cell contact degradation. Further perforation and cell membrane disruption is indicated by a diffuse spheroid-like structure for the remaining time. After 12 hours, the highly diffuse spheroid diameter in dark gray decreases slightly, indicating cellular shrinkage or a final collapse of the entire spheroid body, as it is accompanied by an increase in the central black area. No further morphological changes were observed until 24 hours.

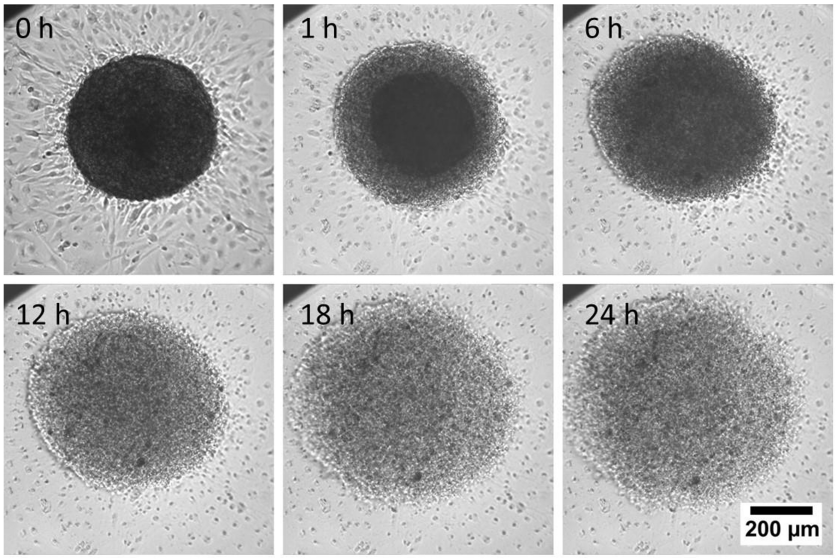

Fig. 7.18 Time-resolved micrographs of the spheroid permeabilization process after the addition of saponin solution (1 mg/mL) to U-373 MG spheroids (7 d, 18,000 c/well). Compound addition was performed at time point zero and the process was documented for 24 hours using the zenCELL owl digital microscope. Experiments were performed in a standard cell culture incubator at 37 °C and 0 % CO_2.

In comparison, a saponin concentration of 1 mg/ml induces equivalent morphological changes in U-373 MG spheroids as displayed in the micrographs (Fig. 7.18). Here, the spheroid diameter increases steadily after detergent addition, while losing the contrasted clear border after the first hour. The entire body becomes brighter in the microscopic images as the spheroid disintegrates into individual cells upon increasing cell membrane perforation and cell contact degradation, as shown after 12 hours. At the 24-hour time point, a diffuse arrangement of cells or cellular fragments is displayed, covering the main portion of the image.

In addition, images of spheroids exposed to different concentrations of saponin for 24 hours were collected (Fig. 7.19 [U-373 MG]; see chapter 11.1, Fig. A-7.8 [MCF-7]). The micrographs illustrate a clear

correlation between the compound dose and the morphological reaction for both cell types, U-373 MG and MCF-7 cells. As the detergent concentration increases, the spheroid shape is stepwise transformed into a diffuse structure with individual cell particles arranged in a disordered manner. In addition, the morphology of the cell monolayer also displays cell disintegration effects, reflected by a change from the typical two-dimensional pattern to an increasing number of single cell spots.

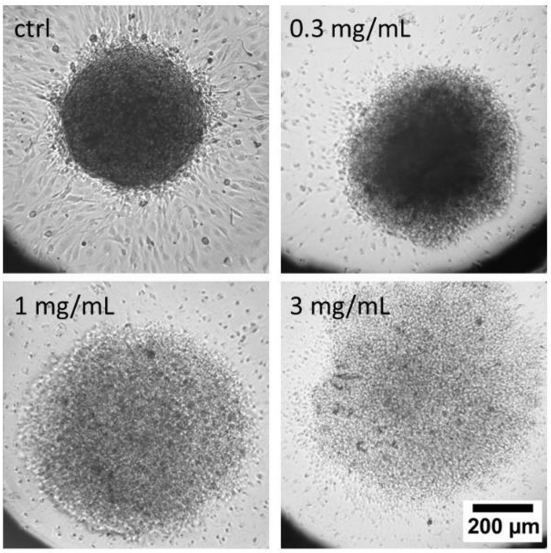

Fig. 7.19 Micrographs of U-373 MG spheroids (7 d, 18,000 c/well) that were exposed to saponin solution at different concentrations (ctrl | 0.3 | 1 | 3 mg/mL) and documented 24 h after the compound addition using the zenCELL owl digital microscope. Experiments were performed in a standard cell culture incubator at 37 °C and 0 % CO_2.

To quantify the spheroid response, the diameter changes were determined according to different saponin concentrations using *ImageJ* software (Rasband, W.S., National Institutes of Health, USA; Fig. 7.20). The results show a dose-dependent effect of the detergent, which induces distinct morphological alterations. Irrespective of the cell type used, the control spheroids retain their size for 24 h, whereas the highest concentration of saponin causes a rapid increase in diameter directly after compound addition, reflecting the disruption of the spheroid body. This strong effect results in a relative increase of the total diameter of 113 (± 4) % for MCF-7 spheroids after 24 hours, whereas an initial maximum of 147 (± 9) % is observed for U-373 MG spheroids after seven hours, followed by a steady decreasing trend, reaching 132 (± 9) % (24 h). Based on this trend, similar increasing/decreasing effects are shown for the time courses of 0.3 mg/mL and 1 mg/mL compound concentration for MCF-7 spheroids, as well as in the case of a saponin concentration of 0.3 mg/mL for U-373 MG spheroids. These diameter changes are more significant as depicted in the respective time-resolved micrographs of MCF-7 spheroids (Fig. 7.17) and may indicate cell shrinkage or collapse of the three-dimensional structure. The time course of U-373 MG spheroids at 1 mg/mL displays a constant increase in diameter corresponding to the description of the micrographs in Fig. 7.18.

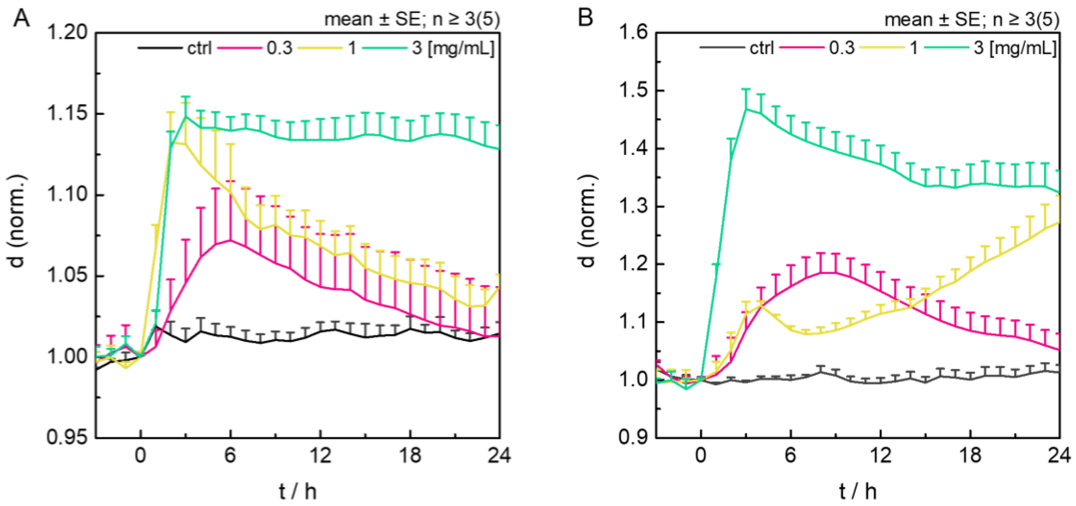

Fig. 7.20 Time course of diameter changes after the addition of saponin solution with different concentrations (ctrl | 0.3 | 1 | 3 mg/mL) to MCF-7 spheroids (A) and U-373 MG spheroids (B) documented for 24 hours using the zenCELL owl digital microscope. Time courses were normalized with respect to the last data point before compound addition at time point zero. Experiments were performed in a standard cell culture incubator at 37 °C and 0 % CO_2. Data sets were averaged after normalization, mean ± SE; n ≥ 3(5).

Overall, the results of the time-resolved microscopy study concerning the influence of saponin demonstrate a clear impact on the spheroid morphology. An increase in the concentration of the compound causes a proportional increase in the permeability of the cell membranes, leading to a gradual permeabilization of the spheroids. As a consequence, the three-dimensional structure of the tissue model is disintegrated and the cell arrangement is disrupted, presenting disassembled cell accumulations.

7.2.6 DISCUSSION: INFLUENCE OF FIXATION

In this chapter, the considerations regarding the choice of either PFA or GA as a suitable fixative for mounting spheroids inside the measurement setup are discussed regarding their reaction mechanisms and time-dependent fixation profiles according to impedimetric measurements. In addition, the influence of fixation on spheroid cell dynamic and changes in intrinsic dielectric parameters are characterized, while the appropriate fixative concentration is determined in the context of the entire spheroid positioning-fixation-permeabilization assay.

I COMPARISON OF FIXATIVES

When comparing the two cross-linking reagents mentioned, the fixation mechanism is similar and non-specific for both reagents. However, GA achieves a higher degree of cross-linking of the same cell

layer compared to PFA because GA has two *-CHO* groups to cross-link the proteins, which is possible over a variable distance due to the intermediate *-$(CH_3)_3$-* group (Kiernan, 2000; Fig. 7.21).

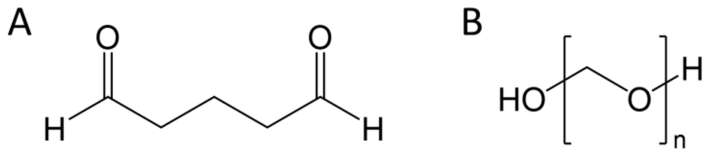

Fig. 7.21 Structural formula of GA (A) and PFA (B).

In the case of PFA, the polymer is fragmented into smaller subunits, enabling rapid penetration into the cells and effective functionality (Pearse, 1980). Upon reaction of the amino groups of a protein with the aldehyde group of PFA, a methylene bridge $-CH_2-$ is formed between the nitrogen atom at the end of the side-chain of lysine and the nitrogen atom of a peptide linkage (Fig. 7.22).

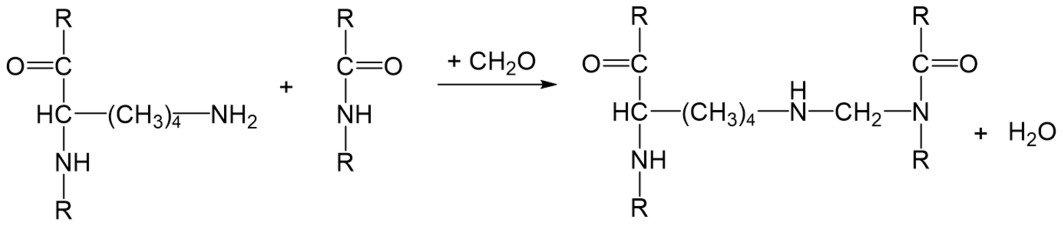

Fig. 7.22 Fixation mechanism of PFA by cross-linking of a lysine side-chain to a peptide nitrogen atom forming a methylene bridge.

The fixation reaction of GA also occurs via the nitrogen atoms of the amino acids, similar to PFA (Fig. 7.23).

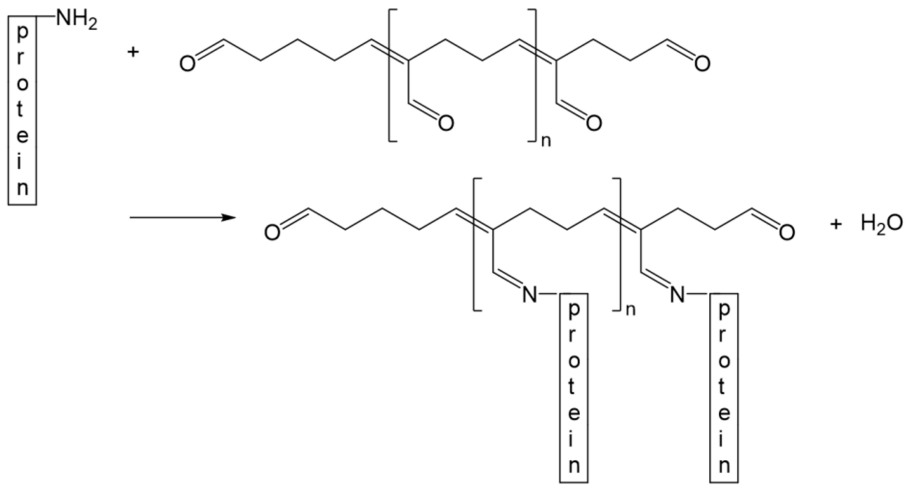

Fig. 7.23 Fixation mechanism of GA in polymeric form in combination with amino groups of proteins.

As GA largely appears in aqueous solution as a polymer with free aldehyde groups and aldehyde side groups, a certain period is required for the molecule to cross the cell membrane (Kiernan, 2000). This determines the depth and rate of penetration into the tissue, which was investigated in experiments

using rat livers. According to Baker, the depth d can be calculated as a function of the time t and the diffusion coefficient K (Eq. 7.1; Baker, 1958). Thus, the specimen must be as thin or small as possible for short fixation times to avoid possible structural changes.

$$d = K \cdot \sqrt{t} \qquad \textbf{Eq. 7.1}$$

The applications of GA include immunocytochemistry and fixation of electron microscopic specimens (Sabatini et al., 1963), while PFA is mainly used in histopathology (Hopwood, 1967).

In the experiments presented in this thesis, the fixation reagent was used to fix the spheroid body inside the funnel, preventing it from passing through the central opening, to perform a complete spheroid positioning-fixation-permeabilization assay. To evaluate which reagent is most suitable for this purpose, three different concentrations of each compound were applied to the spheroids under constant conditions and the recorded impedimetric signal changes over time were analyzed.

In a proof-of-principle experiment, the use of PFA was studied by applying three different concentrations to the spheroids while recording impedance spectra (Fig. 7.24).

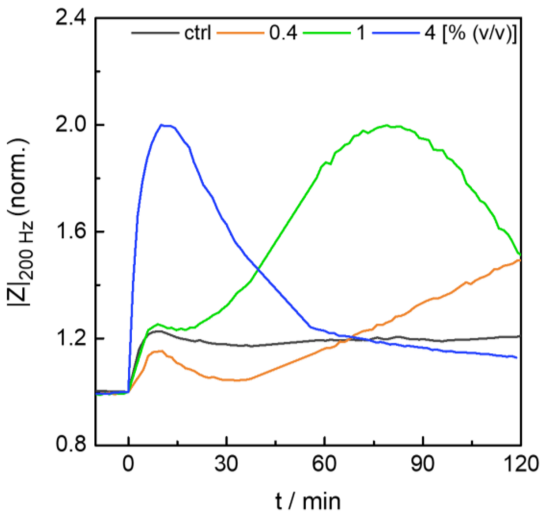

Fig. 7.24 Time course of normalized impedance magnitude at 200 Hz of U-373 MG spheroids after the addition of PFA solutions with different concentrations (ctrl | 0.4 | 1 | 4 % (v/v)). Time courses were normalized with respect to the last data point before compound addition at time point zero. Experiments were performed in a standard cell culture incubator at 37 °C and 0 % CO_2.

The normalized impedance magnitude at 200 Hz as a function of time shows different dose-dependent signals after the addition of the fixative. At the maximum concentration of 4 % (v/v), the impedance signal initially increases to 200 % at time zero and continuously returns to the initial baseline within two hours resulting in a value of 115 %, which is similar to that of the control spheroid. After the addition of 1 % (v/v) PFA solution, or 0.4 % (v/v) respectively, the impedance responses display a similar time

course behavior with time-shifted signal changes compared to the maximum concentration. Here, the 1 % (v/v) solution also causes a maximum peak value of 200 % which is similar to the highest concentration tested, while the lowest concentration shows a constant increase over two hours marked by a smaller slope. The control spheroid displays no signal alterations remaining constant at a level of 120 % after an initial signal increase due to substance addition. As a result, significant dose-dependent signal variations were observed, representing distinct spheroid fixation levels two hours after compound addition.

The impedimetric results indicate progressive cross-linking of the proteins as the impedance values rise in response to increasing barrier formation. After reaching a maximum, the signals decrease steadily, indicating increasing permeability within the spheroid, leading to less hindered current flow paths. This further suggests a compensating effect of progressive fixation processes combined with signal distortion. This assumption is consistent with Oberleitner's findings in conjunction with microscopic studies, which show that PFA fixes and additionally permeabilizes cells to some extent (Oberleitner, 2017). Oberleitner performed dye uptake studies in which membrane-impermeable FITC-labeled dextran (250 kDa) was added to either GA- or PFA-fixed rat kidney cell layers. While no fluorescence of FITC-dextran was seen within cells preserved using GA, intracellular FITC-dextran was detected throughout the cell layer cross-linked with 4 % (v/v) PFA. Based on this, Oberleitner stated that the cross-linking mechanism of PFA possibly causes either a direct or indirect perforation of the plasma membrane and that GA and PFA act in different ways (Oberleitner, 2017). As suggested, this membrane permeabilization effect of PFA may be the reason for the dielectric impedance decreases observed in the proof-of-principle experiment presented. In addition, this statement is consistent with the model studies in this thesis using GA for preserving the spheroid inside the funnel device, since no supplementary permeabilization effects were detected, as the parameter A_{sph} is diminished with increasing GA concentration.

In comparison, Hupf also studied the influence of cross-linking on MCF-7 spheroids using the flow channel-based measurement setup and PFA as a fixative compound (Hupf, 2018). The results revealed that the values for R_{ext} and R_{int} decrease significantly by approximately 90 % with increasing cross-linking using a PFA solution of 0.5 % (v/v), which is in accordance with the model studies on U-373 MG spheroids (Hupf, 2018). In addition, Hupf observed slightly increasing values for A_{sph}, which confirms the theory of increasing perforation of the cell structure induced by PFA.

Moreover, based on the theoretical fixative penetration depth, PFA diffuses more rapidly into the cell interior due to its cleavage into smaller subunits, displaying a diffusion coefficient of 0.78 mm/h for 4 % (v/v) formaldehyde solution (Hou, 2020). In contrast, GA yielded a lower diffusion coefficient of

0.34 mm/h (4 % (v/v)) concerning its molecular structure (Hou, 2020), although less time for the fixation reaction with the proteins is required due to the double reactive aldehyde groups. As a result, GA stiffens more rapidly and the degree of cross-linking is increased, which means that cellular activity is inhibited faster and more strongly than with PFA (Hopwood, 1967).

Overall, the combination of compound efficiency within reduced reaction time and without perforation effects made GA a suitable cross-linking agent for use in spheroid positioning, fixation, and permeabilization assays. Since PFA was not suitable for the required application, no further investigations such as RTC measurements or quantification of the three parameters describing the dielectric spheroid structure were performed.

II INFLUENCE OF FIXATION ON SPHEROIDS

Since GA was selected as an appropriate fixative compound for spheroids when performing a positioning-fixation-permeabilization assay, the influence of the compound was evaluated on U-373 MG spheroids. For these experiments, different dilutions of GA were prepared to investigate the appropriate concentration for securing the spheroid inside the funnel-based measurement setup without disturbing the entire equilibrium. As stated in chapter 7.2.3, the RTC measurements and the calculated variance of increments, as well as the three impedimetric parameters of the spheroid, show significant dose-response dependencies.

- ➔ As the compound concentration increases, the variance of increments decreases.
- ➔ As the compound concentration increases, R_{ext} and R_{int}, as well as A_{sph}, decrease.

The dielectric properties of tissue models exposed to GA change as expected. After the addition of the fixative, the compound diffuses into the cellular structure and causes protein cross-linking, which leads to membrane stiffening and subsequent cell death. Therefore, the greater the amount of fixative available in the cells, the faster the cellular protein is fixed, the more rapidly the cells are immobilized, and the less invasive the effect of cross-linking on the functional integrity of the tight junctions (Oberleitner, 2017). The highest GA concentration of 0.3 % (v/v) caused a significant decrease in cellular micromotion, which was reflected in the smallest signal fluctuation amplitudes in RTC measurements. The normalized impedance signal showed a two-phase time course with an initial signal increase of 120 %, reflecting the resistive increase due to the blockage of the current pathway by the progressive cross-linking of cellular proteins as reported by Oberleitner based on ECIS™ measurements (Oberleitner, 2017). The subsequent impedance signal decrease is not related to an increase in permeability of the spheroids, as the A_{sph} value decreases, but may be related to a contraction of the spheroid due to

stiffening and thus an emerging empty space at the central opening. The 0.1 % (v/v) GA concentration displays a similar biphasic time course, which may also assume morphological spheroid deformation. As a result, the extracellular and intracellular resistance contributions determined three hours after spheroid treatment are reduced and display a decreasing trend with increasing fixative concentrations.

The assumption of spheroid deformation correlates with the finding of Hupf when analyzing the migration depth of fixed spheroids that were pre-incubated with different concentrations of PFA and inserted into the flow channel device (Hupf, 2018). The microscopic study demonstrated that the control spheroid and the 0.01 % (v/v) PFA-treated spheroid migrated deeper into the channel, approximately to the center, whereas at the highest level of fixation with 0.5 % (v/v) PFA, no migration was observed within 45 minutes. These results reflect different levels of spheroid cross-linking depending on the compound concentration used and are generally applicable to the model study using GA fixation.

By performing fundamental model studies with a newly developed ECIS-QCM measurement setup, Oberleitner evaluated signal changes upon exposure of cell monolayer culture to various GA concentrations (Oberleitner, 2017). Oberleitner found a dose-dependent effect of increasing fixative concentrations on the overall impedance increase, with lower concentrations causing a greater reduction in dielectric resistance than higher concentrations. Further, the high-frequency capacitances at 40 kHz were slightly increased by approximately 10 % for the two lowest GA concentrations applied (0.025 % and 0.1 % (v/v)), causing partial detachment of cells from the surface, while 0.25 % (v/v) GA did not induce any change in capacitance. Based on this, Oberleitner assumed that a too slow and less invasive cross-linking action enables a physiological response of the cells (Oberleitner, 2017).

As discussed, this statement cannot be confirmed based on the results of the spheroid studies. Contrary, since the spheroid and thus the impedance signal baseline is too strongly affected by GA concentrations of 0.1 % (v/v) and 0.3 % (v/v), both of these concentrations were not selected for further experiments. Thus, the lowest GA concentration of 0.03 % (v/v) was used, which induces a minimal increase in impedance in combination with a reduction in cellular micromotion. In this way, an appropriate fixation of the spheroid was achieved that was sufficient to secure the body inside the funnel or even to perform fluorescence imaging (see chapter 5.1.1, Fig. 5.2). In addition, the appropriate GA concentration was also confirmed in a proof-of-principle experiment addressing cell dynamic and morphology of either untreated or pre-fixed spheroids affected by permeabilization. For this purpose, spheroid treatment was performed similar to funnel-based impedance measurements using the respective compound concentrations and approximate incubation times, followed by cell viability staining and fluorescence microscopy imaging (see chapter 4.2.3). The experiment reinforced the commonly induced cell death of

the permeabilized spheroids (Fig. A-7.9; B, C) and verified sufficient GA concentration as the spheroids resisted in size during subsequent permeabilization (Fig. A-7.9; C; see chapter 11.1).

Tab. 7.9 Normalized values of R_{ext}, R_{int}, and A_{sph} reflecting the dielectric structure of MCF-7 and U-373 MG spheroids after GA fixation. The values are based on mean values derived from raw data obtained directly after fixation and after 15 hours for the control condition in the model study of saponin. Detailed fitting conditions are provided in the respective raw data information (Tab. 7.8; see chapter 11.1, Tab. A-7.2). Significance was determined by a two-sample t-test of the respective parameters between the cell types using a significance level of 0.1 (*), 0.05 (**), and 0.01 (***).

	0.03 % (v/v)	
	MCF-7	U-373 MG
R_{ext} [%]	90 ± 10$^{n.s.}$	87 ± 6$^{n.s.}$
R_{int} [%]	40 ± 20$^{n.s.}$	50 ± 20$^{n.s.}$
A_{sph} [%]	180 ± 90$^{n.s.}$	140 ± 40$^{n.s.}$
n	4(4)	5(5)

Although the experiments analyzing the influence of fixation on spheroids as a function of compound concentration were only performed with U-373 MG spheroids, the results are also applicable to MCF-7 spheroids, providing optimal treatment by using a 0.03 % (v/v) GA solution. This approach is confirmed by the comparison of the dielectric parameters of the two cell types. The values were obtained 15 hours after spheroid fixation for the control condition in the saponin model study and related to the values directly after the fixation process, respectively (Tab. 7.9). By comparing the respective parameter values, a similar relative signal decrease for R_{ext} and R_{int} respective increase for A_{sph} are observed regardless of the cell type used. This fact is also confirmed by performing a two-sample t-test, which determines no significance ($^{n.s.}$) between the cell types. Thus, the spheroids were affected equally, regardless of the cell type from which they were derived, thereby emphasizing the significance of cell fixation as a fundamental effect at the subcellular level.

7.2.7 DISCUSSION: INFLUENCE OF PERMEABILIZATION

In this model study, the influence of permeabilization on cellular models was investigated using saponin as a detergent compound. For the analysis of the cell monolayer and spheroid response, different experimental approaches such as cell viability assays, impedimetric measurements based on the ECIS™ technique as well as on the novel funnel-based setup, and microscopic observations were performed.

The results are discussed below and provide a comprehensive view of the permeabilization process in relation to the dimensionality of the *in vitro* model.

I CELL VIABILITY EFFECTS

The effects of the compound on cell viability are related to the molecular structure. Saponins are a group of surface-active metabolites that are widely distributed in plants and marine animals (Sparg et al., 2004; Vincken et al., 2007). They are characterized as detergent substances due to the ability of many saponins to form colloidal solutions resulting in the production of soap-like foam. Accordingly, saponins are also used to induce selective permeabilization of cell membranes by cholesterol complexation and subsequent pore formation (Podolak et al., 2010). These features are based on the amphipathic nature of the saponin molecules, as they are composed of a hydrophilic and a lipophilic part.

The first model describing the mechanism of saponin on membranes was proposed by Glauert and coworkers in 1962 (Fig. 7.25; Glauert et al., 1962). Upon addition of saponin, spontaneous complexation reactions occur with cholesterol molecules present in the cell membrane. This results in the formation of micelles and two-dimensional micelle-like structures within the membrane, with the hydrophobic chains oriented towards the center of the clusters. Thus, aqueous pores are generated in the lipid bilayer, leading to an increase in membrane permeability that allows ions and macromolecules to pass through the lipid bilayer. Consequently, cell membranes are degraded and cell death is induced in proportion to the concentration of the compound applied.

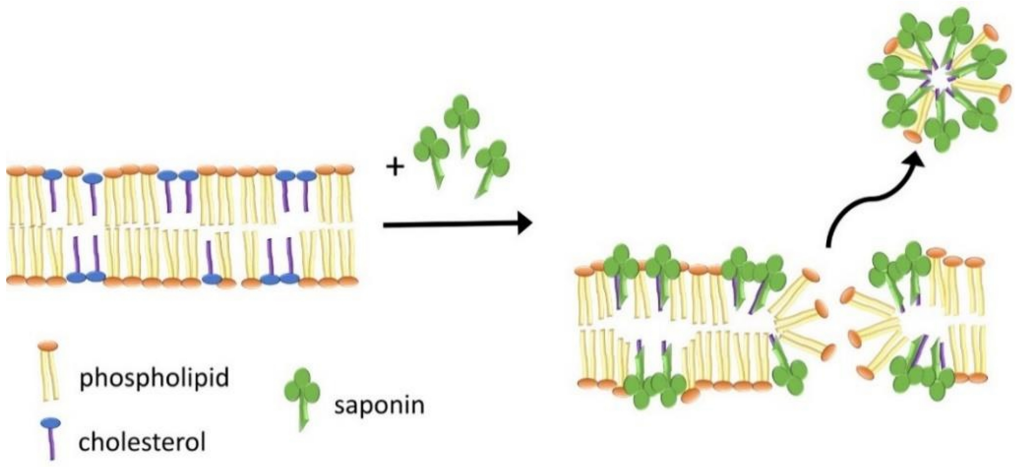

Fig. 7.25 Illustration* of the permeabilization mechanism of saponin on cellular membranes. After compound addition, cholesterol molecules are complexated by saponin leading to the formation of micelles and membrane pores.

*illustration is simplified and not to scale
(adapted from Lorent et al., 2013)

To determine the cytotoxic effect of saponin on the cell types examined within the framework of this thesis, the PrestoBlue™ cell viability assay was performed and the EC_{50} values were calculated (chapter 7.2.1).

➔ The cell viability assay revealed distinct EC_{50} values for MCF-7 and U-373 MG cells depending on the cell type and cell configuration as monolayer culture or spheroids.

The results revealed similar mean values for the cell monolayer culture of 0.034 (± 0.002) mg/mL (MCF-7) and 0.033 (± 0.001) mg/mL (U-373 MG). For spheroids, EC_{50} values of 0.192 (± 0.009) mg/mL (MCF-7) and 0.165 (± 0.008) mg/mL (U-373 MG) were determined, which differ significantly between both cell types and are higher than for the corresponding two-dimensional cell layer. Thus, a five- to six-fold higher concentration of saponin is required to achieve the same 50 % change in response or reduction in cell viability of 3D tissue models in relation to monolayer culture. The difference between spheroids derived from either MCF-7 or U-373 MG cells was as expected. Since the brain has the highest cholesterol content in the body (Björkhem and Meaney, 2004), it is assumed that this also applies to tumor cells, thus enabling a higher level of complexation of the saponin molecules compared to breast cancer cells resulting in a higher degree of pore formation.

For comparison, Hupf also determined the cytotoxicity of saponin on MCF-7 spheroids using an identical assay and determined an EC_{50} value of 0.17 (± 0.01) mg/mL (mean ± SE; n = 3; Hupf, 2018), which is in good agreement with the results of this thesis. In the literature, a large number of saponins with their respective origin and their cytotoxic potential are reported, which were tested on a variety of cell types as cell monolayer (Sparg et al., 2004; Vincken et al., 2007; Podolak et al., 2010). However, as reviewed by Podolak et al., a comparison of cytotoxicity levels is only an approximation as there were notable differences in the evaluated values between the control compounds themselves (Podolak et al., 2010). Furthermore, no defined cytotoxicity values for spheroids could be found in literature, and the preferred assay for investigating compound cytotoxicity on monolayer culture is the colorimetric formazan-based MTT assay, which is reported to be less sensitive compared to the PrestoBlue™ assay (Xu et al., 2015). Therefore, no comparison could be made between the literature data and the results of this work concerning this aspect.

II IMPEDIMETRIC CHARACTERISTICS

In addition to the impairment of saponin on cell viability, the responses of the monolayer culture and spheroids were monitored impedimetrically during the permeabilization process. The time-dependent impedance of the cells changes after the addition of different concentrations of saponin solution and

thus serves as a sensitive indicator of the effect of the detergent and as a basis for the evaluation of acute toxicity.

II.A IMPEDIMETRIC CHARACTERISTICS – 2D TISSUE MODELS

For the experiments on 2D tissue models, saponin solutions in a concentration range of 0.003–0.3 mg/mL were applied and the signal changes were analyzed. As indicated in chapter 7.2.2, the MFT measurements show significant dose-response dependencies for MCF-7 and U-373 MG cells, whereas the calculated variance of increments of the monolayer culture exhibited no clear relationship.

- ➔ As the compound concentration increases, the impedance decreases.
- ➔ As the compound concentration increases, the variance of increments increases and subsequently decreases at concentrations above 0.01 mg/mL saponin solution.

The parameters change as expected when the cells are exposed to a permeabilizing substance. After the addition of the detergent, the compound diffuses into the cell structure and causes increasing pore formation, resulting in less current restriction and decreasing impedance values. Since the calculated variance of increments may not reflect the actual values as cell detachment is indicated in the time course of the capacitance, only the trend of increasing and decreasing values is evaluated. Thus, an initial increase represents an enhanced cellular micromotion upon saponin addition, indicating a higher level of cellular dynamic. As the amount of detergent available in the cells increases, and ultimately exceeds a critical concentration (here: 0.01 mg/mL for MCF-7 cells; 0.03 mg/mL for U-373 MG cells) the cell membranes are degraded more rapidly, as reflected by the time course of impedance values as well as decreasing variance values (see chapter 7.2.2).

For comparison, Oberleitner performed a fixation-permeabilization assay on monolayer culture using the developed ECIS-QCM setup (Oberleitner, 2017). Oberleitner found that saponin treatment after cell layer fixation caused no reduction in the QCM impedance damping signal, whereas it induced a steep increase in capacitance values and a decrease in dielectric resistance recorded in ECIS™ mode. Thus, membrane permeabilization was considered as an instantaneous loss of the dielectric structure of a cell layer (Oberleitner, 2017). Even though the experiments in this work were performed without cell monolayer fixation, the results obtained align with those of Oberleitner.

For further data evaluation, the area under the curve (AUC) of the normalized impedance data within a defined time range was calculated, normalized to the control condition, and plotted as a function of the logarithmic concentration for each cell type (Fig. 7.26). The AUC values indicate the level of permeabilization; low AUC values correlate with a high level of cell perforation. Both cell types show

similar results as the AUC values decrease with increasing saponin concentration. Initially, the data show a plateau up to a concentration of 0.005 mg/mL, followed by a steady decrease to lower values corresponding to a cell-free setup. At a concentration of 0.01 mg/ml, a clear signal increase is observed, which is more significant for U-373 MG cells. This finding can be explained by an excessive overreaction of the cellular response to the addition of the substance, which correlates with the observed trend in the variance of increments, followed by the effect of the substance becoming predominant at higher concentrations.

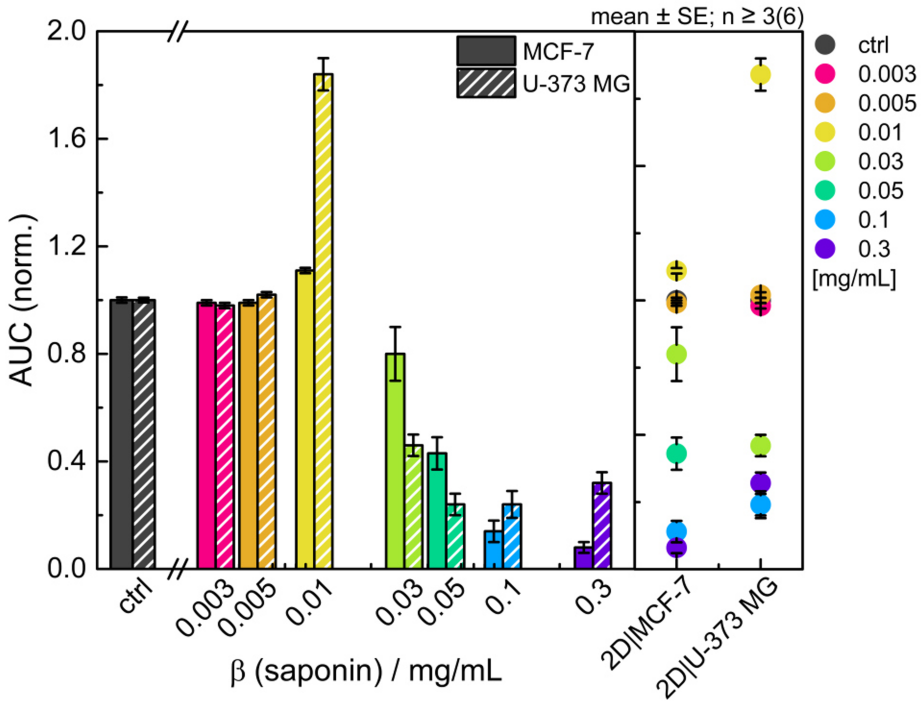

Fig. 7.26 Overview of the normalized results of the area under the curve values derived from the time course of normalized impedance magnitude at 4,000 Hz of MCF-7 and U-373 MG cell monolayer cultures (Fig. 7.9). For integration, a baseline was set at the cell-free level (22 % (MCF-7) respectively 74 % (U-373 MG)) of the normalized impedance, and the values were determined within two hours after the addition of saponin solutions with different concentrations in a range of 0.003–0.3 mg/mL. After averaging, data sets were normalized to the control condition, mean ± SE, n ≥ 3(6). An overview of the distribution of the results is provided in the scatter plot. Significance was determined by a two-sample t-test between the cell types using a significance level of 0.1 (*), 0.05 (**), and 0.01 (***). As a result, a high significance level of 0.01 (***) was determined between the cell types in the concentration range 0.01–0.3 mg/mL, while no significant values ($^{n.s.}$) were obtained at the lower concentrations (symbols not shown in the graph).

An overview of the results for both cell types is shown in the scatter plot. For MCF-7 and U-373 MG cells, a sigmoidal dose-response profile over the entire concentration range is observed. In the case of U-373 MG cells, the values of the highest concentrations remain at a similar higher level and a significant outlier level is displayed, as already noted. The significance between the AUC values of the MCF-7 and U-373 MG monolayer cultures was calculated using a two-sample t-test, which revealed a high

significance level of 0.01 (***) between the cell types in the concentration range 0.01−0.3 mg/mL, while no significant values ($^{n.s.}$) were obtained at the lower concentrations.

Based on the calculated AUC values, a dose-response curve as a function of the saponin concentration was created for each cell line, respectively, and EC_{50} values were determined using the sigmoidal Boltzmann equation (see chapter 11.1, Fig. A-7.10; chapter 4.1.8, Eq. 4.2). The mean values of the EC_{50} are calculated as 0.043 (± 0.003) mg/mL (MCF-7; R^2 = 0.99; mean ± SE; n ≥ 3(6)) and 0.021 (± 0.005) mg/mL (U-373 MG; R^2 = 0.97; mean ± SE; n ≥ 3(6)) in monolayer culture, representing a high significance level of 0.01 (***) compared to each other.

II.B IMPEDIMETRIC CHARACTERISTICS – 3D TISSUE MODELS

For a comprehensive impedimetric characterization, the effect of membrane permeabilization was also analyzed by exposing – in this case – pre-fixed spheroids to different concentrations of the detergent saponin. The experiments were performed with saponin solutions in a concentration range of 0.3–3 mg/mL and the cellular response was recorded using the funnel-based measurement setup. As a result, the analysis of the spheroid micromotion, the calculated variance of increments, and the dielectric spheroid parameters show clear variations as a function of compound concentration for both cell types used, as described in chapter 7.2.4.

- ➔ As the compound concentration increases, the impedance and variance of increments decrease.
- ➔ As the compound concentration increases, R_{ext} and R_{int} decrease, whereas A_{sph} increases.

The dielectric properties of tissue models exposed to saponin change as expected. Based on the explanations for the monolayer culture, the detergent causes pore formation within the cell membrane and leads to decreasing impedimetric signals and variance of increments. The decreasing values indicate a reduced cellular micromotion within the spheroid as demonstrated by the RTC measurements, thereby showing a significant decrease in the fluctuation rate. At saponin concentrations of 1 mg/mL and 3 mg/mL, no micromotion was detected, which confirms the fact that the membrane permeabilization enhances the number of dead cells and is therefore efficient. Furthermore, these findings correlate with the reduction in signal for both parameters R_{ext} and R_{int}, associated with a loss of cell barrier function and decreasing intracellular resistance, thereby enabling the current to flow with less resistance. In addition, the increasing signal of A_{sph} indicates enhanced permeability within the spheroid body associated with a loss of capacitance contribution to the impedance signal. The combination of all signal trends represents the gradual degradation of the cell membrane with increasing saponin concentration.

Accordingly, Hupf performed EIS measurements on spheroids pre-incubated with different concentrations of saponin in the concentration range of 0.01–0.25 mg/mL and evaluated the three spheroid parameters (Hupf, 2018). It was found that R_{ext} and R_{int} decreased with increasing saponin concentrations, while A_{sph} slightly increased at lower concentrations and decreased at the highest saponin concentration. The inconsistent trend of the capacitance parameter was explained by the loss of cells on the spheroid surface, resulting in a reduced spheroid diameter and thus affecting the actual experimental outcome (Hupf, 2018). Therefore, the trends of the resistive parameters align with the results of the model study presented in this thesis. Since Hupf did not use pre-fixed spheroids, the correlation between the experimental approaches performed demonstrates that the fixation of the spheroids does not mask the actual permeabilization process. Furthermore, the use of pre-fixation eliminates the drawback of the need for pre-incubation and enables the performance of online measurements.

Tab. 7.10 Normalized values of R_{ext}, R_{int}, and A_{sph} reflecting the dielectric structure of MCF-7 and U-373 MG spheroids as a function of different saponin concentrations (ctrl | 0.3 | 1 | 3 mg/mL) used for permeabilization. The values are based on mean values derived from raw data obtained 15 hours after the addition of saponin solution. Detailed fitting conditions are provided in the respective raw data information (Tab. 7.8; see chapter 11.1, Tab. A-7.2). Significance was determined by a two-sample t-test of the respective parameters between the cell types using a significance level of 0.1 (*), 0.05 (**), and 0.01 (***).

		$concentration$ [mg/mL]			
		ctrl	0.3	1	3
MCF-7	R_{ext} [%]	100 ± 10$^{n.s.}$	5.2 ± 0.6***	3.9 ± 0.6***	3.7 ± 0.7***
	R_{int} [%]	100 ± 50$^{n.s.}$	3 ± 2**	0.4 ± 0.1*	0.23 ± 0.09**
	A_{sph} [%]	100 ± 80$^{n.s.}$	300 ± 200$^{n.s.}$	600 ± 300**	600 ± 300**
	n	4(4)	4(5)	5(5)	5(5)
U-373 MG	R_{ext} [%]	100 ± 7$^{n.s.}$	44 ± 9***	27 ± 3***	9 ± 1***
	R_{int} [%]	100 ± 50$^{n.s.}$	8 ± 3**	1.0 ± 0.5*	0.1 ± 0.04**
	A_{sph} [%]	100 ± 40$^{n.s.}$	130 ± 60$^{n.s.}$	200 ± 70**	270 ± 80**
	n	5(5)	5(5)	5(5)	5(5)

In order to compare the calculated values of the three spheroid parameters of both cell types, the data were normalized to the respective control condition (Tab. 7.10). The overview reveals that the lowest

saponin concentration of 0.3 mg/mL has a stronger impact on MCF-7 cells, as the extracellular resistance is reduced to 5.2 (± 0.6) %, while the U-373 MG remains at 44 (± 9) %. In addition, the percentage increase in capacitance values is several times higher in MCF-7 cells, indicating a significantly increased permeability within the spheroid body. Based on this strong effect on MCF-7 cells, it is suggested that the saponin molecule penetrates more rapidly into the interior of the tissue model as fewer cells are present. Therefore, at identical concentrations, the effect of the detergent becomes more efficient than in U-373 MG spheroids. This assumption is confirmed by the higher slope values for MCF-7 spheroids, which mimic the kinetic of a stronger impedance signal decrease after saponin addition (see Tab. 7.7). However, this is not consistent with the PrestoBlue™ assay results which show a lower EC_{50} value for U-373 MG spheroids. Thus, the different assay conditions due to spheroid pre-fixation must be considered, which may lead to even stronger cross-linking of the larger number of U-373 MG cells within a spheroid model and thereby less efficient permeabilization compared to MCF-7 spheroids. Regarding the applied saponin concentrations of 1 mg/mL and 3 mg/mL, similar low relative resistance values were observed. The significance of the calculated parameter values was confirmed between the two cell types using a two-sample t-test for each concentration studied, indicating a range of low to high level of significance while no significance ($^{n.s.}$) was determined for A_{sph} at 0.3 mg/mL saponin concentration.

For additional data evaluation, the area under the curve of the normalized impedance data within a defined time range was calculated and discussed in a similar manner as described for the monolayer culture. The normalized AUC values are plotted as a function of the logarithmic concentration for each cell type and indicate the level of permeabilization; low AUC values correlate with a high level of cell perforation (Fig. 7.27). Similar results were obtained for both cell types, demonstrating that the AUC values decrease with increasing saponin concentration approximating a cell-free level at the highest compound concentration of 3 mg/mL. In correlation with the difference of a stronger influence on MCF-7 spheroids, as discussed for the three dielectric spheroid parameters, the AUC values also show a steeper gradient profile. Additionally, this result is also confirmed by the calculated kinetic values concerning the first two hours of compound impact, which demonstrates the faster and higher signal dropdown for MCF-7 spheroids (see Tab. 7.7). Further, this is also illustrated by the scatter plot, which shows the distribution of the MCF-7 results in the lower part only, whereas the U-373 MG spheroid results spread from two concentration values in the middle to one in the lower chapter. The calculation of the significance between the AUC values of the MCF-7 and U-373 MG spheroids using a two-sample t-test revealed a high significance level of 0.01 (***) in the concentration range 0.3–3 mg/mL, while no significance ($^{n.s.}$) was obtained for the control condition.

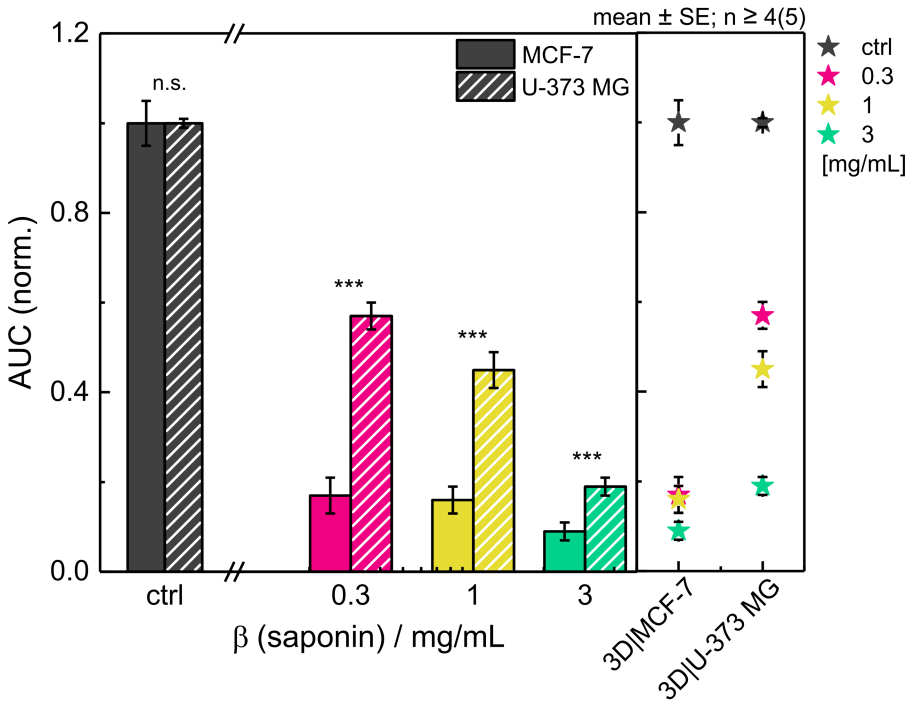

Fig. 7.27 Overview of the normalized results of the area under the curve values derived from the time course of normalized impedance magnitude at 200 Hz with GA (0.03 % (v/v)) pre-fixed MCF-7 and U-373 MG spheroids (Fig. 7.14). For integration, a baseline was set at the cell-free level (13 % (MCF-7) respectively 21 % (U-373 MG)) of the normalized impedance, and the values were determined within 10 hours after the addition of saponin solutions with different concentrations (ctrl | 0.3 | 1 | 3 mg/mL). After averaging, data sets were normalized to the control condition, mean ± SE, n ≥ 4(5). An overview of the distribution of the results is provided in the scatter plot. Significance was determined by a two-sample t-test between the cell types using a significance level of 0.1 (*), 0.05 (**), and 0.01 (***).

In accordance with the dose-response curve of the cell monolayer response, the EC_{50} values were also obtained for spheroids based on the calculated mean AUC values for each cell type (see chapter 11.1, Fig. A-7.11). As a result, the EC_{50} values were calculated as 0.15 (± 0.07) mg/mL (MCF-7; $R^2 = 0.99$; mean ± SE; n ≥ 4(5)) and 0.27 (± 0.08) mg/mL (U-373 MG; $R^2 = 0.98$; mean ± SE; n ≥ 4(5)) in spheroids, representing a significance level of 0.05 (**). Since only four values were taken into account, the sigmoidal fit is not as precise, and the results should be evaluated with caution. For comparison, Hupf also determined the EC_{50} value of saponin on MCF-7 spheroids based on impedance measurements and found an EC_{50} value of 0.10 (± 0.02) mg/mL (mean ± SE; n = 5; Hupf, 2018), which is in good agreement with the results obtained in this chapter.

Overall, a comparison of the impedance signal trends investigated between MCF-7 and U-373 MG monolayer cultures and spheroids revealed that the detergent generally had an identical effect on all parameters, regardless of cell type or cell structure configuration, thereby emphasizing the impact of cell permeabilization as a fundamental effect at the subcellular level (compare the summary in chapter 7.2.8).

III MORPHOLOGICAL PROPERTIES

In addition to the determined cell viability effects and the investigated impedimetric characteristics, the influence of saponin was also studied regarding the morphological properties of spheroids. Therefore, experiments were performed with saponin solutions at concentrations ranging from 0.3–3 mg/mL and the cellular response was measured using the zenCELL owl microscope setup. Based on the analysis of the recorded time-resolved images, a clear dose-response dependency for both cell types used is displayed, as shown in chapter 7.2.5.

➔ As the compound concentration increases, the diameter of the MCF-7 and U-373 MG spheroids increases, and the entire cell assembly disintegrates.

As expected, the morphology of the spheroid bodies changes in response to the exposition of saponin. Correspondingly, the determined spheroid diameter revealed significant changes over time in relation to the detergent concentration applied. The increasing compound concentration leads to a gradual permeabilization of the spheroids and disintegration of the three-dimensional structure of the tissue model. This can be seen in the time-resolved images as the remaining spheroid-like structure becomes progressively more diffuse. The time course of the normalized diameter shows – in addition to the gradual increase in diameter due to continuous perforation at higher concentrations – an increasing/decreasing effect at lower concentrations. Cell shrinkage caused by an osmotic effect, or a final collapse of the entire spheroid body is proposed as an explanation since this effect is accompanied by an increase in the central black area (compare chapter 7.2.5). However, this effect could not be reconstructed using the online recordings as the spheroids were pre-fixed for the funnel-based measurements and no further information was found in the literature.

For a more detailed evaluation, the area under the curve of the normalized diameter time course was calculated for each cell type within 24 hours of saponin exposure and plotted as a function of concentration (Fig. 7.28). In contrast to the impedimetric data analysis, high AUC values correlate with the degree of permeabilization and hence increasing AUC values are displayed with increasing saponin concentration for both cell types demonstrating a dose-response relation. In particular, the AUC of the U-373 MG spheroids at the concentration of 3 mg/mL saponin solution is remarkable, reflecting the rapid increase in diameter after exposure and the strong influence of permeabilization. At the concentrations of 0.3 mg/mL and 1 mg/mL, a similar AUC value for U-373 MG spheroids was obtained, which is based on the different time courses determined for the diameter increase (see Fig. 7.20, B). In contrast, in the case of MCF-7 spheroids, a sigmoidal dose-response profile is obtained, as also displayed in the relevant scatter plot.

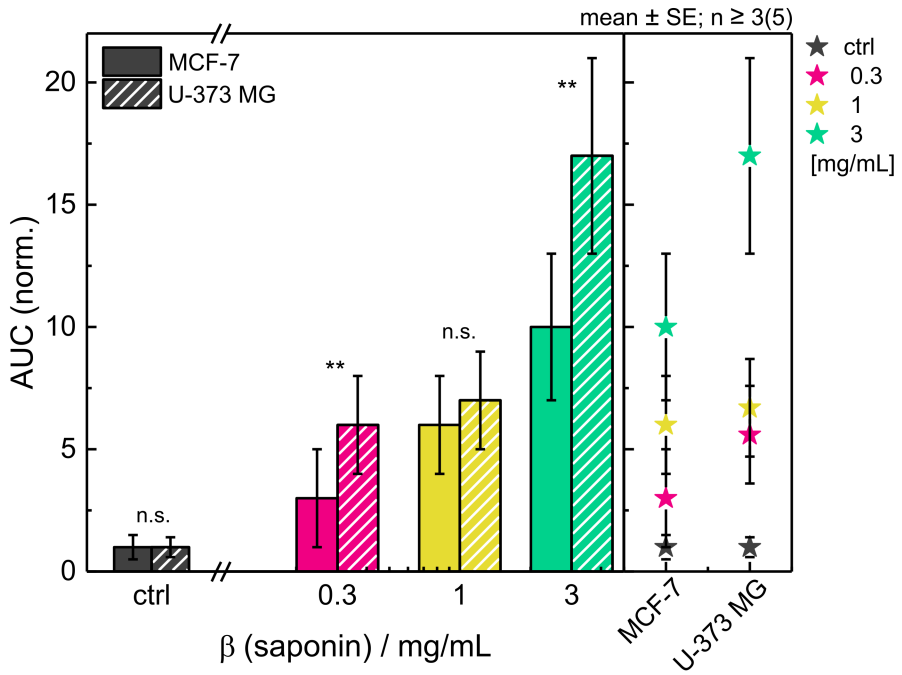

Fig. 7.28 Overview of the normalized results of the area under the curve values derived from the time course of diameter changes of MCF-7 and U-373 MG spheroids documented using the zenCELL owl digital microscope (Fig. 7.20). For integration, a baseline was set at 98 % (MCF-7; U-373 MG) of the normalized diameter and the values were determined within 24 hours after the addition of saponin solutions with different concentrations (ctrl | 0.3 | 1 | 3 mg/mL). After averaging, data sets were normalized to the control condition, mean ± SE, n ≥ 3(5). An overview of the distribution of the results is provided in the scatter plot. Significance was determined by a two-sample t-test between the cell types using a significance level of 0.1 (*), 0.05 (**), and 0.01 (***).

The significance between the AUC values of the MCF-7 and U-373 MG spheroids were calculated using a two-sample t-test, which revealed a significance level of 0.05 (**) for the concentrations of 0.3 mg/mL and 3 mg/mL, while no significance ($^{n.s.}$) was obtained for the values obtained at a saponin concentration of 1 mg/mL and for the control condition.

Based on the AUC values, the EC_{50} values were calculated for each cell type and determined as 0.9 (± 0.2) mg/mL (MCF-7; $R^2 = 0.96$; mean ± SE; n ≥ 3(5)) and 1.1 (± 0.5) mg/mL (U-373 MG; $R^2 = 0.85$; mean ± SE; n ≥ 3(5)), which are not significant ($^{n.s.}$) to each other (see chapter 11.1, Fig. A-7.12). Since only four values were taken into account, the sigmoidal fit is not as precise, and the results should be interpreted with caution.

As the morphological properties of the spheroids cannot be observed during the impedimetric measurements using the funnel-based setup, the results of Hupf are referred to, which used the channel-based setup to take images of the spheroids during the impedance recording (Hupf, 2018). As stated by Hupf, no differences in penetration depth or spheroid size were observed for spheroids incubated with saponin concentrations between 0.01 and 0.1 mg/mL (Hupf, 2018). In contrast,

spheroids pre-incubated for four hours in 0.25 mg/mL saponin solution displayed a reduced diameter, which in some cases led to complete migration of the spheroid into the narrowed space of the aperture and passage through it (Hupf, 2018). Since the spheroids were pre-fixed in the funnel-based EIS device, no body movement would be expected in response to the permeabilization treatment.

Taken together, the results indicate that the spheroid morphology changes in accordance with the concentration of saponin exposure in a dose-response-dependent manner, regardless of the cell type used.

7.2.8 SUMMARY OF THE MODEL STUDY OF PERMEABILIZATION

In this model study, the cellular response to permeabilization was characterized by using saponin as a detergent substance. Based on the investigated results of different experimental approaches and the detailed data evaluation, the following statements were considered in relation to the cell types and cell structure configuration studied.

- ➔ The cell viability assay revealed distinct EC_{50} values depending on the cell type and cell configuration as monolayer culture or spheroids.
- ➔ The impedance decreases with increasing saponin concentrations regardless of cell type and dimensionality.
- ➔ The variance of increments varies in the case of monolayer culture as the results increases with the compound concentration and decreases above 0.01 mg/mL saponin solution, regardless of the cell type. For spheroids, the variance of increments decreases with increasing saponin concentration, regardless of the cell type.
- ➔ The values of R_{ext} and R_{int} decrease, whereas A_{sph} increases with increasing saponin concentration, regardless of the cell type.
- ➔ The diameter of the spheroids increases more rapidly with increasing saponin concentration – regardless of the cell type – and leads to an entire cell assembly disintegration.

To highlight differences and similarities in the cellular responses obtained from monolayer culture and spheroids, the results of the impedance measurements and the calculated EC_{50} values are summarized.

For comparison, an overview of the area under the curve is provided that was obtained from impedance measurements using the ECIS™-based or the funnel-based measurement setup for monolayer cultures and spheroids, respectively (Fig. 7.29). Depending on the cell dimensionality, adjusted saponin concentrations were applied and the AUC values of the detected signal changes were analyzed within

an appropriate time period after compound addition, namely two hours for ECIS™ measurements on monolayer culture and 10 hours for spheroid experiments. The AUC values are thus representative of the permeabilization level and low AUC values correlate with a high level of cell perforation.

In general, the scatter plot shows a decrease in AUC values with increasing saponin concentration, regardless of cell type or dimensionality. Except for the outlier shown for U-373 MG (2D) at 0.01 mg/mL, the absolute range of variation is higher for MCF-7 cells in both dimensionalities. In addition, the results between the monolayer culture and the spheroid models obtained for the identical saponin concentration of 0.3 mg/mL are compared. This reveals that, in the case of two-dimensional cell structures, the lowest AUC values respectively the highest impact in cell morphology was induced, whereas U-373 MG spheroids exhibited a signal decrease to 57 (± 3) % and MCF-7 to 17 (± 4) %. A similar dose-response relationship was found for MCF-7 cells at concentrations of 0.3 mg/mL (2D) and 3 mg/mL (3D), representing a factor of 10 and for U-373 MG cells at concentrations of 0.03 mg/mL (2D) and 1 mg/mL (3D), representing a factor of approximately 30. Thus, an adjustment of the compound concentration in relation to the cell structure dimensionality or a higher concentration of detergent is required to induce an identical response change. In reverse, the multicellular resistance of 3D tissue models is reflected, as discussed in chapter 1.3.

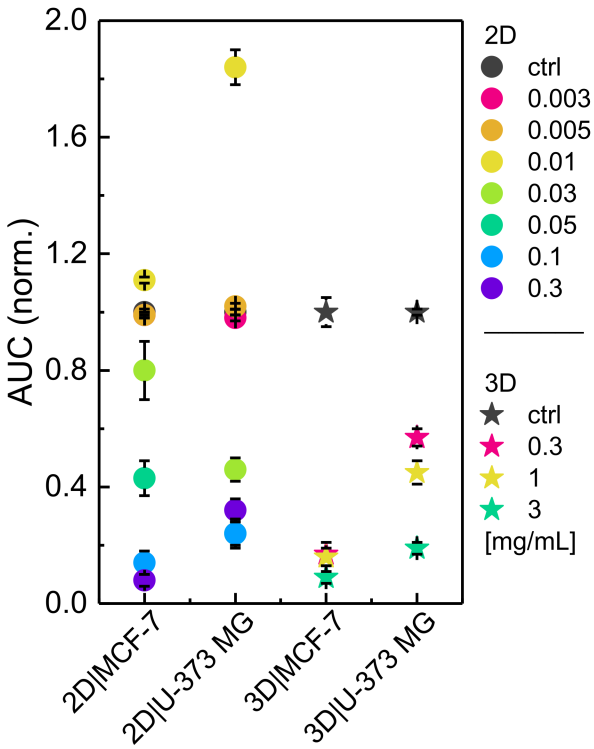

Fig. 7.29 Scatter plot of the normalized area under the curve values, which was derived from the time course of the normalized impedance magnitude recorded by using the ECIS™-based or the funnel-based measurement setup for monolayer cultures and spheroids, respectively, and summarized as individual charts. Detailed experimental conditions are provided in the respective raw data information (Fig. 7.26; Fig. 7.27).

Regarding the distribution of values within the variation range, the results of MCF-7 and U-373 MG cells (2D) as well as spheroids derived from U-373 MG cells (3D) display a sigmoidal dose-response profile, whereas the MCF-7 spheroid model (3D) values are below 20 %. In this case, it is implied that the same concentration of saponin has a greater effect on MCF-7 cells configurated as spheroids than as monolayer cultures. As discussed earlier in this chapter, this assumption should be considered with caution and different assay conditions must be taken into account. In particular, the spheroids must be pre-fixed prior to permeabilization, which may result in even greater cross-linking of the larger number of U-373 MG cells within a spheroid model and thus a lower diffusion of saponin molecules. An indication for this is the correlation between the strong effect of permeabilization on U-373 MG cells, as revealed by the lower EC_{50} value of U-373 MG cells in 2D as well as in 3D obtained by the PrestoBlue™ assay with non-fixed spheroids. As these observations are consistent with the presumed higher cholesterol content of brain tumor cells (Björkhem and Meaney, 2004), which enables a higher level of complexation of saponin molecules, it is concluded that (i) the influence of saponin respective to the level of permeabilization is higher for U-373 MG cells and that (ii) spheroid pre-fixation is required for EIS funnel-based measurements, although the results must be interpreted with caution.

In this model study, the acute toxicity of saponin was investigated using various approaches such as the PrestoBlue™ cell viability assay, impedance measurements, and time-lapse observation. Several dose-response curves were generated from the analyzed area under the curve values or calculated cytotoxicity values, and EC_{50} values were determined using the sigmoidal Boltzmann equation (chapter 4.1.8, Eq. 4.2), whereby the different signal outputs were summarized in one key value. The calculated values are summarized for each experimental setup and listed in relation to the cell monolayer and spheroid models tested (Tab. 7.11).

As indicated, the EC_{50} values obtained from the PrestoBlue™ assay are almost identical for both cell types in monolayer culture. In contrast, the values calculated from the impedance measurements of 2D cell culture differentiate between the cell types, displaying a higher EC_{50} value for MCF-7 cells and a lower value for U-373 MG, which are separated by a factor of two. After averaging, significant values of 0.039 (± 0.004) mg/mL (MCF-7) and 0.027 (± 0.005) mg/mL (U-373 MG) are obtained, indicating that a lower concentration of saponin is required for U-373 MG cells to induce the same response compared to MCF-7 cells. This conclusion is consistent with the presumed higher cholesterol content of brain tumor cells, which allows a higher degree of complexation of saponin molecules and thus a higher degree of pore formation with comparable less amount saponin. In the case of spheroids, the calculated values from the PrestoBlue™ assay and the impedance measurements are in a similar range, whereas the EC_{50} values obtained from time-lapse imaging are approximately five times higher with a relatively

large error. Therefore, these values were used as an indication but are not included in the mean. Remarkably, the results derived from the impedance measurements of spheroids differ by a factor of two. As the U-373 MG value is higher than that of MCF-7 and thus in contrast to the tendency of the monolayer culture, the influence of spheroid pre-fixation has to be considered. The mean values are calculated as 0.17 (± 0.07) mg/mL (MCF-7) and 0.22 (± 0.08) mg/mL (U-373 MG), which are not significant and indicate the opposite influence of saponin on the cell types examined compared to the monolayer culture. Therefore, it is assumed that the results do not reflect the actual values, since the theory of saponin permeabilization states the contrary impact. As stated previously, the values may be distorted by the results of the impedance measurement, and thus it should be emphasized again that only four concentrations were used for the determination of the EC_{50} values.

Tab. 7.11 Overview of the EC_{50} values of saponin determined using the PrestoBlue™ cell viability assay, impedance measurements, and time-lapse observation. The results are categorized by cell type and cell dimensionality, respectively. The coefficient of determination is given in the table respectively for each experiment. Detailed experimental conditions are provided in the respective raw data information (chapter 7.2.1; chapter 7.2.2; chapter 7.2.4; chapter 7.2.5). Mean values were calculated for each cell type and dimensionality without the results presented in parentheses.

EC_{50} [mg/mL]	MCF-7		U-373 MG	
	2D	3D	2D	3D
PrestoBlue™ assay	0.034 ± 0.002	0.192 ± 0.009	0.033 ± 0.001	0.165 ± 0.008
impedance measurements	0.043 ± 0.003 R^2 = 0.99	0.15 ± 0.07 R^2 = 0.99	0.021 ± 0.005 R^2 = 0.97	0.27 ± 0.08 R^2 = 0.98
time-lapse observation	/	(0.9 ± 0.2) R^2 = 0.96	/	(1.1 ± 0.5) R^2 = 0.85
mean value	0.039 ± 0.004	0.17 ± 0.07	0.027 ± 0.005	0.22 ± 0.08

Taken together, distinct EC_{50} values were obtained for both cell types in relation to two- and three-dimensional cell cultures, demonstrating that (i) up to 10 times higher saponin concentration is required for spheroids in contrast to monolayer culture for inducing the identical response, and that (ii) in case of cell monolayer culture, the influence of saponin respective the level of permeabilization is significantly higher for U-373 MG cells than MCF-7 cells, while (iii) in the case of spheroids, the impact may be very similar for both cell types.

To summarize the results of the different approaches used in the permeability model study, all the data were collected and presented with the key parameter *activity level*. Therefore, the to the control condition normalized response to different saponin concentrations such as the AUC values, the variance of increments, or the three dielectric spheroid parameters is plotted on one graph, respectively for each cell type, without further processing the data. Thus, this broad overview serves to highlight the comprehensive concept of the model study, while detailed information and clear comparisons between the cell types used are provided in the individual results and discussion chapters. The charts in the scatter plot are categorized according to the cell dimensionality of the cellular structure, the measurement setup used, such as impedance measurements or time-lapse imaging, and the calculated dielectric parameters. In general, a low *activity level* corresponds to less cellular dynamic; therefore, note the inverted scale for the capacitance parameter and the AUC values obtained from time-lapse imaging, where a signal increase equals this effect. Overall, a decrease in the *activity level* was observed for each parameter upon increasing saponin concentration independently of the cell type or the cell dimensionality derived.

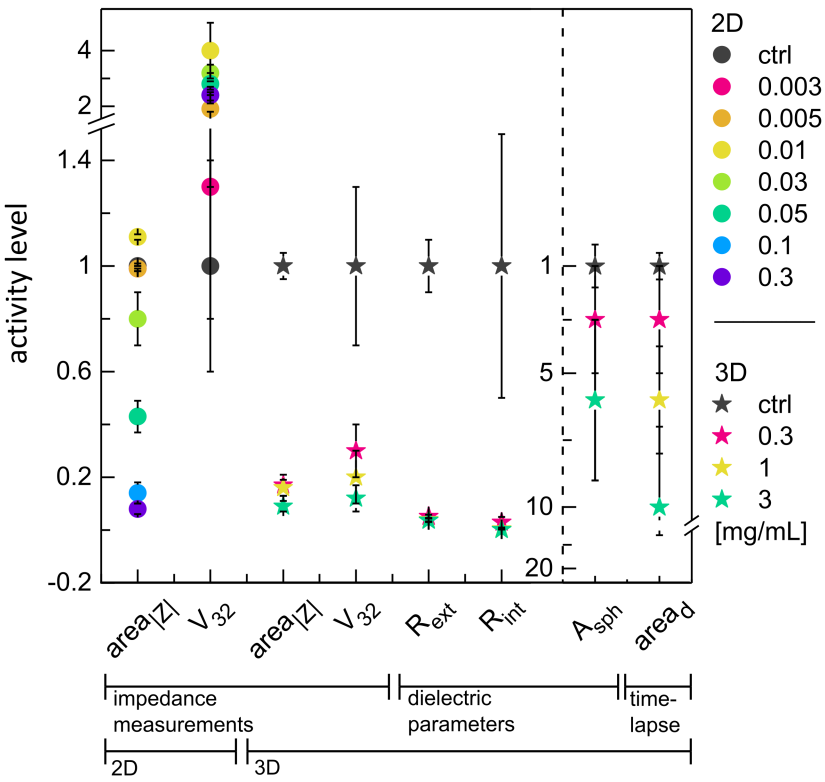

Fig. 7.30 Scatter plot of the normalized *activity level* values that were derived from different approaches applied in the permeability model study by using MCF-7 cells and summarized as individual charts. The charts are categorized according to the dimensionality of the *in vitro* model (2D or 3D tissue models) and the measurement setup used (impedance measurements, calculated dielectric parameters, time-lapse imaging). A low *activity level* corresponds to lower cellular dynamic; note the inverted scale for the capacitance parameter and the AUC values obtained from time-lapse imaging. Detailed experimental conditions are provided in the respective raw data information (Fig. 7.10; Fig. 7.16; Fig. 7.26; Fig. 7.27; Tab. 7.10; Fig. 7.28).

In the case of MCF-7 cells (Fig. 7.30), the values show a sigmoidal dose-response profile for the monolayer culture over the concentration range, which was compromised by an assumed over-reaction in cellular micromotion, indicated by an initial increase in variance values. The AUC values, reflecting the time-resolved impedance measurements of the MCF-7 spheroids, the cellular micromotion reflected by the calculated variance values, as well as the resistive parameters displayed a rapid decrease in activity for saponin-treated spheroids, which indicates a strong effect of the detergent. This effect, combined with a steep increase in permeability as displayed by multiple increases in capacitance values, was contrary to the gradual increase in perforation rate in the monolayer culture, and also to the stepwise perforation level depicted by time-lapse recording. In this context, the influence of the spheroid pre-fixation required to perform funnel-based measurements was considered in terms of making the permeabilization effect efficient. Analysis of the time-lapse images revealed a significant dose-response relationship while illustrating the progress of permeabilization and disruption of the cellular structure.

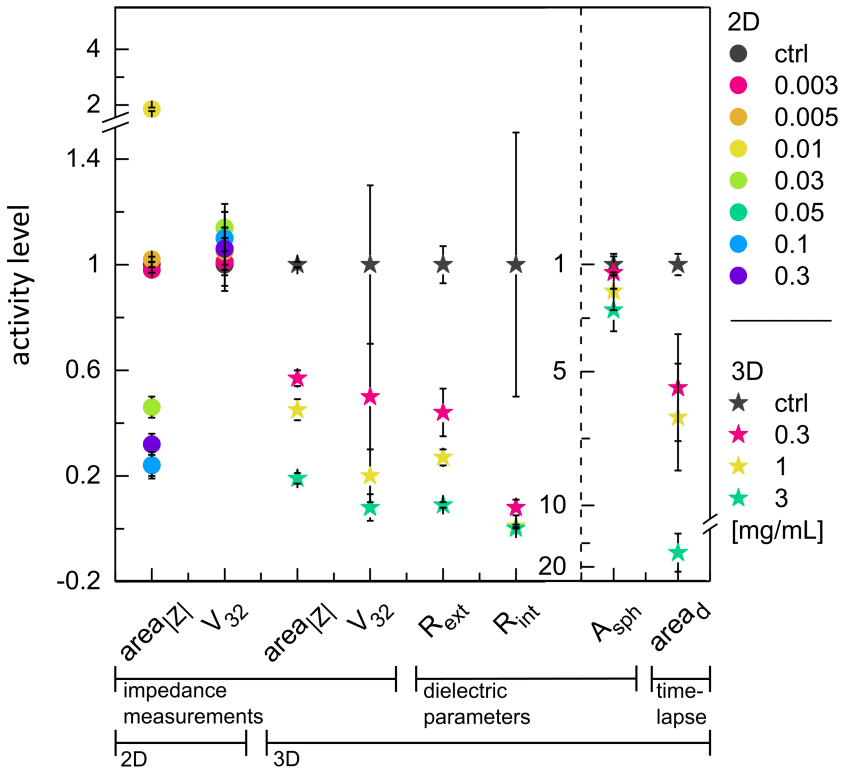

Fig. 7.31 Scatter plot of the normalized *activity level* values that were derived from different approaches applied in the permeability model study by using U-373 MG cells and summarized as individual charts. The charts are categorized according to the dimensionality of the *in vitro* model (2D or 3D tissue models) and the measurement setup used (impedance measurements, calculated dielectric parameters, time-lapse imaging). A low *activity level* corresponds to lower cellular dynamic; note the inverted scale for the capacitance parameter and the AUC values obtained from time-lapse imaging. Detailed experimental conditions are provided in the respective raw data information (Fig. 7.10; Fig. 7.16; Fig. 7.26; Fig. 7.27; Tab. 7.10; Fig. 7.28).

The summary of the model study using U-373 MG cells provides a similar overview (Fig. 7.31). In monolayer culture, the influence of saponin induced a distinct response of either a 200 % increase or decrease towards a cell-free level in combination with not significantly different variations in cellular micromotion, as shown by the value distribution of the variance of increments. In contrast, a sigmoidal dose-response profile for AUC values and the variance of increments within the variation range was revealed, which were obtained by performing experiments with U-373 MG spheroids using the funnel-based measurement setup. Thus, a strong impact of saponin on cell monolayer cultures was found, which was further discussed in the context of the determined EC_{50} values in dependence on cell type and cell dimensionality. The significant dose-response relations induced in spheroids correlate with distinct intrinsic morphological changes within the tissue model. Apart from the stepwise decreasing extracellular resistance and in contrast to MCF-7 spheroids' diminished capacitance increase at the highest saponin concentration, the time-lapse images revealed gradual dose-dependent size changes in accordance with the degree of perforation.

In summary, the findings indicate that changes in cellular morphology due to saponin exposure were detected in a dose-dependent manner in accordance with the gradual perforation of the cellular membranes. This model study included the performance of several assays that provided a comprehensive overview of the effects of the compound from different perspectives, such as cytotoxic specification, impedimetric characterization, and morphological properties. As the experiments were performed using either cell monolayer culture or spheroids, both derived from two different cell types, the individual results were discussed in relation to each other. Based on a detailed analysis of the data, the results were combined into one big picture which either reflected distinct differences or revealed similarities by considering everything together. The influence of saponin on the cellular response was thus clarified in that both monolayer culture and spheroids were equally affected, regardless of the cell type from which they were derived. In this context, it is emphasized that (i) cell permeabilization has a fundamental effect at the subcellular level and (ii) the combination of several assays provides a comprehensive overview of the cellular response induced.

7.3 MODEL STUDY: CELLULAR RESPONSE TO ACTIN CYTOSKELETON DEGRADATION

In this model study, the response of spheroids to actin cytoskeleton degradation was investigated. To this end, the cell membrane permeable compound cytochalasin D was used, which functions as an inhibitor of actin polymerization by binding to the end of actin microfilaments and thereby inhibits the association of actin subunits (Yahara et al., 1982). The influence of different concentrations of the fungal toxin on cell viability was investigated in cell monolayer cultures and attempted in 3D models using the funnel-based impedance setup. Additional time-resolved microscopy studies were performed to correlate the results of impedance measurements accompanied by variance analysis and visual observations.

7.3.1 VIABILITY ANALYSIS OF THE SPHEROID

The impact of cytochalasin D on the metabolic activity of MCF-7 spheroids was investigated in a proof-of-principle experiment by performing a PrestoBlue™ cell viability assay (Invitrogen™, Thermo Fisher Scientific).

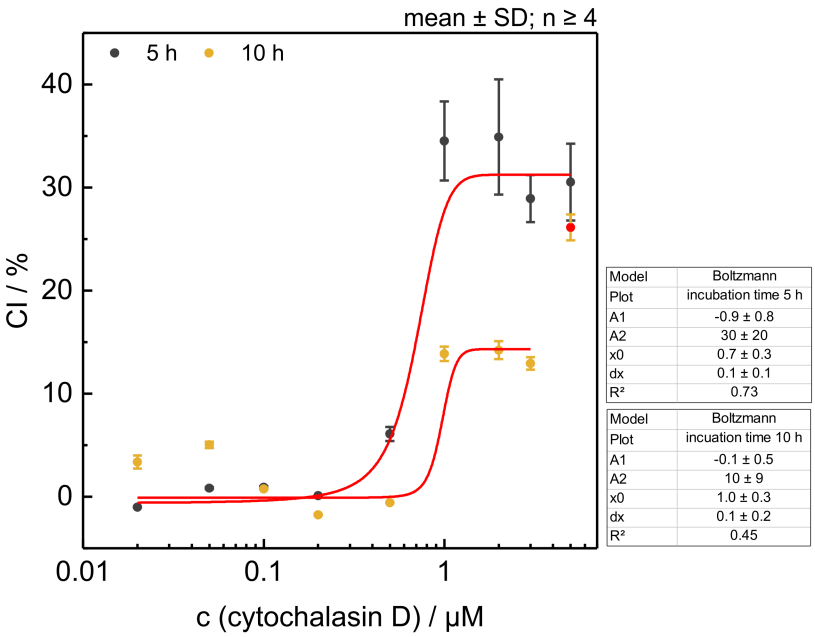

Fig. 7.32 Dose-response curve of the cytotoxicity index CI as a function of the cytochalasin D concentration used to determine the effect of actin cytoskeleton degradation on MCF-7 spheroids' viability. The PrestoBlue™ cell viability assay was performed either five hours or 10 hours after the addition of cytochalasin D solutions at different concentrations (0.02–5 µM). Experiments were performed in a standard cell culture incubator at 37 °C and 0 % CO_2. The results were fitted by the sigmoidal Boltzmann equation and the total EC_{50} value was determined. Data sets of respectively one experiment were averaged, mean ± SD, n ≥ 4; the result for the concentration of 5 µM and 10 hours incubation time was considered as an outlier (marked in red) and was thus not included in the fit function.

The spheroids were incubated with different concentrations of cytochalasin D for either five or 10 hours, respectively, and the measured fluorescence intensities were evaluated individually according to the protocol described in chapter 4.1.8. Each incubation condition was performed once using one 96-well plate, respectively. For data analysis, the calculated CI values were plotted as a function of the logarithmic cytochalasin D concentration and fitted using the sigmoidal dose-response Boltzmann transfer function (Fig. 7.32; chapter 4.1.8, Eq. 4.2).

In both experiments, the maximum cytotoxicity index amounts to less than 100 % and is even diminished from 29 (± 2) % (3 µM, 5 h) to 12.9 (± 0.6) % (3 µM, 10 h) with a longer incubation period. Thus, no complete loss of cell viability is indicated at the highest cytochalasin D concentration, which is accompanied by a certain degree of viability regeneration with increasing exposure time. In the case of a five-hour incubation time, the EC_{50} value was calculated to 0.7 (± 0.3) µM (R^2 = 0.73; mean ± SD, n ≥ 4; 5 h) and in the case of 10 hours to 1.0 (± 0.3) µM (R^2 = 0.45; mean ± SD, n ≥ 4; 10 h), exhibiting no significance to each other.

7.3.2 IMPEDIMETRIC ANALYSIS OF THE CELL MONOLAYER

The effect of actin cytoskeleton depolymerization was analyzed by performing ECIS™ measurements on cell monolayer cultures derived from MCF-7 and U-373 MG cells to compare the cellular response depending on the cell dimensionality of the *in vitro* model. For these experiments, a lower concentration of cytochalasin D (0.3–5 µM) was used compared to the spheroid studies. The induced cellular response was recorded by measurements in MFT and RTC modes, and the respective variance of increments was calculated at different concentrations.

The time course of the normalized impedance magnitude at 4,000 Hz is shown for 15 hours after compound addition (Fig. 7.33). For both cell lines, a dose-response dependency of cytochalasin D is displayed, indicating an increase in tissue model permeability with decreasing impedance signal. For MCF-7 cells (Fig. 7.33, A), the responses of the control and the two lowest concentrations of 0.3 µM and 0.5 µM are similar and therefore unaffected, showing an initial signal increase upon compound addition and reaching 89 (± 5) % (ctrl) after 15 hours. The impedance of the 1 µM and 2 µM cytochalasin D solution also exhibits a compound addition peak, which is diminished with increasing concentration, followed by a signal decrease to significant, constant levels at 82 (± 2) % (1 µM) and 72 (± 2) % (2 µM). A similar signal profile was observed for the three highest concentrations in the range of 3–5 µM cytochalasin D solution, which caused an exponential signal decrease directly after compound addition, resulting in approximately 60 % after 15 hours. In the case of U-373 MG cells, a similar impedance time course is shown (Figure 7.33, B). The signal of the control condition displays a constant baseline at

102 (± 1) %, and for the 0.3 µM cytochalasin D solution, an initial signal increase was observed after the addition of the substance, leading to a constant baseline at 108 (± 1) % after 15 hours. For the concentrations of 0.5 µM and 1 µM cytochalasin D, an initial signal decrease is followed by a linear impedance increase leading to significantly different levels of 112.2 (± 0.8) % (0.5 µM) and 100 (± 2) % (1 µM) after 15 hours. After the application of compound concentrations in the range of 2–5 µM to the cell monolayer, a direct signal decrease was observed, reaching a level of approximately 80 % within two hours after the compound addition.

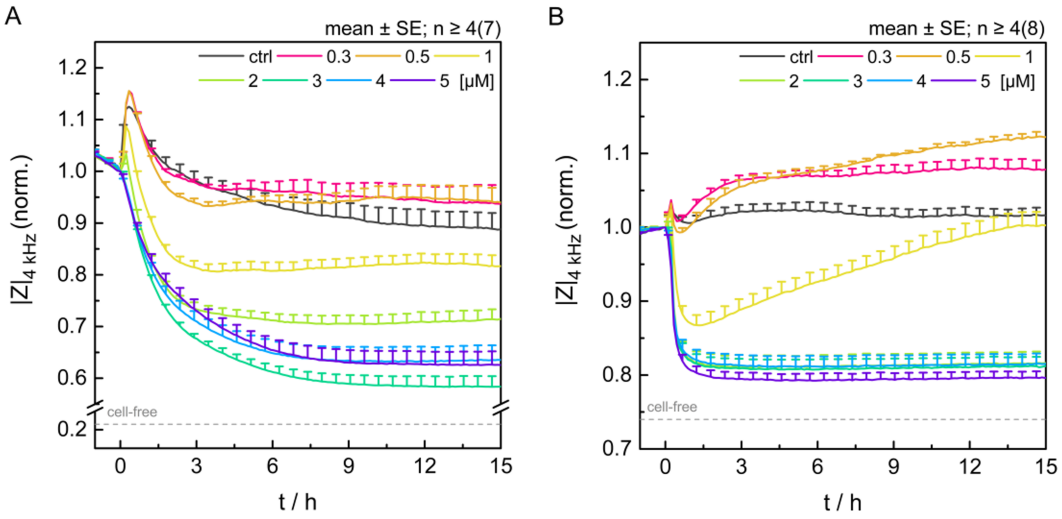

Fig. 7.33 Time course of normalized impedance magnitude at 4,000 Hz of MCF-7 (A) and U-373 MG (B) cell monolayer cultures after the addition of cytochalasin D solutions with different concentrations in a range of 0.3–5 µM. Time courses were normalized with respect to the last data point before compound addition at time point zero. Grey horizontal lines in A and B indicate mean values of cell-free sensors. Experiments were performed in a standard cell culture incubator at 37 °C and 0 % CO_2 using 8W10E arrays. Data sets were averaged after normalization, mean ± SE; A: n ≥ 4(7); B: n ≥ 4(8).

The results showed significant signal variations as a function of compound concentration, representing different degrees of actin cytoskeleton degradation of the cell monolayer. Both cell lines display a similar response to different concentrations of cytochalasin D, remaining either unaffected or completely affected, while the concentration of 1 µM appears to be a transition point. By using the standardized monitoring frequency of 4,000 Hz for comparison of the ECIS™ measurements, differences in relative impedance values between the two cell types are induced due to the lower sensitivity for U-373 MG cells. In addition, it should be noted that capacitance values for the highest concentrations increase after exposure to cytochalasin D, regardless of the cell type used, due to a certain degree of uncovered electrode areas from tight junction disintegration and an accompanied contraction of cells (data sets not shown in this thesis; Oberleitner, 2017).

Apart from MFT measurements, RTC measurements were also performed 15 hours after compound addition (datasets not shown) and the variance of increments was calculated for all concentrations after performing segmented detrending of the data using a time interval of 32 s. The results for both cell types were normalized to the control condition, revealing increasing and decreasing tendencies without a proportional dose-response relationship (Fig. 7.34). After an initial value decrease for the lowest cytochalasin D concentrations of 0.3 µM in the case of MCF-7 cells or 0.3–1 µM in the case of U-373 MG cells, which all display a similar level of approximately 90 %, a stepwise value increase is observed. For both cell types, a maximum value of 140 (± 30) % (MCF-7) respective 150 (± 30) % (U-373 MG) is shown for the 3 µM cytochalasin D concentration. At higher concentrations, the variance of increments is diminished, demonstrating relative values of 120 (± 20) % (MCF-7) and 110 (± 10) % (U-373 MG) at a concentration of 7 µM. Using a two-sample t-test, different levels of significance were found in relation to the control condition, while no significance ($^{n.s.}$) was observed for the three lowest compound concentrations in the MCF-7 cell monolayer culture, and only the maximum in the case of U-373 MG cells was highly significant (***). Significance values between concentration levels were not calculated.

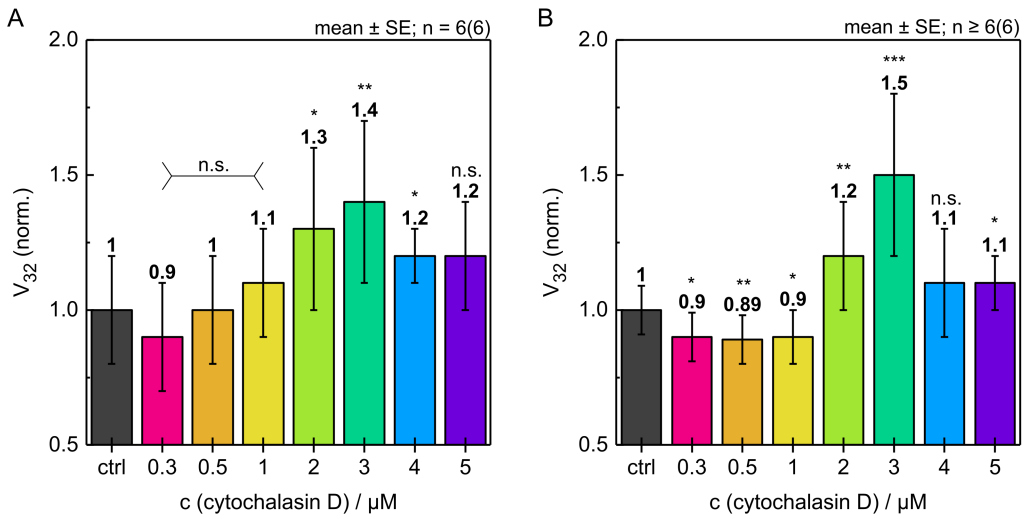

Fig. 7.34 Normalized variance of increments of impedance fluctuations after segmented detrending measured 15 hours after the addition of cytochalasin D solution with different concentrations in a range of 0.3–5 µM to MCF-7 (A) and U-373 MG (B) cell monolayer culture. Significance was determined relative to the control condition by a two-sample t-test using a significance level of 0.1 (*), 0.05 (**), and 0.01 (***). Data sets were averaged after segmented detrending, mean ± SE; n ≥ 6(6).

In general, the ECIS™-based measurements showed an increasing effect of actin cytoskeleton degradation of the cell monolayer as a function of cytochalasin D concentration, represented by decreasing impedance values. However, no clear dose-response relationship can be established from the results and only a trend is indicated. It should be noted that the analysis of cellular micromotion using the 8W10E electrodes is less sensitive due to the large electrode area.

7.3.3 IMPEDIMETRIC ANALYSIS OF THE SPHEROID

The influence of the degradation of the actin cytoskeleton within the spheroids was measured with the funnel-based measurement setup. In a proof-of-principle experiment, cytochalasin D solution with a concentration of 5 µM was applied to an MCF-7 spheroid and the impedance was recorded in MFT mode.

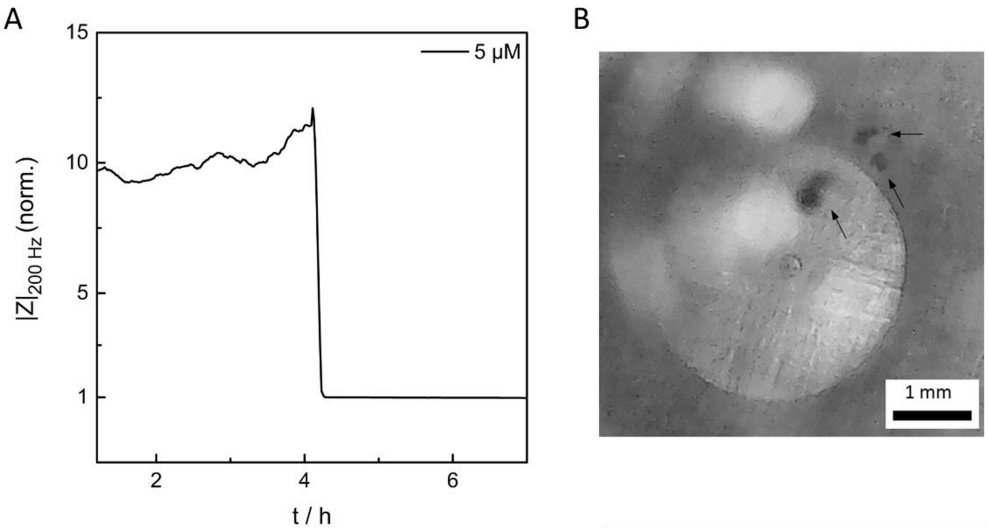

Fig. 7.35 Results of a proof-of-principle experiment regarding the spheroid response to cytochalasin D treatment. Enlarged view of the time course of normalized impedance magnitude at 200 Hz of an MCF-7 spheroid after the addition of cytochalasin D solution with a concentration of 5 µM (A). Time course was normalized with respect to the last data point before compound addition at time point zero, while the impedance was normalized with respect to the value of the spheroid-free setup. Experiment was performed in a standard cell culture incubator at 37 °C and 0 % CO_2. Microscope image of the funnel device taken after the measurement illustrating fragments of the former spheroid body in the lower measurement setup compartment (B).

The time course of the normalized impedance magnitude at 200 Hz shows a fluctuating signal rise followed by a sharp signal drop four hours after compound addition down to a cell-free level of approximately 5,400 Ω (Fig. 7.35, A). After the measurement, a microscope image of the funnel device was taken, illustrating fragments of the former spheroid body in the lower compartment (Fig. 7.35, B). Correlation of the impedance signal with the image reveals that the spheroid was disintegrated by exposure to cytochalasin D, causing fragments to slide through the opening into the lower compartment. During this process, the impedance increases as the degrading spheroid migrates further into the funnel hole until the signal decays as the cellular structure finally collapses. Consequently, as this effect may interfere with the actual signal change of the cytochalasin D reaction, and since the passing through of the spheroid body prohibits time course measurements, the assay cannot be performed with the funnel-based measurement setup.

Thus, in this chapter, the results of Hupf – who investigated the influence of cytochalasin D on MCF-7 spheroids using the channel-based setup – are reported (Hupf, 2018). In this model study, the spheroids were pre-treated with 5 µM cytochalasin D solution for different incubation times from zero to eight hours and were placed into the measurement setup. Hupf noted that measurable but subtle changes were found with different incubation times (Hupf, 2018): (i) the impedance time course showed increasing values for all conditions of the cytochalasin D-treated spheroids after placement, while the control spheroids displayed a stable impedance over time; (ii) with increasing incubation periods of spheroids to cytochalasin D the total change in impedance magnitude decreases.

In addition, the micromotion of the spheroids was examined and demonstrated similar fluctuation characteristics to the control spheroids, except for an increased signal from the spheroids treated for two hours, which is also reflected by the calculated variance of increments. Furthermore, Hupf calculated the dielectric parameters one hour after spheroid placement. Hupf observed an increase in R_{ext} and R_{int} values for two hours of exposure to cytochalasin D, followed by a constant decrease that remained above the values of the control spheroids, while no trend was noticed for A_{sph} (Hupf, 2018). To correlate the impedimetric results, microscopy images were taken at the beginning and end of each measurement which allowed Hupf to demonstrate that spheroids treated with cytochalasin D migrated further into the aperture than control spheroids (Hupf, 2018).

The results reported by Hupf (Hupf, 2018), in combination with the results of the cell monolayer and time-lapse imaging experiments performed in this thesis, serve as a basis for the discussion.

7.3.4 TIME-LAPSE MICROSCOPY ANALYSIS OF THE SPHEROID

The effect of cytochalasin D on cell morphology was monitored by time-lapse imaging using the zenCELL owl digital microscope to obtain a comprehensive characterization of the effect of actin cytoskeleton degradation investigated on spheroids. Spheroids derived from MCF-7 and U-373 MG cells were adhered to an adhesive surface and exposed to a cytochalasin D solution at different concentrations. The response of the spheroids was monitored by taking microscopic images every 10 minutes for 48 hours.

This study yielded different observations for the two cell types used. The montage of time-resolved micrographs of MCF-7 spheroids shows the overall effect of the cytochalasin D solution on the cell structure at a concentration of 10 µM (Fig. 7.36). After the addition of the compound, cytochalasin D inhibits the rate of actin filament polymerization, leading to the opening of cell junctions and a subsequent reduction of mechanical stability. As a result, the entire spheroid structure is disrupted and

the spheroid body disassembles within the first 24 hours, showing an increased diameter with the loss of the outer rim. For the remaining time, the spheroid continues to collapse, as indicated by a diffuse spheroid-like structure. Throughout the progression, an intrinsic central core of the spheroid is maintained, which is framed by a lighter circle and may indicate the necrotic core region. Additionally, the cell monolayer is affected by cytochalasin D, as indicated by the increasing number of single cells and individual clusters surrounding the spheroid core upon the cell-cell contact's degradation. This effect occurs within the first 12 hours, whereas no further changes are evident afterward.

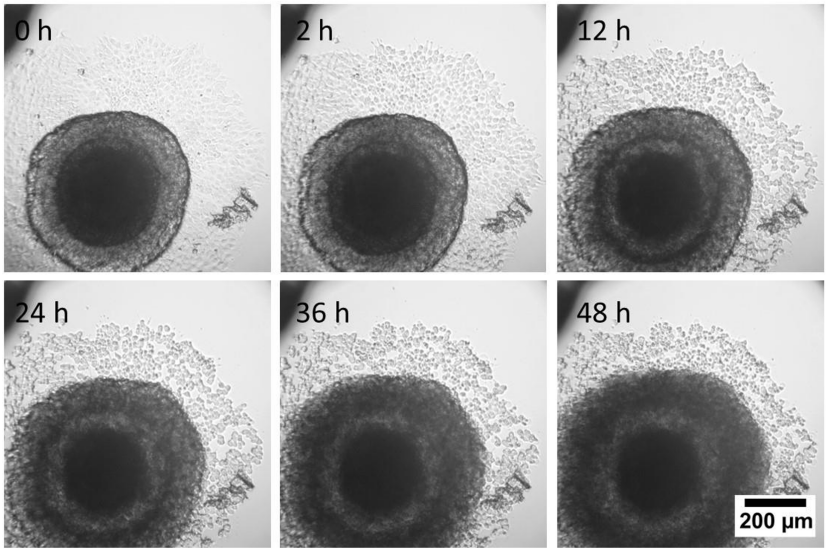

Fig. 7.36 Time-resolved micrographs of the spheroid actin cytoskeleton degradation process after the addition of cytochalasin D solution (10 µM) to MCF-7 spheroid (7 d, 4,000 c/well). Compound addition was performed at time point zero and the process was documented for 48 hours using the zenCELL owl digital microscope. Experiment was performed in a standard cell culture incubator at 37 °C and 0 % CO_2.

For comparison, equivalent but less pronounced morphological changes were observed by exposing U-373 MG spheroids to the identical concentration of 10 µM cytochalasin D, as shown in the time-lapse micrographs (Fig. 7.37). Here, the spheroid diameter begins to increase slowly after compound addition, while the clear outer rim becomes diffuse after the first two hours. No other morphological effect on the spheroid body was observed over the remaining incubation time. In contrast, the cell monolayer is affected within the first 12 hours as evidenced by an increasing separation of the cells through the formation of larger spaces in the cell layer and encapsulation of individual cells from the surface.

In addition, images of spheroids exposed to different concentrations of cytochalasin D for 48 hours were collected (Fig. 7.38 [MCF-7]; see chapter 11.1, Fig. A-7.13 [U-373 MG]). The micrographs show a clear correlation between drug dose and morphological response in MCF-7 cells. The spheroid shape gradually transforms into a diffuse structure and the morphology of the cell monolayer changes from the typical two-dimensional pattern to an increasing number of single cell spots. In contrast, U-373 MG

spheroids display marginal diameter changes with a more pronounced effect on the cell monolayer, showing clear cell disintegration effects with increasing cytochalasin D concentration.

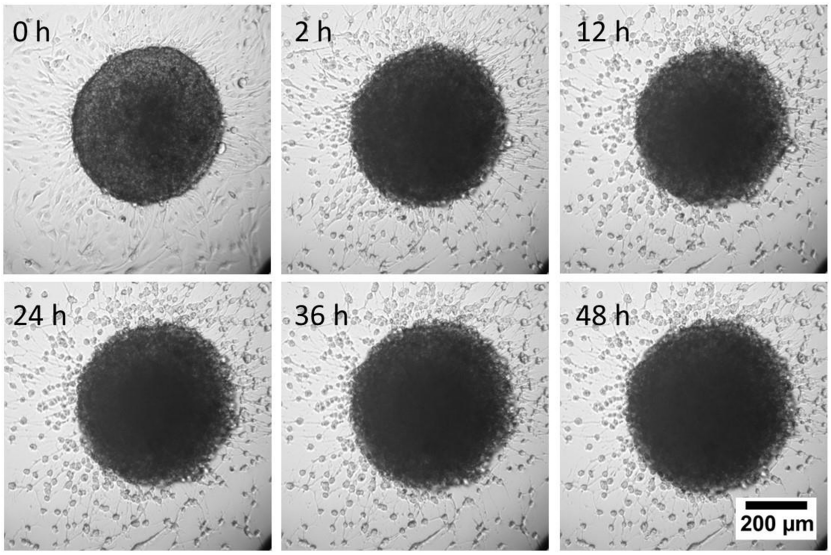

Fig. 7.37 Time-resolved micrographs of the spheroid actin cytoskeleton degradation process after the addition of cytochalasin D solution (10 µM) to U-373 MG spheroid (7 d, 18,000 c/well). Compound addition was performed at time point zero and the process was documented for 48 hours using the zenCELL owl digital microscope. Experiment was performed in a standard cell culture incubator at 37 °C and 0 % CO_2.

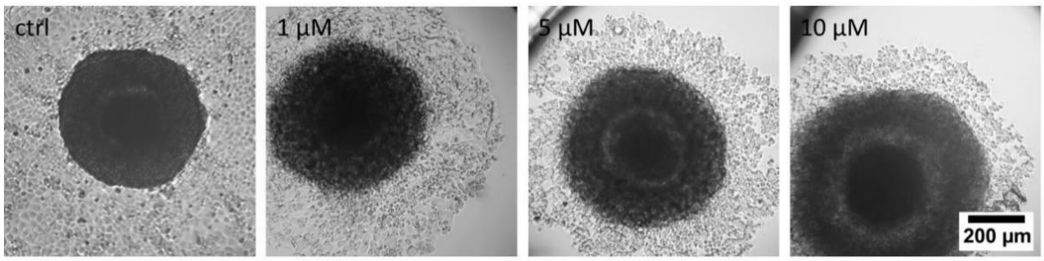

Fig. 7.38 Micrographs of MCF-7 spheroids (7 d, 4,000 c/well) that were exposed to cytochalasin D solution at different concentrations (ctrl | 1 | 5 | 10 µM) and documented 48 hours after the compound addition using the zenCELL owl digital microscope. Experiments were performed in a standard cell culture incubator at 37 °C and 0 % CO_2.

For quantification of the spheroid response, the diameter changes in response to different cytochalasin D concentrations were determined using *ImageJ* software (Rasband, W.S., National Institutes of Health, USA). The results show a dose-dependent effect of the compound that induces a significant increase in the diameter of the MCF-7 spheroid upon spheroid body disruption as observed in the images (Fig. 7.39). While the diameter of the control spheroids shows a steady size increase over time resulting in 104 (± 2) % in total, the spheroid diameter increases with increasing cytochalasin D concentration in a reproducible manner for all conditions, leading to a maximum of 122 (± 2) % (10 µM) after 48 hours. As also displayed in the time-lapse images, the quantification results reflect a less pronounced overall diameter change of cytochalasin D-treated U-373 MG spheroids. The results show

a variable diameter progression for the control spheroids, reaching 101 (± 2) % at 48 hours, and a similar time course with high error bars for each cytochalasin D concentration. Thus, the application of cytochalasin D results in an overall diameter increase of approximately 110 %, which is significant relative to the control condition, but independent of the concentration used.

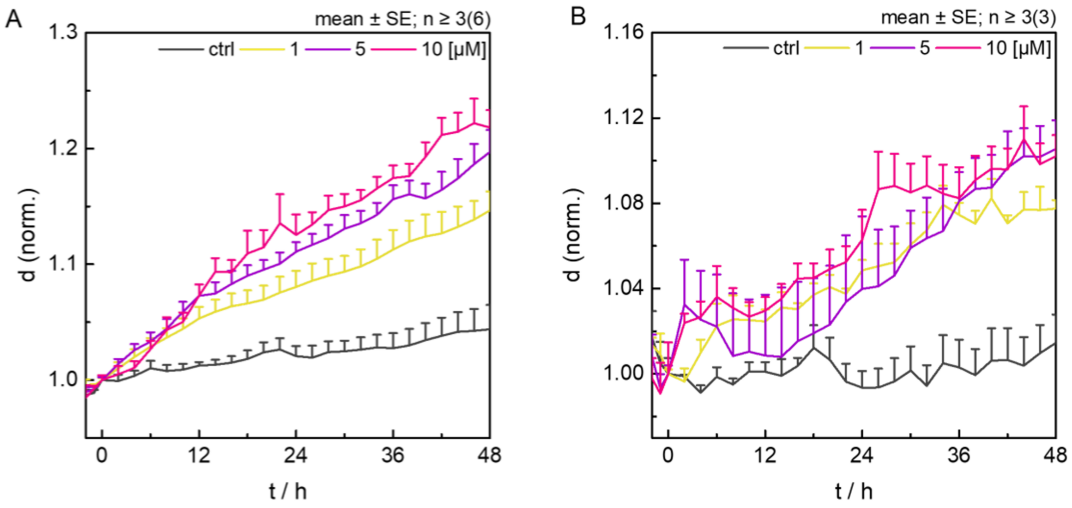

Fig. 7.39 Time course of diameter changes after the addition of cytochalasin D solution with different concentrations (ctrl | 1 | 5 | 10 µM) to MCF-7 (A) and U-373 MG (B) spheroids documented for 48 hours using the zenCELL owl digital microscope. Time courses were normalized with respect to the last data point before compound addition at time point zero. Experiments were performed in a standard cell culture incubator at 37 °C and 0 % CO_2. Data sets were averaged after normalization, mean ± SE; A: n ≥ 3(6); B: n ≥ 3(3).

Overall, the results of the time-resolved microscopy study concerning the influence of cytochalasin D demonstrate a definite effect on spheroid morphology that is dependent on the cell type used. In the case of MCF-7 spheroids, an increase in the concentration of the compound causes a proportional diameter increase induced by an enhanced actin cytoskeleton degradation rate, whereas U-373 MG spheroids are affected to a similar extent regardless of the compound concentration. As a result, the three-dimensional structure of the tissue model is generally disintegrated and disassembled, leading to a diffuse structure.

7.3.5 DISCUSSION: INFLUENCE OF ACTIN CYTOSKELETON DEGRADATION

The influence of actin cytoskeleton degradation on cellular models was investigated in this model study using cytochalasin D as an actin filament polymerization inhibitor. Various experimental approaches such as cell viability assays, impedimetric measurements based on the ECIS™ technique as well as on the channel-based setup reported by the studies of Hupf (Hupf, 2018) and microscopic observations were performed to analyze the cell monolayer and spheroid response. The results are discussed below and provide a comprehensive view of the degradation process in relation to the cell dimensionality.

I CELL VIABILITY EFFECTS

The actin cytoskeletal network plays an important role as a structural element of all eukaryotic cells. Actin filaments are structurally linked to focal adhesions, adherens junctions, and tight junctions by integrins, cadherins, and zonula occludens proteins, respectively, and are thus involved in cell-matrix and cell-cell adhesion processes (Hynes, 1987; Takeichi, 1990; O´Connor et al., 2010). This network dominates the mechanical properties of cells such as cell stiffness and shape (Elson, 1988), maintains junctional permeability, and is required for biological processes such as cell division and migration (Stevenson and Begg, 1994; Gunning et al., 2005; Yamaguchi and Condeelis, 2007). To manipulate this cellular network, the fungal toxin cytochalasin D is used, which is a well-known membrane-permeable drug that causes actin cytoskeleton degradation. The toxicological effect of cytochalasin D on cells initially results from a direct interaction of the drug with the actin filament component, affecting the dynamic treadmilling process of actin monomer assembly and disassembly, and subsequent cellular response. Cytochalasin D specifically binds to the barbed, fast-growing end of filamentous actin, thereby inhibiting the association of actin subunits (Yahara et al., 1982). As a result of actin polymerization inhibition, the ordered actin cytoskeletal network disintegrates, and monomeric actin molecules aggregate. In this way, the stiffness of individual cells and entire cell layers is reduced, and several important cellular processes are inhibited, promoting ferroptosis (Stevenson and Begg, 1994; Wakatsuki et al., 2001). Ferroptosis is an intracellular iron-dependent form of programmed necrotic cell death characterized by an imbalance in the redox state with increased levels of intracellular reactive oxygen species and enhanced amounts of Fe^{2+} ions (Dixon et al., 2012; Zhang et al., 2022). As a result, Ren et al. proposed that high lipid peroxidation and loss of redox state balance induces membrane distortion, leading to cell permeabilization and numerous other perturbations in biological systems, which are still not fully characterized (Ren et al., 2021). However, recent studies are considering the use of cytochalasin D as an additive to current chemotherapy treatments since the compound appears to preferentially damage malignant cells while showing minimal effects on normal epithelial and immune cells (Trendowski, 2015; Zhang et al., 2022).

To determine the cytotoxic effect induced by cytochalasin D on the cell types examined in this thesis, the PrestoBlue™ cell viability assay was performed and the EC_{50} values were calculated (chapter 7.3.1).

➔ The cell viability assay revealed similar, not significantly different EC_{50} values for MCF-7 spheroids exposed to cytochalasin D for either five or 10 hours.

Since the cytotoxicity index changes in a dose-dependent manner without approaching the limit of 100 % dead cells, the EC_{50} value is more appropriate as an indicator of the concentration required to

induce a 50 % cellular response without triggering cell death – at least in the short term. This assumption is also supported by the fact that the overall level of the cytotoxicity index is reduced after 10 hours of incubation compared to five hours, implying a certain degree of regeneration. Accordingly, the EC_{50} values displayed an increase from 0.7 (± 0.3) µM at five hours to 1.0 (± 0.3) µM at 10 hours, indicating reduced cell cytotoxicity at longer incubation times. In the literature, an EC_{50} value in the range of 83–110 nM was calculated for a kidney fibroblast-like cell line treated with cytochalasin D for 24 hours, showing a tenfold higher cytotoxicity (Radnai et al., 2020). This demonstrates a cell type-dependent difference in response to cytochalasin D, which was also reported by White et al. when examining the influence of the identical compound treatment on different cell types. The studies revealed an induced cell death in primary airway epithelial cells, whereas no persistent effect was observed in canine kidney cells (MDCK), showing complete reversibility upon actin filament disruption (White et al., 2001). It was stated that such differences may be related to variations in the regulation of actin filament integrity or to different responses to focal adhesion disassembly.

In this context, it should be noted that in comparison to the model study of permeabilization, no cell death was induced within 48 hours by applying cytochalasin D to the cells. As investigated by impedimetric and time-lapse imaging experiments, mainly morphological alterations were induced in MCF-7 and U-373 MG cells within the distinct concentration range tested.

II IMPEDIMETRIC CHARACTERISTICS

In addition to the cell viability effects of cytochalasin D, the responses of the monolayer culture and the spheroids were monitored impedimetrically during the degradation process. The time-dependent impedance changes of the cells after the addition of different concentrations of cytochalasin D solution serve as a sensitive indicator of the effect of cytochalasin D and thus as a basis for the evaluation of acute toxicity.

II.A IMPEDIMETRIC CHARACTERISTICS – 2D TISSUE MODELS

For the experiments on the 2D tissue models, cytochalasin D solutions were applied in a concentration range of 0.3–5 µM and the signal changes were analyzed. The MFT measurements for MCF-7 and U-373 MG cells showed significant dose-response dependencies, whereas the calculated variance of increments of the monolayer culture revealed no clear correlation, as described in chapter 7.3.2.

➔ As the compound concentration increases, the impedance decreases.

➔ As the compound concentration increases, the variance of increments increases and decreases above 3 µM cytochalasin D solution.

The analyzed key parameters changed as anticipated. After cytochalasin D addition, the compound diffuses into the cell structure and causes an inhibition of actin polymerization processes. This leads to a degradation of barrier-forming tight junctions and thus to a very rapid loss of the barrier resistance of the cell layer, which further results in less current restriction reported by decreasing impedance values.

In addition, a detected increase in capacitance values may indicate cell detachment after exposure to high cytochalasin D concentrations. However, observations made during the microscopy study demonstrate that the monolayer cells remain largely adherent to the surface whereas the intercellular spaces become larger. Stevenson and Begg observed a similar distinct decrease in the transepithelial electrical resistance upon incubation of canine kidney cell (MDCK-II) cultured as cell monolayers in combination with 4 µM cytochalasin D, which was supported by immunostained actin structures showing distinct disruption of actin (Stevenson and Begg, 1994). In accordance with this finding, Oberleitner, who investigated the effect of cytochalasin D also on MDCK-II monolayer cells using a combined QCM-ECIS setup, found a concentration-dependent decrease in normalized resistance and an increase in capacitance (Oberleitner, 2017). Furthermore, Oberleitner stated that capacitance increases within the first two hours after cytochalasin D stimulation are more likely due to uncovered electrode areas instead of cell detachment (Oberleitner, 2017). Cytochalasin D disintegrates the intercellular tight junctions in association with cellular contraction effects as well as rounding-up of cells (Cooper, 1987), giving rise to high-frequency current pathways. Oberleitner confirmed this assumption by applying saponin to the cytochalasin D-treated monolayer, which induces the actual detachment of the remaining cytoskeleton framework from the surface and reveals cell-free measurement signals (Oberleitner, 2017).

In accordance with a partially covered sensor surface, the calculated variance of increments may not reflect the actual values as assuming a confluent monolayer, and only the trend of increasing and decreasing values can be evaluated. The initial increase represents an enhanced level of cellular micromotion upon cytochalasin D addition, indicating a higher level of cellular dynamic as a response to the induced mechanical manipulation. Since the amount of cytochalasin D available in the cells exceeds a critical concentration (in this case, 3 µM) decreasing values reflect an excessive impact on cell dynamic (see chapter 7.3.2).

As indicated by the discussion of the impairment on cell viability of cytochalasin D, a characteristic concentration-dependent impact on the cells is induced. The results of the PrestoBlue™ assay revealed

lower cytotoxicity values accompanied by a higher EC_{50} value for a longer compound incubation time, which may be related to a significant cytomechanical regeneration. This finding is reinforced by the detected impedance time course of U-373 MG cell monolayer culture exposed to cytochalasin D concentrations of 0.5 µM and 1 µM (Fig. 7.33, B). The signals show a similar profile of an initial decrease in impedance with a subsequent linear increase at different offsets. With this, a cellular over-stimulation in the case of 0.5 µM and a complete reversion to pre-stimulation values in the case of 1 µM is indicated. For reference, Oberleitner also describes a partial compensation of initial tight junction disintegration within 12 hours after adding 0.1 µM cytochalasin D to a confluent MCDK-II monolayer culture (Oberleitner, 2017). By performing cytochemical staining of actin, nearly complete intactness of actin filaments in the cell layers treated with 0.1 µM cytochalasin D for one hour and 25 hours was observed. In contrast, higher concentrations of the compound led to a persistent degradation and Oberleitner found a significant difference in the kinetics of signal decrease between 1 µM and 5 µM cytochalasin D solution, which resulted in similar final values after four hours (Oberleitner, 2017). This finding correlates with the slight decay of the impedance signal decrease detected in the ECIS™ measurements after the addition of 3 µM, 4 µM, and 5 µM cytochalasin D solution, respectively, to the MCF-7 monolayer cells. In accordance, the maximum of the variance of increments calculated for both cell lines at 3 µM concentration is assumed to represent a threshold between temporary and permanent induced manipulation. Similar concentration-dependent effects of cytochalasin D in cell culture were examined by Stevenson and Begg when performing reversibility experiments on MDCK cells (Stevenson and Begg, 1994). After exposing the monolayer cells to various concentrations of cytochalasin D for one hour, the compound was washed out of the cultures and a dose-dependent signal increase in the recorded transepithelial electrical resistance was detected, returning to control conditions (Stevenson and Begg, 1994).

For further data evaluation, the area under the curve of the normalized impedance data within a defined time range was calculated, normalized to the control condition, and plotted as a function of the logarithmic concentration for each cell type (Fig. 7.40). The AUC values indicate the level of cytochalasin D impact where low AUC values correlate with enhanced actin cytoskeleton degradation. Both cell types show similar results as the AUC values decrease with increasing cytochalasin D concentration. Initially, the data show a plateau up to a concentration of 0.5 µM, followed by a steady decrease to lower values corresponding to a loss in the barrier resistance of the cell layer and an accompanied contraction of cells.

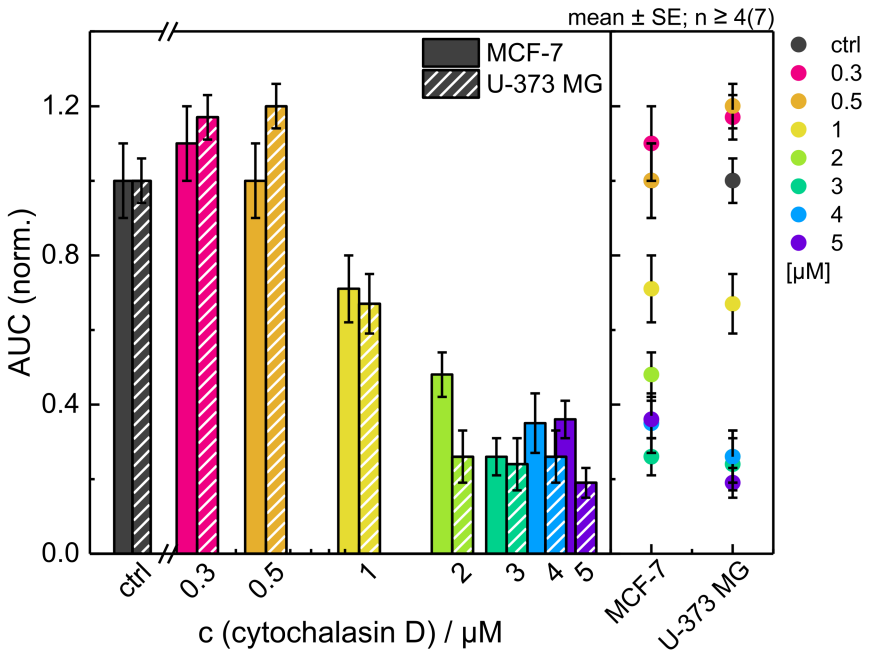

Fig. 7.40 Overview of the normalized results of the area under the curve values derived from the time course of normalized impedance magnitude at 4,000 Hz of MCF-7 and U-373 MG cell monolayer cultures (Fig. 7.33). For integration, a baseline was set at 55 % (MCF-7) respectively 74 % (U-373 MG) of the normalized impedance, and the values were determined within 12 hours after the addition of cytochalasin D solutions with different concentrations in a range of 0.3–5 µM. After averaging, data sets were normalized to the control condition, mean ± SE, n ≥ 4(7). An overview of the distribution of the results is presented in the scatter plot. Significance was determined by a two-sample t-test between the cell types using a significance level of 0.1 (*), 0.05 (**), and 0.01 (***). As a result, a high significance level of 0.01 (***) is determined between the cell types for the cytochalasin D concentrations of 0.5 µM, 2 µM, and 5 µM, while no significant values ($^{n.s.}$) were obtained at the other concentrations (symbols not shown in the graph).

An overview of the results for both cell types is shown in the scatter plot (Fig. 7.40). For MCF-7 and U-373 MG cells, a sigmoidal dose-response profile over the whole concentration range is observed, starting from the reference level at 100 %, in the middle at approximately 70 %, and for higher concentrations above 1 µM at the lowest level at approximately 30 %. The significance between the AUC values of the MCF-7 and U-373 MG monolayer cultures was calculated using a two-sample t-test, which revealed a high significance level of 0.01 (***) between the cell types for the cytochalasin D concentrations of 0.5 µM, 2 µM, and 5 µM, while no significant values ($^{n.s.}$) were obtained at the other concentrations.

Based on the calculated AUC values, a dose-response curve was plotted as a function of cytochalasin D concentration for each cell line, and EC_{50} values were determined using the sigmoidal Boltzmann equation (see chapter 11.1, Fig. A-7.14; chapter 4.1.8, Eq. 4.2). The mean EC_{50} values were calculated revealing not significantly different values of 1.1 (± 0.5) µM (MCF-7; R^2 = 0.96; mean ± SE; n ≥ 4(7)) and 1.0 (± 0.2) µM (U-373 MG; R^2 = 0.98; mean ± SE; n ≥ 4(8)) in monolayer culture.

II.B IMPEDIMETRIC CHARACTERISTICS – 3D TISSUE MODELS

For a comprehensive impedimetric characterization, the effect of actin cytoskeleton degradation was also analyzed by the response of spheroids. As stated, based on the proof-of-principle experiment, the assay could not be performed with the funnel-based measurement setup since interference with either cytochalasin D-induced signal changes and the detected impedance increase due to the spheroid passing through the funnel opening and subsequent disruption of the testimonial body made the signal acquisition of the raw spheroid response to actin cytoskeleton degradation unfeasible. A workaround using spheroid fixation, as used in the membrane perforation model study (chapter 7.2), was not practical since the cytochalasin D reaction only occurs in viable cells respectively regions of active actin polymerization. Thus, the results reported by Hupf using the channel-based measurement setup are included in this model study (Hupf, 2018).

Hupf performed assays by incubating spheroids in 5 µM cytochalasin D solutions for different incubation times between two and eight hours. The experiments showed that the time course of impedance magnitude is constantly increasing for all conditions of cytochalasin D-treated spheroids, while the total change in impedance magnitude decreased with increasing exposure periods to cytochalasin D (Hupf, 2018). In terms of cellular dynamic, the micromotion of the spheroids showed similar fluctuation rates after different incubation durations, with the exception of an increased signal fluctuation of spheroids incubated for two hours. Based on the analysis of the results, Hupf stated that measurable but subtle alterations were found (Hupf, 2018). However, the results did not reflect the intended typical alterations and tendencies such as reduced cell stiffness as well as a decreased resistance in comparison to a control as observed in monolayer cultures by Oberleitner as well as Stevenson and Begg (Oberleitner, 2017; Stevenson and Begg, 1994). Instead, higher impedance values accompanied by increased spheroid resistance values were observed in relation to the control spheroid, especially after two hours of incubation time (Hupf, 2018). Further, the RTC measurement performed revealed similar micromotion activity whereas a dose-dependent fluctuation decrease is expected based on reduced actin polymerization rates as reported by Lo et al. and Opp et al. (Lo et al., 1993; Opp et al., 2009). Since a reduced spheroid stiffness was indicated by the strong penetration into the aperture compared to the control spheroid, this effect also contributed to the recorded slow but constant increase in impedance over time (Hupf, 2018). Therefore, Hupf discussed potential signal interference with a possible decrease in impedance due to cytochalasin D-induced actin degradation and proposed a delayed spheroid response due to limited diffusion of the compound into the spheroid body, indicating that actin filament degradation may only have occurred in the outer cell layers of the spheroid (Hupf, 2018).

Based on this, and in combination with the findings of the funnel-based measurement, Hupf's results are critically reviewed. Similar to the proof-of-principle experiment using the funnel-based assay, the reduction in cell stiffness induced by cytochalasin D was also confirmed using the flow channel-based assay. However, due to the progressive penetration of the spheroids, the final body disruption, and the contraindicative findings of Hupf, no further conclusions can be drawn, making both measurement setups inappropriate for this model study. Thus, no continued data analysis and discussion are provided in this context, as no similar experiments using spheroid models are found in the literature.

III MORPHOLOGICAL PROPERTIES

The influence of cytochalasin D was also studied regarding the morphological properties of spheroids by performing time-lapse imaging using the zenCELL owl digital microscope. To this end, experiments were performed with cytochalasin D solutions at concentrations in a range of 1–10 µM, and the cellular response was observed for 48 hours. Based on the analysis of the recorded time-resolved images, a clear dose-response dependency for both cell types used is displayed, as shown in chapter 7.3.4.

➔ As the compound concentration increases, the diameter of the MCF-7 and U-373 MG spheroids increases, and the entire three-dimensional cell assembly disintegrates.

On exposure to cytochalasin D, the morphology of the spheroid bodies changes as expected. The measured spheroid diameter showed significant alterations by increasing values over time with respect to the control condition. As the concentration of the compound increases, a proportional increase in actin cytoskeleton degradation is induced, leading to a gradual reduction in cytomechanical stiffness and functional integrity of the barrier-forming tight junctions within the three-dimensional structure of the tissue model (Yahara et al., 1982; Stevenson and Begg, 1994). This can be seen in the time-resolved images as the spheroid body is disassembled and the remaining spheroid-like structure becomes progressively more diffuse. The time course of the normalized diameter shows a gradual value increase, which exhibits – in the case of MCF-7 spheroids – a dose-dependent kinetic. Since a morphological change of U-373 MG spheroids is rather apparent, a similar time-dependent diameter increase was investigated regardless of the cytochalasin D concentration applied. In total, relative diameter increases of 122 (± 2) % (MCF-7) and 110 (± 2) % (U-373 MG) were reached at the highest compound concentration of 10 µM (compare Fig. 7.39). The difference between the two cell types in terms of a more pronounced and visible effect on MCF-7 spheroids compared to U-373 MG spheroids may contribute to the increased number of cells in the latter tissue model. Thus, the diffusion and efficacy of the same concentration of cytochalasin D may be limited by denser packed cell layers and thus confined to the outer spheroid region. Furthermore, MCF-7 cells express a higher number of tight

junctions and are therefore more sensitive and accessible compared to U-373 MG cells by providing a higher number of cytochalasin D binding sites (Paterson et al., 2003; Lewis-Tuffin et al., 2010).

In general, the results of cellular effects on 3D tissue models are similar to the literature, as Wakatsuki et al. reported the disruption of almost all long actin filaments in combination with a significantly reduced stiffness of a fibroblast-populated 3D matrix exposed to 2 µM cytochalasin for 30 minutes (Wakatsuki et al., 2001). As mentioned previously, Hupf's findings also relate to a reduced mechanical stiffness of MCF-7 spheroids, which migrated almost completely into the narrowing aperture after exposure to 5 µM cytochalasin D for at least two hours (Hupf, 2018). In addition, a fluorescence staining assay of f-actin in cytochalasin D treated MDCK-II cell monolayer culture demonstrated that incubation with 5 µM cytochalasin D led to the degradation of filamentous actin into clump-like aggregates scattered in the cytoplasm and along the former actin belt around the cells, as well as to the formation of large intercellular openings (Oberleitner, 2017).

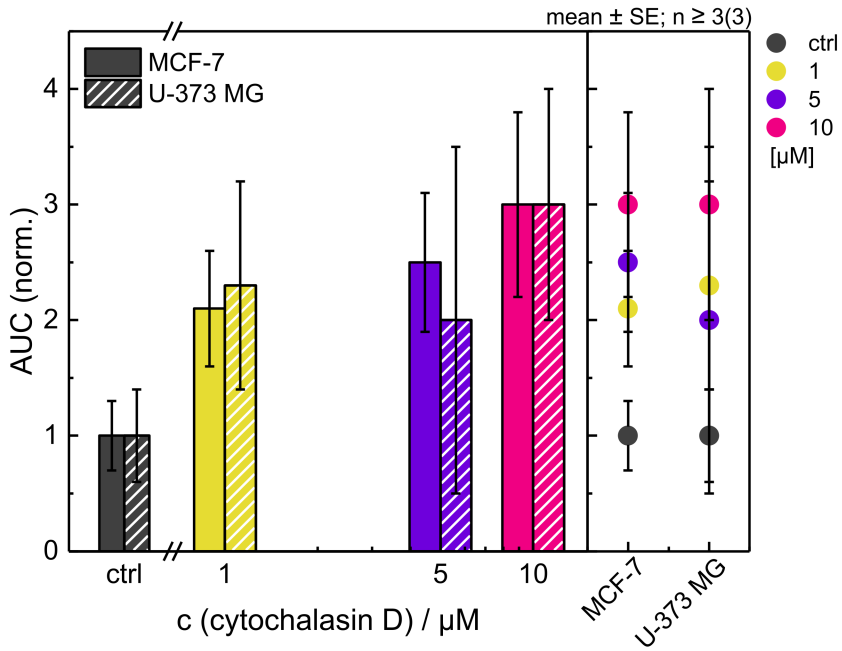

Fig. 7.41 Overview of the normalized results of the area under the curve values derived from the time course of diameter changes of MCF-7 and U-373 MG spheroids documented using the zenCELL owl digital microscope (Fig. 7.39). For integration, a baseline was set at 98 % (MCF-7; U-373 MG) of the normalized diameter, and the values were determined within 24 hours after the addition of cytochalasin D solutions with different concentrations (ctrl | 1 | 5 | 10 µM). After averaging, data sets were normalized to the control condition, mean ± SE, n ≥ 3(3). An overview of the distribution of the results is provided in the scatter plot. Significance was determined by a two-sample t-test between the cell types using a significance level of 0.1 (*), 0.05 (**), and 0.01 (***). As a result, no significant values ($^{n.s.}$) were obtained (symbols not shown in the graph).

To derive additional information, the area under the curve of the time course of the normalized diameter was calculated for each cell type within 48 hours of exposure to cytochalasin D and plotted as a function of concentration (Fig. 7.41). High AUC values correlate with the level of actin degradation,

demonstrating a dose-response relationship with increasing compound concentration for both cell types. In total, a stepwise increase of the normalized AUC values of approximately 200 % (1 µM) to 300 % (10 µM) was calculated. For U-373 MG spheroids, the low reproducibility of the cellular response to cytochalasin D is reflected by the height of the error bars, which corresponds to the similar time course regardless of the concentration applied, whereas for MCF-7 spheroids a more definite difference is given. This is also displayed by the significance between the AUC values of the MCF-7 and U-373 MG spheroids calculated using a two-sample t-test, which revealed no significance between the cell types, irrespective of the compound concentration applied.

Based on the AUC values, the EC_{50} values were calculated for each cell type and determined as 2.1 (± 0.5) µM (MCF-7; R^2 = 0.79; mean ± SE; n ≥ 3(6)) and 1.7 (± 0.4) µM (U-373 MG; R^2 = 0.74; mean ± SE; n ≥ 3(3)), which are not significantly different to each other (see chapter 11.1, Fig. A-7.15). Since only four values were taken into account, the sigmoidal fit is not as precise, and the results should be interpreted with caution.

7.3.6 SUMMARY OF THE MODEL STUDY OF ACTIN CYTOSKELETON DEGRADATION

The cellular response to actin cytoskeleton degradation was characterized in this model study by the use of cytochalasin D. Several experimental approaches were examined, whereby the funnel-based measurement was shown to not be applicable for recording impedance signal changes of cytochalasin D-treated spheroids. It was found that the effect of induced spheroid penetration into the central opening interfered with the actual signal response to the compound applied, while the observed final body collapse demonstrated that the measurement setup was inappropriate. The identical conclusions were obtained based on the results reported by Hupf using the channel-based setup, and thus no impedimetric measurements could be performed in this model study (Hupf, 2018). Therefore, detailed data evaluation was based on cell viability assays performed with MCF-7 spheroids, impedimetric measurements of cell monolayer culture, and time-lapse imaging using spheroids considering the following statements depending on the cell type.

- ➔ The cell viability assay revealed not significantly different EC_{50} values for MCF-7 spheroids exposed to cytochalasin D for either five or 10 hours.
- ➔ The impedance decreases with increasing cytochalasin D concentrations applied to 2D tissue models, regardless of the cell type.
- ➔ The cellular micromotion respective the variance of increments of 2D tissue models initially increases and decreases above 3 µM cytochalasin D solution, regardless of the cell type.

- ➔ The impedance time course in 2D tissue models, as well as the increased EC_{50} values in cell viability assays with longer incubation times, indicate a certain regeneration level from the affected state.
- ➔ The diameter of the spheroids increases with increasing cytochalasin D concentration in either a dose-dependent manner for MCF-7 spheroids by leading to an entire spheroid disintegration or in a concentration-independent way by exhibiting subtle morphological changes using U-373 MG spheroids.

In order to highlight differences and similarities in the cellular responses obtained from monolayer culture and spheroids, the results obtained from different assay approaches were summarized in one key value. Several dose-response curves were generated from the analyzed area under the curve values or calculated cytotoxicity values, and EC_{50} values were determined using the sigmoidal Boltzmann equation (chapter 4.1.8, Eq. 4.2). The calculated values are summarized for each experimental setup and listed in relation to the cell monolayer and spheroid models tested (Tab. 7.12).

Tab. 7.12 Overview of the EC_{50} values of cytochalasin D determined using the PrestoBlue™ cell viability assay, impedance measurements, and time-lapse observations. The coefficient of determination is given in the table respectively for each experiment. The results are categorized by cell type and cell dimensionality, respectively. Detailed experimental conditions are given in the respective raw data information (chapter 7.3.1; chapter 7.3.5).

EC_{50} [µM]	MCF-7		U-373 MG	
	2D	3D	2D	3D
PrestoBlue™ assay	/	5 h: 0.7 ± 0.3 R^2 = 0.73 10 h: 1.0 ± 0.3 R^2 = 0.45	/	/
impedance measurements	1.1 ± 0.5 R^2 = 0.96	/	1.0 ± 0.2 R^2 = 0.98	/
time-lapse observation	/	2.1 ± 0.5 R^2 = 0.79	/	1.7 ± 0.4 R^2 = 0.74

Upon the application of cytochalasin D to cell culture, the cytomechanical stiffness and the functional integrity of barrier-forming tight junctions are affected while ferroptosis as programmed cell death is induced. As revealed from the literature and in coherence with the investigations conducted in the model study, the persistent or reversible impact of cytochalasin D is determined by the applied dose, exhibiting a distinct regeneration level at lower concentrations. In the cellular experiments performed

in this thesis, only morphological changes of the cell network and the cytoskeleton were obtained with respect to the concentration range and within the maximum incubation time of 48 hours tested. Accordingly, in the model study of actin cytoskeleton degradation, the EC_{50} value corresponds to the concentration of the tested substance causing 50 % changes in response and not to a reduction in cell viability as in the case of using, e.g., the permeabilization compound saponin (see chapter 7.2.1).

The EC_{50} values obtained from the PrestoBlue™ assay highlight the previously discussed reversible influence by revealing an increase in the concentration that is necessary for a cellular response from 0.7 (± 0.3) µM after five hours of incubation to 1.0 (± 0.3) µM after 10 hours. In addition, a reduced overall level of the cytotoxicity index was shown. For the cell monolayer culture, EC_{50} values were obtained from the impedance measurements performed, providing similar concentration values of 1.1 (± 0.5) µM (MCF-7) and 1.0 (± 0.2) µM (U-373 MG). In contrast, the values derived from time-lapse observations of spheroids revealed twofold higher values for both cell types in the range of 2.1 (± 0.5) µM (MCF-7) and 1.7 (± 0.4) µM (U-373 MG). Since the interpretation of the values may be biased by the results of the impedance measurement, it should be emphasized again that only four concentrations were used for the determination of the EC_{50} values in terms of time-lapse observation experiments. However, as the concentration levels of the impedance measurements and the PrestoBlue™ assay are similar with respect to the individual errors, a range for the effective concentration of cytochalasin D has to be considered.

As no further studies were performed and taken into account, it is stated that (i) the EC_{50} value concerning the cytochalasin D effective concentration is in the range of approximately 1–2 µM, regardless of the cell dimensionality studied, and that (ii) no cell type-dependent difference was observed between the MCF-7 and U-373 MG cells. Due to limited data availability, no further compilations in terms of the *activity level* were made.

In summary, the findings indicate that changes in cellular morphology due to cytochalasin D exposure were detected in a dose-dependent manner, in accordance with the gradual rate of inhibiting the actin polymerization appearing reversibly or persistently. This model study included the performance of several assays that provided a comprehensive overview of the effects of the compound from different perspectives, such as cytotoxic specification, impedimetric characterization, and morphological properties. Even though the experiments could be performed using either cell monolayer cultures or spheroids, the limitations of the newly developed impedance measurement setup were investigated. After a detailed analysis of the data, the results were summarized in a key value, in this case, the EC_{50} value obtained for each experimental approach, showing either differences or similarities in the overall context. The influence of cytochalasin D on cellular response was confirmed by equally affecting

monolayer cultures and spheroids, regardless of the cell type from which they were derived. These results highlight that (i) actin cytoskeleton degradation has a fundamental effect at the subcellular level, and (ii) the combination of different assays provides a comprehensive view of the cellular response induced.

7.4 MODEL STUDY: CELLULAR RESPONSE TO OSMOTIC PRESSURE

The model study to investigate the response to osmotic pressure in tissue models was carried out by using hyperosmolar buffer solutions. Solutions of varying osmolality were prepared by adding different amounts of sucrose and applied to the 2D and 3D tissue models. This determines the osmotic gradient of the cells, forcing water to flow from the cell inside to the outside. As a result, cell shrinkage is induced, which is associated with an increase in cytoplasmic viscosity and thus cell stiffness, thereby mimicking the initial features of necrotic cell death (Periasamy et al., 1992).

In order to compare the cellular response as a function of the dimensionality of the *in vitro* model, the tissue models were exposed to hyperosmolar buffer solutions with similar final osmolalities. The effect was studied and evaluated in detail using impedimetric and time-lapse analysis. To avoid conductivity alterations by compound addition, the conductivity of each sucrose buffer solution was adjusted to that of the isoosmotic buffer without sucrose.

7.4.1 IMPEDIMETRIC ANALYSIS OF THE CELL MONOLAYER

The influence of osmotic pressure on cell monolayer cultures derived from MCF-7 and U-373 MG cells was analyzed by performing ECIS™ measurements. In this assay, hyperosmolar buffer solutions with a final sucrose concentration in the range of 20–500 mM were used similarly to the spheroid model studies. The osmolalities of these solutions were already provided in chapter 4.1.7 (see Tab. 4.5). Upon exposure to different osmolalities, the changes in cellular properties were recorded by measurements in MFT mode and the corresponding variance of increments was calculated at different sucrose concentrations.

As the cellular response generally occurs within a short time, the MFT measurements were only recorded within a period of 90 minutes after compound addition. The normalized impedance magnitude at 4,000 Hz is shown for both cell types, indicating a clear dose-response dependence of sucrose concentration on the kinetics of the cellular properties' alteration. With increasing signal values, an increasing cellular expansion is reflected.

In the case of MCF-7 cells (Fig. 7.42, A), the responses of the isosmotic control and the two lowest concentrations of 20 mM and 50 mM show a similar, unaffected signal course, resulting in 95.4 (± 0.2) % (ctrl) after 90 minutes. The impedance curve after the addition of the 100 mM, 200 mM, and 300 mM sucrose solutions displays a signal increase reaching a higher value with increasing concentration. While the signal for the 100 mM solution exhibits a delayed signal rise after 10 minutes and a baseline at

109.3 (± 0.1) % (100 mM) within 30 minutes, the signal response of the two higher concentrated buffer solutions is less retarded. Within the time period of measurement, either a plateau at 141 (± 3) % (200 mM) or a continuing constant increase to a maximum magnitude of 163 (± 2) % (300 mM) is shown. In contrast, the total impedance changes are reduced for compound concentrations of 400 mM and 500 mM. Both solutions lead to an initial concentration-dependent signal decrease followed by an increase to 120 (± 2) % (400 mM) and 96.4 (± 0.1) % (500 mM) similar to the isosmotic control condition. As a result, the signal increases more rapidly with increasing osmolality up to a concentration of 300 mM, reflecting faster cell expansion, whereas less pronounced impedance changes were observed at higher sucrose concentrations respectively osmolality values.

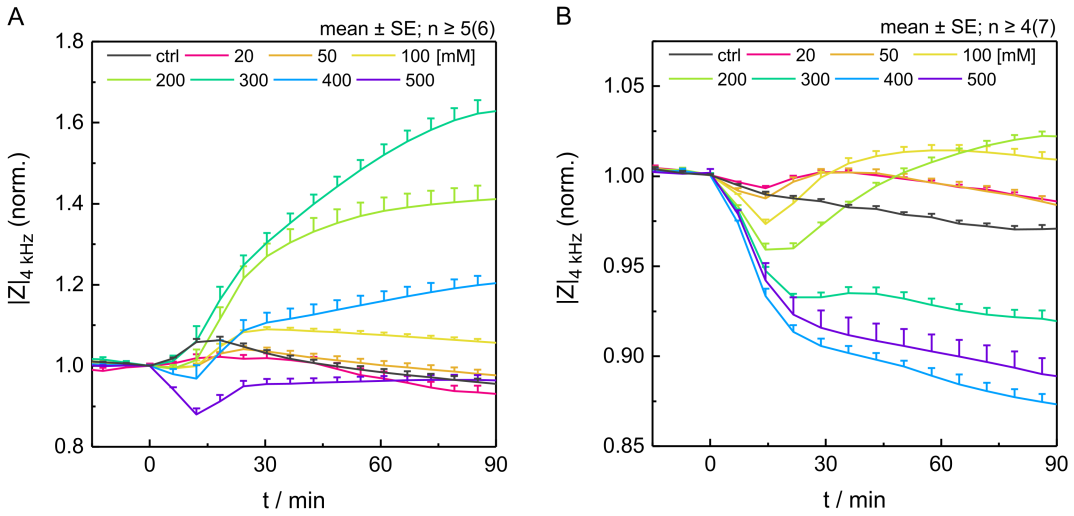

Fig. 7.42 Time course of normalized impedance magnitude at 4,000 Hz of MCF-7 (A) and U-373 MG (B) cell monolayer cultures after the addition of different hyperosmotic buffer solutions in a range of 20–500 mM. Time courses were normalized with respect to the last data point before compound addition at time point zero. Experiments were performed in a standard cell culture incubator at 37 °C and 0 % CO_2 using 8W10E arrays. Data sets were averaged after normalization, mean ± SE; A: n ≥ 5(6); B: n ≥ 4(7).

In comparison, an equivalent impedance time course was found for the U-373 MG cell monolayer, which also reflects a concentration-dependent delay time of the signal responding to the applied sucrose solutions (Fig. 7.42, B). Since the signal from the control condition is constantly decreasing to 96.8 (± 0.2) % (ctrl), the addition of the two lowest concentrations of 20 mM and 50 mM leads to an identical signal course resulting in approximately 98 %. For sucrose solutions in the concentration range of 100–500 mM, a dose-dependent impedance decrease was observed, which is followed by a signal increase for 100 mM and 200 mM or displays a constantly drifting baseline according to the control condition for higher concentrations. By using a buffer solution of 500 mM sucrose concentration, a minimum of 88.1 (± 0.9) % (ctrl) is reached. In summary, the impedance magnitude decreases with increasing sucrose concentration while indicating a signal regeneration for solutions up to 200 mM.

Overall, significant and reproducible signal variations were observed as a function of compound concentration, inducing certain degrees of changes in cellular properties. By modulating the cell diameter and thus the viscosity of the monolayer, different levels of osmotic pressure were reflected. Depending on the cell type used, an ascending signal trend was found for MCF-7 cells, whereas a descending trend was observed for U-373 MG cells. In both cases, a critical concentration of 300 mM (MCF-7) and 200 mM (U-373 MG) was considered at which the signal curve showed a characteristic time course transition. The difference in the relative impedance values between the two cell types is caused by the low sensitivity of the ECIS™ measurements for U-373 MG cells since the standardized monitoring frequency of 4,000 Hz was used for comparison. In addition, it should be noted that the time course of the capacitance shows no signal changes in the case of MCF-7 cells, whereas a slight signal increase over time, and thus cellular detachment of a small fraction from the electrode surface, is displayed after applying 400 mM or 500 mM sucrose solution to U-373 MG cells (data sets not shown in this thesis).

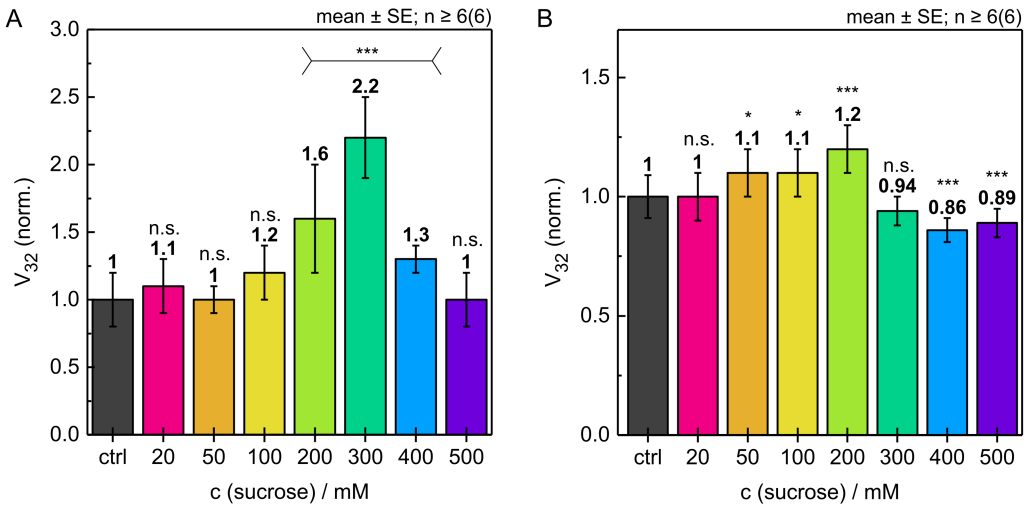

Fig. 7.43 Normalized variance of increments of impedance fluctuations after segmented detrending measured 90 minutes after the addition of different hyperosmotic buffer solutions in a range of 20–500 mM to MCF-7 (A) and U-373 MG (B) cell monolayer cultures. Significance was determined relative to the control condition by a two-sample t-test using a significance level of 0.1 (*), 0.05 (**), and 0.01 (***). Data sets were averaged after segmented detrending, mean ± SE; n ≥ 6(6).

From RTC measurements taken 90 minutes after compound addition (data sets not shown in this thesis), the variance of increments was calculated for all concentrations by performing segmented detrending using a time interval of 32 s. The results for both cell types were normalized to the control condition and the results show a similar dose-dependent pattern (Fig. 7.43). Initially, the variance of increments increases stepwise with a maximum value of 220 (± 30) % at a concentration of 300 mM for MCF-7 cells and 120 (± 10) % for U-373 MG cells at a concentration of 200 mM. This reflects the critical concentration as indicated by the time course measurements. At higher concentrations, the variance of increments is reduced and presents relative values of 100 (± 20) % (MCF-7) and 89 (± 6) % (U-373 MG)

at a sucrose concentration of 500 mM. A two-sample t-test shows that there is high significance (***) for all results relative to the control condition within a concentration range of 200–400 mM determined for the MCF-7 cell monolayer, whereas in the case of U-373 MG cells, only the maximum at 200 mM and the values at 400 mM and 500 mM are highly significant (***) with respect to the isosmotic variance of increments. Significance values between concentration levels were not calculated.

Overall, the ECIS™-based measurements revealed an enhancement of osmotic pressure as represented by changes in impedance values, which reflect either cell shrinkage or expansion as a function of sucrose concentration. However, no proportional dose-response relationship was identified from the impedance analysis since a critical concentration of 300 mM and 200 mM was observed at which the tendencies of either increasing values of the variance of increments or ascending/descending time course profiles changed. It should be noted that the analysis of cellular micromovement is less sensitive with the use of 8W10E electrodes due to the large electrode area.

7.4.2 IMPEDIMETRIC ANALYSIS OF THE SPHEROID

The impedimetric analysis of the spheroid response to induced osmotic pressure was measured using the funnel-based measurement setup. For these experiments, hyperosmolar buffer solutions with a final sucrose concentration in the range of 20–200 mM were used. The osmolalities of these solutions were given in chapter 4.1.7 (see Tab. 4.5). Thus, spheroids at different physiological stages were generated and the results provide comparability with cell monolayer cultures by using similar final osmolalities. The spheroid response was recorded impedimetrically using both MFT and RTC mode measurements to detect changes in cell dynamic and, additionally, the influence on spheroid dielectric properties was calculated.

The MFT mode measurements provide the time course of the impedance magnitude, normalized and plotted at 200 Hz over 90 minutes after compound addition (Fig. 7.44). A clear dependence of the sucrose concentration on the induced osmotic pressure is reflected by the generation of distinct morphological changes for both MCF-7 and U-373 MG spheroids. In general, a decreasing signal value indicates a less restricted current flow influenced by an overall shrinkage of the spheroid body. For MCF-7 spheroids (Fig. 7.44, A), no signal changes were observed for the control condition despite a small initial increase due to substance addition. At the lowest concentration of 20 mM, the impedance initially increases by 120 (± 10) % at time zero, followed by a biphasic downward and upward signal shift by reaching the level of the isosmotic control condition. The concentration of 100 mM sucrose solution caused an impedance signal drop to 33 (± 4) % directly after compound addition, while a signal

regeneration to almost isosmotic values is observed within 90 minutes. After application of the highest concentration of 200 mM, a similar signal decrease is displayed with a progressive signal increase towards 18 (± 2) % after 90 minutes. In the case of U-373 MG spheroids, a similar impedance time course was examined, showing identical signal tendencies with less pronounced minima and maxima values (Fig. 7.44, B). The kinetics of signal regeneration by the addition of 100 mM or 200 mM sucrose solution appears to be faster with respect to MCF-7 spheroids, with a significantly higher rate of signal increase occurring at 100 mM. In general, the impedance signal decays more rapidly with increasing compound concentration, indicating a higher impact on spheroid physiology and morphology. In addition, a certain rate of regeneration is displayed for both cell types.

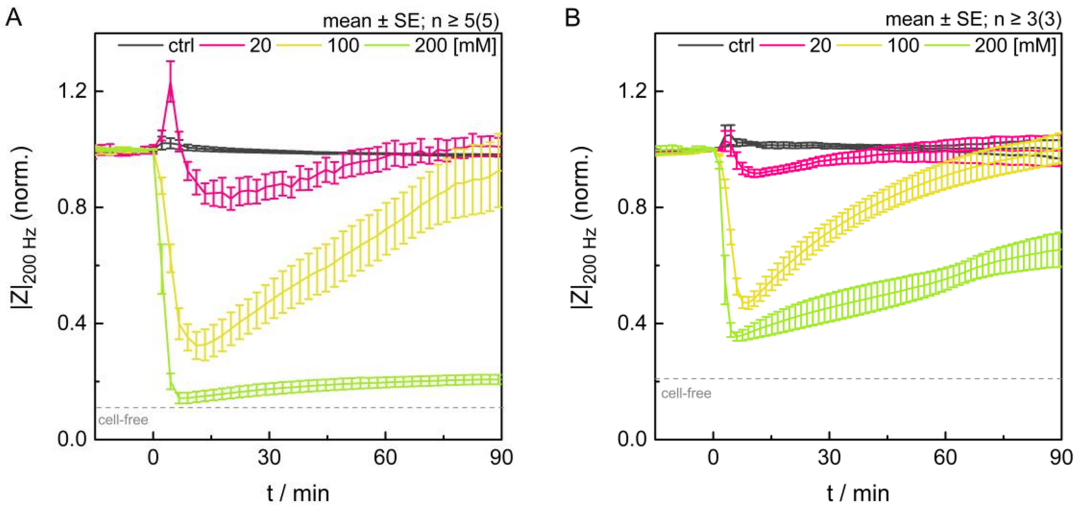

Fig. 7.44 Time course of normalized impedance magnitude at 200 Hz of MCF-7 (A) and U-373 MG (B) spheroids after the addition of different hyperosmotic buffer solutions (ctrl | 20 | 100 | 200 mM). Time courses were normalized with respect to the last data point before compound addition at time point zero. Grey horizontal lines in A and B indicate mean values of spheroid-free micro-traps. Experiments were performed in a standard cell culture incubator at 37 °C and 0 % CO_2. Data sets were averaged after normalization, mean ± SE; A: n ≥ 5(5); B: n ≥ 3(3).

To investigate the influence of osmotic pressure on the micromotion activity of the cells and hence on cell dynamic, high time resolution measurements were analyzed. A dose-response effect is observed in the plots of the detrended RTC data for each sucrose concentration and, in a similar way, for both cell types used. The cellular fluctuations in MCF-7 spheroids (Fig. 7.45) and U-373 MG spheroids (see chapter 11.1, Fig. A-7.16) display a stepwise amplitude increase, exhibiting the maximum range of approximately -200–200 Ω (MCF-7) respective -10–10 Ω (U-373 MG) at a concentration of 100 mM. After application of the highest sucrose concentration of 200 mM, a significant decrease in micromotion activity is observed for both cell types, as reflected by the RTC signal oscillating with a total amplitude range similar to the isosmotic control condition (Fig. 7.45, D).

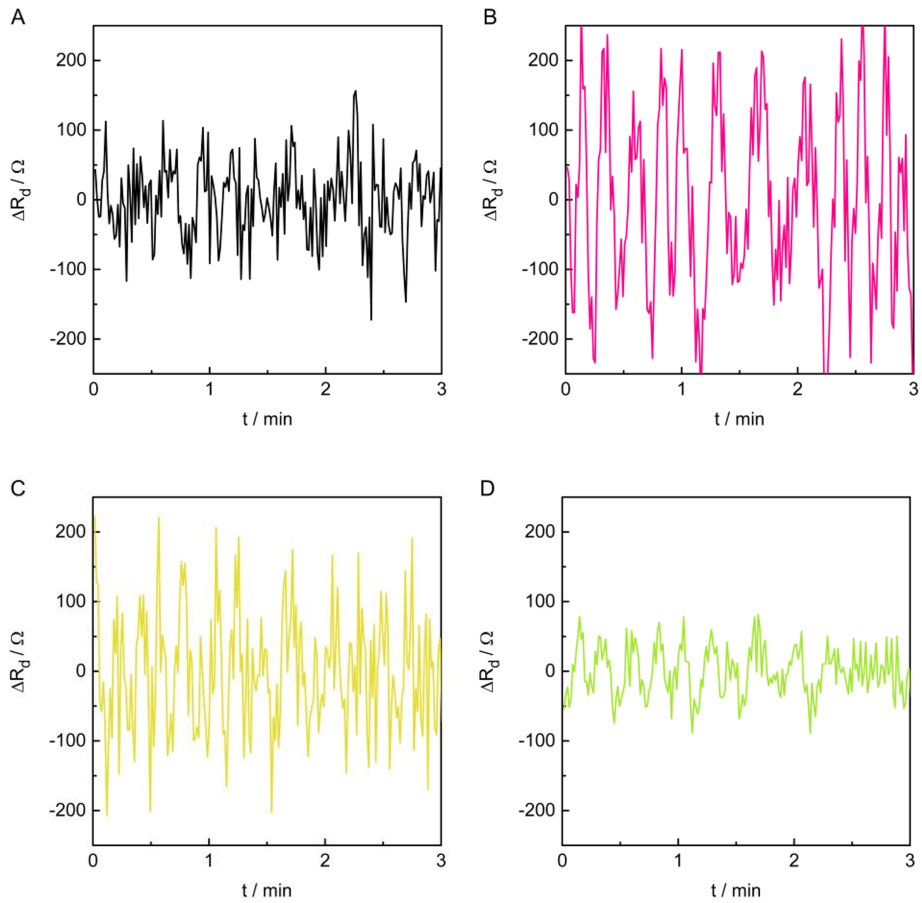

Fig. 7.45 Detrended RTC data at 200 Hz measured 90 minutes after the addition of different hyperosmotic buffer solutions ctrl (A), 20 (B), 100 (C), 200 (D) mM to MCF-7 spheroids. Experiments were performed in a standard cell culture incubator at 37 °C and 0 % CO_2.

Analysis of the variance of increments was performed on the measured RTC data for all conditions by segmented detrending using a time interval of 32 s. For both cell types, the calculated variance of increments was normalized to the control condition and the results reflect the tendency of the cell micromotion behavior discussed previously. In general, an increase is observed with increasing compound concentration, whereas for 200 mM sucrose solution a reduced variance of increments is displayed (Fig. 7.46). With increasing sucrose concentration, a stepwise increase is shown, reaching a maximum at 100 mM with values of 140 (± 70) % (MCF-7) and 120 (± 40) % (U-373 MG) relative to the control condition. At the highest concentration, the values are markedly reduced, calculated as 70 (± 30) % (MCF-7) and 90 (± 40) % (U-373 MG), reflecting reduced cellular micromotion upon enhanced cell stiffening resulting from water efflux. As observed using a two-sample t-test, no significance ($^{n.s.}$) is evident for each condition relative to the control condition and between concentration levels due to high error bands.

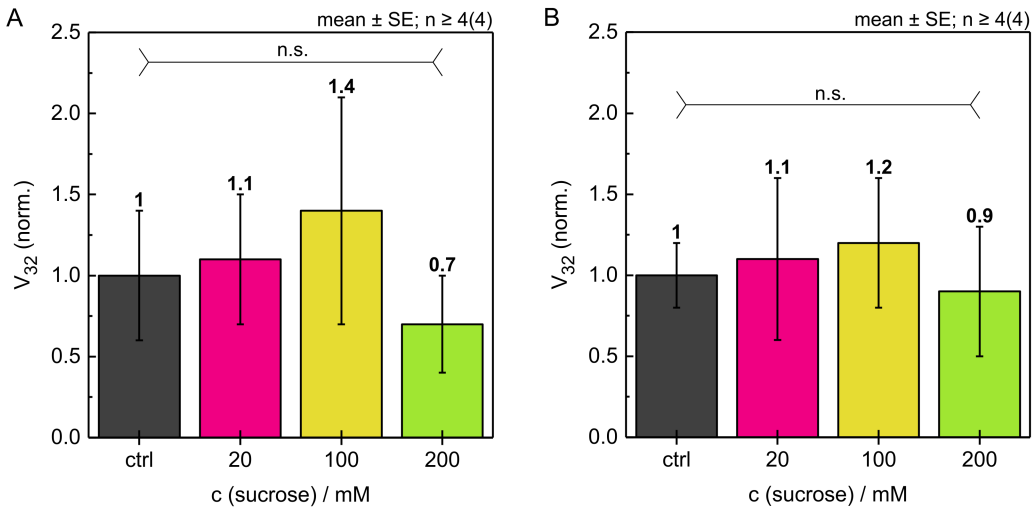

Fig. 7.46 Normalized variance of increments of impedance fluctuations after segmented detrending measured 90 minutes after the addition of different hyperosmotic buffer solutions (ctrl | 20 | 100 | 200 mM) to MCF-7 spheroids (A) and U-373 MG spheroids (B). Significance was determined relative to the control condition and between the different concentrations by a two-sample t-test using a significance level of 0.1 (*), 0.05 (**), and 0.01 (***). Data sets were averaged after segmented detrending, mean ± SE; n ≥ 4(4).

Tab. 7.13 Calculated values of R_{ext}, R_{int}, and A_{sph} reflecting the dielectric structure of MCF-7 spheroids as a function of different hyperosmotic buffer solutions (ctrl | 20 | 100 | 200 mM; 12,000 c/well). The values were determined by fitting each measured impedance spectrum 90 minutes after the addition of different hyperosmotic buffer solutions using a *LabVIEW™*-based software (written by J. Wegener, University of Regensburg) and the following parameter values: A_{el} = 12 (± 1) | 12.4 (± 0.8) | 11 (± 1) | 10.2 (± 0.5) ·10^{-6} $Fs^{n-1}cm^{-2}$; n_{el} = 0.86 (± 0.02) | 0.83 (± 0.03) | 0.86 (± 0.04) | 0.895 (± 0.005); R_{bulk} = 5,400 Ω; A_{para} = 2.4 ·10^{-10} $Fs^{n-1}cm^{-2}$; n_{para} = 0.9; n_{sph} = 0.75. Data sets were averaged after fitting, mean ± SE; see the table for the respective number of experiments.

	$concentration$ [mM]			
	ctrl	20	100	200
R_{ext} [kΩ]	110 ± 10	120 ± 10	80 ± 10	23 ± 2
R_{int} [kΩ]	3 ± 1	2 ± 1	2.5 ± 0.8	2 ± 1
A_{sph} [10^{-9} $Fs^{n-1}cm^{-2}$]	3.1 ± 0.5	3.1 ± 0.4	3.5 ± 0.4	4.2 ± 0.7
n	4(4)	5(6)	4(5)	5(7)

The evaluation of the dielectric spheroid structure based on the recorded data shows an overall decrease in R_{ext} and R_{int} values for both cell types with increasing sucrose concentration, accompanied by an increase in capacitive A_{sph} values (Tab. 7.13). In particular, at the lowest concentration of 20 mM, no significant difference in the values of the dielectric parameters with respect to the isosmotic control condition is observed for either cell type. In the case of MCF-7, the application of sucrose concentrations of 100 mM and 200 mM caused a decreasing trend in the resistance parameters, with values of

80 (± 10) kΩ (100 mM) and 23 (± 2) kΩ (200 mM) obtained. Despite the intracellular resistance exhibiting values that are not highly significant, a decline from 3 (± 1) kΩ (ctrl) to 2 (± 1) kΩ (200 mM) is also observed. The non-ideal capacity of the spheroids A_{sph} increases contrary starting at 3.1 (± 0.5) $\cdot 10^{-9}$ $Fs^{n-1}cm^{-2}$ (ctrl) with a slight increase to 3.5 (± 0.4) $\cdot 10^{-9}$ $Fs^{n-1}cm^{-2}$ (100 mM), up to values around 4.2 (± 0.7) $\cdot 10^{-9}$ $Fs^{n-1}cm^{-2}$ (200 mM). For U-373 MG spheroids, the determined dielectric parameter values display similar trends with respect to the characteristic value level (see chapter 11.1, Tab. A-7.3). As the compound concentration increases, both the extracellular and intracellular resistance values exhibit a descending trend. The extracellular resistance decreases from 36 (± 3) kΩ (ctrl) to 26 (± 2) kΩ (200 mM), whereas the intracellular resistance is reduced in a non-significant way from 8.0 (± 0.5) kΩ (ctrl) to 7 (± 3) kΩ (200 mM) with increasing sucrose concentrations. Identical to the MCF-7 experiments, an inverse trend due to increasing values is reflected by the non-ideal spheroid capacitance A_{sph}. The capacitance values increase constantly with increasing compound concentration from 9.1 (± 0.6) $\cdot 10^{-9}$ $Fs^{n-1}cm^{-2}$ (ctrl) to 18 (± 9) $\cdot 10^{-9}$ $Fs^{n-1}cm^{-2}$ (200 mM). Following the analysis of the dielectric characteristics of MCF-7 and U-373 MG spheroids using varying osmolalities, noticeable divergences between the isosmotic and different hyperosmotic levels were observed, despite the exposition to 20 mM sucrose solution.

The results of impedance time response, spheroid micromotion analysis, and spheroid dielectric properties demonstrate a clear dependence on sucrose concentration respective different osmolality levels. These findings indicate that the amount of sucrose used determines the osmotic pressure of the spheroids in a dose-dependent manner, regardless of whether it is derived from MCF-7 or U-373 MG cells.

7.4.3 TIME-LAPSE MICROSCOPY ANALYSIS OF THE SPHEROID

In addition to impedance analysis, the influence of osmotic pressure on spheroids was observed using time-lapse imaging with the zenCELL owl digital microscope. Spheroids derived from MCF-7 and U-373 MG cells were adhered to the adhesive surface and exposed to sucrose solution at different concentrations (20–400 mM). The response of the spheroids was monitored by taking microscopic images at regular 10-minute intervals over a period of 90 minutes. This time resolution was sufficient for the purposes of the model study. As the time resolution was limited by software settings when the research was conducted, this feature was subsequently improved in collaboration with the manufacturer.

In this study, similar observations were made for both cell types examined. Time-lapse images of MCF-7 spheroids illustrate the overall process following the addition of buffer containing 200 mM sucrose

concentration (Fig. 7.47). Immediately after the addition of the compound, the hyperosmolar solution triggers water outflow from the cells and forces them into a non-physiological state. As a result, the diameter of the entire spheroid body decreases within the first 30 minutes while maintaining its shape. In addition, a slight decrease in the diameter of the central dark gray shaded spheroid core is indicated between 10 and 60 minutes after compound addition. The spheroid body remains in the contracted form for the duration of the measurement, no further morphological changes of the spheroid are observed, and no obvious morphological changes of the cell monolayer are displayed considering the microscopic resolution factor.

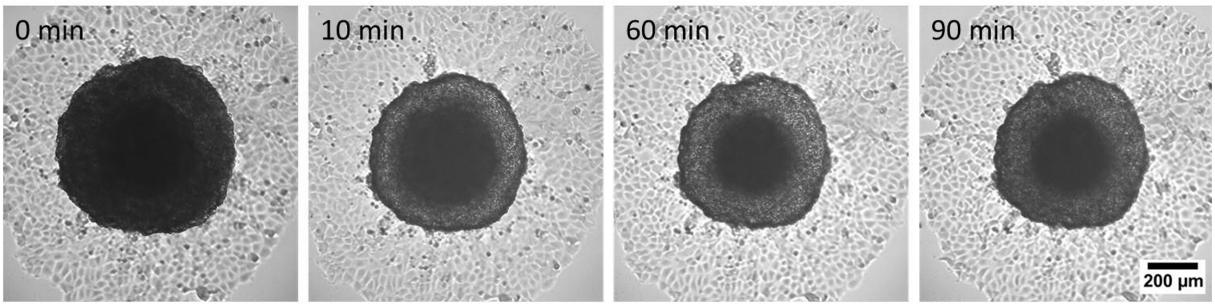

Fig. 7.47 Time-resolved micrographs of the spheroid response to osmotic pressure after the addition of hyperosmotic buffer solution with a final sucrose concentration of 200 mM to MCF-7 spheroid (7 d, 4,000 c/well). Compound addition was performed at time point zero and the process was documented for 90 minutes using the zenCELL owl digital microscope. Experiment was performed in a standard cell culture incubator at 37 °C and 0 % CO_2.

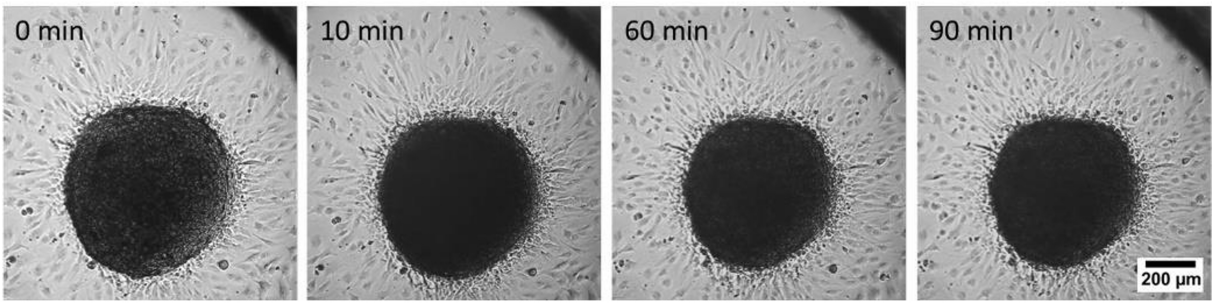

Fig. 7.48 Time-resolved micrographs of the spheroid response to osmotic pressure after the addition of hyperosmotic buffer solution with a final sucrose concentration of 200 mM to U-373 MG spheroid (7 d, 18,000 c/well). Compound addition was performed at time point zero and the process was documented for 90 minutes using the zenCELL owl digital microscope. Experiment was performed in a standard cell culture incubator at 37 °C and 0 % CO_2. The full time-lapse clip is available (see chapter 11.1; Tab. A-6.2).

For comparison, the identical sucrose concentration of 200 mM induced equivalent morphological changes in U-373 MG spheroids as shown in the micrographs (Fig. 7.48). The spheroid diameter decreases within the first 10 minutes after compound addition, while no further morphological changes of the spheroid body or cell monolayer are observed over the remaining measurement period. In addition, time-resolved micrographs of spheroids exposed to a sucrose concentration of 400 mM are

provided in chapter 11.1 (Fig. A-7.17 [MCF-7]; Fig. A-7.18 [U-373 MG]). To optically determine the minimal difference in spheroid diameter induced by the varied osmotic pressure, the total spheroid diameter decrease has to be considered in relation to the initial body size. Thus, a montage of micrographs taken of distinct spheroids exposed to different sucrose concentrations after the same time period would not represent a clear dose-response relation.

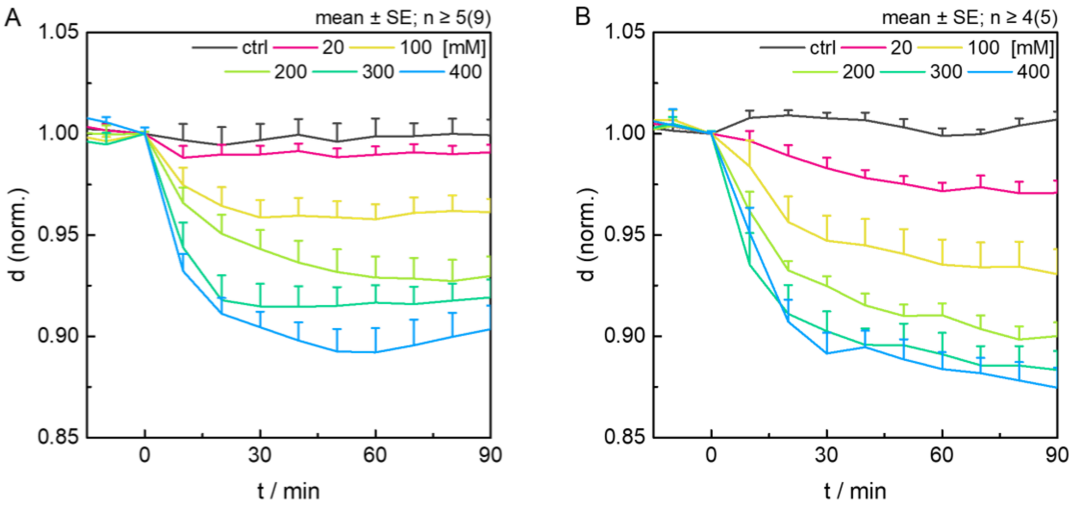

Fig. 7.49 Time course of diameter changes after the addition of different hyperosmotic buffer solutions in a range of 20–400 mM to MCF-7 spheroids (A) and U-373 MG spheroids (B) documented for 90 minutes using the zenCELL owl digital microscope. Time courses were normalized with respect to the last data point before compound addition at time point zero. Experiments were performed in a standard cell culture incubator at 37 °C and 0 % CO_2. Data sets were averaged after normalization, mean ± SE; A: n ≥ 5(9); B: n ≥ 4(5).

As a result, the diameter changes were determined according to different sucrose concentrations using *ImageJ* software (Rasband, W.S., National Institutes of Health, USA) to quantify the spheroid response precisely (Fig. 7.49). For both cell types used, the results show a dose-dependent effect of the osmotic pressure level, inducing distinct morphological changes by a specific diameter reduction of the spheroid body. Irrespective of the cell type used, the control spheroids remain the same size for 90 minutes, whereas the highest concentration of sucrose causes a rapid decrease in diameter immediately after the addition of the compound. As stated by the time-lapse images, no additional diameter alterations were observed within the recorded time period. The application of the highest sucrose concentration leads to a relative decrease in the spheroid diameter of 90 (± 1) % in the case of MCF-7 cells and 88 (± 1) % in the case of U-373 MG cells. Based on this trend, similar decreasing effects are shown for the time courses of the different compound concentrations, demonstrating a dose-dependent response profile.

The results of the time-resolved microscopy study of the effect of different osmolalities demonstrate the influence on spheroid morphology. An increase in the sucrose concentration of the buffer solution

causes a proportional rapid decrease in the spheroid body diameter upon shrinkage of the individual cells.

7.4.4 DISCUSSION: INFLUENCE OF OSMOTIC PRESSURE

In the present model study, the influence of osmotic pressure on cellular models was investigated using hyperosmolar buffer solutions containing different concentrations of sucrose. The analysis of the cell monolayer and the spheroid response was performed using various experimental approaches, including impedimetric measurements based on the ECIS™ technique, as well as the novel funnel-based setup and time-lapse microscopy. The results are discussed in the following, providing a comprehensive view of the influence of different osmolality levels in relation to the dimensionality of the *in vitro* model.

I THEORETICAL BACKGROUND

For a detailed discussion of the results, the theoretical background of osmotic pressure in the presence of cellular tissue models is presented. The osmotic pressure is defined as the pressure of a solvent against a semi-permeable membrane to prevent solvent molecules, such as H_2O molecules, from passing across the membrane. It depends on the osmolality of the solution, which expresses the content of all dissolved molecules. When two solutions of the same osmolality are separated by a semi-permeable membrane, such as the plasma membrane of cells, there is no tendency for water to flow and an isosmotic state exists. By varying the osmolality on one side using hyper- or hypotonic solutions, H_2O molecules will diffuse from the solution with the lower osmolality across the membrane into the solution with the higher osmolality until an equilibrium is reached. This water flux across the membrane is facilitated by integral membrane proteins, termed aquaporins, in either direction.

Based on this principle, cell-based assays have been performed by monitoring the response of 2D and 3D tissue models to osmotically induced changes in cell physiology, the so-called water flux experiments. For this purpose, several measurement approaches were utilized, such as the transwell-filter-based setups performing permeability assays (Urban, 2020), the QCM-technique (Wegener et al., 2000c), and EIS-based-techniques for either 2D tissue models (O´Connor et al., 1993) or in the case of 3D tissue models, the channel-based measurement setup (Hupf, 2018) and the funnel-based measurement setup (investigated in this thesis).

Therefore, hyper- and hypoosmotic buffer solutions with different osmolality values have to be prepared in relation to the isotonic, physiological level, which is in the range of 260–320 mosmol/kg (Freshney, 2010). To obtain higher hypertonic osmolality levels, different amounts of sucrose are added

to the buffer solution, as described in the chapter 4.1.7. For achieving lower hypotonic osmolality levels, a basic buffer solution composed of different ingredients is used in accordance with the protocol of O´Connor et al. (O´Connor et al., 1993). In addition, the specific conductivity of the prepared solutions has to be adjusted by using sodium chloride solution to avoid influences on cell polarity and current resistance contribution.

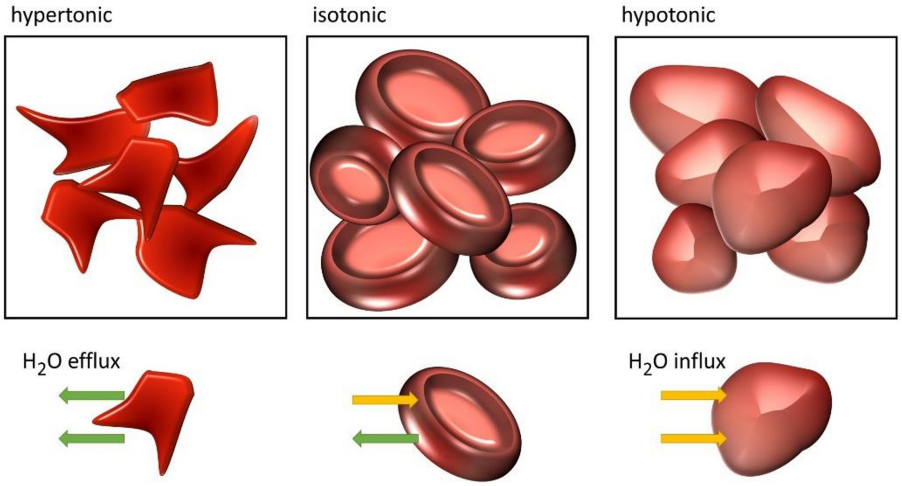

Fig. 7.50 Illustration* of the principle of osmotic pressure applied to blood cells. In a hypertonic environment, the osmotic pressure of the solution outside the blood cells is higher than the osmotic pressure inside the cells, causing a water efflux that leads to cell shrinkage. The isotonic condition corresponds to the physiological state and is associated with an equal distribution of water influx and efflux. When applying hypotonic solutions, water influx and cell volume increase are induced, which may result in cell disruption.

**illustration is simplified and not to scale*
(adapted from Mariana Ruiz Villareal, 2008)

Upon exposition to hyper- or hypotonic solutions, the cells are transferred into a non-physiological state and respond to the osmotically triggered water flux by altering their morphology (Fig. 7.50). In this instance, two different scenarios are obtained in accordance with the direction of the induced osmotic gradient. In the case of extracellular hypertonic conditions, H_2O molecules diffuse from the inside to the outside of the cell, leading to cell body shrinkage and thus enhanced stiffness due to increased cytoplasmic viscosity (Periasamy et al., 1992). Under extracellular hypotonic conditions, the osmotic gradient triggers an influx of H_2O molecules, which is associated with cell body expansion and softening of the entire cell structure. In general, changes in cell volume affect tissue architecture and function by altering the balanced concentrations of substrates and enzymes within the cell body. This can influence biochemical reactions as well as energy metabolism and even cause programmed cell death. Especially in contracted cells, dehydration causes protein unfolding, membrane perturbations, and the generation of reactive oxygen species with consequences for the overall metabolism. Thus, metabolic activity and metabolically driven processes such as cytoskeletal reorganization in combination with cell-cell contacts

and intracellular transport processes are disrupted (Potts, 1994; França et al., 2007). To prevent excessive interferences in cell volume, the initial fast passive response of the cells is followed by an active adaptation through a regulatory volume change (RVC) process that compensates for cell swelling or shrinkage (McCarty and O´Neil, 1992; Mongin and Orlov, 2001). This process acts in a converse direction depending on the initially induced water flux and leads to either regulatory volume decrease (RVD) or regulatory volume increase (RVI). For an acute reaction, membrane ion transporters are used to mediate the release/uptake of osmotically active compounds followed by water flux to regain the original cell volume. Through this mechanism, K^+ and Cl^- channels are utilized in RVD processes, whereas mainly the Na-K-2Cl-cotransporter (NKCC) and the Na^+/H^+ exchanger (NHE1) are involved in RVI processes. Cellular adaptation to long-term hyper- or hypoosmotic stimulation affects the regulation of metabolic pathways involved in osmolyte synthesis and gene expression (Lang et al., 1998; Mongin and Orlov, 2001). The time scale of the initial cell response to osmotic pressure is reported by seconds, whereas the regulatory volume change is measured in minutes as most mammalian cells can regain their original volume within 10 minutes (McCarty and O´Neil, 1992; Fernández-Fernández et al., 2002; Cadart et al., 2019; Liu et al., 2023).

Since cell volume regulation processes are not evident in every cell line, the ability of the cell types used in this thesis has to be reviewed. In the case of U-373 MG cells, and brain cells in general, volume regulation is essential due to the restriction by the rigid skull. Glioma cells exhibit a large Cl^- gradient, which is generated by the high expression of NKCC in glioma cells and is thought to be one of the major driving forces underlying glioma size and shape changes during infiltration and migration (Cuddapah et al., 2014; Elias et al., 2023). In combination with a high K^+ ion concentration within the cells, a large outward driving force for these ions is induced when K^+ or Cl^- channels open, resulting in cell volume reduction (Cuddapah et al., 2014). Upon hyperosmotic stimulation, the NKCC is activated by phosphorylation leading to cell volume increase. In addition, this process has been elucidated by treating U-373 MG cells with high concentrations of NaCl or sorbitol (300–400 mosmol/kg H_2O) and confirming the phosphorylation of αB-Crystallin, a heat shock protein that enables cells to survive and function during hyperosmotic stress (Ito et al., 1997; Burg et al., 2007). In the case of MCF-7 cells, a higher NHE1 activity than in normal human breast cells is present (Reshkin et al., 2000). Under hypertonic cell shrinkage conditions, NHE1 is required to perform net NaCl uptake to maintain the cell volume regulation (Hoffmann et al., 2009). This process takes place in co-operation with anion exchangers, which exchange Cl^- and HCO_3^- 1:1 across the membrane (Hoffmann et al., 2009). In this context, Hoffmann and Pedersen demonstrated, that an inhibition of NHE1 and thus the volume as well as the intracellular pH regulation strongly sensitizes MCF-7 cells to programmed cell death (Hoffmann and Pedersen, 2011)

As confirmed in a proof-of-principle study, the cell viability of the cells may not be apparently affected by the induced osmotic pressure, as shown by cell viability staining and fluorescence microscopy of a U-373 MG spheroid treated with hyperosmotic buffer solution (see chapter 11.1, Fig. A-7.19).

Based on the theoretical background of osmotic pressure, the cellular response is evaluated in terms of the different morphological changes investigated in the model study, whereby different response rates between 2D and 3D tissue models and cell type-dependent variations are expected. It should be noted that in contrast to a transepithelial water flux, as obtained in transwell filter-based experiments, a transmembrane water flux across the apical membrane was generated upon stimulation of the monolayer culture since the basal membrane was not accessible due to adhesion to the surface electrode (Wegener et al., 2000c). The gradient therefore not only affects the cell bodies but also the narrow fluid compartment beneath the cell layer, leading to an additional water flux across the basal membrane, which is associated with a change in the cell-substrate distance (Wegener et al., 2000c).

II IMPEDIMETRIC CHARACTERISTICS

The impact of varying osmotic pressure levels on the response of MCF-7 and U-373 MG cells in the form of monolayer cultures and spheroid models was characterized impedimetrically. In both assays, similar hyperosmotic buffer solutions containing final sucrose concentrations in the range of 20–500 mM (2D tissue models) and 20–200 mM (3D tissue models) were applied. In the case of spheroid model studies, the maximum possible osmolality level was introduced, limited by the fivefold dilution procedure of compound addition in the funnel-based measurement setup. The time-dependent impedance changes of the cells after the addition of different hyperosmotic buffer solutions serve as a sensitive indicator of osmotic pressure effects and thus as a basis for the assessment of cell morphology alterations.

II.A IMPEDIMETRIC CHARACTERISTICS – 2D TISSUE MODELS

In the 2D tissue model water flux experiments, sucrose solutions were applied in a final concentration range of 20–500 mM and the signal changes that were obtained were analyzed. As mentioned in chapter 7.4.1, the MFT measurements show characteristic dose-response dependencies for MCF-7 and U-373 MG cells, and the calculated variance of increments indicates a critical concentration threshold.

- ➔ As the compound concentration increases, an ascending impedance signal trend was investigated for MCF-7 cells, whereas a descending trend was observed for U-373 MG cells.
- ➔ As the compound concentration increases, the variance of increments increases and subsequently decreases above a cell type-specific sucrose concentration of 300 mM (MCF-7) and 200 mM (U-373 MG).

The key parameters change contrary and, at first sight, counterintuitive way when the cells are exposed to different osmotic pressure levels. The addition of hyperosmotic buffer solutions induces a water outflow from the cells, causing a volume shrinkage and an increase in cell stiffness. These morphological changes occur throughout the monolayer, resulting in larger intercellular spaces and thus less current restriction reflected by decreasing impedance values. This acute cellular response is assumed to occur within seconds and is followed by cellular adaptation performing regulatory volume changes, specifically RVI processes upon hyperosmotic stimulation. As a result, the cell volume increases, intercellular gaps become smaller again, and the resistive contribution to the impedance induces a signal increase. This entire process is dose-dependent and amplified by the induced osmolality height, as there is a relationship between the magnitude of the osmotic gradient and that of the water flux (McCarty and O´Neil, 1992).

In the case of MCF-7 cells, the initial signal decline in impedance is shown by zooming in to the time point of compound addition (Fig. 7.51). Compared to the control condition, a significant reduction in signal is observed for lower sucrose concentrations between 20 mM and 100 mM within the first 15 minutes after compound addition. The time course for 200 mM and 300 mM concentrations also shows an initial signal decrease, while the influence of cell volume shrinkage and thus impedance reduction is more pronounced at concentrations above 300 mM. Thus, a higher impact on the cell monolayer, respectively a more intense cell response, is generated with increasing osmolality levels.

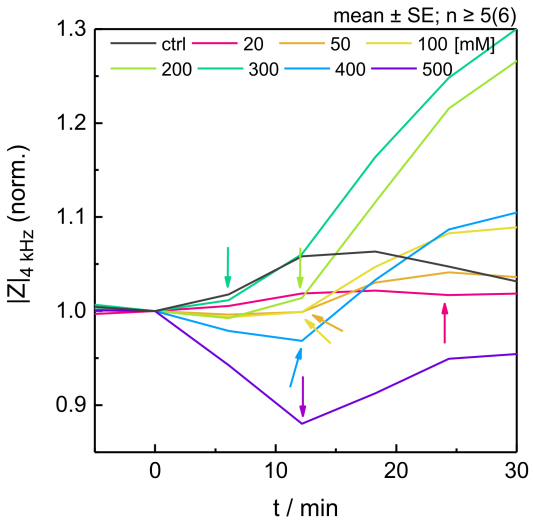

Fig. 7.51 Enlarged view of the time course of the addition of different hyperosmotic buffer solutions in a range of 20–500 mM to MCF-7 cell monolayer cultures (see Fig. 7.42). The inflection point between impedance signal decrease and increase is marked with arrows for each time course reflecting the time point of transition in the manner of a compensation effect between induced cell volume shrinkage and regulated volume increase.

In addition, the inflection point, which displays the transition between impedance signal decrease and increase, is marked with an arrow for each time course. Based on these time points, a decreasing time

period between substance addition and signal increase is shown for increasing sucrose concentrations, signaling a faster reaction time. In contrast, the time period is significantly increased above concentrations of 300 mM by exhibiting periods of six minutes (300 mM) compared to 12 minutes (400 mM). Since the initial cell response to osmotic pressure occurs rapidly in a passive manner within a second range, it is proposed that the inflection point may characterize the point at which the effects of cell volume decrease and increase are no longer compensating each other and the RVI process becomes dominant. This compensation effect is more evident at lower osmotic pressures, showing a reduced signal decrease and a rapid regeneration, whereas compensation is prolonged in the case of a massive impact above the critical concentration of 300 mM. In addition, compensation may also influence the cell volume regeneration, as the absolute increase in impedance with increasing sucrose concentration overwhelms the signal baseline. In this way, a stronger resistance contribution from the cells is reflected upon the RVI process, which may be induced by improved cell-cell contacts, enlarged cell volumes, and a denser packed entire cell monolayer compared to the untreated condition.

For comparison, the U-373 MG cell monolayer measurements show a contrary time course by following the same tendencies. Upon application of hyperosmotic buffer solutions, the measurements display inflection points for sucrose concentrations ranging from 20 mM to 200 mM, whereas no signal change was observed at higher concentrations. This differential response indicates that above the critical concentration of 200 mM, cells are excessively affected and reduced in size, which may delay the effect of the RVI process for several hours before becoming apparent. The slight increase in capacitance values after the addition of 400 mM and 500 mM confirms this assumption, as electrode coverage decreases while no cell detachment or excessive cell death is considered. At lower concentrations, a prolonged time between compound addition and inflection point is observed with increasing osmolality. This fact describes a distinct, but no overcompensation effect in the case of U-373 MG cells compared to MCF-7 cells, as indicated by an opposite effect discussed earlier. In addition, the regulated cell volume increase leads to an enhanced absolute signal increase proportional to the osmolality level applied.

In this context, cell type-dependent differences were observed, considering an overall ascending and descending time course profile. For MCF-7 cells, a general ascending trend was observed based on the impedance increase reflecting the presumably RVI process, whereas in U-373 MG cells, the decreasing impedance curve was predominant due to cell volume shrinkage. These characteristics are mainly based on the individual strength of the cell-cell contacts, which are evident as strong intercellular junctions in MCF-7 cells, whereas no E-cadherin expression is present in U-373 MG cells (Paterson et al., 2003; Lewis-Tuffin et al., 2010). The expression of a higher number of cellular connections, forming a tight and rigid cell network, limits the contraction of individual cells and thereby the absolute shrinkage.

Consistent with this, an increased critical concentration of 300 mM sucrose was found for MCF-7 cells, as an enhanced osmotic pressure has to be induced to overcome the tight cell network and cause a significant signal change. In contrast, the osmotic pressure leads to a more pronounced cell shrinkage in U-373 MG cells due to comparatively weaker cell-cell junctions. This cell contraction was sufficiently compensated by the RVI process, regaining almost isosmotic conditions. In the case of U-373 MG cells, the critical concentration of 200 mM reflects the signal change between regeneration and persistent manipulation as no impedance increase was observed within the recorded time period above this concentration, thus reinforcing the response dependency on the cellular network strength. Overall, the magnitude of both cell volume shrinkage and regulated cell volume increase is amplified by the level of induced osmotic pressure, whereas the resulting cell response, as well as the individual time periods, are difficult to differentiate in impedance measurements due to compensatory effects.

Using a different approach, O´Connor et al. determined the cell volume changes in monolayer cultures of primary astrocytes indirectly by measuring the electrical resistance of the extracellular space (O´Connor et al., 1993). The measurement setup consisted of a flow channel with a central constriction parallel to the bottom of the flow chamber and large gold electrodes on either side of the channel. When the cells were exposed to hyperosmotic solutions in the range of 343–493 mosmol/kg H_2O, equivalent to a sucrose concentration of 100–400 mM, they contracted (O´Connor et al., 1993). As a result, the height of the electrolyte above the cell layer increased, leading to a decrease in the measured resistance across the channel. In addition, no volume-regulating behavior was obtained within 30 minutes, whereas the cells exhibited RVD after exposure to hypoosmotic solutions. This fact was discussed following the statement of Ericson and Spring that fewer cell types show volume regulation after shrinkage than after swelling due to exposition to the respective osmotic media (Ericson and Spring, 1982). Overall, the indirect measurement of osmolality-dependent changes in cell volume confirms the shrinkage of cells observed in this work.

For detailed analysis, the area under the curve of the normalized impedance data within a defined time range was calculated, normalized to the control condition, and plotted as a function of the logarithmic concentration for each cell type (Fig. 7.52). For the integration range of 90 minutes after compound addition, AUC values indicate the relationship between cell shrinkage and cell expansion; AUC values below 100 % predominantly correlate with cell shrinkage, AUC values above 100 % indicate enhanced cell volume regeneration, and AUC values of approximately 100 % represent a state of equal distribution between the two processes. For both cell types, characteristic results were observed corresponding to the ascending and descending tendencies of the time-resolved impedance measurements. Initially, the data show a plateau of approximately 100 % up to a concentration of 50 mM, regardless of the cell type,

reflecting the compensation of induced cell shrinkage and regeneration to isosmotic conditions. In the case of MCF-7 cells, an exponential increase in AUC values is shown, leading to a maximum of 350 % at a sucrose concentration of 300 mM, which corresponds to the excessive RVI process shown in ECIS™ measurements. At higher concentrations, the effect of cell shrinkage associated with decreasing AUC values is pronounced, resulting in 70 (± 10) % (500 mM). For U-373 MG cells, a slight signal increase is obtained at concentrations of 100 mM and 200 mM, consistent with the distinct decrease in impedance and an equal increase in cell regeneration. This is followed by the effect of cell shrinkage at higher concentrations, while no increase in cell volume was observed within the measurement period, as indicated by low AUC values of 45 (± 9) % (500 mM).

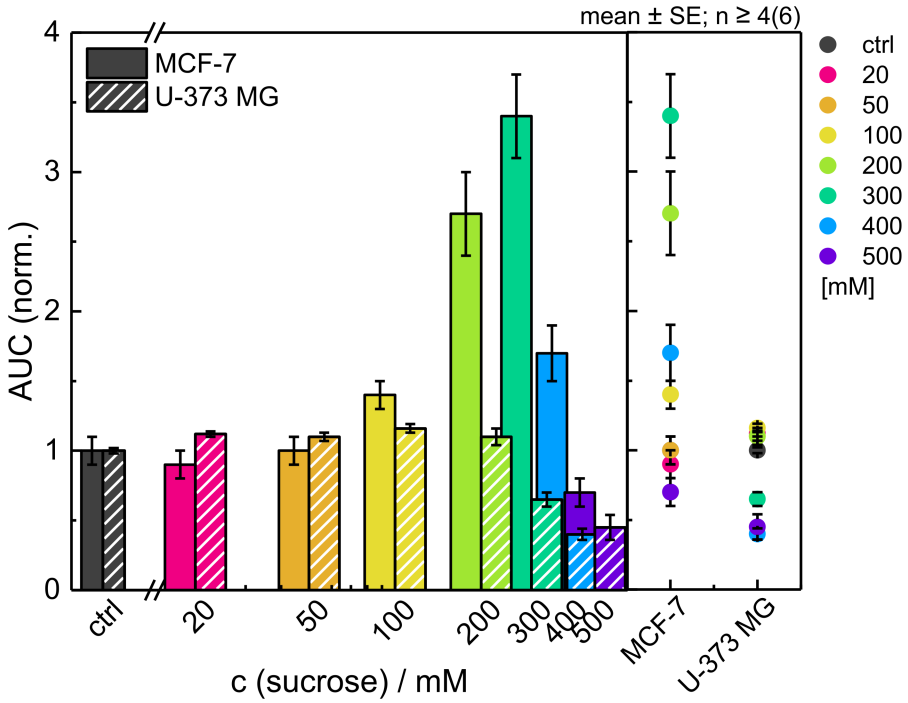

Fig. 7.52 Overview of the normalized results of the area under the curve values derived from the time course of normalized impedance magnitude at 4,000 Hz of MCF-7 and U-373 MG cell monolayer cultures (Fig. 7.42). For integration, a baseline was set at 85 % (MCF-7; U-373 MG) of the normalized impedance, and the values were determined within 90 minutes after the addition of hyperosmotic buffer solutions with different sucrose concentrations in a range of 20–500 mM. After averaging, data sets were normalized to the control condition, mean ± SE, n ≥ 4(6). An overview of the distribution of the results is provided in the scatter plot. Significance was determined by a two-sample t-test between the cell types using a significance level of 0.1 (*), 0.05 (**), and 0.01 (***). As a result, a significance level of 0.05 (**) was determined between the cell types in the concentration range 20–50 mM, while a high significance level of 0.01 (***) was obtained at the sucrose concentrations above 50 mM (symbols not shown in the graph).

An overview of the results for both cell types is shown in the scatter plot (Fig. 7.52). For MCF-7 cells, a characteristic distribution is observed over the concentration range, reflecting the variation of a predominantly induced cell volume increase followed by evident cell shrinkage. In contrast, two significant levels were found for U-373 MG cells, indicating either a balanced system or a dysregulated

state emphasizing cell shrinkage. Thus, as discussed, the results display a high cell type-dependent impact.

Based on the calculated AUC values, a dose-response curve was plotted as a function of sucrose concentration for each cell line. As the results from MCF-7 cells make sigmoidal fitting impossible, the EC_{50} value was only obtained for U-373 MG cells using the sigmoidal Boltzmann equation (see chapter 11.1, Fig. A-7.20; chapter 4.1.8, Eq. 4.2). The EC_{50} value is calculated as 190 (± 20) mM (U-373 MG; $R^2 = 0.79$; mean ± SE; $n \geq 4(7)$) in monolayer culture, following the predicted critical concentration of 200 mM. In accordance, the EC_{50} of MCF-7 cells was also assumed to be in the range of approximately 300 mM, following the critical concentration obtained from the impedance time course.

II.B IMPEDIMETRIC CHARACTERISTICS – 3D TISSUE MODELS

The comprehensive impedimetric characterization also comprised the discussion of the response of 3D tissue models to various osmolality levels by exposing spheroids to different hyperosmotic buffer solutions. The experiments were performed using different concentrations of sucrose with a final range of 20–200 mM and the cellular response was recorded using the funnel-based measurement setup. As a result, the analysis of spheroid micromotion, calculated variance of increments, and spheroid dielectric parameters show clear variations as a function of compound concentration for both cell types examined, as described in chapter 7.4.2.

- ➔ As the compound concentration increases, an enhancement of the decreasing rate as well as the subsequent increasing rate of the impedance signals was observed, regardless of the cell types used.
- ➔ As the compound concentration increases, the cellular micromotion as well as the variance of increments increase and subsequently decrease above 100 mM, regardless of the cell type used.
- ➔ As the compound concentration increases, R_{ext} and R_{int} decrease, whereas A_{sph} increases.

The impedance time course of both cell types displayed a biphasic downward and upward signal change when the cells were exposed to different osmotic pressure levels. This specific curve profile reflects the overall external and internal alterations of the tissue model since the cells within the spheroid are affected in a similar way as in cell monolayer culture. The addition of hyperosmotic buffer solutions induces water efflux from the cells, resulting in volume shrinkage and an increase in cell stiffness. These morphological changes are assumed to occur throughout the spheroid body, initially mainly at the outer

rim, and by correlating the time-lapse images of the MCF-7 spheroid, a later influence on the central spheroid core is assumed. As a result, the entire spheroid body contracts and the central aperture becomes less tightly sealed, which leads to reduced current restrictions and therefore lower impedance values. This acute spheroid reaction is expected to occur within seconds, analogous to a monolayer culture, or at least within a few minutes. The subsequent increasing impedance slope may either reflect the rate of expansion of the spheroid body by RVI processes or the progressive adaptation of the contracted spheroid to the central opening. In both cases, sufficient sealing of the aperture is considered and correlates with an ascending impedance curve. These suggestions were clarified using time-lapse microscopy, as no regeneration of body volume by RVI processes was observed after spheroid shrinkage within the measurement period. In this way, the spheroid acts contrary to the monolayer culture, whereby the inflection point in the time course may reflect the transition between contraction and successive adaptation of the spheroid body to the central opening, which induces a signal increase. The overall spheroid response occurs in a dose-dependent manner, amplified by the applied osmolality height as investigated in monolayer culture and outlined in literature (McCarty and O´Neil, 1992). In order to observe spheroid body expansion upon RVI processes and thus the influence on the impedance signal, the measurement time has to be extended. However, subsequent micrographs of the treated spheroids inside the micro-trap revealed that the spheroids had not slipped through the opening due to their contracted shape -even by a sucrose concentration of 200 mM- as they flexibly adapted to the hole as a result of gravity.

The description of the spheroid response to osmotic pressure applies to the impedance measurements of MCF-7 and U-373 MG cells. In comparison, for both cell types, a similar impedance time course was observed, as stated previously. After the initial decrease in impedance values due to induced spheroid contraction, the inflection point represents a compensatory effect of shrinkage and progressive sealing of the funnel opening by gravity forces. For detailed data analysis, the kinetic values of the time course were determined by defining the time point in relation to the value of the observed signal minima and by calculating the slope values of the decreasing and increasing courses, respectively, as a function of sucrose concentration (Tab. 7.14). The decreasing slope value may reflect the rate of shrinkage of the spheroid body and the increasing slope value may reflect the progressive adaptation of the contracted spheroid to the central opening. These slope values were calculated in the specific time range from either compound addition to signal minimum or from the signal minimum to the end of the measurement. The time course of the isosmotic control condition was not evaluated.

With increasing sucrose concentration, the time of reaching the signal minimum and the minimum values decrease in both cell types. In detail, the time period between compound addition and

impedance minimum is reduced as a result of a stronger effect of the induced higher osmotic pressure. The results show similar time segments according to the concentration used and independent of the cell type, with a minimum response at 6.7 min (MCF-7) and 6.1 min (U-373 MG) after application of the highest sucrose concentration of 200 mM. As an exception, the addition of 20 mM sucrose solution to MCF-7 spheroids resulted in a time period of 20.1 min, which is twice as long as that examined for U-373 MG spheroids. Whilst the initial signal increase is included, the correction yields a period of 15.6 min for the signal decrease only.

Tab. 7.14 Overview of kinetic values as a function of sucrose concentration applied, calculated from the impedance time course (Fig. 7.44). The time period of reaching the signal minima and the relative impedance minima value were determined for MCF-7 and U-373 MG spheroids using the averaged data. By using linear regression in the specific time range from either compound addition to signal minimum or from the signal minimum to the time point 90 minutes after compound addition, the slope values of the decreasing and increasing signal courses were calculated. Here, a decreasing slope value may reflect the rate of shrinkage of the spheroid body and an increasing slope value may reflect the rate of progressive sealing of the funnel opening by contracted spheroid body adaption.

		$concentration$ [mM]		
		20	100	200
MCF-7	$minimum_{time}$ [min]	20.1	11.2	6.7
	$minimum_{value}$ [%]	83 ± 4	32 ± 5	12 ± 2
	$slope_{decrease}$ [%/min]	-1.1 ± 0.1	-7 ± 1	-15.5 ± 0.6
	$slope_{increase}$ [%/min]	0.248 ± 0.005	0.85 ± 0.01	0.066 ± 0.005
U-373 MG	$minimum_{time}$ [min]	10.6	9.1	6.1
	$minimum_{value}$ [%]	92 ± 1	47 ± 2	36 ± 1
	$slope_{decrease}$ [%/min]	-0.9 ± 0.1	-5 ± 1	-11 ± 1
	$slope_{increase}$ [%/min]	0.074 ± 0.009	0.64 ± 0.02	0.339 ± 0.004

As stated earlier, a clear dose-response dependency is revealed for the individual minimum value, exhibiting a lower impedance level with increasing osmotic pressure and thus a stronger impact on the spheroid morphology. Moreover, as indicated by the recorded time courses, the values also reflect the stronger effect on MCF-7 spheroids, which show a significantly greater reduction of the relative impedance values at each concentration in contrast to U-373 MG spheroids. In addition, the slope values demonstrate a steeper decline with increasing sucrose concentration, ranging from 1.1 (± 0.1) % to 15.5 (± 0.6) % per minute for MCF-7 spheroids and from 0.9 (± 0.1) % to 11 (± 1) % per minute for

U-373 MG cells calculated for 20 mM and 200 mM, respectively. By reaching the signal minimum acting as an inflection point, a subsequent increasing time course is observed with various slope values. The highest regeneration rate was calculated for 100 mM sucrose concentration, amounting to 0.85 (± 0.01) % per minute for MCF-7 spheroids and 0.64 (± 0.02) % per minute for U-373 MG spheroids. Based on this, a reduced slope value was examined for the lower and higher concentrations. In comparison, a four times higher regeneration rate was determined in the case of U-373 MG relative to the MCF-7 spheroids for the sucrose concentration of 200 mM, mimicking a more extensive impact on MCF-7 spheroids.

Based on these results, a distinct cell type-related difference was found. The osmotically driven water efflux from the cells leads to cell body shrinkage and thus to enhanced stiffness by increasing cytoplasmic viscosity. Since an overall dose-response relationship on spheroid morphology was examined, an increase in spheroid body stiffness is also expected. As a consequence, the flexibility and therefore the adaptability of the body to the central funnel opening, which determines the impedance signaling, is reduced with ascending osmolality. Hence, a more rapid and less marked decrease in impedance occurs, since the compensation of spheroid body shrinkage and sealing of the central opening is more efficient due to more flexible and less viscous cell structures. Since U-373 MG cells exhibit no tight cell junctions, the contracted spheroid body represents a higher rate of adaptation than MCF-7 spheroids. As a result, the detected period of reaching the inflection point, the value of the minimum and the slope of the signal decrease are smaller in the case of U-373 MG spheroids, demonstrating a faster and more sufficient sealing in comparison to MCF-7 spheroids exposed to the identical hyperosmotic condition. This observation is reinforced by the four times higher regeneration rate of U-373 MG spheroids, as calculated by the increasing slope value for the addition of 200 mM sucrose solution, which emphasizes the influence of the cell network adaptability.

The dielectric properties of tissue models exposed to hypertonic osmotic pressure change as expected and with the same tendency for both cell types. The increasing variance of increments indicates an enhanced cellular *activity level* within the spheroid as demonstrated by the RTC measurements showing a significant increase in the fluctuation rate. This fact is counterintuitive, as the water efflux leads to cell stiffening and should thus induce a decreasing cellular micromotion. In this case, the cellular activity increase may be related to enhanced activated cellular processes involved in adapting the entire spheroid morphology to the funnel opening and is therefore a result of the layout of the measurement setup. Consistent with the prediction, significantly reduced micromotion activity was measured at a sucrose concentration of 200 mM compared to micromotion at 100 mM, representing cell stiffening and reduced adaptation ability to the aperture, consistent with the reduced signal slope increase

revealed by time-resolved impedance measurements. The reduction in signal for R_{ext} values is associated with a loss of cell barrier function upon rapid cell shrinkage, thereby enabling the current to flow with less resistance. Additionally, the intracellular resistance R_{int} decreases following the prediction of Sasser et al., as the water efflux leads to an increased concentration of ions within the cell body and thus an enhanced conductivity (Sasser et al., 1993). An opposite, increasing trend is shown for A_{sph} values indicating increasing permeability within the spheroid body associated with a loss of capacitance contribution to the impedance signal. Thus, a certain amount of programmed cell death has to be considered with increasing osmotic pressure as a result of affecting the tissue architecture and dysregulating cellular functions. The combination of all signal trends represents the gradual shrinking of the spheroid body in combination with the interaction of the measurement setup as a response to increasing sucrose concentrations respectively osmolality.

In the literature, Hupf performed EIS measurements on spheroids in the context of osmotic pressure by introducing the spheroids into the flow channel filled with the respective hypo- or hyperosmotic buffer solution (Hupf, 2018). Both hyperosmotic buffer solutions used offered a similar osmolality level similar to the sucrose concentrations of 100 mM and 200 mM used in the experiments presented in this thesis. Hupf found that the spheroid impedance decreased for increasing osmolality in combination with reduced micromotion activity and diminished values of the variance of increments compared to isosmotic conditions (Hupf, 2018). The evaluation of the dielectric spheroid parameters showed a descending trend of R_{ext} and R_{int} values and an ascending trend of A_{sph} values for increasing osmotic pressure. Even though the decrease of micromotion activity accompanied by reduced variance of increments is only observed at a concentration of 200 mM, the results of Hupf are in good agreement with the results obtained in this model study using the funnel-based setup.

In order to compare the calculated values of the three spheroid parameters of both cell types, the data were normalized to the respective control condition (Tab. 7.15). The overview reveals that the ascending or descending tendencies of certain parameters yield relatively small and very similar changes for both cell types, which remain almost on the basis of the control condition. As shown, no significant alterations were made in comparison to the isosmotic control condition by exposing the spheroids to final sucrose concentrations of 20 mM and 100 mM, taking the error indication into account. In addition, the compound concentration of 200 mM also displays no significant difference for the parameters R_{int} and A_{sph} while the relative changes of the extracellular resistance, calculated as 21 (± 4) % (MCF-7) and 70 (± 10) % (U-373 MG), exhibit distinct alterations towards the control condition and between the cell types used. The significance of the calculated parameter values was confirmed between the two cell types using a two-sample t-test for each concentration studied, indicating a high level of significance

(***) for R_{ext} at a sucrose concentration of 200 mM while no significance ($^{n.s.}$) was determined for the other parameters or concentrations studied.

Tab. 7.15 Normalized values of R_{ext}, R_{int}, and A_{sph} reflecting the dielectric structure of MCF-7 and U-373 MG spheroids as a function of different sucrose concentrations (ctrl | 20 | 100 | 200 mM) used for inducing osmotic pressure. Values are based on mean values derived from raw data obtained 90 minutes after compound addition. Detailed fitting conditions are provided in the respective raw data information (Tab. 7.13; see chapter 11.1, Tab. A-7.3). Significance was determined by a two-sample t-test of the respective parameters between the cell types using a significance level of 0.1 (*), 0.05 (**), and 0.01 (***).

		$concentration$ [mM]			
		ctrl	20	100	200
MCF-7	R_{ext} [%]	100 ± 20$^{n.s.}$	110 ± 20$^{n.s.}$	70 ± 20$^{n.s.}$	21 ± 4***
	R_{int} [%]	100 ± 70$^{n.s.}$	70 ± 60$^{n.s.}$	80 ± 50$^{n.s.}$	70 ± 60$^{n.s.}$
	A_{sph} [%]	100 ± 30$^{n.s.}$	100 ± 30$^{n.s.}$	110 ± 30$^{n.s.}$	140 ± 40$^{n.s.}$
	n	4(4)	5(6)	4(5)	5(7)
U-373 MG	R_{ext} [%]	100 ± 20$^{n.s.}$	100 ± 20$^{n.s.}$	100 ± 30$^{n.s.}$	70 ± 10***
	R_{int} [%]	100 ± 10$^{n.s.}$	100 ± 10$^{n.s.}$	90 ± 10$^{n.s.}$	90 ± 40$^{n.s.}$
	A_{sph} [%]	100 ± 10$^{n.s.}$	110 ± 30$^{n.s.}$	110 ± 30$^{n.s.}$	200 ± 100$^{n.s.}$
	n	4(4)	4(4)	4(4)	3(3)

As the calculation of the dielectric spheroid parameters is based on the raw data acquisition after 90 minutes, the results serve as an endpoint record. Thus, the similar, not significantly different parameter values might indicate either a low dose-dependent effect on the tissue models or, in correlation with the impedance signal regeneration rate, a marked return to approximately isosmotic conditions within 90 minutes after compound addition. A remarkable and unique significant difference was found for the parameter reflecting the extracellular resistance, notably at a sucrose concentration of 200 mM. This fact demonstrates that the main influence of osmotic pressure is exerted in the intercellular junctions as a consequence of excessive cell body shrinkage. Since MCF-7 cells express a higher number and stronger cell-cell contacts, this cell type exhibits a higher sensitivity to morphological alterations. Based on this, the effect of osmotic pressure is particularly pronounced in this cell type compared to U-373 MG cells, although a slightly higher contraction degree was found for U-373 MG spheroids by correlating the time-lapse imaging. In addition, an explanation for the cell type-dependent impedance regeneration after the addition of the highest sucrose concentration is provided. As

discussed previously, the comparatively low percentage value of R_{ext} correlates with the low regeneration rate of the MCF-7 spheroids and explains the final relative impedance signal of 18 (± 2) % after 90 minutes.

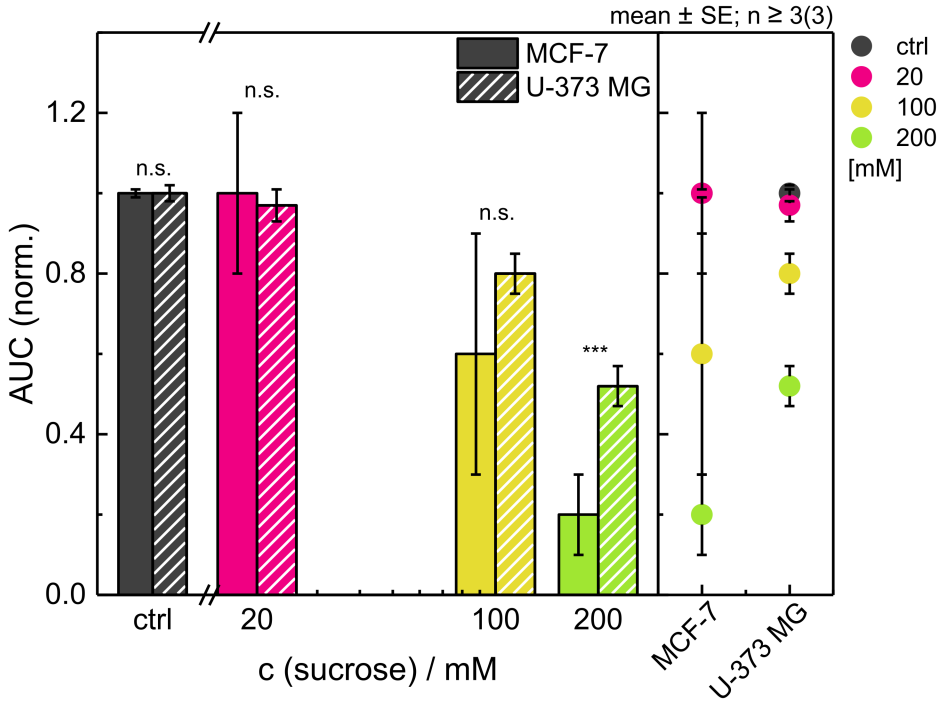

Fig. 7.53 Overview of the normalized results of the area under the curve values derived from the time course of normalized impedance magnitude at 200 Hz of MCF-7 and U-373 MG spheroids (Fig. 7.44). For integration, a baseline was set at 0 % (MCF-7; U-373 MG) of the normalized impedance, and the values were determined within 90 minutes after the addition of hyperosmotic buffer solutions with different final sucrose concentrations (ctrl | 20 | 100 | 200 mM). After averaging, data sets were normalized to the control condition, mean ± SE, n ≥ 3(3). An overview of the distribution of the results is provided in the scatter plot. Significance was determined by a two-sample t-test between the cell types using a significance level of 0.1 (*), 0.05 (**), and 0.01 (***).

For additional data evaluation, the area under the curve of the normalized impedance data within a defined time range was calculated and discussed in a similar manner as described for the monolayer culture. The normalized AUC values are plotted as a function of the logarithmic concentration for each cell type and indicate the level of impedance signal change (Fig. 7.53). The higher the AUC value in relation to the isosmotic control condition, the better the balance between the effect of osmotic pressure resulting in the form of spheroid shrinkage and the adaptation of the contracted spheroid to the funnel opening characterized by cell flexibility. A similar tendency of the results is obtained for both cell types, demonstrating that the AUC values decrease with increasing sucrose concentration. In correlation with the difference of an enhanced dysregulation of MCF-7 spheroids, as discussed for the three dielectric spheroid parameters and confirmed by the calculated kinetic values, the AUC values also show a steeper gradient profile. In the case of a sucrose concentration of 200 mM, the highly significant difference between the cell types used is illustrated by obtaining values of 20 (± 10) %

(MCF-7) and 52 (± 5) % (U-373 MG). Thus, accompanied by the interpretation of the kinetic profiles, a higher impedance signal regeneration is revealed for U-373 MG cells caused by enhanced flexibility of the contracted spheroid, taking an almost similar volume shrinkage of both spheroid types into account. This is further illustrated by the scatter plot (Fig. 7.53), which shows the distribution of the MCF-7 results approximately over the entire range, whereas the U-373 MG spheroid results are located in the upper part. The calculation of significance between the AUC values of the MCF-7 and U-373 MG spheroids using a two-sample t-test showed a high significance level of 0.01 (***) for the 200 mM sucrose concentration, while no significance ($^{n.s.}$) was obtained for the other conditions.

Following the dose-response curve of the cell monolayer response, the EC_{50} values were also obtained for spheroids based on the calculated mean AUC values for each cell type (see chapter 11.1, Fig. A-7.21). As a result, the EC_{50} values were calculated as 70 (± 5) mM (MCF-7; R^2 = 0.99; mean ± SE; n ≥ 5(5)) and 110 (± 10) mM (U-373 MG; R^2 = 0.99; mean ± SE; n ≥ 3(3)) in spheroids, representing a high significance level of 0.01 (***). Since only four values were taken into account, the sigmoidal fit is not as precise, and the results should be evaluated with caution.

III MORPHOLOGICAL PROPERTIES

The influence of osmotic pressure on the morphological properties of spheroids was also investigated in addition to the studied impedimetric characteristics. For this purpose, experiments were performed with hyperosmotic buffer solutions in the range of 20–400 mM and the cellular response was measured using the zenCELL owl microscope setup. Analyses of the recorded time-resolved images revealed a clear dose-response relationship for both cell types used, as shown in chapter 7.3.4.

➔ As the compound concentration increases, the diameter of the MCF-7 and U-373 MG spheroids decreases in a dose-dependent relation.

The morphology of the spheroid bodies changes as expected when exposed to hyperosmotic buffer solutions. Correspondingly, the spheroid diameter determined showed a significant decline over time as a function of the osmolality level applied. With increasing compound concentration, a proportional decrease in cell volume shrinkage is induced, leading to a gradual contraction of the overall structure of the tissue model. These morphological changes are visualized in the time-resolved images or quantitatively analyzed by the time course of the normalized diameter, which shows a rapid dose-dependent decrease within the first 20 minutes after the compound addition. Thus, the higher the osmolality difference to the corresponding isotonic solution, the greater the extent of water efflux and the higher the effect of spheroid size reduction. Despite the theoretical background of regulated cell

volume changes, no volume increase was investigated within the measurement period, and it is assumed to be prolonged by the complex three-dimensional structure compared to that of the monolayer culture.

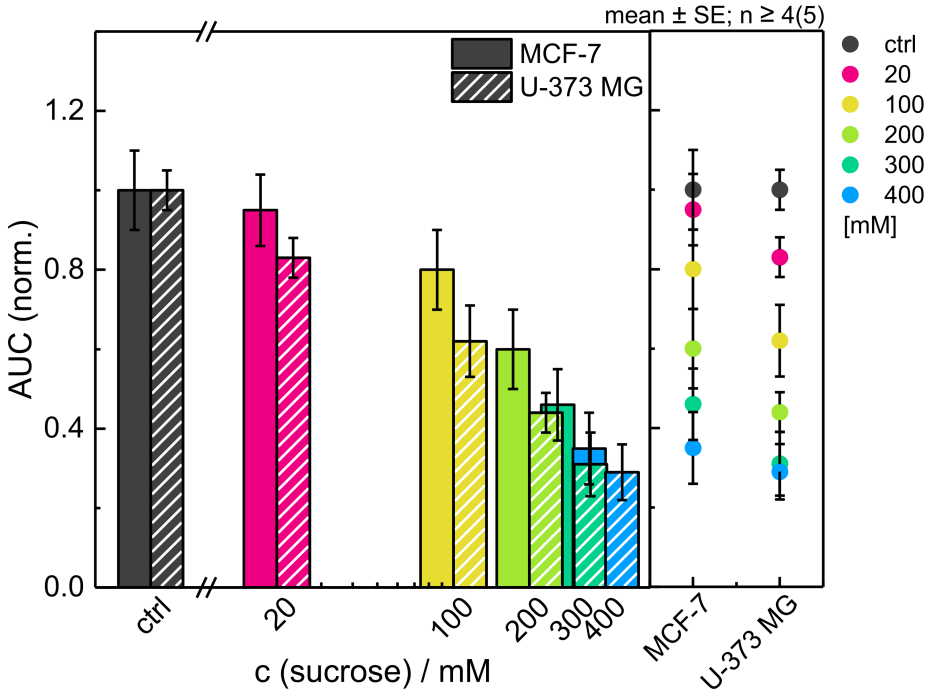

Fig. 7.54 Overview of the normalized results of the area under the curve values derived from the time course of diameter changes of MCF-7 and U-373 MG spheroids documented using the zenCELL owl digital microscope (Fig. 7.49). For integration, a baseline was set at 86 % (MCF-7; U-373 MG) of the normalized diameter, and the values were determined within 90 minutes after the addition of hyperosmotic buffer solutions with different sucrose concentrations in a range of 20–400 mM. After averaging, data sets were normalized to the control condition, mean ± SE, n ≥ 4(5). An overview of the distribution of the results is provided in the scatter plot. Significance was determined by a two-sample t-test between the cell types using a significance level of 0.1 (*), 0.05 (**), and 0.01 (***). As a result, a significance level of 0.05 (**) was determined between the cell types in the concentration range of 20–300 mM, while no significant values ($^{n.s.}$) were obtained at the control condition or at a sucrose concentration of 400 mM (symbols not shown in the graph).

For detailed information, the area under the curve of the normalized diameter time course was calculated for each cell type within 90 minutes of exposure to osmotic pressure and plotted as a function of concentration (Fig. 7.54). The height of AUC values correlates with the spheroid volume alteration, while low values imply a certain volume reduction. Therefore, gradually decreasing AUC values are displayed with increasing sucrose concentration for both cell types, demonstrating a dose-response relation. In particular, the results from MCF-7 spheroids generally exhibit markedly higher AUC values compared to U-373 MG spheroids at each concentration, thus revealing a slightly stronger relative contraction ability of spheroids derived from U-373 MG cells induced upon the identical treatment. This finding is also represented in the relevant scatter plot (Fig. 7.54), providing a sigmoidal dose-response profile regardless of the cell type used with a distinct shift of the U-373 MG values towards lower levels.

Moreover, the slightly higher contraction ability may explain the enhanced capacitive value increase of 200 % after the application of 200 mM sucrose solution as examined by the dielectric spheroid parameter (see Tab. 7.15). During spheroid shrinkage, an increased level of programmed cell death is assumed to be induced by excessive contraction, which is amplified by the overall higher number of cell bodies involved in U-373 MG spheroids. Based on this, the higher degree of non-reproducible permeability is reflected.

The significance was calculated between the AUC values of the MCF-7 and U-373 MG spheroids using a two-sample t-test, which revealed a significance level of 0.05 (**) in the concentration range of 20−300 mM, while no significant values ($^{n.s.}$) were obtained in the control condition and a sucrose concentration of 400 mM. Thus, the difference between both cell types is evident as discussed, indicating the limited contraction of U-373 MG spheroids at the highest sucrose concentration upon the fourfold higher cell concentration by displaying not significantly different AUC values compared to MCF-7 spheroids.

Based on the AUC values, the EC_{50} values were calculated for each cell type and determined as 60 (± 30) mM (MCF-7; R^2 = 0.99; mean ± SE; n ≥ 5(9)) and 50 (± 20) mM (U-373 MG; R^2 = 0.98; mean ± SE; n ≥ 4(5)), which are not significant ($^{n.s.}$) to each other (see chapter 11.1, Fig. A-7.22). Since only four values were taken into account, the sigmoidal fit is not as precise, and the results have to be evaluated with caution.

In the literature, microscopic studies were performed by Hupf, revealing a specific spheroid swelling or shrinking by applying hypoosmotic or hyperosmotic buffer solutions, respectively (Hupf, 2018). By using time-lapse imaging using a self-made setup, she studied the influence over a period of 30 minutes and observed that the spheroids' size alters upon exposition to different osmolality conditions in a dose-response-dependent manner. For example, after 30 minutes of incubation, spheroids in hyperosmotic buffer exhibiting an osmolality of approximately 430 mosmol/kg show a decrease in diameter by 50 (± 8) µm, whereas spheroids in hyperosmotic buffer exhibiting an osmolality of approximately 530 mosmol/kg show a stronger decrease by 70 (± 4) µm (Hupf, 2018). Based on this, the evaluation of the results was in good agreement with the literature regarding the dose dependency of the spheroids´ response.

Taken together, the results indicate that the spheroid morphology changes in accordance with the concentration of sucrose exposure in a dose-response-dependent manner, regardless of the cell type used.

7.4.5 SUMMARY OF THE MODEL STUDY OF OSMOTIC PRESSURE

In this model study, the cellular response to osmotic pressure was characterized by using hyperosmotic buffer solutions with different osmolality levels prepared using varied sucrose concentrations. Based on the investigated results of several experimental approaches and the detailed data evaluation, the following statements were considered in relation to the cell types and cell dimensionality studied.

- ➔ The impedance of the monolayer culture changes individually as a function of sucrose concentration, showing an overall increasing signal trend for MCF-7 cells, whereas a decreasing trend was observed for U-373 MG cells.
- ➔ The impedance of spheroids decreases and subsequently increases with sucrose concentration, regardless of the cell type.
- ➔ The variance of increments increases and then decreases for monolayer cultures above a cell type-dependent concentration of 300 mM (MCF-7) and 200 mM (U-373 MG); for spheroids, the variance of increments increases and then decreases above 100 mM regardless of the cell type.
- ➔ The values of R_{ext} and R_{int} decrease, whereas A_{sph} increases with increasing sucrose concentration, regardless of the cell type.
- ➔ The spheroid diameter decreases more rapidly with increasing sucrose concentration, regardless of the cell type.

To highlight differences and similarities in the cellular responses obtained from monolayer cultures and spheroids, the results of the impedance measurements and the calculated EC_{50} values are summarized. An overview of the area under the curve obtained from impedance measurements using the ECIS™-based or EIS funnel-based measurement setup for monolayer cultures and spheroids, respectively, is provided for comparison (Fig. 7.55). Following the cell dimensionality, appropriate concentrations of sucrose were applied, and the AUC values of the detected signal changes were analyzed within the identical time period of 90 minutes after compound addition. As a result, the AUC values are representative of the magnitude of change of the impedance signal, whereby AUC values of approximately 100 % represent isosmotic conditions or the balance between cell shrinkage and cell expansion in 2D tissue models, whereas in 3D tissue models the balance between spheroid shrinkage and adaptation of the contracted spheroid to the funnel opening is indicated. In general, the scatter plot shows a decrease in AUC values with increasing sucrose concentration, regardless of the cell type or dimensionality (Fig. 7.55). The range of variation is higher for MCF-7 cells in both dimensionalities, indicating either an enhanced affection of the osmotic pressure compared to U-373 MG cells or a higher

degree of counterbalancing. In particular, the ascending versus the descending trend with regard to the individual cell type observed in monolayer culture is displayed.

Based on the distribution and color-coded order of the values within the variation range, the dose-response relationship is illustrated (Fig. 7.55). Three different patterns were observed depending on the cell type and tissue model configuration. The first scatter plot concerns the monolayer culture derived from MCF-7 cells and shows the results distribution of the different concentrations, reflecting the characteristic variation of a predominantly induced cell volume increase at lower concentrations and less pronounced cell shrinkage at higher concentrations. In contrast, the second scatter plot presents a different pattern, with two significant levels for U-373 MG cells, indicating either a balanced system or a dysregulated state emphasizing cell shrinkage. For the spheroid models, a similar pattern is evident, reflecting a sigmoidal dose-response profile over the entire cell type-specific range, which is extended over almost the entire range of 100 % for MCF-7 spheroids, whereas the range of U-373 MG spheroid results is found in the upper part.

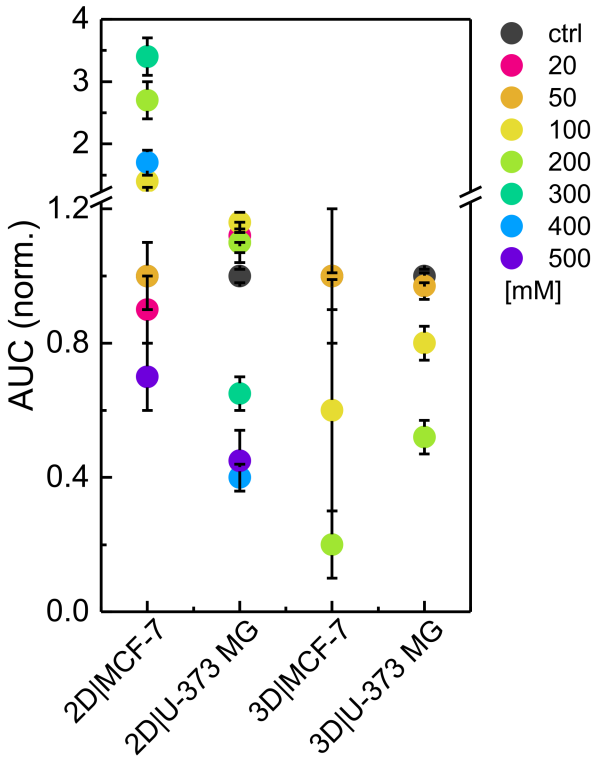

Fig. 7.55 Scatter plot of the normalized area under the curve values, which are derived from the time course of the normalized impedance magnitude recorded by using the ECIS™-based or the EIS funnel-based measurement setup for monolayer cultures and spheroids, respectively, and summarized as individual charts. Detailed experimental conditions are provided in the respective raw data information (Fig. 7.52; Fig. 7.53).

In particular, the results derived for the monolayer culture and the spheroid models obtained for the identical sucrose concentration of 200 mM are compared (Fig. 7.55). The findings show that, in the case

of MCF-7 cells, regardless of the dimensionality of the tissue model derived, the greatest change in AUC values is found, showing either a relative increase to 270 (± 30) % (2D tissue model) or a decrease to 20 (± 10) % (3D tissue model). For U-373 MG cells, AUC values of 110 (± 6) % (2D tissue model) and 52 (± 5) % (3D tissue model) are presented, indicating a higher tendency of approaching the equilibrium at 100 %. In contrast, the application of 50 mM sucrose concentration shows an overall similar cell response, irrespective of the cell type or cell dimensionality studied. In this case, a significant change in osmotic pressure was induced that triggers the cellular system and also enables regeneration close to isosmotic conditions. Thus, an adjustment of the concentration of the compound in relation to the cell type is required at sucrose concentrations above 50 mM to induce an identical change in response.

Based on the discussion, these tendencies were explained by the tightness of cell-cell contacts, which are expressed in a high amount just in MCF-7 cells than in U-373 MG cells (Paterson et al., 2003; Lewis-Tuffin et al., 2010). Thus, the cell shrinkage induced by applying hyperosmotic buffer solutions leads to a more pronounced regulatory cell volume increase (short RVI process) in MCF-7, yielding AUC values above 100 %. In addition, the characteristics of the cellular network also contribute to the investigated kinetics of the impedance signal increase, reflecting the adaptability of contracted spheroids to the central opening of the funnel device. In this way, U-373 MG spheroids were found to exhibit greater flexibility due to less cellular tightness than MCF-7 spheroids, thereby enabling faster impedance signal regeneration and overall higher AUC values. The dependency of the cell-cell contacts contributing to the osmotically induced cellular response was also reflected by the investigated highly significant difference of the extracellular resistance values calculated for both cell types after applying a sucrose concentration of 200 mM. In this case, the relative value decline was higher for MCF-7 spheroids, reflecting the influence of osmotic pressure on the intercellular junctions as a result of excessive cell body shrinkage and consequent damage to the cellular junctions.

As these observations are consistent with the presumed influence of osmotic pressure in different cellular systems, it is concluded that (i) increasing osmolality leads to a higher dysregulation of the cellular system, (ii) the recorded response depends on the layout of the measurement setup used, reflecting in monolayer culture the regulation of cell volume change and in 3D tissue models the adaptation of the contracted spheroid to the funnel opening, (iii) the physiology of the MCF-7 cells is more affected and dysregulated due to stronger intercellular conjugation compared to U-373 MG cells, and therefore (iv) the U-373 MG cells provide a more efficient compensation of the induced cell shrinkage until a certain critical concentration is exceeded.

In this model study, the influence of osmotic pressure was investigated using various approaches such as the impedance measurements of 2D and 3D tissue models and time-lapse observation of spheroids.

Based on the analyzed area under the curve values, several dose-response curves were generated and EC_{50} values were determined. In this way, the various signal outputs are combined into a single key value. The calculated values are summarized for each experimental setup and listed in relation to the cell monolayer as well as spheroid models tested (Tab. 7.16).

Tab. 7.16 Overview of the EC_{50} values of osmotic pressure using impedance measurements and time-lapse observation. The coefficient of determination is given in the table respectively for each experiment. The results are categorized by cell type and cell dimensionality, respectively. Detailed experimental conditions are provided in the respective raw data information (chapter 7.4.1; chapter 7.4.2; chapter 7.4.3). Mean values were calculated for each cell type and dimensionality without the results presented in parentheses. *As in the case of 2D tissue model assays, no EC_{50} value was determined from the results obtained from the MCF-7 cell monolayer, the mean value was set in accordance with the critical threshold concentration obtained from the impedance time course.

EC_{50} [mM]	MCF-7		U-373 MG	
	2D	3D	2D	3D
impedance measurements	/	(70 ± 5) R^2 = 0.99	190 ± 20 R^2 = 0.79	(110 ± 10) R^2 = 0.99
time-lapse observation	/	60 ± 30 R^2 = 0.99	/	50 ± 20 R^2 = 0.98
mean value	*~ 300**	60 ± 30	190 ± 20	50 ± 20

The previous model studies included cell viability experiments based on the PrestoBlue™ assay, which was not appropriate in this case due to the reversibility of the induced cellular response. Therefore, cell viability staining and fluorescence microscopy were used to confirm the persistent cell viability within e.g. spheroids treated with hyperosmotic buffer solution (see chapter 11.1, Fig. A-7.19). Accordingly, no impairment of cell viability is to be expected from the application of different hyperosmotic buffer solutions, except for certain 2D or 3D tissue models respective to the highest sucrose concentration applied, at which reduced cellular micromotion and consequently diminished variance values in combination with an increase of capacitive parameters were observed. As indicated previously, in the case of 2D tissue model assays, no EC_{50} value was determined from the results obtained from the MCF-7 cell monolayer. However, since a clear change in the impedance signal was observed as a function of the sucrose concentration used, either illustrated by the significant change of the impedance signal height or expressed by the absence of a subsequent impedance increase above a certain concentration, a critical concentration threshold was investigated for MCF-7 and U-373 MG cells. This critical concentration was set at 300 mM in the case of the MCF-7 cell monolayer and at 200 mM in the case of

U-373 MG cells. Since this result obtained for U-373 MG cells precisely correlates with the determined EC_{50} of 190 (± 20) mM, the EC_{50} of MCF-7 cells was also assumed to be in the range of approximately 300 mM, following the critical concentration obtained from the impedance time course. Thus, a significantly higher concentration, respective osmolality level, is necessary for changing the cellular response in MCF-7 cell monolayer cultures compared to U-373 MG cells. This conclusion is consistent with the expression of a higher number of intercellular junctions within MCF-7 cells, forming a tight and rigid cell network in which the contraction of individual cells is counteracted, thus requiring an increased osmotic pressure to overcome this effect.

The impedance measurements of spheroids using the new funnel-based measurement setup revealed high significant EC_{50} values for both cell types, yielding a lower EC_{50} value for MCF-7 cells and a higher value for U-373 MG cells (Tab. 7.16). Thus, a contrary relation compared to the 2D tissue models is revealed and indicates that a lower concentration of sucrose is required for MCF-7 cells to induce the same response. However, in this case, the relationship is correlated with the interpretation of the kinetic profiles, which showed that a slower impedance signal regeneration is revealed for MCF-7 spheroids caused by an enhanced cell network strength. Since the results reflect the consequence of the induced cell-specific morphology change rather than the actual osmotic pressure response, these values are used as an indication but are not included in the average of the EC_{50} values. The mean values of the time-lapse imaging are calculated as 60 (± 30) mM (MCF-7) and 50 (± 20) mM (U-373 MG), which are not significant and indicate the identical relation regarding the influence of osmotic pressure on the monolayer culture. Microscopic observations revealed that the rate of absolute diameter reduction is approximately 5–10 % higher in the case of U-373 MG spheroids corresponding to the slightly reduced EC_{50} value investigated. After summarizing the distinct EC_{50} values derived from each assay, the differences between the results indicate a clear relation between the cell types and the cell dimensionality. In general, the results indicate higher EC_{50} values in the case of MCF-7 cells by considering the more pronounced cell-cell connections, as already discussed. Furthermore, a highly significant difference was found between 2D and 3D tissue models by spheroids displaying four to five times lower EC_{50} values, which represents the requirement of lower osmolality by this factor to cause 50 % changes in response. This fact indicates the amplification of the cellular response within the three-dimensional structure after applying the identical sucrose concentration. Furthermore, the appearance of regulatory cell volume changes in cell monolayer culture, while no spheroid size increase was observed within the time period observed, emphasizes the higher impact and dysregulation of the spheroid system.

Taken together, distinct EC_{50} values were obtained for both cell types in relation to two- and three-dimensional cell cultures, demonstrating that (i) up to five times higher sucrose concentration is required for monolayer culture in contrast to spheroids for inducing the identical response, and that (ii) an enhanced osmotic pressure has to be induced to overcome the tight cell network causing a significant signal change in MCF-7 cells.

To summarize the results of the different approaches used in the osmotic pressure model study, all data were combined and presented with the key parameter *compensation degree*. For each cell type, the to the control condition normalized response to different sucrose concentrations, such as the AUC values, the variance of increments, or the three dielectric spheroid parameters, is plotted on a single graph, respectively for each cell type, without further processing the data. In this way, the overall concept of the model study is highlighted in one comprehensive overview, while detailed information and clear comparisons between the cell types used are provided in the individual results and discussion chapters. The scatter plot charts are categorized by the dimensionality of the *in vitro* model, the measurement setup used, such as impedance measurements or time-lapse imaging, and the calculated dielectric parameters. In general, a low *compensation degree* corresponds to greater invasiveness, leading to less regenerative potential; a high *compensation degree* corresponds to enhanced counterbalancing to regain the undisturbed, physiological state. Overall, a general dysregulation by an either increasing or decreasing *compensation degree* was observed for each parameter upon increasing sucrose concentration, independently of the cell type used or the derived cell culture configuration.

In the case of MCF-7 cells (Fig. 7.56), a higher variation range is displayed for all parameters in contrast to U-373 MG cells, mimicking a high impact of manipulation and less counterbalancing. The resulting tendency of 2D tissue models represents a mainly ascending distribution of values over the concentration range, which is also evident from an enhanced cellular micromotion, indicated by increasing values of the variance of increments. In contrast, the results of 3D tissue models are found in the range of a lower *compensation degree*, indicating the excessive influence of osmotic pressure amplified within the three-dimensional structure and the MCF-7 associated lowered adaptability to the funnel device. Moreover, in accordance with gradually decreasing spheroid diameters exhibiting a low *compensation degree*, no regulations of volume changes were observed in 3D tissue models, whereas the ascending tendencies in 2D tissue models indicate the volume increase occurring after osmotic stimulation. By the color-coded order of the variance of increments, a critical concentration of 300 mM in 2D and 100 mM in 3D tissue models was found at which the *compensation degree* changes significantly between excessive cell volume increase regulation towards rather insufficient

compensation. This fact concerns the reduced cellular activity above the critical concentration, while the permeability reflected by the capacitive parameter gradually increased with increasing osmotic pressure, reinforcing the calculated EC_{50} values found in this concentration rate. The steep decrease in extracellular and intracellular resistance implied the relationship between cell shrinkage and the consequent loss of intercellular junctions. With regard to the high number and strength of cellular junctions expressed in MCF-7 cells, the enhanced sensitivity towards osmotic pressure is emphasized, which serves as the basis for the discussion of distinct parameter results and their concentration dependency.

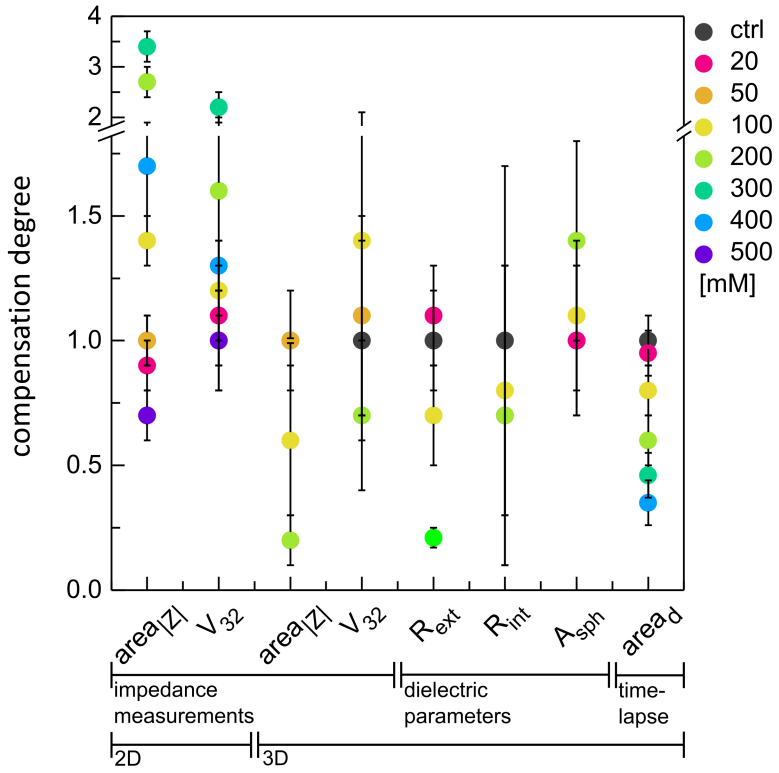

Fig. 7.56 Scatter plot of the normalized *compensation degree* values that were derived from different approaches used in the osmotic pressure model study by using MCF-7 cells and summarized as individual charts. The charts are categorized according to the dimensionality of the *in vitro* model (2D or 3D tissue models) and the measurement setup used (impedance measurements, calculated dielectric parameters, time-lapse imaging). A high or low *compensation degree* corresponds to excessive or insufficient compensation. Detailed experimental conditions are given in the respective raw data information (Fig. 7.43; Fig. 7.46; Fig. 7.52; Fig. 7.53; Tab. 7.15; Fig. 7.54).

The summary of the model study using U-373 MG cells provided a different overview (Fig. 7.57). In comparison to MCF-7 cells, the results mainly vary in the range around a *compensation degree* of 100 %, respectively exhibiting a smaller degree of variation. In this way, a less pronounced manipulation impact in combination with a high level of regulating the induced morphological alterations by regaining physiological equilibrium is demonstrated. For 2D and 3D tissue models, a similar descending tendency

of the impedimetric parameters was obtained. In particular, the results from the cell monolayer cultures demonstrate the change in cell volume regulation to a persistent reduction in cell size without compensation, while the results from the 3D tissue models indicate the adaptation of the contracted spheroids to the funnel opening, resulting in a corresponding equilibrium state.

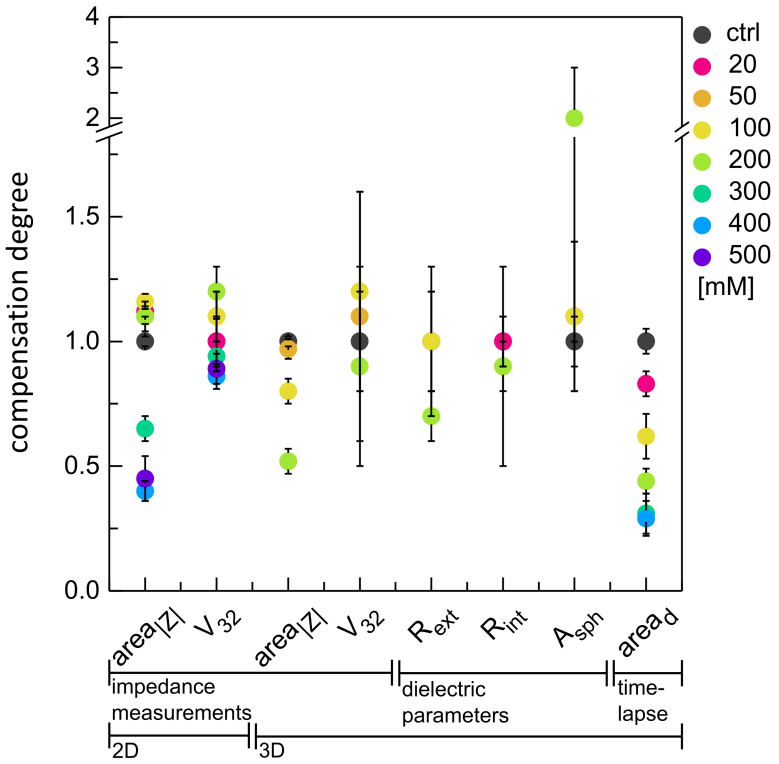

Fig. 7.57 Scatter plot of the normalized *compensation degree* values that were derived from different approaches used in the osmotic pressure model study by using U-373 MG cells and summarized as individual charts. The charts are categorized according to the dimensionality of the *in vitro* model (2D or 3D tissue models) and the measurement setup used (impedance measurements, calculated dielectric parameters, time-lapse imaging). A high or low *compensation degree* corresponds to excessive or insufficient compensation. Detailed experimental conditions are provided in the respective raw data information (Fig. 7.43; Fig. 7.46; Fig. 7.52; Fig. 7.53; Tab. 7.15; Fig. 7.54).

As already discussed, the calculated EC_{50} values emphasized the requirement of higher osmotic pressure to induce a signal change in monolayer culture, which further reveals an enhanced impact of the same osmolality level in spheroids. This fact is related to the observed critical concentration of 100 mM, at which the micromotion activity in spheroids decreases, and to the excessively high capacity, which indicates a distinct twofold degree of permeability inside the body. The height of the capacitance parameter reflects an increased degree of programmed cell death, which is induced by excessive contraction resulting in the dysregulation of cell physiology and architecture. This effect is amplified by the overall higher number of cell bodies involved in U-373 MG spheroids and the gradual, even stronger

spheroid shrinkage in contrast to MCF-7 spheroids with increasing osmotic pressure as shown in time-lapse observations. Since U-373 MG cells do not express a as high number of cellular connections compared to MCF-7 cells, the extracellular resistance was similar and less affected by the osmotic pressure. Thus, the cellular network exhibits high flexibility, as observed in the funnel-based measurements, and less sensitivity upon the manipulation.

In summary, the conclusions indicate that changes in cellular morphology due to hyperosmotic pressure exposure were detected in a dose-dependent manner following the gradual cellular shrinkage and the associated consequences. In this model study, several assays were performed to provide a comprehensive overview of the effects of the compound from different perspectives, such as impedimetric characterization and morphological properties. Since the experiments were performed using either cell monolayer cultures or spheroids, both derived from two different cell types, the individual results were discussed in relation to each other. Based on detailed data analysis, the results were combined into one big picture reflecting either distinct differences or similarities. The influence of osmotic pressure on the cellular response was thus clarified in that both monolayer culture and spheroids were affected similarly, although specific cell type responses and differences in the cell dimensionality were investigated. In this context, it is emphasized that (i) osmotic pressure has a fundamental effect at the subcellular level and (ii) the combination of several assays provides a comprehensive overview of the cellular response induced.

7.5 SUMMARY

In the framework of the experiments presented in this thesis, several model studies were performed to determine the cellular response to different manipulation strategies. For this purpose, different experimental treatments were used that induce previously characterized stimulation processes and consequently known cell responses. By the application of a chemical cross-linker (chapter 7.2), a detergent (chapter 7.2), an actin filament polymerization inhibitor (chapter 7.3), or hyperosmotic buffer solutions (chapter 7.4), different scenarios of cell death were mimicked.

To illustrate the comprehensiveness of the measurement assays used, the main feature of each measurement principle was visualized in one figure (Fig. 7.58). Each assay played a distinct role in the overall model study, providing evidence to explain the results from different perspectives and preliminary information. Specific characteristics and selected results derived from the work presented in this thesis are summarized in this chapter.

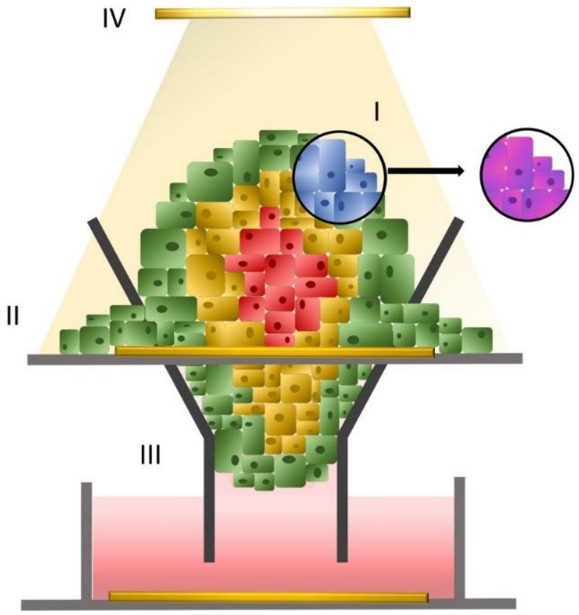

Fig. 7.58 Illustration* of the distinct measurement assays used in the model studies presented in this thesis. The main feature of each measurement principle is visualized and combined in one figure, thereby emphasizing the comprehensiveness of the experiments used. Cell viability of 2D and 3D tissues was determined using the PrestoBlue™ assay by detecting the fluorescence intensity of the non-fluorescent redox indicator resazurin, which is reduced to pink resorufin in metabolically active cells (I). To analyze the cellular response of 2D tissue models, impedimetric measurements based on the ECIS™ technique were performed by cultivating cell monolayers on commercially available planar gold electrode substrates (II). The novel EIS funnel-based setup was used to monitor the impedance signal of spheroids positioned inside the micro-trap device, by additionally allowing compound addition directly during the measurement (III). To continuously monitor the morphological changes of the spheroids during compound treatment, the zenCELL owl digital microscope was used to perform time-lapse microscopy measurements (IV).

**illustration is simplified and not to scale*

The cellular response to the different stimuli was analyzed based on impedance measurements and complementary microscopic images of three-dimensional tissue models, impedance measurements on cell monolayer cultures, or biochemical endpoint assays such as the PrestoBlue™ assay. After data processing and a combination of the results derived from the specific measurement setup signals in one key value, a comprehensive overview of the effects of each stimulation was provided from different perspectives such as cytotoxic specification, impedimetric characterization, and morphological properties. In this context, the sensitivity and applicability of the newly developed funnel-based device were evaluated by considering its advantages and limitations of use.

Based on the assays used, the results show that (i) a standard cell viability assay can also be used for spheroids, (ii) the assessment of cytotoxicity by impedance analysis provides similar results without the use of labels, and (iii) the time-lapse imaging is a supportive tool for discussing morphological changes.

I CELL VIABILITY ASSAY

The PrestoBlue™ cell viability assay (Invitrogen™, Thermo Fisher Scientific) was used to determine the invasiveness of various compound concentrations on the metabolic activity of tissue models. This assay is commonly used to study the cellular response of monolayer culture, whereby it was also used to perform spheroid experiments in the framework of this thesis by adapting the protocol. Based on the evaluation of the measured fluorescence intensities and the calculation of the cytotoxicity indices, the changes in metabolic activity as a function of different compound concentrations applied were investigated. As a result, the inflection point of the sigmoidal dose-response curve determined by the Boltzmann equation represents the EC_{50} value, which corresponds to the concentration of a tested compound causing a 50 % change in response or a 50 % reduction in cell viability (chapter 4.1.8, Eq. 4.2). Therefore, the PrestoBlue™ assay was an ideal tool in the model studies for providing information in advance to classify the specific concentration range at which cells will be affected by the compound. In addition, the dependency of the cellular responses between 2D and 3D tissue models could be evaluated. Since the assay is an endpoint test, only one defined incubation period can be examined per run. In this way, experiments were performed with an appropriate time period after compound addition or by testing two separate approaches with different time periods, for example, five hours for stimulation with saponin or five and 10 hours for stimulation with cytochalasin D. In the case of investigating the cellular response to osmotic pressure, the PrestoBlue™ assay was not appropriate due to the reversibility of the induced cellular response. Therefore, cell viability staining and fluorescence microscopy were used to confirm the persistent cell viability within spheroids treated with hyperosmotic buffer solution.

II ECIS™-BASED MEASUREMENTS OF 2D TISSUE MODELS

To analyze the cellular response of 2D tissue models in a label-free and time-resolved manner, impedimetric measurements based on the ECIS™ technique were performed. Since it is a very sensitive technique to monitor the barrier functionality changes of adherent cell monolayers, it can be applied for the analysis of different kinds of stimuli as shown in this thesis. The measurement setup enables the recording of cellular changes over a variable period and from eight different approaches per array. Using this approach, the influence of a variety of different compound concentrations was studied, thereby providing a representative dose-response dependency. After the application of different compounds, the cellular response is reflected by various signal parameters concerning resistive and capacitive contributions generating specific signal patterns and hence a particular insight into each cell response change. The evaluation and interpretation of the results were in good agreement with the literature findings regarding the predictable stimulation effects in cell models. Based on a well-characterized measurement method and the low complexity of the 2D tissue models studied, the results offer the basis for the characterization of the newly developed funnel-based measurement setup and the interpretation of the cell responses of three-dimensional tissue models made within the same model study. Therefore, similar data structure, signal parameters, and data processing of both measurement setups enable the discussion of signal outputs in relation to the cell dimensionality and the compound concentration applied.

III FUNNEL-BASED MEASUREMENTS OF 3D TISSUE MODELS

In this thesis, a novel impedance-based measurement device was developed for the analysis of spheroid responses. The application of the device was investigated using different model studies demonstrating that the setup enables sensitive, time-resolved monitoring of cellular changes within the tissue model and spheroid body dynamics inside the funnel. To characterize the impedance signal of the measurement setup in terms of signal output and result interpretation, initial fundamental model studies were performed with varying spheroid size, age, and pH. In this way, ideal tissue model conditions were determined and used for subsequent experiments, providing a standardized setting for repeatability and comparability of the measurements (chapter 7.1). The setup was designed to allow the compound addition directly during the measurement, which enables online monitoring of the cellular response without time delay and the requirement for pre-incubation or spheroid repositioning. This is a key advantage of the newly developed setup in comparison to the previous flow channel-based measurements setup, as direct compound addition provides the basis for the simultaneous performance of different stimulations with regard to the measurement of eight approaches in one array.

The responses of the spheroids to various stimuli with known effects were recorded for an appropriate period of time after compound addition, revealing specific signal changes regarding impedance, cellular micromotion, and the dielectric properties of the spheroid body. Based on the model studies performed, a limiting factor in the use of the funnel-based measuring device was observed, as it is crucial for data acquisition that the spheroid body rests in its position sealing the central opening. As shown in the model study of cell membrane permeabilization, the spheroid has to be secured in place by cross-linking the membrane proteins prior to treatment. Thus, a two-step process was required to record the impedance changes during the permeabilization process. Since pre-fixation is not applicable for every subsequent stimulation, as in the case of the application of cytochalasin D to inhibit actin filament polymerization, the spheroid body was disassembled upon treatment and slipped through the central opening. After data processing, the results were interpreted based on the findings in cell monolayer culture and discussed in terms of dose-response dependencies, cell type characteristics, and tissue model dimensionality.

IV TIME-LAPSE MICROSCOPY MEASUREMENTS

The zenCELL owl digital microscope was used to enable continuous observation of multicellular spheroids by performing time-lapse microscopy measurements. The measurement setup allows the monitoring of 24 different samples per plate by capturing images of each well with a time resolution of 10 minutes. This time resolution was sufficient for the purposes of the model studies, although this feature was improved later in collaboration with the manufacturer. After establishing a routine for positioning the spheroids approximately in the field of view of each well, fundamental studies of the spheroid characteristics were performed. Based on this, the influence of different stimuli on the morphological properties of adhered spheroids was investigated, utilizing time-resolved imaging as an additional tool for model studies concerning induced changes in cellular morphology. The recorded images were analyzed, especially concerning the changes in the 3D tissue models, while additionally providing an overview of the changes within the monolayer culture surrounding the spheroid. The results of the observations serve to confirm and explain those of the impedance spectroscopy, making the combination of different approaches an appropriate strategy. For example, in the case of the model study investigating the cellular response to osmotic pressure, the discussion of the impedance time course of either spheroid volume increase or progressive sealing of the funnel aperture was clarified by time-lapse imaging showing no spheroid expansion within this particular time period. Thus, the recording of morphological properties provides a different perspective on cellular responses and completes the model study concept in combination with the determination of cell viability effects and the investigation of impedimetric properties.

V DATA ANALYSIS

For data analysis, the specific parameters of each measurement approach were evaluated and discussed to highlight the characteristic aspects revealed by each application. To compare the cellular responses obtained from monolayer culture and spheroids, the results of the recorded impedance time courses were discussed based on the calculated EC_{50} values. Furthermore, to summarize the results of the different approaches used within the specific model studies, all data were collected and presented with the key parameter *activity level* for permeabilization effects and the key parameter *compensation degree* for osmotic pressure-induced effects. Therefore, the normalized response to different compound concentrations, such as the AUC values, the variance of increments, or the three dielectric spheroid parameters, are plotted in a single graph for each cell type. This overview serves to highlight the comprehensive concept of the model studies performed, while detailed information and clear comparisons between the cell types used are provided in the individual results and discussion chapters. In this context, it should be noted that the time period evaluated is highly dependent on the treatment and the cellular structure being studied. In the optimal case, identical periods are used within the model study regardless of the approach, as shown by the application of different hyperosmotic buffer solutions, while different time periods specific to each experiment are also similar.

7.6 OUTLOOK

The results of the model studies, which combine different experimental approaches, demonstrate the applicability of the measurement techniques used and the strategy of gaining specific insights for a comprehensive overview of the cellular response. Based on the findings of this work, the new EIS-based micro-trap device was characterized as a promising setup for the non-invasive and time-resolved readout of spheroid responses. It was shown that the developed setup is applicable for fundamental research on 3D tissue models.

Based on the demonstrated cellular model studies, additional manipulation methods are feasible. For instance, in addition to the exposure to osmotic pressure using hypertonic buffer solutions, the application of hypotonic solutions would provide a complementary study. In this case, an opposite effect is induced, resulting in an immediate increase in cell volume upon water influx. Thus, a contrary signaling response regarding the impedimetric characterization and diameter changes in time-lapse observations would be expected. Additionally, the influence of compounds causing inhibitory effects on specific aspects of water flux can be addressed in a combined assay, as examined by Kade studying aquaporin AQP1 inhibition in canine kidney MDCK-I and trabecular meshwork HTM-N cells detected by QCM measurements (Kade, 2023). Another example is the cellular response to hyperthermia applying enhanced temperatures of 45 °C, as demonstrated by Hupf performing impedance measurements with the flow channel-based setup and pre-stimulated spheroids (Hupf, 2018). This approach is utilized in cancer therapy to sensitize cells for subsequent tumor treatment. In this context, the duration of exposure and the temperature applied can be analyzed, which will have a particular effect on cell dynamic, as reflected in changes in cell micromotion, and less influence on overall cell morphology. Based on the multistep assay of spheroid fixation and subsequent permeabilization performed in the experiments presented in this thesis, the performance of a serial compound addition protocol as developed by Stolwijk et al. in the context of stimulating G-protein-coupled receptors would also be feasible in 3D tissue models through the use of the new micro-trap device (Stolwijk et al., 2019). In serial mode, the compound is added stepwise to a population of cells at successively increasing concentrations at equal time intervals. This procedure is applicable to most compound additions, making a full concentration-response relationship available from one cell population (Stolwijk et al., 2019). In particular, the signal response of U-373 MG spheroids to histamine solutions was demonstrated in a proof-of-principle experiment, investigating the typical time course of impedance change upon compound addition (datasets not shown).

In this thesis, two different cell types, namely MCF-7 and the U-373 MG cells, were used for the model studies investigating cell type-dependent differences and similarities. Since the measurement setups and the model studies presented are independent of the cell type studied, the experiments are applicable to a variety of different spheroid-forming cell types. For example, upon the formation of cardiospheres derived from Cor.At® cells, 3D tissue models of regularly beating cells are generated. Since these spheroids are also accessible via the funnel-based measurement setup, various parameters such as beats per minute and the amplitude of beating-related fluctuations are determined by recording RTC measurements, as tested by Hupf (Hupf, 2018). This enables the analysis of the influence of different compounds modulating the beating efficiency.

The use of varied experimental approaches provides a comprehensive view of different perspectives such as cytotoxic specification, impedimetric characterization, and morphological properties, which were evaluated within the distinct model studies. This combination of diverse techniques could be supplemented by the determination of oxygen consumption rates recorded by the use of fluorescence ratiometric imaging. In cooperation with PreSens Precision Sensing GmbH (Regensburg), Schmittlein developed an imaging system based on microscopy optics (VisiSens TD mic) and investigated its applicability for non-invasive monitoring of oxygen gradient formation in 2D and 3D tissue models (Schmittlein, 2018). In addition to fundamental model studies, cell manipulation by the addition of blockers or uncouplers of oxidative phosphorylation was also performed (Schmittlein, 2018). Thus, the measurement technique would serve as a suitable complement to the devices used in this thesis to obtain further supplementary information from the cellular system under investigation.

CHAPTER 8

SUMMARY

The use of 3D tissue models as *in vitro* models provides a powerful tool for numerous cell-based assays in biomedical research and drug screening. Based on their characteristic microenvironment, spheroids mimic tumor behavior more effectively than conventional two-dimensional monolayer cultures and are therefore applied in preclinical screening experiments for assessing drug safety while identifying potential cancer therapeutics. A challenging aspect in this context is the development of applicable techniques and measurement setups capable of extracting significant biological information from such models and detecting morphological or biochemical changes upon stimulation.

This thesis presents the design of a newly developed impedance-based device for the non-invasive and label-free analysis of spheroids. The measurement setup is based on an existing flow channel device developed by C. Hupf (Hupf, 2018), in which the orientation of the system was shifted from a horizontal to an upright position. As a result, an upright funnel-shaped micro-trap with a central opening between two electrodes was produced. For the purpose of setup characterization, various aspects such as specific dimensions of the funnel-based micro-trap, the choice of the manufacturing material, or the overall measurement principle were investigated in detail and adjusted to achieve optimal settings. As a result, spheroid measurements could be conducted in a highly sensitive and reproducible manner, detecting the impedimetric responses of up to eight spheroids respective experiments in parallel.

When a spheroid is inserted into the device, it is retained at the aperture and seals the opening by adapting to the smaller diameter of the funnel hole through gravitational forces. In this way, EIS analysis of the trapped spheroid is enabled by forcing the electric current to flow through the 3D tissue model, thereby yielding a significant impedance signal increase due to spheroid positioning in a time-resolved manner. In addition, the overall impedance contribution of the system and signal changes obtained by intrinsic spheroid changes are addressed. To quantify the dielectric properties of spheroids, a transfer function is used that describes the equivalent circuit model of a spheroid in the EIS device, representing both the extracellular and intracellular resistance combined with the capacitance contribution of the tissue model.

The impedance signaling of the newly developed funnel-based measuring device was determined in relation to basic spheroid features. Therefore, the spheroids derived from breast cancer and brain tumor cells were characterized in a comprehensive microscopic study, investigating the spheroid formation procedure, their growth behavior, and the kinetics of their adhesion to a surface. In addition, fundamental model studies on three different aspects of the tissue model conditions, namely spheroid size, spheroid age, and pH, were performed by analyzing their influence on the impedimetric parameters. As a result, the optimal setting for the tissue model conditions in the context of this thesis

was obtained while investigating the signal output and result interpretation of the new measurement setup.

In addition to the design and characterization of the new setup, the application of the device has to be evaluated. Since the setup has the crucial advantage of allowing stimulation studies during an impedance measurement, the respective compound solution was applied via the upper compartment to induce cellular responses without removing the spheroid from the trap. The cellular response to the varied stimuli mimicking different cell death scenarios was analyzed based on spheroid impedance measurements and complementary time-lapse microscopy, impedance measurements on cell monolayer cultures, and biochemical endpoint assays determining cell viability. This provided a comprehensive overview of the effects of each stimulation from different perspectives, such as cytotoxic specification, impedimetric characterization, and morphological properties, by summarizing the specific measurement setup signals into a single key parameter. In this context, the sensitivity and applicability of the newly developed funnel-based device were evaluated by considering its advantages and limitations of use.

In conclusion, the funnel-based impedance measurement device provides a non-invasive, label-free, and time-resolved novel sensing method for monitoring 3D tissue models and their changes during biomedical experiments.

CHAPTER 9

ZUSAMMENFASSUNG

Dreidimensionale Gewebemodelle werden in Form von *in vitro* Modellen für viele verschiedene zellbasierte Tests in der biomedizinischen Forschung und der Arzneimittelentwicklung verwendet. Aufgrund ihrer charakteristischen Mikroumgebung imitieren Sphäroide das Verhalten von Tumoren im Vergleich zu zweidimensionalen, planaren Zellmodellen besser und werden daher bevorzugt zur Bewertung der Arzneimittelsicherheit sowie zur Identifizierung potenzieller Krebstherapeutika eingesetzt. Eine große Herausforderung hierbei ist die Entwicklung geeigneter Techniken und Messsysteme, die in der Lage sind, signifikante biologische Informationen der verwendeten Gewebemodelle zu erfassen und mittels Stimulation induzierte, morphologische bzw. biochemische Veränderungen zu erkennen.

In dieser Arbeit wird die Entwicklung eines neuen, impedanzbasierten Messsystems für die nicht-invasive und markierungsfreie Analyse von Sphäroiden dargestellt. Der Messaufbau basiert auf einem von C. Hupf entwickelten Fließkanal (Hupf, 2018), indem die Orientierung des Gesamtsystems von einer horizontalen zu einer vertikalen Ausrichtung geändert wurde. Dadurch entstand eine trichterförmige Messvorrichtung mit einer zentralen Öffnung, welche zwischen zwei Elektroden platziert wird. Zur Charakterisierung des Aufbaus wurden verschiedene Aspekte wie die spezifischen Abmessungen der Apparatur, die Wahl des Herstellungsmaterials und das generelle Messprinzip im Detail untersucht und entsprechend angepasst, um optimale Einstellungen zu erreichen. So konnten die Messungen mit hoher Empfindlichkeit und Reproduzierbarkeit durchgeführt werden, wobei das Impedanzsignal von bis zu acht Sphäroiden bzw. Experimenten parallel erfasst wurde.

Sobald ein Sphäroid in die Vorrichtung eingesetzt wird, wird dieser von der zentralen Trichteröffnung zurückgehalten und verschließt diese, indem sich der Sphäroid bedingt durch die Schwerkraft an den kleineren Durchmesser des Trichterlochs anpasst. Auf diese Weise ist es möglich, impedimetrische Messungen des eingesetzten Sphäroids durchzuführen, indem der applizierte Stromfluss direkt durch das dreidimensionale Gewebemodell geleitet wird. Somit wird durch die Positionierung des Sphäroids in der Messvorrichtung ein signifikanter Anstieg des Impedanzsignals erzeugt und Signaländerungen, die durch intrinsische Veränderungen des Sphäroids verursacht werden, werden zeitaufgelöst erfasst. Zur Quantifizierung der dielektrischen Eigenschaften von Sphäroiden wird eine mathematische Übertragungsfunktion verwendet, die das Ersatzschaltbild eines Sphäroids im Messsystem beschreibt und sowohl den extrazellulären als auch den intrazellulären Widerstand zusammen mit dem Kapazitätsbeitrag des Gewebemodells darstellt.

Die Empfindlichkeit des Impedanzsignals des neu entwickelten trichterbasierten Messsystems wurde in Abhängigkeit von grundlegenden Merkmalen der Sphäroide bestimmt. Dazu wurden Sphäroide aus Brustkrebs- und Gehirntumorzellen gebildet und in einer umfassenden mikroskopischen Studie

charakterisiert, in der der Prozess zur Bildung von Sphäroiden, deren Wachstumsverhalten und die Kinetik der Anhaftung von Sphäroiden an einer Oberfläche untersucht wurden. Durch die Impedanzanalyse von Sphäroiden mit unterschiedlicher Größe, Alter und pH-Wert wurde deren Einfluss auf die impedimetrischen Messgrößen analysiert. Hierdurch konnten die optimalen Bedingungen für den Sphäroid als Testobjekt zur Anwendung in weiterführenden Experimenten ermittelt werden.

Neben dem Design und der Charakterisierung des neuen Messsystems wurde zudem dessen Anwendbarkeit getestet. Das neu entwickelte System besitzt den entscheidenden Vorteil, Sphäroide direkt während einer Messung durch die Zugabe von Substanzlösungen über das obere Trichterkompartiment zu stimulieren und zu manipulieren, ohne dass der Sphäroid aus der Messvorrichtung entfernt werden muss. Dadurch kann die zelluläre Reaktion ausgelöst und zeitgleich detektiert werden. Dies ermöglichte die Durchführung von Modellstudien, in denen durch die Verwendung unterschiedlicher Stimulanzien verschiedene Zelltodszenarien nachgeahmt wurden. Innerhalb einer Studie wurden unterschiedliche Messmethoden angewendet, welche einerseits die resultierende Zellantwort anhand der Veränderung des Impedanzsignals von drei- und zweidimensionalen Zellstrukturen messen, und andererseits den Einfluss auf die Zellvitalität sowie die zeitabhängige morphologische Veränderung der Sphäroide darstellen. Durch die Kombination der Ergebnisse aus der erhaltenen zytotoxischen Spezifikation, impedimetrischen Charakterisierung und visuellen Darstellung der Gewebemodelle zu einem aussagekräftigen, übergeordneten Kennwert konnte die Auswirkung der verschiedenen Manipulationsstrategien gesamtheitlich betrachtet werden. In diesem Zusammenhang wurde die Empfindlichkeit sowie die Verwendbarkeit des neu entwickelten trichterbasierten Messsystems unter Berücksichtigung seiner Vorteile und Einschränkungen in der Anwendung validiert.

Auf Grundlage der Ergebnisse ist festzustellen, dass das impedanzbasierte Messsystem eine nicht-invasive, markierungsfreie und zeitlich hochaufgelöste Analysemethode darstellt, die zur Überwachung von dreidimensionalen Gewebemodellen und deren Veränderungen während biomedizinischer Experimente angewendet werden kann.

CHAPTER 10

REFERENCES

A

Abdalla, S., Al-Ameer, S.S. and Al-Magaishi, S.H., **2010**. Electrical properties with relaxation through human blood. *Biomicrofluidics*, 4(3).

Achilli, T.M., McCalla, S., Meyer, J., Tripathi, A. and Morgan, J.R., **2014**. Multilayer spheroids to quantify drug uptake and diffusion in 3D. *Molecular pharmaceutics*, 11(7), pp.2071-2081.

Aijian, A.P. and Garrell, R.L., **2015**. Digital microfluidics for automated hanging drop cell spheroid culture. *Journal of laboratory automation*, 20(3), pp.283-295.

Amaral, D.B.J., Urabayashi, S.M. and Machado-Santelli, M.G., **2010**. Cell death and lumen formation in spheroids of MCF-7 cells. *Cell biology international*, 34(3), pp.267-274.

Anil-Inevi, M., Yaman, S., Yildiz, A.A., Mese, G., Yalcin-Ozuysal, O., Tekin, H.C. and Ozcivici, E., **2018**. Biofabrication of in situ self assembled 3D cell cultures in a weightlessness environment generated using magnetic levitation. *Scientific reports*, 8(1), p.7239.

Antoni, D., Burckel, H., Josset, E. and Noel, G., **2015**. Three-dimensional cell culture: a breakthrough in vivo. *International journal of molecular sciences*, 16(3), pp.5517-5527.

Arias-Montaño, J.A., Berger, V. and Young, J.M., **1994**. Calcium-dependence of histamine-and carbachol-induced inositol phosphate formation in human U373 MG astrocytoma cells: comparison with HeLa cells and brain slices. *British journal of pharmacology*, 111(2), pp.598-608.

Arndt, S., Seebach, J., Psathaki, K., Galla, H.J. and Wegener, J., **2004**. Bioelectrical impedance assay to monitor changes in cell shape during apoptosis. *Biosensors and Bioelectronics*, 19(6), pp.583-594.

B

Bain, G., Ray, W.J., Yao, M. and Gottlieb, D.I., **1994**. From embryonal carcinoma cells to neurons: the P19 pathway. *Bioessays*, 16(5), pp.343-348.

Barsoukov, E. and Macdonald, J.R. eds., **2018**. *Impedance spectroscopy: theory, experiment, and applications*. John Wiley & Sons.

Bartholomä, P., Impidjati, Reininger-Mack, A., Zhang, Z., Thielecke, H. and Robitzki, A., **2005**. A more aggressive breast cancer spheroid model coupled to an electronic capillary sensor system for a high-content screening of cytotoxic agents in cancer therapy: 3-dimensional in vitro tumor spheroids as a screening model. *Journal of biomolecular screening*, 10(7), pp.705-714.

Beaumont, K.A., Anfosso, A., Ahmed, F., Weninger, W. and Haass, N.K., **2015**. Imaging-and flow cytometry-based analysis of cell position and the cell cycle in 3D melanoma spheroids. *JoVE (Journal of Visualized Experiments)*, (106), p.e53486.

Berrier, A.L. and Yamada, K.M., **2007**. Cell–matrix adhesion. *Journal of cellular physiology*, 213(3), pp.565-573.

Bigner, D.D., Bigner, S.H., Ponten, J., Westermark, B., Mahaley Jr, M.S., Ruoslahti, E., Herschman, H., Eng, L.F. and Wikstrand, C.J., **1981**. Heterogeneity of genotypic and phenotypic characteristics of fifteen permanent cell lines derived from human gliomas. *Journal of Neuropathology & Experimental Neurology*, 40(3), pp.201-229.

Birchler, A., Berger, M., Jäggin, V., Lopes, T., Etzrodt, M., Misun, P.M., Pena-Francesch, M., Schroeder, T., Hierlemann, A. and Frey, O., **2016**. Seamless combination of fluorescence-activated cell sorting and hanging-drop networks for individual handling and culturing of stem cells and microtissue spheroids. *Analytical chemistry*, 88(2), pp.1222-1229.

Björkhem, I. and Meaney, S., **2004**. Brain cholesterol: long secret life behind a barrier. *Arteriosclerosis, thrombosis, and vascular biology*, 24(5), pp.806-815.

Black, J. and Andreas, H.A., **2009**. Effects of charge redistribution on self-discharge of electrochemical capacitors. *Electrochimica Acta*, 54(13), pp.3568-3574.

Boghaert, E.R., Lu, X., Hessler, P.E., McGonigal, T.P., Oleksijew, A., Mitten, M.J., Foster-Duke, K., Hickson, J.A., Santo, V.E., Brito, C. and Uziel, T., **2017**. The volume of three-dimensional cultures of cancer cells in vitro influences transcriptional profile differences and similarities with monolayer cultures and xenografted tumors. *Neoplasia*, 19(9), pp.695-706.

Breslin, S. and O'Driscoll, L., **2016**. The relevance of using 3D cell cultures, in addition to 2D monolayer cultures, when evaluating breast cancer drug sensitivity and resistance. *Oncotarget*, 7(29), p.45745.

Brophy, C.M., Luebke-Wheeler, J.L., Amiot, B.P., Khan, H., Remmel, R.P., Rinaldo, P. and Nyberg, S.L., **2009**. Rat hepatocyte spheroids formed by rocked technique maintain differentiated hepatocyte gene expression and function. *Hepatology*, 49(2), pp.578-586.

Bruns, T., Schickinger, S., Wittig, R. and Schneckenburger, H., **2012**. Preparation strategy and illumination of three-dimensional cell cultures in light sheet–based fluorescence microscopy. *Journal of Biomedical Optics*, 17(10), pp.101518-101518.

Burg, M.B., Ferraris, J.D. and Dmitrieva, N.I., **2007**. Cellular response to hyperosmotic stresses. *Physiological reviews*, 87(4), pp.1441-1474.

Bürgel, S.C., Kim, J.Y., Hierlemann, A. and Frey, O., **2013**. Electrical impedance spectroscopy for label-free, continuous monitoring of drug impact on 3D tissue spheroids. In *17th International Conference on Miniaturized Systems for Chemistry and Life Sciences, MicroTAS 2013*, Chemical and Biological Microsystems Society., pp.1797-1799.

Bürgel, S.C., Schmid, Y., Agarkova, I., Fluri, D.A., Kelm, J.M., Hierlemann, A. and Frey, O., **2015**, January. Simultaneous impedance spectroscopy and stimulation of human iPS-derived cardiac 3D spheroids in hanging-drop networks. In *2015 28th IEEE International Conference on Micro Electro Mechanical Systems (MEMS)*, IEEE, pp.226-229.

Bürgel, S.C., Diener, L., Frey, O., Kim, J.Y. and Hierlemann, A., **2016**. Automated, multiplexed electrical impedance spectroscopy platform for continuous monitoring of microtissue spheroids. *Analytical chemistry*, 88(22), pp.10876-10883.

C

Cadart, C., Venkova, L., Recho, P., Lagomarsino, M.C. and Piel, M., **2019**. The physics of cell-size regulation across timescales. *Nature Physics*, 15(10), pp.993-1004.

Caliari, S.R. and Burdick, J.A., **2016**. A practical guide to hydrogels for cell culture. *Nature methods*, 13(5), pp.405-414.

Campbell, C.E., Laane, M.M., Haugarvoll, E. and Giaever, I., **2007**. Monitoring viral-induced cell death using electric cell–substrate impedance sensing. *Biosensors and Bioelectronics*, 23(4), pp.536-542.

Carlsson, J., Nilsson, K., Westermark, B., Ponten, J., Sundström, C., Larsson, E., Bergh, J., Påhlman, S., Busch, C. and Collins, V.P., **1983**. Formation and growth of multicellular spheroids of human origin. *International journal of cancer*, 31(5), pp.523-533.

Carlsson, K., Danielsson, P.E., Lenz, R., Liljeborg, A., Majlöf, L. and Åslund, N., **1985**. Three-dimensional microscopy using a confocal laser scanning microscope. *Optics letters*, 10(2), pp.53-55.

Casey, R.C., Burleson, K.M., Skubitz, K.M., Pambuccian, S.E., Oegema Jr, T.R., Ruff, L.E. and Skubitz, A.P., **2001**. β1-integrins regulate the formation and adhesion of ovarian carcinoma multicellular spheroids. *The American journal of pathology*, 159(6), pp.2071-2080.

Casey, J.R., Grinstein, S. and Orlowski, J., **2010**. Sensors and regulators of intracellular pH. *Nature reviews Molecular cell biology*, 11(1), pp.50-61.

Cole, K.S., **1940**, January. Permeability and impermeability of cell membranes for ions. In *Cold Spring Harbor symposia on quantitative biology, Cold Spring Harbor Laboratory Press,* 8, pp.110-122.

Cole, K.S., **1972**. *Membranes, ions and impulses: a chapter of classical biophysics* (Vol. 1). Univ of California Press.

Comşa, Ş., Cimpean, A.M. and Raica, M., **2015**. The story of MCF-7 breast cancer cell line: 40 years of experience in research. *Anticancer research*, 35(6), pp.3147-3154.

Cooper, J.A., **1987**. Effects of cytochalasin and phalloidin on actin. *The Journal of cell biology*, 105(4), pp.1473-1478.

Costa, E.C., Gaspar, V.M., Coutinho, P. and Correia, I.J., **2014**. Optimization of liquid overlay technique to formulate heterogenic 3D co-cultures models. *Biotechnology and bioengineering*, 111(8), pp.1672-1685.

Costa, E.C., Moreira, A.F., de Melo-Diogo, D., Gaspar, V.M., Carvalho, M.P. and Correia, I.J., **2016**. 3D tumor spheroids: an overview on the tools and techniques used for their analysis. *Biotechnology advances*, 34(8), pp.1427-1441.

Costa, E.C., de Melo-Diogo, D., Moreira, A.F., Carvalho, M.P. and Correia, I.J., **2018**. Spheroids formation on non-adhesive surfaces by liquid overlay technique: Considerations and practical approaches. *Biotechnology journal*, 13(1), p.1700417.

Costa, E.C., Silva, D.N., Moreira, A.F. and Correia, I.J., **2019**. Optical clearing methods: an overview of the techniques used for the imaging of 3D spheroids. *Biotechnology and bioengineering*, 116(10), pp.2742-2763.

Cuddapah, V.A., Robel, S., Watkins, S. and Sontheimer, H., **2014**. A neurocentric perspective on glioma invasion. *Nature Reviews Neuroscience*, 15(7), pp.455-465.

Cui, P. and Wang, S., **2019**. Application of microfluidic chip technology in pharmaceutical analysis: A review. *Journal of pharmaceutical analysis*, 9(4), pp.238-247.

Curto, V.F., Ferro, M.P., Mariani, F., Scavetta, E. and Owens, R.M., **2018**. A planar impedance sensor for 3D spheroids. *Lab on a Chip*, 18(6), pp.933-943.

D

Deo, K.A., Singh, K.A., Peak, C.W., Alge, D.L. and Gaharwar, A.K., **2020**. Bioprinting 101: design, fabrication, and evaluation of cell-laden 3D bioprinted scaffolds. *Tissue Engineering Part A*, 26(5-6), pp.318-338.

Desoize, B. and Jardillier, J.C., **2000**. Multicellular resistance: a paradigm for clinical resistance?. *Critical reviews in oncology/hematology*, 36(2-3), pp.193-207.

Devanny, A.J., Vancura, M.B. and Kaufman, L.J., **2021**. Exploiting differential effects of actomyosin contractility to control cell sorting among breast cancer cells. *Molecular Biology of the Cell*, 32(21), p.ar24.

Dixon, S.J., Lemberg, K.M., Lamprecht, M.R., Skouta, R., Zaitsev, E.M., Gleason, C.E., Patel, D.N., Bauer, A.J., Cantley, A.M., Yang, W.S. and Morrison, B., **2012**. Ferroptosis: an iron-dependent form of nonapoptotic cell death. *cell*, 149(5), pp.1060-1072.

Düchting, W. and Vogelsaenger, T., **1981**. Three-dimensional pattern generation applied to spheroidal tumor growth in a nutrient medium. *International Journal of Bio-Medical Computing*, 12(5), pp.377-392.

Düchting, W. and Vogelsaenger, T., **1984**. Modeling and simulation of growing spheroids. In *Spheroids in Cancer Research: Methods and Perspectives* (pp.168-179). Berlin, Heidelberg: Springer Berlin Heidelberg.

E

Edmondson, R., Broglie, J.J., Adcock, A.F. and Yang, L., **2014**. Three-dimensional cell culture systems and their applications in drug discovery and cell-based biosensors. *Assay and drug development technologies*, 12(4), pp.207-218.

Eichler, M., Jahnke, H.G., Krinke, D., Müller, A., Schmidt, S., Azendorf, R. and Robitzki, A.A., **2015**. A novel 96-well multielectrode array based impedimetric monitoring platform for comparative drug efficacy analysis on 2D and 3D brain tumor cultures. *Biosensors and Bioelectronics*, 67, pp.582-589.

Elias, A.F., Lin, B.C. and Piggott, B.J., **2023**. Ion channels in gliomas—from molecular basis to treatment. *International Journal of Molecular Sciences*, 24(3), p.2530.

Elson, E.L., **1988**. Cellular mechanics as an indicator of cytoskeletal structure and function. *Annual review of biophysics and biophysical chemistry*, 17(1), pp.397-430.

Ende, D. and Mangold, K.M., **1993**. Impedanzspektroskopie. *Chemie in unserer Zeit*, 27(3), pp.134-140.

Ericson, A.C. and Spring, K.R., **1982**. Coupled NaCl entry into Necturus gallbladder epithelial cells. *American Journal of Physiology-Cell Physiology*, 243(3), pp.C140-C145.

F

Fang, G., Lu, H., Law, A., Gallego-Ortega, D., Jin, D. and Lin, G., **2019**. Gradient-sized control of tumor spheroids on a single chip. *Lab on a Chip*, 19(24), pp.4093-4103.

Fernández-Fernández, J.M., Nobles, M., Currid, A., Vázquez, E. and Valverde, M.A., **2002**. Maxi K+ channel mediates regulatory volume decrease response in a human bronchial epithelial cell line. *American Journal of Physiology-Cell Physiology*, 283(6), pp.C1705-C1714.

Foster, K.R. and Schwan, H.P., **1989**. Dielectric properties of tissues and biological materials: a critical review. *Critical Reviews in Biomedical Engineering*, 17(1), pp.25-104.

Foty, R., **2011**. A simple hanging drop cell culture protocol for generation of 3D spheroids. *JoVE (Journal of Visualized Experiments)*, (51), p.e2720.

França, M.B., Panek, A.D. and Eleutherio, E.C.A., **2007**. Oxidative stress and its effects during dehydration. *Comparative Biochemistry and Physiology Part A: Molecular & Integrative Physiology*, 146(4), pp.621-631.

Frankel, A., Man, S., Elliott, P., Adams, J. and Kerbel, R.S., **2000**. Lack of multicellular drug resistance observed in human ovarian and prostate carcinoma treated with the proteasome inhibitor PS-341. *Clinical Cancer Research*, 6(9), pp.3719-3728.

Franko, A.J. and Sutherland, R.M., **1979**. Oxygen diffusion distance and development of necrosis in multicell spheroids. *Radiation Research*, 79(3), pp.439-453.

Freshney, R.I., **2015**. Culture of animal cells: a manual of basic technique and specialized applications. *John Wiley & Sons*.

Fricke, H. and Morse, S., **1925**. The electric resistance and capacity of blood for frequencies between 800 and 4½ million cycles. *The Journal of general physiology*, 9(2), p.153.

Friedrich, J., Seidel, C., Ebner, R. and Kunz-Schughart, L.A., **2009**. Spheroid-based drug screen: considerations and practical approach. *Nature protocols*, 4(3), pp.309-324.

Froehlich, K., Haeger, J.D., Heger, J., Pastuschek, J., Photini, S.M., Yan, Y., Lupp, A., Pfarrer, C., Mrowka, R., Schleußner, E. and Markert, U.R., **2016**. Generation of multicellular breast cancer tumor spheroids: comparison of different protocols. *Journal of mammary gland biology and neoplasia*, 21, pp.89-98.

G

Ganjali, H. and Ganjali, M., **2013**. Fixation in tissue processing. *Intl J Farm & Alli Sci*, 2, pp.686-689.

Gaskell, H., Sharma, P., Colley, H.E., Murdoch, C., Williams, D.P. and Webb, S.D., **2016**. Characterization of a functional C3A liver spheroid model. *Toxicology research*, 5(4), pp.1053-1065.

Geiger, B. and Yamada, K.M., **2011**. Molecular architecture and function of matrix adhesions. *Cold Spring Harbor perspectives in biology*, 3(5), p.a005033.

Gerasimenko, T., Nikulin, S., Zakharova, G., Poloznikov, A., Petrov, V., Baranova, A. and Tonevitsky, A., **2020**. Impedance spectroscopy as a tool for monitoring performance in 3D models of epithelial tissues. *Frontiers in bioengineering and biotechnology*, 7, p.474.

Giaever, I. and Keese, C.R., **1984**. Monitoring fibroblast behavior in tissue culture with an applied electric field. *Proceedings of the National Academy of Sciences*, 81(12), pp.3761-3764.

Giaever, I. and Keese, C.R., **1991**. Micromotion of mammalian cells measured electrically. *Proceedings of the National Academy of Sciences*, 88(17), pp.7896-7900.

Giaever, I. and Keese, C.R., **1993**. A morphological biosensor for mammalian cells. *Nature*, 366(6455), pp.591-592.

Gilazieva, Z., Ponomarev, A., Rutland, C., Rizvanov, A. and Solovyeva, V., **2020**. Promising applications of tumor spheroids and organoids for personalized medicine. *Cancers*, 12(10), p.2727.

Glauert, A.M., Dingle, J.T. and Lucy, J.A., **1962**. Action of saponin on biological cell membranes. *Nature*, 196(4858), pp.953-955.

Glicklis, R., Merchuk, J.C. and Cohen, S., **2004**. Modeling mass transfer in hepatocyte spheroids via cell viability, spheroid size, and hepatocellular functions. *Biotechnology and bioengineering*, 86(6), pp.672-680.

Gompertz, B., **1825**. XXIV. On the nature of the function expressive of the law of human mortality, and on a new mode of determining the value of life contingencies. *In a letter to Francis Baily, Esq. FRS &c. Philosophical transactions of the Royal Society of London*, (115), pp.513-583.

Graf, B.W. and Boppart, S.A., **2010**. Imaging and analysis of three-dimensional cell culture models. *Live Cell Imaging: Methods and Protocols*, pp.211-227.

Green, S.K., Francia, G., Isidoro, C. and Kerbel, R.S., **2004**. Antiadhesive antibodies targeting E-cadherin sensitize multicellular tumor spheroids to chemotherapy in vitro. *Molecular cancer therapeutics*, 3(2), pp.149-159.

Greenwood, M., **1928**. " Laws" of mortality from the biological point of view. *The Journal of hygiene*, 28(3), pp.267-294.

Griffith, L.G. and Swartz, M.A., **2006**. Capturing complex 3D tissue physiology in vitro. *Nature reviews Molecular cell biology*, 7(3), pp.211-224.

Grimmes, S. and Martinsen, R.G., **2008**. *Bioimpedance and Bioelectricity, university of Oslo and Department of biomedical and clinical engineering*.

Gstraunthaler, G., Lindl, T. and van der Valk, J., **2013**. A plea to reduce or replace fetal bovine serum in cell culture media. *Cytotechnology*, 65, pp.791-793.

Gunning, P.W., Schevzov, G., Kee, A.J. and Hardeman, E.C., **2005**. Tropomyosin isoforms: divining rods for actin cytoskeleton function. *Trends in cell biology*, 15(6), pp.333-341.

Gunti, S., Hoke, A.T., Vu, K.P. and London Jr, N.R., **2021**. Organoid and spheroid tumor models: Techniques and applications. *Cancers*, 13(4), p.874.

H

Hamilton, G., **1998**. Multicellular spheroids as an in vitro tumor model. *Cancer letters*, 131(1), pp.29-34.

Han, S.J., Kwon, S. and Kim, K.S., **2021**. Challenges of applying multicellular tumor spheroids in preclinical phase. *Cancer cell international*, 21, pp.1-19.

Hardelauf, H., Frimat, J.P., Stewart, J.D., Schormann, W., Chiang, Y.Y., Lampen, P., Franzke, J., Hengstler, J.G., Cadenas, C., Kunz-Schughart, L.A. and West, J., **2011**. Microarrays for the scalable production of metabolically relevant tumour spheroids: a tool for modulating chemosensitivity traits. *Lab on a Chip*, 11(3), pp.419-428.

Hari, N., Patel, P., Ross, J., Hicks, K. and Vanholsbeeck, F., **2019**. Optical coherence tomography complements confocal microscopy for investigation of multicellular tumour spheroids. *Scientific Reports*, 9(1), p.10601.

Hayes, J.S., Czekanska, E.M. and Richards, R.G., **2012**. The cell–surface interaction. *Tissue engineering III: cell-surface interactions for tissue culture*, pp.1-31.

Hayman, E.G., Pierschbacher, M.D., Suzuki, S. and Ruoslahti, E., **1985**. Vitronectin—a major cell attachment-promoting protein in fetal bovine serum. *Experimental cell research*, 160(2), pp.245-258.

Heitmann, V., Reiß, B. and Wegener, J., **2007**. The quartz crystal microbalance in cell biology: basics and applications. *Piezoelectric sensors*, pp.303-338.

Hickman, J.A., Graeser, R., de Hoogt, R., Vidic, S., Brito, C., Gutekunst, M. and van der Kuip, H., **2014**. Three-dimensional models of cancer for pharmacology and cancer cell biology: capturing tumor complexity in vitro/ex vivo. *Biotechnology journal*, 9(9), pp.1115-1128.

Hildebrandt, C., Büth, H., Cho, S. and Thielecke, H., **2010**. Detection of the osteogenic differentiation of mesenchymal stem cells in 2D and 3D cultures by electrochemical impedance spectroscopy. *Journal of biotechnology*, 148(1), pp.83-90.

Hirschhaeuser, F., Menne, H., Dittfeld, C., West, J., Mueller-Klieser, W. and Kunz-Schughart, L.A., **2010**. Multicellular tumor spheroids: an underestimated tool is catching up again. *Journal of biotechnology*, 148(1), pp.3-15.

Hirschhaeuser, F., Sattler, U.G. and Mueller-Klieser, W., **2011**. Lactate: a metabolic key player in cancer. *Cancer research*, 71(22), pp.6921-6925.

Ho, W.Y., Yeap, S.K., Ho, C.L., Rahim, R.A. and Alitheen, N.B., **2012**. *Development of multicellular tumor spheroid (MCTS) culture from breast cancer cell and a high throughput screening method using the MTT assay*.

Hoffmann, E.K., Lambert, I.H. and Pedersen, S.F., **2009**. Physiology of cell volume regulation in vertebrates. *Physiological reviews*, 89(1), pp.193-277.

Hoffmann, E.K. and Pedersen, S.F., **2011**. Cell volume homeostatic mechanisms: effectors and signalling pathways. *Acta physiologica*, 202(3), pp.465-485.

Holopainen, I.E., **2005**. Organotypic hippocampal slice cultures: a model system to study basic cellular and molecular mechanisms of neuronal cell death, neuroprotection, and synaptic plasticity. *Neurochemical research*, 30, pp.1521-1528.

Homan, K.A., Gupta, N., Kroll, K.T., Kolesky, D.B., Skylar-Scott, M., Miyoshi, T., Mau, D., Valerius, M.T., Ferrante, T., Bonventre, J.V. and Lewis, J.A., **2019**. Flow-enhanced vascularization and maturation of kidney organoids in vitro. *Nature methods*, 16(3), pp.255-262.

Horning, J.L., Sahoo, S.K., Vijayaraghavalu, S., Dimitrijevic, S., Vasir, J.K., Jain, T.K., Panda, A.K. and Labhasetwar, V., **2008**. 3-D tumor model for in vitro evaluation of anticancer drugs. *Molecular pharmaceutics*, 5(5), pp.849-862.

Hou, J., **2020**. A Laboratory Guide to the Tight Junction. *Academic Press*.

Hoyer, M., Meier, C., Breier, A., Hahner, J., Heinrich, G., Drechsel, N., Meyer, M., Rentsch, C., Garbe, L.A., Ertel, W. and Lohan, A., **2015**. In vitro characterization of self-assembled anterior cruciate ligament cell spheroids for ligament tissue engineering. *Histochemistry and cell biology*, 143, pp.289-300.

https://www.bf3r.de/en/about_the_bf3r-282533.html; 31.12.2023.

https://cordis.europa.eu/project/id/746876; 14.10.2023.

https://omnexus.specialchem.com/polymer-properties/properties/water-absorption-24-hours; 02.07.2022.

https://www.vanderveerplastics.com/assets/docs/Technical-Date-Sheets-Plexiglas®-Revised.pdf; 02.07.2022.

https://www.vanderveerplastics.com/assets/docs/Technical-Date-Sheets-Polycarbonate-Revised.pdf; 02.07.2022.

https://www.vanderveerplastics.com/assets/docs/Technical-Date-Sheets-Teflon®-Revised.pdf; 02.07.2022.

Huang, J., Li, Z., Liaw, B.Y. and Zhang, J., **2016**. Graphical analysis of electrochemical impedance spectroscopy data in Bode and Nyquist representations. *Journal of Power Sources*, 309, pp.82-98.

Hupf, C., **2018**. Impedance-based analysis of 3D tissue models: A novel measurement setup for novel measurement modes (*Doctoral dissertation, Regensburg*).

Hynes, R.O., **1987**. Integrins: a family of cell surface receptors. *Cell*, 48(4), pp.549-554.

I

Instruments, G., **2007**. Basics of electrochemical impedance spectroscopy. G. *Instruments, Complex impedance in Corrosion, 1*, pp.1-30.

Imamura, Y., Mukohara, T., Shimono, Y., Funakoshi, Y., Chayahara, N., Toyoda, M., Kiyota, N., Takao, S., Kono, S., Nakatsura, T. and Minami, H., **2015**. Comparison of 2D-and 3D-culture models as drug-testing platforms in breast cancer. *Oncology reports*, 33(4), pp.1837-1843.

Ito, H., Okamoto, K., Nakayama, H., Isobe, T. and Kato, K., **1997**. Phosphorylation of αB-crystallin in response to various types of stress. *Journal of Biological Chemistry*, 272(47), pp.29934-29941.

Ivascu, A. and Kubbies, M., **2006**. Rapid generation of single-tumor spheroids for high-throughput cell function and toxicity analysis. *SLAS Discovery*, 11(8), pp.922-932.

Ivascu, A. and Kubbies, M., **2007**. Diversity of cell-mediated adhesions in breast cancer spheroids. *International journal of oncology*, 31(6), pp.1403-1413.

J

Jahnke, H.G., Steel, D., Fleischer, S., Seidel, D., Kurz, R., Vinz, S., Dahlenborg, K., Sartipy, P. and Robitzki, A.A., **2013**. A novel 3D label-free monitoring system of hES-derived cardiomyocyte clusters: a step forward to in vitro cardiotoxicity testing. *PLoS One*, 8(7), p.e68971.

Jakab, K., Neagu, A., Mironov, V., Markwald, R.R. and Forgacs, G., **2004**. Engineering biological structures of prescribed shape using self-assembling multicellular systems. *Proceedings of the National Academy of Sciences*, 101(9), pp.2864-2869.

Jauković, A., Abadjieva, D., Trivanović, D., Stoyanova, E., Kostadinova, M., Pashova, S., Kestendjieva, S., Kukolj, T., Jeseta, M., Kistanova, E. and Mourdjeva, M., **2020**. Specificity of 3D MSC spheroids microenvironment: impact on MSC behavior and properties. *Stem cell reviews and reports*, 16, pp.853-875.

K

Kade, C., **2023**. Sensing for Disease Models of Glaucoma (*Doctoral dissertation, Regensburg*).

Kapałczyńska, M., Kolenda, T., Przybyła, W., Zajączkowska, M., Teresiak, A., Filas, V., Ibbs, M., Bliźniak, R., Łuczewski, Ł. and Lamperska, K., **2018**. 2D and 3D cell cultures–a comparison of different types of cancer cell cultures. *Archives of Medical Science*, 14(4), pp.910-919.

Keese, C.R., Wegener, J., Walker, S.R. and Giaever, I., **2004**. Electrical wound-healing assay for cells in vitro. *Proceedings of the National Academy of Sciences*, 101(6), pp.1554-1559.

Khaitan, D., Chandna, S., Arya, M.B. and Dwarakanath, B.S., **2006**. Establishment and characterization of multicellular spheroids from a human glioma cell line; Implications for tumor therapy. *Journal of translational medicine*, 4, pp.1-13.

Kloß, D., Kurz, R., Jahnke, H.G., Fischer, M., Rothermel, A., Anderegg, U., Simon, J.C. and Robitzki, A.A., **2008a**. Microcavity array (MCA)-based biosensor chip for functional drug screening of 3D tissue models. *Biosensors and Bioelectronics*, 23(10), pp.1473-1480.

Kloß, D., Fischer, M., Rothermel, A., Simon, J.C. and Robitzki, A.A., **2008b**. Drug testing on 3D in vitro tissues trapped on a microcavity chip. *Lab on a Chip*, 8(6), pp.879-884.

Koliakos, G., Paletas, K. and Kaloyianni, M., **2008**. NHE-1: a molecular target for signalling and cell matrix interactions. *Connective tissue research*, 49(3-4), pp.157-161.

Krinke, D., Jahnke, H.G., Mack, T.G., Hirche, A., Striggow, F. and Robitzki, A.A., **2010**. A novel organotypic tauopathy model on a new microcavity chip for bioelectronic label-free and real time monitoring. *Biosensors and Bioelectronics*, 26(1), pp.162-168.

Kyle, A.H., Chan, C.T. and Minchinton, A.I., **1999**. Characterization of three-dimensional tissue cultures using electrical impedance spectroscopy. *Biophysical journal*, 76(5), pp.2640-2648.

Kyle, U.G., Bosaeus, I., De Lorenzo, A.D., Deurenberg, P., Elia, M., Gómez, J.M., Heitmann, B.L., Kent-Smith, L., Melchior, J.C., Pirlich, M. and Scharfetter, H., **2004**. Bioelectrical impedance analysis—part I: review of principles and methods. *Clinical nutrition*, 23(5), pp.1226-1243.

L

Lacaille-Dubois, M.A. and Wagner, H., **1996**. A review of the biological and pharmacological activities of saponins. *Phytomedicine*, 2(4), pp.363-386.

Landry, J., Freyer, J.P. and Sutherland, R.M., **1982**. A model for the growth of multicellular spheroids. *Cell Proliferation*, 15(6), pp.585-594.

Lang, F., Busch, G.L., Ritter, M., Volkl, H., Waldegger, S., Gulbins, E. and Haussinger, D., **1998**. Functional significance of cell volume regulatory mechanisms. *Physiological reviews*, 78(1), pp.247-306.

Langhans, S.A., **2018**. Three-dimensional in vitro cell culture models in drug discovery and drug repositioning. *Frontiers in pharmacology*, 9, p.6.

Lapicque, L., **1907**. Recherches quantitatives sur lexcitation electrique des nerfs traitee comme une polarization. *J. Physiol. Pathol. Gen.*, 9, p.620.

Laurent, J., Frongia, C., Cazales, M., Mondesert, O., Ducommun, B. and Lobjois, V., **2013**. Multicellular tumor spheroid models to explore cell cycle checkpoints in 3D. *BMC cancer*, 13(1), pp.1-12.

Lee, S.Y., Jeong, E.K., Jeon, H.M., Kim, C.H. and Kang, H.S., **2010**. Implication of necrosis-linked p53 aggregation in acquired apoptotic resistance to 5-FU in MCF-7 multicellular tumour spheroids. *Oncology reports*, 24(1), pp.73-79.

Lee, K.H. and Kim, T.H., **2021**. Recent advances in multicellular tumor spheroid generation for drug screening. *Biosensors*, 11(11), p.445.

Lee, S.Y., Koo, I.S., Hwang, H.J. and Lee, D.W., **2023**. In Vitro three-dimensional (3D) cell culture tools for spheroid and organoid models. *SLAS Discovery*.

Levenson, A.S. and Jordan, V.C., **1997**. MCF-7: the first hormone-responsive breast cancer cell line. *Cancer research*, 57(15), pp.3071-3078.

Lewis, E.E.L., Wheadon, H., Lewis, N., Yang, J., Mullin, M., Hursthouse, A., Stirling, D., Dalby, M.J. and Berry, C.C., **2016**. A quiescent, regeneration-responsive tissue engineered mesenchymal stem cell bone marrow niche model via magnetic levitation. *ACS nano*, 10(9), pp.8346-8354.

Lewis-Tuffin, L.J., Rodriguez, F., Giannini, C., Scheithauer, B., Necela, B.M., Sarkaria, J.N. and Anastasiadis, P.Z., **2010**. Misregulated E-cadherin expression associated with an aggressive brain tumor phenotype. *PloS one*, 5(10), p.e13665.

Li, C.L., Tian, T.A.O., Nan, K.J., Zhao, N.A., Guo, Y.H., Cui, J.I.E., Wang, J. and Zhang, W.G., **2008**. Survival advantages of multicellular spheroids vs. monolayers of HepG2 cells in vitro. *Oncology reports*, 20(6), pp.1465-1471.

Lieb, S., Littmann, T., Plank, N., Felixberger, J., Tanaka, M., Schäfer, T., Krief, S., Elz, S., Friedland, K., Bernhardt, G. and Wegener, J., **2016**. Label-free versus conventional cellular assays: Functional investigations on the human histamine H1 receptor. *Pharmacological research*, 114, pp.13-26.

Lin, R.Z., Chou, L.F., Chien, C.C.M. and Chang, H.Y., **2006**. Dynamic analysis of hepatoma spheroid formation: roles of E-cadherin and β1-integrin. *Cell and tissue research*, 324, pp.411-422.

Lin, R.Z. and Chang, H.Y., **2008**. Recent advances in three-dimensional multicellular spheroid culture for biomedical research. *Biotechnology Journal: Healthcare Nutrition Technology*, 3(9-10), pp.1172-1184.

Liu, Y., Wu, W., Feng, S., Chen, Y., Wu, X., Zhang, Q. and Wu, S., **2023**. Dynamic response of the cell traction force to osmotic shock. *Microsystems & Nanoengineering*, 9(1), p.131.

Lo, C.M., Keese, C.R. and Giaever, I., **1993**. Monitoring motion of confluent cells in tissue culture. *Experimental cell research*, 204(1), pp.102-109.

Lorent, J., Le Duff, C.S., Quetin-Leclercq, J. and Mingeot-Leclercq, M.P., **2013**. Induction of highly curved structures in relation to membrane permeabilization and budding by the triterpenoid saponins, α-and δ-Hederin. *Journal of Biological Chemistry*, 288(20), pp.14000-14017.

Lu, P., Weaver, V.M. and Werb, Z., **2012**. The extracellular matrix: a dynamic niche in cancer progression. *Journal of cell biology*, 196(4), pp.395-406.

Lukic, S. and Wegener, J., **2015**. Impedimetric monitoring of cell-based assays. *eLS*, pp.1-8.

Luongo, K., Holton, A., Kaushik, A., Spence, P., Ng, B., Deschenes, R., Sundaram, S. and Bhansali, S., **2013**. Microfluidic device for trapping and monitoring three dimensional multicell spheroids using electrical impedance spectroscopy. *Biomicrofluidics*, 7(3).

Lvovich, V.F., **2012**. Impedance spectroscopy: applications to electrochemical and dielectric phenomena. *John Wiley & Sons*.

M

Ma, H.L., Jiang, Q., Han, S., Wu, Y., Tomshine, J.C., Wang, D., Gan, Y., Zou, G. and Liang, X.J., **2012**. Multicellular tumor spheroids as an in vivo–like tumor model for three-dimensional imaging of chemotherapeutic and nano material cellular penetration. *Molecular imaging*, 11(6), pp.7290-2012.

Ma, X., Liu, J., Zhu, W., Tang, M., Lawrence, N., Yu, C., Gou, M. and Chen, S., **2018**. 3D bioprinting of functional tissue models for personalized drug screening and in vitro disease modeling. *Advanced drug delivery reviews*, 132, pp.235-251.

Madshus, I.H., **1988**. Regulation of intracellular pH in eukaryotic cells. *Biochemical journal*, 250(1), p.1.

Malda, J. and Frondoza, C.G., **2006**. Microcarriers in the engineering of cartilage and bone. *Trends in biotechnology*, 24(7), pp.299-304.

Mammoto, T., Jiang, A., Jiang, E., Panigrahy, D., Kieran, M.W. and Mammoto, A., **2013**. Role of collagen matrix in tumor angiogenesis and glioblastoma multiforme progression. *The American journal of pathology*, 183(4), pp.1293-1305.

Mariana Ruiz Villareal, **2008**. https://de.wikipedia.org/wiki/Datei:Erythrozyten_und_Osmotischer_Druck.svg; 12.08.2023.

McAdams, E.T. and Jossinet, J., **1995**. Tissue impedance: a historical overview. *Physiological measurement*, 16(3A), p.A1.

McCarty, N.A. and O´Neil, R.G., **1992**. Calcium signaling in cell volume regulation. *Physiological reviews*, 72(4), pp.1037-1061.

Michaelis, S., Wegener, J. and Robelek, R., **2013**. Label-free monitoring of cell-based assays: Combining impedance analysis with SPR for multiparametric cell profiling. *Biosensors and Bioelectronics*, 49, pp.63-70.

Miklavčič, D., Pavšelj, N. and Hart, F.X., **2006**. Electric properties of tissues. *Wiley encyclopedia of biomedical engineering*.

Minami, N., Maeda, Y., Shibao, S., Arima, Y., Ohka, F., Kondo, Y., Maruyama, K., Kusuhara, M., Sasayama, T., Kohmura, E. and Saya, H., **2017**. Organotypic brain explant culture as a drug evaluation system for malignant brain tumors. *Cancer medicine*, 6(11), pp.2635-2645.

Mironov, V., Kasyanov, V., Drake, C. and Markwald, R.R., **2008**. Organ printing: promises and challenges.

Mistry, I.N., Thomas, M., Calder, E.D., Conway, S.J. and Hammond, E.M., **2017**. Clinical advances of hypoxia-activated prodrugs in combination with radiation therapy. *International Journal of Radiation Oncology* Biology* Physics*, 98(5), pp.1183-1196.

Mittler, F., Obeïd, P., Rulina, A.V., Haguet, V., Gidrol, X. and Balakirev, M.Y., **2017**. High-content monitoring of drug effects in a 3D spheroid model. *Frontiers in oncology*, 7, p.293.

Mongin, A.A. and Orlov, S.N., **2001**. Mechanisms of cell volume regulation and possible nature of the cell volume sensor. *Pathophysiology*, 8(2), pp.77-88.

Moysidou, C.M., Barberio, C. and Owens, R.M., **2021**. Advances in engineering human tissue models. *Frontiers in bioengineering and biotechnology*, 8, p.620962.

Mueller-Klieser, W.F. and Sutherland, R.M., **1982**. Influence of convection in the growth medium on oxygen tensions in multicellular tumor spheroids. *Cancer research*, 42(1), pp.237-242.

Mueller-Klieser, W., **1987**. Multicellular spheroids: a review on cellular aggregates in cancer research. *Journal of cancer research and clinical oncology*, 113, pp.101-122.

Murphy, G.J., Johnson, T.W., Chamberlain, M.H., Rizvi, S.I., Wyatt, M., George, S.J., Angelini, G.D., Karsch, K.R., Oberhoff, M. and Newby, A.C., **2007**. Short-and long-term effects of cytochalasin D, paclitaxel and rapamycin on wall thickening in experimental porcine vein grafts. *Cardiovascular research*, 73(3), pp.607-617.

N

Napolitano, A.P., Chai, P., Dean, D.M. and Morgan, J.R., **2007**. Dynamics of the self-assembly of complex cellular aggregates on micromolded nonadhesive hydrogels. *Tissue engineering*, 13(8), pp.2087-2094.

Nath, S. and Devi, G.R., **2016**. Three-dimensional culture systems in cancer research: Focus on tumor spheroid model. *Pharmacology & therapeutics*, 163, pp.94-108.

Nirmala, C., Rao, J.S., Ruifrok, A.C., Langford, L.A. and Obeyesekere, M., **2001**. Growth characteristics of glioblastoma spheroids. *International journal of oncology*, 19(6), pp.1109-1115.

Nunes, A.S., Barros, A.S., Costa, E.C., Moreira, A.F. and Correia, I.J., **2019**. 3D tumor spheroids as in vitro models to mimic in vivo human solid tumors resistance to therapeutic drugs. *Biotechnology and bioengineering*, 116(1), pp.206-226.

O

O´Connor, E.R., Kimelberg, H.K., Keese, C.R. and Giaever, I.V.A.R., **1993**. Electrical resistance method for measuring volume changes in monolayer cultures applied to primary astrocyte cultures. *American Journal of Physiology-Cell Physiology*, 264(2), pp.C471-C478.

O´Connor, C.M., Adams, J.U. and Fairman, J., **2010**. How do cells decode genetic information into functional proteins. *Essentials of Cell Biology; NPG Education: Cambridge, MA, USA*, 1, p.54.

Oberleitner, M., **2017**. Label-free and Multi-parametric Monitoring of Cell-based Assays with Substrate-embedded Sensors. *Springer*.

O´Brien, L.E., Zegers, M.M. and Mostov, K.E., **2002**. Building epithelial architecture: insights from three-dimensional culture models. *Nature reviews Molecular cell biology*, 3(7), pp.531-537.

Ong, S.M., Zhao, Z., Arooz, T., Zhao, D., Zhang, S., Du, T., Wasser, M., van Noort, D. and Yu, H., **2010**. Engineering a scaffold-free 3D tumor model for in vitro drug penetration studies. *Biomaterials*, 31(6), pp.1180-1190.

Opp, D., Wafula, B., Lim, J., Huang, E., Lo, J.C. and Lo, C.M., **2009**. Use of electric cell–substrate impedance sensing to assess in vitro cytotoxicity. *Biosensors and Bioelectronics*, 24(8), pp.2625-2629.

Ouyang, L., Armstrong, J., Salmeron-Sanchez, M. and Stevens, M., **2020**. Assembly of living building blocks to engineer complex tissues. *Advanced Functional Materials*.

Owen, G.R., Meredith, D.O., Ap Gwynn, I. and Richards, R.G., **2005**. Focal adhesion quantification-a new assay of material biocompatibility? Review. *European cells & materials*, 9, pp.85-96.

P

Pampaloni, F., Reynaud, E.G. and Stelzer, E.H., **2007**. The third dimension bridges the gap between cell culture and live tissue. *Nature reviews Molecular cell biology*, 8(10), pp.839-845.

Paterson, A.D., Parton, R.G., Ferguson, C. and Stow, J.L., **2003**. Characterization of E-cadherin endocytosis in isolated MCF-7 and chinese hamster ovary cells: the initial fate of unbound E-cadherin. *Journal of Biological Chemistry*, 278(23), pp.21050-21057.

Periasamy, N., Kao, H.P., Fushimi, K.I.Y.O.H.I.D.E. and Verkman, A.S., **1992**. Organic osmolytes increase cytoplasmic viscosity in kidney cells. *American Journal of Physiology-Cell Physiology*, 263(4), pp.C901-C907.

Petry, F. and Salzig, D., **2022**. Large-scale production of size-adjusted β-cell spheroids in a fully controlled stirred-tank reactor. *Processes*, 10(5), p.861.

Piccinini, F., Tesei, A., Arienti, C. and Bevilacqua, A., **2015**. Cancer multicellular spheroids: volume assessment from a single 2D projection. *Computer methods and programs in biomedicine*, 118(2), pp.95-106.

Podolak, I., Galanty, A. and Sobolewska, D., **2010**. Saponins as cytotoxic agents: a review. *Phytochemistry Reviews*, 9, pp.425-474.

Polonchuk, L., Chabria, M., Badi, L., Hoflack, J.C., Figtree, G., Davies, M.J. and Gentile, C., **2017**. Cardiac spheroids as promising in vitro models to study the human heart microenvironment. *Scientific reports*, 7(1), p.7005.

Potts, M., **1994**. Desiccation tolerance of prokaryotes. *Microbiological reviews*, 58(4), pp.755-805.

Puri, G., Chaudhary, S.S., Singh, V.K. and Sharma, A.K., **2015**. Effects of fetal bovine serum and estrus buffalo serum on maturation of buffalo (Bubalus bubalis) oocytes in vitro. *Veterinary world*, 8(2), p.143.

Pütz, L., **2022**. Imaging Microphysiometry of 2D and 3D Tissue Models: Method Development and Application (*Doctoral dissertation, Regensburg*).

R

Radnai, L., Stremel, R.F., Vaissiere, T., Lin, L., Cameron, M., Martin, W.H., Rumbaugh, G., Kamenecka, T.M., Griffin, P.R. and Miller, C.A., **2020**. A simple and robust cell-based assay for the discovery of novel cytokinesis inhibitors. *Journal of Biological Methods*, 7(3).

Raghavan, S., Mehta, P., Horst, E.N., Ward, M.R., Rowley, K.R. and Mehta, G., **2016**. Comparative analysis of tumor spheroid generation techniques for differential in vitro drug toxicity. *Oncotarget*, 7(13), p.16948.

Ralph, A.C.L., Valadão, I.C., Cardoso, E.C., Martins, V.R., Oliveira, L.M.S., Bevilacqua, E.M.A.F., Geraldo, M.V., Jaeger, R.G., Goldberg, G.S. and Freitas, V.M., **2020**. Environmental control of mammary carcinoma cell expansion by acidification and spheroid formation in vitro. *Scientific Reports*, 10(1), p.21959.

Rape, A., Ananthanarayanan, B. and Kumar, S., **2014**. Engineering strategies to mimic the glioblastoma microenvironment. *Advanced drug delivery reviews*, 79, pp.172-183.

Reiß, B., **2004**. Mikrogravimetrische Untersuchung des Adhäsionskontakts tierischer Zellen: eine biophysikalische Studie (*Doctoral dissertation, Münster*).

Ren, W., Zhao, W., Cao, L. and Huang, J., **2021**. Involvement of the actin machinery in programmed cell death. *Frontiers in Cell and Developmental Biology*, 8, p.634849.

Reshkin, S.J., Bellizzi, A., Albarani, V., Guerra, L., Tommasino, M., Paradiso, A. and Casavola, V., **2000**. Phosphoinositide 3-kinase is involved in the tumor-specific activation of human breast cancer cell Na+/H+ exchange, motility, and invasion induced by serum deprivation. *Journal of Biological Chemistry*, 275(8), pp.5361-5369.

Richardson, D.S. and Lichtman, J.W., **2015**. Clarifying tissue clearing. *Cell*, 162(2), pp.246-257.

Robinson, E.E., Foty, R.A. and Corbett, S.A., **2004**. Fibronectin matrix assembly regulates α5β1-mediated cell cohesion. *Molecular biology of the cell*, 15(3), pp.973-981.

Roos, A. and Boron, W.F., **1981**. Intracellular pH. *Physiological reviews*, 61(2), pp.296-434.

Roy, M., Alix, C., Bouakaz, A., Serrière, S. and Escoffre, J.M., **2023**. Tumor Spheroids as Model to Design Acoustically Mediated Drug Therapies: A Review. *Pharmaceutics*, 15(3), p.806.

Ruckdäschel, S., Michaelis, S. and Wegener, J., **2017**. Time lapse imaging of spheroids–zencellowl incubator microscope. *OMNI Life Sci*.

Russell, W.M.S. and Burch, R.L., **1959**. The principles of humane experimental technique. *Methuen*.

S

Sasser, D.C., Gerth, W.A. and Wu, Y.C., **1993**. Monitoring of segmental intra-and extracellular volume changes using electrical impedance spectroscopy. *Journal of Applied Physiology*, 74(5), pp.2180-2187.

Schmittlein, C., **2018**. Sensors and Actuators for 2D and 3D Cell Culture Models based on Oxygen Sensitive Culture Substrates (*Doctoral dissertation, Regensburg*).

Schumacher, Z., Frey, O. and Hierlemann, A., **2011**, October. Microfluidic impedance spectroscopy scanner for spherical microtissues. In *Proceedings of 15th International Conference on Miniaturized Systems for Chemistry and Life Sciences, Seattle, WA, USA* (Vol. 26).

Schwan, H.P., **1957**. Electrical properties of tissue and cell suspensions. In *Advances in biological and medical physics; Elsevier*, 5, pp.147-209).

Shamir, E.R. and Ewald, A.J., **2014**. Three-dimensional organotypic culture: experimental models of mammalian biology and disease. *Nature reviews Molecular cell biology*, 15(10), pp.647-664.

Sharma, M., Astekar, M., Soi, S., S Manjunatha, B., C Shetty, D. and Radhakrishnan, R., **2015**. pH gradient reversal: an emerging hallmark of cancers. *Recent patents on anti-cancer drug discovery*, 10(3), pp.244-258.

Shen, H., Cai, S., Wu, C., Yang, W., Yu, H. and Liu, L., **2021**. Recent advances in three-dimensional multicellular spheroid culture and future development. *Micromachines*, 12(1), p.96.

Soule, H.D., Vazquez, J., Long, A., Albert, S. and Brennan, M., **1973**. A human cell line from a pleural effusion derived from a breast carcinoma. *Journal of the national cancer institute*, 51(5), pp.1409-1416.

Souza, G.R., Molina, J.R., Raphael, R.M., Ozawa, M.G., Stark, D.J., Levin, C.S., Bronk, L.F., Ananta, J.S., Mandelin, J., Georgescu, M.M. and Bankson, J.A., **2010**. Three-dimensional tissue culture based on magnetic cell levitation. *Nature nanotechnology*, 5(4), pp.291-296.

Souza, A.G., Ferreira, I.C., Marangoni, K., Bastos, V.A.F. and Goulart, V.A., **2016**. Advances in cell culture: more than a century after cultivating cells. *Journal of Biotechnology & Biomaterials*, 6(2), p.1000221.

Souza, A.G., Silva, I.B.B., Campos-Fernandez, E., Barcelos, L.S., Souza, J.B., Marangoni, K., Goulart, L.R. and Alonso-Goulart, V., **2018**. Comparative assay of 2D and 3D cell culture models: proliferation, gene expression and anticancer drug response. *Current pharmaceutical design*, 24(15), pp.1689-1694.

Sparg, S., Light, M.E. and Van Staden, J., **2004**. Biological activities and distribution of plant saponins. *Journal of ethnopharmacology*, 94(2-3), pp.219-243.

Steinem, C., Janshoff, A., Wegener, J., Ulrich, W.P., Willenbrink, W., Sieber, M. and Galla, H.J., **1997**. Impedance and shear wave resonance analysis of ligand–receptor interactions at functionalized surfaces and of cell monolayers. *Biosensors and Bioelectronics*, 12(8), pp.787-808.

Stevenson, B.R. and Begg, D.A., **1994**. Concentration-dependent effects of cytochalasin D on tight junctions and actin filaments in MDCK epithelial cells. *Journal of cell science*, 107(3), pp.367-375.

Stock, C. and Schwab, A., **2006**. Role of the Na+/H+ exchanger NHE1 in cell migration. *Acta physiologica*, 187(1-2), pp.149-157.

Stolwijk, J.A., Hartmann, C., Balani, P., Albermann, S., Keese, C.R., Giaever, I. and Wegener, J., **2011**. Impedance analysis of adherent cells after in situ electroporation: non-invasive monitoring during intracellular manipulations. *Biosensors and Bioelectronics*, 26(12), pp.4720-4727.

Stolwijk, J.A., **2012**. Electric manipulation and impedance analysis of adherent cells on gold-film electrodes (*Doctoral dissertation, Regensburg*).

Stolwijk, J.A., Michaelis, S. and Wegener, J., **2012**. Cell growth and cell death studied by electric cell-substrate impedance sensing. *Electric cell-substrate impedance sensing and cancer metastasis*, pp.85-117.

Stolwijk, J.A., Skiba, M., Kade, C., Bernhardt, G., Buschauer, A., Hübner, H., Gmeiner, P. and Wegener, J., **2019**. Increasing the throughput of label-free cell assays to study the activation of G-protein-coupled receptors by using a serial agonist exposure protocol. *Integrative Biology*, 11(3), pp.99-108.

Stoppini, L., Buchs, P.A. and Muller, D., **1991**. A simple method for organotypic cultures of nervous tissue. *Journal of neuroscience methods*, 37(2), pp.173-182.

Sutherland, R.M., McCredie, J.A. and Inch, W.R., **1971**. Growth of multicell spheroids in tissue culture as a model of nodular carcinomas. *Journal of the National Cancer Institute*, 46(1), pp.113-120.

Sutherland, R.M. and Durand, R.E., **1984**. Growth and cellular characteristics of multicell spheroids. *Spheroids in Cancer Research: Methods and Perspectives*, pp.24-49.

Sutherland, R.M., **1988**. Cell and environment interactions in tumor microregions: the multicell spheroid model. *Science*, 240(4849), pp.177-184.

Swaminathan, S., Hamid, Q., Sun, W. and Clyne, A.M., **2019**. Bioprinting of 3D breast epithelial spheroids for human cancer models. *Biofabrication*, 11(2), p.025003.

Swisher, J.W. and Rannels, D.E., **1997**. Assembly of exogenous fibronectin into type II cell extracellular matrix. *American Journal of Physiology-Lung Cellular and Molecular Physiology*, 272(5), pp.L908-L915.

T

Takeichi, M., **1990**. Cadherins: a molecular family important in selective cell-cell adhesion. *Annual review of biochemistry*, 59(1), pp.237-252.

Tarantola, M., Marel, A.K., Sunnick, E., Adam, H., Wegener, J. and Janshoff, A., **2010**. Dynamics of human cancer cell lines monitored by electrical and acoustic fluctuation analysis. *Integrative Biology*, 2(2-3), pp.139-150.

Thielecke, H., Mack, A. and Robitzki, A., **2001a**. A multicellular spheroid-based sensor for anti-cancer therapeutics. *Biosensors and Bioelectronics*, 16(4-5), pp.261-269.

Thielecke, H., Mack, A. and Robitzki, A., **2001b**. Biohybrid microarrays–impedimetric biosensors with 3D in vitro tissues for toxicological and biomedical screening. *Fresenius' journal of analytical chemistry*, 369, pp.23-29.

Timm, D.M., Chen, J., Sing, D., Gage, J.A., Haisler, W.L., Neeley, S.K., Raphael, R.M., Dehghani, M., Rosenblatt, K.P., Killian, T.C. and Tseng, H., **2013**. A high-throughput three-dimensional cell migration assay for toxicity screening with mobile device-based macroscopic image analysis. *Scientific reports*, 3(1), p.3000.

Toda, S., Watanabe, K., Yokoi, F., Matsumura, S., Suzuki, K., Ootani, A., Aoki, S., Koike, N. and Sugihara, H., **2002**. A new organotypic culture of thyroid tissue maintains three-dimensional follicles with C cells for a long term. *Biochemical and biophysical research communications*, 294(4), pp.906-911.

Trendowski, M., **2015**. Using cytochalasins to improve current chemotherapeutic approaches. *Anti-Cancer Agents in Medicinal Chemistry (Formerly Current Medicinal Chemistry-Anti-Cancer Agents)*, 15(3), pp.327-335.

Tung, Y.C., Hsiao, A.Y., Allen, S.G., Torisawa, Y.S., Ho, M. and Takayama, S., **2011**. High-throughput 3D spheroid culture and drug testing using a 384 hanging drop array. *Analyst*, 136(3), pp.473-478.

Tzanakakis, E.S., Hansen, L.K. and Hu, W.S., **2001**. The role of actin filaments and microtubules in hepatocyte spheroid self-assembly. *Cell motility and the cytoskeleton*, 48(3), pp.175-189.

U

Urban, F., **2020**. Expanding the Scope of Impedance Analysis of Epithelial Barrier Function: Novel Assays and Devices (*Doctoral dissertation, Regensburg*).

Uroukov, I.S. and Patton, D., **2008**. Optimizing environmental scanning electron microscopy of spheroidal reaggregated neuronal cultures. *Microscopy research and technique*, 71(11), pp.792-801

V

Vaira, V., Fedele, G., Pyne, S., Fasoli, E., Zadra, G., Bailey, D., Snyder, E., Faversani, A., Coggi, G., Flavin, R. and Bosari, S., **2010**. Preclinical model of organotypic culture for pharmacodynamic profiling of human tumors. *Proceedings of the National Academy of Sciences*, 107(18), pp.8352-8356.

Valero, T., Moschopoulou, G., Kintzios, S., Hauptmann, P., Naumann, M. and Jacobs, T., **2010**. Studies on neuronal differentiation and signalling processes with a novel impedimetric biosensor. *Biosensors and Bioelectronics*, 26(4), pp.1407-1413.

Valley, M.P., Kupcho, K.R., Zimprich, C.A., Leippe, D., Niles, A.L., Vidugiriene, J., Cali, J.J., Kelm, J.M., Moritz, W. and Lazar, D.F., **2014**. Luminescent cell health assays for tumor spheroid evaluation. *Cancer Res.*, 74(19_Supplement).

Vanaei, S., Parizi, M.S., Salemizadehparizi, F. and Vanaei, H.R., **2021**. An overview on materials and techniques in 3D bioprinting toward biomedical application. *Engineered Regeneration*, 2, pp.1-18.

Velasco, V., Shariati, S.A. and Esfandyarpour, R., **2020**. Microtechnology-based methods for organoid models. *Microsystems & nanoengineering*, 6(1), p.76.

Vincken, J.P., Heng, L., de Groot, A. and Gruppen, H., **2007**. Saponins, classification and occurrence in the plant kingdom. *Phytochemistry*, 68(3), pp.275-297.

von Euler, H., Söderstedt, A., Thörne, A., Olsson, J.M. and Yongqing, G., **2002**. Cellular toxicity induced by different pH levels on the R3230AC rat mammary tumour cell line. An in vitro model for investigation of the tumour destructive properties of electrochemical treatment of tumours. *Bioelectrochemistry*, 58(2), pp.163-170.

W

Wakatsuki, T., Schwab, B., Thompson, N.C. and Elson, E.L., **2001**. Effects of cytochalasin D and latrunculin B on mechanical properties of cells. *Journal of cell science*, 114(5), pp.1025-1036.

Walpita, D. and Hay, E., **2002**. Studying actin-dependent processes in tissue culture. *Nature reviews Molecular cell biology*, 3(2), pp.137-141.

Walzl, A., Unger, C., Kramer, N., Unterleuthner, D., Scherzer, M., Hengstschläger, M., Schwanzer-Pfeiffer, D. and Dolznig, H., **2014**. The resazurin reduction assay can distinguish cytotoxic from cytostatic compounds in spheroid screening assays. *Journal of biomolecular screening*, 19(7), pp.1047-1059.

Wan, Z., Floryan, M.A., Coughlin, M.F., Zhang, S., Zhong, A.X., Shelton, S.E., Wang, X., Xu, C., Barbie, D.A. and Kamm, R.D., **2023**. New strategy for promoting vascularization in tumor spheroids in a microfluidic assay. *Advanced healthcare materials*, 12(14), p.2201784.

Warburg, E., **1901**. Ueber die polarisationscapacität des platins. *Annalen der Physik*, 311(9), pp.125-135.

Ward, J.P. and King, J.R., **1997**. Mathematical modelling of avascular-tumour growth. *Mathematical Medicine and Biology: A Journal of the IMA*, 14(1), pp.39-69.

Wartenberg, M., Richter, M., Datchev, A., Günther, S., Milosevic, N., Bekhite, M.M., Figulla, H.R., Aran, J.M., Pétriz, J. and Sauer, H., **2010**. Glycolytic pyruvate regulates P-Glycoprotein expression in multicellular tumor spheroids via modulation of the intracellular redox state. *Journal of cellular biochemistry*, 109(2), pp.434-446.

Webb, B.A., Chimenti, M., Jacobson, M.P. and Barber, D.L., **2011**. Dysregulated pH: a perfect storm for cancer progression. *Nature Reviews Cancer*, 11(9), pp.671-677.

Wegener, J., **1998**. Impedanzspektroskopische und mikrogravimetrische Untersuchungen an barrierebildenden Zellen auf planaren Goldelektroden (*Doctoral dissertation, Münster*).

Wegener, J., Hakvoort, A. and Galla, H.J., **2000a**. Barrier function of porcine choroid plexus epithelial cells is modulated by cAMP-dependent pathways in vitro. *Brain research*, 853(1), pp.115-124.

Wegener, J., Keese, C.R. and Giaever, I., **2000b**. Electric cell–substrate impedance sensing (ECIS) as a noninvasive means to monitor the kinetics of cell spreading to artificial surfaces. *Experimental cell research*, 259(1), pp.158-166.

Wegener, J., Seebach, J., Janshoff, A. and Galla, H.J., **2000c**. Analysis of the composite response of shear wave resonators to the attachment of mammalian cells. *Biophysical journal*, 78(6), pp.2821-2833.

Wegener, J., Keese, C.R. and Giaever, I., **2002**. Recovery of adherent cells after in situ electroporation monitored electrically. *Biotechniques*, 33(2), pp.348-357.

White, S.R., Williams, P., Wojcik, K.R., Sun, S., Hiemstra, P.S., Rabe, K.F. and Dorscheid, D.R., **2001**. Initiation of apoptosis by actin cytoskeletal derangement in human airway epithelial cells. *American Journal of Respiratory Cell and Molecular Biology*, 24(3), pp.282-294.

X

Xu, M., McCanna, D.J. and Sivak, J.G., **2015**. Use of the viability reagent PrestoBlue in comparison with alamarBlue and MTT to assess the viability of human corneal epithelial cells. *Journal of pharmacological and toxicological methods*, 71, pp.1-7.

Y

Yahara, I., Harada, F., Sekita, S., Yoshihira, K. and Natori, S., **1982**. Correlation between effects of 24 different cytochalasins on cellular structures and cellular events and those on actin in vitro. *The Journal of Cell Biology*, 92(1), pp.69-78.

Yamada, K.M. and Cukierman, E., **2007**. Modeling tissue morphogenesis and cancer in 3D. *Cell*, 130(4), pp.601-610.

Yamaguchi, H. and Condeelis, J., **2007**. Regulation of the actin cytoskeleton in cancer cell migration and invasion. *Biochimica et Biophysica Acta (BBA)-Molecular Cell Research*, 1773(5), pp.642-652.

Yaman, S., Anil-Inevi, M., Ozcivici, E. and Tekin, H.C., **2018**. Magnetic force-based microfluidic techniques for cellular and tissue bioengineering. *Frontiers in bioengineering and biotechnology*, 6, p.192.

Yuhas, J.M., Li, A.P., Martinez, A.O. and Ladman, A.J., **1977**. A simplified method for production and growth of multicellular tumor spheroids. *Cancer research*, 37(10), pp.3639-3643.

Yuhas, J.M., Tarleton, A.E. and Molzen, K.B., **1978**. Multicellular tumor spheroid formation by breast cancer cells isolated from different sites. *Cancer Research*, 38(8), pp.2486-2491.

Z

Zagaynova, E.V., Druzhkova, I.N., Mishina, N.M., Ignatova, N.I., Dudenkova, V.V. and Shirmanova, M.V., **2017**. Imaging of intracellular pH in tumor spheroids using genetically encoded sensor SypHer2. *Multi-Parametric Live Cell Microscopy of 3D Tissue Models*, pp.105-119.

Zahn, I., Braun, T., Gögele, C. and Schulze-Tanzil, G., **2021**. Minispheroids as a tool for ligament tissue engineering: Do the self-assembly techniques and spheroid dimensions influence the cruciate ligamentocyte phenotype?. *International Journal of Molecular Sciences*, 22(20), p.11011.

Zhang, J., Li, J. and Han, Y., **2004**. Superhydrophobic PTFE surfaces by extension. *Macromolecular Rapid Communications*, 25(11), pp.1105-1108.

Zhang, C., Liu, X., Jin, S., Chen, Y. and Guo, R., **2022**. Ferroptosis in cancer therapy: a novel approach to reversing drug resistance. *Molecular cancer*, 21(1), p.47.

Zhao, L., Xiu, J., Liu, Y., Zhang, T., Pan, W., Zheng, X. and Zhang, X., **2019**. A 3D printed hanging drop dripper for tumor spheroids analysis without recovery. *Scientific reports*, 9(1), p.19717.

Zhou, X., Zhu, W., Nowicki, M., Miao, S., Cui, H., Holmes, B., Glazer, R.I. and Zhang, L.G., **2016**. 3D bioprinting a cell-laden bone matrix for breast cancer metastasis study. *ACS applied materials & interfaces*, 8(44), pp.30017-30026.

Zhu, C., **2000**. Kinetics and mechanics of cell adhesion. *Journal of biomechanics*, 33(1), pp.23-33.

Zhu, J., Wang, Y., Zhong, L., Pan, F. and Wang, J., **2021**. Advances in tissue engineering of vasculature through three-dimensional bioprinting. *Developmental Dynamics*, 250(12), pp.1717-1738.

CHAPTER 11

APPENDIX

11.1 SUPPLEMENTARY INFORMATION 304

11.2 LIST OF ABBREVIATIONS AND SYMBOLS 321

11.3 MATERIALS AND INSTRUMENTATIONS 324

11.1 SUPPLEMENTARY INFORMATION

Tab. A-4.1 Pipetting scheme for a 96-well plate with (w/) and without (w/o) MCF-7 spheroids (3D) incubated with cytochalasin D (diluted with L15), Triton™ X-100 (diluted with PBS^{++}/glc), or PBS^{++}/glc.

column	well content 3D		column	well content 3D	
1	0.02 µM cytochalasin D	w/	7	2 µM cytochalasin D	w/
2	0.05 µM cytochalasin D	w/	8	3 µM cytochalasin D	w/
3	0.1 µM cytochalasin D	w/	9	5 µM cytochalasin D	w/
4	0.2 µM cytochalasin D	w/	10	2 % (v/v) Triton™ X-100	w/
5	0.5 µM cytochalasin D	w/	11	PBS^{++}/glc	w/
6	0.1 µM cytochalasin D	w/	12	PBS^{++}/glc	w/o

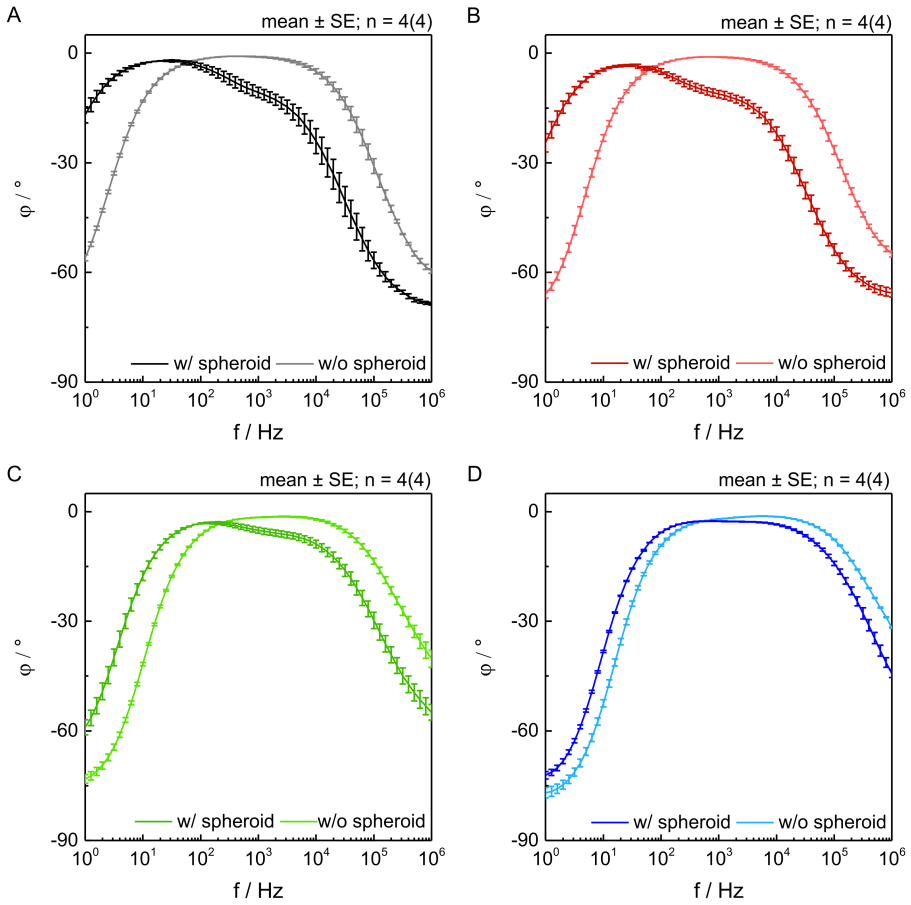

Fig. A-5.1 Recorded phase spectra of the funnel-shaped micro-trap prototypes with different hole diameters of 100 µm (A), 250 µm (B), 400 µm (C), and 500 µm (D), which were filled with buffer medium and measured with U-373 MG spheroids (w/; recorded three hours after positioning) and without (w/o) a spheroid using the final measurement setup. Data sets were averaged, mean ± SE; n = 4(4).

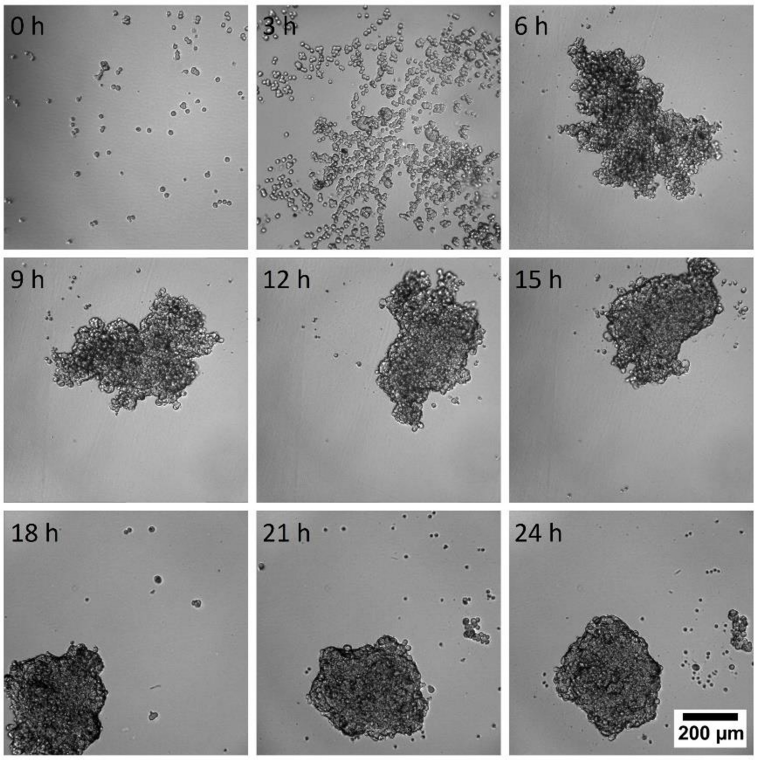

Fig. A-6.1 Time-resolved micrographs of the spheroid formation process of MCF-7 cells (seeding density: 4,000 c/well) documented for 24 hours using the zenCELL owl digital microscope. Experiment was performed in a standard cell culture incubator at 37 °C and 5 % CO_2.

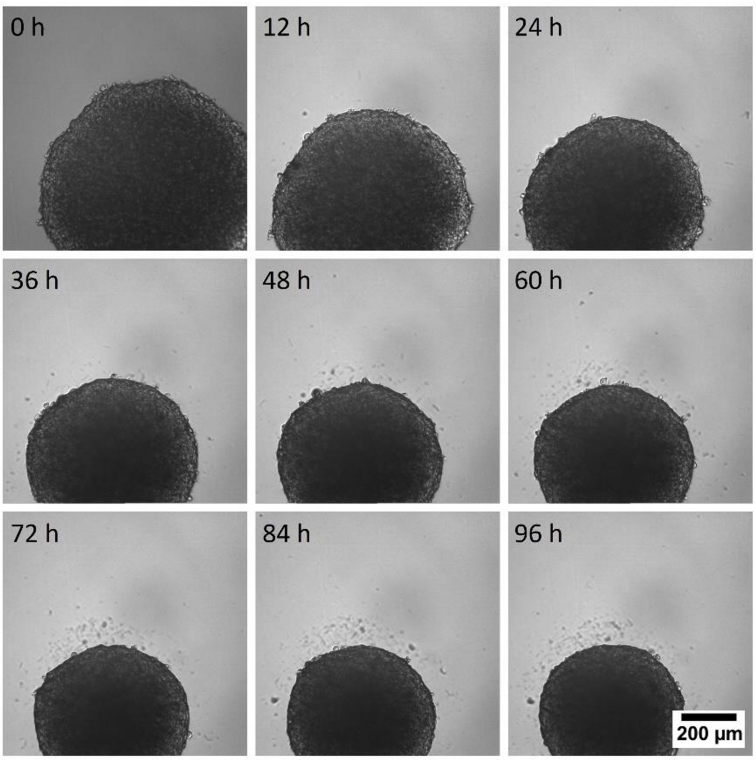

Fig. A-6.2 Time-resolved micrographs of the spheroid growth process of a U-373 MG spheroid (1 d, 18,000 c/well) documented for 96 hours using the zenCELL owl digital microscope. Experiment was performed in a standard cell culture incubator at 37 °C and 5 % CO_2.

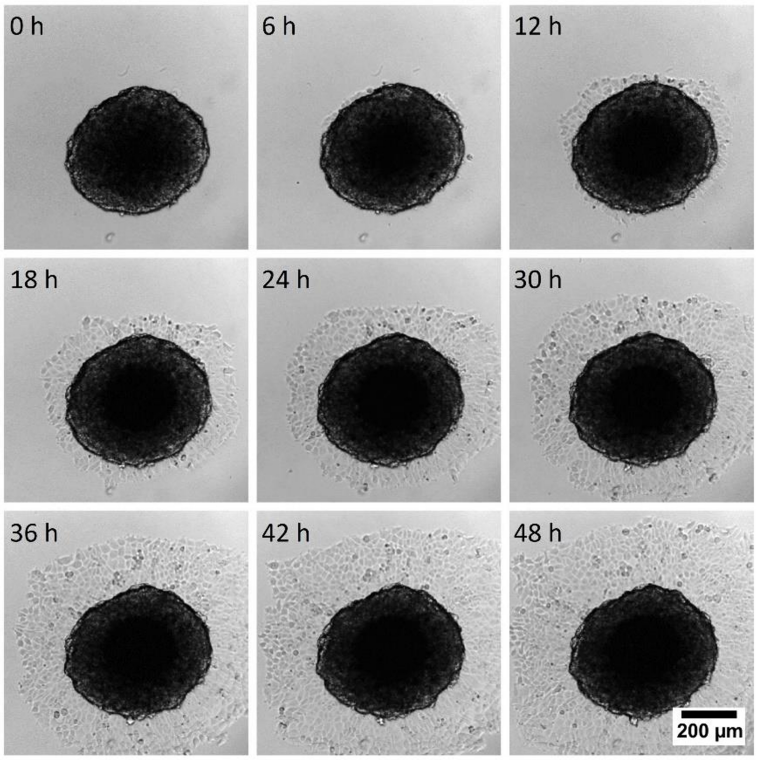

Fig. A-6.3 Time-resolved micrographs of the spheroid adhesion process of an MCF-7 spheroid (5 d, 4,000 c/well) documented for 48 hours using the zenCELL owl digital microscope. Experiment was performed in a standard cell culture incubator at 37 °C and 5 % CO_2. The full time-lapse clip is available by scanning the QR code (see Tab. A-6.2 for the password).

Tab. A-6.1 Resulting values of the calculated linear equations, slope and intercept, describing the kinetic growth curves of MCF-7 spheroids from different seeding densities (4,000–20,000 c/well) between day 2 and day 8 after spheroid formation. The coefficient of determination is given in the table respectively for each cell number.

	cell number [c/well]						
	4k	**10k**	**12k**	**14k**	**16k**	**18k**	**20k**
slope [µm/d]	34 ± 1	26.4 ± 0.8	22.5 ± 0.9	18 ± 1	12 ± 1	10.2 ± 0.6	9 ± 1
intercept [µm]	324 ± 6	436 ± 5	490 ± 4	554 ± 7	617 ± 6	653 ± 3	682 ± 5
R^2	1.00	1.00	0.99	0.98	0.94	0.98	0.92

Tab. A-6.2 Overview of the full time-lapse clips, which have been generated based on the time resolved images taken during the distinct experiments recorded by the zenCELL owl digital microscope using *ImageJ* software (Rasband, W.S., National Institutes of Health, USA). The data files are provided by following the link. It has to be taken into account that the image resolution has been reduced by file size compression.

time-lapse clips	
Fig. 6.2	Time-resolved micrographs of the spheroid formation process of U-373 MG cells.
Fig. 6.3	Time-resolved micrographs of the spheroid growth process of an MCF-7 spheroid.
Fig. 6.4	Time-resolved micrographs of the spheroid growth process of a U-373 MG spheroid.
Fig. A-6.3	Time resolved micrographs of the spheroid adhesion process of an MCF-7 spheroid.
Fig. 7.17	Time-resolved micrographs of the spheroid permeabilization process after the addition of saponin solution (3 mg/mL) to MCF-7 spheroid.
Fig. 7.48	Time-resolved micrographs of the spheroid response to osmotic pressure after the addition of hyperosmotic buffer solution (200 mM) to U-373 MG spheroid.
password	ThesisBaeumler2024!
QR-Code and link	https://1drv.ms/f/s!Aie6C3et0LB3gbt8MlLWXoTTcqckCQ

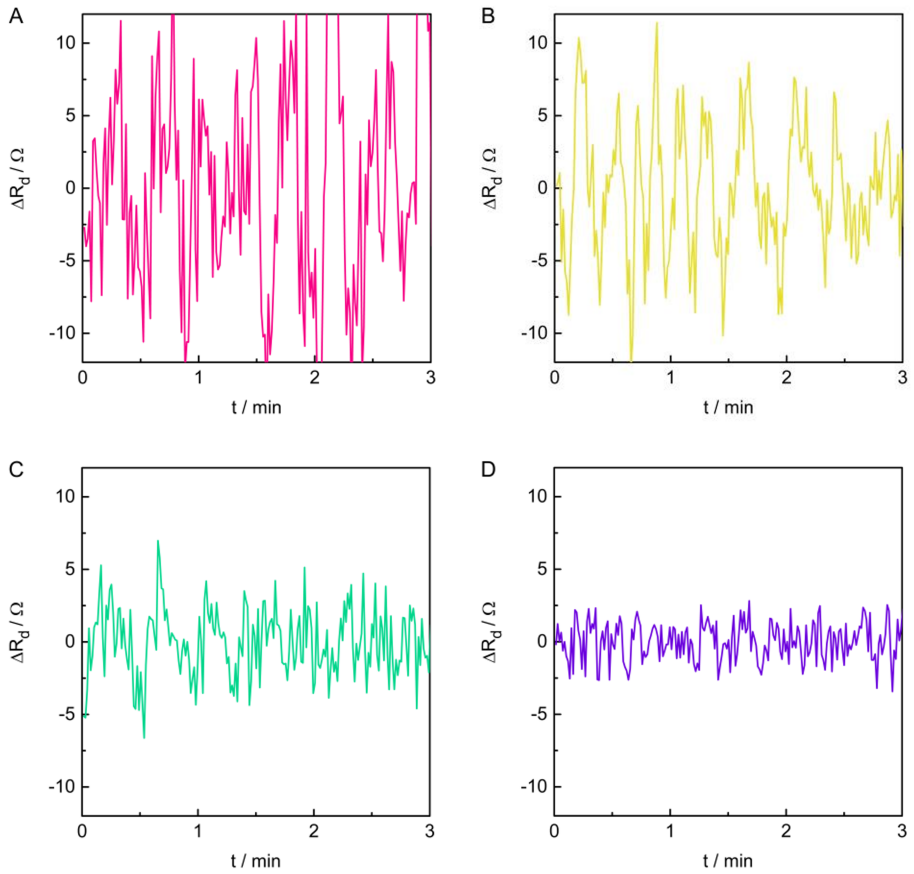

Fig. A-7.1 Detrended RTC data at 200 Hz three hours after positioning of U-373 MG spheroids (30,000 c/well) at different ages of five (A), six (B), seven (C), and eight (D) days after spheroid formation. Experiments were performed in a standard cell culture incubator at 37 °C and 0 % CO_2.

Tab. A-7.1 Calculated values of R_{ext}, R_{int}, and A_{sph} reflecting the dielectric structure of U-373 MG spheroids as a function of different spheroid ages (day 5 | day 6 | day 7 | day 8; 30,000 c/well). The values were determined by fitting each measured impedance spectrum three hours after spheroid insertion using a *LabVIEW™*-based software (written by J. Wegener, University of Regensburg) and the following parameter values: A_{el} = 12.0 (± 0.7) | 11.2 (± 0.4) | 10 (± 1) | 8.9 (± 0.6) ·10^{-6} $Fs^{n-1}cm^{-2}$; n_{el} = 0.851 (± 0.006) | 0.868 (± 0.004) | 0.880 (± 0.009) | 0.903 (± 0.007); R_{bulk} = 5,400 Ω; A_{para} = 2.4 ·10^{-10} $Fs^{n-1}cm^{-2}$; n_{para} = 0.9; n_{sph} = 0.75. Data sets were averaged after fitting, mean ± SE; see the table for the respective number of experiments.

	spheroid age			
	day 5	day 6	day 7	day 8
R_{ext} [kΩ]	41 ± 2	38 ± 11	32 ± 2	27 ± 1
R_{int} [kΩ]	8.0 ± 0.5	7.5 ± 0.6	3.3 ± 0.4	2.6 ± 0.4
A_{sph} [10^{-9} $Fs^{n-1}cm^{-2}$]	8.9 ± 0.5	9.6 ± 0.5	10 ± 1	13 ± 2
n	7(12)	14(25)	3(7)	4(9)

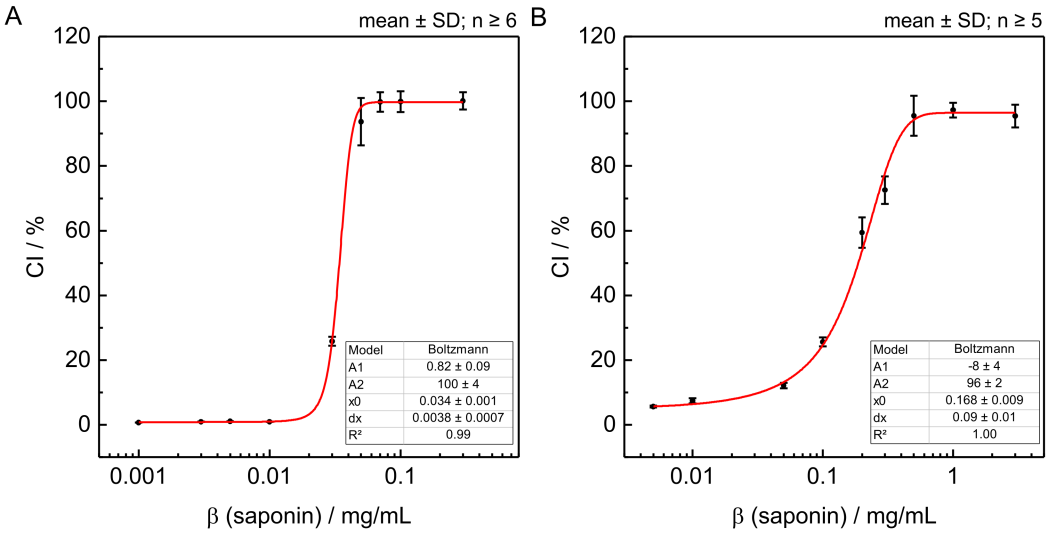

Fig. A-7.2 Dose-response curve of the cytotoxicity index CI as a function of the saponin concentration used to determine the effect of permeabilization on U-373 MG cell monolayer culture (A) and spheroid (B) viability. One of three independent experiments is shown for each cell dimensionality, respectively. The PrestoBlue™ cell viability assay was performed five hours after the addition of saponin solution at different concentrations (2D: 0.001–0.3 mg/mL; 3D: 0.005–3 mg/mL). Experiments were performed in a standard cell culture incubator at 37 °C and 0 % CO_2. Data sets of respectively one experiment were averaged, mean ± SD; A: n ≥ 6; B: n ≥ 5. The results were fitted by sigmoidal Boltzmann equation and the overall EC_{50} value was determined.

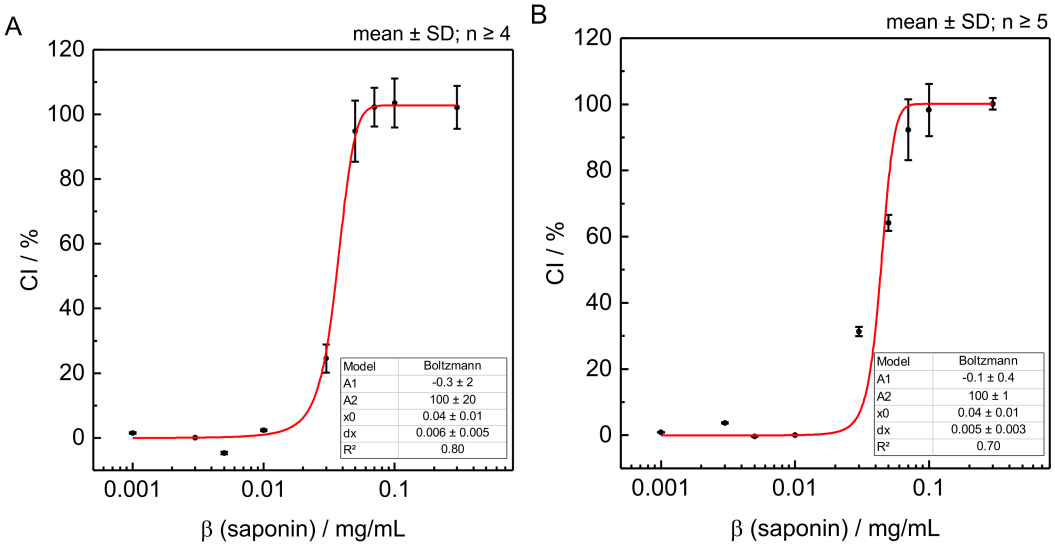

Fig. A-7.3 Dose-response curve of the cytotoxicity index CI as a function of the saponin concentration used to determine the effect of permeabilization on MCF-7 cell monolayer viability. Two independent experiments are shown (A, B) as replicates of Fig. 7.8, A (see chapter 7.2.1). The PrestoBlue™ cell viability assay was performed five hours after the addition of saponin solution at different concentrations (2D: 0.001–0.3 mg/mL). Experiments were performed in a standard cell culture incubator at 37 °C and 0 % CO_2. Data sets of respectively one experiment were averaged, mean ± SD; A: n ≥ 4; B: n ≥ 5. The results were fitted by sigmoidal Boltzmann equation and the overall EC_{50} value was determined.

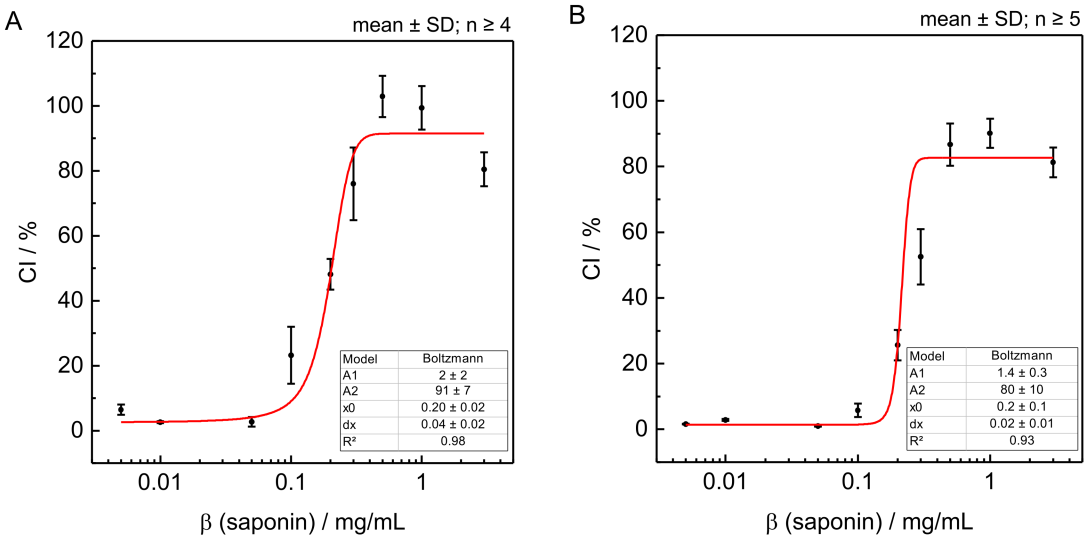

Fig. A-7.4 Dose-response curve of the cytotoxicity index CI as a function of the saponin concentration used to determine the effect of permeabilization on MCF-7 spheroids viability. Two independent experiments are shown (A, B) as replicates of Fig. 7.8, B (see chapter 7.2.1). The PrestoBlue™ cell viability assay was performed five hours after the addition of saponin solution at different concentrations (3D: 0.005–3 mg/mL). Experiments were performed in a standard cell culture incubator at 37 °C and 0 % CO_2. Data sets of respectively one experiment were averaged, mean ± SD; A: n ≥ 4; B: n ≥ 5. The results were fitted by sigmoidal Boltzmann equation and the overall EC_{50} value was determined.

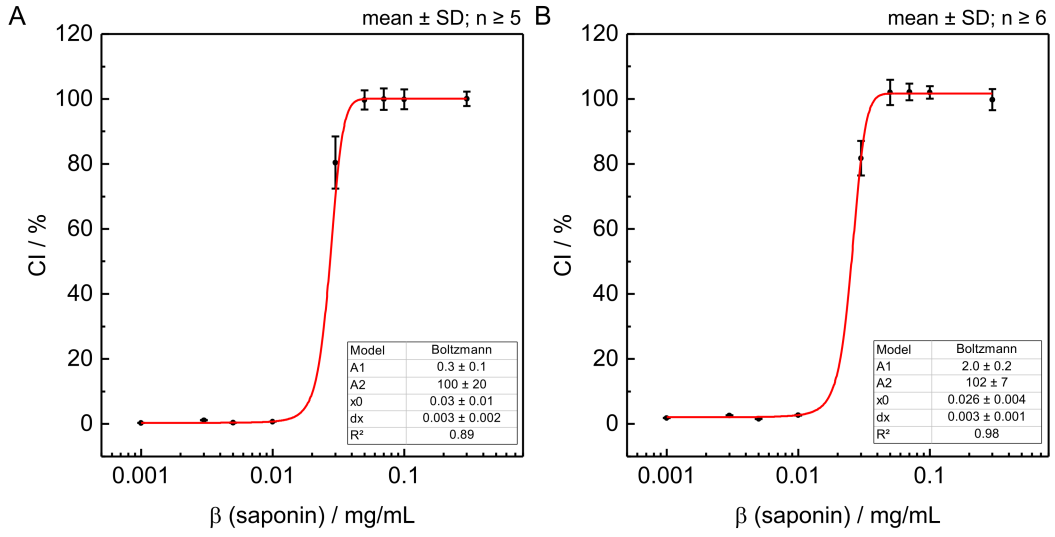

Fig. A-7.5 Dose-response curve of the cytotoxicity index CI as a function of the saponin concentration used to determine the effect of permeabilization on U-373 MG cell monolayer viability. Two independent experiments are shown (A, B) as replicates of Fig. A-7.2, A (see chapter 11.1). The PrestoBlue™ cell viability assay was performed five hours after the addition of saponin solution at different concentrations (2D: 0.001–0.3 mg/mL). Experiments were performed in a standard cell culture incubator at 37 °C and 0 % CO_2. Data sets of respectively one experiment were averaged, mean ± SD; A: n ≥ 5; B: n ≥ 6. The results were fitted by sigmoidal Boltzmann equation and the overall EC_{50} value was determined.

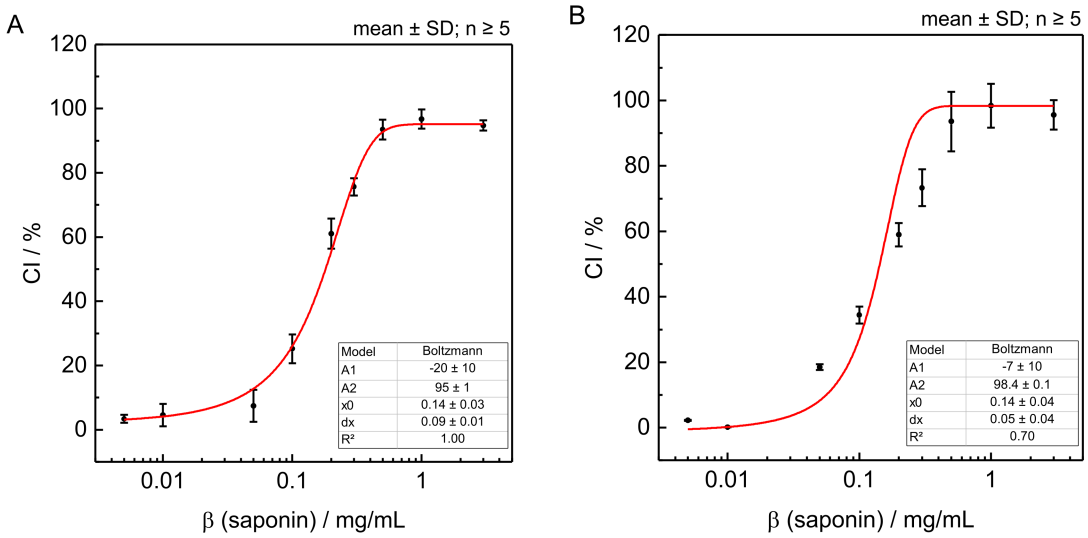

Fig. A-7.6 Dose-response curve of the cytotoxicity index CI as a function of the saponin concentration used to determine the effect of permeabilization on U-373 MG spheroids viability. Two independent experiments are shown (A, B) as replicates of Fig. A-7.2, B (see chapter 11.1). The PrestoBlue™ cell viability assay was performed five hours after the addition of saponin solution at different concentrations (3D: 0.005–3 mg/mL). Experiments were performed in a standard cell culture incubator at 37 °C and 0 % CO_2. Data sets of respectively one experiment were averaged, mean ± SD, A and B: n ≥ 5. The results were fitted by sigmoidal Boltzmann equation and the overall EC_{50} value was determined.

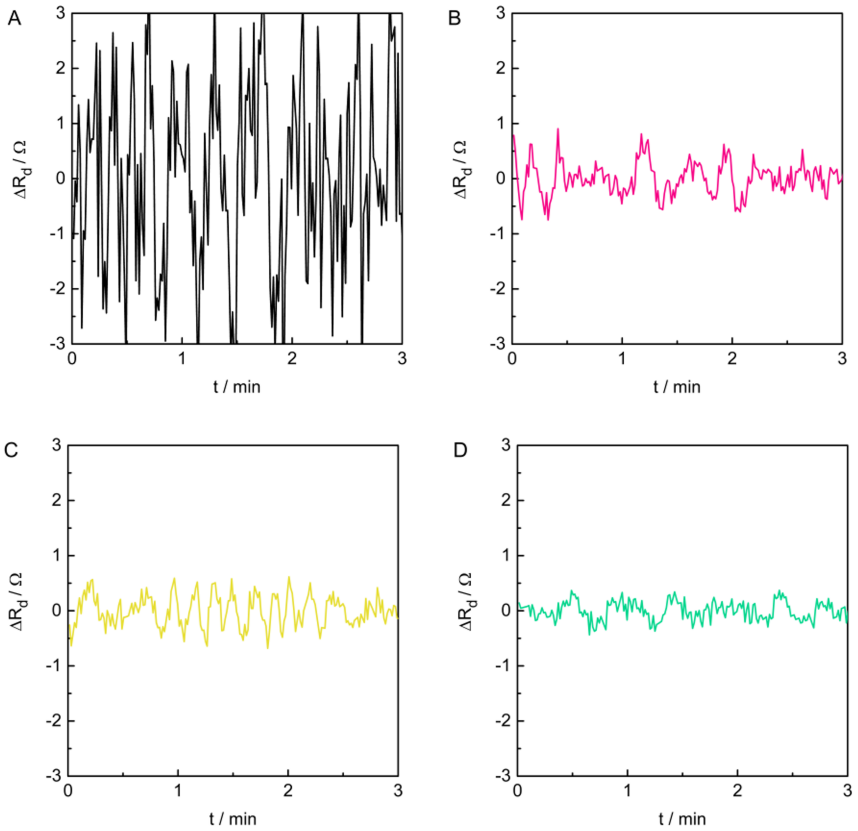

Fig. A-7.7 Detrended RTC data at 200 Hz, 15 hours after the addition of saponin solution with different concentrations (ctrl (A) | 0.3 (B) | 1 (C) | 3 (D) mg/mL) to with GA (0.03 % (v/v)) pre-fixed U-373 MG spheroids. Experiments were performed in a standard cell culture incubator at 37 °C and 0 % CO_2.

Tab. A-7.2 Calculated values of R_{ext}, R_{int}, and A_{sph} reflecting the dielectric structure of U-373 MG spheroids as a function of different saponin concentrations (ctrl | 0.3 | 1 | 3 mg/mL; 30,000 c/well) used for permeabilization. The values were determined by fitting each measured impedance spectrum three hours after spheroid fixation with GA (0.03 % (v/v)) and impedance spectrum 15 hours after the addition of saponin solution respective 18 hours after spheroid fixation using a *LabVIEW™*-based software (written by J. Wegener, University of Regensburg) and the following parameter values: A_{el} = 10.6 (± 0.5) | 9.5 (± 0.9) | 12 (± 1) | 11 (± 2) | 12.7 (± 0.7) ·10^{-6} $Fs^{n-1}cm^{-2}$; n_{el} = 0.885 (± 0.005) | 0.896 (± 0.009) | 0.87 (± 0.02) | 0.88 (± 0.02) | 0.897 (± 0.005); R_{bulk} = 5,400 Ω; A_{para} = 2.4 ·10^{-10} $Fs^{n-1}cm^{-2}$; n_{para} = 0.9; n_{sph} = 0.75. Data sets were averaged after fitting, mean ± SE; see the table for the respective number of experiments.

		$concentration$ [mg/mL]			
	after fixation	ctrl	0.3	1	3
R_{ext} [kΩ]	31 ± 1	27 ± 1	12 ± 2	7.2 ± 0.5	2.3 ± 0.3
R_{int} [kΩ]	7.3 ± 0.2	4 ± 1	0.33 ± 0.05	0.04 ± 0.01	0.002 ± 0.001
A_{sph} [10^{-9} $Fs^{n-1}cm^{-2}$]	8.0 ± 0.7	11 ± 2	14 ± 4	22 ± 4	30 ± 4
n	8(16)	5(5)	5(5)	5(5)	5(5)

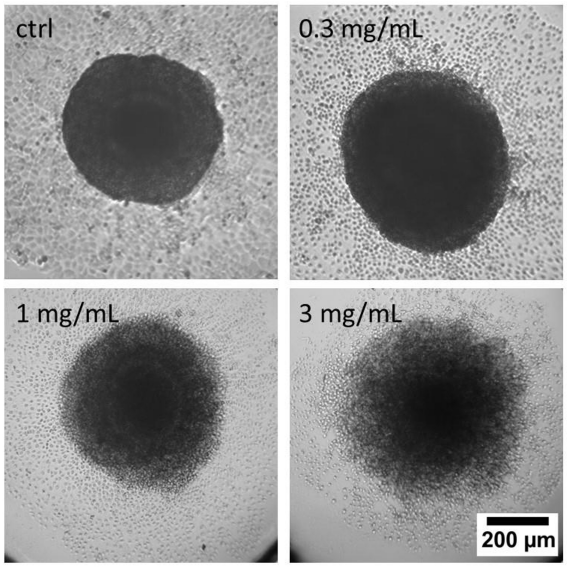

Fig. A-7.8 Micrographs of MCF-7 spheroids (7d, 4,000 c/well) that were exposed to saponin solution at different concentrations (ctrl | 0.3 | 1 | 3 mg/mL) and documented 24 h after the compound addition using the zenCELL owl digital microscope. Experiments were performed in a standard cell culture incubator at 37 °C and 0 % CO_2.

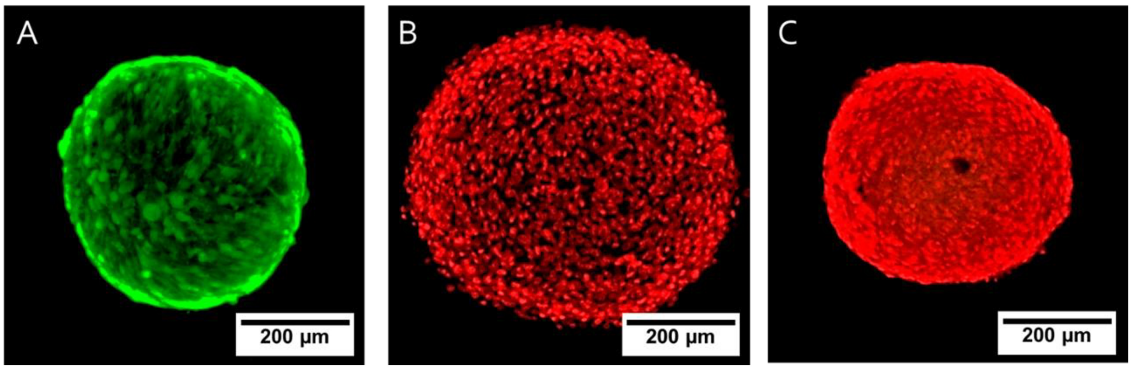

Fig. A-7.9 Proof-of-concept study addressing cell viability and morphology of either untreated or pre-fixed spheroids affected by permeabilization. Confocal microscopy micrographs of U-373 MG spheroids after the addition of buffer solution as a control (A, 5 h), treated with saponin solution (B; 3 mg/mL, 4 h), or GA solution (0.03 % [v/v], 60 min) and subsequent saponin solution (C; 3 mg/mL, 4 h). For fluorescence microscopy, the spheroid body was prepared using the cell viability staining protocol for spheroids (see chapter 4.2.3). The cytosol of viable cells emits a green fluorescence and the cell nuclei of dead cells appear red after excitation of the applied probes. The experiment reinforced the commonly induced cell death of the permeabilized spheroids (B, C) and verified sufficient GA concentration as the spheroids resisted in size during subsequent permeabilization (C).

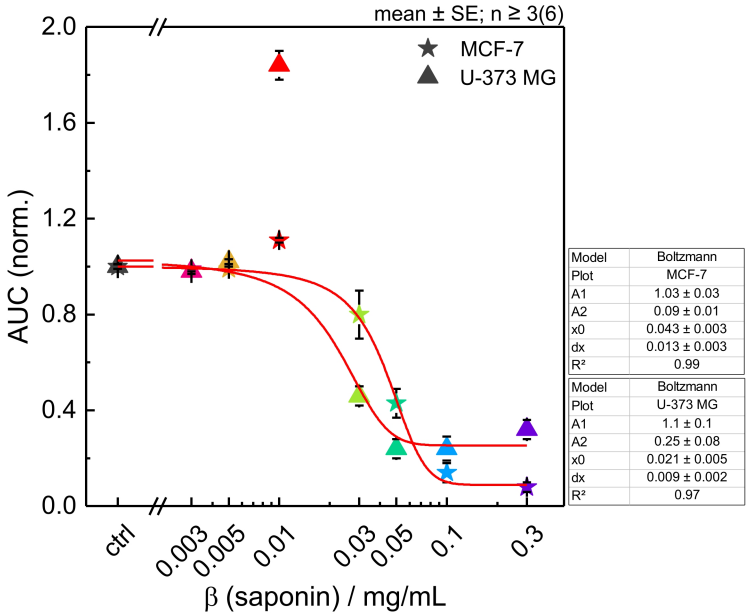

Fig. A-7.10 Dose-response curve of the normalized area under the curve values derived from the time course of normalized impedance magnitude at 4,000 Hz of MCF-7 and U-373 MG cell monolayer culture (Fig. 7.9). For integration, a baseline was set at the cell-free level (22 % (MCF-7) respectively 74 % (U-373 MG)) of the normalized impedance, and the values were determined within two hours after the addition of saponin solutions with different concentrations in a range of 0.003–0.3 mg/mL. After averaging, data sets were normalized to the control condition, mean ± SE, n ≥ 3(6). The results were fitted by sigmoidal Boltzmann equation and the respective EC_{50} value was determined; the results for the saponin concentration of 0.01 mg/mL were considered as outliers (marked in red) and were thus not included in the fit function.

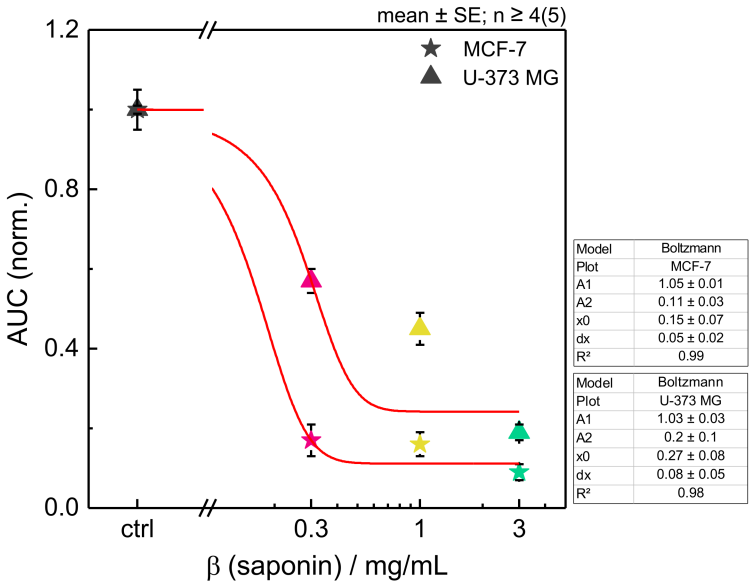

Fig. A-7.11 Dose-response curve of the normalized area under the curve values derived from the time course of normalized impedance magnitude at 200 Hz of GA (0.03 % (v/v)) pre-fixed MCF-7 and U-373 MG spheroids (Fig. 7.14). For integration, a baseline was set at the cell-free level (13 % (MCF-7) respectively 21 % (U-373 MG)) of the normalized impedance, and the values were determined within 10 hours after the addition of saponin solutions with different concentrations (ctrl | 0.3 | 1 | 3 mg/mL). After averaging, data sets were normalized to the control condition, mean ± SE, n ≥ 4(5). The results were fitted by sigmoidal Boltzmann equation and the respective EC_{50} value was determined.

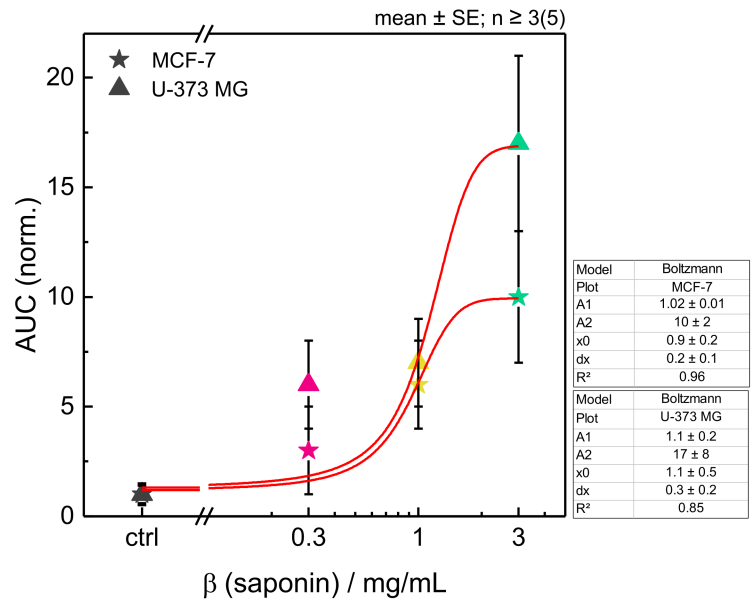

Fig. A-7.12 Dose-response curve of the normalized area under the curve values derived from the time course of diameter changes of MCF-7 as well as U-373 MG spheroids documented using the zenCELL owl digital microscope (Fig. 7.20). For integration, a baseline was set at 98 % (MCF-7; U-373 MG) of the normalized diameter and the values were determined within 24 hours after the addition of saponin solutions with different concentrations (ctrl | 0.3 | 1 | 3 mg/mL). After averaging, data sets were normalized to the control condition, mean ± SE, n ≥ 3(5). The results were fitted by sigmoidal Boltzmann equation and the respective EC_{50} value was determined.

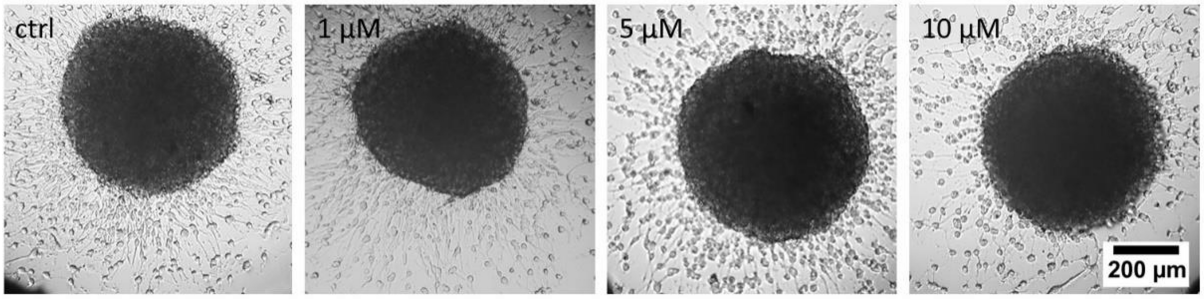

Fig. A-7.13 Micrographs of U-373 MG spheroids (7d, 18,000 c/well) that were exposed to cytochalasin D solution at different concentrations (ctrl | 1 | 5 | 10 µM) and documented 48 hours after the compound addition using the zenCELL owl digital microscope. Experiments were performed in a standard cell culture incubator at 37 °C and 0 % CO_2.

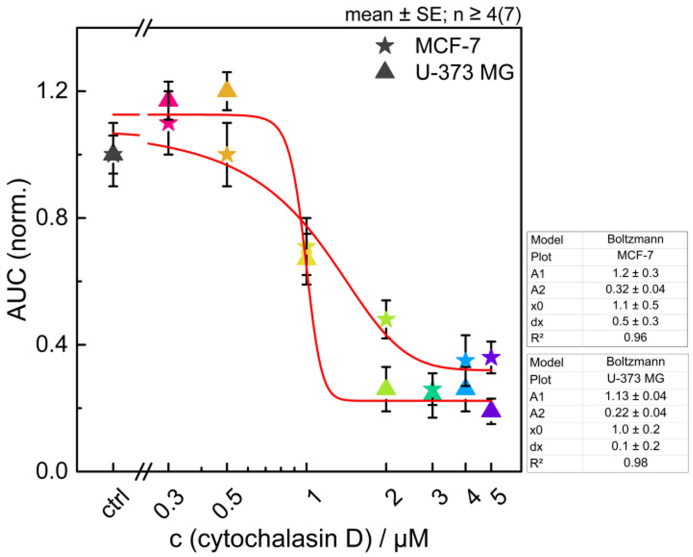

Fig. A-7.14 Dose-response curve of the normalized area under the curve values derived from the time course of normalized impedance magnitude at 4,000 Hz of MCF-7 and U-373 MG cell monolayer culture (Fig. 7.33). For integration, a baseline was set at 55 % (MCF-7) respectively 74 % (U-373 MG) of the normalized impedance, and the values were determined within 12 hours after the addition of cytochalasin D solutions with different concentrations in a range of 0.3–5 µM. After averaging, data sets were normalized to the control condition, mean ± SE, n ≥ 4(7). The results were fitted by sigmoidal Boltzmann equation and the respective EC_{50} value was determined.

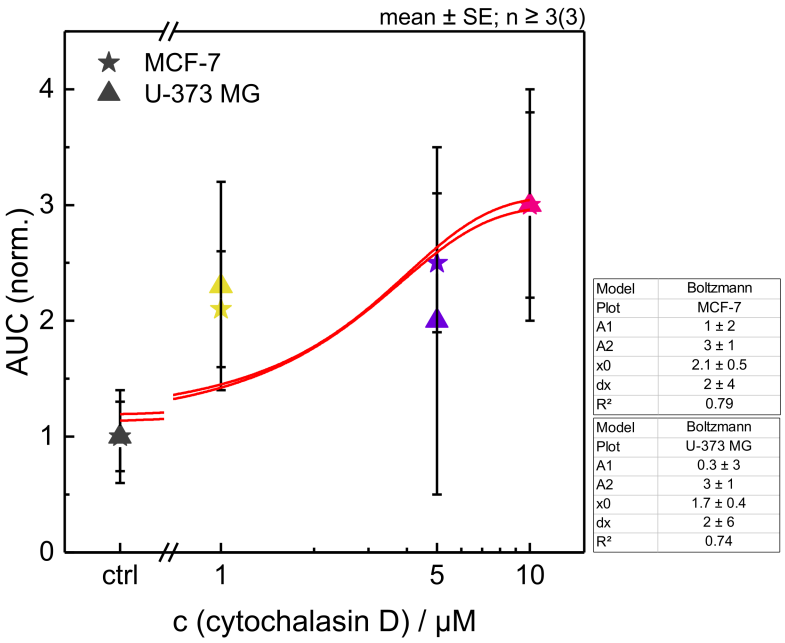

Fig. A-7.15 Dose-response curve of the normalized area under the curve values derived from the time course of diameter changes of MCF-7 as well as U-373 MG spheroids documented using the zenCELL owl digital microscope (Fig. 7.39). For integration, a baseline was set at 98 % (MCF-7; U-373 MG) of the normalized diameter, and the values were determined within 24 hours after the addition of cytochalasin D solutions with different concentrations (ctrl | 1 | 5 | 10 µM). After averaging, data sets were normalized to the control condition, mean ± SE, n ≥ 3(3). The results were fitted by sigmoidal Boltzmann equation and the respective EC_{50} value was determined.

Tab. A-7.3 Calculated values of R_{ext}, R_{int}, and A_{sph} reflecting the dielectric structure of U-373 MG spheroids as a function of different hyperosmotic buffer solutions (ctrl | 20 | 100 | 200 mM; 30,000 c/well). The values were determined by fitting each measured impedance spectrum 90 minutes after the addition of different hyperosmotic buffer solutions using a *LabVIEW™*-based software (written by J. Wegener, University of Regensburg) and the following parameter values: A_{el} = 12 (± 1) | 13 (± 1) | 11 (± 2) | 10 (± 4) ·10^{-6} $Fs^{n-1}cm^{-2}$; n_{el} = 0.811 (± 0.01) | 0.85 (± 0.01) | 0.89 (± 0.02) | 0.90 (± 0.01); R_{bulk} = 5,400 Ω; A_{para} = 2.4 ·10^{-10} $Fs^{n-1}cm^{-2}$; n_{para} = 0.9; n_{sph} = 0.75. Data sets were averaged after fitting, mean ± SE; see the table for the respective number of experiments.

	$concentration$ [mM]			
	ctrl	20	100	200
R_{ext} [kΩ]	36 ± 3	37 ± 5	36 ± 8	26 ± 2
R_{int} [kΩ]	8.0 ± 0.5	8.3 ± 0.4	7.3 ± 0.7	7 ± 3
A_{sph} [10^{-9} $Fs^{n-1}cm^{-2}$]	9.1 ± 0.6	10 ± 2	10 ± 2	18 ± 9
n	4(4)	4(4)	4(4)	3(3)

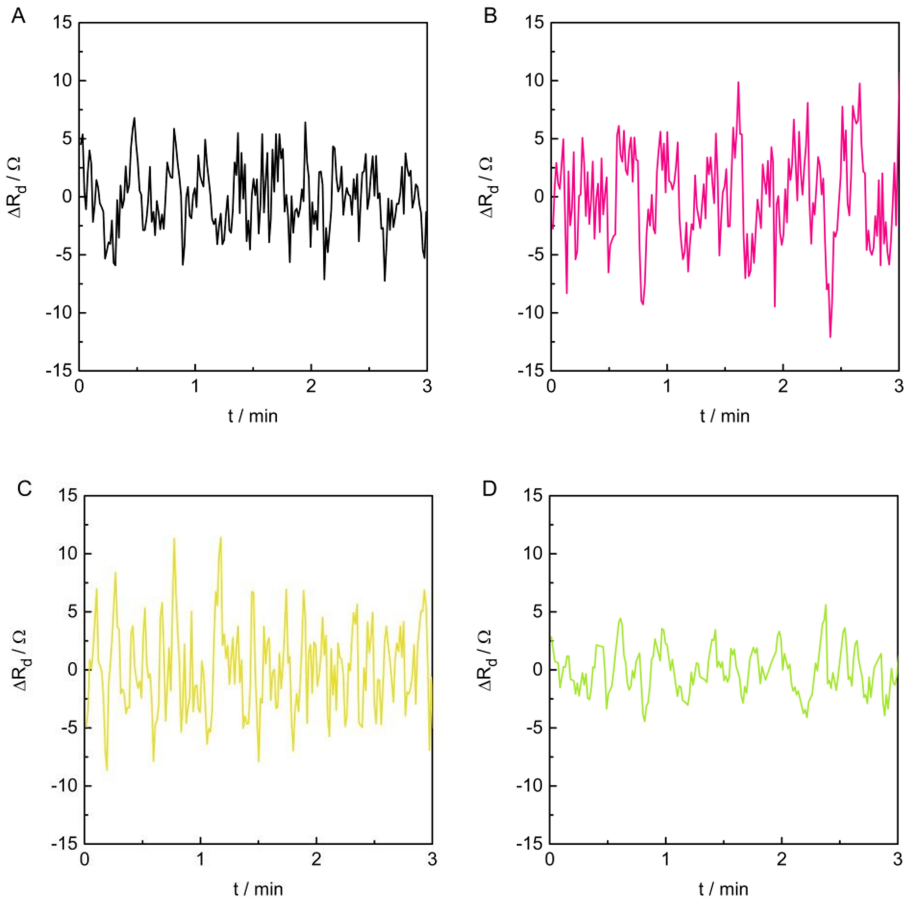

Fig. A-7.16 Detrended RTC data at 200 Hz measured 90 minutes after the addition of different hyperosmotic buffer solutions ctrl (A), 20 (B), 100 (C), 200 (D) mM to U-373 MG spheroids. Experiments were performed in a standard cell culture incubator at 37 °C and 0 % CO_2.

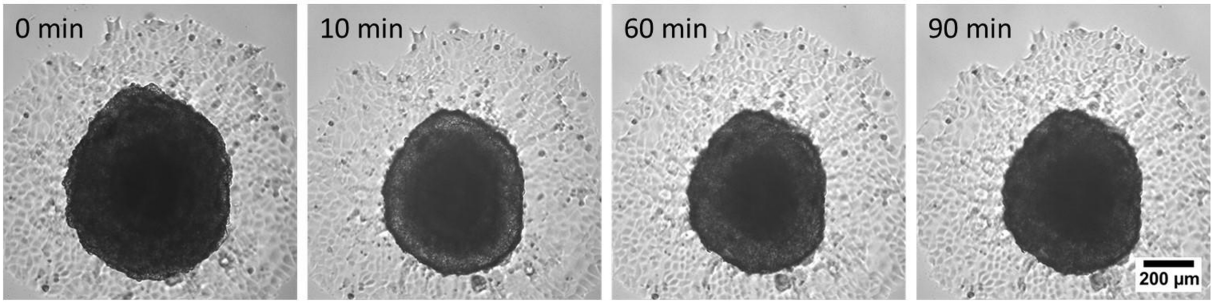

Fig. A-7.17 Time-resolved micrographs of the spheroid response to osmotic pressure after the addition of hyperosmotic buffer solution with a final sucrose concentration of 400 mM to MCF-7 spheroid (7 d, 4,000 c/well). Compound addition was performed at time point zero and the process was documented for 90 minutes using the zenCELL owl digital microscope. Experiment was performed in a standard cell culture incubator at 37 °C and 0 % CO_2.

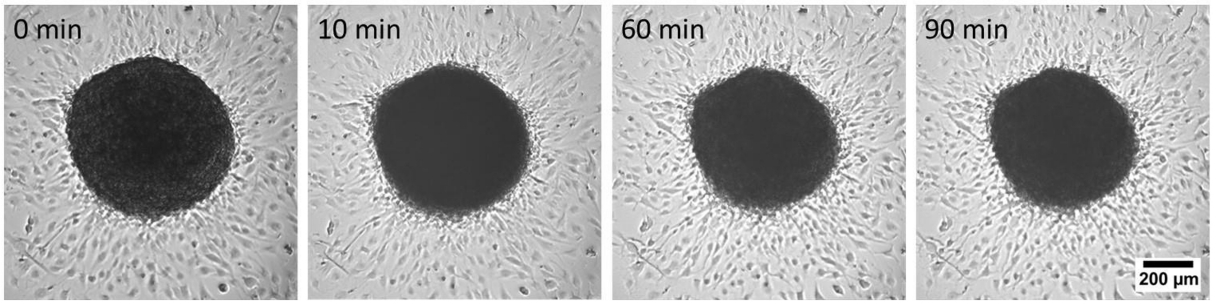

Fig. A-7.18 Time-resolved micrographs of the spheroid response to osmotic pressure after the addition of hyperosmotic buffer solution with a final sucrose concentration of 400 mM to U-373 MG spheroid (7 d, 18,000 c/well). Compound addition was performed at time point zero and the process was documented for 90 minutes using the zenCELL owl digital microscope. Experiment was performed in a standard cell culture incubator at 37 °C and 0 % CO_2.

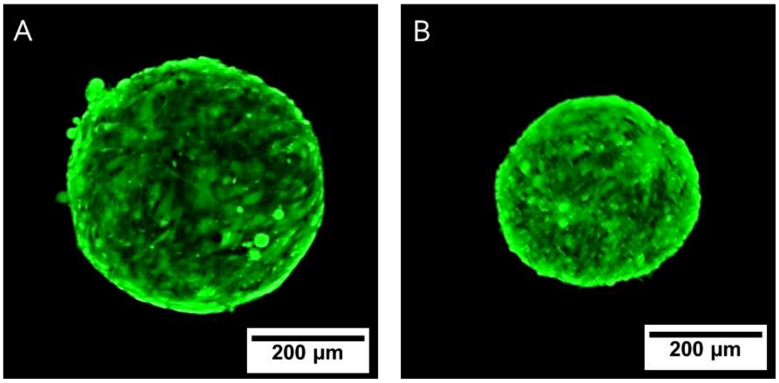

Fig. A-7.19 Proof-of-concept study addressing cell viability and morphology of spheroids affected by osmotic pressure. Confocal microscopy micrographs of U-373 MG spheroids two hours after the addition of either buffer solution as a control (A) or hyperosmotic buffer solution with a final sucrose solution of 1000 mM (B). For fluorescence microscopy, the spheroid body was prepared using the cell viability staining protocol for spheroids (see chapter 4.2.3). The cytosol of viable cells emits a green fluorescence and the cell nuclei of dead cells appear red after excitation of the applied probes As a result, the cell viability of the cells may not be apparently affected by the induced osmotic pressure, as shown by cell viability staining displaying green-fluorescent viable cells.

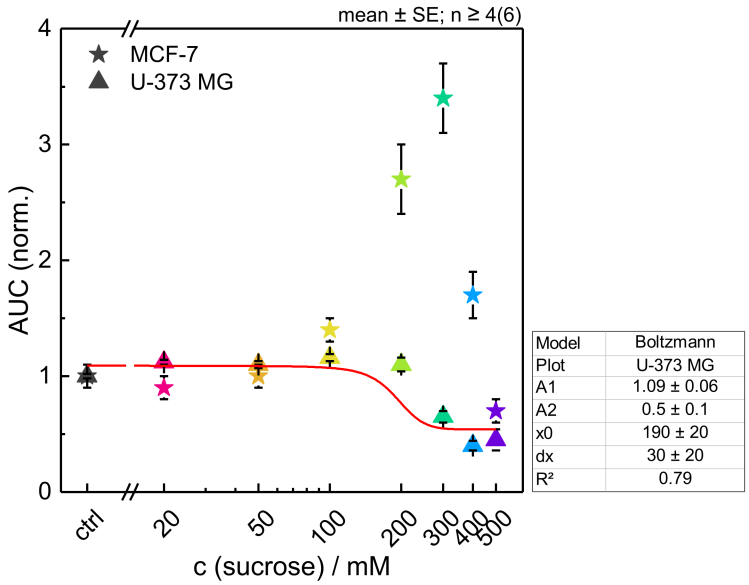

Fig. A-7.20 Dose-response curve of the normalized area under the curve values derived from the time course of normalized impedance magnitude at 4,000 Hz of MCF-7 and U-373 MG cell monolayer culture (Fig. 7.42). For integration, a baseline was set at 85 % (MCF-7; U-373 MG) of the normalized impedance, and the values were determined within 90 minutes after the addition of hyperosmotic buffer solutions with different sucrose concentrations in a range of 20–500 mM. After averaging, data sets were normalized to the control condition, mean ± SE, n ≥ 4(6). The results were fitted by a sigmoidal Boltzmann equation and the respective EC_{50} value was determined for the U-373 MG cell monolayer, whereas no sigmoidal fit was possible for the MCF 7 cell results.

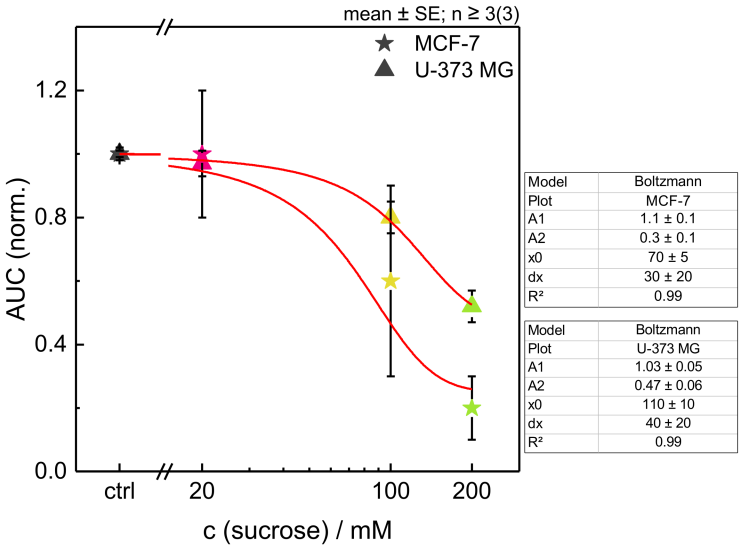

Fig. A-7.21 Dose-response curve of the normalized area under the curve values derived from the time course of normalized impedance magnitude at 200 Hz of MCF-7 and U-373 MG spheroids (Fig. 7.44). For integration, a baseline was set at 0 % (MCF-7; U-373 MG) of the normalized impedance, and the values were determined within 90 minutes after the addition of hyperosmotic buffer solutions with different final sucrose concentrations (ctrl | 20 | 100 | 200 mM). After averaging, data sets were normalized to the control condition, mean ± SE, n ≥ 3(3). The results were fitted by sigmoidal Boltzmann equation and the respective EC_{50} value was determined.

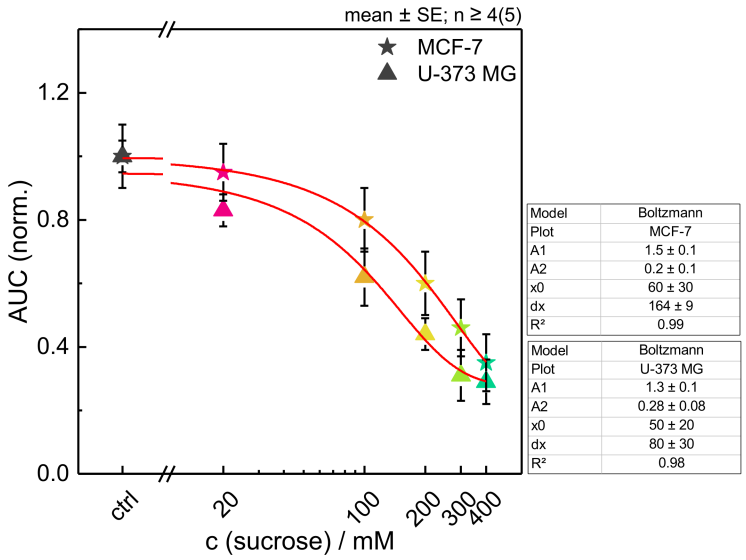

Fig. A-7.22 Dose-response curve of the normalized area under the curve values derived from the time course of diameter changes of MCF-7 as well as U-373 MG spheroids documented using the zenCELL owl digital microscope (Fig. 7.49). For integration, a baseline was set at 86 % (MCF-7; U-373 MG) of the normalized diameter, and the values were determined within 90 minutes after the addition of hyperosmotic buffer solutions with different sucrose concentrations in a range of 20–400 mM. After averaging, data sets were normalized to the control condition, mean ± SE, n ≥ 4(5). The results were fitted by sigmoidal Boltzmann equation and the respective EC_{50} value was determined.

11.2 LIST OF ABBREVIATIONS AND SYMBOLS

A

A	area, ampere, amplitude
AC	alternating current
ANOVA	analysis of variance
AUC	area under the curve

B

β	mass concentration

C

C	capacitor, capacitance
c	concentration
CaAM	calcein acetoxymethyl ester
CI	cytotoxicity index
CLSM	confocal laser scanning microscope
CPE	constant phase element
ctrl	control condition

D

d	diameter
DC	direct current
DMEM	Dulbecco's Modified Eagle's Medium
DMSO	dimethyl sulfoxide
DSMZ	Deutsche Sammlung von Mikroorganismen und Zellkulturen
Δ	difference

E

EC_{50}	half maximal effective concentration
ECIS™	electric cell-substrate impedance sensing
ECM	extracellular matrix
EDTA	ethylenediaminetetraacetic acid
EIS	electrochemical impedance spectroscopy
e.g.	(Lat.: *exempli gratia*) for example
Eq.	equation
et al.	(Lat.: *et alii*) and others
EthD-1	ethidium homodimer-1

F

F	Farad
f	frequency
FCS	fetal calf serum
Fig.	figure

G

g	gram, gravity
glc	glucose
GA	glutaraldehyde

H

H	Henry
h	height, hour
Hz	Hertz
HEPES	4-(2-hydroxyethyl)-1-piperazineethane-sulfonic acid

I

I	current
i	imaginary factor
Im	imaginary part
ITO	indium tin oxide

J

Φ	phase shift

L

L	liter, inductance
L-15	Leibovitz medium
λ	wavelength

M

M	molarity (mol/g), mega
m	milli, meter
min	minute
MFT	multiple-frequency/time
M_W	molecular weight
μ	micro

N

n	number of experiments
n.s.	non-significant

P

PBS^{--}	Dulbecco´s Phosphate Buffered Saline (without Ca^{2+} and Mg^{2+})
PBS^{++}	Dulbecco´s Phosphate Buffered Saline (with Ca^{2+} and Mg^{2+})
PFA	paraformaldehyde

R

R	resistor, resistance
R_{bulk}	bulk resistance

Re	real part
rpm	rounds per minute
RT	room temperature
RTC	rapid time collect

S

s	second
SD	standard deviation
SE	standard error
σ	Warburg impedance

T

t	time
Tab.	table

V

V	voltage
V_{32}	variance of increments (time interval of 32 s)

W

w/	with
w/o	without
Ω	Ohm

Z

Z	impedance
|Z|	impedance magnitude

Others

°	degree
°C	degree Celsius
%	percent
(v/v)	volume concentration
(w/v)	weight concentration
8W10E	ECIS™ array consisting of 8 wells with ten single electrodes in each well

11.3 MATERIALS AND INSTRUMENTATIONS

A	
agarose	Sigma-Aldrich Chemie GmbH, Munich, Germany
Alexa Fluor™ 488 phalloidin	Invitrogen™, Thermo Fisher Scientific, Hanau, Germany
argon	Linde AG, Pullach, Germany
Argon Plasma Cleaner PDC 32G-2	Harrick Plasma Inc., Ithaca, USA
Aspiration System for Cell Culture	HLC Biotech, Bovenden
Autoclave DX-45	Systec GmbH & Co. KG, Wettenberg, Germany
B	
bovine serum albumin (BSA)	Sigma-Aldrich Chemie GmbH, Munich, Germany
bunsen burner for cell culture	IBS Tecnomara GmbH, Fernwald, Germany
butane/propane camping gas	Cavagna Group S.p.A., Viadana di Calvasano (I)
C	
carbolfuchsin	Sigma-Aldrich Chemie GmbH, Munich, Germany
carbon dioxid	Linde AG, Pullach, Germany
cell culture flasks (25 cm^2, 75 cm^2)	Sarstedt AG & Co. KG, Nümbrecht, Germany
cell culture incubator	Thermo Fisher Scientific, Hanau, Germany
cell culture medium (MEM Eagle)	Sigma-Aldrich Chemie GmbH, Munich, Germany
cell culture Petri dishes (d = 9 cm)	Sarstedt AG & Co. KG, Nümbrecht, Germany
cell culture plate (96-well)	Sarstedt AG & Co. KG, Nümbrecht, Germany
cell culture plate (24-well)	Eppendorf SE, Hamburg, Germany
cell line MCF-7	Prof. Göpferich, Department of Pharmaceutical Technology; University of Regensburg, Germany
cell line U373-MG	Prof. Buschauer, Department of Pharmaceutical/Medicinal Chemistry; University of Regensburg, Germany
centrifuge Heraeus Multifuge 1 S-R	Thermo Fisher Scientific, Hanau, Germany
centrifuge tube (15 mL, 50 mL)	Greiner Bio-One GmbH, Frickenhausen
cover slip (d = 15 mm)	Paul Marienfeld GmbH & Co. KG, Lauda-Königshofen, Germany
conductivity meter inoLab Multi 720	WTW Weilheim, Weilheim, Germany
CryoBox™ (Nalgene®)	Sigma-Aldrich Chemie GmbH, Munich, Germany
cryovial	Techno Plastic Products AG (TPP), Trasadingen, Switzerland
cytochalasin D	Sigma-Aldrich Chemie GmbH, Munich, Germany
L-cystein	Sigma-Aldrich Chemie GmbH, Munich, Germany
D	
dimethyl sulfoxide	Carl Roth GmbH & Co. KG, Karlsruhe, Germany
E	
ECIS™ Impedance Analyzer	Applied BioPhysics Inc., Troy, USA
ECIS™ Trans Filter Adapter device	Applied BioPhysics Inc., Troy, USA
EDTA	Sigma-Aldrich Chemie GmbH, Munich, Germany
Electrode Arrays (8W10E)	Applied BioPhysics Inc., Troy, USA
Elma Clean 10	Elma Schmidbauer GmbH, Singen, Germany
ethanol	Merck KGaA, Darmstadt, Germany

F

fetal calf serum	Sigma-Aldrich Chemie GmbH, Munich, Germany
fetal calf serum for MCF-7 cell culture	Biochrom AG, Berlin, Germany
fibronectin from human plasma	Sigma-Aldrich Chemie GmbH, Munich, Germany

G

D-Glucose	Merck KGaA, Darmstadt, Germany
gelatine	Sigma-Aldrich Chemie GmbH, Munich, Germany
glass pipettes	VWR International GmbH, Ismaning, Germany
D-Glucose	Merck KGaA, Darmstadt, Germany
L-Glutamine	Biochrom KG, Berlin, Germany
glutaraldehyde	Sigma-Aldrich Chemie GmbH, Munich, Germany

H

4-(2-hydroxyethyl)-1-piperazineethane-sulfonic acid (HEPES)	Carl Roth GmbH & Co. KG, Karlsruhe, Germany
hemocytometer (Bürker)	Paul Marienfeld GmbH & Co. KG, Lauda-Königshofen, Germany

I

Impedance Analyzer SI-1260	Solartron Instruments, Farnborough, UK
indium tin oxide coated polyethylene terephthalate foils	Sigma-Aldrich Chemie GmbH, Munich, Germany
isopropanol	Merck KGaA, Darmstadt, Germany

L

laminar air flow work bench HERAsafe®	Thermo Fisher Scientific, Hanau, Germany
latex gloves	VWR International GmbH, Ismaning, Germany
Leibovitz Medium	Sigma-Aldrich Chemie GmbH, Munich, Germany
liquid nitrogen tank GC-BR2150 M	Jutta Ohst german-cryo GmbH, Jüchen, Germany
LIVE/DEAD™ Viability/Cytotoxicity Kit	Invitrogen™, Thermo Fisher Scientific, Hanau, Germany

M

measurement setup flow channel-based	ibidi GmbH, Gräfelfing, Germany
measurement setup funnel-based	Feinmechanik-Werkstatt, University of Regensburg, Germany
microscope Digital USB	Shenzhen Supereyes Technology Co. Ltd, Guangdong, China
microplate Reader GENios™	Tecan Group Ltd., Männedorf, Switzerland
microscope Nikon Diaphot	Nikon Instruments Inc., Melville, USA
microscope Nikon Eclipse 90i	Nikon Instruments Inc., Melville, USA
microscope Nikon SMZ 1500 C-DXD230 CMO	Nikon Instruments Inc., Melville, USA
microscope zenCELL owl	innoME GmbH, Espelkamp, Germany
Minimum Essential Medium Eagle	Sigma-Aldrich Chemie GmbH, Munich, Germany

N

Nalgene® CryoBox™	Sigma-Aldrich Chemie GmbH, Munich, Germany
nitrogene	Linde AG, Pullach, Germany

O

Orbital shaker KM-2 AKKU	Edmund Bühler GmbH, Bodelshausen, Germany
osmometer Osmomat™ 030	Gonotec Meß- und Regeltechnik GmbH, Berlin, Germany

P

Parafilm®	Pechiney Plastic Packaging, Chicago, USA
paraformaldehyde	Sigma-Aldrich Chemie GmbH, Munich, Germany
Dulbecco´s phosphate-buffered saline	Sigma-Aldrich Chemie GmbH, Munich, Germany
penicillin/streptomycin solution	Sigma-Aldrich Chemie GmbH, Munich, Germany
pipette Controller accu-jet® pro	Brand GmbH, Wertheim, Germany
pipettes (10 µL, 200 µL, 1000 µL)	Brand GmbH, Wertheim, Germany & Eppendorf AG, Hamburg, Germany
pipette tips (10 µL, 200 µL, 1000 µL)	Sarstedt AG & Co. KG, Nümbrecht, Germany
poly-L-Lysine Hydrobromide (M_W = 30000 – 70000 g/mol)	Sigma-Aldrich Chemie GmbH, Munich, Germany
positioning disks for zenCELL owl digital microscope	Feinmechanik-Werkstatt, University of Regensburg, Germany
PrestoBlue™ HS Cell Viability Reagent	Invitrogen™, Thermo Fisher Scientific, Hanau, Germany

R

reaction tubes (500 µL – 2 mL)	Sarstedt AG & Co. KG, Nümbrecht, Germany
Relay	Elektronik-Werkstatt, University of Regensburg, Germany

S

saponin	Sigma-Aldrich Chemie GmbH, Munich, Germany
serological pipettes (5 mL, 10 mL, 25 mL)	Greiner Bio-One GmbH, Frickenhausen
silicon glue Aquadicht PROBAU	Bauhaus, Regensburg, Germany
sodium chloride	Merck KGaA, Darmstadt, Germany
sodium dihydrogen phosphate	Sigma-Aldrich Chemie GmbH, Munich, Germany
sodium sulfite	Merck KGaA, Darmstadt, Germany
Sputter Coater Bal-Tec SCD 050	Capovani Brothers Inc., Scotia, USA
sterile filter (pore diameter 0.2 µm)	Techno Plastic Products AG (TPP), Trasadingen, Switzerland
Sylgard® 182 Silicone Elastomer Kit	Dow Corning, Midland, USA
software ECIS	Applied BioPhysics Inc., Troy, USA
software *EZ-C1*	Nikon Instruments Inc., Melville, USA
software *ImageJ*	Rasband, W.S., National Institutes of Health, Maryland, USA
software *LabVIEW™ software*	National Instruments™, Austin, USA
software *supereyes 3.54*	Shenzhen Supereyes Technology Co. Ltd, Guangdong, China
software *zencell-owl v2.0*	innoME GmbH, Espelkamp, Germany

T

Triton™ X-100	Sigma-Aldrich Chemie GmbH, Munich, Germany
trypsin 0.05 % (w/v), 0.25 % (w/v)	Sigma-Aldrich Chemie GmbH, Munich, Germany

U

Ultrasonic Bath Sonorex Digitec	Bandelin Electronics GmbH & Co. KG, Berlin, Germany

V

Vortex Mixer	Heidolph Elektro GmbH & Co. KG, Kelheim, Germany

W

water bath TW12	Julabo GmbH, Seelbach, Germany
Weighting Instrument PL1200	Mettler-Toledo GmbH, Gießen, Germany

DANKSAGUNG

Hiermit möchte ich mich ganz herzlich bei allen Menschen bedanken, die mich während meiner Doktorarbeit unterstützt haben und mir mit Rat und Tat zur Seite gestanden sind!

An erster Stelle möchte ich mich bei Prof. Dr. Joachim Wegener bedanken, der es mir ermöglicht hat dieses Promotionsthema zu bearbeiten. Vielen Dank für die Aufnahme in die AG Wegener und Deine fachliche Unterstützung.

Ich möchte mich ebenfalls bei Herrn Prof. Dr. Göpferich für die freundliche Übernahme des Zweitgutachtens und bei Herrn Apl. Prof. Dr. Müller für die Übernahme des Amts als Drittprüfer bedanken. Vielen Dank, dass Sie sich Zeit für mich genommen haben.

Mein Dank gilt allen Mitgliedern und ehemaligen Mitstreitern der AG Wegener. Vielen Dank für die entspannte Arbeitsatmosphäre, den Mensa- bzw. Kaffeetratsch und die gemeinsamen Ausflüge. Ganz besonderer Dank gilt Dr. Stefanie Michaelis und Dr. Judith Stolwijk für Eure Unterstützung, Beratung und Euer stets offenes Ohr!

Ein großes Dankeschön und Lob gehen an die Glasbläserei, Elektronik- und Feinmechanik-Werkstatt der Universität Regensburg für die Unterstützung zur Umsetzung meiner Ideen. Besonders bedanken möchte ich mich bei Matthias Kainz, denn Dein Engagement und Perfektionismus haben maßgeblich zur Entwicklung des ersten Prototyps bis hin zur Vervielfältigung des finalen Trichterlayouts beigetragen!

Vielen herzlichen Dank an all meine Arbeitskollegen bei Labor Kneißler, vor allem an das Prüfleitung IA/Chemie-Team, für Eure Unterstützung und die Verpflegung mit immer ausreichend Kaffee und Kuchen. Mein besonderer Dank gilt Dr. Nicole Meißner für das Verständnis, Felix Kaltenhäuser für die Vertretungen und Dr. Thomas Hofmann sowie Anke Gettinger für die steten Aufmunterungen!

Ein herzliches Dankeschön geht an meine Familie und meine Freunde für Eure Ermutigungen und Euer Verständnis. Vielen lieben Dank an meine Eltern für den Rückhalt, Euren Glauben an mich und dafür, dass ihr mir das Studium überhaupt ermöglicht und bis zum Schluss mitgefiebert habt. Mein größter Dank gilt meinem Mann Markus für Deine bedingungslose Unterstützung während der gesamten Studienzeit – ohne Dich wäre diese Arbeit niemals angefangen, geschweige denn abgeschlossen worden!

CURRICULUM VITAE



PERSONAL INFORMATION

Name	Simone Bäumler
Maiden Name	Ruckdäschel
Date of Birth	September 15th 1992
Place of Birth	Weiden i. d. Opf., Germany
Nationality	German

UNIVERSITY STUDIES AND SCHOOL EDUCATION

since 10/2017	PhD thesis (Dr. rer. nat.) in Chemistry, University of Regensburg Institute of Analytical Chemistry, Chemo- und Biosensors, Prof. Dr. J. Wegener *"A Novel Measurement Setup for Impedance-Based Analysis of 3D Tissue Models: Design, Characterization and Application"*
10/2014 - 09/2016	Master of Science in Chemistry, University of Regensburg Institute of Analytical Chemistry, Chemo- und Biosensors, Prof. Dr. J. Wegener *"Mikrogravimetrie: Beiträge zum Verständnis der Signalentstehung".*
10/2011 – 10/2014	Bachelor of Science in Chemistry, University of Regensburg, Institute of Analytical Chemistry, Chemo- und Biosensors, Prof. Dr. J. Wegener *"Mikrogravimetrische Ganz-Zell-Sensoren: Beiträge zum Verständnis der Signalentstehung".*
07/2011	University Entrance Diploma (Abitur) Gymnasium Neustadt, Neustadt a. d. Waldnaab

EIDESSTATTLICHE ERKLÄRUNG

Ich erkläre hiermit an Eides statt, dass ich die vorliegende Arbeit ohne unzulässige Hilfe Dritter und ohne Benutzung anderer als der angegebenen Hilfsmittel angefertigt habe; die aus anderen Quellen direkt oder indirekt übernommenen Daten und Konzepte sind unter Angabe des Literaturzitats gekennzeichnet.

Weitere Personen waren an der inhaltlich-materiellen Herstellung der vorliegenden Arbeit nicht beteiligt. Insbesondere habe ich hierfür nicht die entgeltliche Hilfe eines Promotionsberaters oder anderer Personen in Anspruch genommen. Niemand hat von mir weder unmittelbar noch mittelbar geldwerte Leistungen für Arbeiten erhalten, die im Zusammenhang mit dem Inhalt der vorgelegten Dissertation stehen.

Die Arbeit wurde bisher weder im In- noch im Ausland in gleicher oder ähnlicher Form einer anderen Prüfungsbehörde vorgelegt.

Ich versichere an Eides statt, dass ich nach bestem Wissen die reine Wahrheit gesagt und nichts verschwiegen habe.

Regensburg, den

Ort, Datum

Simone Bäumler